



HAL
open science

Thermal and structural performance energy tunnels

Alessandra Insana

► **To cite this version:**

Alessandra Insana. Thermal and structural performance energy tunnels. Thermics [physics.class-ph]. Université Paris-Est; Politecnico di Torino, 2020. English. NNT : 2020PESC2058 . tel-03245445

HAL Id: tel-03245445

<https://theses.hal.science/tel-03245445v1>

Submitted on 1 Jun 2021

HAL is a multi-disciplinary open access archive for the deposit and dissemination of scientific research documents, whether they are published or not. The documents may come from teaching and research institutions in France or abroad, or from public or private research centers.

L'archive ouverte pluridisciplinaire **HAL**, est destinée au dépôt et à la diffusion de documents scientifiques de niveau recherche, publiés ou non, émanant des établissements d'enseignement et de recherche français ou étrangers, des laboratoires publics ou privés.



ScuDo
Scuola di Dottorato ~ Doctoral School
WHAT YOU ARE, TAKES YOU FAR



Doctoral Dissertation
Doctoral Program in Civil and Environmental Engineering (32nd Cycle)

Thermal and Structural Performance of Energy Tunnels

Alessandra Insana

Supervisor

Prof. Marco Barla

Co-supervisor

Prof. Jean Sulem

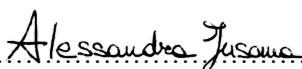
Doctoral Examination Committee:

Prof. Stefano Aversa, Università di Napoli Parthenope
Dr. Sébastien Burlon, Referee, Terrasol, Paris
Prof. Hussein Mroueh, Université de Lille
Prof. Iulia Prodan, Technical University of Cluj-Napoca
Prof. Donatella Sterpi, Referee, Politecnico di Milano

Politecnico di Torino
June 25, 2020

This thesis is licensed under a Creative Commons License, Attribution - Noncommercial - NoDerivative Works 4.0 International: see www.creativecommons.org. The text may be reproduced for non-commercial purposes, provided that credit is given to the original author.

I hereby declare that, the contents and organisation of this dissertation constitute my own original work and does not compromise in any way the rights of third parties, including those relating to the security of personal data.


.....

Alessandra Insana
Turin, June 25, 2020

Abstract

The present era embodies a critical decision point for mankind who has to reckon with the negative impacts of past energy choices. To make a shift and to shape the future of energy, a move towards carbon-free and renewable resources has to be boosted. In this framework geothermal energy is a key inspiring actor that has seen innovative, effective technological developments in recent years to capture the Earth's heat buried at shallow depths, among which energy geostructures are noteworthy. Turning a geostructure, i.e. foundations, tunnel linings, walls, into a heat extraction and storage system, notwithstanding, puts forward unmatched challenges and unsolved questions related to the effects emerging from this original new role.

This Doctoral Thesis focuses on the investigation of a dual-purpose technology that couples the roles for the structural support and energy supply, i.e. energy tunnels, with a major interest on thermal and structural performance. Energy tunnels involve the coexistence of both mechanical and thermal loads, that cause seasonally cyclic alterations of temperature, solicitation and deformation patterns within the surrounding ground and the lining itself that should be accounted for during analysis and design. The additional thermal loading being the essence of all energy geostructures, under any circumstances can the necessary structural stability of the tunnel lining be jeopardized.

Despite prior to this work a substantial amount of research had been made available to address the energy and structural performance of energy piles and walls, little or even no guidance has been proposed to advise in the design of energy tunnels. Limited knowledge, if available, was present to address the energy linings behaviour and performance under thermal loads.

To address such challenges, this research is focused on the experimental and numerical investigation of energy tunnel linings over typical timescales of practical applications, and on the formulation of a comprehensive procedural outline to be used in performance-based design practice. The objective of this Thesis is to identify, quantify and analyse the principal aspects that are involved in the design, construction and performance of energy tunnels as against traditional tunnels.

Following the introduction of the most recent advances, mostly based on contributions related to technological aspects and thermal performance, with plenty of numerical explorations and very rare experimental studies, the research examines the basic principles of tunnel linings design to pave the way for the ensuing extension to energy tunnel linings. The bibliographic study highlights that significant contributions were given in the field of thermo-mechanical behaviour of soils.

The acknowledgement of a gap in the full understanding of energy tunnels thermal-based and structural-based performance led to the setup of a new full-scale experimental prototype that represents the first Italian attempt to show the maturity of a still unfamiliar technology. The chance offered by the tunnel of Turin Metro Line 1 South Extension under construction was taken to put in practice the novel Enertun concept defining a new layout of the networks of geothermal pipes. The design stages and construction details have been presented to show the relatively simple implementation of the primary and secondary circuits. The monitoring plan has been described with the intent to characterize the response in terms of additional thermally induced mechanical effects when subjected to thermal loading in the range between 0 and 35 °C. Indeed, an experimental program has been performed, involving tests able to mimic the real operation of the closed loop system, recovery time-lags and natural trends in absence of any external forcing. Particular attention has been posed on the quantification of thermally induced stresses and strains, as well as temperature within the lining and at the circuit inlet and outlet.

The knowledge acquired throughout the previous experimental campaign was included into a series of numerical analyses performed on a three-dimensional, coupled thermo-hydraulic numerical model that was first validated and then used to further generalize the results to different ground and environmental conditions, including the unstudied role of groundwater flow direction. The effect of the most important design parameters allowed to update existing parametric design charts and to develop a simple method for preliminary evaluation of the energy tunnels potential.

The last part of the Thesis allows one to draw some important conclusions on the structural design of energy tunnels. With the purpose of numerically reproducing the response experimentally observed, a thermo-elastic model was built and validated, to allow for a deeper understanding of the thermo-mechanical interactions. Hence, the interest is moved to the assessment of the structural effects of long-term operation of energy tunnels. This aspect is of great importance from the engineering point of view, which is why in the final part of the Thesis design verifications are performed and some practical recommendations for future designers enunciated. The results presented in this Thesis suggest the conclusion that, in the normal working conditions of current applications, (a) thermal loads do have a visible effect on the thermo-mechanical behaviour though (b) they do not seem to represent a serviceability nor an ultimate limit state problem in the conditions investigated, as internal actions are acceptable with respect to the norms in force. Hence (c) the thermo-mechanical behaviour and performance of energy tunnels is not critically threatened by thermal loads.

Keywords: energy tunnels, geothermal energy, thermo-hydraulic behaviour, thermo-mechanical behaviour, performance, soil-structure interaction, in situ testing, numerical modelling, performance-based design, design charts, thermo-elasticity.

Résumé

L'ère actuelle incarne un point de décision critique pour l'humanité qui doit rendre compte des impacts négatifs des choix énergétiques passés. Pour marquer un virage et façonner l'avenir de l'énergie, il faut accélérer la transition vers des ressources décarbonées et renouvelables. Dans ce cadre, la géothermie peut apporter une contribution majeure et a connu, ces dernières années, des développements technologiques innovants et efficaces pour capter la chaleur de la Terre enfouie à de faibles profondeurs, en particulier pour les géostructures énergétiques. Transformer une géostructure, c'est-à-dire des fondations, des revêtements de tunnel, des murs, en un système d'extraction et de stockage de chaleur, présente des défis inédits et des questions non résolues.

Cette thèse de doctorat se concentre sur la recherche d'une technologie à double usage qui couple les rôles de support structurel et d'approvisionnement énergétique, pour une application aux tunnels énergétiques, avec un intérêt particulier pour les performances thermiques et structurelles. Les tunnels énergétiques impliquent la coexistence de charges mécaniques et thermiques, qui provoquent des altérations cycliques saisonnières de la température, des sollicitations et des modes de déformation dans le sol environnant et dans le revêtement lui-même qui doivent être pris en compte lors de l'analyse et de la conception. La charge thermique supplémentaire étant l'essence de toutes les géostructures énergétiques, la stabilité structurelle nécessaire du revêtement du tunnel ne peut en aucun cas être compromise.

Un nombre important de travaux de recherche ont déjà porté sur la performance énergétique et structurelle des pieux et des murs énergétiques, mais peu ou même aucune orientation n'a été proposée pour guider la conception des tunnels énergétiques. Des connaissances limitées, le cas échéant, étaient disponibles pour traiter le comportement et les performances des revêtements énergétiques sous des charges thermiques.

Pour relever ces défis, cette recherche est axée sur l'étude expérimentale et numérique des revêtements de tunnels énergétiques sur des échelles de temps typiques des applications pratiques, et sur la formulation d'un schéma procédural complet à utiliser en pratique dans la conception. L'objectif de cette thèse est d'identifier, de quantifier et d'analyser les principaux aspects impliqués dans la conception, la construction et la performance des tunnels énergétiques par rapport aux tunnels traditionnels.

Après l'introduction des avancées les plus récentes, principalement basées sur des contributions liées aux aspects technologiques et aux performances thermiques, avec de nombreuses explorations numériques et quelques rares études expérimentales, ce travail examine les principes de base de la conception des revêtements de tunnels et leur extension aux revêtements de tunnel énergétiques. L'étude bibliographique souligne les contributions importantes apportées dans le domaine du comportement thermo-mécanique des sols.

La reconnaissance d'une lacune dans la compréhension complète des performances thermiques et structurelles des tunnels énergétiques a conduit à la mise en place d'un nouveau prototype expérimental à grande échelle qui représente la première tentative italienne de montrer la maturité d'une technologie encore inconnue. L'occasion offerte par le tunnel de Turin Métro Ligne 1 Extension Sud en construction a été saisie pour mettre en pratique le nouveau concept Enertun définissant un nouveau tracé des réseaux de tuyaux géothermiques. Les étapes de conception et les détails de construction ont été présentés pour montrer la mise en œuvre relativement simple des circuits primaire et secondaire. Le plan de surveillance a été décrit avec l'intention de caractériser la réponse en termes d'effets mécaniques supplémentaires induits thermiquement lorsque des charges thermiques comprises entre 0 et 35°C sont appliquées. En effet, un programme expérimental a été réalisé, impliquant des tests capables de simuler le fonctionnement réel du système en boucle fermée, les délais de récupération et les tendances naturelles en l'absence de tout forçage externe. Une attention particulière a été portée à la quantification des contraintes et déformations induites thermiquement, ainsi qu'à la température à l'intérieur du revêtement et à l'entrée et à la sortie du circuit.

Les connaissances acquises tout au long de cette campagne expérimentale ont été incluses dans une série d'analyses numériques effectuées sur un modèle thermo-hydraulique couplé tridimensionnel qui a d'abord été validé puis utilisé pour généraliser les résultats à des conditions différentes du terrain et de l'environnement, y compris le rôle de la direction de l'écoulement de la nappe. L'analyse de l'effet des paramètres de conception les plus importants a permis de mettre à jour les courbes de calcul paramétrique existantes et de développer une méthode simple pour l'évaluation préliminaire du potentiel des tunnels énergétiques.

La dernière partie de la thèse permet de tirer des conclusions importantes sur la conception structurelle des tunnels énergétiques. Dans le but de reproduire numériquement la réponse observée expérimentalement, un modèle thermo-élastique a été construit et validé, pour permettre une meilleure compréhension des interactions thermo-mécaniques. Par conséquent, l'intérêt est porté à l'évaluation des effets structurels de l'exploitation à long terme des tunnels énergétiques. Cet aspect est d'une grande importance du point de vue de l'ingénierie, c'est pourquoi dans la dernière partie de la thèse, des vérifications de conception sont effectuées et quelques recommandations pratiques pour les futurs concepteurs sont énoncées. Les résultats présentés dans cette thèse suggèrent la conclusion que, dans les conditions normales des applications actuelles, (a) les charges thermiques ont un effet visible sur la réponse thermo-mécanique de la structure bien que (b) elles ne semblent pas représenter un problème d'état limite ultime ou de service dans les conditions étudiées, car les actions internes sont acceptables par rapport aux normes en vigueur. Par conséquent, (c) le comportement et les performances thermomécaniques des tunnels énergétiques ne sont pas menacés de manière critique par les charges thermiques.

Mots-clés: tunnels énergétiques, géothermie, comportement thermo-hydraulique, comportement thermo-mécanique, performance, interaction sol-structure, essais in situ, modélisation numérique, conception basée sur les performances, courbes de calcul, thermo-élasticité.

Sommario

L'epoca attuale incarna un punto di decisione critico per l'umanità che deve fare i conti con gli impatti negativi delle scelte energetiche passate. Per attuare un cambiamento e plasmare il futuro del panorama energetico, è necessario potenziare l'utilizzo di risorse rinnovabili tali da non comportare emissioni di anidride carbonica. In questo contesto, l'energia geotermica è un attore chiave che negli ultimi anni ha visto sviluppi tecnologici innovativi ed efficaci per catturare il calore a basse profondità, tra i quali le geostrutture energetiche sono degne di nota. Trasformare una geostruttura, come ad esempio fondazioni, rivestimenti di gallerie, muri, in un sistema di estrazione e immagazzinamento del calore, tuttavia, pone sfide senza precedenti e domande irrisolte relative agli effetti che emergono da questo nuovo ruolo.

Questa tesi di dottorato si concentra sull'indagine di una tecnologia caratterizzata da una duplice funzione, in quanto abbina i ruoli per il supporto strutturale e la fornitura di energia, per un'applicazione alle gallerie energetiche, con un'attenzione rivolta in particolare alle prestazioni termiche e strutturali. Le gallerie energetiche implicano la coesistenza di carichi meccanici e termici, che causano alterazioni cicliche stagionali della temperatura, delle sollecitazioni e delle deformazioni nel terreno circostante e nel rivestimento stesso che dovrebbero essere presi in considerazione durante l'analisi e la progettazione. Dal momento che il carico termico addizionale è l'essenza di tutte le geostrutture energetiche, la stabilità strutturale del rivestimento della galleria non deve, in nessuna circostanza, essere messa a repentaglio.

Nonostante prima di questo lavoro fossero state messe a disposizione numerose ricerche per affrontare il comportamento energetico e strutturale di pali e pareti energetiche, pochissime o addirittura nessuna indicazione è stata fornita per guidare la progettazione di gallerie energetiche. Scarse conoscenze, ove disponibili, erano dunque presenti in merito al comportamento dei rivestimenti energetici e alle prestazioni sotto carichi termici.

Per affrontare tali sfide, questa ricerca si concentra sullo studio sperimentale e numerico del rivestimento di gallerie energetiche su scale temporali tipiche di applicazioni pratiche e sulla formulazione di una struttura procedurale completa da utilizzare nella pratica di progettazione. L'obiettivo di questa tesi è quello di identificare, quantificare e analizzare i principali aspetti coinvolti nella progettazione, costruzione e comportamento di gallerie energetiche rispetto a gallerie tradizionali.

Dopo aver introdotto i più recenti sviluppi, basati principalmente su contributi relativi agli aspetti tecnologici e alle prestazioni termiche, con numerose esplorazioni numeriche e studi sperimentali molto rari, la ricerca esamina i principi di base della progettazione dei rivestimenti delle gallerie per spianare la strada alla successiva estensione ai rivestimenti di gallerie

energetiche. Lo studio bibliografico evidenzia contributi significativi nel campo del comportamento termo-meccanico dei terreni.

Le evidenti lacune nella comprensione delle prestazioni energetiche e strutturali delle gallerie energetiche hanno portato all'installazione di un nuovo prototipo sperimentale a scala reale che rappresenta il primo tentativo italiano di mostrare la maturità di una tecnologia ancora poco nota. L'opportunità offerta dalla galleria dell'Estensione Sud della Linea 1 della Metropolitana di Torino in fase di costruzione è stata colta per mettere in pratica il nuovo concetto Enertun che definisce un nuovo layout della rete di serpentine geotermiche. Le fasi di progettazione e i dettagli di costruzione sono stati presentati per mostrare l'implementazione relativamente semplice dei circuiti primario e secondario. Il piano di monitoraggio è stato descritto con l'intento di caratterizzare la risposta in termini di ulteriori effetti meccanici indotti termicamente in presenza di carichi termici nell'intervallo tra 0 e 35 ° C. Si è portato a termine un programma sperimentale, che ha incluso test in grado di simulare il funzionamento reale del sistema a circuito chiuso, le fasi di recupero termico e i trend naturali in assenza di forzanti esterne. Particolare attenzione è stata rivolta alla quantificazione di sollecitazioni e tensioni indotte termicamente, nonché sulla temperatura all'interno del rivestimento e all'ingresso e all'uscita del circuito.

Le conoscenze acquisite durante la suddetta campagna sperimentale si sono rivelate utili per una serie di analisi numeriche eseguite su un modello termoidraulico accoppiato tridimensionale che è stato prima validato e poi utilizzato per generalizzare ulteriormente i risultati a diverse condizioni geologiche e ambientali, incluso il ruolo non indagato in letteratura della direzione del flusso dell'acqua di falda. L'effetto dei parametri di progettazione più rilevanti ha permesso di aggiornare i design charts parametrici già esistenti e di sviluppare un metodo semplice per la valutazione preliminare del potenziale delle gallerie energetiche.

L'ultima parte della tesi ha consentito di trarre alcune importanti conclusioni sulla progettazione strutturale delle gallerie energetiche. Allo scopo di riprodurre numericamente la risposta osservata sperimentalmente, è stato costruito e validato un modello termo-elastico, per consentire una comprensione più dettagliata delle interazioni termo-meccaniche. L'interesse è stato dunque rivolto alla valutazione degli effetti strutturali del funzionamento a lungo termine delle gallerie energetiche. Questo aspetto è di grande importanza dal punto di vista ingegneristico, motivo per il quale nella parte finale della tesi vengono eseguite le verifiche di progetto e vengono enunciate alcune raccomandazioni pratiche rivolte ai futuri progettisti. I risultati presentati in questa tesi ventilano la conclusione che, nelle normali condizioni di lavoro delle attuali applicazioni, (a) i carichi termici hanno un effetto visibile sul comportamento termo-meccanico sebbene (b) non sembrino rappresentare un problema né a stato limite ultimo né a stato limite di esercizio nelle condizioni investigate, poiché le azioni interne sono accettabili rispetto alle norme in vigore. Pertanto (c) il comportamento termo-meccanico e le prestazioni delle gallerie energetiche non risultano criticamente minacciati dalle azioni termiche indotte dalla loro attivazione energetica.

Parole chiave: gallerie energetiche, energia geotermica, comportamento termo-idraulico, comportamento termo-meccanico, prestazioni, interazione terreno-struttura, prove in situ, modellazione numerica, progettazione basata sulle prestazioni, grafici di progetto, termo-elasticità.

Acknowledgments

First and foremost, I want to thank my advisor Professor Marco Barla who offered me the opportunity to work on a theme that I loved right away and that was an irreplaceable point of reference for completing it. He has taught me, both consciously and unconsciously, to be joyful and enthusiastic even during tough times in the Ph.D. pursuit. I thank him for the encouragement and teachings of life that led me to take things with more irony and that profoundly changed me. Thanks also for the opportunity to experiment teaching experiences and to apply knowledge to almost unique real cases.

I wish to express my deep gratitude to my co-supervisor, Professor Jean Sulem, who has shown a great willingness to welcome me at the ENPC Laboratoire Navier. I am especially grateful for numerous remote conversations to reason together about the details of the work. I appreciate all his contributions of time and ideas. It has been an honor to work with him.

For this Dissertation I would like to thank the referees Prof. Donatella Sterpi and Dr. Sébastien Burlon for their thoughtful comments and efforts towards improving the manuscript, as well as Prof. Stefano Aversa, Prof. Hussein Mroueh and Prof. Iulia Prodan for agreeing to be my committee members, for their time and for discussing the work together.

Thanks also to the internal commission formed by Professors Luca Giordano and Claudio Scavia for validating the study each year with useful comments. Thanks to Professor Giordano also for the valuable advice during the quarantine time.

Thanks to Professor Alice Di Donna, with whom I shared the office for a year, for the fundamental role of guide in the development of the experimental field also as co-founder of the Enertun patent together with Professor Barla, and, last but not least, for the thousand laughs that could be heard several offices away.

The high interdisciplinary nature of the work has allowed me to meet many people from DISEG and other departments that I wish to thank for the mutual exchange of knowledge and for the good moments spent together: Prof. Marco Zerbinatti from DISEG, Dr. Riccardo Vesipa from DIATI, Prof. Guido Perrone, Prof. Alberto Vallan, Dr. Giuseppe Rizzelli and Prof. Roberto Gaudino from DET and PhotoNext Inter-Dipartimental Center for Photonic technologies, Prof. Alberto Poggio and Prof. Marco Simonetti from DENERG, together with Dr. Giulio Cerino, Dr. Stefano Fantucci and Federico Neirrotti. Special thanks go to Dr. Massimo Olivero from DET, always available to work with me in the field and, subsequently, to the interpretation of fiber optics data. His excellent hazelnuts are always very welcome.

I am willing to acknowledge the help of the large number of people and companies that, in different ways, contributed to accomplish the installation of the first prototype of energy tunnel in Italy. The site installation was the result of an agreement set by the Politecnico di Torino with InfraTo, the owner, and Consorzio Integra, the contractor, within a 'proof of

concept' project. In this respect, special thanks are devoted to Vanni Cappellato, Roberto Crova and Giovanni Currado (from InfraTo), Guido Bay and Lorenzo Fiorentino (from CMC). Particular thanks are also devoted to Stefania Di Giovanni (from CMC) for the hints and suggestions provided on technical issues and details. Specific contribution and expertise were provided by Generali Prefabbricati, where the Enertun segments were casted, by the contractor at the site, by suppliers (Arco Green Energy, Sisgeo) and by colleagues at the Politecnico. With the purpose of thanking all of them, an alphabetical list of the persons involved at various stages is given below.

Giovanni Anglani, Francesco Antolini, Luigia Arpone, Lorenzo Aversa, Emilio Avitabile, Matteo Baralis, Ivan Battolla, Ales Besednjac, Valentino Buldum, Alberto Buonamano, Manuel Carrara, Alessandra D'Elia, Silvio D'Elcio, Stefano Dellea, Stefania Di Giovanni, Paolo Fagioli, Gianni Finelli, Paolo Garavini, Roberto Gaudino, Claudia Gennaro, Giorgio Gianni, Maurizio Guerrini, Georgios Kalamaras, Agnes Lee, Luca Lessona, Eusebio Ligorio, Paolo Masserano, Elena Nava, Massimo Olivero, Jesus Alejandro Palomino, Andrea Palumbo, Paolo Pavinato, Guido Pecetti, Guido Perrone, Enrico Petelio, Pavel Quibus, Alessandro Reale, Damiano Rendina, Andrea Sanulli, Michele Schippa, Giovanni Tofani, Samuele Trento, Alberto Vallan, Fabrizio Zacco, Alessandro Zampieri.

In view of the permanent arrangement of the experimental plant, I would like to thank Eng. Emiliano Di Lorenzo, Eng. Matteo Zanini Astaldi and Gennaro Brigante (Sinergo), Eng. Carmine Cafaro (Pagano e Ascolillo), and Eng. Massimiliano Cudia, Luigi Guerino, Roberto Crova together with Paolo Pavinato (InfraTo), as well as Eng. Gian Piero Fantini and Fulvio Grinzato (GTT). Thanks also to Renzo Pallara and Giampiero Bianchi from DISEG for helping me in moving the heat pump.

Thanks to the COST Gabi TU1405 Group with which I shared the passion for energy geostructures in the common mission of trying to make them reality and common practice. Thanks to this international experience I was lucky enough to meet a sincere friend, Yvon. Thanks for welcoming me on my arrival in Paris and for inviting me to the wedding with Julie, I am deeply grateful for the good experiences I have had the chance to live.

My time at ENPC was made enjoyable in large part due to many friends and groups that became a part of my life. I am grateful for time spent with wonderful people: Agustin, Alexandre, Anais, Axelle, Benjamin, Edoardo, Hao, Manuel, Nick, Philipp, Radja, Xiu, Yichun, Youssef, Yu and Zi. The dinner on the bateau at the end of the JNGG, the Vietnamese dinner with Xiu, Zi and Yu, the dinners with the Chinese guys at the residence with Chinese food, meeting again Edoardo, Yichun and Manuel at the WTC in Naples are moments I will never forget. I thank Professor Jean-Michel Pereira for the discussions during the numerous consultations. Thanks also to Robin, travelmate to and from Clermont-Ferrand for Yvon's wedding, those were unique moments.

The guys of the PoliTo group have contributed immensely to enrich my personal and professional time. It has been a source of friendships as well as good advice and collaboration. Special thanks go to Matteo, Fabrizio, Francesco, Giovanni and Silvio. Matteo, with whom I have shared and still share, apart from the coronavirus time, the office, but also anxieties, fears and successes related to the PhD. The technical debates I had with him have always stimulated and allowed me to grow, as well as the first ski lessons. Fabrizio, sincere and humble friend, with whom I shared the passion for energy tunnels and who helped me a lot with the experimental campaign during my time in Paris. He delighted us with tasty meals from Sicily, among which the unforgettable "gelo di mellone" which I will try to replicate one day. Francesco, point of reference of the group, from whom I learned not only technical aspects related to geotechnics but also the passion for snow and mountains. Thanks for the amazing porcini mushrooms kindly offered to my family. Giovanni, also a doctoral fellow, with whom I shared lunches, laughter and witty jokes that made history. I met him during our first day of

work at Politecnico as research fellows and I believe that since that moment the third floor of DISEG became much more joyful and, probably, also a little bit more noisy! Silvio, the best administrative ever, ready to help in any event and without whom the beautiful DISEG group would have never existed. I must thank Silvio and Erica for the amazing online exercise classes that offered me healthy distraction moments during the quarantine. I am very happy to have found in both of them great friends and points of reference. Thanks to Fabio, Paolo and Diego for their suggestions on Thesis redaction, prestressed reinforced concrete behaviour and limit state verifications. Thanks to Marco for our chats during difficult times. Even if the joke related to the state of the art theft irritated me a little bit at the beginning, now I smile thinking of it.

The doctoral path thanks to the experimental activity also led me surprisingly to (re-)meet a fellow student. "Galeotto fu il cantiere", one might say. Thanks Luca, for having supported me, encouraged me, helped me, loved me. You have always been there, and you were the only one who understood me in times of difficulty. The weekends spent with your family were always lovely. Thanks also to Tina and Paolo for letting me work in the kitchen, showing they cared about me when asking how I was doing and how the work was going on. I very much appreciate them, not to mention the delicious pumpkin rice and pasta with eggplants and swordfish.

If I got this far it is thanks to my parents because they have always believed in me and have always encouraged me to shoot for the stars. They saw me rejoicing and losing hope, thinking and reflecting, getting angry and getting up again. They were the first ones to listen to my presentations, possibly to criticize them and to give me constructive suggestions. Thank you for your patience and your love, you supported me in all my pursuits, you are my lighthouse in the storm.

To my grandparents Giuseppe, Giuseppina,
Antonino and Santina

*« Nous avons trois moyens principaux:
l'observation de la nature, la réflexion et l'expérience.
Il faut que l'observation de la nature soit assidue,
que la réflexion soit profonde,
et que l'expérience soit exacte »*

Denis Diderot

Contents

CONTENTS.....	XVII
LIST OF TABLES	XXI
LIST OF FIGURES	XXIII
LIST OF SYMBOLS	XXVIII
CHAPTER 1.....	1
INTRODUCTION.....	1
1.1. FRAMEWORK.....	1
1.2. PROBLEM STATEMENT.....	2
1.3. THESIS SCOPE AND OBJECTIVES	2
1.4. ORGANIZATION OF THESIS.....	3
CHAPTER 2	5
ENERGY TUNNELS	5
2.1. INTRODUCTION.....	5
2.2. ENERGY GEOSTRUCTURES	5
2.3. THERMAL ACTIVATION OF TUNNEL LININGS	7
2.3.1. <i>Energy geotextile</i>	9
2.3.2. <i>Energy segmental linings</i>	11
2.3.3. <i>Technical aspects</i>	16
2.3.4. <i>Working principle of a heat pump</i>	18
2.4. THERMAL BEHAVIOUR	20
2.4.1. <i>Case studies</i>	25
2.4.2. <i>Governing equations</i>	31
2.4.3. <i>Analytical models</i>	34
2.4.4. <i>Sensitivity studies</i>	36
2.4.5. <i>The role of groundwater flow</i>	40
2.4.6. <i>The role of internal air</i>	43
2.4.7. <i>Other applications: mountain tunnels</i>	44
2.5. STRUCTURAL BEHAVIOUR.....	45
2.6. DESIGN CONCEPTS	50
2.6.1. <i>General aspects of tunnel linings</i>	50
2.6.2. <i>Tunnel lining design</i>	51
2.6.3. <i>Current design approaches for energy tunnels</i>	57
2.7. SUMMARY.....	59
CHAPTER 3	61
THERMO-MECHANICAL BEHAVIOUR OF SOILS AND CONCRETE	61
3.1. INTRODUCTION.....	61
3.2. EXPERIMENTAL EVIDENCES ON SOILS.....	61
3.2.1. <i>Volumetric thermal response</i>	62
3.2.2. <i>Deviatoric thermal response</i>	66
3.2.3. <i>Cyclic thermal response</i>	68
3.2.4. <i>Constitutive modelling</i>	70
3.2.5. <i>Other effects of temperature</i>	71

3.2.6.	<i>Soil-structure interaction</i>	72
3.3.	EXPERIMENTAL EVIDENCES ON CONCRETE.....	74
3.4.	DESIGN PROPERTIES FOR ENERGY TUNNELS.....	76
3.4.1.	<i>Design parameters</i>	77
3.4.2.	<i>In situ tests</i>	80
3.4.3.	<i>Laboratory tests</i>	82
3.5.	SUMMARY.....	83
CHAPTER 4	85
THE FIRST ITALIAN PROTOTYPE OF ENERGY TUNNEL	85
4.1.	INTRODUCTION.....	85
4.2.	DESCRIPTION OF THE PROTOTYPE.....	86
4.2.1.	<i>Background of Turin ML1 SE project</i>	87
4.2.2.	<i>Energy segments manufacturing</i>	89
4.2.3.	<i>Site implementation</i>	92
4.2.4.	<i>Monitoring and acquisition system</i>	95
4.3.	OPERATION OF THE PROTOTYPE.....	113
4.4.	SUMMARY.....	117
CHAPTER 5	119
THERMAL DESIGN	119
5.1.	INTRODUCTION.....	119
5.2.	ENERGY PERFORMANCE OF THE PROTOTYPE.....	119
5.3.	NUMERICAL INVESTIGATION ON THE THERMAL BEHAVIOUR OF THE PROTOTYPE.....	125
5.4.	GENERALIZATION TO DIFFERENT GROUND AND ENVIRONMENTAL CONDITIONS.....	135
5.4.1.	<i>Developing design charts</i>	135
5.4.2.	<i>Sensitivity analyses</i>	139
5.4.3.	<i>Validation against existing data</i>	141
5.5.	SUMMARY.....	143
CHAPTER 6	145
STRUCTURAL DESIGN	145
6.1.	INTRODUCTION.....	145
6.2.	EXPERIMENTAL DATA.....	145
6.2.1.	<i>Construction site measurements</i>	146
6.2.2.	<i>Experimental site measurements</i>	149
6.3.	INTERPRETATION OF EXPERIMENTAL DATA.....	157
6.3.1.	<i>Conventional sensors</i>	157
6.3.2.	<i>Optical sensors</i>	166
6.4.	NUMERICAL INVESTIGATION ON THE STRUCTURAL BEHAVIOUR OF THE PROTOTYPE.....	169
6.4.1.	<i>Modelling procedure and input parameters</i>	169
6.4.2.	<i>Mechanical analysis</i>	172
6.4.3.	<i>Thermo-mechanical analysis</i>	173
6.5.	ULS AND SLS DESIGN VERIFICATIONS.....	187
6.6.	SUMMARY.....	198
CHAPTER 7	201
SUMMARY AND CONCLUSIONS	201
7.1.	SUMMARY.....	201
7.2.	CONCLUSIONS.....	202
7.2.1.	<i>Energy tunnels thermal performance</i>	202
7.2.2.	<i>Energy tunnels structural performance</i>	203
7.2.3.	<i>Consequences of numerical and experimental results on design analyses of energy tunnels</i>	205
7.3.	RECOMMENDATIONS FOR FURTHER DEVELOPMENT.....	207

SELECTED LIST OF PUBLICATIONS	209
REFERENCES.....	211
APPENDIX A.....	221
EXPERIMENTAL DATA.....	221
A.1 CONTENTS	221
<i>Undisturbed phase (winter 2017)</i>	223
<i>Test GH1</i>	232
<i>Test GH2</i>	244
<i>Test GH3</i>	256
<i>Test GH4</i>	268
<i>Test GH5</i>	277
<i>Test GH6</i>	289
<i>Test GH7</i>	301
<i>Test GH8</i>	313
<i>Test GH9 – cyclic test</i>	325
<i>Test GH10 – cyclic test</i>	337
<i>Test GC1</i>	349
<i>Test AH1</i>	358
<i>Test AH2</i>	370
<i>Test GC2</i>	380
<i>Undisturbed phase (summer 2018)</i>	389
APPENDIX B.....	393
IN SITU TESTING EQUIPMENT	393
B.1 CONTENTS.....	393

List of Tables

Table 2.1: Thermal performance of the main case studies documented in literature (*=summer mode).	24
Table 2.2: Lining characteristics, groundwater flow and ground temperature for the main case studies documented in literature.	24
Table 2.3: Pipes geometry and soil type for the main case studies documented in literature.	25
Table 2.4: Typical uniform initial ground temperature values used in numerical models retrieved from literature.	33
Table 2.5: Thermal boundary conditions used for ground and tunnel lining in numerical models retrieved from literature.	33
Table 2.6: Thermal boundary conditions used for pipes circuit in numerical models retrieved from literature.	34
Table 2.7: Hydraulic boundary conditions used in numerical models retrieved from literature.	34
Table 2.8: Variations in tunnel vertical diameter for the Ce and Ce _{i,j} cycles on clay and silt (from Mimouni et al., 2013).	48
Table 2.9: Invert slab top horizontal displacements for the Ce and Ce _{i,j} cycles on clay and silt (from Mimouni et al., 2013).	48
Table 2.10: Variations in Crossrail tunnel diameter for the no heat extraction and the 30 W/m ² heat extraction cases (from Nicholson et al., 2014).	49
Table 2.11: Typical ULS and SLS (AFTES, 1997).	53
Table 2.12: Partial coefficients for actions of effect of actions (from NTC2018, 2018).	55
Table 2.13: Partial coefficients for geotechnical parameters (from NTC2018, 2018).	55
Table 3.1: Key design properties needed for energy geostructures (modified from Loveridge et al., 2017).	77
Table 3.2: Volumetric thermal expansion coefficients in literature.	79
Table 4.1: Strength and deformability properties of the four GU for Turin subsoil (from Barla and Barla, 2012).	89
Table 4.2: Location of sensors installed in ring 179.	97
Table 4.3: Location of sensors installed in ring 180.	97
Table 4.4: Operation of all sensors involved in the experimental site: timespan and observed failures.	100
Table 4.5: Maximum and minimum values of temperatures, strains and stresses during the undisturbed phase.	114
Table 4.6: List of the tests performed.	115
Table 5.1: Main features of the example test GH8.	120
Table 5.2: Temperatures during the test GH8.	122
Table 5.3: Energy performance of the prototype in terms of heat flux and thermal energy for each of the tests performed.	123
Table 5.4: COP/EER and total COP/EER calculation.	125
Table 5.5: Technical specifications of heat flow meter Lasercomp FOX600.	130
Table 5.6: Concrete sample thickness measured by the flow meter.	132
Table 5.7: Set points fixed for the heat flow meter.	132
Table 5.8: Computation of concrete thermal conductivity and thermal resistance.	132
Table 5.9: Material properties used during the calibration phase of the numerical model.	133
Table 5.10: Main properties of the base and sensitivity analyses models.	137
Table 5.11: Parameters investigated in the sensitivity analyses.	139
Table 5.12: Validation of the design charts against available data of energy tunnels thermal power exchanged with the ground.	142

Table 6.1: Available stress, strain and surface settlements data.....	146
Table 6.2: Nomenclature of the strain gauges and pressure cells in ring 181 (BEC=in hoop direction, BEL=in longitudinal direction, BEA=no stress, E=extrados, I=intrados, 1=side close to ring 182, 2=side close to ring 180, CPR=in radial direction, CPT=in hoop direction, *in MPa).	147
Table 6.3: Strains measurements (i) in the precast concrete plant, (ii) before connecting the datalogger and (iii) after connecting the datalogger.....	150
Table 6.4: Strains differences between the second and the first reading.....	150
Table 6.5: Stress measurements (i) in the precast concrete plant, (ii) before connecting the datalogger and (iii) after connecting the datalogger.....	153
Table 6.6: Stress differences between the second and the first reading.....	154
Table 6.7: FBGs sensors sensitivities.....	156
Table 6.8: Optical sensing experimental campaigns.....	157
Table 6.9: Main segment 6 (ring 179) TM results at the end of test GH8.....	165
Table 6.10: Mechanical and thermal material properties.....	171
Table 6.11: Numerical modelling calculation stages.....	171
Table 6.12: Comparison between experimental and numerical results.....	178
Table 6.13: Convergences obtained numerically at the lining intrados and extrados.....	179
Table 6.14: Thermal effect on tunnel diameter change (modified from Nicholson et al. 2014).....	180
Table 6.15: Triplets of internal forces at the end of excavation and of the simulated tests needed for ULS verifications.....	180
Table 6.16: Triplets of internal forces at specific timeframes of model A and B for ULS verifications.	186
Table 6.17: Design approach proposal for underground earthworks according to Sciotti (2010).....	192
Table 6.18: Concrete characteristics.....	192
Table 6.19: Concrete mechanical properties.....	192
Table 6.20: Steel mechanical properties.....	193
Table 6.21: ULS shear verification – tests.....	195
Table 6.22: ULS shear verification – long-term models A and B.....	195
Table 6.23: SLS stress limitation verification – tests.....	196
Table 6.24: SLS stress limitation verification – long term models A and B.....	196
Table 6.25: Criteria to choose the crack limit state.....	197

List of Figures

Figure 2.1: Basic principle of tunnel lining ground heat exchangers (from Zhang et al., 2014).....	8
Figure 2.2: Examples of energy geotextile installations: (a,b) Lainzer Tunnel (from Adam and Markiewicz, 2009); (c,d) Stuttgart-Fasanenhof Tunnel (from www.bine.info; Schneider and Moormann, 2010); (e,f) Seocheon tunnel (from Lee et al., 2016; Lee et al., 2012) and (g,h) Linchang tunnel (from Zhang et al., 2013; Zhang et al., 2014).	10
Figure 2.3: (a) Schematic view of the HUT system and (b) thermal picture showing the difference between temperature-controlled and non temperature-controlled pavement (from Islam et al., 2006).....	11
Figure 2.4: Details from Jenbach TBM-driven energy tunnel: (a) absorber pipes, (b-c) connection among adjacent segments, (d) connection circuits before invert slab installation, (e-f) conventional and geothermal view during operation (from Frodl et al., 2010).	12
Figure 2.5: Energy segmental lining: (a) pipes with main direction parallel to tunnel axis, (b) pipes with main direction perpendicular to tunnel axis, together with plant view of their connection to the consumer (modified from Barla and Di Donna, 2016; Frodl et al., 2010).....	13
Figure 2.6: Schematic pipework connections with subcircuits made up of five in series-rings (from Nicholson et al., 2014).	13
Figure 2.7: Comparison between Enertun and previous configurations in terms of heat (modified from Barla et al., 2019).	15
Figure 2.8: Configurations of the Enertun patent: (a) ground, (b) air and (c) ground&air.	16
Figure 2.9: Illustration of cold (left) and hot (right) tunnels (modified from Nicholson et al., 2013)....	17
Figure 2.10: Time and spatial distribution of energy geostructures (modified from Di Donna et al., 2017).	18
Figure 2.11: Scheme of operation of a compression heat pump (Brandl, 2006).	19
Figure 2.12: Main heat transfer mechanisms involved in the problem of energy tunnel systems.....	21
Figure 2.13: Temperature at the tunnel extrados and 5 m far from the lining over three years in different modes of operation (modified from Franzius and Pralle, 2011).	23
Figure 2.14: Monitoring plan at Stuttgart-Fasanenhof tunnel and soil temperature during winter natural (top right) and working (bottom right) conditions at Stuttgart-Fasanenhof tunnel (modified from Buhmann et al., 2016).	26
Figure 2.15: (a) Cooling and (b) heating mode test at Stuttgart-Fasanenhof tunnel (modified from Buhmann et al., 2016).....	27
Figure 2.16: Layout of the demonstration project at Jenbach tunnel (modified from https://www.bft-international.com ; Moormann et al., 2016).	27
Figure 2.17: Heating mode test performed at Jenbach tunnel (modified form Moormann et al., 2016).	28
Figure 2.18: Cyclic cooling mode test performed at Seocheon tunnel in 2010 (from Lee et al., 2012). 29	
Figure 2.19: Cyclic heating and cooling mode test performed at Seocheon tunnel in 2011 (Lee et al., 2016).....	29
Figure 2.20: Correlation between average heat exchange obtained at Seocheon tunnel and difference between air and inlet temperatures (modified from Lee et al., 2016).	30
Figure 2.21: Monitoring system installed at Linchang tunnel (from Zhang et al., 2014).	30
Figure 2.22: THM problem couplings.	31
Figure 2.23: Scheme of the model for the analytical calculation of (a) rock mass, tunnel lining and (b) heat carrier fluid temperature (modified from Zhang et al., 2013).	36
Figure 2.24: Design charts for the preliminary assessment of heating and cooling potential for energy tunnels (from Di Donna and Barla, 2016).....	37

Figure 2.25: Extracted thermal power obtained by varying pipes layout, pipes diameter, pipes embedment and heat carrier fluid flow rate (modified from Cousin et al., 2019).	38
Figure 2.26: Web-based calculation (a) tool and (b) model (modified from Moormann et al., 2018).	39
Figure 2.27: Effect of groundwater flow velocity on average fluid temperature (Bidarmaghz and Narsilio, 2018).	40
Figure 2.28: Turin ML1 SE model: (a) geometry and pipes inlet thermal boundary condition, (b) temperature distribution over time at several distances from the tunnel alignment (modified from Barla et al., 2016). NE extension Warsaw metro: (c) effect of thermal plume in the case of twin tunnels (Baralis et al., 2018).	41
Figure 2.29: (a) Setup of laboratory scale experiment and (b) effect of pipes layout (modified from Zhang et al., 2016).	42
Figure 2.30: (a) Thermal and hydrodynamic entry length and stabilised area within a tube (from Brandl, 2006), (b) correlations between heat transfer coefficient, wall roughness and airflow velocity (from Peltier et al., 2019).	44
Figure 2.31: Effect of flow rate and user temperature level on thermal performance for the case study of Mules Access Tunnel (from Tinti et al., 2017).	45
Figure 2.32: (a) FDM mesh of the TM model and (b) stresses variations output (modified from Barla et al., 2018).	47
Figure 2.33: Axial stress for clay and silt in extraction only and injection and extraction cases (modified from Mimouni et al., 2013; compression is negative).	47
Figure 2.34: (a) Geometry of the thermo-mechanical FE numerical model and (b) maximum principal stress distribution during summer without and with heat extraction (modified from Nicholson et al., 2013).	49
Figure 2.35: Main issues involved in the geotechnical design of energy tunnels (modified from Soga and Rui, 2016).	49
Figure 2.36: Tunnel lining design procedure (modified from ITA, 2000).	52
Figure 3.1: Effect of (a,b) OCR, drained heating and (b) drained heating-cooling cycles on thermal volumetric strain (modified from (a) Cekerevac and Laloui, 2004, (b) Abuel-Naga et al., 2007).	63
Figure 3.2: Variation of the apparent preconsolidation stress with temperature (modified from Laloui and Cekerevac, 2003).	64
Figure 3.3: Effect of temperature on isotropic compression line for a saturated Illite (modified from Campanella and Mitchell, 1968).	65
Figure 3.4: Stress path in the isotropic plane (modified from Laloui and Di Donna, 2013).	65
Figure 3.5: Effect of OCR on pore water pressure development (modified from Abuel-Naga et al., 2007).	66
Figure 3.6: Stress path in the temperature-deviatoric stress-mean effective stress plane (modified from Laloui and Di Donna, 2013).	67
Figure 3.7: Effect of temperature on friction angle at critical state (modified from Cekerevac and Laloui, 2004).	67
Figure 3.8: Cyclic thermal effects on normalconsolidated clay.	68
Figure 3.9: Effect of drained cyclic thermal loading on a NC sample compared to a sample left free to deform in isothermal conditions (modified from Burghignoli et al., 2000).	69
Figure 3.10: Effect of temperature on hydraulic conductivity (modified from Towhata et al., 1993).	71
Figure 3.11: Effect of temperature on (a) undrained secant modulus of NC specimens and (b) drained secant modulus ((a) from Bergado et al., 2007; (b) from Cekerevac and Laloui, 2004).	72
Figure 3.12: Thermo-mechanical stress path for the soil-concrete tests (a) at room temperature and (b) at high temperature (modified from Di Donna et al., 2016).	73
Figure 3.13: Summary of results of direct shear tests at different temperatures for (a) sand-concrete specimens and (b) clay-concrete specimens (from Di Donna et al., 2016).	74
Figure 3.14: Sketch of a TRT test.	81
Figure 3.15: (a) Guarded hot plate and (b) divided cut-bar methods (modified from Vieira et al., 2017).	82
Figure 4.1: View of the Enertun experimental site and its location along the Turin Metro Line 1.	86

Figure 4.2: Partial layout of the Lingotto-Bengasi section with a particular focus on Bengasi station. .87	87
Figure 4.3 Monitored tunnel internal temperature in the Metro (a) in 2010-2011 (modified from Barla et al., 2016;) and (b) in 2018-2019 in a well close to Lingotto (courtesy from GTT).....87	87
Figure 4.4: Cross-section of the tunnel.....89	89
Figure 4.5: Pipes layout in the two energy rings, (a) section corresponding to the extrados and (b) section corresponding to the intrados.....90	90
Figure 4.6: Example of steel cage equipped with pipes before casting (segment 1, ring 180) with detail of box-outs.....91	91
Figure 4.7: Preparation stages of energy segments: (a) moulding, (b) casting, (c) demoulding and (d) circulation test.....92	92
Figure 4.8: Pipes connections between adjacent segments.93	93
Figure 4.9: Flow and return pipes.....94	94
Figure 4.10: Details of the experimental plant geometry and junctions.94	94
Figure 4.11: The control room, hosting the heat pump, the datalogger and the secondary circuit, view from the mezzanine (left) and a close-up view (right).....95	95
Figure 4.12: Design layout of sensors in the two energy rings: (a) extrados plan view, (b) intrados plan view, (c) single-mode fiber optics chains and (d) vertical cross sections showing the sensors location.....96	96
Figure 4.13 Laboratory check of the wavelengths correctness: (a) undeformed signal and (b) example of deformed signal (tension).98	98
Figure 4.14: Energy segments equipped with the three types of monitoring system.99	99
Figure 4.15: Location of the temperature probes.99	99
Figure 4.16: Energy segments construction details: ring 179, segment 1 (1/12). 101	101
Figure 4.17: Energy segments construction details: ring 179, segment 2 (2/12). 102	102
Figure 4.18: Energy segments construction details: ring 179, segment 3 (3/12). 103	103
Figure 4.19: Energy segments construction details: ring 179, segment 4 (4/12). 104	104
Figure 4.20: Energy segments construction details: ring 179, segment 5 (5/12). 105	105
Figure 4.21: Energy segments construction details: ring 179, segment 6 (6/12). 106	106
Figure 4.22: Energy segments construction details: ring 180, segment 1 (7/12). 107	107
Figure 4.23: Energy segments construction details: ring 180, segment 2 (8/12). 108	108
Figure 4.24: Energy segments construction details: ring 180, segment 3 (9/12). 109	109
Figure 4.25: Energy segments construction details: ring 180, segment 4 (10/12). 110	110
Figure 4.26: Energy segments construction details: ring 180, segment 5 (11/12). 111	111
Figure 4.27: Energy segments construction details: ring 180, segment 6 (12/12). 112	112
Figure 4.28: Temperatures, thermally induced strains and thermally induced stresses (a) in segment 4 and (b) in segment 6 (ring 179) during the Sep-Oct 2017 undisturbed conditions..... 113	113
Figure 4.29: Standard view (a), (c), (e) and thermal picture (b), (d), (f) during the operation of the prototype ((a),(b) air heating; (c),(d) ground cooling; (e),(f) air heating)..... 116	116
Figure 5.1: Monitored temperatures in the primary and secondary circuits during test GH8. 121	121
Figure 5.2: Monitored upstream groundwater temperature T6 in the area of the construction site. ... 121	121
Figure 5.3: Energy tunnel thermal performance dependence on (a) heat carrier fluid volumetric flow rate, (b) test duration and (c) period of the year..... 124	124
Figure 5.4: Energy balance scheme for the heat pump..... 124	124
Figure 5.5: Comparison among different boundary conditions - temperature along horizontal profile (a) after 30 days and (c) after 60 days, temperature along vertical profile (b) after 30 days and (d) after 60 days. 126	126
Figure 5.6: Comparison among different boundary conditions, (a) inlet and (b) outlet temperature. 127	127
Figure 5.7: Cross section of the 3D FEM model with indication of thermal and hydraulic boundary conditions. 127	127
Figure 5.8: Thickness of grout specimens extracted after lining installation. 128	128
Figure 5.9: 3D view of the pipes circuit (expansion factor along longitudinal axis for a better view of the pipes network). 129	129

Figure 5.10: Thermal conductivity measurement: (a) Concrete sample, (b) Heat flow meter used, (c) optical encoders for automatic thickness measurement, (d) thin film heat flux transducers, (e) placement of the concrete sample, (f) thermal picture during a test.	131
Figure 5.11: Comparison between measured and computed circuit outlet temperature: test GH8 (calibration phase).....	134
Figure 5.12: Comparison between measured and computed data: (a) test GH5, (b) test GH6, (c) test GC1 and (d) AH2 (validation phase).....	134
Figure 5.13: Comparison between measured and computed lining temperature at the extrados and at the intrados and computed downstream temperature at the end of the simulated tests.	135
Figure 5.14: Geometry of the network of pipes embedded in the model adopted for the construction of design charts (only inlets and outlets of rings 1 and 15 are highlighted for illustrative purposes).	136
Figure 5.15: Updated preliminary design charts showing geothermal potential in W/m^2 for winter and summer conditions and for different groundwater flow directions with respect to the tunnel axis (0° , 45° and 90°).	138
Figure 5.16: Effect of (a) fluid inlet temperature, (b) fluid velocity, (c) pipes size and (d) heat transfer coefficient on geothermal potential during winter and summer conditions expressed in terms of heat flux variations in the case perpendicular flow.	141
Figure 6.1: Stress and strain gauges deployed in ring 181 by the construction site.	146
Figure 6.2: Temporal trend of face and ring installation advancement (only data available are shown).	147
Figure 6.3: Strain outputs in ring 181 referred to the pre-installation reading.	148
Figure 6.4: Stress outputs in ring 181, 222, 322, 437.....	149
Figure 6.5: Evolution of the surface settlements profile with time.	149
Figure 6.6: Location of the strain gauges and pressure cells in the experimental site and view of the pipes network.	150
Figure 6.7: Monitored strains and temperature without compensation.	152
Figure 6.8: Monitored strains and temperature with compensation – Method 1.....	152
Figure 6.9: Monitored strains and temperature with compensation – Method 2.....	153
Figure 6.10: Monitored stresses and transducers temperatures.....	154
Figure 6.11: Location of FBGs and electrical strain sensors.	156
Figure 6.12: Heating test GH8 and cooling test GC1 with corresponding lining temperatures, thermally induced strains and thermally induced stresses.	158
Figure 6.13: Relationship strains-temperature for the ground heating tests.	159
Figure 6.14: Relationship strains-temperature for the ground cooling tests.	160
Figure 6.15: Relationship strains-temperature for the air heating tests.	161
Figure 6.16: Relationship stress-temperature for the ground heating tests.	162
Figure 6.17: Relationship stress-temperature for the ground cooling tests.	163
Figure 6.18: Relationship stress-temperature for the air heating tests.	164
Figure 6.19: Temperatures, strains and stress in segment 6 (ring 179) during test GH8.....	165
Figure 6.20: Comparison among electrical and optical fiber sensors during experimental campaign A3.	166
Figure 6.21: Bragg wavelength and correspondent temperature variation detected by two embedded FBGs vs time. The curve is compared to the heat pump activity (expressed as the temperature variation produced at the heat pump inlets of the primary circuit).	167
Figure 6.22: Temperature variation (with respect to the beginning of the acquisition) as recorded by comparable optical and electrical sensors. The air temperature in the tunnel is also reported.	167
Figure 6.23: Bragg wavelengths from an optical sensor containing a strain and a temperature FBG.	168
Figure 6.24: Comparison among electrical and optical fiber sensors during experimental campaign B.	168
Figure 6.25: Comparison among electrical and optical fiber sensors during experimental campaign C.	168
Figure 6.26: Finite difference mesh of the thermo-mechanical numerical model with stratigraphy. ...	169

Figure 6.27: Longitudinal profile of the area of interest with indication of the stratigraphy.....	171
Figure 6.28: Geostatic state of stress at the end of Stage 1 along any vertical axis.....	172
Figure 6.29: State of stress in the tunnel lining at the end of the excavation.	173
Figure 6.30: Computed and monitored surface settlements at the end of the excavation.	173
Figure 6.31: Conceptual scheme of the steps needed to import the temperature field from FEFLOW to FLAC.....	175
Figure 6.32: Matching of the temperature field at the end of heating and cooling season for long term operation in the TH and TM model.....	176
Figure 6.33: Computed hoop strains and stresses at the end of test GH8.....	177
Figure 6.34: Computed hoop strains and stresses at the end of test GC1.	178
Figure 6.35: Deformed lining at the end of the excavation phase and at the end of experimental tests with indication of maximum convergences (additional convergences with respect to the end of excavation are shown for all the tests).	179
Figure 6.36: Internal actions at the end of the excavation phase and at the end of the simulated tests with indication of maximum values.....	181
Figure 6.37: Monitoring data and sinusoidal interpolation for (a) external air and (b) tunnel air temperature.	182
Figure 6.38: Geothermal circuit inlet temperature in model B over one year.	183
Figure 6.39: Deformed lining for models A (first row) and B (second row) at specific timeframes with indication of maximum convergences (additional convergences with respect to the end of excavation are shown).	183
Figure 6.40: Internal actions acting within the energy lining for model A at different timeframes with indication of maximum values.	184
Figure 6.41: Internal actions acting within the energy lining for model B at different timeframes with indication of maximum values.	185
Figure 6.42: Computed surface settlements at different timeframes of model A and model B.	187
Figure 6.43: Combinations cases of congruence and compatibility in presence of thermal actions. ..	188
Figure 6.44: Examples of possible temperature profiles (EN 1991-1-5).....	188
Figure 6.45: Profiles of temperature and hoop stresses computed from the numerical analyses (tests).	189
Figure 6.46: Profiles of temperature and hoop stresses computed from the numerical analyses (long- term).	190
Figure 6.47: Scheme of a typical segment rebars arrangement.....	192
Figure 6.48: ULS - bending moment with axial force verification – tests and long term.....	193
Figure 7.1: Methodology for thermal and structural design.....	206

List of Symbols

Roman symbols

Symbol	Variable name	Unit measure
a_d	nominal geometric quantities	m
A	area	m^2
b	hydraulic aperture	m
c	cohesion	Pa
c_u	undrained cohesion	Pa
c_p	heat capacity of the heat carrier fluid	$J/(kg\ ^\circ C)$
C_d	serviceability prescribed limit design value	-
d	pipes diameter	mm
D	ring external diameter	m
D_R	relative density	%
E	Young's modulus	Pa
E_d	design value of the effect of actions	-
f_{cd}	design compression strength	Pa
f_{ck}	cylindric characteristic compression strength	Pa
f_{cm}	average compression strength	Pa
f_{ctd}	design tensile strength	Pa
$f_{ctk0.05}$	lower bound of characteristic tensile strength	Pa
f_{ctm}	average tensile strength	Pa
f_{yk}	characteristic yielding strength of steel	Pa
f_{yd}	steel design strength	Pa
F_0	Fourier number	-
F_d	design actions	-
g_i	gravity vector	m/s^2
G	permanent action	-
G_0	shear modulus of the soil	Pa
h	convective heat transfer coefficient	$W/(m^2K)$
	<i>or</i> hydraulic head	m
h_G	joint thickness	m
\dot{H}	enthalpy flow	W
J_2	second deviatoric stress invariant	Pa
k_0	coefficient of lateral earth pressure at rest	-
k_w	hydraulic conductivity	m/s
K	stiffness of the far-field spring	Pa
	<i>or</i> hydraulic conductivity	m/s
	<i>or</i> coefficient for thermal correction	$MPa/^\circ C$
	<i>or</i> bulk modulus	Pa
K_ε	strain sensitivity of the loosen FBG	$pm/\mu\varepsilon$

K_T	temperature sensitivity of the loosen FBG	pm/°C
l_0	reading with the cell in air before the installation	Pa
L	ring thickness	m
L_{es}	pressure cell reading	Pa
L_{hyd}	hydrodynamic entrance region	m
L_{th}	thermal entrance regions	m
m	Hoek and Brown constant	-
	<i>or</i> mass flow rate	kg/s
M	bending moment	kNm
\dot{M}	mass flow rate	kg/s
n	porosity	-
n_G	number of joints	-
N	axial force	kN
p	pressure	Pa
p'	volumetric stress	Pa
P_c	power consumption	W
P_t	temperature correction	Pa
q	deviatoric stress	Pa
	<i>or</i> heat transfer rate	W/m
\dot{q}	power per tunnel lining unit area	W/m ²
Q	Variable action	-
	<i>or</i> thermal energy	kWh
\dot{Q}	thermal power or heat flow	W
Q_a	heat absorbed from the low temperature source	W
Q_l	thermal losses	W
Q_r	heat rejected into the high temperature sink	W
r_b	borehole radius	m
R_d	design capacity	-
R_{ck}	cubic characteristic compression strength	Pa
R	pile radius	m
	<i>or</i> thermal resistance	°C/W
s_{ij}	deviatoric stress component	Pa
S	specific storage coefficient	1/m
	<i>or</i> sensitivity factor	digit/MPa
S_c	specific heat capacity	J/kgK
S_r	degree of saturation	%
t	time	s
	<i>or</i> pipes thickness	mm
T	shear force	kN
	<i>or</i> temperature	°C
T_0	undisturbed temperature	°C
T_i	inlet temperature of pipe circuit	°C
T_o	outlet temperature of pipe circuit	°C
v_{gw}	groundwater flow velocity	m/s
v_w	fluid velocity	m/s
y	vertical coordinate	m
v	Darcy velocity	m/s
v_f	fluid velocity	m/s

V	shear force	kN
w_k	calculated crack width	mm
w_{max}	crack width limiting value	mm
\dot{W}	heat source	W
X_d	design material properties	-

Greek symbols

Symbol	Variable name	Unit measure
α	coefficient of volumetric thermal expansion	1/°C
α_{cc}, α_{ct}	coefficient for reduction of strength	-
α_i	thermal diffusivity	m ² /s
α_L	longitudinal thermal dispersivity	m
α_T	trasverse thermal dispersivity	m
β_w	water thermal expansion coefficient	1/°C
δ_{ij}	Kronecker delta	-
$\epsilon_{th,f}$	free thermal strain	-
$\epsilon_{th,o}$	observed thermal strain	-
$\epsilon_{th,r}$	restrained thermal strain	-
ϵ_v^{Te}	elastic expansion component	-
ϵ_v^{Tp}	plastic contraction component	-
Φ	heat transfer coefficient	W/m ² K
γ	unit weight	kN/m ³
	<i>or</i> partial safety factor	-
φ	friction angle	°
λ	thermal conductivity	W/(mK)
λ_ϵ	strain wavelength	nm
λ_T	temperature wavelength	nm
Ψ	dilatancy	°
	<i>or</i> combination factor	-
ρ	density	kg/m ³
σ^e	effective stress	Pa
σ	total stress	Pa
σ_c	unconfined compressive strength	Pa
$\sigma_{c,max}$	maximum stresses in concrete	Pa
σ_p	preconsolidation stress	Pa
$\sigma_{s,max}$	maximum stresses in reinforcement	Pa
σ_{v0}	current vertical effective stress	Pa
Υ_w	water compressibility	m ² /N
Υ_s	solid compressibility	-
ν	Poisson's ratio	-

Operators and functions

Symbol	Name
$\bar{\quad}$	average
$d(\quad)$	increment operator

∂	derivative
Δ	difference operator
Σ	sum
$\ln()$	natural logarithm
$\log()$	common logarithm
∇	gradient
$\nabla \cdot ()$	divergence

Acronyms

AH	air heating
ASHP	air source heat pump
BHE	borehole heat exchanger
Ce	only extraction
Cei-i	both injection-extraction Cei-i starting by injection
COP	coefficient of performance
CNL	constant normal stress
CNS	constant normal stiffness
CSL	critical state line
DA	Design Approach
DOF	degree of freedom
DTRT	Distributed Thermal Response Test
EER	energy efficiency ratio
EPB	Earth Pressure Balance
ETRT	Enhanced Thermal Response Test
EU	European Union
FBG	Fiber Bragg Grating
FEM	finite element method
GC	ground cooling
GH	ground heating
GHE	ground heat exchanger
GSHP	ground source heat pump
GU	Geotechnical Unit
HUT	horizontal U-tube
HVAC	heating, ventilation and air conditioning
IR	intermittent ratio
NAN	not available number
NATM	new Austrian tunnelling method
NC	normalconsolidated
NCL	normal compression line
OC	overconsolidated
OCR	overconsolidation ratio
PE	polyethylene
PI	plasticity index
PT100	platinum thermal resistance
RES	renewable energy sources
REV	representative elementary volume
SCOP	seasonal coefficient of performance
SEER	seasonal energy efficiency ratio

SLS	Serviceability Limit State
SPF	seasonal performance factor
TBM	tunnel boring machine
TH	thermo-hydraulic
THM	thermo-hydro-mechanical
TM	thermo-mechanical
TRT	thermal response test
ULS	Ultimate Limit State
VAL	automatic light vehicle

Chapter 1

Introduction

1.1. Framework

The slow growth of renewable energy in the heating and cooling context is a challenge, yet addressing it is mandatory for decarbonisation. However, this sector is still heavily reliant on fossil fuels on a global scale. In the light of the EU directive for renewable energy (2009/28/EC), aerothermal, geothermal and hydrothermal heat energy captured by heat pumps is established as one of the mainstream options to meet the thermal needs of buildings and industry for heating and cooling.

The technology of energy geostructures, which harvests shallow renewable geothermal energy, that is the energy buried in the first hundred of meters below ground surface, fits perfectly in this picture. It is a unique technology developed in recent years that can provide an extraordinary capability in meeting international agreements aimed at achieving a low carbon-built environment. This generic designation connotes all geostructure that couples the structural support role of conventional geostructures to the performance of typical geothermal heat exchangers. Not only can the operation of energy geostructures provide reinforcement to soils for supporting a building, as in the case of energy piles, or stabilising the excavation of a tunnel, as in the case of energy tunnels, but also it can store and supply energy for several purposes, such as residential heating and cooling to reach comfort levels, the production of domestic hot water for anthropogenic uses and deicing of infrastructures pavements and decks.

Focusing the attention on energy tunnels, research in this field is still a largely unexplored land. There are no clearly defined rules and recommendations for their design and it has to be recognised that, despite the principle of the technology is known since decades, no projects at the city scale can be mentioned, except some pilot testbeds and feasibility studies, even if significant efforts have been made in the recent past.

Considering the need to boost innovation and develop breakthrough solutions to support the heating and cooling strategies, the present Thesis is to address research to demonstrate the readiness level of the energy tunnels technology.

1.2. Problem statement

Despite the potential of energy tunnels to contribute to the so-called sustainable development goals, given also their much higher heat exchange surface in comparison to other homothetic energy geostructures, tremendously limited applications can currently be observed because of several challenges. Indeed, their dual-purpose role involves additional thermal loads applied that cause changes in the temperature, stress, deformation patterns within the surrounding soil and the lining itself, thus bringing to the attention of engineers unprecedented questions. The energy and structural response of energy tunnels is strongly affected by the thermally induced alterations subsequent to the heat carrier fluid circulation from and to the heat pump and requires multidisciplinary competences to finalise the analysis and design. It is therefore clear that, from the design point of view, an additional element is introduced compared to traditional tunnels, as it is necessary to guarantee adequate efficiency and sustainability to the geothermal plant, incorporated, as already mentioned, within the lining itself.

Most of the available studies have addressed the behaviour of energy tunnels by using numerical methods, although expertise required is typically a niche competence and simplified methods are mainly needed to capture the behaviour of these geostructures in a broad range of situations.

This Doctoral Dissertation is intended to investigate and characterise the thermal and the structural performance of energy tunnels by means of experimental and numerical approaches. Considering that the ratio of full-scale in situ and physical tests to numerical analyses existing in the literature is exceedingly biased towards this latter, the added value of performing a real-scale experiment in an attempt to provide additional knowledge in this context can be evidently appreciated.

1.3. Thesis scope and objectives

This Thesis is devoted to the understanding of energy tunnels thermal and structural performance with major interest being placed on the design of such fascinating underground structures. Their structural-energy double role implies that a correct design must consider at the same time the structural safety and the energy aspects. Some efforts have already been done in the past, or are in progress, to study and optimise the performance of these geostructures, but few advancements have been achieved in the understanding of their thermo-mechanical behaviour through in-situ monitoring of real scale cases and development of design tools. The objective of this Thesis is to contribute to the investigation on the behaviour of energy tunnels from the energy efficiency and the thermo-mechanical point of view, by extending the knowledge on their response, highlighting the most important design aspects and providing scientific-based design recommendations. Prior to this work, no comprehensive summary about the role of thermal and mechanical loads in the structural performance and performance-based design of energy tunnels was available.

The problem will be analysed from the experimental point of view, by means of the implementation of a prototype in the tunnel of Turin Metro Line 1 South Extension, followed by numerical analyses to enlarge the picture to different ground and environmental conditions and to real timescales of practical applications. Reference is made to urban tunnels excavated with precast segmental lining. The main tasks undertaken, i.e. design, construction and monitoring of the testbed, together with the development of a comprehensive experimental programme which aimed at testing all possible configurations of the recently patented Enertun

concept, will be described with emphasis placed on the energy performance of the prototype as well as on structural implications.

Analysis and synthesis of the results obtained will allow to identify the elements to be introduced in performance-based design according to the Eurocodes, that lack recognised rules that can be straightforwardly applied to energy tunnels.

1.4. Organization of Thesis

The Thesis is divided into 7 chapters and two appendices. Following the present chapter, which has the purpose to provide a general introduction to the work carried out, *Chapter two* is to give a brief overview on the subject of energy tunnels, provide the current state of knowledge about technical aspects and identify the key points of thermal and structural design, with emphasis on design methods currently employed for the dimensioning of conventional tunnels. The goal is to identify the aspects of such procedures which will have to be adapted to take into account the additional aspects related to the geothermal exploitation.

Chapter three is devoted to the understanding of the effects of temperature on the behaviour of soils and concrete, by presenting experimental evidences resulting from laboratory tests performed that can be found in literature. After an up-to-date state of knowledge in this field, the design parameters needed for designing energy tunnels and methodologies available for their assessment are depicted.

Chapter four is the main core of the doctoral work, illustrating a description of the newly developed energy tunnel prototype installed in Turin with its special features and the testing equipment used during this Thesis. The pilot demonstrator has the goal to go a step forward into the understanding of the behaviour of tunnels subjected to the thermo-mechanical conditions imposed by thermal loads. The main points of the prototype operation during the experimental campaign carried out are presented, by outlining the various tests performed.

Chapter five presents the energy efficiency interpretation of the results of the experimental tests in the different configurations analyzed with the intent to show its promising value. Numerical investigation follows to study the problem from a broader perspective, first by reproducing numerically the behaviour observed experimentally during the tests then by enlarging the view to different conditions in order to formulate a methodology for preliminary evaluation of energy tunnel projects.

The presentation and analysis of monitored data pertaining to the thermo-mechanical behaviour are illustrated in *Chapter six*, followed by the development of numerical models for the simulation of the observed response. Similarly to *Chapter five* for the energy performance, the main goal is to integrate the knowledge acquired through the studies to investigate the structural response in applications real timescales. Insights into performance-based design are hence inferred.

The results obtained in the different chapters are summarised in the conclusion of the Thesis and their consequences and applications to the design of energy tunnels are discussed in *Chapter seven*. Finally, also the possible future developments and new perspectives are described.

In line with the ongoing transition towards policies of open access to research data (European Commission, 2012), full data from the testing program are listed in Appendix A in the form of charts and reduced datasheets. Appendix B describes the monitoring instrumentation used for the in situ testing activities presented in *Chapter four*, *Chapter five* and *Chapter six*.

The adopted sign convention in this manuscript considers compressive stresses, contractive strains and downward displacements (settlements) as positive.

Chapter 2

Energy tunnels

2.1. Introduction

Energy tunnels are a relatively new technology that has been under a magnifying glass during the last decades. Most of the studies found in literature have focused on the evaluation of thermal performance of energy tunnels, whereas the reported studies on their thermo-mechanical behaviour are extremely few, in contrast for instance with the more advanced knowledge and widespread use of energy piles.

The main purpose of this chapter is to present an up-to-date review of the various numerical investigations and experimental applications of energy tunnels, focusing on thermal and mechanical behaviour and identifying the key aspects for their analysis, design and application. Attention is also paid to design guidelines already existing for standard tunnels and that could be adapted and extended to include the additional phenomena related to the thermal activation of the lining.

This review forms the background for the experimental and numerical research on energy tunnels technology and for the development of a new design procedure, which is proposed in the following.

2.2. Energy geostructures

In the next decades new solutions involving the use of renewable energy sources (RES) will be crucial to achieve a noticeable increase in clean energy production aimed at reducing carbon dioxide emissions against climate change and at meeting other targets, such as energy supply security. Every European country agreed to elaborate a National Renewable Energy Action Plan to reach the goal, as required by the EU (Directive 2009/28/EC, 2009).

In this context, shallow geothermal energy is getting more and more attractive, given that it is accessible everywhere in the world (below 10–15 m up to 400 m depth). Today, the use of shallow geothermal energy is common to many countries. Usually, heat is extracted from the ground for domestic heating or to produce hot water by means of open or closed loop systems. Therefore, it can potentially contribute to decrease the heating and cooling carbon footprint, leading to important environmental benefits (European Commission, 2016;

Eurostat, 2017; IEA and World Bank, 2015; REN21, 2017). A major advantage of shallow geothermal energy lies in the reliability of its supply as well as its nearly unlimited availability. It is a local form of energy that would reduce the import of supplies from other countries, thus leading to independence from economical and political situations. Furthermore, a review carried out in 2010 showed the important role that geothermal energy can play in a country's energy mix, given also the increasing economic competitiveness (Lund et al., 2011).

A branch of shallow geothermal energy has been gaining increasing popularity in recent decades, that is energy geostructures (Brandl, 2006; Laloui and Di Donna, 2013, Barla and Perino, 2015). Energy geostructures can be defined as all those ground-contact structures that provide both a structural support and an energy contribution to climatization of buildings. The ground temperature at a depth of 10-15 m is relatively constant, around 10-15°C in most European climate zones, up to approximately 50 m (Sanner, 2001; Banks, 2012; Lee, 2013) and is unaffected by seasonal temperature fluctuations. Therefore, the ground can provide refrigeration in summer working as a heat sink and heat supply in winter. Moreover, concrete is characterised by a fairly good thermal conductivity and thermal storage capacity (Brandl, 2006), making it ideal for heat exchange applications.

This multifunctional technology represents an interesting alternative to traditional shallow geothermal technologies, well fitting in the context of an energy system transition that will bring important modifications to the way homes and other spaces will be heated and cooled. By thermally activating the structural elements of a construction in direct contact with the ground, a low enthalpy geothermal system can be achieved. This is obtained by embedding a circuit of pipes into the concrete members and by circulating a heat carrier fluid along it.

The idea of extracting, reinjecting and storing heat from/into the ground through geostructures belongs to the 1980s, when the first base slabs, piles and diaphragm walls were thermally activated, as reported by Brandl (2006). Piles, micropiles, diaphragm walls, anchors, tunnel linings can be mentioned among this technology. Most current applications are related to energy piles and diaphragm walls and many are already operational especially in Austria, UK, Germany and Switzerland, countries that made major pioneering efforts in the field of thermo-active geostructures.

A wide state of the art exists on the structural and thermal performance of energy piles. The thermo-mechanical behaviour was investigated by Laloui et al. (2003) who tested a real-scale energy pile in Lausanne, Switzerland, and also by Bourne-Webb et al. (2009), who performed a pile-loading test in London. Good thermal performances were found in the energy piles installation at Dock Midfield, Zurich airport (Pahud, 2013), confirming economic convenience compared to traditional heating and cooling systems. Knellwolf et al. (2011) developed a tool called Thermopile that computes thermally induced stresses and strains based on the load-transfer curves method, by discretizing the pile in segments and taking into account interaction with the supported structure. A comprehensive study about the thermo-mechanical effects of pile groups, instead of single piles, can be found in Rotta Loria (2017), while Di Donna (2014) focused on the response under thermal cyclic loadings. Support for building cost-effective energy piles can be found in literature (Alberdi-Pagola, 2018). Simplified thermo-mechanical design charts are provided by Mroueh et al. (2018) for the assessment of head settlements and variations in axial load and the impact of the thermal solicitation choice on structural design of energy piles is addressed by Rammal et al. (2018a). The importance in the way the pile-soil contact is modelled emerges in Suryatriyastuti et al (2012). Adinolfi et al. (2018) investigated the geotechnical long-term behaviour of a single energy pile installed in the Neapolitan area through coupled THM numerical analyses after validating them against experimental data related to the above-mentioned experimental site in London (Bourne-Webb et al., 2009).

The possibility of equipping walls as ground heat exchangers has been explored in the last years. Through a parametric numerical study Di Donna et al. (2016) identified the main factors that can affect the energy performance of diaphragm walls, namely pipe spacing, temperature difference between air and soil and concrete thermal properties. The importance of pipe layout and of thermal boundary conditions at the excavation boundary is highlighted by Sterpi et al. (2017), who also recommend caution in the assessment of thermally induced additional displacements and internal forces that, albeit likely not detrimental, are not negligible. Bourne-Webb et al. (2015) agree about the importance of the excavation boundary condition stating that most of the heat exchange occurs with the underground void system, but do not believe that thermo-mechanical effects are significant, as most of these are produced by the natural temperature variations compared to which thermal activation adds very little contribution. Sterpi et al. (2018,2019) analysed field data concluding that the excavation side highly affects the heat transfer process changing the heat flux direction and that a major component in thermal efficiency is given by the below excavation portion, whose thermal boundary condition is given entirely by the temperature stable surrounding soil. For this reason, they suggest enhanced Single-W and Double-W layouts that minimise interference between branches where fluid is at different temperature and takes advantage of the ground-embedded portion. Other studies are those by Barla et al. (2018), about the thermal and structural performance, and by Delerablée et al. (2018), discussing the possibility of equipping the Grand Paris metro stations with thermoactive walls. Additionally, Rammal et al. (2018b) investigated the hydro-thermal behaviour of geothermal walls by developing a new approach to distinguish conductive and advective exchanged heat. A similar strategy is adopted by Delerablée et al. (2019) to investigate the energy performance of a metro station.

Some researchers analysed the performances of energy micropiles (Ronchi et al., 2018) finding specific heat fluxes similar to energy piles. Studies on thermal management and impact of energy geostructures at the city-scale are provided by Epting et al. (2013) and by Ryzynski and Bogusz (2016). The noticeable diversity in regulations on shallow geothermal energy systems and institutional support emerges in the review by Tsagarakis et al. (2020).

The difficulties met in boosting the use of the technology in practice might be related to its multi-disciplinary nature, requiring coordination among multiple experts and research in several disciplines, both technical, juridical and humanistic. As discussed in Tsagarakis (2020) and Tsagarakis et al. (2020), issues hindering a wide spread of shallow geothermal energy installation in general are related to some barriers such as high installation and investment costs, lack of legal framework, stakeholders' lack of knowledge, lack of an in-depth financial analysis, lack of experience. Financial incentives should be also stimulated at the institutional level.

Recently, an interest in applying this technology to tunnels has grown, as witnessed by the number of studies that investigate thermal exploitation through tunnels and that will be presented hereafter.

2.3. Thermal activation of tunnel linings

By taking advantage of the nearly constant temperature of the ground up to approximately 50 m, the tunnel lining can be turned into a ground heat exchanger by including heat exchange pipes to form a close loop, as in standard low enthalpy geothermal applications such as vertical or horizontal borehole heat exchangers (BHE). Unlike these, the construction cost is significantly lower as no boreholes need to be drilled for this specific purpose and no additional space for construction is required, which makes this technology an interesting alternative to conventional shallow geothermal systems, especially in central, densely populated urban areas,

where possible end users are in the immediate vicinity and their heating and cooling demand can be easily met. Previous forecasts show that the increased costs of the tunnel infrastructure related to the geothermal activation amount to about 1-2% (Barla et al., 2016; Barla and Di Donna, 2018; Geimer, 2013; Moormann et al., 2018), while savings of about 73% can be reached compared to vertical closed loop GHE (Tinti et al., 2017). Therefore, the payback times are comparable with conventional geothermal applications, amounting to around 5-15 years, which is still low compared to the longevity of such infrastructures (Barla et al., 2016; Bourne-Webb et al., 2013; Moormann et al., 2016). A major advantage in comparison to thermal activation of building foundations, is that larger ground-contact activated volumes can be achieved. Energy tunnels thus take over an energy function in addition to the main static one with little added technical outlay. Also, the shallow location, especially in aquiferous soil, represents an ideal condition for geothermal exploitation. As in traditional closed loop no interferences with groundwater are created, with great benefits for the environment, in contrast with open loop systems.

The system consists of a primary geothermal circuit, a secondary circuit and a water-source heat pump unit coupled with the ground heat exchangers collectors and/or a cooling machine (Figure 2.1). A heat carrier fluid (water, water with anti-freeze as glycol or saline solution that can work down to -20°C) is circulated by a hydraulic pump in the loop, extracting heat in winter. The warmed fluid is then further heated thanks to the heat pump to increase its energy level, typically from $10\text{-}15^{\circ}\text{C}$ to $25\text{-}35^{\circ}\text{C}$ as stated by Brandl (2006) and a distribution pipes network delivers the heat to the final users through the secondary circuit. In summer, excess heat is withdrawn from the building via air- or water-cooling systems embedded in floors, walls and ceilings and dissipated/stored into the soil via the absorber pipes. In this case the heat pump reduces fluid temperature below that in the conditioning system, thus improving reinjection effectiveness. In the case of free heating or free cooling the heat pump can be omitted thanks to favourable soil temperatures and the only electricity input is that needed to run circulation pumps. For instance, in free cooling mode the warm fluid is directly dissipated in the ground by skipping the heat pump and gaining in efficiency.

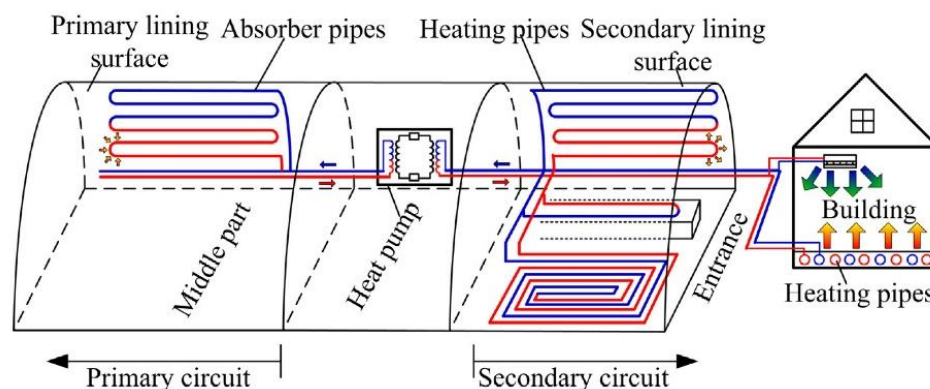


Figure 2.1: Basic principle of tunnel lining ground heat exchangers (from Zhang et al., 2014).

Different HVAC uses of the extracted and injected heat can be mentioned, such as heating and cooling of subway stations or buildings near the tunnel (Nicholson et al., 2014; Barla et al., 2016), heating the lining itself (Zhang et al., 2014), de-icing at the tunnel portals (Islam et al., 2006), road pavements, bridge decks (Dupray et al., 2013; Bowers and Olgun, 2013), platforms etc. (Figure 2.1). Temperatures needed for these applications are around 40 to 50°C ,

although direct heating can be applied to keep traffic surfaces free of ice and snow (Franzius and Pralle, 2011).

Usually, the operating temperatures can be considered in the range 4-30°C (Knellwolf et al., 2011), but in some cases temperatures up to 40 and 50°C can be reached, either because of a non-optimised operation or because heat is recharged in the ground from waste heat or solar panels.

While for cut-and-cover tunnels already existing methods for pipes installation can be adopted (bored piles, diaphragm walls, base slabs), for mined tunnels, depending on the tunnelling technique, pipes can be laid according to different configurations. In 2.3.1 and 2.3.2 two technological solutions, pertaining to conventional and mechanized tunnelling methods, are described, energy geotextile and energy segmental lining.

2.3.1. Energy geotextile

For tunnels excavated with conventional techniques (NATM) the concept of energy fleece (Markiewicz, 2004), energy geo-textile (Markiewicz and Adam, 2003; Markiewicz et al., 2005; Lee et al., 2016) or in general of tunnel lining ground heat exchanger (Zhang et al., 2014) can be found in literature. The energy textile is a textile-type ground heat exchanger placed between a guided drainage geotextile for easier mounting and a shotcrete primary layer, that is installed together with the tunnel support systems. First experiences dealing with mounting and efficiency of the energy geotextile date back to 2003, when a test facility was included in LT22 of the Lainzer Tunnel in Vienna (Figure 2.2a,b). Here the first worldwide energy geotextile was installed, as illustrated by Adam and Markiewicz (2009) and Unterberger et al. (2004). Pipes were fixed to non-woven geosynthetics off site and then located between the primary and the secondary lining. Schneider and Moormann (2010) reported about a geothermal test section at the Stuttgart-Fasanenhof urban rail Tunnel, the first of its kind in Germany, within the framework of the GeoTU6 research project (underground line U6, 380 m long). Pipes were mounted on a geotextile by taking advantage of assembly rails and installed in two 10 m-long sections (B73 and B82) between the outer shotcrete shell and the concrete one, forming four partial circuits for redundancy reasons, for a total of 800 m of pipes covering a surface of 360 m² (Figure 2.2c,d). High-pressure cross-linked PE pipes (25 x 2.3 mm) were used. The two blocks were connected in parallel to optimise the system from the hydraulic point of view. The Authors state that beside catering for a lower output for circulation pumps operation, venting of the pipes is simplified. The main pipe running on the slab connects the pipes to the heat pump being part of the test rig located in a service room of the nearby tunnel station. A heat accumulator and various valves can also be found in the room. In Schneider and Moormann (2010) it is said that the 2 blocks should support the air-conditioning in the service room of Europaplatz station, whereas Moormann et al. (2016) point out that they exclusively work as a test plant without a specified consumer. Lee et al. (2012) and Lee et al. (2016) described the construction of a test bed of energy textile in the middle of an abandoned 200 m-long railroad tunnel in Seocheon, in west South Korea, where three different pipes layouts (transverse, longitudinal and slinky) and four pipes locations within the lining (wall-attached and centered, with or without drainage layer) were tested to evaluate thermal performance, for a total of six modules (Figure 2.2e,f). Each module was 10 m-long and 1.5 m-high, with polyethylene (PE) pipes 15 mm in diameter and 2.5 mm-thick. This example demonstrates that if no (or limited) shape constraints are to be fulfilled, this system can even be introduced a posteriori on the already existing tunnel wall. Zhang et al. (2014) illustrated the setup of a 200 m-long section equipped with polyethylene absorber pipes 600 m away from Linchang Tunnel's entrance in the city of Yakeshi in Inner Mongolia Autonomous Region, China (Figure

2.2g,h). The aim was to avoid the risk of freezing damage that often threatens tunnels in this region, by using a new economic and environmentally friendly heating system as an alternative to traditional electrical-driven or coal carbon-driven systems. In the middle of the tunnel temperatures are much higher than at its entrance, as in this cold region the annual air mean is -2.2°C . Pipes were 25 mm in diameter and 2.3 mm-thick and they were placed between the primary and the secondary lining. The secondary circuit is formed by a lining heating section and a ditch heating section, both insulated from the tunnel inner environment. The heat carrier fluid flow rate was 0.6 m/s.

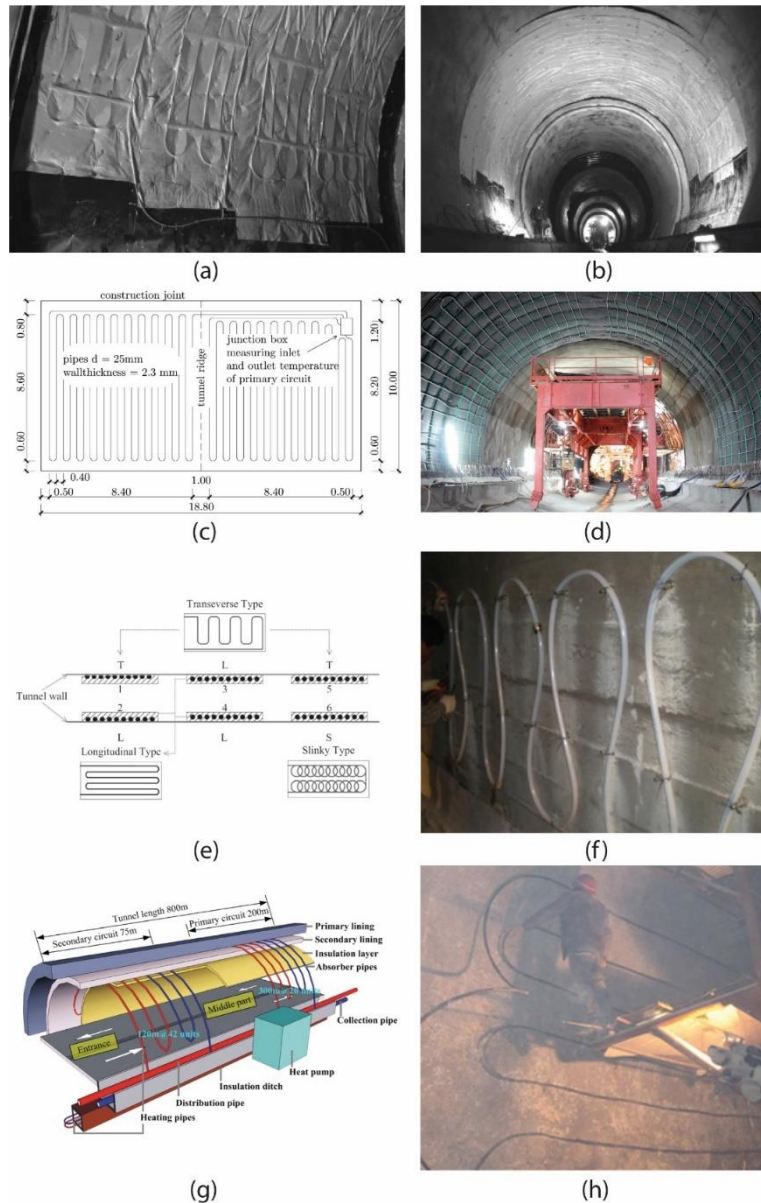


Figure 2.2: Examples of energy geotextile installations: (a,b) Lainzer Tunnel (from Adam and Markiewicz, 2009); (c,d) Stuttgart-Fasanenhof Tunnel (from www.bine.info; Schneider and Moormann, 2010); (e,f) Seocheon tunnel (from Lee et al., 2016; Lee et al., 2012) and (g,h) Linchang tunnel (from Zhang et al., 2013; Zhang et al., 2014).

An interesting use of tunnel as a heat exchanger is described in Islam et al. (2006). Horizontal U-Tube (HUT) were developed to control pavement temperature, prevent road from freezing, avoid winter accidents and were installed in Nanaori-Toge tunnel in Japan in 2002. As shown in Figure 2.3a, HUTs were buried 1.2 m below the road surface in the central part of the tunnel, while an anti-freezing pavement was incorporated at the tunnel portal at a depth of 70 mm. Road temperature is automatically controlled: the system activates when the temperature at a depth of 10 mm falls below 5°C and stops when the threshold of 8°C is reached. Figure 2.3b exemplifies the effect of the pavement heating system compared to a section that is not equipped with the same technology.

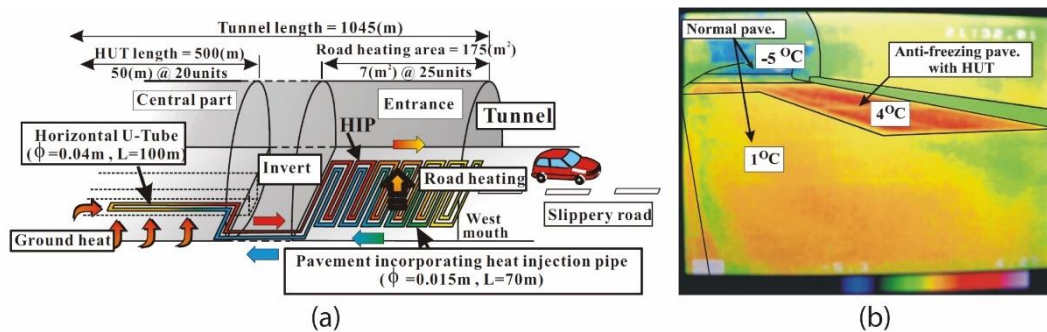


Figure 2.3: (a) Schematic view of the HUT system and (b) thermal picture showing the difference between temperature-controlled and non temperature-controlled pavement (from Islam et al., 2006).

2.3.2. Energy segmental linings

If the tunnels are built by using tunnel boring machines (TBM) and segmental linings, absorber pipes are integrated in the prefabricated concrete segments during manufacturing, before casting (Nicholson et al., 2014; Barla and Perino, 2014; Barla and Perino, 2015; Barla et al., 2016; Di Donna and Barla, 2016), as shown by the experience gained at Katzenberg Tunnel (Karlsruhe-Basle new high speed railway) and at Jenbach tunnel in Austria (Franzius and Pralle, 2011; Frodl et al., 2010; Moormann et al., 2016), on the northern approach route to the Brenner Base Tunnel in the Tyrol. In the former a short semi-circular test section made of five segments for a total surface of 60 m² was activated for a field trial in 2009 before tunnel opening using a temporary monitoring system and heat pump. In the latter a 54 m-long section (2000 m²) was dimensioned to cover the heat demand of the nearby city council (43 kW are being supplied since 2012, 15 of which extracted from the ground – Frodl et al., 2010). This was the first worldwide energy lining segmental heating system. Cross-linked polyethylene (PE-Xa) pipes are laid in the segments in loops by mounting them on the reinforcement cage (Figure 2.4a) or on a light support mesh (e.g. in the case of fibre reinforced segments) and special waterproof coupling elements connect them hydraulically between different segments and different rings (Figure 2.4b-c). The cover is not affected as pipes are fixed inside the reinforcement outer layer. The PE-Xa pipes are characterized by high durability and are able to resist corrosion, high pressures and temperatures. As tunnel lifetime is designed to be more than 100 years, it is important to use a likewise durable material for the geothermal plant. Typically, at the start and return end of the high-density polyethylene plastic pipes loops, a manometer and locking valves are fixed: the circuit is pressurized for checking integrity and to avoid collapse under the concrete mix. The same reinforcement cages and moulds as for standard segments can be used, without affecting the efficiency in the production process.

A box-out is installed into the formwork to create the coupling pockets facing the tunnel's interior. The size of the pockets should be kept as small as possible so as not to reduce the longitudinal joint contact. Pressure tests can be done to verify that the pipe fails earlier than the joint (as for the Everloc permanent connection described in Nicholson et al., 2014). Great accuracy is needed to ensure the connection between pipe-ends of adjacent segments. Usually the connection takes place from the TBM backup as soon as segments have been erected at the tunnel face. The backfilling of the annular gap provides the thermal bridge between the energy segments and the soil. At Jenbach tunnel 27 rings were instrumented and connected in pairs to a distribution module. An insulated collector pipe 170 m-long runs through a rescue shaft from this module to the yard of the heated building, where the heat pump is located. Responsibilities between parties were contractually defined: the owner of the tunnel is also the owner of the pipework and collector system, while the owner of the heat pump system is the consumer (Frodl et al., 2010). Therefore, the rescue shaft represents a kind of boundary line of ownership and responsibilities. An external and independent energy supplier could operate and maintain the plant by accessing the collector system, acting as a go-between operator-consumer. An alternative to this model is that the tunnel owner directly acts as energy supplier selling the heat to the consumer.

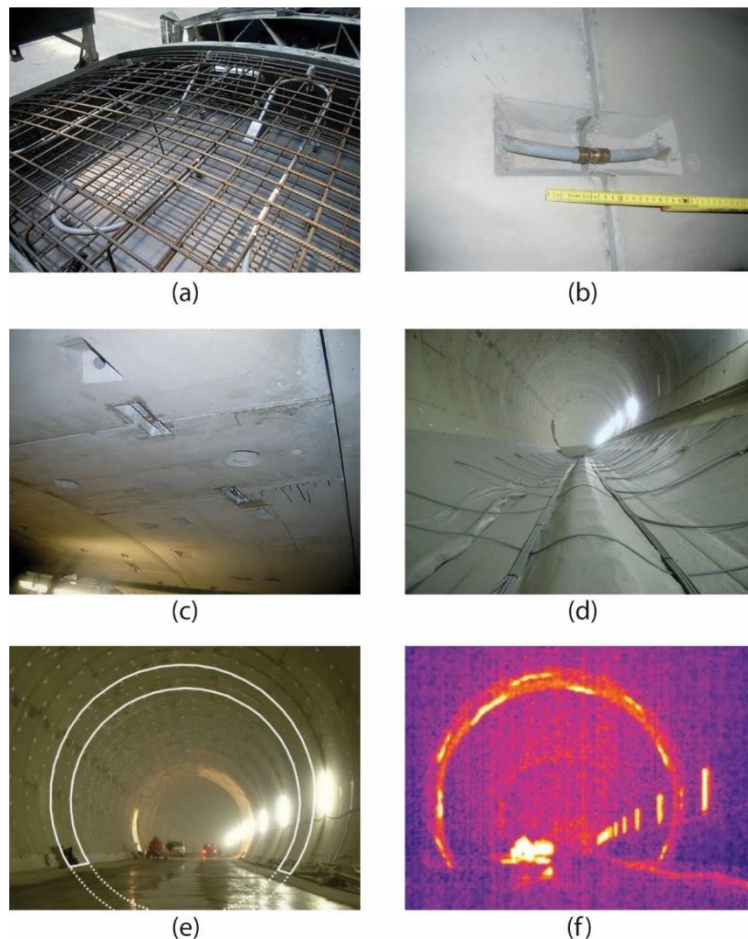


Figure 2.4: Details from Jenbach TBM-driven energy tunnel: (a) absorber pipes, (b-c) connection among adjacent segments, (d) connection circuits before invert slab installation, (e-f) conventional and geothermal view during operation (from Frodl et al., 2010).

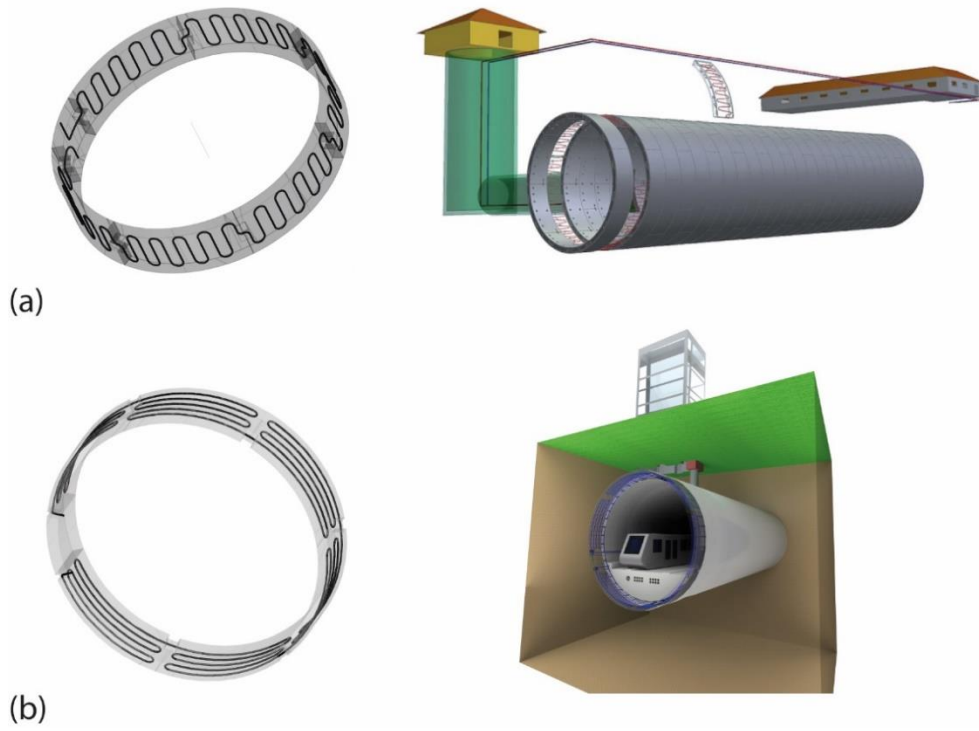


Figure 2.5: Energy segmental lining: (a) pipes with main direction parallel to tunnel axis, (b) pipes with main direction perpendicular to tunnel axis, together with plant view of their connection to the consumer (modified from Barla and Di Donna, 2016; Frodl et al., 2010).

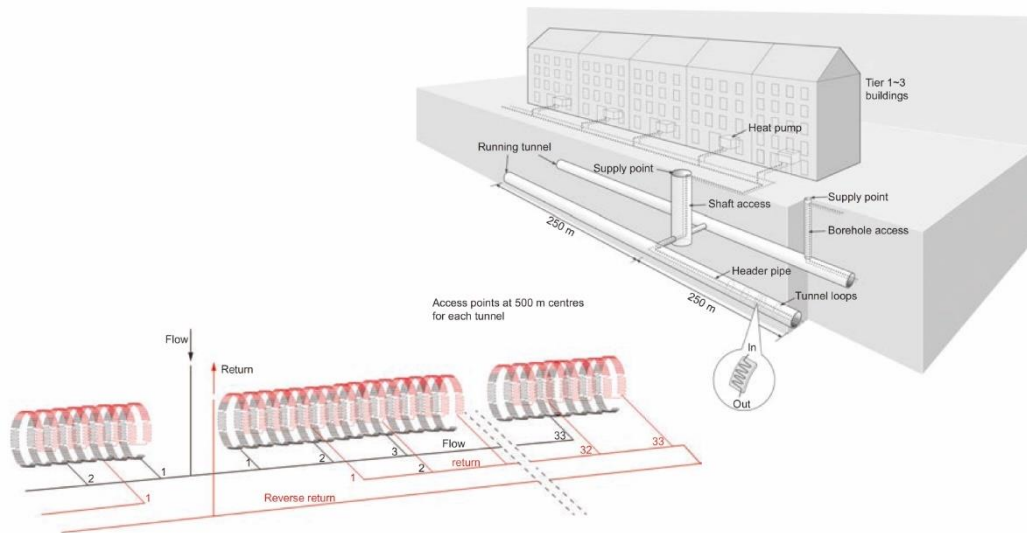


Figure 2.6: Schematic pipework connections with subcircuits made up of five in series-rings (from Nicholson et al., 2014).

A schematic representation of energy segmental lining is given in Figure 2.5. Usually 6-7 segments compose each ring, with a thickness of 30-50 cm and a width of 1-2 m, and two or more rings can be connected in parallel so that a sub-circuit is created, thus reducing the number of connections on the main conduit and the consequent head losses. No specifications can be found in literature on the ideal number of rings that should be connected in series to optimize the plant from a thermal and a hydraulic point of view. The sole, though not very well argued, technical solution in this direction is given in Nicholson et al. (2014), where five neighbouring rings are connected in series to form a single circuitry, then connected to the main flow and return pipes (Figure 2.6); control valves are suggested to isolate individual subcircuits in case of local failure and for de-airing. Indeed, flushing operations have to be envisaged to remove air bubbles trapped in the pipes. Nicholson et al. (2014) recommend doing this in two phases, first for the individual ring circuit then for the header pipes.

2.3.2.1. Enertun: a new concept of energy segmental lining

When designing an energy geostructure, many factors could be considered to enhance thermal exchange and make it optimal, such as surface and width of concrete members or choice of materials according to thermal conductivity. However, very few projects have taken into account the geothermal design as a priority aspect to maximise energy output (Amis and Loveridge, 2014). Most of the times, the thermal design follows the structural and geotechnical design and thermal capacity should be evaluated starting from a given layout. In this situation, the need to optimize heat exchanger elements configuration is essential to make the geostructure more efficient and to be able to answer more adequately to buildings thermal loadings. In the case of energy tunnels (but this applies to every energy geostructure) the clients will be conscious of the value added thanks to the almost free harvesting of ground-trapped energy, which allows to take advantage of a reliable amount of energy that would otherwise remain unexploited. However, they will surely require that the preparation and installation of energy segments do not affect the production timeline and/or delay the delivery of the work (Bourne-Webb et al., 2013). Moreover, safety aspects, such as the measures to be undertaken in case of possible malfunctioning of a section of the geothermal circuit, will be asked to be envisaged. Transforming a tunnel lining into a heat exchanger thus requires a specific, viable and efficient design strategy.

Based on these assumptions, some solutions have been presented to the market. Recently, given the increasing number of tunnels excavated by means of TBMs, a novel energy tunnel precast segmental lining, named Enertun, has been designed and patented (Patent Priority number: 102016000020821) at Politecnico di Torino (Barla and Di Donna, 2016; Barla and Di Donna, 2018). The aspect of novelty, compared to previous configurations (Franzius and Pralle, 2011; Figure 2.5a), lies in the pipes layout, whose main direction is circumferential (see Figure 2.5b, whereas it is longitudinal in Figure 2.5a), as it is said to reduce head losses by 20-30% because of the lower number of bends and increase thermal efficiency when groundwater flow is perpendicular to the tunnel axis (by 5-10% for the same material employed and the same pipes length, based on coupled thermo-hydraulic numerical analyses - Barla and Di Donna, 2016; Barla and Di Donna, 2018).

The role of groundwater flow will be discussed later (see 2.4.5), but it can be anticipated that it is well known that groundwater flow contributes significantly to the energy efficiency of geothermal systems (Di Donna and Barla, 2016), subsequently the interest in installing energy tunnels increases in zones where a groundwater flow exists. Improving the energy efficiency of these applications in such conditions becomes consequently of primary importance. Figure 2.7 shows the heat exchanged by a ring of energy tunnel lining, comparing

Enertun configuration with the one employed in the past. The numerical approach, geometry and materials considered are those illustrated in Barla et al. (2016). If no difference is shown in the absence of groundwater flow, an increase of about 10% is found when considering Enertun in the case of groundwater flow perpendicular to the tunnel axis, as the heat carrier fluid flows parallel to the direction of the groundwater flow for most of its path.

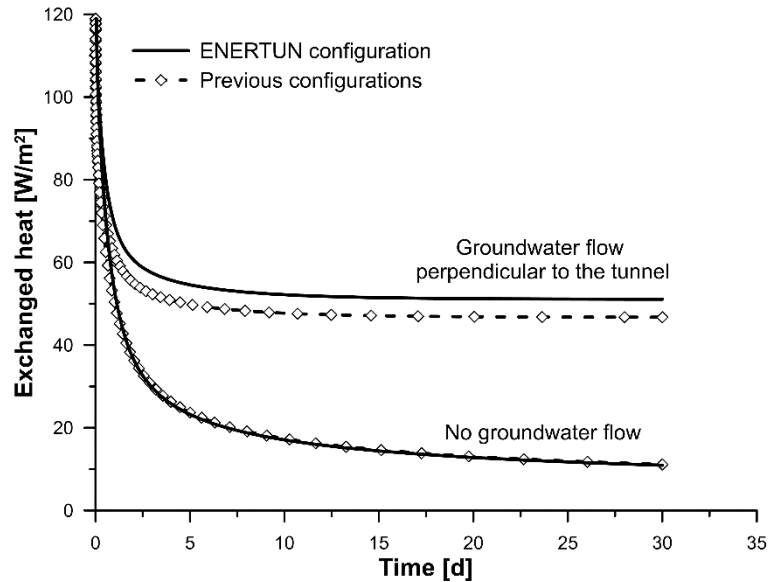


Figure 2.7: Comparison between Enertun and previous configurations in terms of heat (modified from Barla et al., 2019).

The Enertun segment is innovative in proposing three different layouts, each of which is designed for a specific purpose and can therefore fulfil different needs:

- the ground configuration (Figure 2.8a), which is conceived to facilitate heat exchange mainly with the ground, making it dominant, has a unique pipes circuit positioned close to the segment's extrados and to the ground;
- the air configuration (Figure 2.8b), which allows to operate mainly on the air inside the tunnel, has a unique pipes circuit positioned close to the intrados and was conceived with the purpose to combine this application with the need for decreasing internal temperature of hot tunnels, limiting inner overheating due to traffic and ventilation costs;
- the ground&air configuration (Figure 2.8c), which is a combined solution that fulfils both previously mentioned tasks, thanks to a double circuit which can be either fully activated to exchange heat simultaneously with the ground and the air inside the tunnel or partially activated to endorse one or the other side.

The selection of the most adequate configuration depends on the purpose. In the case of a metro tunnel, the surface space will be characterized by an urban environment and the need to extract, inject and store heat in the ground for the conditioning of buildings will be of primary importance. The solution called “ground” would be appropriate in this case. Moreover, this solution could also have a beneficial effect by limiting the long term thermal disturbance of subway transport on the surrounding ground environment (Fouché et al., 2018) on one side and the rise in tunnel air temperature due to the operation of the trains (Nicholson

et al., 2014) on the other side. The “air” configuration results to be more appropriate for those situations where the tunnel’s air needs to be cooled down, which can occur for example in the case of mountain tunnels, hundreds of meters deep. In a mountain environment, potential users can be very far compared to urban tunnels, but the need for tunnel cooling is particularly critical and the air configuration can represent an attractive solution to improve self-sustainability of the infrastructure.

The present research focuses on Enertun thermal and structural behaviour.

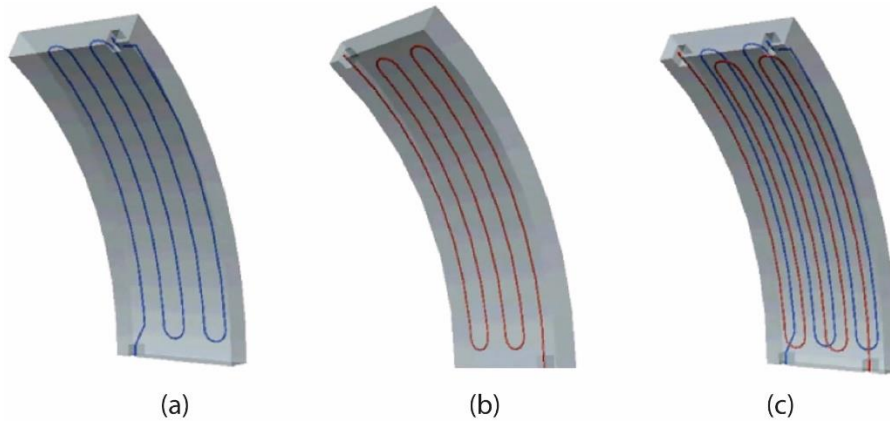


Figure 2.8: Configurations of the Enertun patent: (a) ground, (b) air and (c) ground&air.

2.3.3. Technical aspects

As for every energy geostructure, three different operating regimes can exist, depending on the scope and on the user: pure geothermal energy extraction (usually for small properties), pure energy input or seasonal operation (for larger structures). In the latter the thermodynamic inertia of the soil can be used to store energy in the ground to be used again later and to reach energy balance over the annual period (Markiewicz et al., 2005; Brandl 2006; Bouazza et al., 2011; Adam and Markiewicz, 2009; Loveridge et al., 2017). For instance, by conveying waste heat derived from buildings cooling, this energy can be later used during winter operation, enhancing cost-effectiveness especially for low-permeable soils.

The linear parts of the pipes can range from 3 to 7. Pipes external diameter ranges from 15 to 35 mm and their thickness between 1.5 and 3 mm. The distance from intrados/extrados can be 5-15 cm and the mutual distance between pipes is 20-40 cm to meet minimum bending radius. Pipes lengths of 20-30 m occupy each segment. To guarantee efficient heat exchange, a turbulent flow has to be maintained in the circuits. Figure 2.5a,b exemplifies the connection of the two different solutions of energy segmental lining, with main development direction hoop and longitudinal, to the consumers through shafts, stations or dedicated access boreholes.

Depending on the temperature inside the tunnel, hot and cold tunnels can be distinguished (Figure 2.9): in the former inner temperature is higher than that of the ground due to the passage of trains/cars and internal diameter typically is 7 m, while in the latter it is closer to that of the ground (Barla et al., 2016) or of external air (Barla and Perino, 2014; Nicholson et al., 2013) and, in any case, relatively low (about 15°C) all year round. While cold tunnels can be efficiently used both for heating and cooling purposes, hot tunnels are only efficient for heating, but their internal environment can also be cooled, such as in the case of Alpine tunnels where temperatures of between 30 and 50°C can be encountered. It goes without saying that

the more different are tunnel and soil temperature in comparison to ambient temperature, the more efficient and suitable is the system. An example of hot tunnel is given by Nicholson et al. (2014), as at Crossrail the waste heat rejected from trains is remarkable, especially due to braking, accelerating and waiting close to the stations, and can warm the ground. They state that in some parts of the tunnel, temperature can reach 30°C and computed that thanks to the base and peak heat output from trains on a 500 m-long section, the heat demand of 100 family apartments could be satisfied by extracting excess heat from the tunnel and subsequently cooling the tunnel. In this context heating of nearby buildings and simultaneous cooling of the tunnel is beneficial, while the injection of heat could cause problems to the tunnel operator. Cold tunnels typically are road tunnels or, more in general, short-run tunnels, with a large internal diameter of 10-12 meters and their effect on the surrounding ground is limited. An example is given by Jenbach tunnel.

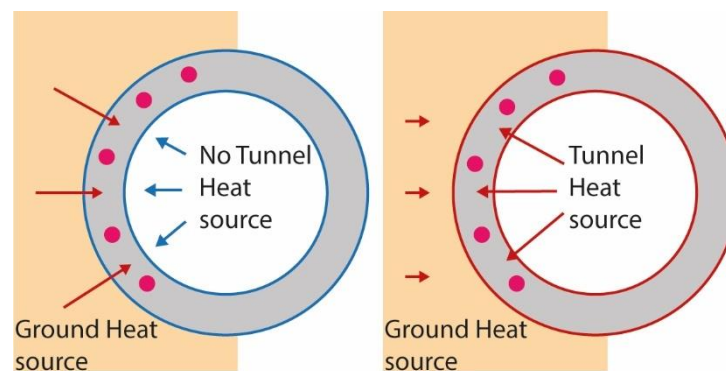


Figure 2.9: Illustration of cold (left) and hot (right) tunnels (modified from Nicholson et al., 2013).

The implementation of energy segments deals with a number of technical and management challenges (Franzius and Pralle, 2011; Nicholson et al., 2014; Bourne-Webb et al., 2013; Amis and Loveridge, 2014; Adam and Markiewicz, 2009):

- lining structural integrity and durability must not be altered and watertightness must be ensured;
- fire, heat and ventilation requirements still must be met;
- normal tunnel construction must not be delayed due to pipes integration in factory and to pipes connection in situ and costs should remain sustainable. This issue could be cancelled with good early coordination;
- potential users have to be identified and managed; the heat withdrawn from the tunnel could be supplied to blocks of buildings along the tunnel axis through a district heating network and sold to district heating companies, ensuring a revenue to the tunnel operator that finances the implementation of the energy tunnels technology. The exploration of innovative business models is still an open issue;
- roles and responsibilities should be clearly set and accurately defined in advance.

The interaction of the system with the ground has to be studied, together with its sustainability in the long term (implications on infrastructure lifetime, temperature alterations in the ground, subsidence in the surrounding buildings).

Another type of geothermal exploitation through tunnel structure is the direct use of warm groundwater, especially in many Alpine tunnels in Switzerland (Moormann et al., 2016;

Wilhelm and Rybach, 2001; Rybach, 1995), where drainage water can be used for heating of tunnel control centres, public buildings or residential properties instead of discharging it, with ecological and economical advantages. However, their description is not in the scope of the present study.

Figure 2.10 illustrates the cumulative number of energy geostructures since 1993 and their spatial distribution (Di Donna et al., 2017). As highlighted by Di Donna et al. (2017) energy tunnels appeared more recently compared to energy piles and energy walls and attribute their slower evolution to technical difficulties such as identifying the owner of the heat and distributing the heat. This is the reason why design and applicability concepts for construction of energy tunnels are not well established yet. As stated by Markiewicz et al. (2005), scientific monitoring of real-scale installations is essential to better adapt energy tunnels to each site-specific hydrogeologic condition and to optimize their design. Barla et al. (2016) claim that the number of real implementation cases is limited probably because a cost-effective analysis strongly depends on the specific characteristics of the site, not easy to assess. This same argument is reported by Moormann et al. (2018): according to them, in fact, the proposal of equipping tunnels with absorbers fails at the design stage, as complex tools such as numerical simulations, out of normal engineering practice, are required to estimate the possible extraction rate, although it would be easy to integrate thermal activation in the design process if considered at an early stage. In the next chapters available studies will help the reader to shed some light on these topics.

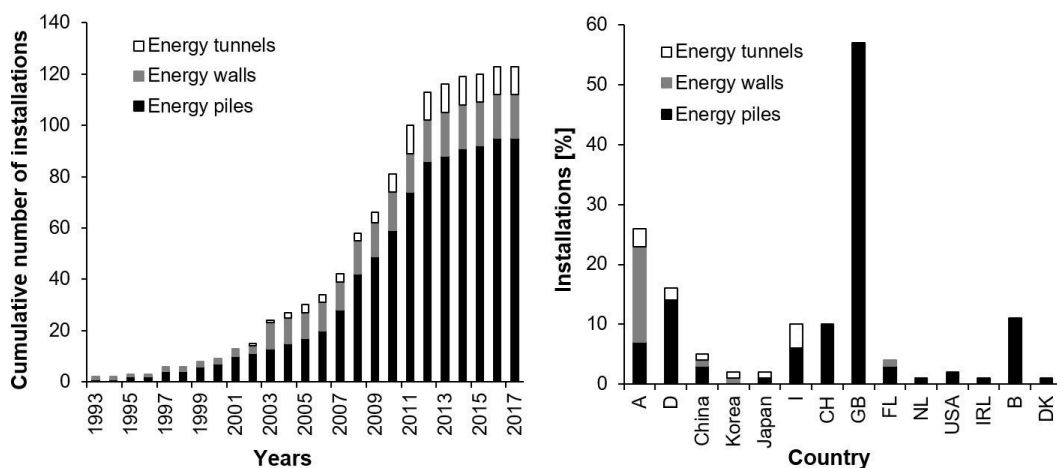


Figure 2.10: Time and spatial distribution of energy geostructures (modified from Di Donna et al., 2017).

2.3.4. Working principle of a heat pump

A heat pump is a device that absorbs heat from a low temperature source and rejects it to a high temperature sink. For instance, during winter it transfers heat at $-5\div 15^{\circ}\text{C}$ from the ground (Ground Source Heat Pump, GSHP) or the ambient air (Air Source Heat Pump, ASHP) to an interior building's space at $19\div 23^{\circ}\text{C}$. In summer the opposite operation takes place, heat is absorbed from the building's interior at $26\div 29^{\circ}\text{C}$ and rejected to the ground or ambient air at $25\div 40^{\circ}\text{C}$ to cool that space. While in winter the ground is the low temperature source, in summer it becomes the high temperature sink.

Heat pumps denomination is based on the heat transfer medium for the outdoor heat exchanger, indicated first, and that for the indoor heat exchanger (UNI EN 14511-1:2018,

2018). In shallow geothermal applications water-to-air and water-to-water heat pumps are commonly used.

The working principle of a heat pump is not very different from that of a reverse refrigerator. However, in the heat pump evaporator heat absorption and condenser heat emission occur at a higher temperature. Thanks to a low electrical energy input, the originally non-usable heat temperature is raised to higher, usable levels. In the general case of a reversible heat pump, suitable also for cooling, it can be said that the temperature is adapted to an appropriate level for heating, ventilation and air conditioning applications.

The operation of a heat pump needs power consumption to produce heat transfer. The following relationship holds true:

$$Q_r = Q_a + P_c - Q_l \quad \text{Eq. 2.1}$$

where Q_r is the heat rejected into the high temperature sink, Q_a is the heat absorbed from the low temperature source, P_c is power consumption and Q_l are thermal losses.

The operational scheme of a compression heat pump is exemplified in Figure 2.11. A working fluid, called refrigerant, is used. The refrigerant is a substance able to evaporate at low temperatures and to condensate at high ones. Heat exchange from the primary circuit to the refrigerant fluid occurs in the evaporator, while heat exchange from the refrigerant fluid to the secondary circuit takes place in the condenser. The basic principle is that when a fluid evaporates into a gas it absorbs heat, while the gas gives it off when condensing back to a liquid. This circular closed-loop process is the vapour compression cycle or refrigerant evaporation cycle.

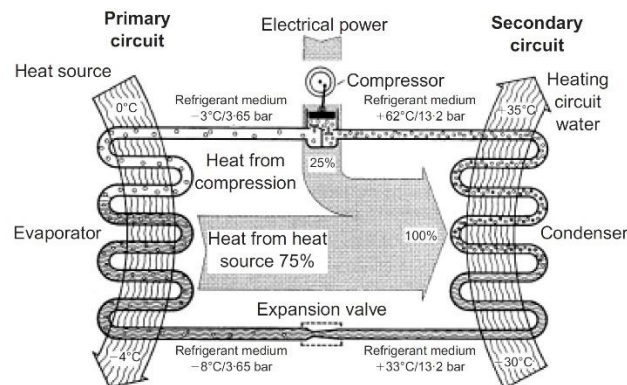


Figure 2.11: Scheme of operation of a compression heat pump (Brandl, 2006).

The main heat pump components are the compressor, the evaporator, the condenser, the expansion valve, the reversing valve and the control system. The evaporator is a coil where the refrigerant (initially liquid or gas/liquid mixture) absorbs heat from the heat source and boils becoming a low-temperature vapour. The compressor is the step that requires power, provided by an electrically driven engine, increases pressure and temperature of the refrigerant. As the evaporator, the condenser is a coil where the refrigerant (initially high-temperature superheated vapour) gives off heat to the heat sink and becomes a gas/liquid mixture or subcooled liquid. The expansion valve reduces the pressure that was created in the compressor, as a consequence temperature drops, and the refrigerant becomes a low-temperature liquid or

gas/liquid mixture. The reversing valve is a four-way valve that allows to perform both heating and cooling by reversing the direction of the refrigerant flow.

The typical parameter that is used to evaluate the heat pump performance is the coefficient of performance, COP, defined as:

$$\text{COP} = \frac{\text{heating capacity of the condenser [W]}}{\text{power input of the compressor [W]}} \quad \text{Eq. 2.2}$$

This is typically used for heating operation, while for cooling the energy efficiency ratio, EER, is used:

$$\text{EER} = \frac{\text{cooling capacity of the evaporator [W]}}{\text{power input of the compressor [W]}} \quad \text{Eq. 2.3}$$

Both the COP and the EER are instantaneous energy performance indicators, not able to describe long-term operation performance. The COP should be at least four for economic reasons, meaning that three quarters of the usable energy in the secondary circuit originates from the ground heat and one quarter comes from electricity. The efficiency is strongly affected by the difference between the actually used and the extracted temperature: if the former is high and the latter is too low, the efficiency decreases. For this reason the acceptable temperature levels should be 0-5°C for the primary circuit and 35-45°C for the secondary circuit. Of course, low-temperature heating (and cooling) systems can profit more from these types of ground heat exchangers.

The seasonal performance factor (SPF) or seasonal COP (SCOP) is defined as:

$$\text{SCOP} = \frac{\text{annual heating demand [kWh]}}{\text{annual electricity consumption for heating [kWh]}} \quad \text{Eq. 2.4}$$

and includes all the energy-consuming components, such as circulation pumps. Standard electric pumps allow to reach SPF values in the range 3.8-4.3. For cooling the seasonal EER (SEER) is used:

$$\text{SEER} = \frac{\text{annual cooling demand [kWh]}}{\text{annual electricity consumption for cooling [kWh]}} \quad \text{Eq. 2.5}$$

In winter thermal capacity and COP increase with an increase in water temperature within the primary circuit, while in summer cooling capacity and EER increase with a decrease of it.

2.4. Thermal behaviour

Energy tunnels are systems characterized by three main elements, that is the heat carrier fluid in the pipes, the surrounding soil or rock-mass and the tunnel air (Tinti et al., 2017; Bidarmaghz and Narsilio, 2018). Their thermal performance is affected by a number of factors, among which arrangement of the pipes, thermo-hydraulic properties of the ground, presence and velocity of the groundwater flow, tunnel air temperature, far field ground temperature and thermal load curve.

The main heat transfer mechanisms involved in the problem are illustrated in Figure 2.12. Conduction takes place in the ground, lining and pipe wall, while convection is characteristic

of tunnel air, heat carrier fluid (forced convection) and ground in the presence of a groundwater flow. These mechanisms are investigated in the paper by Bidarmaghz and Narsilio (2018), whose results are described later. For the sake of clarity, it is pointed out that the main heat transfer mechanisms in soils are:

- heat conduction (or diffusion), whereby heat energy is transferred from one region of the medium to another, without visible motion in the medium, by means of the movement of atomic particles (most important contribution in heat transfer for thermoactive geo-structures);
- heat convection, given by the sum of conduction and advection, referred to the transport of heat in a fluid by means of circulation flows. It can be free or forced if driven by internal (groundwater flow) or external forces (pumps), and internal or external if occurring in a pipe for example or around a body;
- radiation, where heat energy is propagated as electromagnetic waves.

Heat transfer occurs when there is a temperature gradient. Conduction is often the dominant mechanisms within the ground, but groundwater flow provides a remarkable contribution by advection. Radiation is usually neglected.

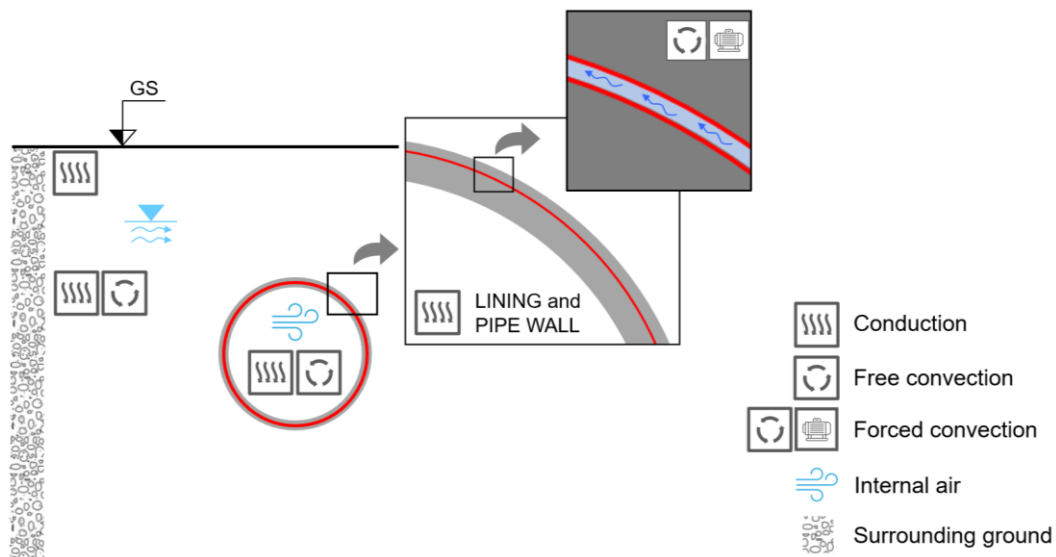


Figure 2.12: Main heat transfer mechanisms involved in the problem of energy tunnel systems.

The operation of the geothermal system has an influence on both the ground and the tunnel climate. In hot tunnels, as seen for the Crossrail (Nicholson et al., 2014) the effect on the second is of vital importance.

The assessment of energy tunnels thermal performance deals with the estimation of the exploitable heat, that can be achieved numerically, analytically or experimentally (real-scale or laboratory-scale). From the numerical standpoint, as it can be read in Barla and Di Donna (2018), it is useless to perform a complete THM simulation, despite structural and thermal response would be obtained at once, as the improvement in the results would not counterbalance the increased difficulty degree.

In all cases the thermal power \dot{Q} in W extracted from the ground in winter and injected in summer can be computed from the following relationship:

$$\dot{Q} = \dot{m} c_p |T_o - T_i| \quad \text{Eq. 2.6}$$

where T_i , T_o are inlet and outlet temperature of pipe circuit in °C, \dot{m} is the mass flow rate expressed in kg/s and c_p is the heat capacity of the heat carrier fluid in J/(kg °C). The power per tunnel lining unit area in W/m² is obtained by dividing by the ring outer (or inner, as in Cousin et al., 2018) surface:

$$\dot{q} = \frac{\dot{Q}}{L\pi D} \quad \text{Eq. 2.7}$$

where L and D are the ring thickness and external diameter. As Tinti et al. (2017) pointed out, it can be seen from Eq. 2.6 that the maximum temperature spread and maximum power occur in different conditions, as a high difference in temperature is obtained with low flow rate that decreases the power and viceversa.

Some results of thermal performance available in literature are shown in Table 2.1, while Table 2.2 and Table 2.3 summarize some relevant geometric and thermo-hydrogeologic characteristics of the same case studies (blank cells mean that no data were found). For the Turin ML1 SE case (Barla et al., 2016), the favourable groundwater flow direction, perpendicular to the tunnel, and the totally submerged location of the tunnel work in favour of thermal exchange compared to other case studies (Buhmann et al., 2016; Moormann et al., 2016; Franzius and Pralle, 2011). In the same study the positive effect of seasonal alternative use of the geothermal resource is mentioned, as no progressive heating or cooling occurs, but winter heat extraction is refilled by summer heat injection. Nicholson et al. (2014) performed a 10-years simulation for the Crossrail tunnel in London where they varied thermal extraction rate from 5 to 50 W/m². For the highest extraction rate, average fluid temperatures were predicted to fall at -6°C, thus operation should be limited to 30 W/m² in order to avoid freezing and to 20 W/m² to achieve good performances of the heat pump thanks to the higher temperatures in the primary circuit. Baralis et al. (2018) estimated the deliverable thermal energy from activating Warsaw SE metro twin tunnels. The peculiarity of the study lies on the definition of a number of representative cross-sections along the line, homogeneous in terms of geothermal parameters, then extending the obtained results for the length of occurrence of those sections. It resulted that more than 11 buildings could be served by the thermal activation of the 1651 m-long line. As in Nicholson et al. (2014) a GIS spatial analysis allowed to identify potential customers falling within 25 m-wide buffer zones around stations and ventilation shafts. Moreover, relative effects of one single-track tunnel on the other were assessed by showing that in permeable soils the downstream tunnel is able to extract up to 17% more thermal energy due to the thermal plume originating from the upstream tunnel. Cousin et al. (2018) dealt with the case study of the Grand Paris Express line, building transient 3D numerical models with constant boundary conditions in order to achieve steady-state solutions at 16 days. They claim that the advantage of proceeding in this way is that more complex thermal loads can be subdivided in constant unit-step loads whose response is known thanks to a number of steady solutions. Steady solutions after 30 days are also considered in Barla et al. (2016) and Di Donna and Barla (2016). However, as pointed out in Bidarmaghz and Narsilio (2018), the groundwater flow rate may affect the time needed to reach steady-state. It is also true that considering the heat flux at the end of the simulation means neglecting the higher fluxes obtained during the transient initial days and this is conservative. Franzius and Pralle

(2011) give a brief description of the test phases at Katzenberg tunnel, where monitoring data, including temperatures in the segments, the ground and the tunnel, showed that heat extraction does not affect the ground at a distance higher than 5 m.

Other results are extracted by Bracq et al. (2017), Fouché et al. (2018), Lee et al. (2012), Zhang et al. (2014). The application of energy tunnels to Grand Paris Express line (Bracq et al., 2017) demonstrated a positive reduction of the impact of tunnel and trains circulation on the surrounding ground temperature from $+2.5^{\circ}\text{C}$ to $+1.5^{\circ}\text{C}$ (-1°C in heating only) at a distance of 6 m from the extrados of the lining, which recalls the study by Nicholson et al. (2014). Interestingly, they provide the heat flux exchanged as the sum of that at the intrados and at the extrados of the lining, which are proportional to the inlet-air and inlet-soil temperature difference respectively. They also raise questions about the management model to be adopted, finding solutions similar to Frodl et al. (2010).

Franzius and Pralle (2011) performed a finite-difference calculation assuming an axisymmetric temperature field around the tunnel, not varying longitudinally, thermally isotropic and homogeneous ground and neglecting the contribution of convection. The cases of i) continuous heat extraction (10 W/m^2), ii) cyclic heat extraction with summer break and iii) cyclic heat extraction and injection were considered, similarly to what was done by Barla and Perino (2015). In Figure 2.13 it is clear that case i) is unviable as it leads to dramatic drops in the extrados temperature and in a premature depletion of the geothermal resource. In case ii) the trend is decreasing, but the extrados temperature remains above 0°C . Similar results are shown for case iii) but heat injection helps in maintaining the extrados temperature higher during the following heat extraction.

In the following the most relevant case studies will be outlined and the governing equation of the TH coupled problem will be enounced. Parametric studies together with the role of groundwater flow, the role of internal air and other applications such as mountain tunnels will be presented and described.

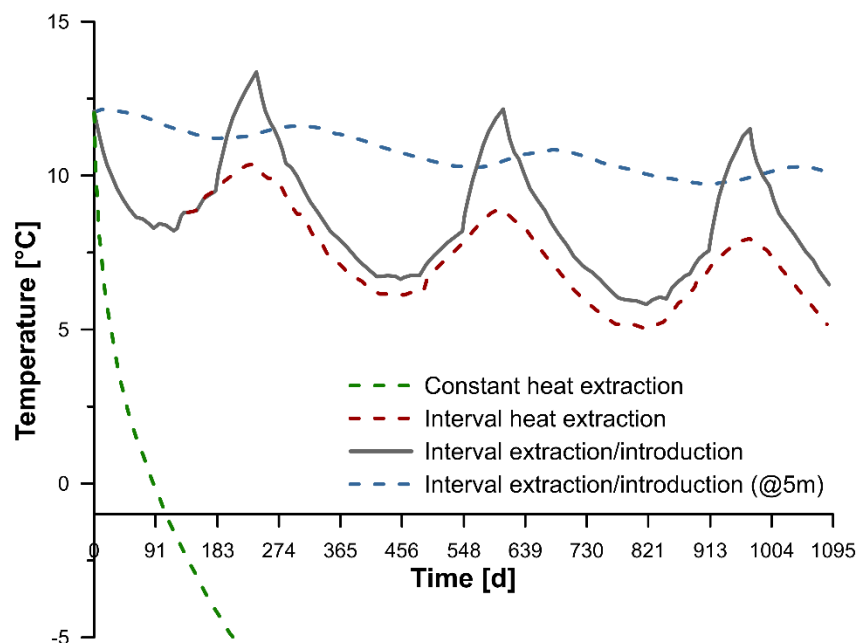


Figure 2.13: Temperature at the tunnel extrados and 5 m far from the lining over three years in different modes of operation (modified from Franzius and Pralle, 2011).

Table 2.1: Thermal performance of the main case studies documented in literature (*=summer mode).

Case study	Study type	Activated length/surface	Q [kW]	q [W/m ²]
Turin ML1 SE - previous configurations (Barla et al., 2016)	Numerical	1350 m	1.67, 2.34*	52.8, 73.9*
Turin ML1 SE - ENERTUN configuration (Barla and Di Donna, 2016)	Numerical	1350 m	1.77	56.0
Katzenberg tunnel (Franzius and Pralle, 2011)	Real	60 m ²	1.0-1.5	17-25
Jenbach tunnel (Buhmann et al., 2016)	Real	54 m, 2200 m ²		10-20
Stuttgart-Fasanenhof tunnel (Buhmann et al., 2016)	Real	2x10 m, 360 m ²		20,5-30*
Crossrail tunnel (Nicholson et al., 2014)	Numerical			5-30
Warsaw NE extension (Baralis et al., 2018)	Numerical	Model 1: 288 m Model 2: 968 m Model 3: 396 m		13.2, 29.5* 15.2, 42.1* 13.6, 36.6*
Grand Paris Express (Bracq et al., 2017; Fouché et al., 2018)	Numerical			15-30, 9-15*
Grand Paris Express (case 2.2 in Cousin et al., 2019)	Numerical	2 m		60-70
Seocheon tunnel (Lee et al., 2012)	Real	10x2 m	0.59-0.71*	
Linchang tunnel (Zhang et al., 2012)	Real	8 m	(10-30 W/m)L*	

Table 2.2: Lining characteristics, groundwater flow and ground temperature for the main case studies documented in literature.

Case study	Lining type	Inner diameter/thickness	Average cover	Groundwater	Ground temperature
Turin ML1 SE (Barla et al., 2016)	Precast	6.8/0.3 m	17.8	Perpendicular flow	14°C
Katzenberg tunnel (Franzius and Pralle, 2011)	Precast				13°C
Jenbach tunnel (Buhmann et al., 2016)	Precast	12/0.5 m	16 m	Below gw table, high velocities, direction unknown	12°C
Stuttgart-Fasanenhof tunnel (Schneider and Moormann, 2010)	Cast in-situ		10 m	Below gw table, no flow	
Crossrail tunnel (Nicholson et al., 2014)	Precast	6.2/0.3 m	15-20 m		14.8°C
Warsaw NE extension (Baralis et al., 2018)	Precast	5.4/0.3 m	7.7-16 m	Perpendicular flow	12°C
Grand Paris Express (Bracq et al., 2017; Fouché et al., 2018)	Precast	8.7/0.4 m		No flow	12°C

Case study	Lining type	Inner diameter/ thickness	Average cover	Groundwater	Ground temperature
Grand Paris Express (case 2.2 in Cousin et al., 2019)	Precast	8.7/0.4 m	15.0-24.5 m	No flow	13°C
Seocheon tunnel (Lee et al., 2012)	Cast in-situ	-/0.2 m		No flow	15°C
Linchang tunnel (Zhang et al., 2014)	Cast in-situ	0.5/0.6 m	100 m	Flow	5.6°C

Table 2.3: Pipes geometry and soil type for the main case studies documented in literature.

Case study	Pipes location	Spacing	External diameter/ thickness	Internal diameter	Geology
Turin ML1 SE (Barla et al., 2016)	10 cm from extrados	30 cm	25/2.3 mm		Sand and gravel
Katzenberg tunnel Jenbach tunnel (Franzius and Pralle, 2011; Moormann et al., 2016)		25-30 cm	20/2 mm		Sand and gravel
Stuttgart-Fasanenhof tunnel (Buhmann et al., 2016; Moormann et al., 2016)			25/2.3 mm		Mudstone, sandstone and marlstone
Crossrail tunnel (Nicholson et al., 2014)	20 cm from intrados	30 cm		20 mm	
Warsaw NE extension (Baralis et al., 2018)		30 cm	25/2.3 mm		1) pliocene clays, 2) fluvioglacial sands, 3) sands (top) and clays (bottom)
Grand Paris Express (Bracq et al., 2017; Fouché et al., 2018)	5 cm from extrados			21 mm	
Grand Paris Express (case 2.2 in Cousin et al., 2019)	at mid-thickness	200 mm	20/1.9 mm		Limestone and sands
Seocheon tunnel (Lee et al., 2012)	wall-attached and centered		15/2.5 mm		
Linchang tunnel (Zhang et al., 2012)	Between primary and secondary lining	50-100 cm	25/2.3 mm		Slightly weathered sandstone

2.4.1. Case studies

2.4.1.1. Stuttgart-Fasanenhof tunnel

This energy tunnel project was instrumented with a number of sensors to measure tunnel air, tunnel lining and ground temperature, as sketched in Figure 2.14, together with volume flow rate, inlet and outlet primary circuit temperatures (Buhmann et al., 2016; Schneider and Moormann, 2010). The aim was to test thermal efficiency, validate numerical models and understand the effect of thermal loads on the subsoil. Three probes 5 to 10 m-long measure

the subsoil thermal field along the springlines and the crown directions. Measurements results from April 2011 to April 2015 were reported.

From Figure 2.15a showing a test in cooling mode with constant inlet temperature of about 20.5°C it is evident how the outlet temperature and the energy extraction rate are strictly dependent on tunnel air and, what is more, outlet, subsoil and tunnel air temperature are very similar. When tunnel temperature increases, energy extraction rate reduces from 30 to 5 W/m². By doubling the flow rate this overlapping reduces and the outlet follows tunnel air in a damped way, as the residence time reduces. In a cyclic 7-days heating mode test (Figure 2.15b), that simulates the typical heating operation covering demand during daytime, with constant inlet temperature and flow rate (0.5°C and 500 L/h) no effects on the subsoil can be detected during heat extraction. A heat flux of 20 W/m², slightly decreasing in the evening, is shown. As before, the subsoil follows tunnel air temperature in a damped form showing fluctuations between day and night as the tunnel communicates with external air.

The tunnel itself alters the undisturbed thermal field in the surrounding ground (Figure 2.14, top right) in an annulus 7 m wide by maximum of 5.5 °C very near to the tunnel. Thermal activation slightly exacerbates this collateral effect (Figure 2.14, bottom right) in the closest 2.5 m by an additional 3°C. This experimental result was confirmed qualitatively in the research by Ogunleye et al. (2019), who claim that heat flux from the tunnel environment itself has an impact on the surrounding ground not very different from the one caused by heat extraction.

The take-home message gained from this field trial is that understanding the tunnel climate evolution is a major task when designing a geothermal plant and that thermal exploitation only has minor effects on surrounding subsoil compared to the anthropogenic only heat flux. Also, the tunnel GHE operation plays a key role on thermal efficiency.

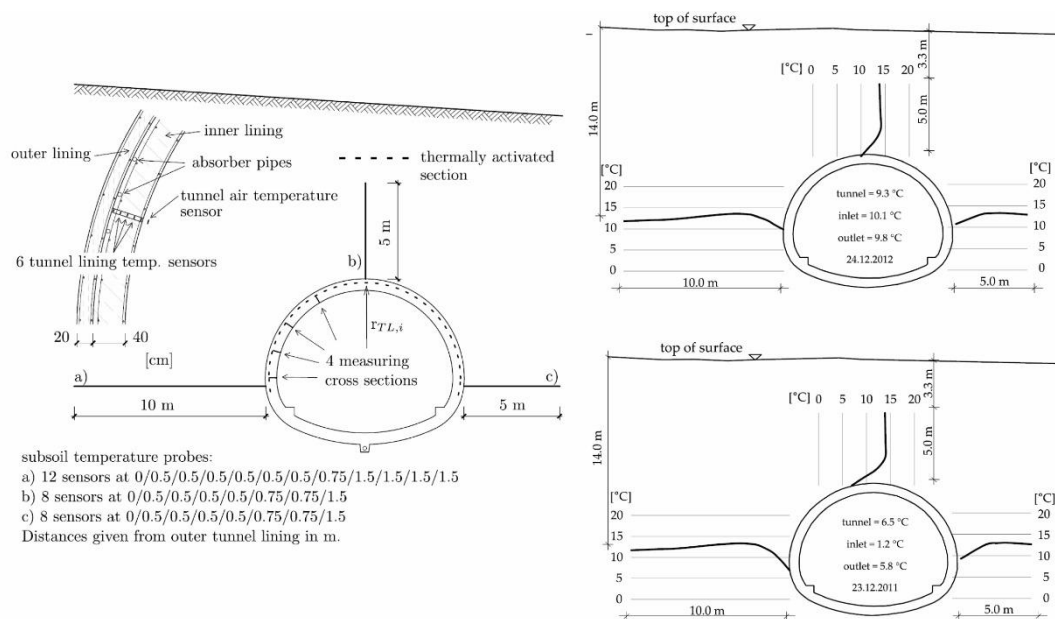


Figure 2.14: Monitoring plan at Stuttgart-Fasanenhof tunnel and soil temperature during winter natural (top right) and working (bottom right) conditions at Stuttgart-Fasanenhof tunnel (modified from Buhmann et al., 2016).

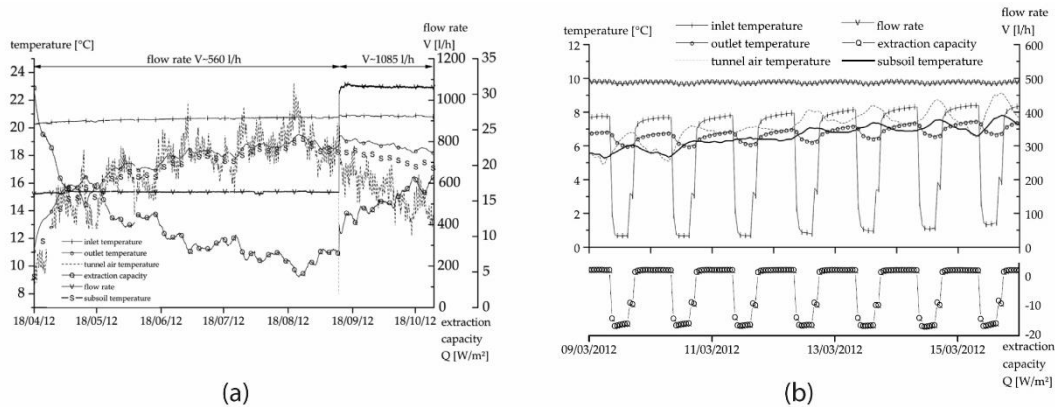


Figure 2.15: (a) Cooling and (b) heating mode test at Stuttgart-Fasanenhof tunnel (modified from Buhmann et al., 2016).

2.4.1.2. Jenbach tunnel

The overall length of this demonstration project was inferred from the results of the field trial at Katzenberg tunnel, yielding 10-20 W/m². For a tunnel with inner diameter of 12 m, around 55 m were needed to provide 40 kW in the hypothesis of COP=4. The scheme of the demonstration project is shown in Figure 2.16. Eight temperature probes were installed in the lining and two were devoted to the record of tunnel air temperature. Inlet and outlet temperatures, together with flow rate were also measured. The main monitoring results are reported in Moormann et al. (2016), who clarify that compared to Stuttgart-Fasanenhof tunnel, here the main heat transport mechanism is convection.

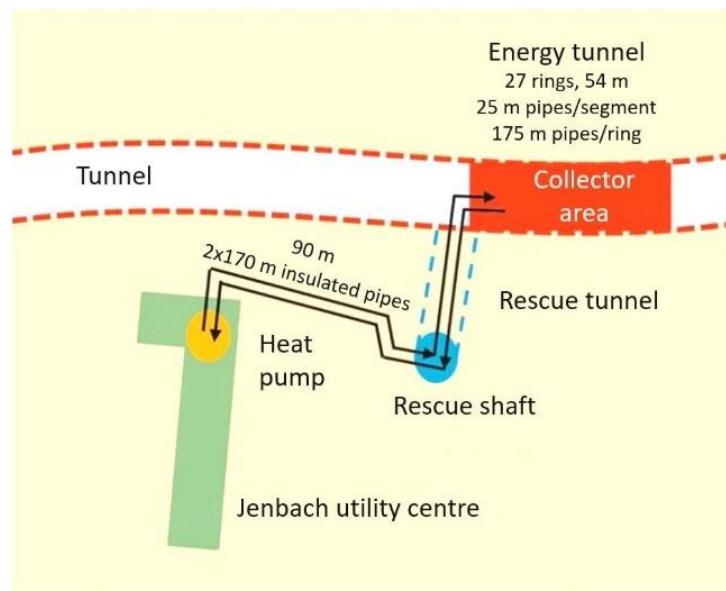


Figure 2.16: Layout of the demonstration project at Jenbach tunnel (modified from <https://www.bft-international.com>; Moormann et al., 2016).

In Figure 2.17 an example of heating mode test performed between August and October 2013 indicates a heat flux of 20-25 kW corresponding to about 12.5 W/m^2 , for inlet temperatures between 2.5 and 5.5°C . They also varied the fluid flow rate between the laminar and the turbulent range and observed a 60% increase in performance, from 10 to 16 W/m^2 at inlet temperatures of 6°C . Higher rates are expected at lower feed temperatures ($18\text{-}40 \text{ W/m}^2$ were computed for a hot tunnel with 25°C as tunnel air temperature, 10°C for the subsoil and 5°C for the inlet). Indicators of higher rates in turbulent regime were the more pronounced cooling of the segments (less than 8°C compared to the laminar case of 10°C) and the reduced inlet-outlet spread (3°C compared to 6°C) since the residence time of the fluid reduces. The heating demand of 100 to 150 houses could be met by thermally activating a 500 m-long section.

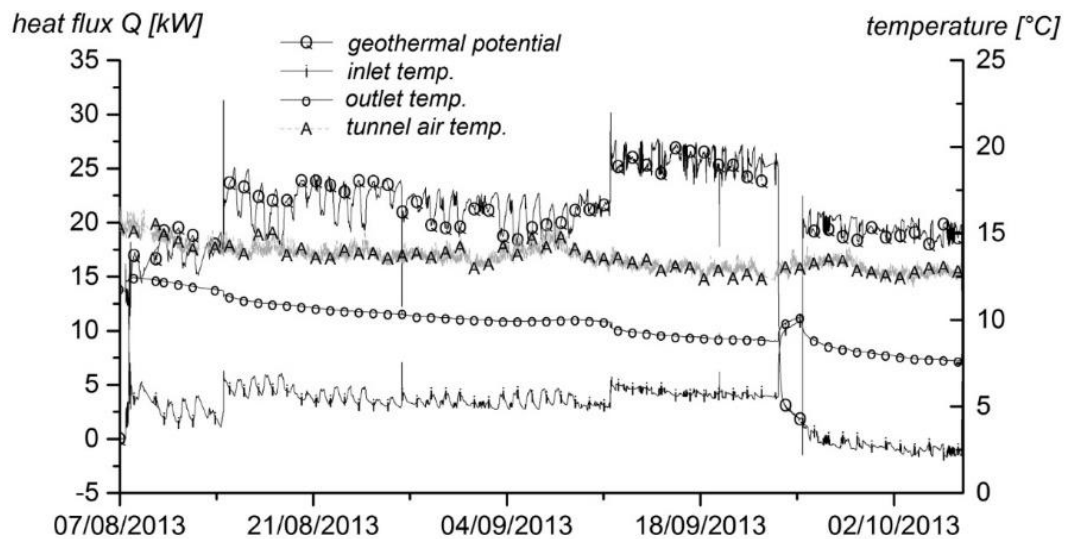


Figure 2.17: Heating mode test performed at Jenbach tunnel (modified from Moormann et al., 2016).

2.4.1.3. Seocheon tunnel

After a 2-months preliminary test in 2010 aimed at evaluating the adequate fluid flow rate, the system was run twice in a typical daily cyclic cooling mode (as for the heating test at Stuttgart-Fasanenhof tunnel, Figure 2.15b) with inlet temperature less than 30°C and flow rate 1.5 and 2 lpm ($0.09\text{-}0.12 \text{ m}^3/\text{h}$) during the two tests (Figure 2.18). Two textile units (transverse and longitudinal) were linked to obtain feasible outlet temperatures. Energy textile inlet and outlet temperatures, flow rate, temperature in the tunnel were monitored during the tests (Lee et al., 2012). Temperature in the tunnel was about 17.5°C during the first test and 15°C during the second one. Temperature spreads are higher in the first test, up to 5°C . Despite this, the authors report that the average total heat power is 713 W during the second test, while it is 592 during the first test, probably because of the difference in flow rate. The tunnel wall temperature field is highly affected by the operation of the energy geotextile.

A 3D numerical model built in FLUENT to reproduce a one-day-long cooling cycle showed good agreement with monitored data.

More experimental outcomes dating 2011 are reported in Lee et al. (2016) and include both heating and cooling tests on a transverse layout (Figure 2.19, see Figure 2.2 for transverse layout). Inlet temperature was 5 and 30°C respectively, temperature spreads were around 3

heating and 5°C in cooling. Tunnel temperature was nearly constant at 20°C during cooling, while it exhibits a marked cyclic trend during heating, especially during the execution of the test. The average heat exchange is 58.2 W during heating and 362.3 W during cooling (six times greater) due to the higher flow rate and temperature difference. At Seocheon tunnel the energy textiles are more efficient in summer than in winter. Figure 2.20 focuses on the effect caused by the difference between tunnel air and inlet temperature on heat exchange and demonstrates that tunnel climate is one of the most influential factors when exploiting geothermal energy from a tunnel.

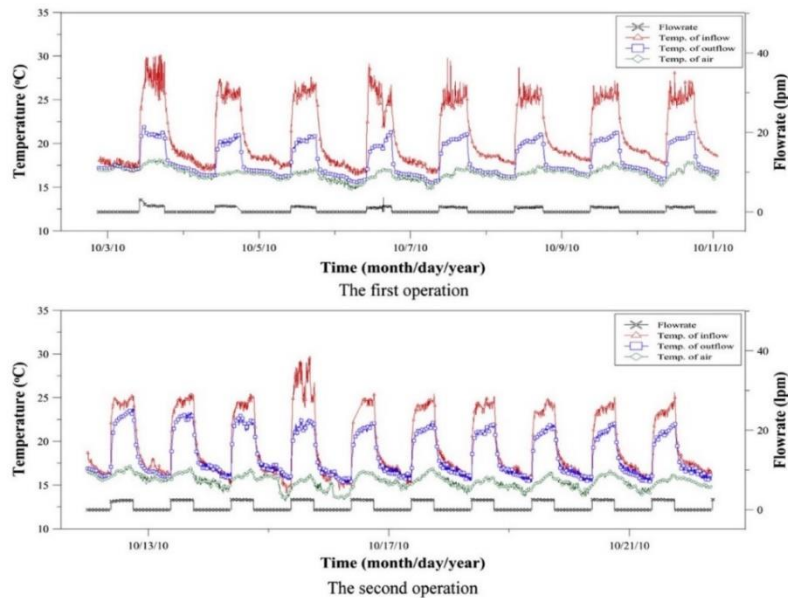


Figure 2.18: Cyclic cooling mode test performed at Seocheon tunnel in 2010 (from Lee et al., 2012).

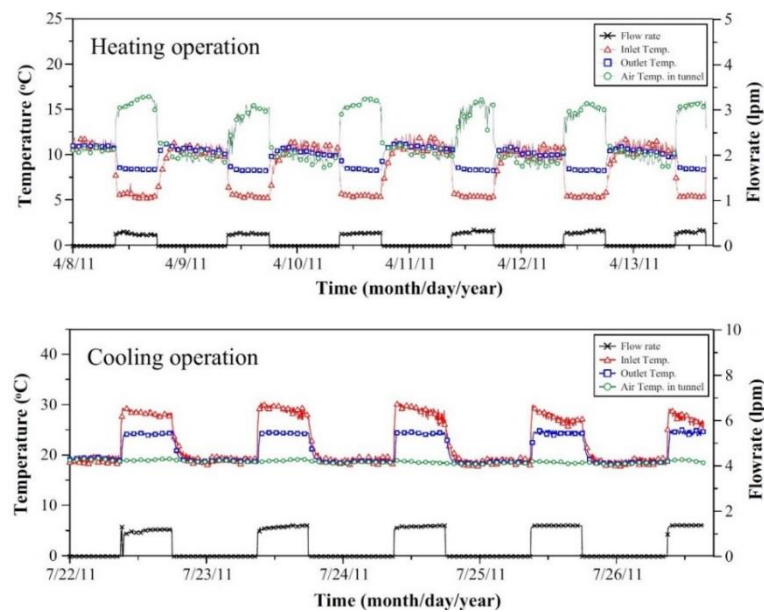


Figure 2.19: Cyclic heating and cooling mode test performed at Seocheon tunnel in 2011 (Lee et al., 2016).

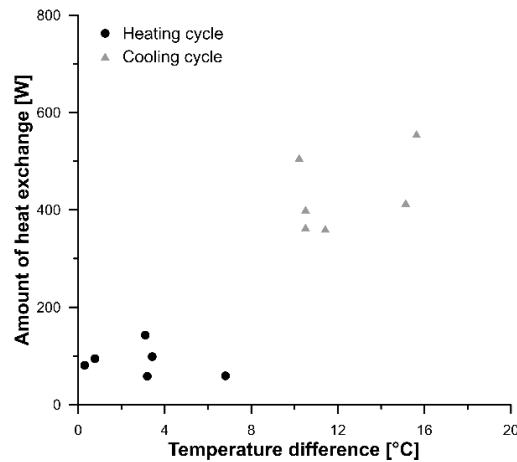


Figure 2.20: Correlation between average heat exchange obtained at Seocheon tunnel and difference between air and inlet temperatures (modified from Lee et al., 2016).

2.4.1.4. Linchang tunnel

At Linchang tunnel the energy geotextiles underwent some thermal response tests with constant inlet temperature with the goal of evaluating their efficacy, as well as the action of inlet temperature (16-18-20°C), fluid velocity (0.487-0.673-0.953-1.25 m³/h) and pipes spacing (50-100 cm) on the neighbouring materials and on performance. To do this the thermistors shown in Figure 2.21 were deployed and inlet and outlet temperatures were tracked.

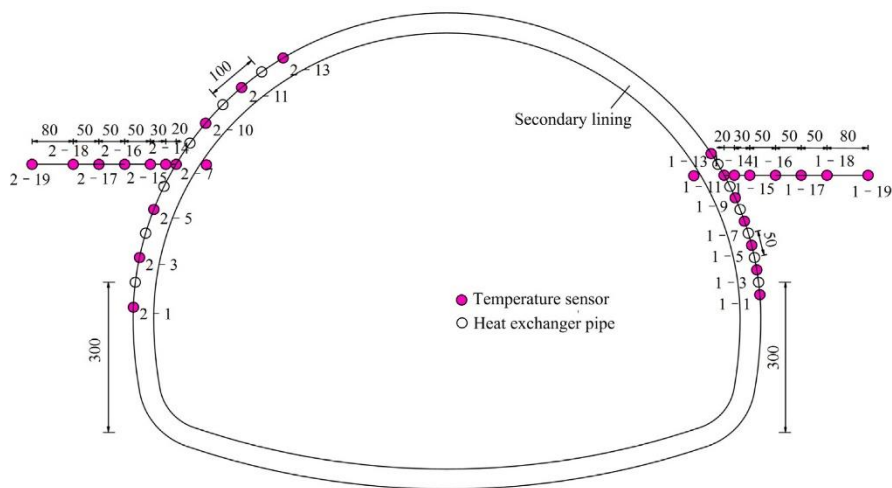


Figure 2.21: Monitoring system installed at Linchang tunnel (from Zhang et al., 2014).

With a pipe spacing of 50 cm, temperature at the secondary lining intrados increases by a maximum of 1.29°C, twice as much as with 100 cm spacing. Likewise, the surrounding ground heats up more with 50 cm spacing, although the effects disappear at a distance of more than 1 m and a recovery phase of two-days allows to restore the initial temperature field, at least from 1 m distance. Intermittent operation, also adopted at Stuttgart-Fasanenhof tunnel (Figure 2.15b) and Seocheon tunnel (Figure 2.19), is of advantage for the surrounding ground initial temperature re-establishment and for the preservation of the geothermal resource. Smaller

pipes distances lead to a higher heat exchange. According to the authors, this is related to the higher ground and air temperatures on the side with 100 cm pipes spacing:

$$Q_{i,l}(t) = \frac{T_{i,l}(t) - T_{\text{ground}}(t)}{R_{\text{ground}}} + \frac{T_{i,l}(t) - T_{\text{air}}(t)}{R_{\text{air}}} \quad \text{Eq. 2.8}$$

that shows the dependence of the total heat power $Q_{i,l}(t)$ in pipe i from the difference between its temperature $T_{i,l}(t)$ and the ground/air temperatures $T_{\text{ground}}(t)$, $T_{\text{air}}(t)$ and the thermal resistances R_{ground} , R_{air} on both sides (a similar relationship can be found in Tinti et al., 2017). Conductive thermal resistance is defined as the ratio between the thickness of the layer over which conduction takes place and the thermal conductivity multiplied by the area:

$$R_{\text{cond}} = \frac{\delta}{\lambda A} \quad \text{Eq. 2.9}$$

while convective thermal resistance is

$$R_{\text{conv}} = \frac{1}{hA} \quad \text{Eq. 2.10}$$

2.4.2. Governing equations

Given the physical processes involved in energy tunnels-related problems, including thermal, hydraulic and mechanical aspects (Figure 2.22), coupled approaches are needed to study the problem in a holistic way. In particular, the thermo-hydraulic problem mathematical formulation is ruled by the following equations governing fluid flow and heat transport coupling:

- Mass conservation equation (continuity equation)
- Darcy's law
- Energy conservation equation

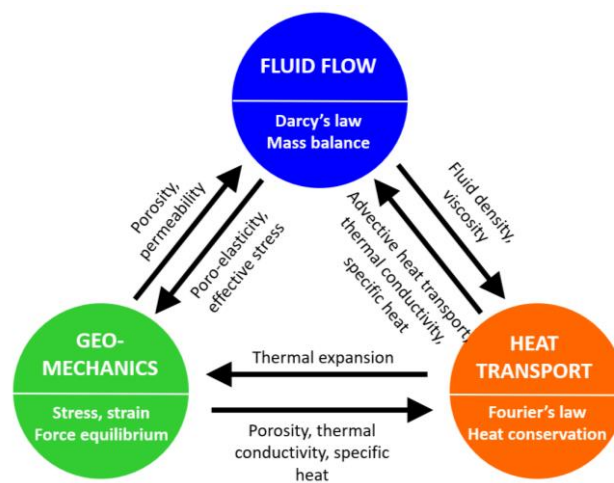


Figure 2.22: THM problem couplings.

The continuity equation for a two-phase fully saturated medium (soil skeleton and water with constant and uniform density) can be written as:

$$S \cdot \frac{\partial p}{\partial t} + \frac{\partial n v_{w,x}}{\partial x} + \frac{\partial n v_{w,y}}{\partial y} + \frac{\partial n v_{w,z}}{\partial z} - n \beta_w \frac{\partial T}{\partial t} - \beta_w [n v_w] \{\nabla T\} = 0 \quad \text{Eq. 2.11}$$

where $S = [n Y_w + (1-n) Y_s]$ is the specific storage coefficient, Y_w and Y_s the water and solid compressibility, p the pressure, n the porosity, β_w the water thermal expansion coefficient, T the temperature, $n v_{w,x}$, $n v_{w,y}$, $n v_{w,z}$ are the fluid apparent velocity components in the three directions and t the time. Eq. 2.11 is nothing but the equation of mass conservation in non-isothermal conditions, where the last two terms represent the role of temperature. $n v_w$ is an apparent velocity, smaller than the real one, because the area of the pores crossed by the fluid is lower than the considered one ($v_f = n v_w$).

The fluid flow velocity field is governed by Darcy's law:

$$\{v_f\} = \{n v_{w,x}, n v_{w,y}, n v_{w,z}\} = -[k_w] \{\nabla h\} \quad \text{Eq. 2.12}$$

where $[k_w]$ is the hydraulic conductivity tensor and h is the hydraulic head, defined as:

$$h = y + \frac{p}{\rho_w g_i} \quad \text{Eq. 2.13}$$

with y the vertical coordinate, ρ_w the water density and g_i the gravity vector.

The energy conservation, including both conduction and convection, can be written as:

$$[n \rho_w c_{pw} + (1-n) \rho_s c_{ps}] \frac{\partial T}{\partial t} - \nabla \cdot ([\lambda] \{\nabla T\}) + \rho_w c_{pw} [n v_w] \cdot \{\nabla T\} = 0 \quad \text{Eq. 2.14}$$

where ρ_w and ρ_s are water and solid densities, c_{pw} and c_{ps} water and solid heat capacities, λ is the thermal conductivity tensor whose components are both conductive and dispersive:

$$\lambda_{ij} = [n \lambda_w + (1-n) \lambda_s] \delta_{ij} + \rho_w c_w \left(\alpha_T \sqrt{q_{f,i} q_{f,j}} \delta_{ij} + (\alpha_L - \alpha_T) \frac{q_{f,i} q_{f,j}}{\sqrt{q_{f,i} q_{f,j}}} \right) \quad \text{Eq. 2.15}$$

with λ_w , λ_s the water and solid thermal conductivities, δ_{ij} the Kronecker delta and α_T , α_L the longitudinal and trasverse thermal dispersivities. The concept of dispersivity allows to keep into account microscale and macroscale inhomogeneities, such as pore directions not parallel to flow direction or layers and lenses not considered due to poor knowledge or to model discretization (Diersch, 2009).

Through the combination of the above equations the finite-element formulation for coupled thermo-hydraulic problems can be obtained. To solve the coupled problem, appropriate boundary conditions, both thermal and hydraulic, need to be set. As known, ground farfield boundary should be placed far enough from the area of interest to avoid any edge effect on the numerical outputs. Temperature boundary conditions can be of three types:

- Dirichlet-type or temperature boundary condition, $T=\text{constant}$ ($^{\circ}\text{C}$);
- Neumann-type or heat flux boundary conditions, $q=\text{constant}$ (W/m^2);
- Cauchy-type or heat-transfer boundary condition, where a reference temperature is given together with a heat transfer parameter h ($\text{W}/\text{m}^2\text{C}$).

Some common initial and boundary conditions gathered from the literature can be found in Tables 2.4-2.7. Typically, to simulate energy tunnels operation, inlet temperature and velocity are fixed and the outlet temperature is computed. Some exceptions can be found in Nicholson et al. (2014) who let the average pipes temperature vary according to a prescribed heat flux, and in Lee et al. (2012) who set the temperature difference observed in the thermal response tests (TRT) and the initial inlet temperature and computed the inlet and outlet temperature trends.

Table 2.4: Typical uniform initial ground temperature values used in numerical models retrieved from literature.

Case study	Initial temperature	Reference
Fasanenohf–Stuttgart tunnel (Germany)	10 $^{\circ}\text{C}$	Bidarmaghz and Narsilio, 2018
Fasanenohf–Stuttgart tunnel (Germany)	9 $^{\circ}\text{C}$	Bidarmaghz et al., 2017
Metro Torino line tunnel	14 $^{\circ}\text{C}$	Barla et al., 2016
Crossrail (UK)	14.8 $^{\circ}\text{C}$	Nicholson et al., 2014
NE extension Warsaw metro tunnel	12 $^{\circ}\text{C}$	Baralis et al., 2018
Grand Paris Express	12 $^{\circ}\text{C}$	Bracq et al., 2017; Fouché et al., 2018
Grand Paris Express	13 $^{\circ}\text{C}$	Cousin et al., 2019

Table 2.5: Thermal boundary conditions used for ground and tunnel lining in numerical models retrieved from literature.

Case study	Left	Right	Bottom	Top	Tunnel lining
Bidarmaghz and Narsilio, 2018	Thermal insulation	Thermal insulation	Thermal insulation	Thermal insulation or $T_0=10^{\circ}\text{C}$	-
Bidarmaghz et al., 2017	Thermal insulation	Thermal insulation	Thermal insulation	Thermal insulation	$T_{\text{wall}}(t)=17.5\text{-}25^{\circ}\text{C}$
Barla et al., 2016	-	-	-	-	30 cm-thick air layer + Cauchy BC from monitoring data
Nicholson et al., 2014	14.8 $^{\circ}\text{C}$	14.8 $^{\circ}\text{C}$	-	-	Cauchy boundary condition with seasonal variation and $h_c=5 \text{ W}/(\text{m}^2\text{C})$
Baralis et al., 2018	Thermal insulation	Thermal insulation	12 $^{\circ}\text{C}$	Monthly average air temperature variation	Thermal insulation
Bracq et al., 2017; Fouché et al., 2018			12 $^{\circ}\text{C}$ (circular model)		Cauchy boundary condition with measured tunnel air temperature
Cousin et al., 2019	13 $^{\circ}\text{C}$	13 $^{\circ}\text{C}$	13 $^{\circ}\text{C}$	13 $^{\circ}\text{C}$	Cauchy boundary condition with constant tunnel air temperature of 18.96 $^{\circ}\text{C}$ and $h_c=15.13 \text{ W}/(\text{m}^2\text{C})$

Table 2.6: Thermal boundary conditions used for pipes circuit in numerical models retrieved from literature.

Case study	Inlet temperature	Inlet velocity	Flow rate
Bidarmaghz and Narsilio, 2018	$T_{in}(t) = T_{out}(t) - \frac{Q_{tunnel-GHE}(t)}{(Q_w V_w \Delta C_{p,w})}$	0.48 m/s	0.56 m ³ /h
Bidarmaghz et al., 2017	$T_{in}(t) = T_{out}(t) - \frac{Q_{tunnel-GHE}(t)}{(Q_w V_w \Delta C_{p,w})}$	0.3 m/s	-
Barla et al., 2016	4, 28°C	0.4 m/s	0.6 m ³ /h
Baralis et al., 2018	4, 26.5°C	0.7 m/s	-
Bracq et al., 2017; Fouché et al., 2018	4, 20-28°C	-	0.36 m ³ /h
Cousin et al., 2019	2	0.31-1.00 m/s	-

Table 2.7: Hydraulic boundary conditions used in numerical models retrieved from literature.

Case study	Left	Right	Bottom	Top
Bidarmaghz and Narsilio, 2018	H ₁	H ₀ <H ₁	No flow	No flow
Bidarmaghz et al., 2017	H ₁	H ₀ <H ₁	No flow	No flow
Barla et al., 2016	H ₁	H ₀ <H ₁	-	-
Baralis et al., 2018	H ₁	H ₀ <H ₁	-	-
Nicholson et al., 2014	-	-	-	-
Bracq et al., 2017; Fouché et al., 2018	-	-	-	-
Cousin et al., 2019	-	-	-	-

2.4.3. Analytical models

For energy tunnels the classical line heat source and hollow cylinder model (Carslaw and Jaeger, 1959) adopted for BHE are not applicable, which calls for new analytical solutions. A new 2D line heat source model was developed and validated on TRT tests performed in Linchang tunnel by Zhang et al. (2013), based on the following underlying simplifying assumptions:

- homogeneous rock and tunnel lining, with thermally inert properties;
- negligible heat conduction in the longitudinal direction;
- negligible heat conduction in the pipes wall and heat carrier fluid by virtue of the pipes small size compared to the tunnel domain.

The base geometry for the analytical model is represented in Figure 2.23a. Transient heat conduction equation for bodies with constant material properties can be written as:

$$\frac{\partial T}{\partial t} = \alpha \nabla^2 T + \frac{\dot{W}}{c\rho} \quad \text{Eq. 2.16}$$

and in cylindrical coordinates, dividing by thermal diffusivity, as:

$$\frac{1}{\alpha_i} \frac{\partial T_i}{\partial t}(r, \theta, t) = \frac{\partial^2 T_i}{\partial r^2}(r, \theta, t) + \frac{1}{r} \frac{\partial T_i}{\partial r}(r, \theta, t) + \frac{1}{r^2} \frac{\partial^2 T_i}{\partial \theta^2}(r, \theta, t) + \frac{\partial^2 T_i}{\partial z^2} + \frac{\dot{W}_i(r, \theta, t)}{\lambda_i} \text{ for } i=1,2,3 \quad \text{Eq. 2.17}$$

where T is the temperature, $\alpha_i = \frac{\lambda}{\rho c}$ [m²/s] is the thermal diffusivity that relates the temperature change in time with the temperature gradient in space in the transient conduction equation, r ,

θ are the radial and circumferential directions, t is time, \dot{W} is a heat source (the extracted geothermal energy in this specific case) and λ is thermal conductivity. The ticked term is temperature variation in the longitudinal direction that was said to be neglected. It is reminded that the thermal diffusivity measures how quick a material responds to a temperature change and that it is equivalent to the coefficient of consolidation in the consolidation theory. Indeed, the Terzaghi's equation or equation of consolidation is a second-order partial differential equation of parabolic type that can describe all the diffusion phenomena such as, in this case, heat diffusion.

To define the temperature field not only the differential equation is needed, but several boundary conditions, including initial-value condition and local conditions, must be imposed and fulfilled by its solution. The initial-value condition is:

$$T_i(r, \theta, t=0) = f_i(r, \theta) \quad \text{for } i=1,2,3,4 \quad \text{Eq. 2.18}$$

This temperature can change during the transient heat conduction process. The local boundary conditions are:

$$-\lambda_1 \frac{\partial T_1}{\partial r}(r_0, \theta, t) = h[f(t) - T_1(r_0, \theta, t)] \quad \text{Eq. 2.19}$$

$$T_3(r_3, \theta, t) = T_0 \quad \text{Eq. 2.20}$$

$$T_i(r, 0, t) = T_i(r, 2\pi, t) \quad \text{Eq. 2.21}$$

$$\frac{\partial T_i}{\partial t}(r, 0, t) = \frac{\partial T_i}{\partial t}(r, 2\pi, t) \quad \text{Eq. 2.22}$$

$$T_i(r_i, \theta, t) = T_{i+1}(r_i, \theta, t) \quad \text{for } i=1,2 \quad \text{Eq. 2.23}$$

$$\lambda_i \frac{\partial T_i}{\partial r}(r_i, \theta, t) = \lambda_{i+1} \frac{\partial T_{i+1}}{\partial r}(r_i, \theta, t) \quad \text{for } i=1,2 \quad \text{Eq. 2.24}$$

where h is the convective heat transfer coefficient and $f(t)$ is tunnel air temperature. By expliciting tunnel air temperature and extracted geothermal energy, the problem can be solved by superimposing the results of two simpler decomposed problems, that is:

$$T_i(r, \theta, t) = \zeta_i(r, \theta, t) + \psi_i(r, \theta, t) \quad \text{Eq. 2.25}$$

where ζ_i is the solution of a transient heat-conduction problem with heat source (see Eq. 2.17) and ψ_i is the solution of a transient heat-conduction problem without heat source (see Eq. 2.17 without last term). The temperature of the surrounding rock and of the tunnel lining can thus be calculated. The pipes wall temperature T_{wall} is also known, as considered identical to inner secondary lining temperature. The fluid in the absorbers is governed by:

$$qc v \frac{dT_f(z)}{dz} = \lambda(T_{\text{wall}} - T_f(z)) \quad \text{Eq. 2.26}$$

with v flow rate of the fluid and $T_f(z)$ temperature of the fluid at distance z , from which outlet temperature $T_f(z)$ can be derived using an iterative method. A first-trial outlet temperature is used to compute the heat source term in Eq. 2.17 and the wall temperature from Eq. 2.25. If this wall temperature yields a different outlet temperature through the solution of Eq. 2.26,

then the process is repeated until trial and computed outlet temperature differ less than a certain threshold. It has to be reminded that in this analytical solution groundwater flow is not considered.

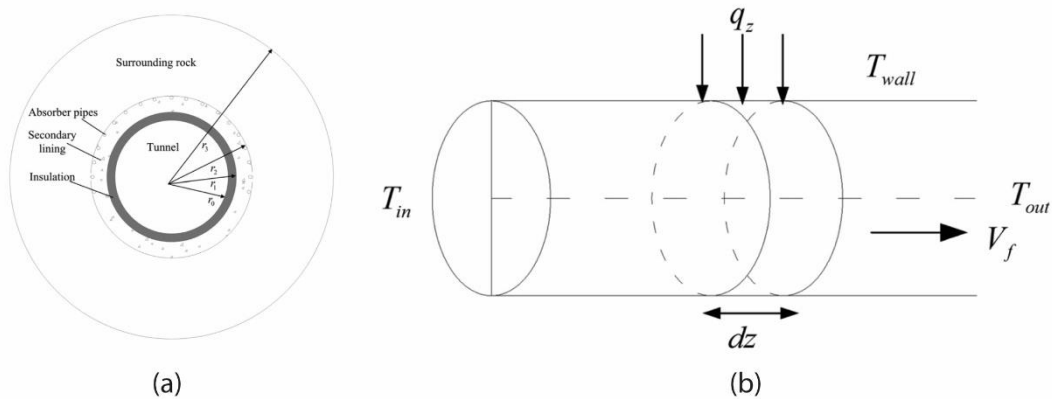


Figure 2.23: Scheme of the model for the analytical calculation of (a) rock mass, tunnel lining and (b) heat carrier fluid temperature (modified from Zhang et al., 2013).

2.4.4. Sensitivity studies

As already mentioned, a number of parameters affect the heat transfer process, such as the pipes geometry, hydrogeological conditions and ground thermal properties. In literature it is possible to find some researches focusing the attention on the role of some of them. Di Donna and Barla (2016) and Barla et al. (2016) investigated the effect of ground initial temperature, groundwater flow velocity, thermal conductivity and fluid flow velocity by parametric analyses in the case of perpendicular groundwater flow. Their results can be summarized as follows:

- in predominantly conductive soils a primary role is played by ground thermal conductivity as it can be observed that heat exchange when $\lambda=3.9$ W/mK is twice as much than when it is 0.9 W/mK, both in summer and in winter;
- groundwater flow intensity becomes the most influencing factor if ground convection is present in addition to ground conduction and heat exchange multiplies by 3 to 8 times for flows ranging from 0 to 2 m/d, though the risk of thermal pollution becomes noticeable;
- a 1°C of ground temperature variation improves heat exchange by 7% in winter and reduces it in summer;
- the efficiency increases/decreases linearly with ground temperature in winter/summer;
- heat exchange increases in a non-linear way with increasing heat carrier fluid velocity and with increasing groundwater flow.

Similar results, though with a lower level of detail, are described in Fouché et al. (2018) who studied the influence of i) fluid's inlet temperature and flow rate and ii) rock's initial temperature and thermal conductivity in the absence of groundwater flow. Heat flux increases with increasing fluid velocity, decreasing inlet temperature, and to a lesser extent with increasing rock thermal conductivity, as confirmed by Zhang et al. (2014), and increased/decreased initial temperature in winter/summer. Lee et al. (2012) found that performance increases with increasing thermal conductivity of primary and secondary lining, while fluid velocity negatively affects heat exchange in the range analyzed. This is not in agreement with other studies (Di Donna and Barla 2016; Cousin et al., 2019; Zhang et al.,

2014). Zhang et al. (2013) applied their newly validated analytical model to explore the effect of i) ground temperature, ii) pipes flow rate, and iii) inlet temperature on extraction rates, learning that these linearly increase with i), exponentially increase with ii) especially in the short-term and linearly decrease with iii) by 0.39 W/m every 1°C. However, operating costs should be kept in mind when increasing fluid flow through the roof (>0.8 m/s). If lower inlet temperatures are beneficial for enhancing thermal performance, special care should be taken as freezing of the soil and underground water could occur. Experimental injection tests in Linchang tunnel (Zhang et al., 2014) revealed a 2.5 W/m increase for 1°C increase in inlet temperature.

Di Donna and Barla (2016) suggested some preliminary design charts resulting from numerical analyses (Figure 2.24), valid for groundwater flow perpendicular to tunnel axis only. These charts were conceived to support designers and city planners in understanding the potential deriving from energy tunnels installation based on the most relevant site-specific conditions. Of course, as they point out, this preliminary evaluation should be followed by detailed and site-specific numerical analyses at a later stage of the design.

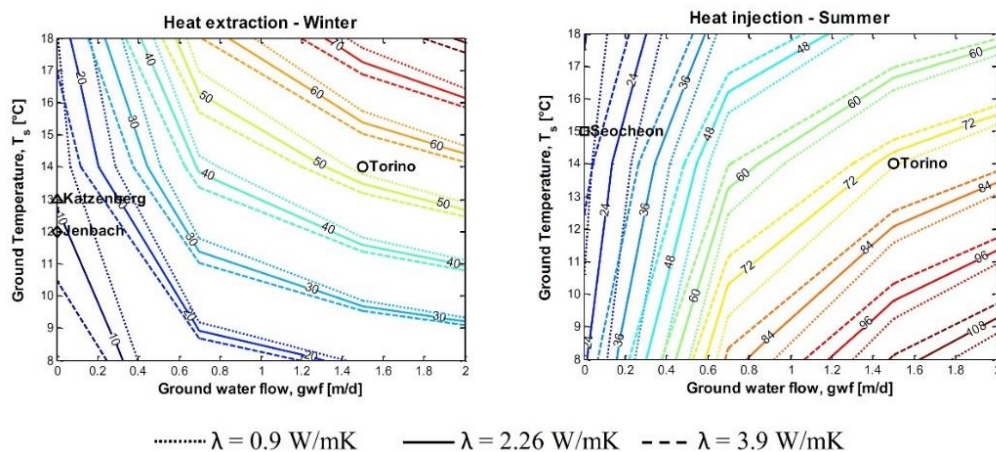


Figure 2.24: Design charts for the preliminary assessment of heating and cooling potential for energy tunnels (from Di Donna and Barla, 2016).

During design another aspect to consider is the configuration of the rings, whether in series or in parallel and how many rings to connect in each subcircuit. Barla et al. (2016) carried out an optimization study considering a number of layouts and concluded that the solution with rings connected in parallel is the best one, as the temperature gradient of the heat carrier fluid decreases along its path. Therefore, connecting the rings in series means that the efficiency is progressively reduced, as the increase in temperature difference between inlet and outlet is not comparable to the increase in exchange area. Their analysis is focused on the thermal efficiency and does not include technical and plant aspects.

The effect of pipe configuration (diameter, layout and embedment) and heat carrier fluid flow rate were investigated by Cousin et al. (2019), who found a difference of nearly 50% between the highest and the lowest extracted thermal power among 36 considered designs (Figure 2.25). The highest heat flux was obtained with the so-called Enertun layout, with pipes 20 mm in diameter, the highest flow rate and embedment close to the tunnel intrados. This last clearly affects the amount of heat exchange with the tunnel air, whose value of 18.96°C considered in this study was very favourable for heating. This is why the closer pipes location to the intrados facilitates heat transfer with the air and increases it, reducing the lining thermal

resistance. The higher velocity and Reynolds number reduce convective thermal resistance in the pipes. It is meaningful to highlight that the configuration with pipes 20 mm in diameter was also the longest one (207.8 m of pipes laid in the energy ring). In fact, larger diameter pipes lead to higher thermal power per meter. An optimization accounting both for heat exchange and head losses would be needed and the Enertun concept goes in this direction.

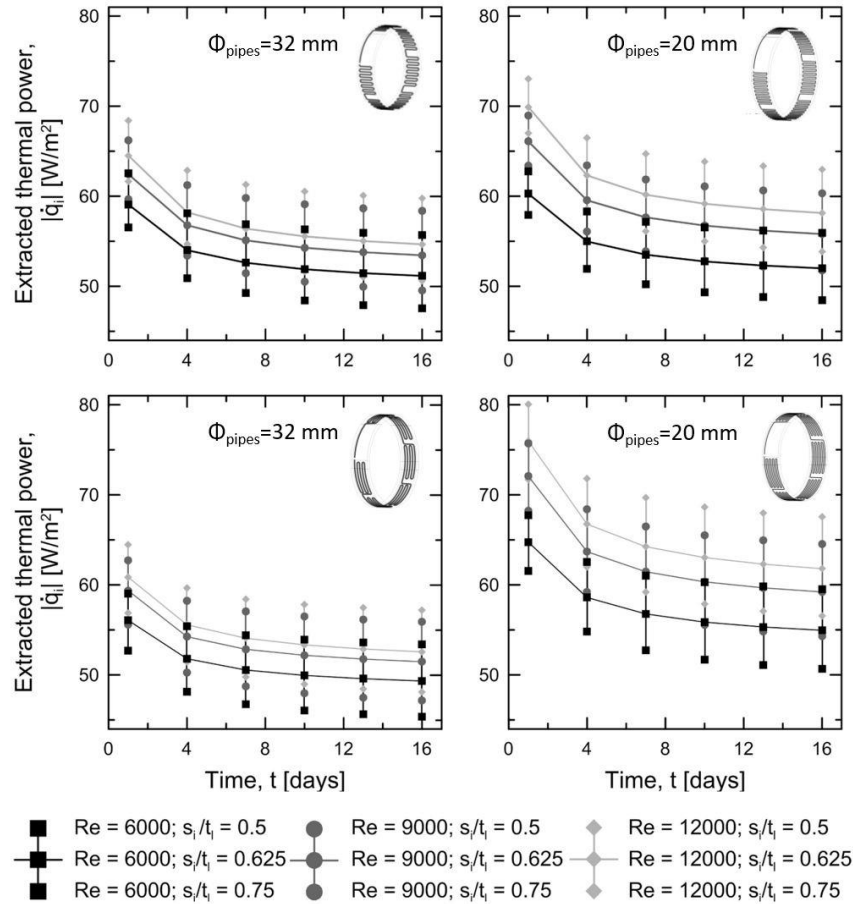
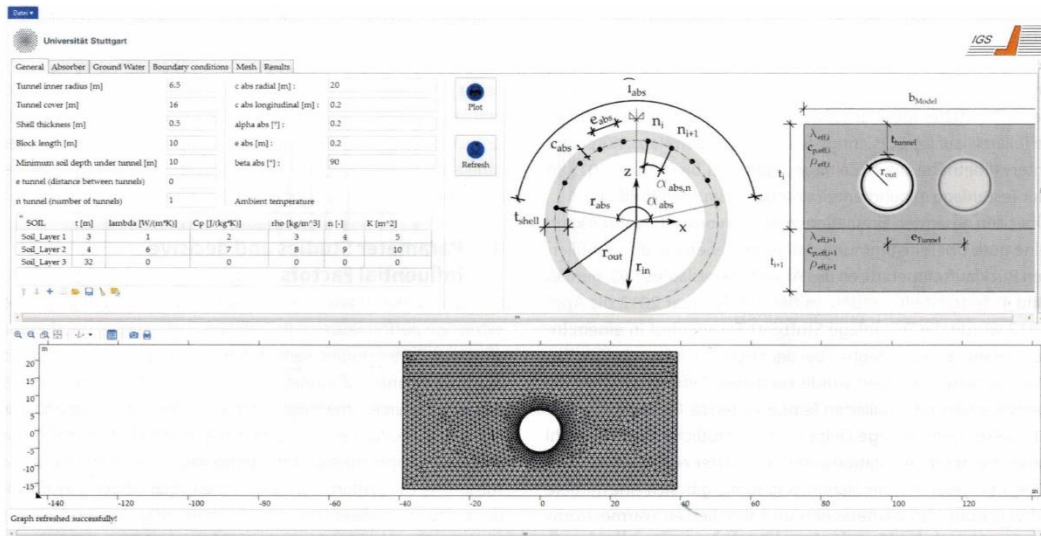


Figure 2.25: Extracted thermal power obtained by varying pipes layout, pipes diameter, pipes embedment and heat carrier fluid flow rate (modified from Cousin et al., 2019).

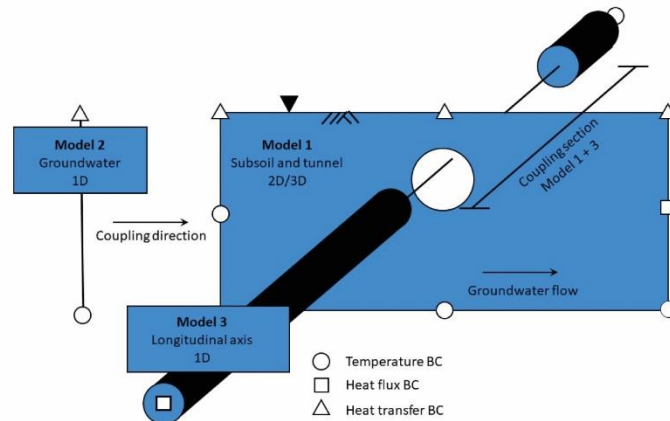
At the University of Stuttgart a web-based simulation parametrised tool to estimate energy tunnels thermal efficiency is under development (Figure 2.26a), that is claimed to be quick for practical applications and does not require deep insights into the heat transfer mechanisms between the ground, the lining and the tunnel air (Moormann et al., 2018). A sketch of the model is depicted in Figure 2.26b: model 1 couples heat transfer and groundwater flow, model 2 is to consider transient boundary conditions related to the groundwater flow temperature field and model 3 is to compute temperature distribution along the tunnel. The validation on Stuttgart-Fasanenhof 1.5 years measurements gave satisfactory results, allowing for parametric studies (groundwater flow was neglected). As in Cousin et al. (2019) the pipes radial embedment strongly affects heat exchange: if placed close to the intrados, heat exchange increases up to 66%. While in Di Donna and Barla (2016) and Cousin et al. (2019) inlet temperature was fixed at 4 and 2°C, Moormann et al. (2018) obtained that this parameter has

a linear effect on the extraction rate of about $3 \text{ W}/(\text{m}^2\text{C})$. The tunnel diameter negligibly affects heat flux density. The same goes for the tunnel overburden, as the solar storage zone is relatively shallow. Moreover, according to them, thermal conductivity slightly influences the achievable heat extraction, though in this study the tunnel climate has a predominant effect.

Another interesting aspect that can influence thermal performance is the operation mode. Taking inspiration by Zhang et al. (2014), Ogunleye et al. (2019) analyzed in detail the role of an intermittent ratio IR varying from 0.5 to 2, where IR is defined as the daily ratio between the heat pump off and on phase. For instance, the intermittent ratio is 2 if the heat pump works for 8 hours/day. They found that an intermittent working mode can increase thermal efficiency and help soil to recover (more quickly) by minimising its thermal perturbation.



(a)



(b)

Figure 2.26: Web-based calculation (a) tool and (b) model (modified from Moormann et al., 2018).

2.4.5. The role of groundwater flow

Groundwater flow can have a three-fold effect: on the operation of the geothermal system, on the surrounding ground temperature distribution and on internal air temperature distribution. Bidarmaghz and Narsilio (2018), after validating a TH three-dimensional FE model against Stuttgart-Fasanenhof tunnel recorded data, studied these aspects by varying hydraulic conductivity of the porous ground to yield gradually increasing flow rates, from 0.05 to 4.3 m/d. For each of these values the average fluid temperature within pipes was calculated. This information is crucial for thermal design as it has to be verified (i) that it falls within the range of operation of the heat pump (typically $-2\div 40^{\circ}\text{C}$) and (ii) that the COP remains optimal. It was found that a faster groundwater flow leads to a rapid recharge of the ground around the tunnel and to higher/lower fluid temperatures in winter/summer (Figure 2.27). In other words, less pronounced temperature differences are needed to fulfil the thermal demand, with beneficial effects on the heat pump performance. In the case of the slowest flow there is a considerable risk that the fluid temperature dramatically drops below 0°C making the shallow geothermal solution unfeasible and unpractical as the design size would be unbearable. Another great difference between fast and slow groundwater flow is the average fluid temperature trend over time: in the first case a steady state is reached very quickly in each cycle as an equilibrium between demand and resource is established and temperature does not need to vary further. These results demonstrate the importance of accounting for groundwater flow, collecting reliable data in this regard, and that sites with favourable groundwater movement are more prone to host an energy tunnel system. On the other hand, this environment is less appropriate for storage purposes.

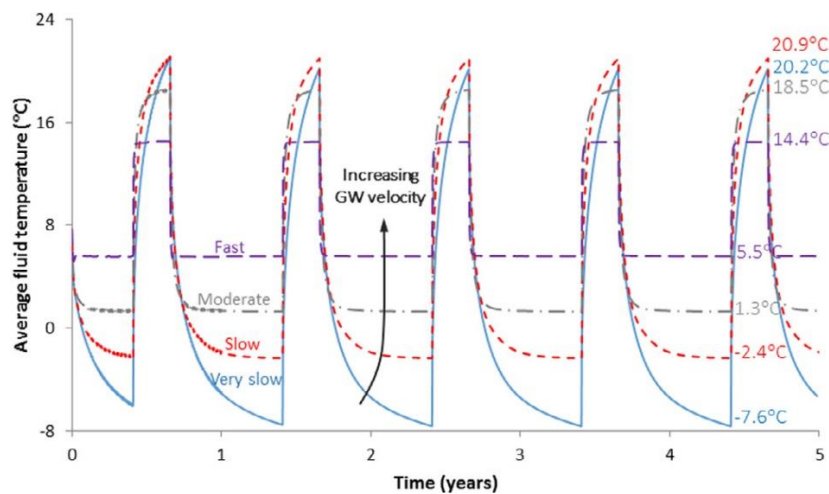


Figure 2.27: Effect of groundwater flow velocity on average fluid temperature (Bidarmaghz and Narsilio, 2018).

Groundwater flow velocity and direction also affect temperature distribution in the surrounding soil. Bidarmaghz et al. (2018) point out that areas of significant temperature gradient in the ground should be detected to verify that the ground can be used as a source of energy in a sustainable and viable manner. In low-permeability soils with no groundwater flow, summer injection may be needed to restore thermal equilibrium in the ground, so that its mean does not vary year after year (see also Laloui and Di Donna, 2011). In fact the faster the groundwater flow the smoother and less visible are the residual effects of previous cycles. For a slow flow peaks occur relatively close to the lining and relevant variations from ground

undisturbed temperature are shown, as also obtained by Barla and Perino (2015) in the total absence of groundwater flow. This opens the path to research at a bigger scale than that of the single energy tunnel plant, as these alterations could guide a well-planned strategy for the use of this resource. For instance, a very slow flow would increase the downstream ground temperature in heating dominated operation, but on the other hand it was highlighted how this hydrology condition is not optimal for heat pump operation. On the contrary a very fast flow is the best condition for thermal efficiency, as confirmed also by the studies for the Turin case (Barla et al., 2016; Di Donna and Barla, 2016; Barla and Perino, 2014; Barla and Perino, 2015; Barla and Di Donna, 2018), though the dissipation rate is noticeably high and only effects of the current operation mode can be seen in the ground. The reciprocal influence of an energy tunnel and of a close-by BHE, situated either upstream or downstream, is looked into in Bidarmaghz et al. (2017). If the BHE is located upstream, similar results as for standalone BHE are obtained. However, if it is located downstream it could experience higher average temperatures, beneficial in heating dominant operations improving their thermal performance.

Barla et al. (2016) simulated three years of operation of Turin ML1 SE tunnel geothermal plant considering different hypotheses of operation and evaluated the effects on the surrounding ground due to the presence of groundwater flow. In the heating and cooling case, the optimal solution to avoid depleting of the geothermal reservoir, temperature variations are around 1°C at a distance of 22 m and within 5°C at a distance of 10 m (Figure 2.28a,b).

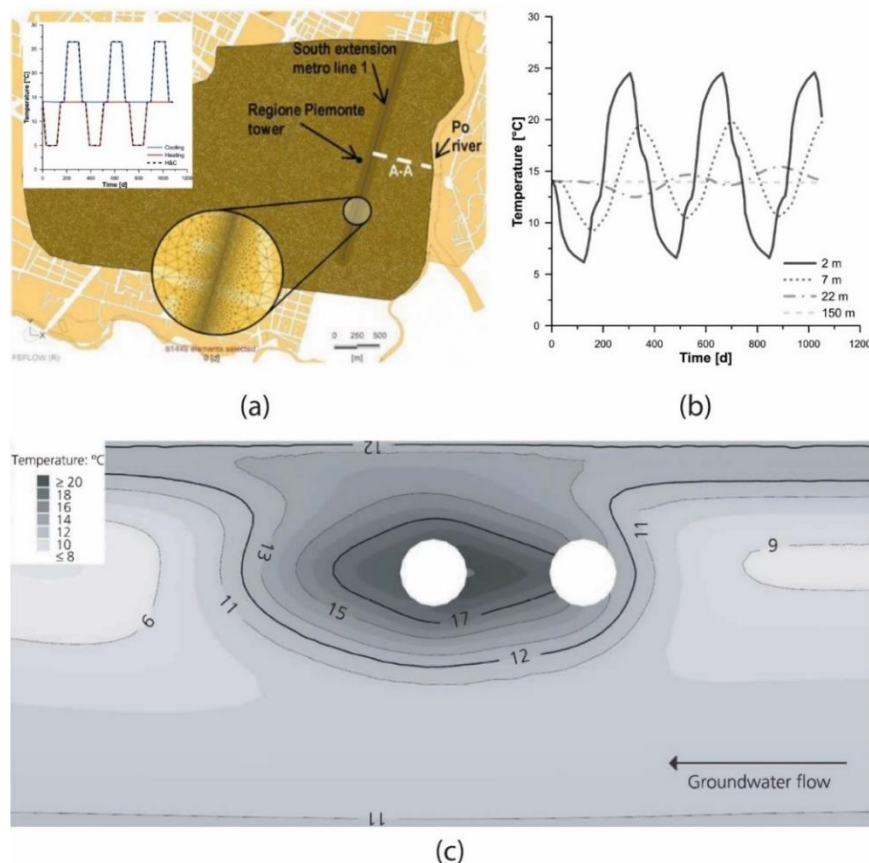


Figure 2.28: Turin ML1 SE model: (a) geometry and pipes inlet thermal boundary condition, (b) temperature distribution over time at several distances from the tunnel alignment (modified from Barla et al., 2016). NE extension Warsaw metro: (c) effect of thermal plume in the case of twin tunnels (Baralis et al., 2018).

The disturbance effect of thermal plume in a twin tunnels case study can be seen in Baralis et al. (2018). Indeed, among all the models analyzed in their study, those including sandy layers involve the origination of a hot thermal plume from the upstream to the downstream tunnel due to the cooling cycle (Figure 2.28c). As a consequence, in winter, the downstream tunnel increases its heat extraction performance.

Bidarmaghz et al. (2018) studied the role of groundwater flow velocity on tunnel air temperature distribution. As they considered GHE embedded only in the upper half of the lining, for slow flow rates higher top-bottom temperature gradients and a faster airflow arise inside the tunnel due to the slower dissipation rate of accumulated thermal energy. For faster groundwater flows this effect disappears and a more homogeneous temperature field, similar to the undisturbed ground temperature, recreates. The consideration of convection in addition to conduction in the tunnel air has an influence on air distribution, which would influence ventilation systems and therefore, in a loop, the geothermal response.

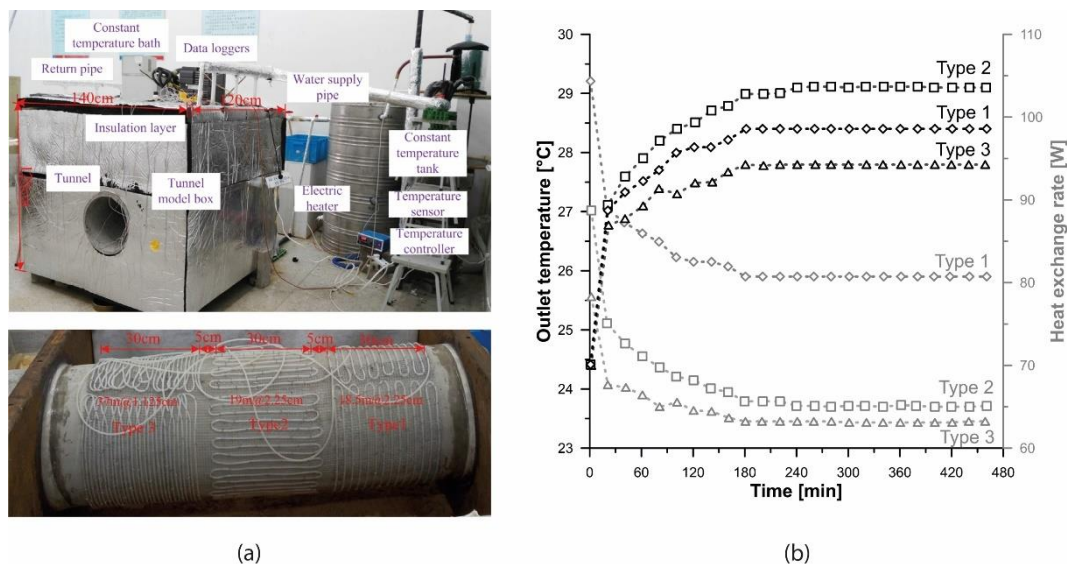


Figure 2.29: (a) Setup of laboratory scale experiment and (b) effect of pipes layout (modified from Zhang et al., 2016).

A curious experience involves a laboratory model test performed on a small-scale energy tunnel (Figure 2.29a) to clarify the effect of groundwater flow on thermal performance, which is discussed in Zhang et al. (2016). The small-scale tunnel (1:20) was embedded in an insulated sand box connected to two circuits, one for tackling flow in the ground heat exchangers and the other for creating a constant temperature groundwater flow through the sandy soil with different velocities depending on the height of a water tank. Water was pumped in the pipes with a constant temperature and thanks to a number of PT100 sensors temperature was monitored in the surrounding ground, in the lining and in the tunnel air. It was found that for a groundwater flow of 10^{-4} m/s (fast) a certain stability is reached in the ground and recovery is very quick, while for 10^{-5} - 10^{-6} m/s (slow) recovery is slow all around and a risk of continuous heating/cooling in summer/winter does exist, with possible consequences on the stress state on the structure because of the change in soil properties. A slow hydraulic regime causes high alterations in the thermal field close to the tunnel, especially upstream, while a fast groundwater flow diminishes these variations but extends them to higher distances downstream. With a slow flow, due to the persisting heat around pipes, tunnel air and lining temperature show

rising tendencies, as a steady condition is not reached, similarly to the ground. The groundwater flow has positive implications both on thermal efficiency and on the time needed to reach stability, improving the long-term GHE performance. The higher the distance between inlet and ground temperature, the higher thermal efficiency, independently from the groundwater velocity, and the relationship is linear. However, a fast flow contributes to have constant and higher heat exchange rates with time. In their experiments different pipes layouts (transverse pipes to tunnel axis direction with spacing 2.5 cm, parallel pipes with spacing 2.5 cm, transverse pipes with spacing 1.125 cm) were also tested and the Enertun one – pipes transverse to tunnel axis - with larger distance among pipes resulted the most favourable case (Figure 2.29b) and was also confirmed to be the one with the lowest head losses and the highest fluid flow velocity, as claimed by Barla and Di Donna (2016) when describing their patent.

An important remark is that based on the hydrogeological regime there can be or not the possibility of using the tunnel geothermal plant for storage purposes. In case of absence of flow, the stored energy in summer sourced by the buildings could improve economic efficiency in winter months.

2.4.6. The role of internal air

An essential difference of energy tunnels from other energy geostructures is that not only is the heat extracted from the ground but also from the internal air (Bidarmaghz and Narsilio, 2018; Buhmann et al., 2016; Cousin et al., 2019). The utilization of heat fluxes from the tunnel air and from the subsoil is such that they could be regarded as duo-hybrid-systems (Buhmann et al., 2016). This feature makes the technology flexible yet challenging, as both aerothermal and geothermal sources can be exploited but multiple phenomena govern the thermal performance. The interaction of the absorber pipes with these external boundary conditions regulates the direction and the intensity of heat fluxes. Based on analytical calculations carried out in the context of the Stuttgart 21 project (Schlosser et al., 2007) the tunnel air supplies a not neglectable contribution to heat extraction ranging from 20 to 30% of the energy output. For the same project measurements suggest that values of up to 80% can be attained during long-term heat extraction (Moormann et al., 2018). An effect of internal air was also highlighted by Berg et al. (2017) and by Nicholson et al. (2013) who claim that the efficiency of the energy tunnel depends both on the surrounding ground temperature and on the tunnel air temperature, in addition to ground permeability and hydraulic gradient. The relevance of tunnel air, especially in hot tunnels, is emphasised by Ogunleye et al. (2019), as in their study on hot tunnels its seasonal variation helps the recovery process and influences thermal efficiency. According to Bracq et al. (2017) who worked on the Grand Paris Express project, in winter 75% of the extracted energy originated from the tunnel because of the high temperature in the tunnel and to the fast cooling of the ground that reduces to about 1 month the period of efficient thermal exchange. On the contrary, in summer, as they supposed an air temperature very similar to that of the inlet, almost all energy comes from the soil.

Monitoring experiences from the few pilot projects of energy tunnels show that the rock mass thermal properties and the tunnel climate are crucial for determining the extraction rates (Buhmann et al., 2016). In the numerical models the tunnel climate boundary condition is of great significance to correctly predict energy performance.

The paper by Peltier et al. (2019) focuses on the concept of thermal and velocity boundary layers, involving the thermal L_{th} and hydrodynamic L_{hyd} entrance regions and the stabilised or fully developed regions, also described in Brandl (2006) and shown in Figure 2.30a. In the thermal and hydrodynamic entry length, flow velocity and temperature profile can vary with the chainage, while they are constant in the stabilised area. Depending on the wall roughness,

the airflow velocity (or else the Reynolds number) and the shape of tunnel cross-section, different thermal and hydrodynamic entry lengths can be obtained. This is important as convective heat transfer between the tunnel lining and the tunnel air is a function of both the velocity of the air through the heat transfer coefficient and the difference between the air undisturbed temperature and the temperature at the tunnel wall. If these lengths change, the aerothermal energy than can be harvested does change too. For example, the Reynolds number does not affect the value of L_{th} and L_{dyn} , but it influences the way the convection heat transfer coefficient varies longitudinally as this increases with increasing air velocities, as known in literature. Typical thermal entry lengths are between 100 and 400 m.

In Figure 2.30b some established correlations between the convective heat transfer coefficient and the average airflow velocity are depicted. The convective heat transfer coefficient increases not only with increasing airflow but also with increasing roughness. Moreover, comparing the average heat transfer coefficient along L_{th} and L_{hyd} , little differences can be found, then the average energy flux exploitable through energy tunnels is practically unaffected by the development of velocity and thermal boundary layers. Constant values of convection heat transfer coefficient are appropriate to describe heat transfer in energy tunnels. This is what Nicholson et al. (2014), Zhang et al. (2014) and Cousin et al. (2019) did in their studies, by considering 5, 15 and 15.13 W/m^2K respectively. Ogunleye et al. (2019) considered 15 W/m^2K too.

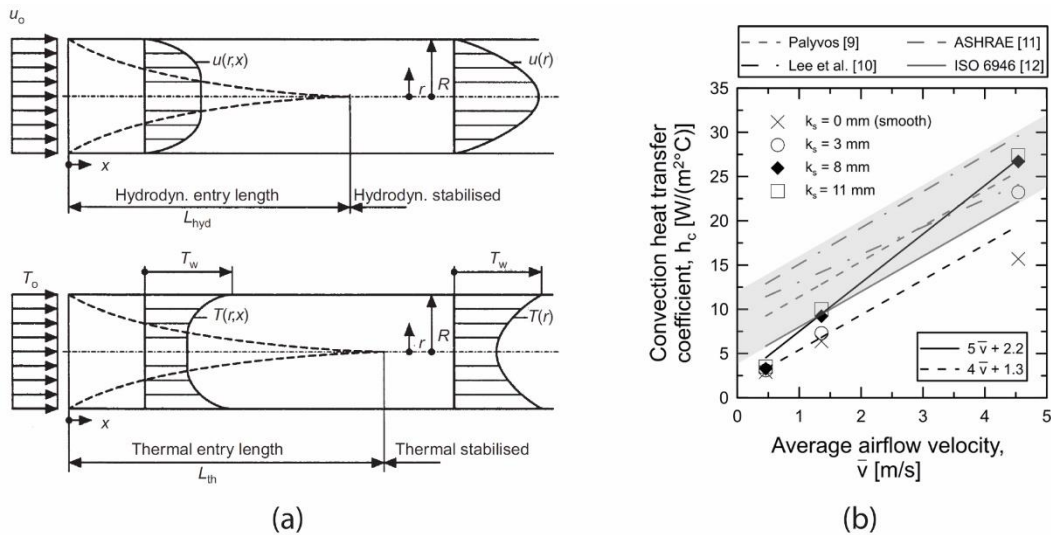


Figure 2.30: (a) Thermal and hydrodynamic entry length and stabilised area within a tube (from Brandl, 2006), (b) correlations between heat transfer coefficient, wall roughness and airflow velocity (from Peltier et al., 2019).

2.4.7. Other applications: mountain tunnels

Some authors performed feasibility studies for the thermal activation of deep tunnels (Barla et al., 2018; Tinti et al., 2017). In particular Barla et al. (2018) tested the efficiency of Enertun air configuration for cooling on the case study of Turin-Lyon new railway tunnel, where temperature is expected to exceed 32°C in many sections. They imagined to activate the system when internal temperature is higher than 30°C and to turn it off when reaching about 25°C, estimating savings of between 10 and 20 k€/ (km·year). Moreover, the extracted heat for 1 km, about 6500 MWh/year after the initial 50 days of operation, could be delivered to any user in

the vicinity of the tunnel portals. The wider presence of potential users in urban areas makes urban tunnels the best application, although deep tunnel cooling could allow big savings on ventilation systems. Tinti et al. (2017) suggested an optimization strategy for the design of energy tunnels and reconstructed the initial tunnel and rock-mass temperature field by Kriging spatial interpolation techniques in the framework of a preliminary design study for implementing energy lining in the Mules Access Tunnel that is part of the Brenner Base Tunnel (BBT), excavated by drill and blast. The crown, invert and rock-mass temperatures allowed to set tunnel intrados and extrados boundary conditions. Some results are presented in Figure 2.31 for an inlet temperature of 0°C: higher flow rates reduce outlet temperature, but globally the thermal power is enhanced, up to 560 kW. The higher the user required temperature level, the lower the heat pump COP. The total efficiency balance should also consider the circulation pump consumption, not only that of the compressor, that could be threatened by the considerable pressure drops, increasing with flow rate, as also stated by Zhang et al. (2014). A small village of potential users was supposed, and it was verified that the energy lining be able of providing the needed thermal energy based on a typical thermal load profile. The modulation of flow rate can help in fulfilling the energy needs and in attaining good seasonal efficiencies. Temperature tuning can be an option to avoid geothermal resource depletion around the heat exchangers in the short and long term.

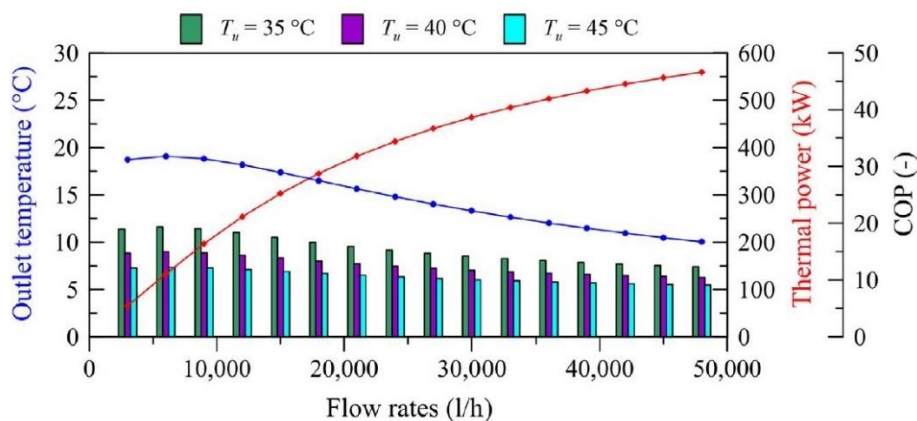


Figure 2.31: Effect of flow rate and user temperature level on thermal performance for the case study of Mules Access Tunnel (from Tinti et al., 2017).

The potential of mountain tunnels for geothermal exploitation is noticeable, nevertheless no users can be usually found in the immediate vicinity. This drawback can be solved by imagining low-temperature district heating networks and by adequately accounting for feed and return heat losses. Heat pump for temperature rising would be located downstream, close to buildings and villages.

2.5. Structural behaviour

The effects produced by tunnel thermal activation in terms of structural integrity have to be investigated to ensure the long-term behaviour of the segments is not jeopardised. A relevant imbalance exists in literature between studies on thermal efficiency and researches on structural integrity of energy tunnels, as little work was carried out in this latter area. To the Author's best knowledge, the only references in this respect are Barla and Di Donna (2018), Mimouni

(2014), Mimouni et al. (2013), Dupray et al. (2013) and Nicholson et al. (2013, 2014). In all cases thermo-mechanical (TM) or thermo-hydro-mechanical (THM) numerical analyses were undertaken, because of the complexity of pipe geometry as well as soil-structure interaction. No experimental data are available.

In general, from the theoretical point of view, the governing equations for the mechanical problem are:

$$\text{Equilibrium equation} \quad \text{div}(\sigma'_{ij}) + \rho \cdot g_i = 0 \quad \text{Eq. 2.27}$$

$$\text{Compatibility equation} \quad \epsilon_{ij} = \frac{1}{2} \cdot \left(\frac{\partial u_i}{\partial x_j} + \frac{\partial u_j}{\partial x_i} \right) \quad \text{Eq. 2.28}$$

$$\text{Constitutive equation} \quad d\sigma'_{ij} = C_{ijkl} (d\epsilon_{kl} - d\epsilon_{kl}^p) \quad \text{Eq. 2.29}$$

where σ'_{ij} is the effective stress tensor, ρ is the material unit weight, g_i is gravity vector, ϵ_{ij} is the strain tensor, u_k are the displacements along the coordinate x_k ($k=i,j$), C_{ijkl} is the fourth order elastic tensor, $d\epsilon_{kl}$ is the increment of total strain, $d\epsilon_{kl}^p$ is the increment of plastic strain. Together with Eq. 2.27, Eq. 2.28 and Eq. 2.29 appropriate boundary conditions need to be specified. For the thermo-mechanical problem, the thermal strains must be included (Figure 2.22). For an isotropic material the thermal strain corresponding to an infinitesimal thermal variation dT can be expressed as:

$$d\epsilon_{kl}^T = \alpha_t dT \delta_{kl} \quad \text{Eq. 2.30}$$

where α_t is the coefficient of linear thermal expansion and δ_{kl} is the Kronecker delta. Hence also Eq. 2.29 changes according to the following expression:

$$d\sigma'_{ij} = C_{ijkl} (d\epsilon_{kl} - d\epsilon_{kl}^p + d\epsilon_{kl}^T) \quad \text{Eq. 2.31}$$

In absence of pore pressure, the stress change associated to a temperature change is defined as:

$$d\sigma_{ij} = -3 \cdot K \cdot \alpha_t \cdot dT \cdot \delta_{ij} \quad \text{Eq. 2.32}$$

where K is the bulk modulus.

In Barla and Di Donna (2018) the finite difference software FLAC (Itasca, 2016) was adopted for transient, purely conductive TM coupled analyses with the aim to evaluate stresses and strains due to cyclic thermal variations across the thickness of the ring. As stated in Itasca (2016), the coupling is one-way, that is mechanical changes resulting from force application cannot produce temperature changes, while the opposite can occur. The underlying assumption is that in quasi-static mechanical problems energy changes can be neglected. After building the real problem geometry where the layout in Figure 2.5a and a deep tunnel were considered (Figure 2.32a), assigning ground and concrete adequate constitutive parameters and simulating construction sequence, the temperature module was activated together with the already active mechanical one and temperature changes resulting from TH analyses were applied at the pipe contour as a temperature boundary condition. Pipes are located at 12.5 cm from the lining extrados, the lining thickness is 35 cm and the ring diameter is 7.4 m. The additional variations in horizontal and vertical stresses consequent to a full summer-winter cycle are shown in Figure 2.32b. It can be seen that in summer compression increases and in

winter compression decreases. Moreover, the order of magnitude of these variations is lower than 1 MPa in summer and than 0.75 MPa in winter. The difference is due to the higher temperatures reached in summer during cooling operation.

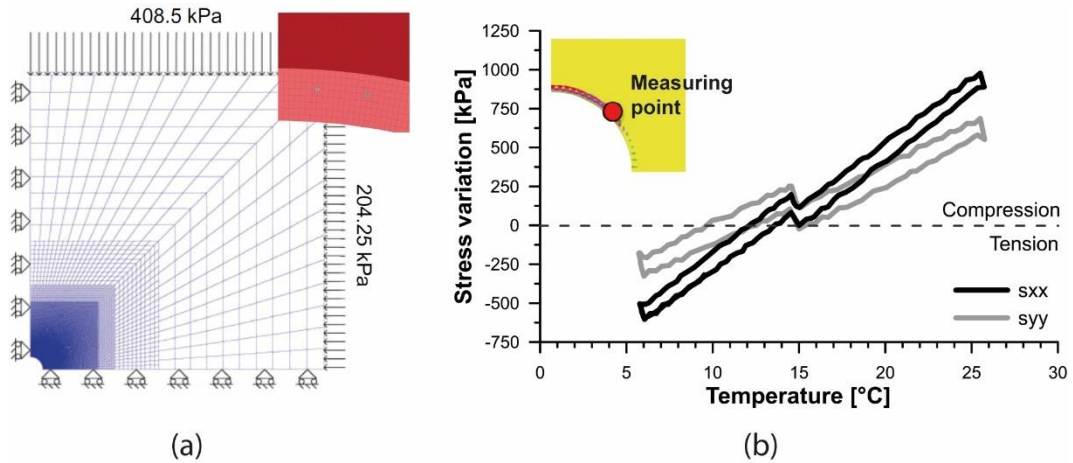


Figure 2.32: (a) FDM mesh of the TM model and (b) stresses variations output (modified from Barla et al., 2018).

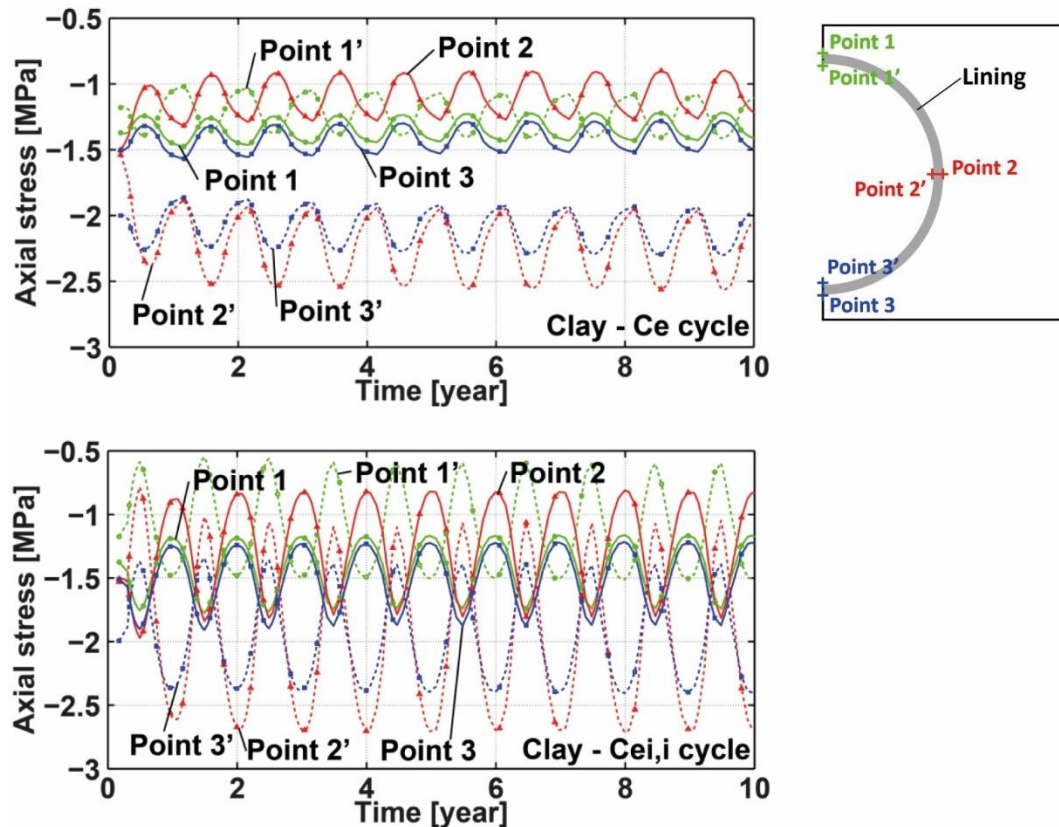


Figure 2.33: Axial stress for clay and silt in extraction only and injection and extraction cases (modified from Mimouni et al., 2013; compression is negative).

Similar ranges were found by Mimouni (2014) and Mimouni et al. (2013) who analyzed numerically the mechanical response of soil and tunnel lining and related geotechnical issues in the case of a deep bored tunnel whose anchors are thermally activated. The tunnel was considered deep as they estimated that the thermal influence reaches 6 m, while the tunnel crown is 14 m deep. Creep was not investigated, and the constitutive thermal model was assumed as thermoelastic, so no irreversible phenomena arise. Due to the much higher water thermal expansion coefficient in comparison to soil and concrete, when temperature increases excess pore pressure reduces effective stresses in the soil matrix and vice versa. This means that the load on the lining will vary cyclically, which should be taken into account in the design. Figure 2.33 illustrates the results obtained in terms of axial stresses in the lining for a clayey soil following 10-years thermal activation (only extraction Ce and both injection-extraction Ce_i-i starting by injection respectively). It can be noticed that extrados and intrados stresses are in antiphase as the loading causes bending in the lining and subsequent additional compression at the intrados and traction at the extrados. Moreover, in the extraction only cycle, soil effective stresses increase and the load on the tunnel increases. The opposite occurs in the injection-extraction cycle as injection takes place first. Depending on the thermal load curve considered (Ce or Ce_i), the stress variations can range between 0.5 and 1.5 MPa.

Vertical and horizontal displacements were also examined. Although points 1-1' and 3-3' show the same vertical and in-phase displacements, there are differences between crown and invert. This means that the lining all moves in a certain direction, but cyclic compression and dilation of the vertical diameter occurs. Table 2.8 summarizes the tunnel vertical diameter variations for the Ce and Ce_i,i cycles on clay and silt. It can happen that the vertical diameter remains compressed, but in the case of Ce_i,i cycle on silt it can extend. Horizontal displacement at the top of the invert slab are indicated in Table 2.9.

Table 2.8: Variations in tunnel vertical diameter for the Ce and Ce_i,i cycles on clay and silt (from Mimouni et al., 2013).

Operation	Clay		Silt	
	Max	Min	Max	Min
Ce	-0.5 mm	-1.1 mm	-0.2 mm	-0.6 mm
Ce _i ,i	0 mm	-1.5 mm	+0.25 mm	-0.6 mm

Table 2.9: Invert slab top horizontal displacements for the Ce and Ce_i,i cycles on clay and silt (from Mimouni et al., 2013).

Operation	Clay	Silt
Ce	+0.02 mm	+0.07 mm
Ce _i ,i	+0.1 mm	+0.18 mm

At the ground surface, above the tunnel crown, vertical displacements are greater for clay with Ce_i,i cycle than for silt, by 4-5 times, oscillating between -5 and 5 mm. The reason is that the lower permeability hampers water dissipation, whose expansion and contraction amplifies vertical displacements.

In the geotechnical conditions analysed by Barla and Di Donna (2018), no substantial precautions need to be taken as thermal loads can be neglected in the short and long term. In silt and clay, according to Mimouni (2014), the mechanical implications of seasonal heat storage are relatively relevant and should be taken into account in design.

In both previous cases 2D numerical models were performed. Nicholson et al. (2014) carried out a 3D coupled thermo-mechanical FE model of the Crossrail tunnel (6.2 m in diameter and 300 mm in thickness, see Figure 2.34a) with a typical London stratigraphy, with

drained and undrained layers (e.g. London clay). The concrete liner is assigned a linear elastic model and a novelty compared to previously mentioned models is the representation of the segments joint through interface elements to permit rotational movements among them. They followed a different approach compared to, for instance, Barla and Di Donna (2018), as they fixed the extraction rate rather than a temperature boundary condition. The variations in vertical and horizontal tunnel diameter are shown in Table 2.10, from which it emerges that the extraction case leads to a further 1 mm horizontal contraction compared to the no extraction case.

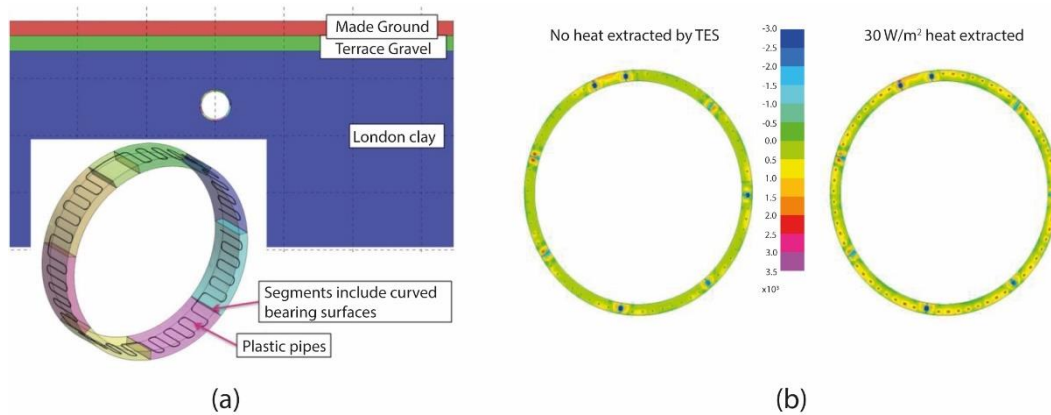


Figure 2.34: (a) Geometry of the thermo-mechanical FE numerical model and (b) maximum principal stress distribution during summer without and with heat extraction (modified from Nicholson et al., 2013).

Table 2.10: Variations in Crossrail tunnel diameter for the no heat extraction and the 30 W/m² heat extraction cases (from Nicholson et al., 2014).

Season	0 W/m ² (natural conditions)		30 W/m ²	
	Crown-invert	Springlines	Crown-invert	Springlines
Summer	+0.1	-1.1	+0.3	-1.9
Winter	-0.5	-1.6	-0.6	-2.6

+ expansion outward
- contraction inward

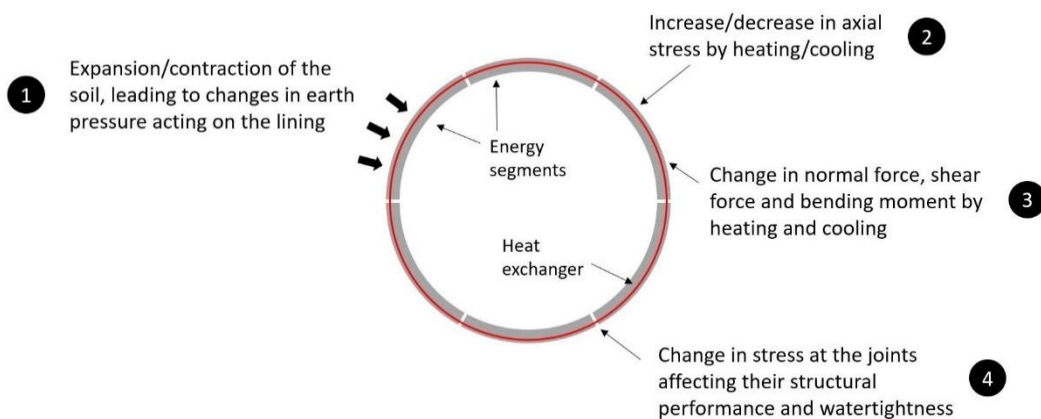


Figure 2.35: Main issues involved in the geotechnical design of energy tunnels (modified from Soga and Rui, 2016).

The maximum hoop stress occurring at the segmental joints is pointed out. Under natural conditions this is 7% higher in summer than at the end of the construction, rising to 9% if heat extraction takes place. No substantial differences are highlighted in winter. They obtained that hoop stresses remain compressive both at the extrados and at the intrados. The tensile (bursting) stress is also maximum at convex to convex joints (Figure 2.34b) and proportional to hoop stresses. Around the pipes where heat is extracted, local tensile stresses are also expected due to cooling, but the obtained value of 3.5 MPa still remains below the design limit of 5 MPa.

The main issues related to geotechnical design and highlighted in the above-mentioned studies are summarized in Figure 2.35.

2.6. Design concepts

The brief review in this chapter includes fundamentals from AFTES (1997), ITA (2000) DAUB (2013) and from European and Italian regulations.

2.6.1. General aspects of tunnel linings

In TBM-driven tunnels, precast concrete linings have several functions: prevent rock falls, hydraulically seal the tunnel, absorb TBM forces both during excavation and steering, handling rock and groundwater loads, allow mounting of equipment, ecc. They are composed by a series of side-by-side rings, divided into elementary units called segments. Generally, the ring length is 0.60-2 m according to AFTES (1997) and 0.75-2.50 m according to DAUB (2013). The segment thickness is 15-75 cm (AFTES, 1997; DAUB, 2013).

Segments can come in different shapes. The rectangular and trapezoidal shapes include rectangular identical standard segments, two counter segments and a trapezoidal key segment to ensure key closure. In most cases, the location of the segments is offset longitudinally, to prevent water leakages and to apply a certain pressure on the nearby already installed segments. The universal and the left-and-right rings can be mentioned among this category. As the name itself says, the universal ring requires only one set of rings to achieve any longitudinal and altimetric path. Another shape is the parallelogrammatic and trapezoidal one, involving the adoption of plugs between successive rings contact face. In this case parallelogrammatic standard segments, a key segment and a reversed key segment are comprised in the lining. Finally, the use of trapezoidal segments allows simultaneous tunnel excavation and lining erection. In this case half segments are counter type, that is their width decreases in the direction of TBM advance, and the remaining half is key type, that is their width increases in the direction of TBM advance.

Of great significance are contact surfaces or joints, divided into i) circumferential (or transverse) contact joints between segments of different rings and ii) radial (or longitudinal) contact joints between segments of the same ring. In i) compressive and shear forces are beared, originating from the longitudinal thrust of the TBM and from the adjacent rings' differential deformations. In ii) compressive loads, transverse shear forces and bending forces are to be sustained. The presence of waterproofing sealing profiles called gaskets all around the segment perimeter, several centimetres from its extrados, guarantees watertightness thanks to their compression during erection and the whole infrastructure lifetime. Longitudinal and transverse assembly mechanisms at contact joints help achieving sufficient erection accuracy, maintaining compression at waterproofing gaskets, guaranteeing segments stability at the erection stage and ensuring correct relative positions between segments. Examples are bolts and threaded rods whose installation takes place using pockets at the intrados, or plugs that

do not need pockets with subsequent reinforcement simplification, but as they cannot be removed they inhibit some degrees of freedom and lead to excessive stresses in the lining that should be taken into account during design. Pockets inevitably represent sources of weakened strength, whose impact on the structural behaviour through all construction phases, not only during ring erection, should be examined. It is reminded that, if not needed for standard assembly reasons or else (grouting, erection, precutting, traceability, instrumentation...) these are needed in energy rings for connecting the individual segments pipes circuits. Recommendations (AFTES, 1997) suggest limiting their number to a minimum, given that reinforcement in these area needs ad hoc consideration. A compromise could be found regarding the size of these pockets.

The annular gap between the extrados of the lining and the excavated profile is back-grouted to block the lining against the ground, reduce ring displacements during construction and in the long term, equalize effectively the actions on the lining, reduce deformations in the surrounding ground to a minimum, help controlling confinement pressure, ensure imperviousness at the back of the TBM.

If ground stability and water inflows are not restrictive, segments can be mounted outside the area of the TBM.

Tunnel structure durability requires that load bearing capacity and serviceability are met over the useful life, avoiding spalling, water leakages, corrosion and ageing damages. Segments concrete durability is related to concrete mix design, permeability, as well as from temperature, frost, salts, fire, sulphate, aggressive chemicals contained in the ground and in the groundwater. In the case of energy tunnels, the action of temperature on segments durability should be investigated and the risk of freezing prevented. Admixtures could be considered to ensure adequate performance. Steel bars durability also needs to be guaranteed against the above-mentioned agents and by controlling concrete cover (exposure classes according to UNI EN 1992, 2008) and permeability. A minimum concrete cover of 40 mm, with 5 mm tolerance, should be maintained.

2.6.2. Tunnel lining design

Segments are subjected to a number of operations between the initial casting in the precast plant and the final erection by the TBM. Many of them recur systematically in different projects, such as segments flipping after demoulding, lifting and relocation to storage areas, stacking by insertion of timber blocks to distance the segments, unloading on site, supply to the workface. Each of these stages should be carefully examined from the reinforced concrete design standpoint, by computing internal forces induced within segments and considering the effective age and strength of concrete. Although in most cases this is just a design check, as segments are conceived for tunnel operation and TBM mounting, it might lead to improvements in short-term concrete properties or to redesign of certain mid-phases. During ring building, loads acting on the segments should take into account their pick-up, possible accidental impacts, actions of the assembly systems and TBM jacks thrust.

The structural behaviour of a precast concrete segmental ring is governed by the confinement pressure and the external hydrostatic pressure. For each geological unit crossed, a comprehensive geotechnical characterization with determination of characteristic values is therefore essential.

In addition to this, segment structural properties (sectional area, inertia – accounting for more or less large pockets, deformation modulus - based on concrete class, strength, creep, shrinkage, relative humidity, Poisson's ratio) and contact joint structural properties (sectional area, inertia and ring composition) are of relevance. The discontinuous peculiarity of a ring

reduces its bending stiffness, while compression stiffness is in general only marginally affected. The use of rigid assembly mechanisms limits the reduction in bending stiffness.

Soil-structure interaction is primarily affected by:

- contact conditions between the ground and the back-grouting material (from total slippage to total adherence);
- environment (existence or planning of nearby underground or surface structures, superimposed loads such as buildings or traffic).

A flow chart summarizing the iterative tunnel lining design procedure is shown in Figure 2.36. Given the high complexity and unpredictability of geotechnical materials, careful monitoring and interpretation is a crucial prerequisite during the construction phases for checking design predictions and achieving construction works safely and cost-effectively. In this framework the observational method has to be reminded which includes not only modern measuring sensors but also back analysis techniques (Sakurai et al., 2003).

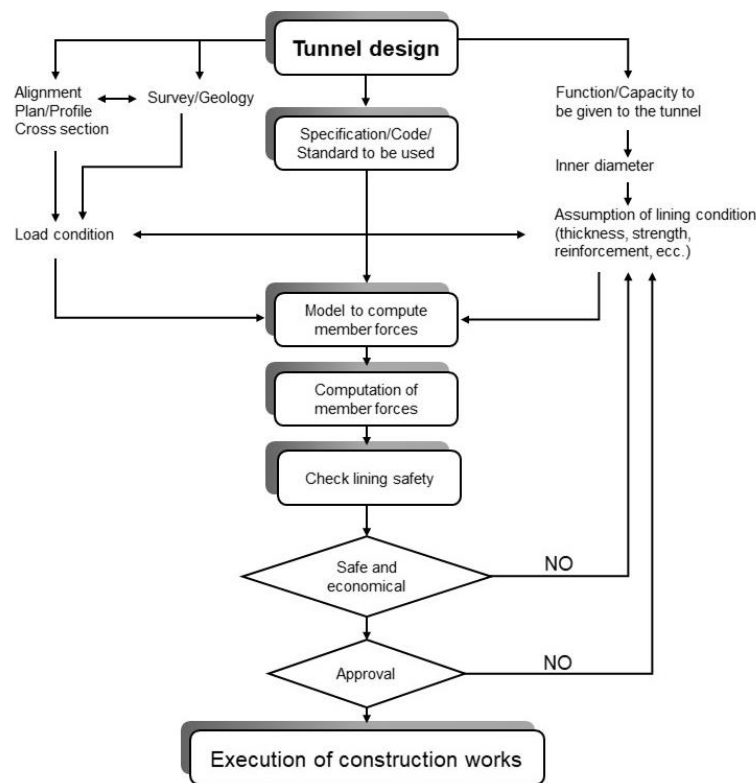


Figure 2.36: Tunnel lining design procedure (modified from ITA, 2000).

2.6.2.1. Limit State Design method

Safety and performance of tunnel structures must be checked with reference to the limit states that can eventually occur. When a limit state is reached, the structure can no longer fulfil the specified requirements (NTC2018, 2018), that is safety with respect to failure (Ultimate Limit State, ULS), serviceability (Serviceability Limit State, SLS), fire, durability and robustness.

Overcoming of a ULS is irreversible, while it could be reversible in case of a SLS. Typical examples of ULS and SLS can be found in Table 2.11.

Table 2.11: Typical ULS and SLS (AFTES, 1997).

ULS	SLS
Failure of a section due to concrete crushing	Excessive cracks opening (corrosion, infiltration)
Excessive deformation of steel	Excessive concrete compression (microcracking)
Loss of static equilibrium at ring erection	Excessive ring deformation
Shape instability (buckling, bulging-only for thin linings in very deformable ground)	

The basic concept of the semiprobabilistic limit state design method, based on the use of partial coefficients, is the comparison between the design capacity R_d , that is a function of design material properties X_d and of nominal geometric quantities a_d , and design action effect E_d , function of design actions F_d and nominal geometric quantities. For ULS safety is verified according to:

$$R_d \geq E_d \quad \text{Eq. 2.33}$$

with

$$E_d = E \left[\gamma_F F_k; \frac{X_k}{\gamma_M}; a_d \right] \quad \text{or} \quad E_d = \gamma_E \cdot E \left[F_k; \frac{X_k}{\gamma_M}; a_d \right] \quad \text{Eq. 2.34}$$

$$R_d = \frac{1}{\gamma_R} \cdot R \left[\gamma_F F_k; \frac{X_k}{\gamma_M}; a_d \right] \quad \text{Eq. 2.35}$$

The design strength X_d is computed from the characteristic strength (fractile 0.05 of its statistic distribution) divided by the strength partial safety factor:

$$X_d = X_k / \gamma_M \quad \text{Eq. 2.36}$$

The same applies to the design actions F_d (in this case the characteristic value is assumed as the fractile 0.95 of its statistic distribution or is related to a specific return period):

$$F_d = F_k \gamma_F \quad \text{Eq. 2.37}$$

If more than one action occurs simultaneously, a combination factor $\psi \leq 1$ is also applied to the characteristic value of the action, to keep in mind the reduced possibility that all actions occur at once with their characteristic value.

For SLS performances are guaranteed according to:

$$C_d \geq E_d \quad \text{Eq. 2.38}$$

where C_d is the prescribed limit design value of the serviceability aspect under exam and E_d the design value of the effect of actions.

Today, the technical regulations in force in Italy are the so-called NTC2018 (Norme Tecniche per le Costruzioni) or D.M. 17-01-2018, transposing the European directive in a

single organic text. In particular, the following European regulations are involved in reinforced concrete segments Limit State Analysis:

- Eurocode 0 – Basis of structural design (UNI EN 1990, 2006);
- Eurocode 1 – Actions on structures (UNI EN 1991, 2004);
- Eurocode 2 – Design of concrete structures (UNI EN 1992, 2008);
- Eurocode 7 – Geotechnical design (UNI EN 1997, 2009).

Actions and loadings on the lining can be divided in the following groups:

a) Permanent actions (G)

- Dead weight of the structure
It is the vertical load at the centroid of the tunnel cross-section

$$p_g = \frac{W}{2\pi R_c} \quad \text{Eq. 2.39}$$

- Surrounding ground loads
- Loads induced by close structures
- Hydrostatic pressure (maximum and minimum water levels)
The resultant water pressure acting on the tunnel lining is the buoyancy
- Back-grouting pressures (if higher than ground pressure)

b) Variable actions (Q)

- Working loads inside the tunnel (suspended facilities or inner water pressure)
- Surcharges on ground surface (road and railway traffic load, buildings)
- Loads applied during construction (segment handling, turning, storage, relocation, transportation, loading, unloading, pick-up, installation, longitudinal thrust force of shield jacks, passage of TBM back-up, annular gap back-grouting pressure)
- Temperature-induced actions (uniform and non-uniform temperature variations)
In the case of special thermal actions, design should take into account temperature distributions corresponding to working conditions (NTC2018, 2018). This is the case of energy tunnels.

c) Accidental actions (FA)

- Earthquakes
- Explosions
- Vehicle impacts
- Loss of lining permeability
- Temperature actions in the case of fire
- Accidental actions related to tunnel installations

2.6.2.2. Ultimate Limit State (ULS)

For segmental linings, verifications should be accomplished in the limit states STR (strength reached in the lining), GEO (strength reached in the ground) and UPL (hydraulic limit state produced by hydraulic loads at the face and at the tunnel boundary during advancement) (NTC2018, 2018). The determination of resistances is done using material parameters and partial safety factors indicated in UNI EN 1992 (2008). Two approaches exist, Design

Approach 1 and Design approach 2, and Design Approach 1 includes 2 combinations. In DA1-C1 the coefficients γ_F in column A1 are used, while in DA1-C2 those reported in column A2 (Table 2.12). In DA2 the coefficients γ_F in column A1 of are used. The ULS checks should be done using DA1-C1 (A1+M1+R1) and DA2-C2 (A2+M2+R2) with the partial coefficients in Table 2.12 and Table 2.13, while the coefficients γ_R are taken equal to 1.

Table 2.12: Partial coefficients for actions of effect of actions (from NTC2018, 2018).

	Effect	Coefficient γ_F	EQU	A1	A2
Permanent loads G1	Favourable	γ_{G1}	0.9	1.0	1.0
	Unfavourable		1.1	1.3	1.0
Permanent loads G2 (non-structural)	Favourable	γ_{G2}	0.8	0.8	0.8
	Unfavourable		1.5	1.5	1.3
Variable actions Q	Favourable	γ_Q	0.0	0.0	0.0
	Unfavourable		1.5	1.5	1.3

Table 2.13: Partial coefficients for geotechnical parameters (from NTC2018, 2018).

Parameter	Coefficient γ_M	M1	M2
Tangent of friction angle $\tan\varphi'_k$	γ_φ	1.0	1.25
Effective cohesion c'_k	γ_c	1.0	1.25
Undrained strength c_{uk}	γ_{cu}	1.0	1.4
Unit weight γ_y	γ_y	1.0	1.0

The following action combination should be used (basic and accidental combination):

$$\gamma_{G1}G_1 + \gamma_{G2}G_2 + \gamma_{Q1}Q_{k1} + \sum_i \gamma_{Qi}\Psi_{0i}Q_{ki} \quad \text{Eq. 2.40}$$

$$G_1 + G_2 + A_d + \Psi_{21}Q_{k1} + \sum_i \Psi_{2i}Q_{ki} \quad \text{Eq. 2.41}$$

where G_1 and G_2 are the structural and non-structural permanent actions (dead weight, ground pressure...), Q_{k1} is the main variable action, Q_{ki} are the accompanying variable actions and A_d is the nominal value of accidental actions.

Limit State Design analysis requires that design stresses derived from basic or accidental combinations of actions do not exceed the reinforced concrete sections ultimate limit capacities, defined by the limiting strains ($10 \cdot 10^{-3}$ for steel bars elongation, $3.5 \cdot 10^{-3}$ for partially compressed sections with a strength of less than 60 MPa, $2 \cdot 10^{-3}$ for concrete fully compressed sections).

The analyses whose aim is the structural design considering soil-structure interaction are to be carried out using the characteristic values of geotechnical parameters, where the effect of actions is multiplied by using partial coefficients of group A1 in Table 2.12.

2.6.2.3. Serviceability Limit State (SLS)

Verifications at serviceability limit states refer to the checking of displacements and deformations. In particular, the crack width verification is of relevance. The following combinations of actions apply (characteristic, frequent and quasi-permanent combinations used for irreversible SLE, reversible SLE and long-term effects respectively):

$$G_1 + G_2 + Q_{k1} + \sum_i \Psi_{0i} Q_{ki} \quad \text{Eq. 2.42}$$

$$G_1 + G_2 + \Psi_{11} Q_{k1} + \sum_i \Psi_{2i} Q_{ki} \quad \text{Eq. 2.43}$$

$$G_1 + G_2 + \Psi_{21} Q_{k1} + \sum_i \Psi_{2i} Q_{ki} \quad \text{Eq. 2.44}$$

where the first and second term are permanent actions, the third term is the dominant variable action and the fourth term are accompanying variable actions. For cracking state limit the quasi-permanent and frequent combinations are used. The allowed calculated crack width depends on exposure classes (UNI EN 1992, 2008), but in any case should not exceed 0.2 mm.

The following cracking limit states can be distinguished:

- decompression limit state, where normal stresses are compressive or equal to 0;
- crack formation limit state, where tensile normal stress in the most solicited fiber is $\sigma_t = f_{ctm}/1.2$;
- crack opening limit state, where the computed limit opening is between 0.2 and 0.4 mm depending on environmental conditions and reinforcement sensibility to corrosion.

Thanks to the concrete alkaline environment ($\text{pH} \approx 12$), steel bars are protected by passivation, that is the formation of $\text{Fe}(\text{OH})_2$ at its surface. Nevertheless, special care must ensure an adequate concrete cover in relation to the environment, a satisfactory concrete mix and a limited crack opening. To this aim, reinforcement tensile stress should not exceed certain values.

Another serviceability limit state is the stress limitation limit state, evaluated based on the characteristic and quasi-permanent combinations of actions. To fulfil safety against this limit state, the maximum stresses both in concrete and in reinforcement must be smaller than defined limit values:

$$\sigma_{c,\max} \leq 0.60 f_{ck} \quad \text{for the characteristic combination} \quad \text{Eq. 2.45}$$

$$\sigma_{c,\max} \leq 0.45 f_{ck} \quad \text{for the quasi-permanent combination} \quad \text{Eq. 2.46}$$

$$\sigma_{s,\max} \leq 0.80 f_{yk} \quad \text{for the characteristic combination} \quad \text{Eq. 2.47}$$

2.6.2.4. Stresses in the tunnel lining

The calculation of the tunnel cross-section should include the critical sections, such as those with greatest/lowest cover, highest/lowest groundwater level, large surcharge, eccentric loads, unlevel surface, present or planned adjacent tunnel. Two methods can be used for the determination of stresses in the lining due to soil-structure-interaction, the hyperstatic reaction method and the composite solid method.

In the first one the lining alone is analysed with the ground as an external load. The ground, modeled through mutually independent springs, is considered as elastic. Best applications regard shallow tunnels in weak soils or very fractured rocks. The numerous drawbacks (not possible to estimate ground surface settlements or to take into account the construction stage, behaviour of the ground after failure with time is neglected) make it ideal for preliminary design and for selection of critical sections.

In the second one the global soil-structure system can be studied. The surrounding soil or rock-mass is considered a continuous medium. Analytical solutions arising from soil and rock

mechanics theories for continuous media allow to compute the lining forces under the assumptions of circular and uniform (no joints) tunnel, single elastic ground layer, total adherence or total slippage at soil-lining contact, uniform isotropic or anisotropic loads. These can be derived from the convergence-confinement method, together with the ring radial displacements. This method is not valid for shallow tunnels, heterogeneous ground, uneven external loads and lining. As for the first method, it can be used for its quickness to select critical sections and for sensitivity studies.

An alternative to analytical solutions is given by finite element or finite difference numerical simulation, that allows to perform 2D and 3D analyses. These methods are complex, though very versatile, as they apply to any tunnel depth, heterogeneous grounds with isotropic or anisotropic stresses, behaving variously (elastic, fully elasto-plastic...), uneven surfaces and loads, linings of any stiffness and can represent soil-structure interaction realistically. The stress-strain state of the ground, its displacements and its behaviour after failure and with time can be taken into account, as well as loads redistribution due to lining deformation, 3D nature of the excavation process, excavation stages and influence of tunnel construction on adjacent or overlying structures. These methods are typically resorted to during final design of few specific sections. If empirical methods to estimate settlements are excluded, numerical methods represent the sole tool to tackle these issues.

Other methods are the bedded frame model method, the elastic equation method, the Schultze and Duddeck model and the Muir Wood model (ITA, 2000).

Once member forces are computed, the safety of the most critical sections characterized by maximum positive moment, maximum negative moment and maximum axial force can be assessed using the limit state design method. The relationship between the design reinforced concrete section axial and flexural capacity is described by a curve. The safety of the member section is guaranteed if the point representing acting member forces (M_d, N_d) locates inside that curve. A different approach was the allowable stress design method which considered the comparison between the extreme fiber concrete and reinforcement stress σ_c, σ_s and their allowable stress σ_{ca}, σ_{sa} :

$$\sigma_c \leq \sigma_{ca} = f_{ck} / F_c \quad \text{Eq. 2.48}$$

$$\sigma_s \leq \sigma_{sa} = f_{yk} / F_s \quad \text{Eq. 2.49}$$

where f_{ck} is the characteristic compressive strength of concrete, F_c the concrete safety factor, f_{yk} the yield strength of steel and F_s the steel safety factor.

The effect of shield jacks thrust force should also be checked:

$$f_{ck} / F_c \leq F_a / A \quad \text{Eq. 2.50}$$

where F_a and A are the total thrust force of jacks and the cross-section area of the lining, together with safety of joints and fire resistance to state the lining stability to fire. Usually, temperature-time curves are adopted to describe the fire thermal action.

2.6.3. Current design approaches for energy tunnels

Thermal activation of tunnels could involve potentially serious implications in terms of ground freezing, excessive deformations in the ground, additional thermally induced stresses and strains that cannot be safely sustained by the structure and that need to be considered to ensure a proper design and guarantee structure integrity, together with the change in soil properties

with temperature and in their long-term behaviour. The soil around the tunnel represents a constraint to free thermal deformation, leading both to thermal strains and to thermal stresses. If thermal effects are not accounted for, the safety margin of a conventional design could be reduced. However, no evidence of structural or serviceability issues exists to date for energy tunnels, albeit their limited number does not allow for a representative sample. Due to the fact that the design of the energy tunnels case studies analyzed in all cases did not account for the presence of pipes and their thermo-mechanical effects, the reason does not lie in conservative assumptions or in increased geotechnical factors of safety.

In the thermal design the intention is never to define the geometric restraints of the structure based on the geothermal requirement, but to determine the amount of thermal energy that could be provided by the energy tunnel. To this aim, literature values for initial ground thermal properties, such as temperature, thermal conductivity and heat capacity, are often used instead of collecting site-specific geotechnical input through laboratory and in-situ testing, and monthly thermal loads are used in lieu of appropriate timestepping and realistic analyses (Preene and Powrie, 2009). Misestimation of loads or thermal parameters could lead to short- and long-term failures that should not be seen as outright collapses but as the equivalent of a serviceability limit state in geotechnical design. For example the thermal load applied may not be fulfilled, the ground temperature could keep decreasing due to continuous heating until freezing with subsequent deformations in the ground in the structures above, or there could be an annual heat flow imbalance that alters the ground temperature field and reduces thermal efficiency with impacts on the foreseen costs.

Today the dimensioning of energy tunnels is still based on empirical considerations and the understanding of their thermo-mechanical behaviour is dramatically limited. Except for boreholes and piles (GSHPA, 2012; NHBC, 2010; SIA, 2005), there are no standard design practice rules, guidance for routine use or analyses procedures. Nevertheless, also for piles, for instance, Habert et al. (2018) highlight the variety in the results deriving from the number of possible assumptions in their benchmark exercise for an isolated thermoactive pile and claim the need for further guidance for practitioners. Recently a comprehensive collection of recommendations was published in France, but energy tunnels are classified as peculiar structures that are not addressed in the actual version of the document (CFMS/SYNTEC INGENIERIE/SOFFONS-FNTP, 2016). Some valuable indications can be found in Barla and Di Donna (2018), where the authors clarify that two additional efforts are required to energy tunnels designers: the quantification of exploitable heat, that is efficiency, and the evaluation of long-term integrity of the lining following to thermal actions. The first is defined as thermal design and the second one as mechanical or structural (this latter designation will be adopted in the present Thesis) design.

Usually, every energy tunnel study is individually processed by taking advantage of sophisticated coupled numerical analyses (Nicholson et al., 2014; Barla et al., 2016) or analytical solutions whose underlying assumptions are highly binding and hardly ever applicable (Zhang et al., 2013). Loveridge et al. (2017) make clear that the starting point of what they call the “desk study” should always be the reference to Eurocodes, and in particular to Eurocode 7 (UNI EN 1997, 2009), with the addition of further consulting sources to evaluate the key parameters that are peculiar of energy tunnels and that will be described in Chapter 3. Loveridge and Powrie (2013) point out the need to define operational temperature limits to avoid adverse effects on the geotechnical performance, for example in this direction NHBC (2010) and SIA (2005) set the limit of 2°C to the minimum fluid temperature, even if this is a conservative approach.

2.7. Summary

Energy tunnels are a technology that has been gaining attention in the last decades. The present Chapter has presented a detailed review of the latest developments, with the description of the main case studies and findings related to thermal and structural performance, by devoting a special space to the role of both internal air and groundwater flow. In the last part of the Chapter, design aspects of traditional tunnels have been mentioned, with the aim to prepare the field for successive implementation of guidelines specifically oriented to energy tunnels design.

The equipment of tunnels with ground heat exchangers adds value to the construction of such infrastructures, that is often linked to projects of urban regeneration along their path. This confluence of events makes it even easier and convenient to match the low-grade energy coming from the tunnel with the low energy demand of the new envisaged buildings, transforming this still developing technology into an attractive, reliable answer for meeting both the economic interest of the operator of the tunnel and the energy demand of future potential recipients. However, a fragmented landscape emerges from this review. Many authors focused on similar issues and, what is more, so far, few results from documented implemented projects have been available. Despite the incredible growth in the background on the topic of energy geostructures in the last 50 years, none of the attempts that can be found in the literature managed to spread the application of this technology in order to make it a proven and sound utilization of tunnels infrastructures against the climate change challenge.

Chapter 3

Thermo-mechanical behaviour of soils and concrete

3.1. Introduction

The behaviour of soil and concrete plays a primary role in the design of tunnels. In the case of energy tunnels, an energy supply function is added to the structural function. The understanding of soil and concrete response when undergoing a thermo-mechanical solicitation and the variation of their strength, deformability and thermal properties with temperature is therefore essential, as well as the development of constitutive models able to describe and recreate all identified peculiar aspects.

The results of laboratory experimental campaigns on soils and concrete are reviewed in this chapter, with the aim to highlight the main aspects related to energy tunnels applications. Particular attention will be then paid to presenting the parameters and related laboratory and in situ tests that are needed for energy tunnels design in addition to those routinely assessed during geotechnical investigation.

3.2. Experimental evidences on soils

Soil is a porous material consisting of a solid skeleton and pores that are filled with air or with water in saturated conditions. The case of partial saturation is also possible but will not be dealt with in this review. A major distinction is between granular soils (sand, gravel) and fine-grained soils (silt, clay).

When a sandy soil is heated, both water and grains dilate thermo-elastically according to their thermal expansion coefficient. Normally, the thermal expansion coefficient of water is higher than that of grains (10-15 times), but by virtue of the drained conditions (that is always the case in static conditions for coarse soils) the water expansion dissipates. This explains the reduced number of experimental results for sandy soils. The effect of temperature variations on strength and deformability is rather limited.

On the contrary, clay response to thermal variations is much more complex. This is to be ascribed to their microstructure and to the electrochemical equilibrium among clay particles, whose surface forces are more important than the self-weight ones (it is the opposite for granular soils). Indeed, heating causes a dilation of all soil components, but in the case of clays an alteration of the equilibrium between attractive and repulsive forces changes the distance between particles and strength of the adsorbed layers decreases. Therefore, for clays, understanding of microstructural phenomena is required.

Research in this field started with the aim of understanding effects of temperature variations in specimens sampled and transported to the laboratory (Campanella and Mitchell, 1968). Then it saw a noticeable development during the last decades in reaction to the considerable number of applications involving thermal effects, such as, to name a few, radioactive waste disposal (Tang et al., 2008; Delage et al., 2010), energy geostructures (Laloui et al., 2004), heat storage (Knödler, 2019), underground power cables (Ahmad et al., 2019) and CO₂ sequestration plants (Favero et al., 2016). Today, a conspicuous knowledge is available on the thermo-mechanical behaviour of soils. It is very well known that the response of clay to heat is non-linear and irreversible and is ruled by the temperature influence on free and adsorbed water.

In the following a summary of the experimental evidences emerging from the literature regarding the thermo-mechanical behaviour of clays is reported. The effects of temperature on volume change, stiffness, shear strength and hydraulic response are depicted. These were obtained by performing laboratory tests in which traditional soil mechanics apparatus were adapted for non-isothermal conditions (triaxial tests, oedometer tests, direct shear tests). A comprehensive review on the topic can be found in Laloui (2001). Undrained conditions and unsaturated soils are addressed by Hueckel and Pellegrini (1992) and François and Laloui (2008) respectively.

The analyzed temperature can be said to range, in general, from 4 to 95°C with no phase change, although the typical temperature range for energy geostructures is 5÷40°C (Vieira et al., 2017). This incongruence is due to the fact that, as said earlier, an interest in the thermo-mechanical behaviour of soils initially arose in relation to nuclear waste disposal, in which case higher temperatures are involved. Therefore, if the most important behavioural trends will be highlighted, caution should be adopted when evaluating the results, which will have to be “damped” in a certain way to adapt to the lower ranges of temperatures occurring in energy tunnels.

3.2.1. Volumetric thermal response

It has been extensively proved experimentally (Campanella and Mitchell, 1968; Plum and Esrig 1969; Baldi et al., 1988; Bergado et al., 2007; Burghignoli et al., 1992; Burghignoli et al., 2000; Cekerevac and Laloui, 2004) that when heated in drained conditions, clays can exhibit either a contractive or a dilative volume change. The discriminant parameter is represented by the overconsolidation ratio (OCR), that summarizes the loading history of the soil:

$$\text{OCR} = \frac{\sigma'_p}{\sigma'_{v0}} \quad \text{Eq. 3.1}$$

where σ'_p is the preconsolidation stress, that is the maximum vertical stress experienced and recorded by the soil corresponding to the lowest void ratio e , and σ'_{v0} is the current vertical effective stress. If $\text{OCR}=1$ the soil is normal-consolidated (NC), if $\text{OCR}>1$ it is over-

consolidated (OC). In the first case the soil has never experienced stresses higher than the current one, then any load increment applied will produce relevant elasto-plastic (partially irreversible) deformations. In the second case, the soil is in the elastic domain and any load increment applied will produce modest elastic (reversible) deformations until σ'_p is reached. The preconsolidation stress delimits the elastic domain from the elasto-plastic domain. Based on OCR, different thermal volumetric responses are shown, whose magnitude is a function of soil type, OCR, temperature and soil plasticity (Figure 3.1):

- if the soil is NC, heating in drained conditions is followed by a predominantly irreversible non-linear contraction (thermoplasticity);
- if it is OC, heating produces an expansion that is reversible upon cooling, however after a certain temperature it contracts (the exact threshold is still object of research);
- if clays are slightly OC, during heating the initial dilation is followed by a contraction at higher temperatures, while during cooling they contract.

According to Abuel-Naga et al. (2007) the thermal volumetric strain can be expressed as the sum of a thermoelastic and of a thermoplastic contribution:

$$\epsilon_v^T = \epsilon_v^{Te} + \epsilon_v^{Tp} \quad \text{Eq. 3.2}$$

where ϵ_v^{Te} is the elastic (reversible) expansion component and ϵ_v^{Tp} is the plastic (irreversible) contraction component. The former is related to the thermal expansion of clay minerals and pore water and to the repulsive forces among clay particles upon heating. The latter is due to particles rearrangement. The expansive term is dominant in overconsolidated soils, while in normally consolidated soils the contractive term is more important.

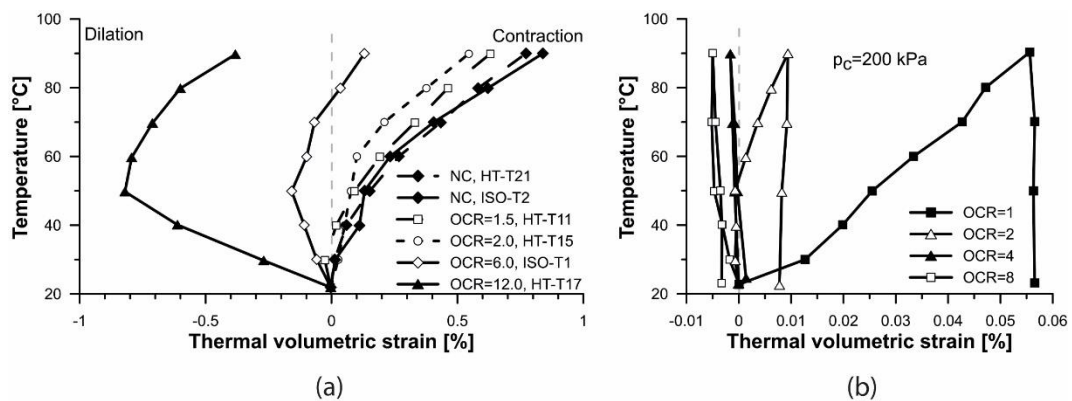


Figure 3.1: Effect of (a,b) OCR, drained heating and (b) drained heating-cooling cycles on thermal volumetric strain (modified from (a) Cekerevac and Laloui, 2004, (b) Abuel-Naga et al., 2007).

Campanella and Mitchell (1968) first attributed the contractive thermal strains to physicochemical changes of adsorbed water and stated that the drained volume change could be computed from the volume of expelled water from the specimen. The OCR at which the behaviour moves from contractive to dilative is not unique for different soil types. The thermal volumetric strain increases with plasticity index PI and does not vary with the stress applied (Abuel-Naga et al., 2007). It is interesting to notice that thermal consolidation curves in terms of volume of expelled water with time are analogous to mechanical consolidation curves

(Shetty et al., 2019; Baldi et al., 1988), probably because pore pressure with a thermal and a mechanical origin dissipate in an identical manner.

It can be seen from Figure 3.1b that under a constant mechanical loading equal to σ'_p or slightly lower, an increase in temperature can cause irreversible deformations. This behaviour was explained by a reduction (nonlinear) in apparent preconsolidation stress as temperature increases (some experimental results are depicted in Figure 3.2). This phenomenon is called thermal softening. The term “apparent” is linked to the fact that the mechanical loading is constant. Di Donna (2014) performed oedometer tests on natural clays and observed a generally decreasing trend in the preconsolidation pressure with temperature. Laloui and Cekerevac (2003) normalised the results and found a linear logarithmic relationship for each material in Figure 3.2 defined by a unique parameter γ :

$$\sigma'_c(T) = \sigma'_c(T_0) \{1 - \gamma \log[T/T_0]\} \quad \text{Eq. 3.3}$$

This relationship is able to express the decrease in preconsolidation pressure with heating.

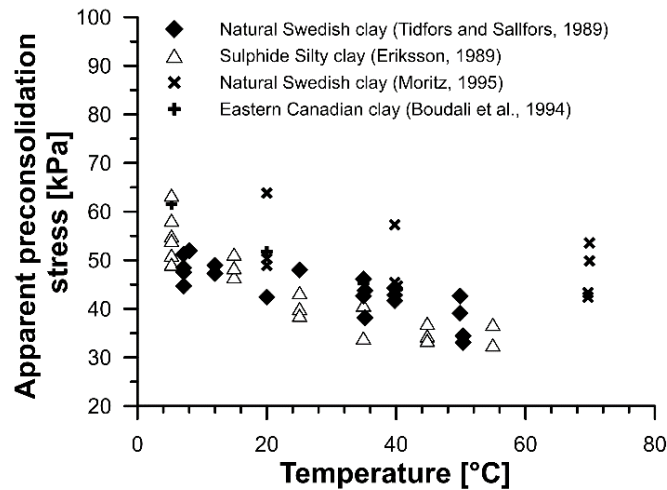


Figure 3.2: Variation of the apparent preconsolidation stress with temperature (modified from Laloui and Cekerevac, 2003).

Through isothermal oedometer tests at different temperatures, Campanella and Mitchell (1968) demonstrated that the compression index (slope of the normal compression line or NCL) is independent of temperatures, but lower void ratios occur (Figure 3.3), as confirmed by Di Donna (2014), Eriksson (1989), Tidfors and Sallfors (1989), Cekerevac and Laloui (2004) and Burghignoli et al. (2000), which is a consequence of induced thermal compaction. In other words, densification is produced. The latter reference added that a higher liquid limit emphasizes temperature influence on preconsolidation pressure. A contradictory result was obtained by Plum and Esrig (1968), who state that the compression index varies with temperature.

Figure 3.4 shows the evolution of the apparent preconsolidation stress with temperature. The mean effective stress is defined as:

$$p = \frac{\sigma'_v + 2\sigma'_h}{3} \quad \text{Eq. 3.4}$$

The preconsolidation stress represents the boundary between the elastic pre-yield and the elastoplastic post-yield domains in isotropic or oedometric conditions. Cekerevac and Laloui (2004) call it “pseudo-elastic limit”. Point A is characterized by an initial temperature T_0 and by an overconsolidated stress condition ($p'_A < p'_{prec}$). After heating, point A moves to A' remaining in the elastic domain and experiencing reversible dilation. If point B or C is considered, the initial stress condition is normalconsolidated or slightly overconsolidated and upon heating the stress path is given by B-B' or C-C'. For point B the response is thermoelastoplastic since the beginning of heating, while for point C the response is elastic until C'', on the yield limit at the edge of the two domains, and then thermoelastoplastic until C'.

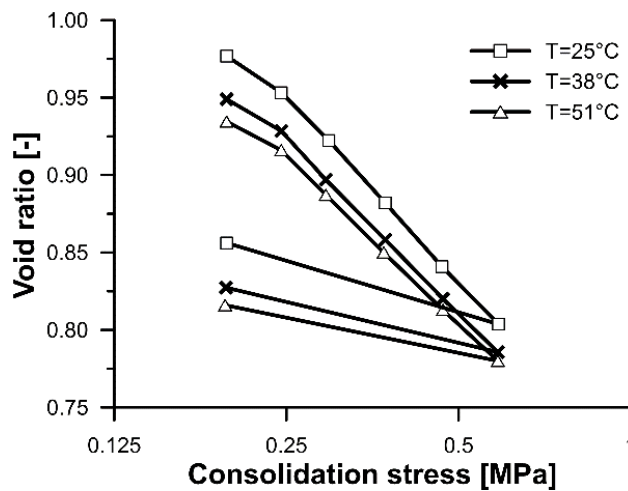


Figure 3.3: Effect of temperature on isotropic compression line for a saturated Illite (modified from Campanella and Mitchell, 1968).

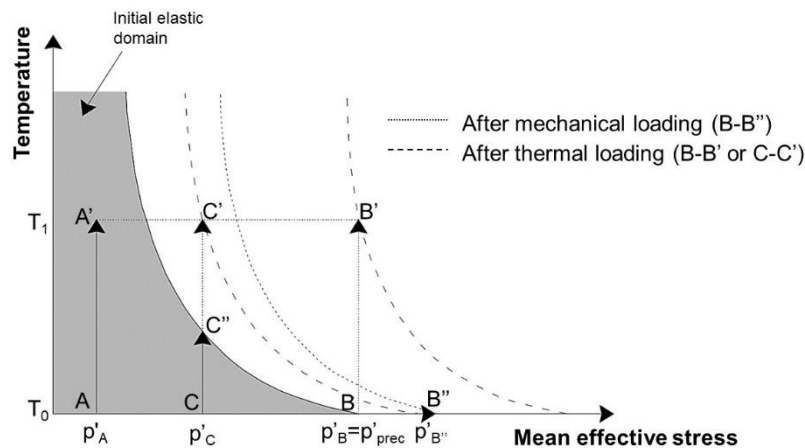


Figure 3.4: Stress path in the isotropic plane (modified from Laloui and Di Donna, 2013).

If thermal softening is the reduction in preconsolidation stress and, subsequently, of the elastic domain (yield limit in the isotropic plane), the increase in the elastic domain following to plastic deformations is called thermal hardening. As well as an isothermal mechanical loading from B to B'' in Figure 3.4 leads to a new preconsolidation pressure $p'_{B''}$ and to an extension

of the initial elastic domain, a thermal loading from B to B', produces the same effect, called thermal hardening, with subsequent densification, although the effective stress does not vary.

Undrained heating causes increases in pore water pressure, with a corresponding reduction in effective mean stresses, that are reversible upon cooling but could lead to failure if the specimen carries shear stresses as they are not always irreversible in this circumstance (Hueckel and Pellegrini, 1992). Abuel-Naga et al. (2007) demonstrated through triaxial undrained heating tests that pore water pressure is a function of the stress history and is reversible for NC specimens, irreversible for OC specimens (Figure 3.5) as observed by Hueckel and Pellegrini (1992). The mean effective stress applied has a strong influence on the amount of pore pressure developed as it represents a restraint to thermal expansion of soil skeleton. By normalizing the results in Figure 3.5, it was observed that results are coincident for i) heating for different OCR, but they are not for ii) cooling in OC specimens. For i) Campanella and Mitchell (1968) introduced the parameter F, that is the variation of thermal induced pore pressure per unit variation of temperature and of effective stress. The reason of ii) is the permanent fabric disintegration induced by temperature change at low stresses.

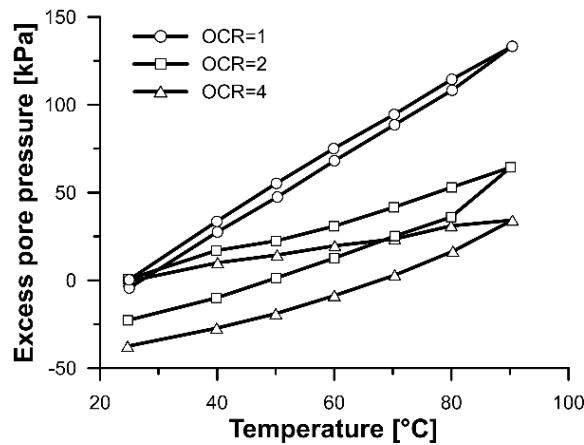


Figure 3.5: Effect of OCR on pore water pressure development (modified from Abuel-Naga et al., 2007).

3.2.2. Deviatoric thermal response

When a non-null deviatoric stress is present, that is an anisotropic stress state, then a further axis corresponding to the deviatoric stress q , defined as follows, has to be added to Figure 3.4:

$$q = \sqrt{3J_2} = \sqrt{3 \cdot \frac{1}{2} s_{ij}s_{ij}} \quad \text{Eq. 3.5}$$

where J_2 is the second deviatoric stress invariant and s_{ij} is the deviatoric stress component (note that Einstein's notation is adopted here). The thermomechanical yield limit shrinks at higher temperatures (Figure 3.6), which is once again an evidence of the thermal softening phenomenon. For overconsolidated materials it can be seen from Figure 3.6 that shearing at higher temperatures (stress path A'A'' compared to AA'') means earlier plastic strains as the boundary between the elastic and the elastoplastic domain is reached at a lower deviatoric stress. For normalconsolidated or slightly overconsolidated specimens (points B and C respectively) both thermal softening and thermal hardening occur.

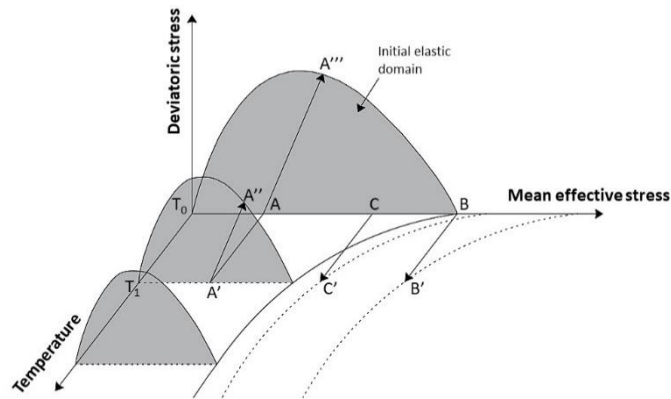


Figure 3.6: Stress path in the temperature-deviatoric stress-mean effective stress plane (modified from Laloui and Di Donna, 2013).

The effect of temperature on soils shear strength is a controversial land. At the origin of the conflicting conclusions there might be the consideration of soil type, mineralogic composition, OCR, drainage conditions, as well as the unclear definition of the thermal and mechanical loading paths of the specimens (Hueckel et al., 2009). According to some authors, irrespective of the OCR, the undrained shear strength increases with soil temperature (Bergado et al., 2007; Abuel-Naga et al., 2007b – drained heating + undrained shearing) Others report no significant changes due to heating and cooling, especially as strains increase (Burghignoli et al., 2000). Campanella and Mitchell (1968) obtained a decrease in Illite clay strength (drained heating + undrained shearing). Cekerevac and Laloui (2004) performed drained triaxial shear tests, by obtaining higher shear strength at high temperatures, especially for lower OCR samples, although the same behaviour is shown at large strains tending to the same critical state (same results obtained by Burghignoli et al., 1992). Moreover, the slope of the critical state line (CSL) is not a function of temperature, that is they found an independency of friction angle from temperature, as supported by other results in the literature (Figure 3.7). At failure, there is no influence of temperature and temperature history on shear strength envelope (Burghignoli et al., 2000).

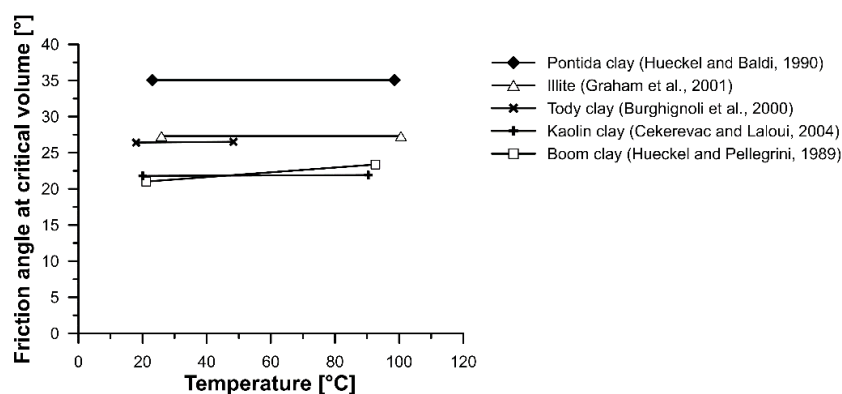


Figure 3.7: Effect of temperature on friction angle at critical state (modified from Cekerevac and Laloui, 2004).

3.2.3. Cyclic thermal response

In the framework of energy geostructures, in addition to the thermo-mechanical behaviour of soils subjected to monotonic thermal loading, it is of interest the investigation of that consequent to cyclic thermal loadings, akin to those occurring seasonally and daily. As reported in Laloui and Di Donna (2013), it was shown in literature (Campanella and Mitchell, 1968; Hueckel et al., 1998; Burghignoli et al., 1992; Burghignoli et al., 2000; Towhata et al., 1993; Di Donna, 2014) that for normalconsolidated clays a large part of the irreversible volumetric contraction occurs during the first cycle and the following cycles result in an increase of irreversible volumetric deformations, though with a progressively smaller entity (accommodation). This concept is called thermal cyclic stabilization (Campanella and Mitchell, 1968). Volume deformations during heating are due to rearrangement of particles, which does not reverse during subsequent cooling, hence producing irreversible deformations (Burghignoli et al., 2000). An example for a saturated Illite specimen is depicted in Figure 3.8: following temperature increase and decrease, a permanent volume variation of 1% occurred, due to irreversible structural rearrangements aimed at sustaining the applied effective stress. Further irreversible volume decrease was small (about 0.1%) but could have an impact on the long-term behaviour of thermo-active systems (Laloui et al., 2014). This behaviour recalls the effect of stress history on volume changes, therefore when a soil undergoes a heating and cooling cycle it becomes overconsolidated. Towhata et al. (1993) observed an independency of the amount of volumetric contraction from the stress level.

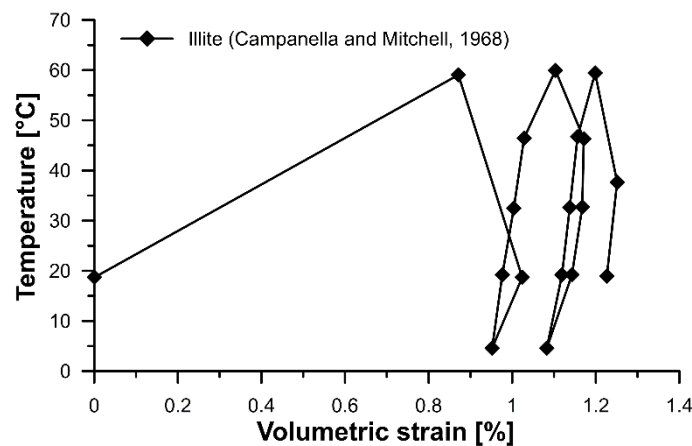


Figure 3.8: Cyclic thermal effects on normalconsolidated clay.

It can be said that in general cyclic thermal loadings generate volume changes, but it was observed that while NC samples always contract (irreversibly), OC can either dilate or contract. Burghignoli et al. (1992) and Burghignoli et al. (2000) tried to clarify this issue for NC and OC clays performing temperature-controlled triaxial tests on Todi clay. Temperature in the samples, pore water pressure and volume changes were measured by embedding a thermocouple, a needle micropiezometer and by measuring the volume of water expelled respectively. They obtained that the magnitude and sign of the volume change after a heating-cooling cycle depends on the amplitude of the thermal cycle, on OCR, on plasticity index, recent stress history. Unloading causes dilation, bigger with bigger OCR; loading and reloading cause contraction. Time (thermal cycle duration and elapsed time from last mechanical consolidation) and history of thermal stresses (number of cycles) also influence soil response

to thermal cycles. Di Donna (2014) verified that initial void ratio and plasticity index increase thermoplastic deformations, confirming the relationship between microstructure and macroresponse.

It can be seen from Figure 3.6 that a heating-cooling cycle performed on an overconsolidated specimen (A-A'-A) does not produce any plastic deformation, therefore the elastic domain and the deviatoric response stay the same at the end of the cycle. A heating-cooling cycle performed from B or C produces both plastic deformations and thermal hardening, with an expansion of the thermal yield surface, then at the end of the cycle the stress state has become overconsolidated. In other words, a thermal consolidation takes place, as demonstrated experimentally by Abuel-Naga et al. (2006), Plum and Esrig (1968), Di Donna (2014) and Burghignoli et al. (1992). When cyclic thermal loading is performed on a NC specimen, an increased stability is reached, with reduction in the void space and in probability of collapse (accommodation), with a transition to an OC condition. After thermal cycling and reloading, the yield threshold locates on the right of the one before thermal cycling (see Figure 3.9). With an increase in stress, the soil gradually forgets the temperature treatment. Burghignoli et al. (1992) found qualitative analogies with isothermal volumetric creep deformation, as the origin lies in the same phenomenon that is the soil skeleton structural changes. The drained thermal behaviour can be related with the creep behaviour of solid skeleton. Further thermal cyclic loadings at temperatures lower than the previous one will lead only to elastic, expansive thermal deformations. Moreover, it was proved, through a drained heating-cooling followed by triaxial shearing, that a beneficial collateral effect of thermal consolidation is the increase in undrained shear strength (Burghignoli et al., 2000). Also Bergado et al. (2007) found an increase in undrained shear strength for soils that undergo a heating-cooling cycle $T_0-T_1 > T_0-T_0$ compared to soils at temperature T_0 and the highest T_1 the highest the undrained shear strength whatever the OCR. In this case, the excess pore water pressure always decreases independently from the OCR.

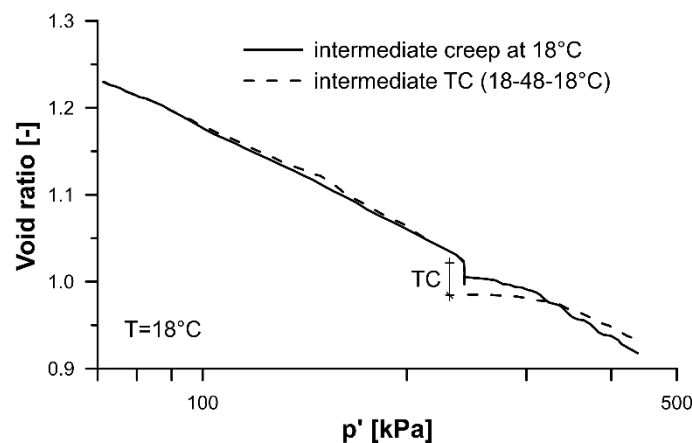


Figure 3.9: Effect of drained cyclic thermal loading on a NC sample compared to a sample left free to deform in isothermal conditions (modified from Burghignoli et al., 2000).

In undrained conditions, pore pressure increases with temperature increases and decreases with temperature decreases, following a hysteresis loop (Campanella and Mitchell, 1968). Pore pressure increase is followed by an effective stress decrease if external forces are constant. Burghignoli et al. (2000) noticed that pore water pressure variation during heating is larger than those during cooling for NC samples and viceversa for OC samples. Thermally induced pore water pressure variations can lead to plastic strains and thermal failure (Hueckel and Pellegrini,

1992). Plum and Esrig (1968) performed undrained cyclic thermal loading between 14 to 35°C in a triaxial cell and their results highlight that pore water pressure gradually increases for the first cycles and that no more increase manifests with additional thermal cycling. They also gave a possible explanation of the closed hysteresis loop observed by some: this probably appears only when the material is overconsolidated.

Different is the case of cyclic mechanical loadings carried out at room or high temperature. An interesting study in this direction is reported by Cekerevac and Laloui (2010) and Laloui (2001). They show that when a sample is heated in drained conditions and then cyclically sheared undrained, the induced strains are lower than the equivalent unheated samples, as well as the developed pore pressures, as the heated sample experiences some sort of densification (thermal hardening). Therefore, failure occurs at the same strain level, but much later for heated samples. However, this is not of great interest in the case of energy geostructures.

3.2.4. Constitutive modelling

Various studies are available that introduce models able to capture the thermomechanical response of saturated clays, mainly because of the high interest in nuclear energy applications. A first attempt to model the constitutive behaviour of soils subjected to temperature was done by Campanella and Mitchell (1968), who wrote theoretical equations for calculating the volume change or pore pressure development based on the distinction of each phase's coefficient of dilation, porosity and water compressibility. However, at that time few experimental results were available.

The critical state model by Schofield and Wroth (1968) was generalized by Hueckel and Borsetto (1990) to model for the first time macroscopic thermomechanical behaviour of saturated clays skeleton in drained conditions including thermo-plasticity based on phenomenological experiments. Some updates of this model followed later on, as in Hueckel et al. (2009) who address into more detail the dependence of strength on temperature. This appears to be dependent on the material, stress state and heating drainage condition. The coefficient M (or the internal friction angle) in some materials increases with increasing temperature, probably because of the structural role played by adsorbed water in different clay minerals.

Modaressi and Laloui (1997) developed a cyclic thermo-viscoplastic model. Again, this is a generalization of previous isothermal elastoviscoplastic models for such materials. The model was validated on experimental results for Boom clay and Pontida clay.

Cui et al. (2000) improved the existing thermomechanical elastoplastic models for saturated clays focusing on the aspect of the plastic deformations at higher OCR and paying attention to the thermal hardening and overconsolidation phenomena. They showed that the model is able to account for the OCR effects by overlapping modelling and experimental results.

Graham et al. (2001) presented a thermal elasto-plastic model relying on their own testing results about the thermomechanical behaviour of illite. Viscosity was neglected in this case, although the authors admit it should be addressed extensively. Their model is inspired by Hueckel and Borsetto (1990), but they affirm that greater emphasis is placed on the behaviour in the v - $\ln(p')$ compression space. Their model well predicts heating and cooling effects on volume changes, strength and pore water pressure for both NC and OC saturated clays, by providing qualitative explanations about some unclear temperature effects.

In 2003 Laloui and Cekerevac (2003) mentioned the importance of thermo-mechanical behaviour of soils not only applied to nuclear waste isolation, but also to geothermal structures. Their thermoplastic model is specific for isotropic thermo-mechanical paths and include thermal hardening in the yield mechanism. The change in preconsolidation pressure due to

temperature is reproduced using a logarithmic law based on the above-mentioned material parameter γ . The model is able to capture the thermal volumetric changes in a soil NC or OC.

An evolution of the previous constitutive models by Laloui and Cekerevac (2003) and Modaressi and Laloui (1997) is the ACMEG-T model (Laloui and François, 2009), where the acronym stands for “Advanced Constitutive Model For Environmental Geomechanics – Thermal effects”. Here, thermoplastic strains develop as soon as the yield limit is reached. As previous models, it belongs to the family of Cam Clay models and originates from the critical state theory. Both nonlinear thermoelasticity and coupled volumetric and deviatoric thermoplasticity are taken into account in a unified approach. Validation against experimental results from Baldi et al. (1991) and Abuel-Naga et al. (2006) showed good agreement, especially with respect to the volumetric deformation upon drained heating and cooling, thermal consolidation and shear strength at different temperatures. The authors are convinced that the ACMEG-T model can be used to model any thermomechanical loading path, in drained or undrained conditions. Di Donna (2014) enhanced this model by including the possibility to reproduce cyclic thermal effects based on the experimental results obtained in her work.

3.2.5. Other effects of temperature

Secondary compression. Towhata et al. (1993) studied the effects of temperature during secondary compression for a MC clay. Consolidation was continued beyond primary consolidation by increasing temperature at 90°C under constant stress level. Heating stimulates a substantial reactivation of volume change (contraction), as if it still was primary consolidation. However, within a short time the rate of volume contraction went back to the one observed for room temperature tests. Hence, usually, the secondary consolidation coefficient is assumed to be independent of temperature and this is coherent with the results by Di Donna (2014).

Hydraulic conductivity. Bergado et al. (2007) carried out hydraulic conductivity tests on normally consolidated specimens of soft Bangkok clay at different temperatures and found that, following temperature increase, water viscosity diminishes and hydraulic conductivity increases. Similar results are exposed in Di Donna (2014) and Towhata et al. (1993), as depicted in Figure 3.10. In their research they found that primary consolidation takes place more quickly at higher temperature, because the permeability of clay increases upon heating.

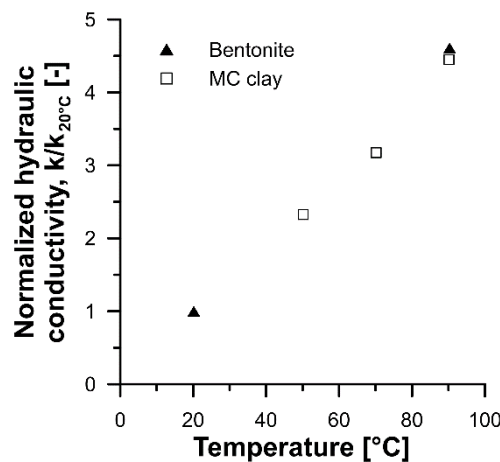


Figure 3.10: Effect of temperature on hydraulic conductivity (modified from Towhata et al., 1993).

Stiffness. The undrained secant modulus of NC specimens increases with temperature and is higher for specimens subjected to a temperature cycle before shearing than for those simply subjected to high temperatures (Figure 3.11a, Bergado et al., 2007; confirmed by Burghignoli et al., 1992). Cekerevac and Laloui (2004) observed an increase of initial secant modulus, computed at 0.5% axial strain from the stress-strain curves obtained from drained triaxial tests, with temperature (Figure 3.11b). The same behaviour was reported by Burghignoli et al. (1992). Burghignoli et al. (2000) discovered that higher temperatures do not affect the tangent bulk moduli, while a thermal cycle produces an initial stiffening that disappears at higher effective stresses. For the secant undrained Young's moduli, the same considerations as for the bulk moduli apply. Hence, thermal history influences soil deformability, while temperature in itself does not. The oedometric modulus did not appear to depend on temperature (Di Donna, 2014)

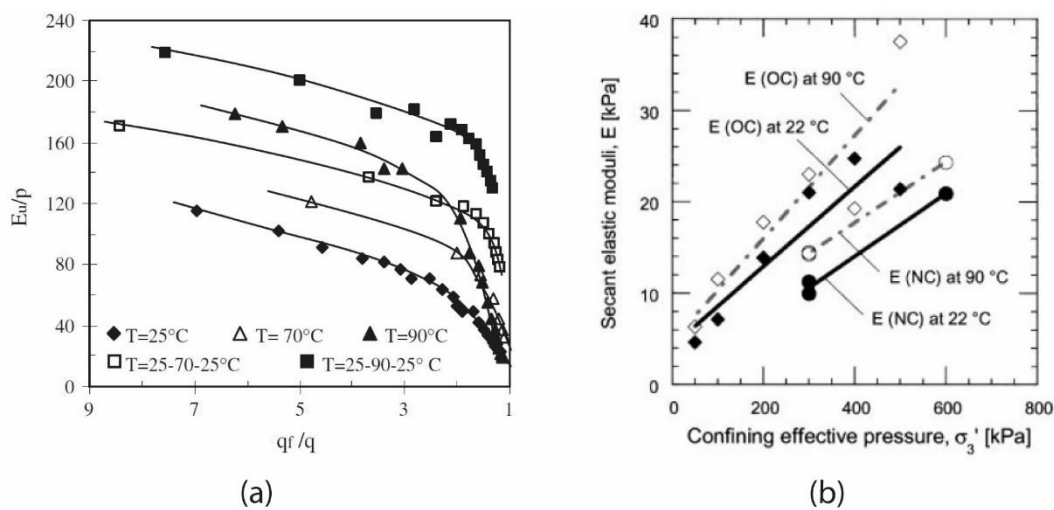


Figure 3.11: Effect of temperature on (a) undrained secant modulus of NC specimens and (b) drained secant modulus ((a) from Bergado et al., 2007; (b) from Cekerevac and Laloui, 2004).

3.2.6. Soil-structure interaction

With special reference to energy piles, the impact of temperature on soil-concrete behaviour was studied by some authors with the aim to predict displacements and shaft capacity. Di Donna et al. (2016) and Yavari et al. (2016) developed and calibrated a new direct shear box adapted with heating system, to investigate the influence of temperature on soil and soil-concrete behaviour at different temperatures for sand and clay, for which no results were available. In particular, in the work by Di Donna et al. (2016) the effect of roughness, temperature, loading conditions (constant normal loading/constant normal stiffness), loading type (monotonic or cyclic) and normal stiffness was investigated in the soil-concrete tests. The thermomechanical stress path for the cases at ambient and at high temperature can be seen in Figure 3.12a,b and were characterized by isotropic consolidation, increase in temperature up to the desired level (with particular care in the case of clay to avoid excess pore pressure generation), shearing at constant normal stress (CNL) or constant normal stiffness (CNS). About the CNS case, the idea is to simulate in situ conditions where the surrounding ground acts like a spring with a certain stiffness reacting to the volumetric soil-structure response. The following relationships hold true (Di Donna et al., 2016):

$$\sigma'_n = \sigma'_{n0} + \Delta\sigma'_n = \sigma'_{n0} - K\Delta\delta_n \quad \text{Eq. 3.6}$$

$$K = \frac{2G_0}{R} \quad \text{Eq. 3.7}$$

where σ'_n is the normal effective stress applied, σ'_{n0} is the initial vertical effective stress, $\Delta\sigma'_n$ is its variation, K is the stiffness of the far-field spring representing the ground, G_0 is the shear modulus of the soil and R is the pile radius.

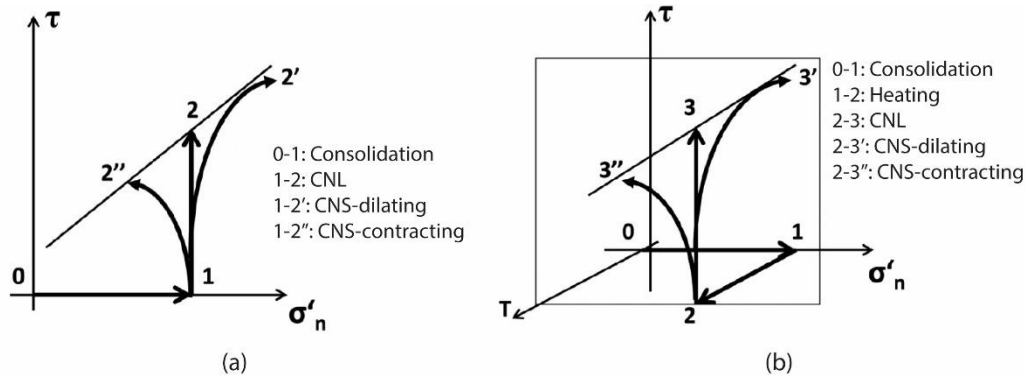


Figure 3.12: Thermo-mechanical stress path for the soil-concrete tests (a) at room temperature and (b) at high temperature (modified from Di Donna et al., 2016).

It appeared that the sand-concrete shear stress and volumetric behaviour are not affected by temperature changes, and failure envelopes (namely friction angle) obtained at 20 and 60°C are coincident for each roughness tested (Figure 3.13a), as expected due to their thermoelastic behaviour and limited effect of temperature on sandy soils, though never verified earlier. When comparing clay-concrete tests at ambient and high temperature, an increase in interface shear strength (both at small displacements, where a peak strength arises, and at constant volume) and a reduction in volumetric contraction during shearing are highlighted in the latter case due to thermal consolidation effect. On the contrary, clay-clay samples heating does not produce significant effects on soil strength at constant volume (Burghignoli et al., 2000). In particular, cohesion (or adhesion) between concrete and clay increases as the consolidation effect increases the contact surface, whereas the friction angle slightly decreases (Figure 3.13b). Under shearing cyclic loading at higher temperatures, lower volumetric contractions are shown, making cyclic degradation slower. From this study it is inferred that temperature plays a favourable role when dealing with energy piles as no effects are present for piles in sands and an increase in interface strength is evident in clay. Under cyclic loading clays have an advantage with respect to sand, that is cyclic contraction is lower and is even reduced by an increase in temperature. Similar results were obtained by Yavari et al. (2016) in the sense that temperature was not found to have any evident effect on the shear strength of sand-sand, clay-clay and clay-concrete samples, and this was proved to be coherent with data in the literature by putting together their and other data. The ranges of temperature they investigated were even closer to those in which energy geotechnical structures work, that is 5-40°C. A major difference from the work by Di Donna et al. (2016) is the fact that the specimens were first heated at 40°C, before being led to the desired temperature (5, 20 or 40°C) to avoid the effects of thermal consolidation and work in elastic conditions. For this reason, they did not observe the increase in cohesion reported by the Swiss team.

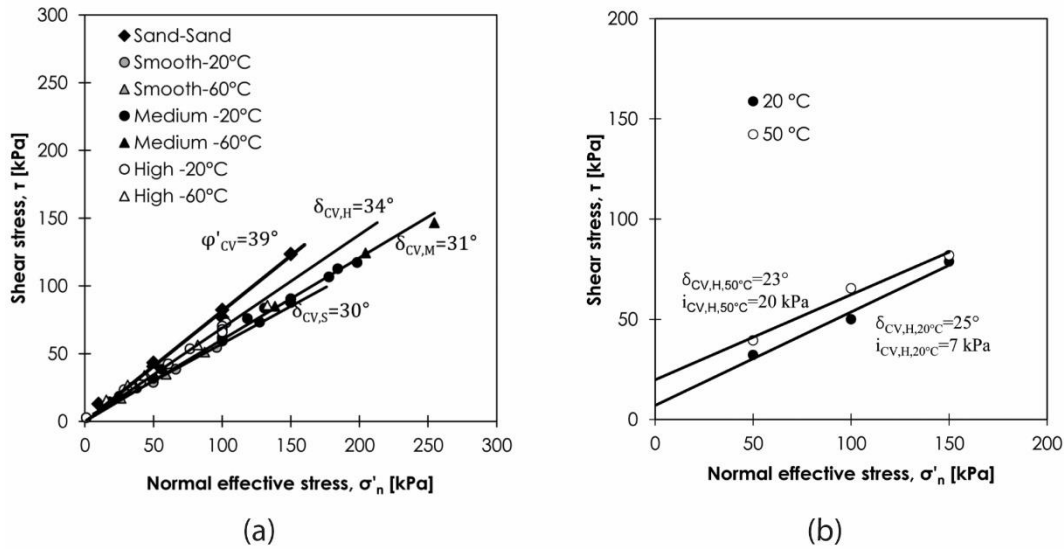


Figure 3.13: Summary of results of direct shear tests at different temperatures for (a) sand-concrete specimens and (b) clay-concrete specimens (from Di Donna et al., 2016).

3.3. Experimental evidences on concrete

Not many studies are reported in literature on the effects of moderate temperatures such as those involved by energy geotechnical systems on concrete, the highest interest being undeniably on the impacts of high temperatures developing in case of fire.

An interesting study on the effect of temperature and pipes embedment on concrete used for energy foundations and thermo-active building systems can be found in Cobo et al. (2015), who performed compression tests and pull-out tests on cubic and cylindrical specimens at different temperatures (20, 40, 70, 100°C) and with pipes placed both parallel and perpendicular to the load. They concluded that an increase of temperature decreases the mechanical properties of concrete, by more than 20% over 70°C, and that pipes reduce the mechanical capacity especially when placed perpendicular to the load. However, they point out that as the working temperatures of thermally activated systems is lower than 55°C it can be assumed that the mechanical properties of concrete are not jeopardised by strength losses of more than 20%.

From the review by Kassir et al. (1996) the response of concrete to temperature can be summarized as follows:

- the compressive strength decreases with an increase in temperature, but this markedly appears beyond 38°C;
- the tensile strength decreases at high temperatures and this reduction is larger under thermal cycling due to differential thermal expansion of cement paste and aggregates and to subsequent cracking, though in the range 23-71-23°C no significant cyclic effects were observed and at 38°C tensile strength is about 90% of that at 21°C;
- the modulus of elasticity permanently reduces at high temperatures, but a maximum reduction of 5% is highlighted at 38°C;
- the stress-strain curve shape remains unchanged upon heating, but the peak strength reduces and occurs at higher strains, thus showing increasing ductility;

- creep, influenced by water/cement ratio and type of aggregates, increases with temperature and strains at 43°C were found to be 1.15-1.3 times those at 23°C;
- shrinkage magnitude increases with temperature until 105°C. As an order of magnitude 65 microstrains were recorded after 5 years at room temperature by Browne (1968);
- the coefficient of thermal expansion is affected by the type of aggregates and remains approximately constant up to 300°C. Typically, it is bigger for the first cycle of heating compared to cooling and following thermal cycles. The range of variation is 2.2 to $3.9 \cdot 10^{-6}/^{\circ}\text{C}$ with an average value of $3.1 \cdot 10^{-6}/^{\circ}\text{C}$;
- thermal conductivity depends on composition (quartzitic and basalts aggregates give highest and lowest conductivities respectively) and degree of saturation. High thermal conductivity allows rapid dissipation of heat fluxes, minimization of thermal gradients across the thickness, and lower thermal stresses. The influence of temperature up to 315°C can be neglected;
- thermal diffusivity variation with temperature can be neglected for the application under study;
- specific heat variation with temperature can be neglected;
- thermal cycling was observed to progressively damage concrete even at moderate temperature rise (65°C) and the degradation process particularly affects compressive strength rather than the modulus of elasticity, especially during the first few cycles.

According to EN 1992-1-2, strength and deformation properties of uniaxially stressed concrete modify starting from 100°C, as well as tensile strength and specific heat. Practically no variations of thermal conductivity and thermal elongation exist in the range of temperatures of interest for the present study.

In general, as for piles, in principle when a tunnel is heated it will expand and when it is cooled it will contract. The entity of these deformations will be:

$$\varepsilon_{th,f} = \alpha \cdot \Delta T \quad \text{Eq. 3.8}$$

where $\varepsilon_{th,f}$ is the free thermal strain, α the coefficient of volumetric thermal expansion and ΔT the temperature variation. Nevertheless, due to the soil restraints, free expansion and contraction will not occur thus resulting in just a part of the theoretical free strain, called observed thermal strain $\varepsilon_{th,o}$ (Knellwolf et al., 2011 related to piles, but here applied to tunnels) and in an increase of stress originating from the portion of strain that was not allowed. This stress will be a reduction in compression upon cooling and an increase in compression upon heating. For piles, the concept of degree of freedom DOF was introduced (Laloui et al., 2003), defined as the ratio between the observed thermal strain and the free thermal strain:

$$\text{DOF} = \frac{\varepsilon_{th,o}}{\varepsilon_{th,f}} \quad \text{Eq. 3.9}$$

This parameter is equal to zero when the deformation is completely blocked and to one when it is totally permitted. Combining Eq. 3.8 with Eq. 3.9 (Knellwolf et al., 2011):

$$\varepsilon_{th,o} = \text{DOF} \cdot \alpha \cdot \Delta T \quad \text{Eq. 3.10}$$

so that the restrained thermal strain $\varepsilon_{th,r}$, given by the difference between the free one and the observed one is (Knellwolf et al., 2011):

$$\varepsilon_{th,r} = (1-DOF) \cdot \alpha \cdot \Delta T \quad \text{Eq. 3.11}$$

and in the hypothesis of a linear elastic behaviour the additional thermal stress is (Knellwolf et al., 2011):

$$\sigma_{th} = -(1-DOF) \cdot \alpha \cdot \Delta T \cdot E_{\text{lining}} \quad \text{Eq. 3.12}$$

in which E_{lining} is the Young modulus of the lining. However, the evaluation of DOF cannot be done but experimentally, as it is difficult to define the degree of restraint due to the surrounding soil.

The tests performed by Bourne-Webb et al. (2009) and by Laloui et al. (2006) on energy piles demonstrated that the thermomechanical response of the pile was reversible and that the pile-soil system behaved thermo-elastically, which would suggest implausible permanent deformation from the ground energy system operation, given the realistic ranges of temperatures adopted in the tests. Nevertheless, long-term monitoring and experimental laboratory campaigns covering the structure lifetime would definitely shed more light on this topic (Loveridge and Powrie, 2013).

The magnitude of thermally induced additional stresses and strains on energy geostructures depend on many factors, such as heat conduction parameters, contrast between volumetric thermal expansion coefficients of concrete and of the different phases of the soil, permeability, drainage conditions and structure's boundary constraints.

3.4. Design properties for energy tunnels

When carrying out investigations for a project of energy tunnel, additional information compared to traditional geotechnical investigations is required, involving both the ground and the geostructure. Careful analysis of input parameters needed in energy tunnel design should be tackled (Cairo et al., 2018). In energy geostructures design it is possible to distinguish two main objectives (Loveridge et al., 2017), clearly defined in the recent standard for energy piles (GSHPA, 2012) but applicable to every geostructure:

- assess the energy output that should be compliant with adequate soil and operating temperatures;
- guarantee the non-exceedance of any structural/geotechnical limit states as a consequence of the additional temperature variations in the geostructure.

For accomplishing i), called energy design, and ii), called structural/geotechnical design, the key design parameters reported in Table 3.1 need to be accounted for during investigations, with in mind the need to know how temperature changes (likely $\pm 20^\circ\text{C}$ for energy geostructures) affect the thermo-mechanical behaviour of soils. Loveridge et al. (2017) affirm that practically there are no significant thermal-related consequences on soils engineering properties, as emerges from the review in 3.2, and that the most relevant impact is the thermal volume change which could even preclude a site from being potentially a candidate for an energy geostructure project. Of course, the level of detail depends on the stage of the project. Thermal demand and balance/imbalance between heating and cooling is also of equal importance given that it affects the way the ground responds and behaves. Adverse impacts on adjacent structures and on the environment should also be assessed.

Table 3.1: Key design properties needed for energy geostructures (modified from Loveridge et al., 2017).

Property	Symbol	Unit	Materials	Required for
Thermal conductivity	λ	W/mK	Soil, concrete	Energy design
Specific heat capacity (volumetric heat capacity)	S_c	J/kgK (J/(m ³ K))	Soil, concrete	Energy design
Undisturbed temperature	T_0	°C	Soil	Energy design
Groundwater flow, Darcy velocity	v	m/s		Energy design
Thermal resistance	R_b	K/W	Fluid, pipes, concrete, soil	Energy design
Soil strength			Soil	Geotechnical design
Soil stiffness			Soil	Geotechnical design
In situ stresses (K_0) and pore water regime			Soil	Geotechnical design
Stress history			Soil	Geotechnical design
Over-consolidation ratio	OCR		Soil	Geotechnical design
Coefficient of thermal expansion (linear, volumetric)	α, β	1/°C	Soil, concrete	Geotechnical design
Concrete limiting stress		MPa	Concrete	Structural design

3.4.1. Design parameters

3.4.1.1. Thermal conductivity

Thermal conductivity is the parameter characteristic of conductive heat transfer measuring how well a material conducts heat, accordingly to hydraulic conductivity and electrical conductance. It is the constant of proportionality in 1D Fourier's law, the basic law of conduction, that applies at steady state and describes the relationship existing between the heat transfer rate and the profile of temperature (analogous to Darcy's law for groundwater flow):

$$\frac{\dot{Q}}{A} = -\lambda \frac{dT}{dx} \quad \text{Eq. 3.13}$$

where \dot{Q} is the heat flow rate along x (W), A is the area normal to x (m²), $\frac{dT}{dx}$ is the temperature gradient (K/m). Its determination can derive both from national databases including laboratory and field measurements or from correlations based on phase proportions (Loveridge et al., 2017), adequate for early-stage projects only:

$$\lambda_{\text{eff(max)}} = (1-n)\lambda_s + nS_r\lambda_w + (1-S_r)n\lambda_a \quad \text{upper bound} \quad \text{Eq. 3.14}$$

$$\frac{1}{\lambda_{\text{eff(min)}}} = \frac{1-n}{\lambda_s} + \frac{nS_r}{\lambda_w} + \frac{1-S_r}{\lambda_a} \quad \text{lower bound} \quad \text{Eq. 3.15}$$

where n is the porosity, S_r the degree of saturation, $\lambda_s, \lambda_w, \lambda_a$ are the soil, water and air thermal conductivity. Upper and lower bounds come from two opposite assumptions that are not made for other coefficients. Indeed, beyond being able to state that $\lambda_w < \lambda_s$ and then $\lambda_w < \lambda < \lambda_s$ (hypothesis of a two-phase porous material), two simple phase distributions can be considered. These are the series distribution and the parallel distribution, in which the phases are thermally in series (minimum value of λ) or in parallel (maximum value of λ) with respect to heat flow direction (Woodside and Messmer, 1961). The first one is obtained from a weighted harmonic mean of each phase's conductivity, while the second one from a weighted arithmetic mean of them.

As a drawback the thermal conductivity of each phase, and in particular of soil for which ranges are quite wide (1÷8 W/mK, Loveridge et al., 2017), have to be determined. Moreover, moisture migration can affect phase proportions and modify thermal conductivity, i.e. heating consequent to heat injection can cause drying and a reduction in λ (Vieira et al., 2017). Its value has a strong impact on ground energy design and system size in case of absence of groundwater flow and it is directly related to the thermal performance and to the ground recover capacity.

For concrete the thermal conductivity ranges between 1 to 4 W/(mK), based on mix design, water content, aggregate lithology and volume ratio.

3.4.1.2. Volumetric heat capacity

It is defined as the amount of heat that is needed to increase the unit mass temperature by one degree. As for thermal conductivity, volumetric heat capacity can be expressed by weighting the relative phase proportions:

$$S_{cv} = (1-n)S_{cv,s} + nS_r S_{cv,w} + (1-S_r)nS_{cv,a} \quad \text{Eq. 3.16}$$

Nevertheless the same drawbacks holds as ranges are 650-950 J/(kg K) (Loveridge et al., 2017). For concrete values of between 840 and 1170 J/(kg K) can be met, with higher values for increasing temperature and water content.

3.4.1.3. Undisturbed temperature

Undisturbed temperature is generally considered as a single-value parameter, even if it is possible to distinguish three areas of the ground based on depth, the surface one, the shallow one and a relatively-deep one (Vieira et al., 2017). In the surface and shallow zone (up to a few meters below ground surface) temperature varies according to daily and seasonal fluctuations, while in the relatively deep zone (up to hundreds of meters down) it increases with the geothermal gradient. However, it can vary due to geology conditions, presence of buildings and infrastructures (urban heat island effect, see Epting and Huggerberger, 2013). The latter could lead to an increase of the stored exploitable heat.

3.4.1.4. Thermal resistance

Thermal resistance is a concept analogous to electrical resistance, usually evaluated at steady state so that it can be said to be constant, and is given by:

$$R = \frac{T_1 - T_2}{q} \quad \text{Eq. 3.17}$$

where $T_1 - T_2$ is the difference between the heat exchangers fluid temperature and the temperature at the geostructure boundary and q is the heat transfer rate applied in W/m. By replacing Fourier's law:

$$R = \frac{L}{\lambda A} \quad \left[\frac{K}{W} \right] \quad \text{Eq. 3.18}$$

or

$$R = \frac{1}{\lambda S} \quad \text{Eq. 3.19}$$

where S is a dimensionless shape factor that takes into account the geometry, hence R depends on both geometry and thermal properties. A low thermal resistance increases thermal performance and reduces the plant size. It can be determined analytically, numerically or experimentally. Resistance of multiple components can be composed in series to give the overall resistance, given in this case by the sum of concrete/grout and pipe/fluid resistances. This parameter is commonly used for piles but can also be adapted to thermal analysis of other energy geostructures (see for example Shafagh and Rees, 2018 and Kürten et al., 2015 for an application of the concept of thermal resistance to the thermal analysis of walls). The fact that it is determined at steady state may lead to overly conservative conclusions about the energy output of the geostructure, because the ground response is usually transient and an extra information as against geometry and thermal conductivity is needed, that is the specific heat capacity.

A “contact resistance” also exists when there is an imperfect interface between two materials (Loveridge and Powrie, 2013).

3.4.1.5. Thermal expansion coefficient

The linear/volumetric coefficient of thermal expansion represents the change in length/volume due to a change in temperature of 1°C . If it is low, it means that induced thermal stresses and strains are lower. The volumetric thermal expansion coefficient is the constant of proportionality between the temperature rate and the volumetric strain rate:

$$\dot{\epsilon}_v = -\beta \dot{T} \quad \text{Eq. 3.20}$$

and can be determined by performing non-isothermal drained isotropic tests in OC specimens.

Table 3.2: Volumetric thermal expansion coefficients in literature.

Lithotype or mineral	Min	Max	Average	Reference
Bentonitic clay	2.50E-04	6.50E-04		Dixon et al., 1993
Calcite			1.38E-05	Fei, 1995
Chlorite			3.12E-05	McKinstry, 1965
Clay			3.40E-05	McTigue, 1986
Clay particles			2.90E-05	Horseman and McEwen, 1996
COx claystone			4.20E-05	Gens et al., 2007
Dickite			2.67E-05	McKinstry, 1965
Felspar			1.11E-05	Fei, 1995
Halloysite			2.20E-05	McKinstry, 1965
Illite clay	4.50E-04	5.00E-04		Dixon et al., 1993
Inorganic clay medium plasticity			1.80E-05	Di Donna and Laloui, 2015
Kaolin			2.10E-05	Chiu (1990)
Kaolinite			2.90E-05	McKinstry, 1965
Montmorillonite			<3.9E-05	
Muscovite			2.48E-05	McKinstry, 1965
MX80 bentonite			2.00E-04	Tang et al., 2008
Opalinus clay (solid grains)			4.2E-05	
Opalinus clay (undrained at 25°C)			1.47E-04	Monfared et al., 2011
Phlogopite			4.58E-05	McKinstry, 1965
Pyrophyllite			3.93E-05	McKinstry, 1965
Quartz			3.34E-05	Palciauskas and Domenico, 1982

Lithotype or mineral	Min	Max	Average	Reference
Quartz sand			5.30E-04	Dixon et al., 1993
Rothbach sandstone			2.80E-05	Ghazebloo and Sulem, 2009
Sandstone	6.00E-06	1.25E-05		Maruyama et al., 2013 (depends on quartz content)
Saturated silt			3.50E-05	Khalili et al., 2010
Serpentine			2.40E-05	McKinstry, 1965
Talc			2.37E-05	McKinstry, 1965
Water			5.80E-04	Chiu (1990)
Water			2.70E-04	Delage (2013)

In the case of concrete this coefficient, or more properly the linear thermal expansion coefficient α , rules the additional stresses arising in the concrete members of the geostructure. It is a function of the concrete mix, cement aggregate ratio, water content, age, but in general it goes from 7 to $13 \cdot 10^{-6}$ (Loveridge et al., 2017). Some typical thermal expansion coefficients, including that of water, are shown in Table 3.2. Experimental techniques for evaluating this coefficient can be found in Aversa and Evangelista (1993).

3.4.2. In situ tests

3.4.2.1. Thermal response testing (TRT)

This technique is useful for the evaluation of ground thermal conductivity and heat exchanger thermal resistance. A constant heat rate is usually applied for 2-3 days in a borehole for injecting heat and the temperature trend of the heat carrier fluid in the borehole is monitored and recorded, as well as flow rate, ambient temperature, heat pump and pump power (Figure 3.14). Several alternative ways of performing the test exist, as described in Vieira et al. (2017), the aim remaining the same, namely measuring ground response to a thermal loading. Interpretation of results is based on the infinite line source (ILS) theory, that is the borehole acts as if it was a thin and infinitely long heat power source and the ground is assumed homogeneous in terms of properties and of initial temperature field. By solving the heat diffusion equation under these assumptions, it is found that the temperature gradient becomes a linear function of the natural logarithm of time after the dimensionless elapsed time F_0 (Fourier number):

$$\Delta T = I + k \cdot \ln(t) \quad \text{Eq. 3.21}$$

$$F_0 = \frac{\alpha t}{r_b^2} > 5 \quad \text{Eq. 3.22}$$

where I is the intercept, k the slope, α the thermal diffusivity in m^2/s , t the time in s and r_b the borehole radius in m . Hence, thermal conductivity and thermal resistance can be determined as:

$$\lambda = \frac{q}{4\pi k} \quad \text{Eq. 3.23}$$

$$I = q \left\{ R_b + \frac{1}{4\pi\lambda} \left[\ln \left(\frac{4\alpha}{r_b^2} \right) - \gamma \right] \right\} \quad \text{Eq. 3.24}$$

where γ is the Euler's constant. Despite the simplicity of the approach, errors to the simplified assumptions can arise but were estimated to be in the order of 10% (Loveridge et al., 2017).

However, the cylindrical heat source approach, in view of its greater complication, does not offer improved estimations of the parameters. In both cases major limits are encountered in assuming constant thermal resistance and constant heat flux, which is very far from reality. Parameter estimation methods, both analytical and numerical, can also be used, aiming at matching the experimental and the simulated fluid temperatures.

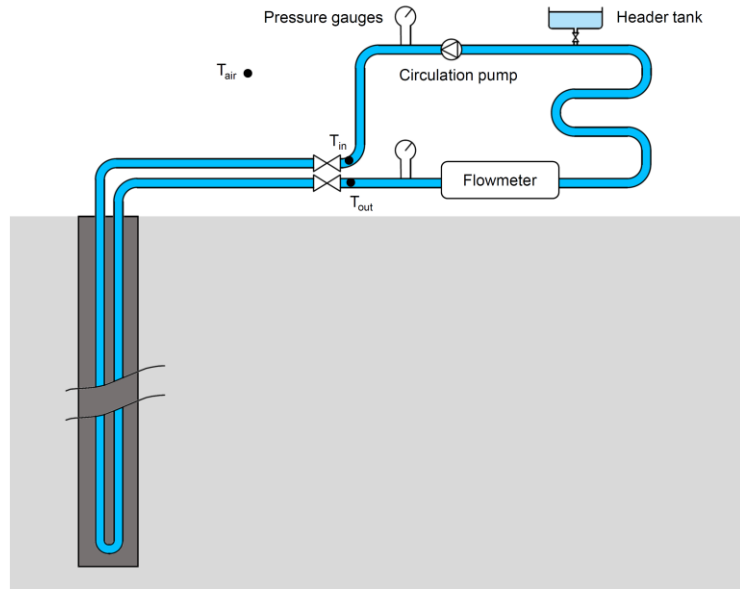


Figure 3.14: Sketch of a TRT test.

TRTs also allow to determine the undisturbed ground temperature, by adding a preliminary phase to the test during which natural heat carrier fluid temperatures fluctuations are recorded during circulation prior to the injection phase. The undisturbed temperature is estimated as the temperature at steady state, but different interpretations of the test exist, such as considering the temperature at the end of the first cycle in order to avoid environmental effects (Vieira et al., 2017). This is called fluid circulation method. As an alternative, downhole temperature logging can be used for evaluating the undisturbed ground temperature by lowering a temperature sensing system (wired or wireless probes, fiber optics) in a groundwater-filled borehole and computing a simple or a weighted average of the measured values. In grouted boreholes either a temperature sensor is embedded before grouting or temperature of the fluid within the pipes can be measured once it has reached thermal equilibrium with the ground.

The drawback of TRTs performed as described earlier is that a unique, average value of thermal conductivity is found. To improve design, Distributed and Enhanced Thermal Response Tests (DTRT, ETRT) exist, that measure temperature at a certain number of locations to get the response all along the depth. Vieira et al. (2017) compared results for standard TRT, DRT and ETRT and found quite good agreement. More details can be found in Vieira et al. (2017).

The possibility of performing TRTs on piles is discussed in Loveridge et al. (2017), who highlight time issues for large piles, with cost-benefits consequences, and the shorter length compared to BHE, which could cause overheating and stops. Group of piles could be tested to virtually extend the length of the heat exchangers and solve this problem, even if in this case heat losses and thermal interferences among the piles should be considered.

3.4.3. Laboratory tests

Laboratory tests are quicker and less expensive than in situ tests, but also present a number of drawbacks. Loveridge et al. (2017) warn about the comparison between laboratory and in situ tests, in the sense that if a scale and site-specific issue is intrinsically evident (heterogeneous materials and groundwater flow are not accounted for in laboratory tests) care is needed in both approaches so that suitable results are obtained. Vieira et al. (2017) collected many laboratory and in situ results and concluded that in situ thermal conductivities are greater. Reasons are attributed to small representative elementary volume (REV) in the lab, absence of advective groundwater contribution, always resulting in higher values, environmental influences during TRTs. As for traditional geotechnical laboratory tests, one should keep in mind that quality of the samples is crucial for the interpretation of thermal properties. Moisture content, structure and density all have relevant effects.

Steady-state methods and transient methods can be distinguished, as described hereafter. A comprehensive summary of advantages and disadvantages of each technique can be found in Vieira et al. (2017).

3.4.3.1. Steady-state methods

The peculiar aspect of steady-state methods is the measurement of a steady temperature field across the sample, so that Fourier's law can be applied straightforwardly. One of the steady-state methods is the guarded hot plate method, where a specimen is located between a heat source and a heat sink (Figure 3.15a) and protected laterally by the "guards" to prevent lateral heat flow and favor vertical, 1D flow. The supplied heating unit power and the temperature gradient across the specimen are measured and thermal conductivity is determined from this. The comparative cut-bar method is similar, though a material with known conductivity is interposed between the sample and the heat sink (Figure 3.15b). This method is rather applied to rock samples.

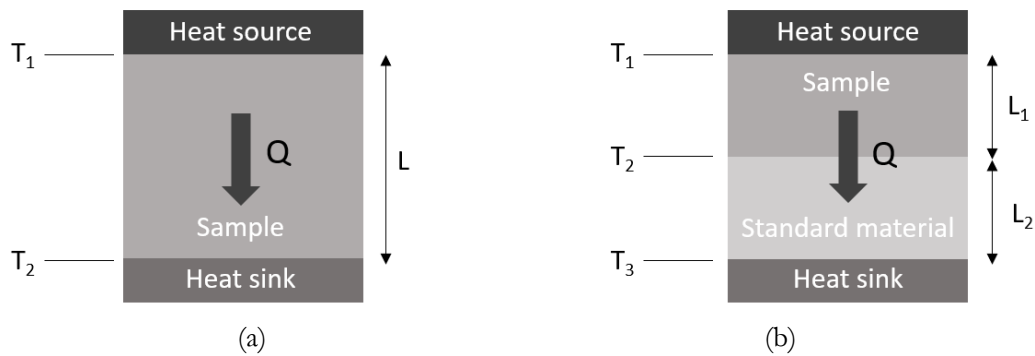


Figure 3.15: (a) Guarded hot plate and (b) divided cut-bar methods (modified from Vieira et al., 2017).

The major drawbacks are (Vieira et al., 2017):

- long time needed before attaining steady-state (hours to days);
- moisture migration for unsaturated soil specimens affecting results accuracy;
- big sizes of the samples (300 mm for the guarded hot plate), often incompatible with ordinary ground investigations;

- complicated apparatus and thermal resistances;
- need to account for heat losses given the times involved.

There is actually no evidence that these methods are more accurate than transient methods, especially for soils, but they are usually used for rocks.

3.4.3.2. Transient methods

An alternative to steady-state methods particularly employed for soils are the transient methods, such as the needle probe (or hot wire method) and the dual needle probe. In these tests the time-dependent temperature of the sample is monitored with time. Similarly to a thermal response test, but at the laboratory scale, a needle provided with both a heater and a temperature sensor is put in the sample to record resulting temperature variations (further details are given in Vieira et al., 2017). Interpretation is done via the line source approach already described. Despite its quickness and minimization of moisture migration, very small volumes of soil are tested, which could arise questions about the representativeness of the results. In the dual needle probe a second needle with just a temperature sensor is located at very short distance from the first one, allowing to assess thermal diffusivity and specific heat capacity too. Given the short distance, results highly depend on it.

Comparison with steady-state outcomes, particularly for soils with high moisture content, often leads to discrepancies in the order of 10-20% whose origin is not always clear, some of which could lie in drying effects and soil anisotropy. Vieira et al. (2017) emphasised the fact that there are no standardised procedures for thermal laboratory testing and that awareness of advantages and limitations of each testing technique is of vital importance.

3.5. Summary

The purpose of the present Chapter was to understand the role of non-isothermal conditions on the behaviour of both soils and concrete and to identify the additional knowledge that is required at the investigation stage when designing energy tunnels. The description of the techniques commonly adopted for the study of the key thermal properties was also one of the aims of this Chapter. A comparison between in situ and laboratory techniques was depicted, by outlining advantages and limitations.

Thanks to the rapid growing in the topic of energy geotechnics, often for other reasons than energy geostructures, at least at the beginning, a significant literature is available especially for clays, that exhibit the most complex thermo-mechanical response. It emerges that the volumetric behaviour of soils has reached a mature understanding, while pending questions still exist on the deviatoric behaviour. A number of constitutive models were developed to reproduce many of the peculiar aspects highlighted through experimental campaigns. The observation of thermoelastic deformations in energy piles suggest the same behaviour in the case of energy linings and the effect of temperature on mechanical and thermal properties appears to be rather limited. For concrete it is rather difficult to find data in the temperature ranges of interest in this study, but the main consequences of exposition to temperature were summarized.

This review will be particularly useful for the examination of the thermomechanical behaviour of energy tunnels, investigated experimentally and numerically in Chapter 6.

Chapter 4

The first Italian prototype of energy tunnel

4.1. Introduction

In recent years, energy tunnels have shown potential to work as both structural supports and geothermal heat exchangers and as such they can be subjected to both mechanical and thermal loads. Nevertheless, the behaviour of energy tunnels is still very little studied and represents a niche topic. There is no doubt that an increasing amount of modelling research has investigated the previously unexplored capabilities of tunnels to exchange heat and have highlighted the most important features and challenges. However, practical energy tunnels applications can almost be counted on one hand and very limited field data have been available to analyse their thermo-mechanical behaviour, of which none addresses the structural impacts.

To investigate this problem, a full-scale in situ test of a thermally activated and monitored energy tunnel prototype was performed and is presented in this work. The novel Enertun segments described in Chapter 2 were tested for the first time in the tunnel under construction of the Turin Metro Line 1 South Extension. The project was achieved in the framework of a “Proof of Concept” funding with scientific responsible Prof. Barla, thanks to a Memorandum of Understanding signed between Politecnico di Torino, Consorzio Integra and Infratrasporti.To. As part of the project, cooperation with Generale Prefabbricati, Ingegneria&Controlli Italia and Cmc was set up. For the peculiarity of monitoring through optical sensors, a collaboration with PhotoNext, the Inter-Dipartimental Center for Photonic technologies of Politecnico di Torino, was established.

The ensuing sections present i) the features of the experimental site, ii) a comprehensive view of the different phases needed for the installation of the prototype, iii) the main characteristics of the testing equipment, iv) the details of the real-scale tests. Part of the work presented in this Chapter comes from Barla et al. (2019). Detailed information about experimental tests is reported in Appendix A.

4.2. Description of the prototype

In Chapter 2 the results of preliminary thermo-hydraulic numerical analyses carried out to investigate the energy efficiency of thermal activation of tunnels and their influence on the surrounding ground were presented. From these outcomes it was possible to demonstrate on one hand the profitable conditions existing in Turin, related to the favorable groundwater flow, and on the other hand the convenience of employing the Enertun scheme compared to other solutions (see Figure 2.7 and Table 2.1).

In order to test the thermal performance of the newly patented energy segment, an experimental site of Enertun segmental lining was installed in the tunnel of Turin Metro Line 1 South Extension under construction, about 42 m northwards from Bengasi station, in the Lingotto-Bengasi section, as shown in Figure 4.1 and in the layout of Figure 4.2.

According to the monitored data shown in Barla et al. (2016) (Figure 4.3a), Turin metro tunnel can be classified as a cold tunnel, that is internal air temperature is similar to ground surface temperature and thermal influence due to fast-moving trains operation is negligible. This is also testified by the more recent data of temperature collected by GTT, the operator of the line (Figure 4.3b).



Figure 4.1: View of the Enertun experimental site and its location along the Turin Metro Line 1.

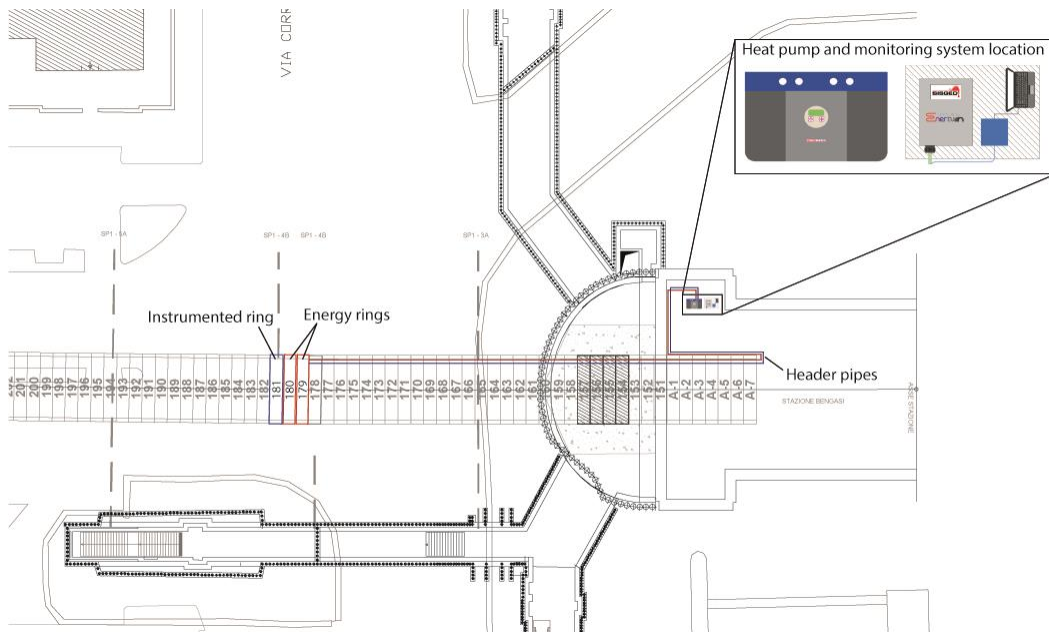


Figure 4.2: Partial layout of the Lingotto-Bengasi section with a particular focus on Bengasi station.

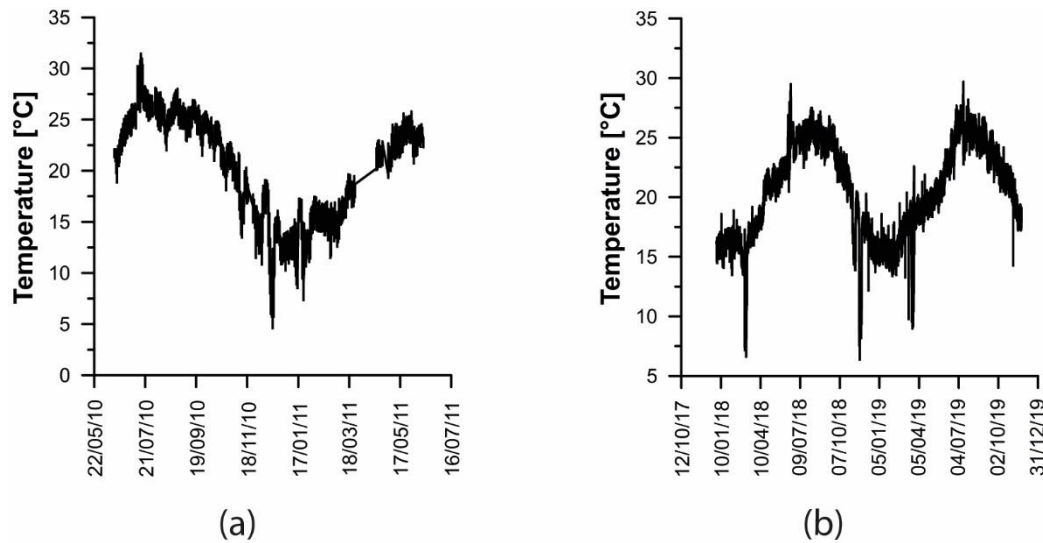


Figure 4.3 Monitored tunnel internal temperature in the Metro (a) in 2010-2011 (modified from Barla et al., 2016;) and (b) in 2018-2019 in a well close to Lingotto (courtesy from GTT).

4.2.1. Background of Turin ML1 SE project

ML1 connects the North-Western part of the city with the South-Eastern one, from Fermi station in Collegno to Lingotto multifunctional centre, for a total length of 13.4 km and 21 stations. The construction started in 2000, in view of Turin 2006 Winter Olympic Games. In 2006 the first section from Fermi to XVIII Dicembre was opened, immediately followed by

the second one up to Porta Nuova in 2007. The last part of the line towards Lingotto was completed in 2011. Two additional stations located in the Southern districts of the city, Italia '61, planned to serve the future Piedmont Region Headquarters, and Bengasi, are currently under construction.

The Lingotto-Bengasi section is characterized by a 1728 m length, with 8 m of altitude difference and linear planimetric development (Infratrasporti.To S.r.l., 2015), 2 intermediate ventilation shafts (PB1 and PB2) and a terminal shaft of end section (PBI) located approximately 200 m beyond Bengasi station. The terminal tunnel will allow the inversion of trains behind Bengasi station, in the section between the station itself and the terminal shaft. This solution will make it possible to fully exploit the potential of the VAL system (automatic light vehicle): at peak times it will be possible to guarantee a train frequency every 69 seconds. Additionally, the length of the concerned section will enable parking of four trains, ready to get in service depending on the users flows fluctuations.

At the time of writing the single-shield EPB (Earth Pressure Balance) TBM has completed the excavation and has been dismantled. It is 100 meters long, with a weight of 400 tons and an excavation diameter of the cutterhead of 7.76 m. Excavation took place under the water table. The average depth of the tunnel is in the range 16-20 m. The tunnel lining is 30 cm thick and each ring, universal type, is made of 6 precast concrete segments (5 plus a key, of which 4 parallelogrammatic and 2 trapezoidal, with 15 possible positions of the key, as the minimum rotation angle is 24°) mounted by the TBM itself while excavating and permanently sealed to protect tunnel tube against groundwater. There are 2 or 3 longitudinal connectors between the segments according to their length. Each ring is 1.4 m wide; the internal diameter is 6.88 m and the external one is 7.48 m. The concrete used is strength class C40/50, with $R_{ck} \geq 50$ MPa, slump class S4, water/cement ratio ≤ 0.5 , maximum aggregates diameter 30 mm and minimum cover 40 mm (following the standards UNI EN 206-1, 2006 and UNI 11104, 2004) according to Infratrasporti.To S.r.l. (2015). Steel bars are characterized by a diameter lower than 40 mm, steel FeB44k, tensile strength $f_{tk} = 540$ MPa and yield limit $f_{yk} = 430$ MPa according to the same reference.

The geological profile in the area within which the work is to take place is quite well-known, especially in the first 40-50 m thanks to the geotechnical investigations carried out for the design of the Underground Railway Link and of the Metro Line 1 (Barla and Barla, 2012) and to the inspection of boreholes drilled ad hoc by the construction site. It is characterized by a plain area originated by subsequent contributions of the alluvial cones located at the base of alpine valleys (Infratrasporti.To S.r.l., 2015). The cones are made of quaternary fluvioglacial deposits whose shallow layer is modelled by the action of rivers. The fluvioglacial deposits are 35-40 m thick, mainly made of loose material alternated to some cemented lens in the order of the centimeter-decimeter. Below this layer, clayey silt and sandy-gravelly layers are present, followed by marine, cohesive deposits (Barla and Barla, 2012; Infratrasporti.To S.r.l., 2015). A more detailed description can be found in Barla and Barla (2012), who came up with four homogeneous classes, called Geotechnical Units (GU), summarized in Table 4.1. In the cross section of the Enertun prototype, below a shallow backfill layer, a sand and gravel unit from loose to weakly cemented (cementation included in the range 0-25%, i.e. GU2) can be highlighted. The tunnel is located within an aquifer, completely below the groundwater table surface. Based on the data recorded by nearby piezometers, it is possible to detect a West-to-East groundwater flow and a hydraulic gradient in the range 0.3-0.5%. In the area of interest, the groundwater table can be found at a depth of 11.70-12.40 m and flows towards East to reach the Po river with an average velocity of 1.4 m/day, see Figure 4.4.

Table 4.1. Strength and deformability properties of the four GU for Turin subsoil (from Barla and Barla, 2012).

Geotechnical Unit	C% [%]	D _R [%]	γ [kN/m ³]	E _d [MPa]	ν [-]	σ _c [MPa]	m [-]	c [kPa]	φ [°]
GU1	-	50-60	17-19	10-20	0.35	0	-	0	36-37
GU2	0-25	50-70	18-21	190-240	0.30	0-0.03	3-4.8	0-30	37-39
GU3	25-50	60-80	19-22	240-300	0.30	0.03-0.14	4.8-7.8	15-80	37-42
GU4	50-75	60-80	19-22	300-370	0.30	0.14-0.67	7.8-12.5	50-200	39-48

C%=cementation degree, D_R=relative density, γ=unit weight, E_d=deformation modulus, ν=Poisson's ratio, σ_c=unconfined compressive strength, m=Hoek and Brown constant, c=cohesion, φ=friction angle.

In the following, the Enertun experimental prototype will be described by focusing the attention on three main stages of the works:

1. energy segments manufacturing
2. site implementation
3. monitoring and acquisition system

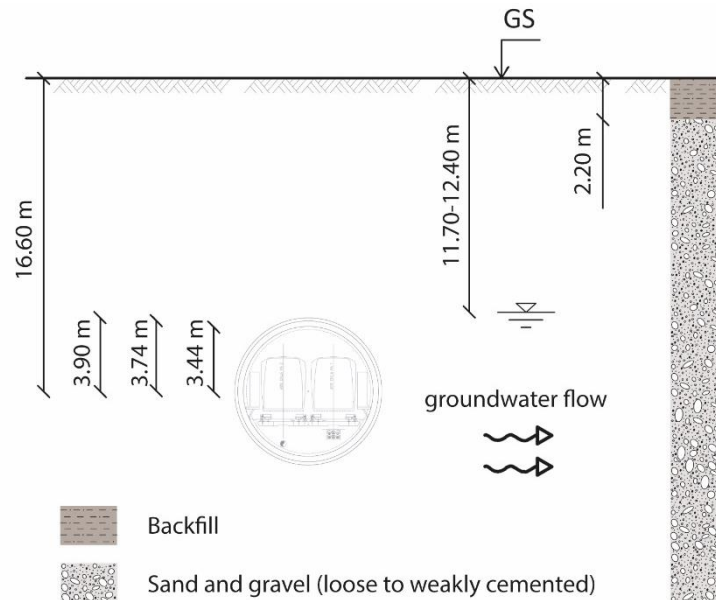


Figure 4.4: Cross-section of the tunnel.

4.2.2. Energy segments manufacturing

Two rings of segmental lining were fully equipped with the ground&air net of pipes for a total of 12 Enertun segments. The two nets of pipes, one close to the extrados (tunnel surface in contact with the ground), the other close to the intrados (tunnel surface in contact with the air) allowed to test alternatively all three different configurations (see Enertun concept at paragraph 2.3.2).

Segments manufacturing was the result of a 5-months phase (from December 2016 to April 2017) characterized by several meetings with the client, the contractors, the consultants and the staff in charge of precasting. Discussions mainly focused on i) technical viability of the project, ii) drafting and signature of a memorandum of understanding between parties

involved, iii) integrity and serviceability of the final work, iv) exact location of the energy segments, chosen unanimously so as not to cause interferences with the works execution, v) development of design drawings useful to undertake the required adjustments and implement the equipment (pipes layout, position of monitoring sensors and box-outs geometry to hydraulically connect adjacent segments) and vi) operational details.

As pipes configuration design took place after reinforced concrete segments design, their exact location and spacing was dictated by rebars position. The two pins for segments uplift, handling and mounting from the TBM forced the arrangement of the pipes not to be uniformly spaced. This is not likely to have any significant impact on the tests results, although little interference is to be foreseen between the closest coils; however, some construction details could be avoided by designing the energy segments at an early stage, as stated also by Frodl et al. (2010). Pipes were placed inside bending rebars, towards the segment interior so as not to reduce the 4 cm wide cover and run in between the hoop rebars with the intention of preserving concrete-rebars adherence. No critical issues were found to be associated with the project by the designers, neither during transient phases nor in the long term, given the minimal section of the pipes.

The pipes layout for the two energy rings is illustrated in Figure 4.5. The segments name A-E and the key name K were changed to 1-6 for simplicity. The code 1 corresponds to the first segment of each ring where the circuit enters and the code 6 to the last segment from which the pipes exit. It follows that homologous segments will have the same letter, but different numbers, for instance the key is segment 2 in ring 179 and 1 in segment 180. Due to a mistake in pipes placement, their spacing is reversed in segment 1 of ring 179 and segment 6 of ring 180. Details of the design of segments equipped with pipes in the Enertun ground&air configuration are given for each segment in Figures 4.16-4.27, together with pictures before casting.

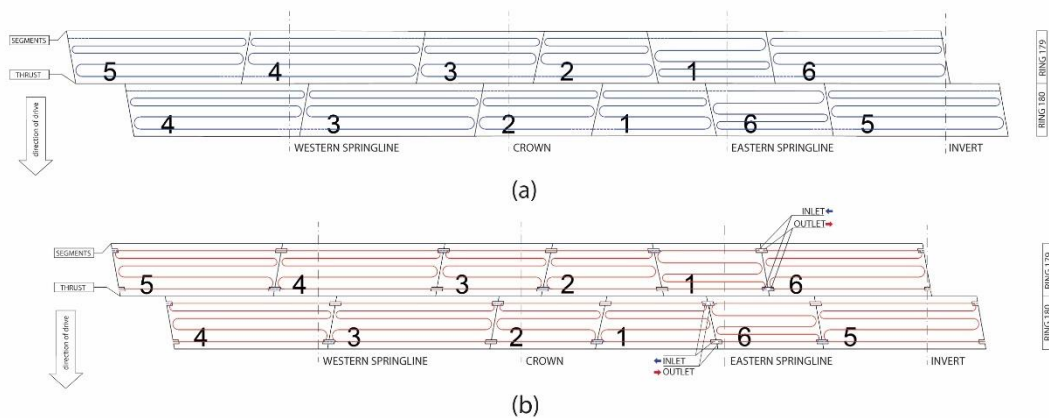


Figure 4.5: Pipes layout in the two energy rings, (a) section corresponding to the extrados and (b) section corresponding to the intrados.

During the preparation stage, all the equipment to be embedded within the segments was purchased: pipes, manifolds and monitoring sensors (whose description can be found in the following paragraphs). The pipes used are fabricated in reticulated polyethylene (PE-Xa) with antioxygen barrier, have an external diameter of 20 mm and a thickness of 2 mm. PE-Xa, obtained by crosslinking of polyethylene using peroxides, is a material characterized by high resistance to corrosion, uniform and high reticulation over the whole section and is suitable for radiative heating and cooling. They were simply tied to rebars through wire by hand in the

precast concrete plant on a separate line to avoid delaying segment production schedule. This process was time-consuming (2 days needed) if compared to the production of a standard segment and can be optimized for the case of an industrial scale installation. About 116 m/ring of pipes were laid at the extrados and 110 m/ring at the intrados. The bends between each row of pipes took into account the minimum allowable bending radius based on the pipes' specifications (five times the external diameter). The distance of the ground circuit from the extrados is 6 cm, as well as the distance of the air circuit from the intrados.

Each segment represents an individual hydraulic circuit, in which the air net of pipes runs at the intrados and the ground one at the extrados. However, each ring must eventually form a single, continuous, completely connected circuit. The ground&air nets of pipes in each segment need to be connected to the adjacent segments' ones once the TBM has mounted them on site. To do so, four special coupling box-outs were envisaged, specifically designed and included at the intrados of each segment along longitudinal joints. Box-outs are no more than 4-sided aluminum boxes with a circular hole on one side from which pipes (and also sensors cables) can go through, exit the segment and be handled for the following in situ connection by means of manifolds. At the end, two continuous circuits are available, one at the extrados and the other at the intrados. The boundary of the hole was adequately sealed before casting to prevent the concrete mix from entering the box. For the same reason the whole box was filled with some soft filling material and then protected by means of tape.

An example of steel cage equipped with pipes before casting is provided in Figure 4.6. While the air circuit already lays at the level of box-outs, the first and fifth rows of the ground circuit need to bend to reach the same level and exit at the intrados.



Figure 4.6: Example of steel cage equipped with pipes before casting (segment 1, ring 180) with detail of box-outs.

Once all the steel cages with embedded pipes were ready, they were moved inside moulds (Figure 4.7a), where casting of the twelve Enertun segments took place in May 2017 (Figure 4.7b). It should be noted that great care was taken during this process and the flow rate of the concrete mix was a bit lower than usual, to avoid any damages such as pipes collapse. After casting, energy segments were demoulded (Figure 4.7c) and circulation tests were carried out to ensure pipes integrity (Figure 4.7d), with a successful outcome. Continuity of the water flow through the segment, from one side to the other, indicated no collapse of pipes had occurred

during casting. Then, at the end of the 28-days curing period, they were transported to the construction site.



Figure 4.7: Preparation stages of energy segments: (a) moulding, (b) casting, (c) demoulding and (d) circulation test.

4.2.3. Site implementation

As previously mentioned, the prototype of energy tunnel consists of two rings, completely thermally activated and equipped with the double ground&air configuration, for a total longitudinal length of 2.80 m. Energy rings were placed on site by the TBM on July 3rd 2017 (rings 179 and 180, as shown in Figure 4.1), about 42 m from the entrance of the station. Installation chainage was decided in accordance with the construction site managers with the intention to minimize impact on the construction operations. As of this date, fiber optics and electrical sensors connections together with hydraulic connections between adjacent segments were completed. This task was achieved by taking advantage of the TBM backup to reach the highest, hardly accessible points.

Fiber optics sensors (described in detail in 4.2.4) were connected both by means of fusion splicing (for multi-mode fibers) and through simple FC-APC adapters (for single-mode fibers). In fusion splicing a machine is used to precisely align the two glass fiber ends, then welded

together using some type of heat or electric arc, thus producing a continuous connection between the fibers. This method of splicing provides for the lowest loss, less reflectance, strongest and most reliable joint between two fibers. An 80 m cable (customized to have 4 inlets and 4 outlets, but a unique body) connects the single-mode fibers to a control room out of the tunnel.

Electrical sensors cables were linked through a fireproof, multipolar cable to a multiplexer fixed at the tunnel wall close to the energy rings, and then from here to the datalogger, located outside the tunnel, thanks to a single cable running all along the Eastern springline towards the entrance of Bengasi station.

As concerns pipes, connections between segments were done by placing a union tube connector in between the two opposite portions of pipes exiting each segment. The handling of pipes, albeit limited, compensated for the possible alignment imperfections. Afterwards, the pockets, hosting pipes and sensors connections, were protected by means of a layer of insulation to avoid heat losses along the circuit (Figure 4.8).



Figure 4.8: Pipes connections between adjacent segments.

As a result, two circuits per ring were obtained, air and ground, characterized by one inlet and one outlet each. After segments installation and hydraulic connections, the two rings were connected in parallel to the main conduit, made up of two flow and two return pipes (one for the ground circuit and one for the air circuit), for a total of four header pipes (Figure 4.9 and Figure 4.10). These pipes are 32 mm in external diameter, 2.9 mm in thickness, are made of the same material of the 20 mm pipes and are located outside the segments, hanging on steel brackets fixed at the tunnel Eastern springline (Figure 4.9). They have the aim to collect heat carrier fluid coming from both rings and to lead it to the heat pump. Their length is about 70 m from the energy rings to the heat pump. Also, header pipes were insulated to minimize heat losses. An advantage of connecting rings in parallel is the possibility of excluding some of them in case of unexpected glitches, but also the capability to test them separately or together. In fact, two hydraulic valves were added between the two inlet header pipes and each ring, that can be opened or closed depending on the desired configuration to be tested.

The different types of junctions installed are represented in Figure 4.10. The elevated number of connections requires further attention in the hydraulic head losses assessment.

So far, the ground loop heat exchanger has been described, that is the primary circuit embedded in the ground. Header pipes have the role to connect the primary circuit to the heat pump, which in turn is coupled with the secondary circuit, represented by the building to be heated or cooled. The working principle of a heat pump is described in 2.3.4. A heat pump device type KRONOTERM WPG-07-1 HT, characterized by a useful thermal power in the range 4.8 and 7.4 kW (datasheet shown in Appendix B), was installed together with two hydraulic pumps, (i) model DAB EVOPLUS 120/250.40 M and (ii) model Lovara HP 0.6 220, that circulate the heat carrier fluid along the primary circuit. This fluid is a propylene

glycol mixed with water allowing to work down to a temperature of -20°C. Exact measurement of the percentages of water and glycol was not performed, but the Author believes that a 10% of glycol can be reasonably assumed. The second circulation pump was required to provide sufficient hydraulic head, limited to a maximum of 12 m for (i) as can be seen in Appendix B, but reaching around 20 m for the studied plant. Of course, to optimize the energy efficiency of the system, a single circulation pump should be used.



Figure 4.9: Flow and return pipes.

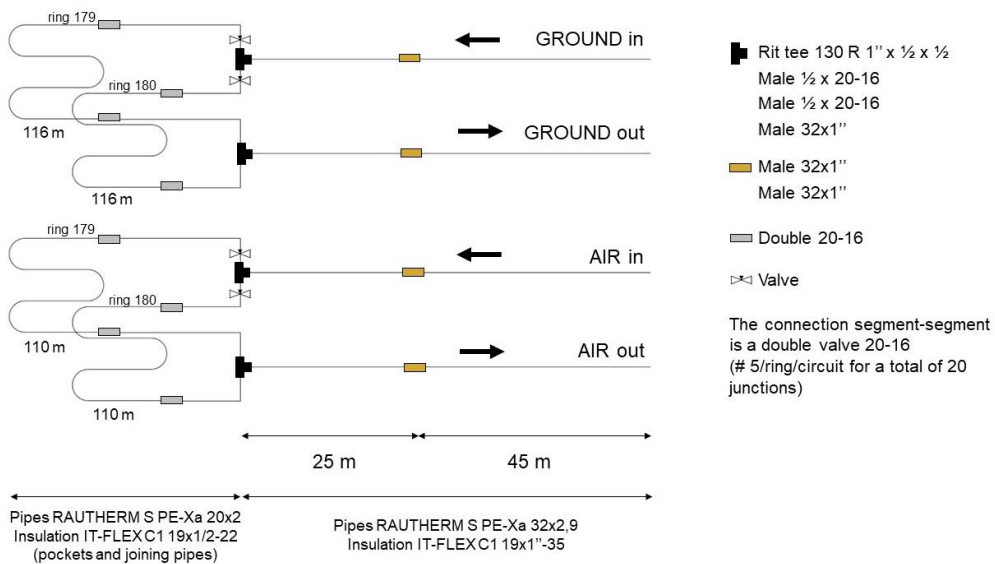


Figure 4.10: Details of the experimental plant geometry and junctions.

The “control room” hosting both the heat pump and the datalogger is an open space located close to the future elevator shaft (at present stairs are located here to allow access to the tunnel entrance). In this space, the ground&air hydraulic circuit starting and ending points can be found and management of the heat pump and of the data acquisition system are possible without interfering with the muck train going back and forth from the TBM backup in the tunnel. The control room with the test rig are depicted in Figure 4.11.

Because of the experimental nature of the project, the secondary circuit of the heat pump is represented by a fan coil unit located close to the heat pump. Therefore, at present there are no real end users benefitting from the tests, but the heat is dissipated in or extracted from the air.



Figure 4.11: The control room, hosting the heat pump, the datalogger and the secondary circuit, view from the mezzanine (left) and a close-up view (right).

Once the heat pump had been installed, the circuit was charged. A total fluid volume (water-glycol mixture) of about 123 l per circuit circulates in the absorber system. It is worth noting that the issue of air bubbles inside the pipes was not negligible and required a phase of pre-circulation to be reduced. The presence of a number of vent valves along the circuit was helpful to reach the scope.

4.2.4. Monitoring and acquisition system

Given the complexity of the system to be investigated and the experimental nature of the project, a comprehensive monitoring system was installed to monitor the energy tunnel performance both from a thermal and a structural point of view. The two energy rings were instrumented with a specifically designed monitoring system to observe stresses, strains and temperatures in the lining. Plan and cross-sections view of the sensors' layout in the two energy rings are shown in Figure 4.12 and their location is listed in Table 4.2-4.3. It is possible to divide the description of the sensors installed based on their type, that is i) conventional sensors, ii) single-mode fiber optics and iii) multi-mode fiber optics. Indeed, thanks to a collaboration with the Department of Electronics and Telecommunications, fiber-optics sensors were installed. Figures 4.16-4.27 depict the actual location of each sensor (note that the ring sketch is referred to the view towards Lingotto station).

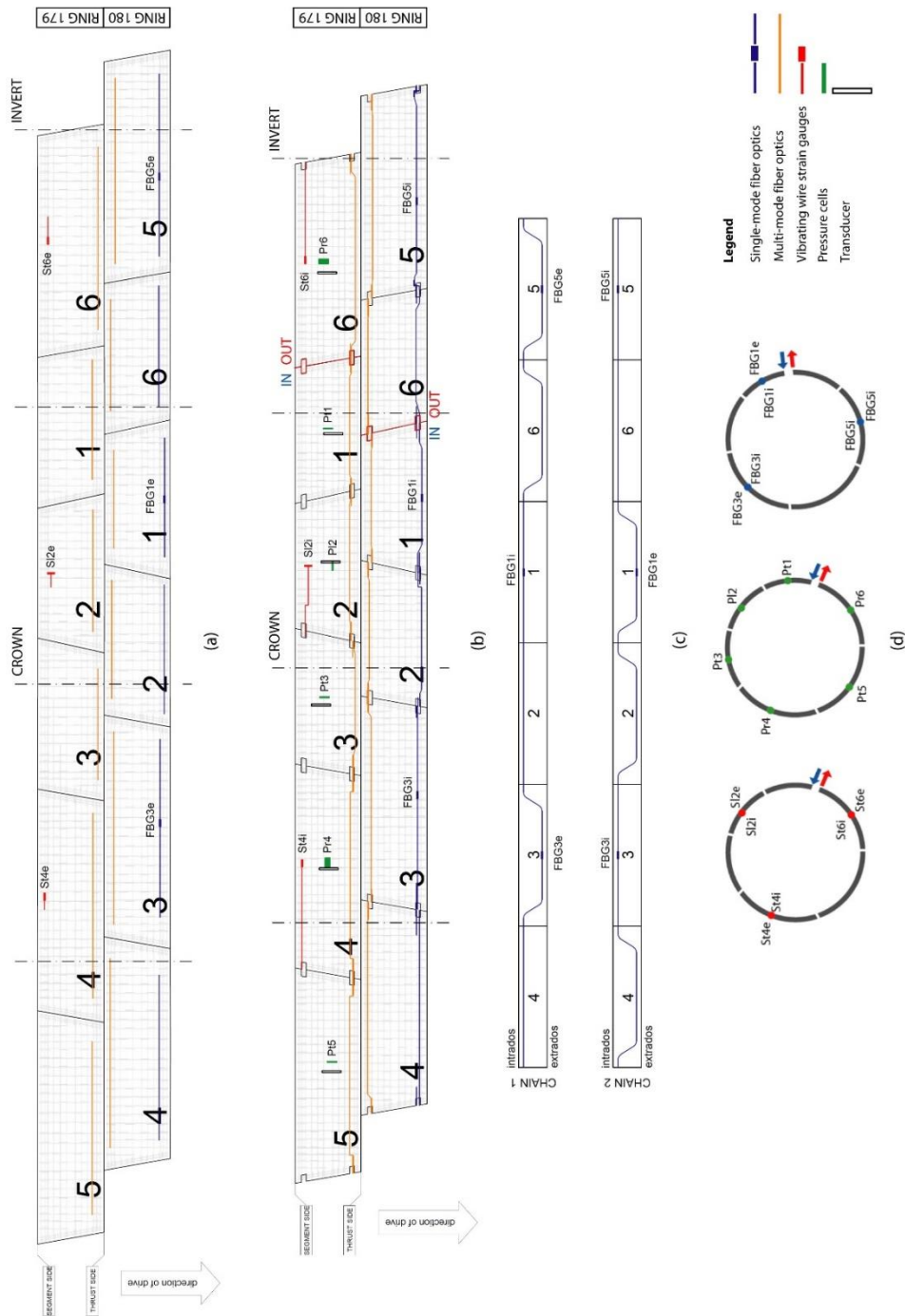


Figure 4.12: Design layout of sensors in the two energy rings: (a) extrados plan view, (b) intrados plan view, (c) single-mode fiber optics chains and (d) vertical cross sections showing the sensors location.

Table 4.2: Location of sensors installed in ring 179.

ENERGY RING 179			
Segment	Instrument	Orientation	Code
1	pressure cell	circumferential	Pt1
2	strain gauge	longitudinal (extra+intra)	Sl2e, Sl2i
	pressure cell	longitudinal	Pl2
3	pressure cell	circumferential	Pt3
4	strain gauge	circumferential (extra+intra)	St4e, St4i
	pressure cell	radial	Pr4
5	pressure cell	circumferential	Pt5
6	strain gauge	circumferential (extra+intra)	St6e, St6i
	pressure cell	radial	Pr6

Table 4.3: Location of sensors installed in ring 180.

ENERGY RING 180			
Segment	Instrument	Orientation	Code
1	FBG strain gauge	circumferential (extra+intra)	FBG1e, FBG1i (1549-1553 nm, 1547-1551 nm)
2	-	-	-
3	FBG strain gauge	circumferential (extra+intra)	FBG3e, FBG3i (1539-1543 nm, 1541-1545 nm)
4	-	-	-
5	FBG strain gauge	circumferential (extra+intra)	FBG5e, FBG5i (1555-1559 nm, 1557-1561 nm)
6	-	-	-

Type i) is represented by vibrating wire strain gauges and pressure cells. The energy ring 179 was equipped with these sensors. A schematic view of their arrangement in the cross-section can be seen in Figure 4.12d. On one hand, vibrating wire strain gauges with active length 150 mm and measurement range $\pm 1500 \mu\epsilon$ were welded to reinforcement bars in the precast concrete plant and placed longitudinally (segment 2) and circumferentially (segments 4 and 6), both close to the extrados and to the intrados. Resolution is $< 1 \mu\epsilon$, repeatability $< \pm 1 \mu\epsilon$ and accuracy is $\pm 0.5\%$ FS, that is $15 \mu\epsilon$. The coefficient of thermal expansion is $12 \cdot 10^{-6}/^\circ\text{C}$. The strain gauges have a built-in NTC thermistor to provide temperature data for thermal corrections with an accuracy of $\pm 0.5^\circ\text{C}$. Indeed, compensation of temperature is not performed automatically. Strain and temperature correspondent to their location can be obtained. On the other hand, hydraulic pressure cells were tied by wire to the steel cage before casting and placed radially (segments 4 and 6), circumferentially (segments 1, 3 and 5) and longitudinally (segment 2) in the central section of the concrete elements. The stress cell consists of a deaired oil filled pad connected to a vibrating wire pressure transducer by a hydraulic tube. The shape of the cell is rectangular, 100x200 mm. The transducer is made by a stainless-steel diaphragm to which a steel wire is connected. The change of pressure is transmitted to the oil into the pad and then to the diaphragm causing its deflection. The deflection is measured as a change in tension and then in frequency of vibration of the wire. The square of the frequency is directly proportional to the applied pressure. The vibrating wire pressure transducer is placed in a steel sealed box at the segments' intrados (where also temperature is measured) then reopened after segments demoulding, making it accessible. Sensitivity of the transducer is 0.03% FS, that is 1.5 kPa, and accuracy is $< \pm 0.25\%$ FS, that is 12.5 kPa. Of course, the sensors record variations induced by multiple phenomena (temperature, creep, ground load, etc.). A clear distinction among these actors cannot be made, but it can be assumed that since more than three months passed by from the time of energy segments installation the effect of creep and ground load are negligible, in favour of the

remaining effect of temperature. Then, both pressure and strain measurements will represent thermally induced strains and thermally induced stresses.

Data were recorded by the data logger every 10 minutes and transmitted every morning by FTP to a server located at Politecnico di Torino, so that they could be easily and remotely downloaded.

Type ii) is constituted by single-mode embedded Fiber Bragg Grating (FBG) sensors with temperature compensation, that were installed circumferentially in ring 180 (segments 1, 3 and 5) both at the extrados and at the intrados (Figure 4.12d). The FBG sensors design was tailor-made (cables length and measuring strain). A laboratory check was carried out before casting to verify the correctness of the requested wavelengths and their translation when subject to tension (higher wavelength, Figure 4.13b) and compression (lower wavelength). Two chains were designed to avoid losing all data in case of malfunctioning, by diversifying extrados and intrados sensors on each chain (Figure 4.12c). Embedment took place by means of zip ties around reinforcement bars, so that the sensors can extend or contract following concrete movements in a solidary way. Straps with no sensors run along the non-equipped segments, for providing connection continuity with the following one. These sensors are provided with two built-in FBG inside, one for strain measurement and another one for temperature compensation. A 6 mm armored cable was used to ensure more robustness during casting. Measurements of temperature and strain take place locally thanks to an interrogation system connected to a computer and occur only occasionally, depending on the availability of the interrogation system. Wavelengths are measured with time and a post-processing phase is needed to convert them into quantities of physical significance. Thermal coefficients in $\text{pm}/^\circ\text{C}$ are provided by suppliers for both gratings, together with strain calibration (wavelength as a function of strain, see Appendix B). Resolution is $1 \mu\text{e}$.

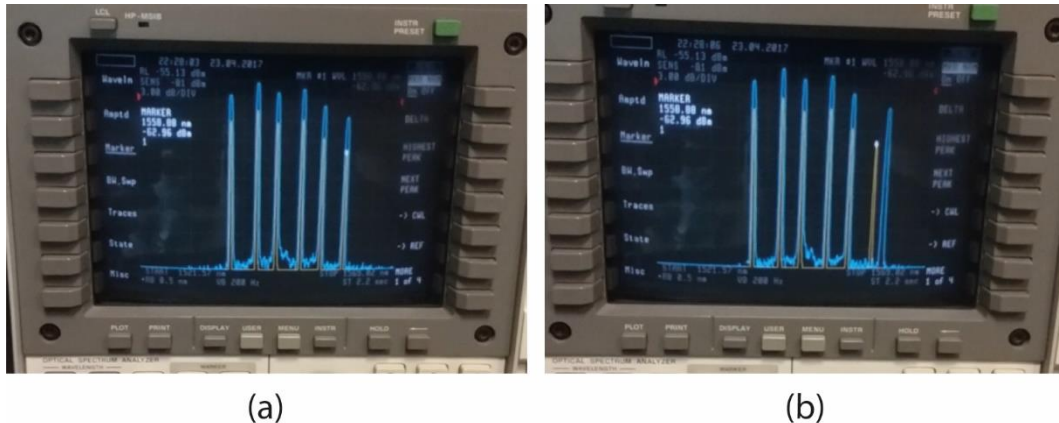


Figure 4.13 Laboratory check of the wavelengths correctness: (a) undeformed signal and (b) example of deformed signal (tension).

Type iii) comprises multi-mode fiber optics. Both rings were provided with two chains of multimodal fibers, one at the extrados and one at the intrados. They are supposed to be able to return distributed measurements of strain and temperature, all along their length. However, data have not been gathered yet, because of the current unavailability of the interrogation system. In Figure 4.14 some pictures of the three types of monitoring system can be seen.



Figure 4.14: Energy segments equipped with the three types of monitoring system.



Figure 4.15: Location of the temperature probes.

Not only what happens in the lining is observed, but also what occurs in the pipes and in the ground. Five PT100 class B temperature probes were devoted to the measurement of tunnel air temperature (T1), inlet/outlet temperature in the ground circuit (T2, T3) and inlet/outlet temperature in the air circuit (T4, T5). One more probe (T6) was located inside a piezometer well within the construction site to monitor the upstream groundwater temperature continuously. The accuracy is 0.3°C. Data are recorded continuously and sent hourly to a web server for storage. Measurements frequency can be regulated remotely. During testing the acquisition frequency is in the order of two minutes. The location of the above-described temperature probes can be observed in Figure 4.15.

The heat pump is equipped with a flow meter (indicated in Figure 4.11) whose screen can be only read in situ and gives the flow rate in m³/h and a thermal energy meter providing punctual values. A temperature probe measuring air temperature close to the heat pump is also available (T_{air}). Temperature of the heat carrier fluid leaving and entering the heat pump both on the primary circuit (IN, OUT) and on the secondary circuit side (U1, U2) are recorded continuously and transmitted through the same router adopted for the sensors within the lining.

Table 4.4 summarizes the monitoring timespan and the experienced failures for each of the installed sensors. Some bad electrical connections to the multiplexer were observed at the beginning. Later, specific interventions allowed to restore strain sensor St4e.

Table 4.4. Operation of all sensors involved in the experimental site: timespan and observed failures.

	Sensor	Timespan [dd/mm/yyyy]	Observed failures
Strain and temperature	Sl2i	31/08/2017-09/08/2018	Strain often skips from 300 to 3000 $\mu\epsilon$. Temperature ok.
	Sl2e	31/08/2017-09/08/2018	Sometimes strain skips from 2590 to 48000, frequent NAN (not available number). Temperature ok.
	St4i	31/08/2017-09/08/2018	-
	St4e	24/09/2017-09/08/2018	Strain started working on Sep 24, 2017, stopped on Oct 7, 2017, then ok from Nov 10 2017. Temperature ok.
	St6i	31/08/2017-09/08/2018	-
	St6e	31/08/2017-09/08/2018	-
Stress and temperature	Pt1	31/08/2017-09/08/2018	-
	Pl2	31/08/2017-09/08/2018	-
	Pt3	31/08/2017-09/08/2018	Stress never recorded. Temperature ok.
	Pr4	31/08/2017-09/08/2018	-
	Pt5	31/08/2017-09/08/2018	-
	Pr6	31/08/2017-09/08/2018	-
Temperature	T _{datalogger}	31/08/2017-09/08/2018	-
	T1	23/11/2017-20/08/2018	-
	T2	23/11/2017-20/08/2018	-
	T3	14/11/2017-20/08/2018	Started working on Dec 14, 2017.
	T4	23/11/2017-20/08/2018	-
	T5	23/11/2017-20/08/2018	-
	T6	01/12/2017-11/05/2018	Started working on Dec 1, 2017 and ended earlier due to wire failure.
	IN	16/09/2017- 09/08/2018	-
	OUT	16/09/2017- 09/08/2018	-
	U1	16/09/2017- 09/08/2018	-
U2	16/09/2017- 09/08/2018	-	
T _{heat pump}	16/09/2017- 09/08/2018	-	

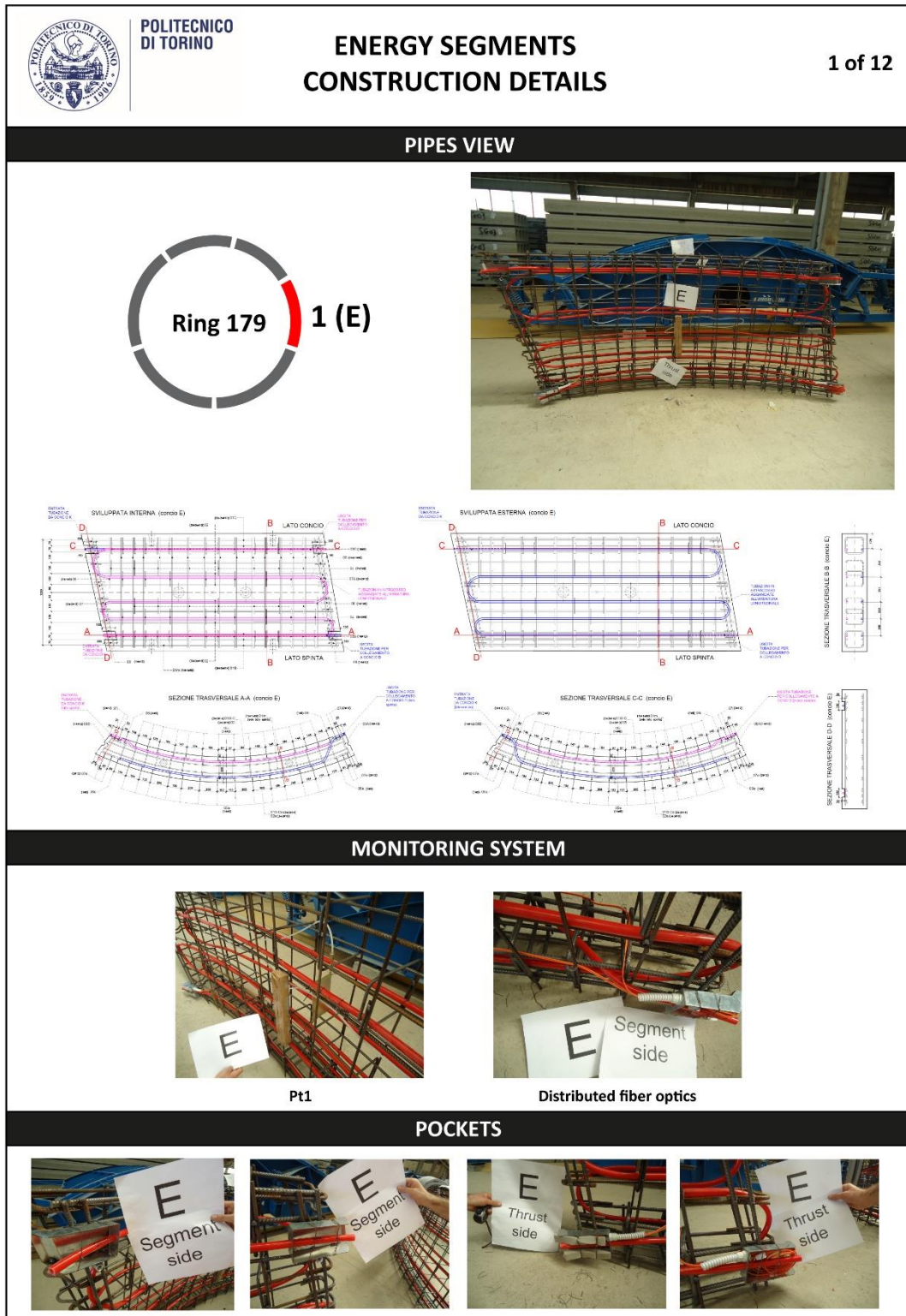


Figure 4.16: Energy segments construction details: ring 179, segment 1 (1/12).

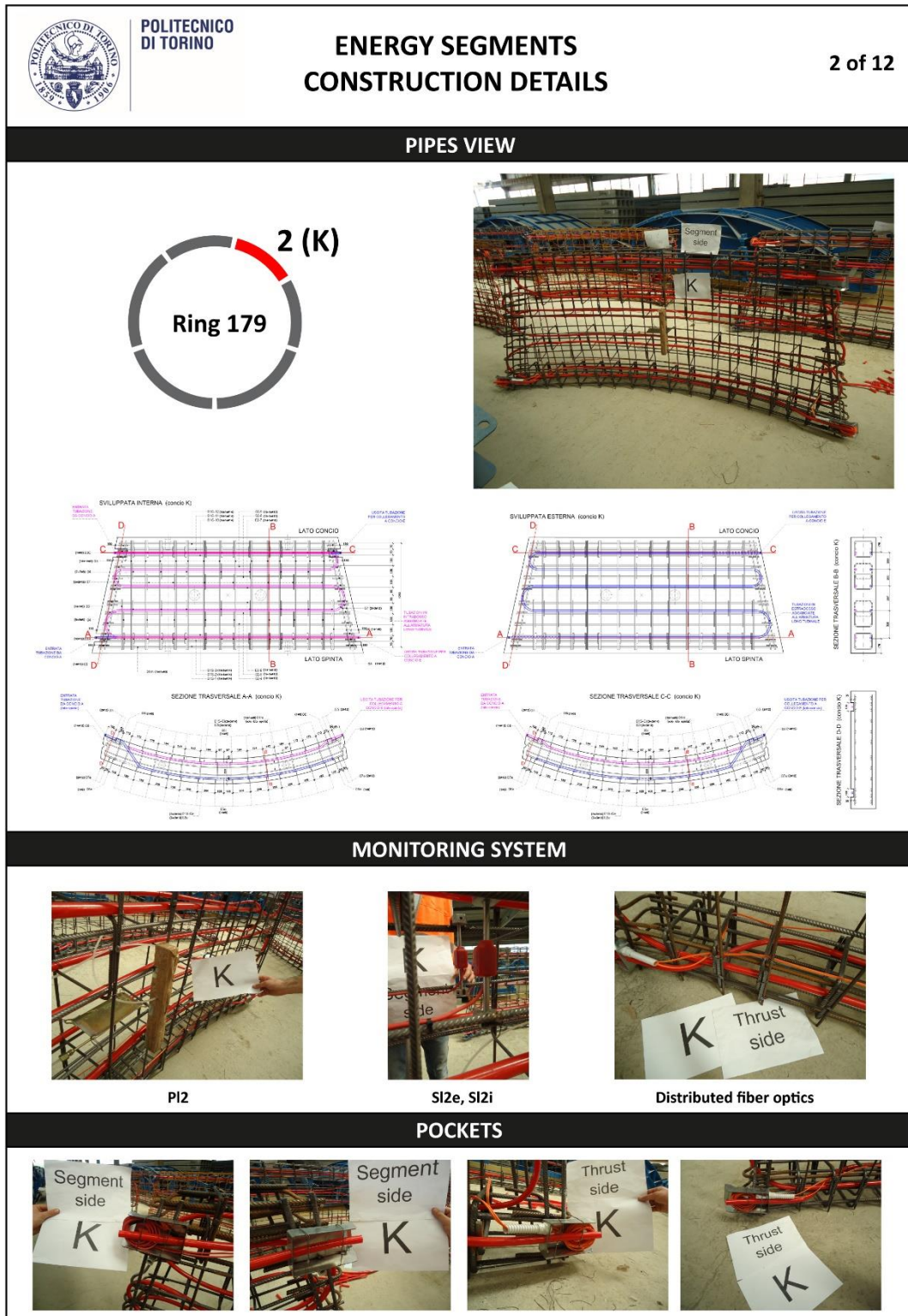



Figure 4.17: Energy segments construction details: ring 179, segment 2 (2/12).




**POLITECNICO
DI TORINO**

ENERGY SEGMENTS CONSTRUCTION DETAILS


3 of 12

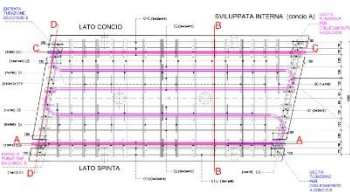
PIPES VIEW

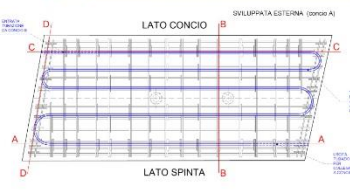
3 (A)

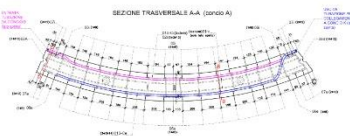


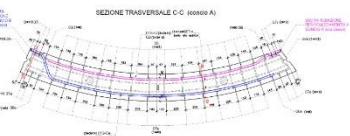
Ring 179













MONITORING SYSTEM





Pt3




Distributed fiber optics

POCKETS







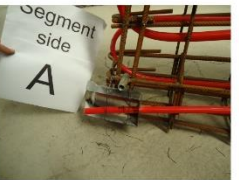


Figure 4.18: Energy segments construction details: ring 179, segment 3 (3/12).

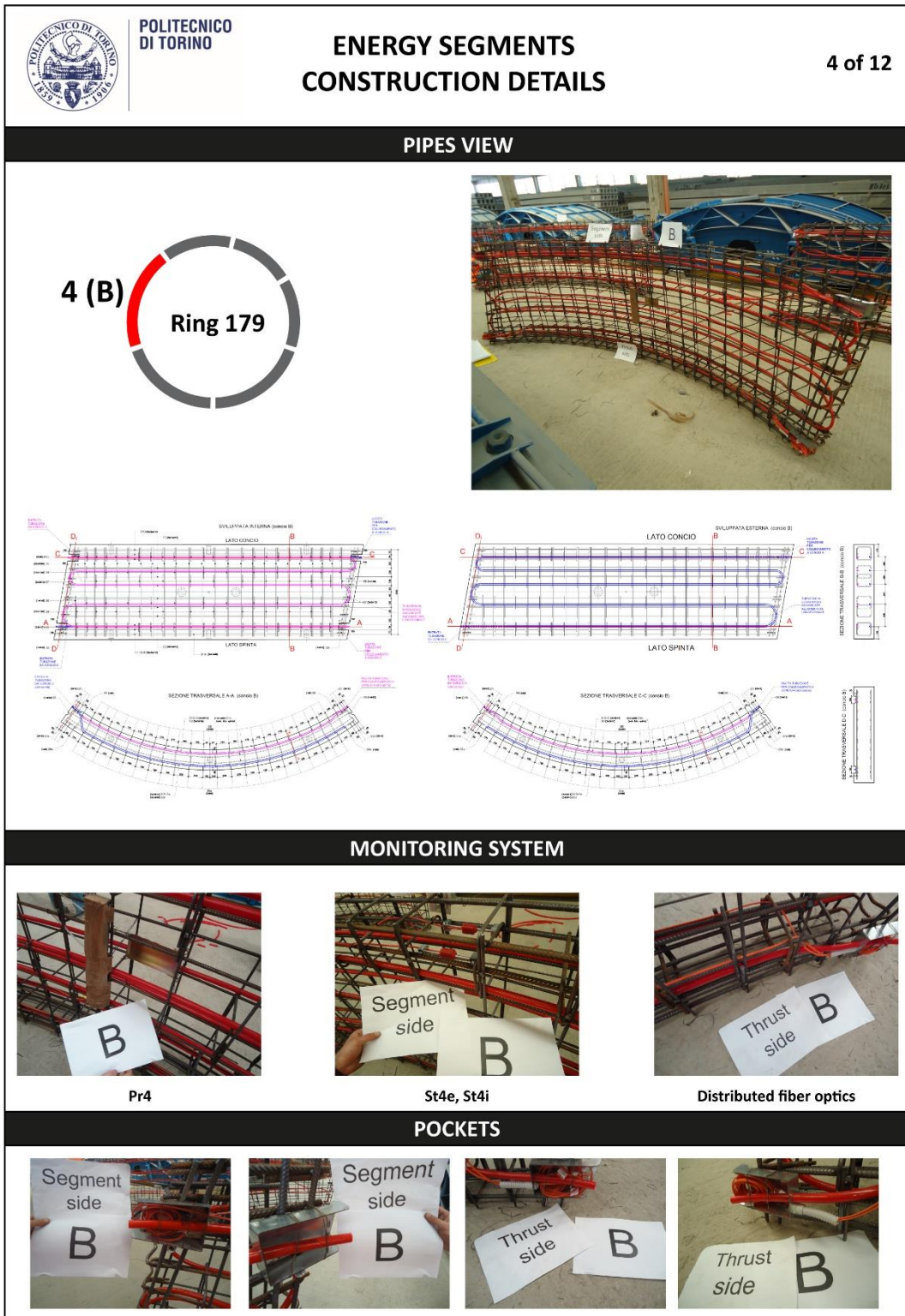


Figure 4.19: Energy segments construction details: ring 179, segment 4 (4/12).

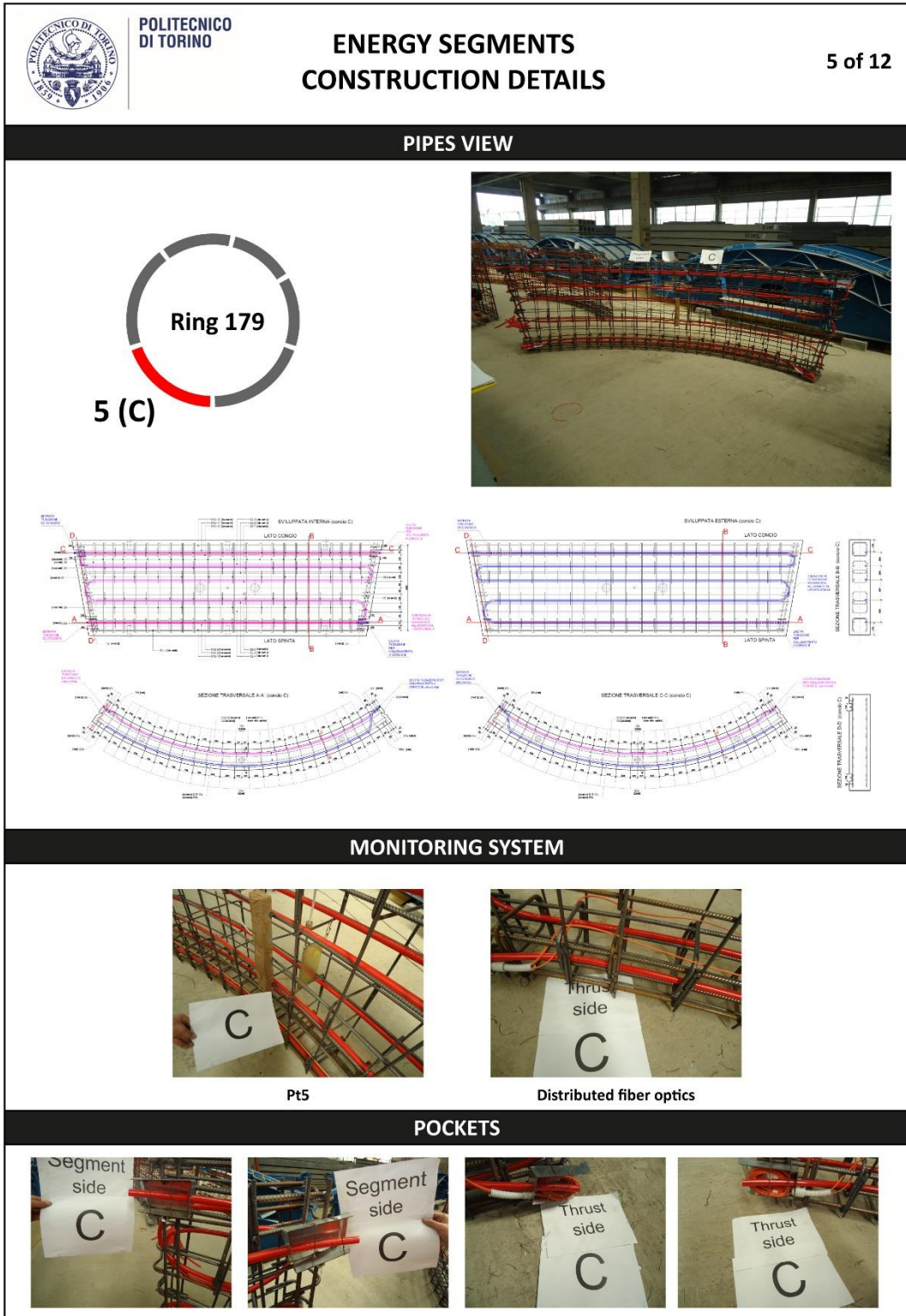


Figure 4.20: Energy segments construction details: ring 179, segment 5 (5/12).

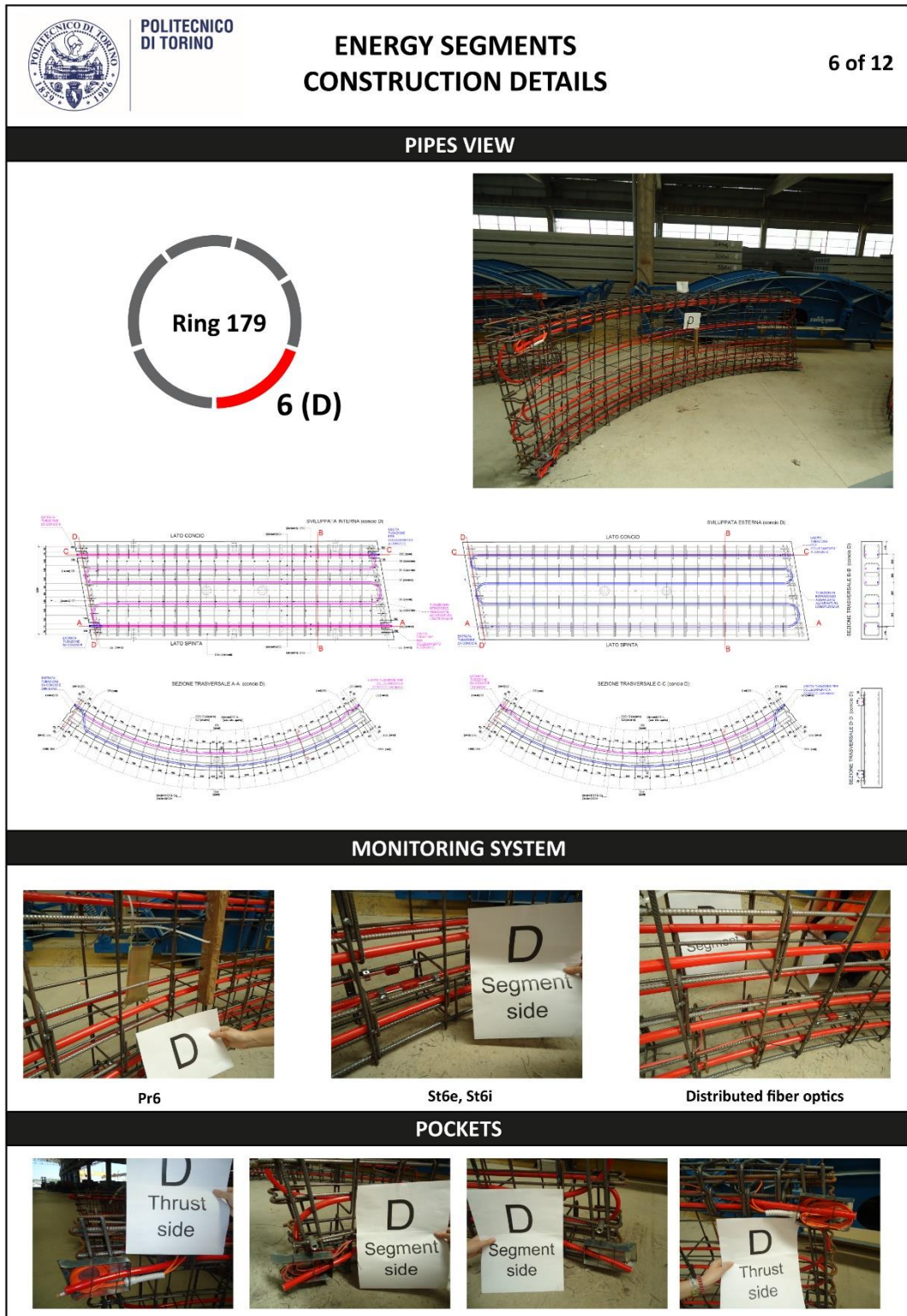


Figure 4.21: Energy segments construction details: ring 179, segment 6 (6/12).

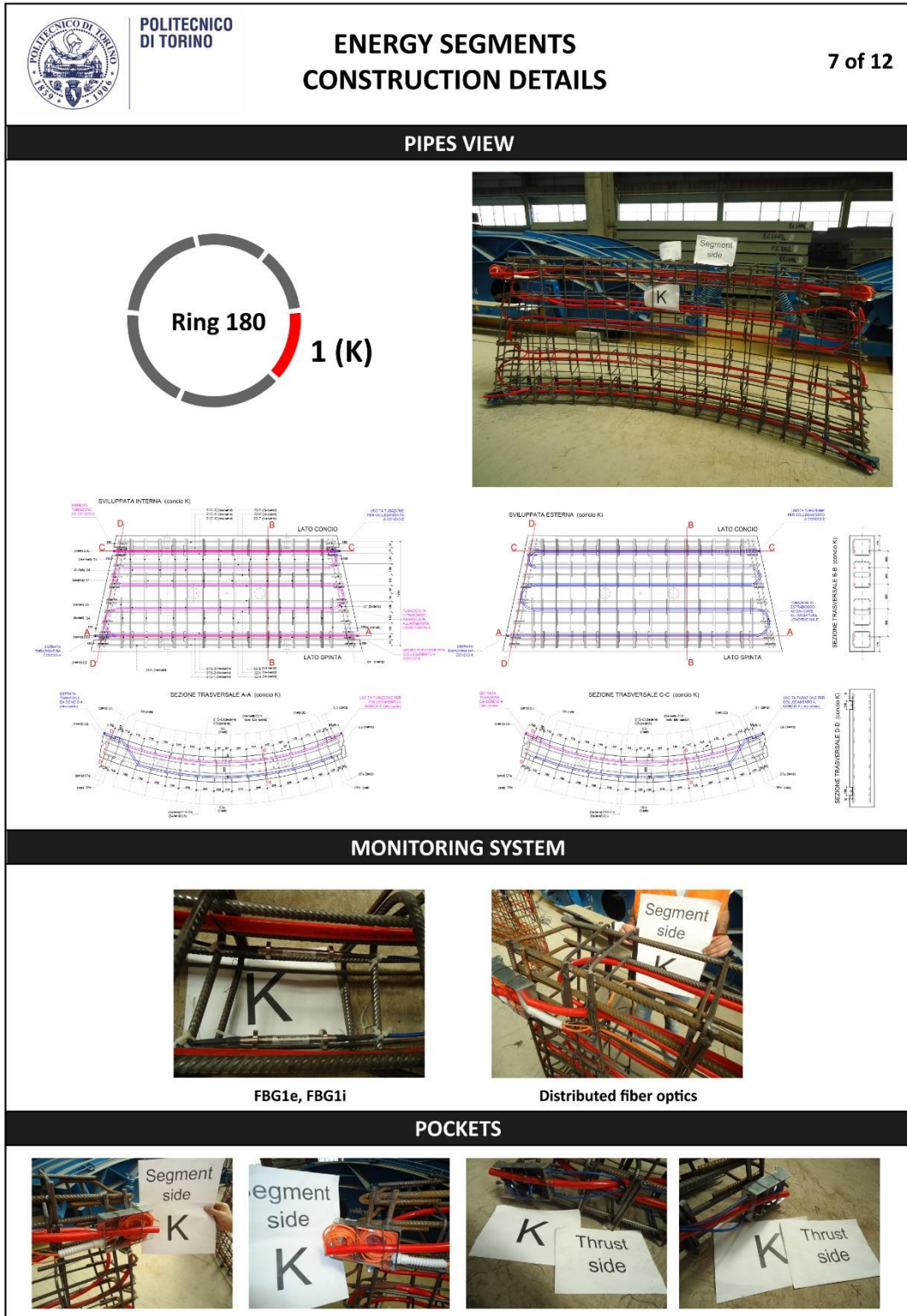


Figure 4.22: Energy segments construction details: ring 180, segment 1 (7/12).

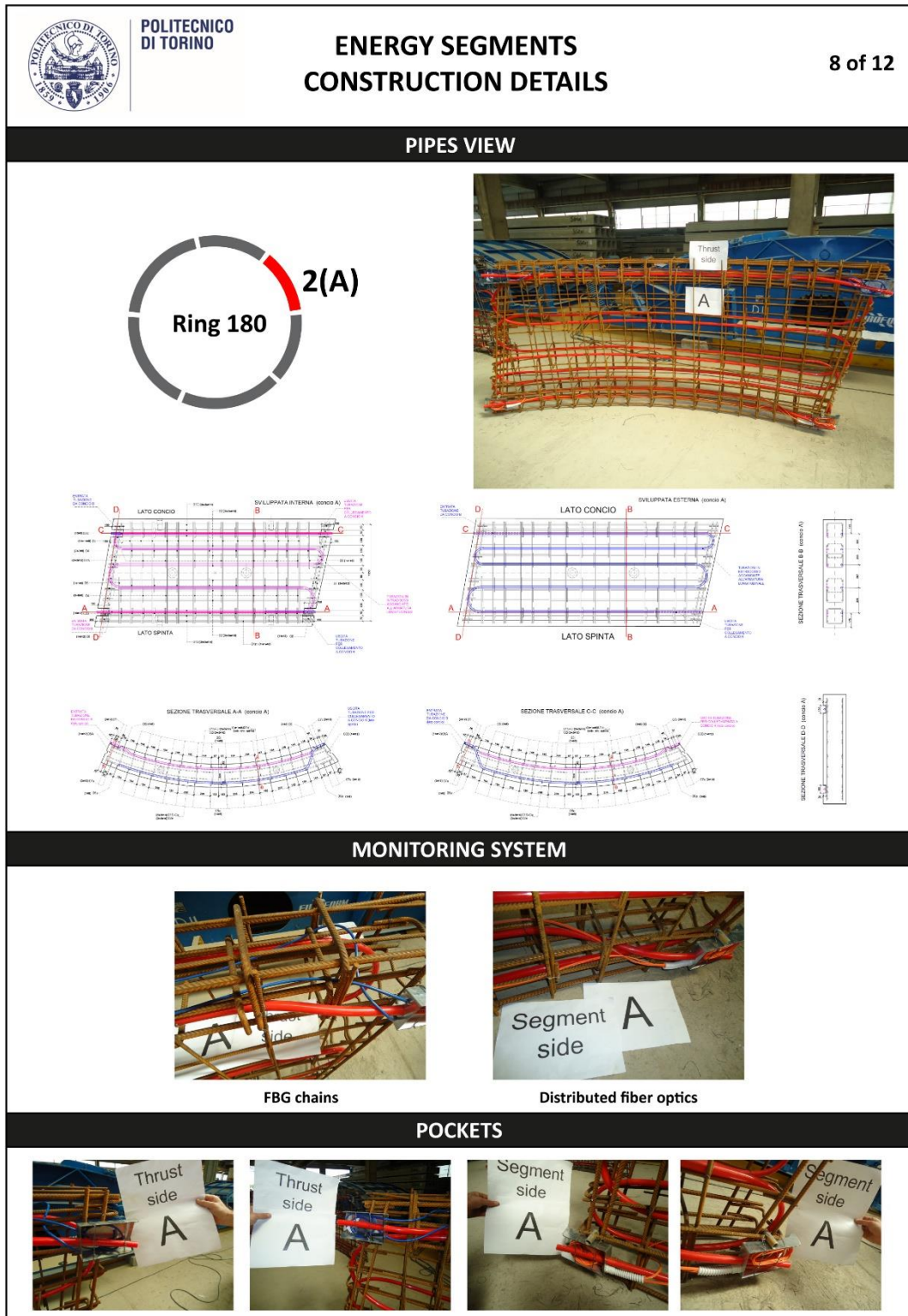



Figure 4.23: Energy segments construction details: ring 180, segment 2 (8/12).

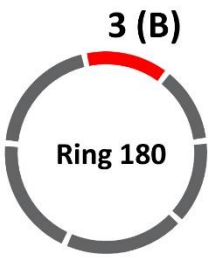


**POLITECNICO
DI TORINO**


ENERGY SEGMENTS CONSTRUCTION DETAILS


9 of 12

PIPES VIEW

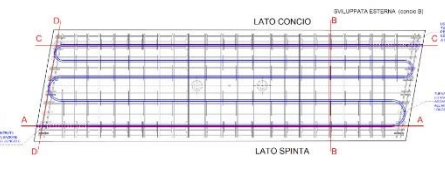


3 (B)
Ring 180

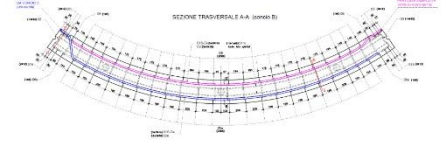




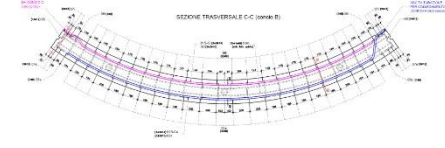
SVILUPPO A INTERNA (LATO CONCA)



SVILUPPO A ESTERNA (LATO SPINTA)




SEZIONE TRASVERSALE A-A




SEZIONE TRASVERSALE C-C

MONITORING SYSTEM




FBG3e, FBG3i




Distributed fiber optics


POCKETS




B Thrust side



B Thrust side



B Segment side



B Segment side

Figure 4.24: Energy segments construction details: ring 180, segment 3 (9/12).

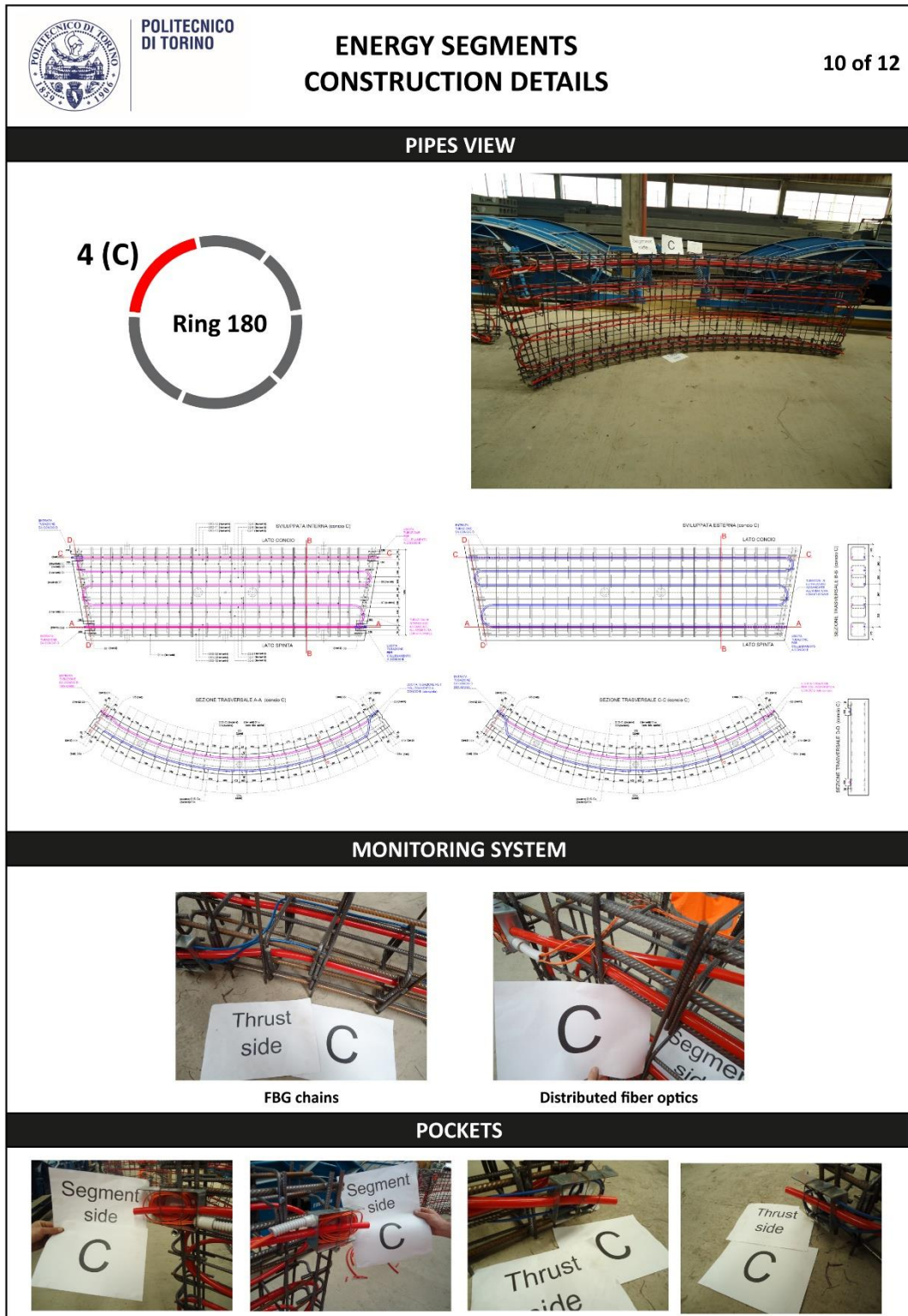


Figure 4.25: Energy segments construction details: ring 180, segment 4 (10/12).

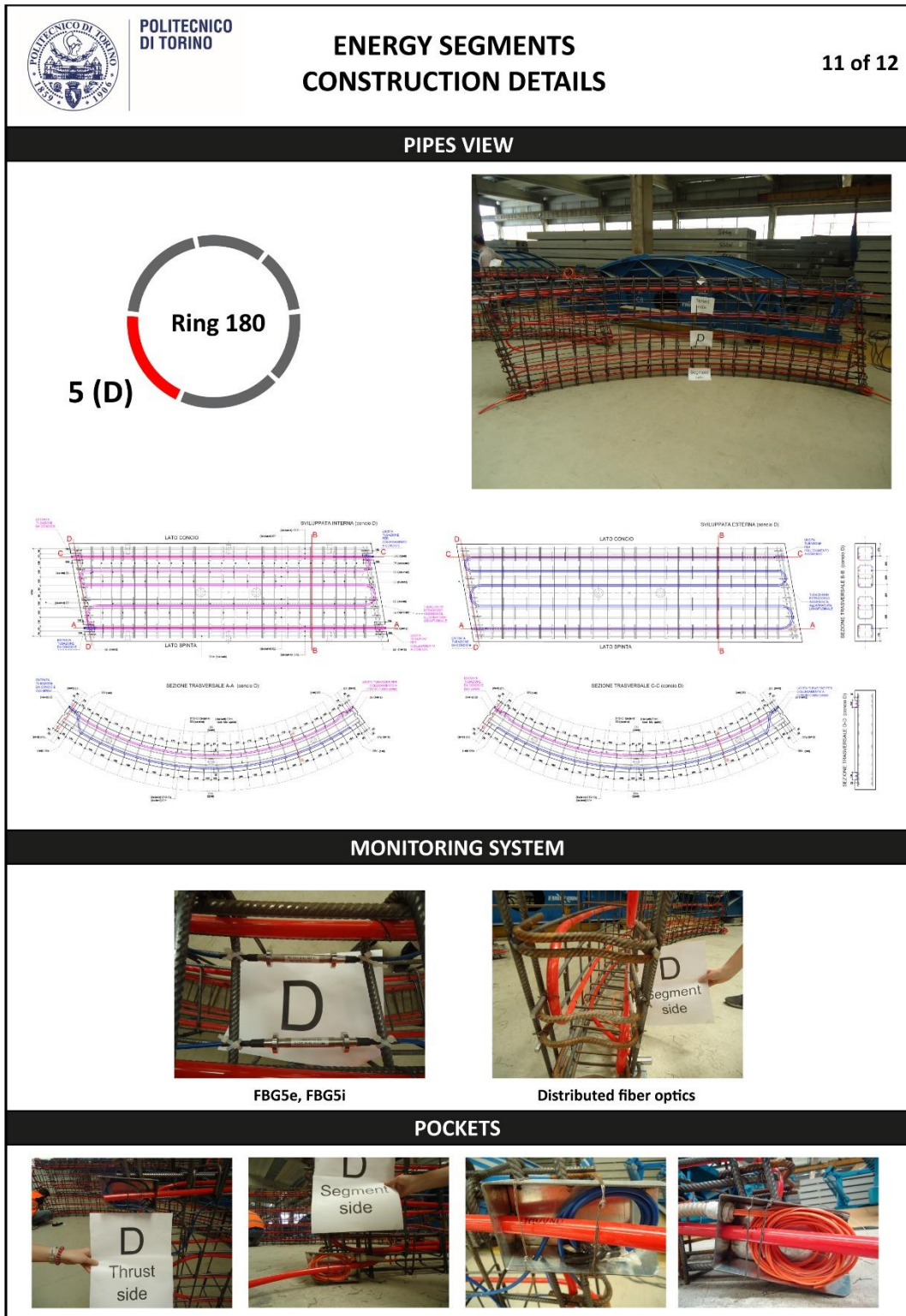


Figure 4.26: Energy segments construction details: ring 180, segment 5 (11/12).

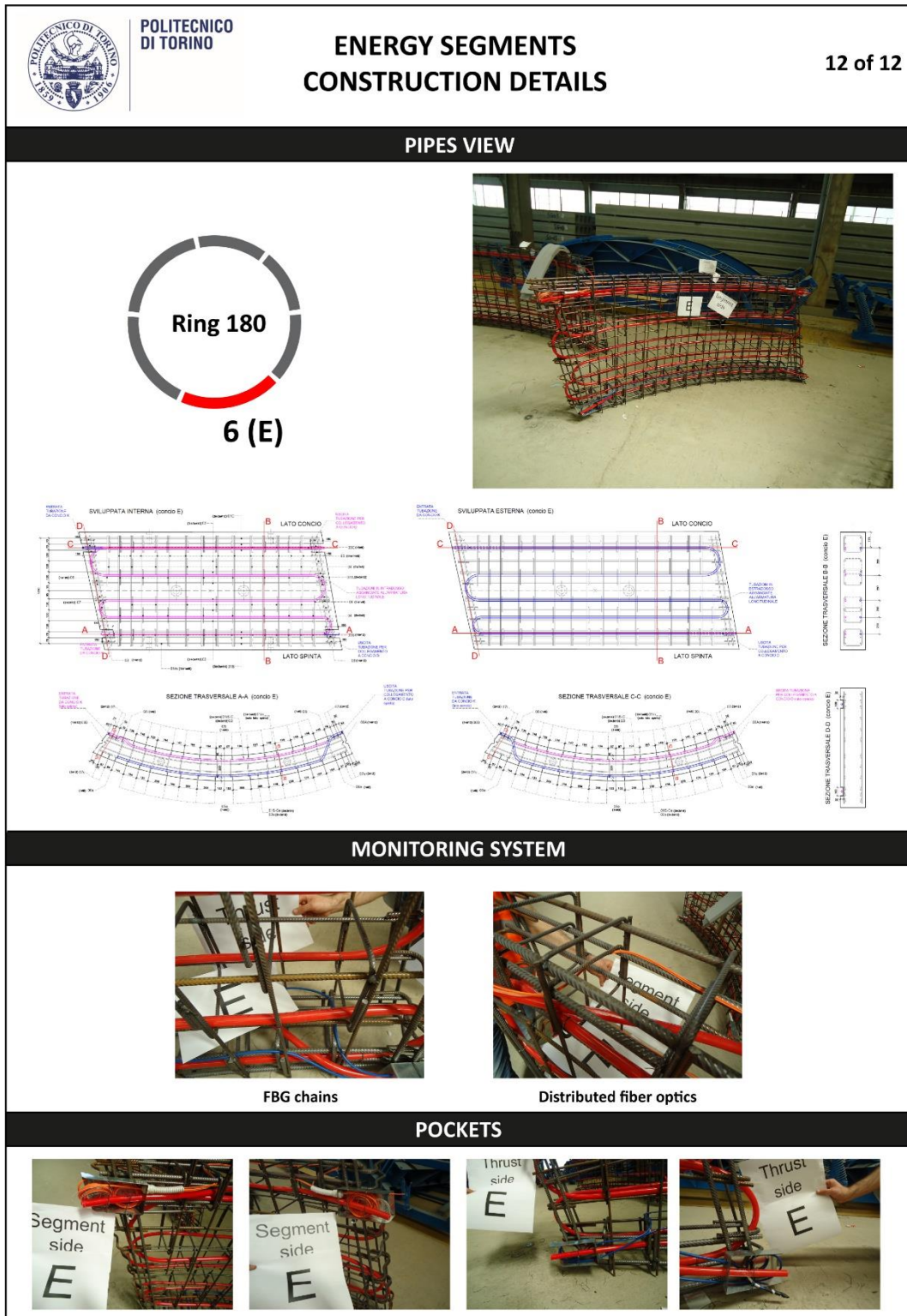


Figure 4.27: Energy segments construction details: ring 180, segment 6 (12/12).

4.3. Operation of the prototype

The aim of the experimental campaign was to evaluate efficiency and reliability of the prototype thermal activation together with its possible impacts on the lining.

Monitoring started in September 2017 with the assessment of undisturbed conditions at the site. Thermally induced stresses, thermally induced strains and temperatures in the lining were recorded under natural fluctuations of tunnel air temperature (it has to be recalled that the site is still under construction, therefore external air temperatures are strongly reflected in tunnel air). The purpose of this one-and-a-half-month phase was also to verify the regular functioning of the system. As already mentioned, a preliminary phase of flushing was necessary to eliminate most of air bubbles from the hydraulic circuit.

Figure 4.28 presents the recording of temperatures, strains and stresses (positive stresses indicate an increase in compression, positive strains indicate contraction) in two segments during this one-and-a-half month. Complete data are reported in Appendix A.

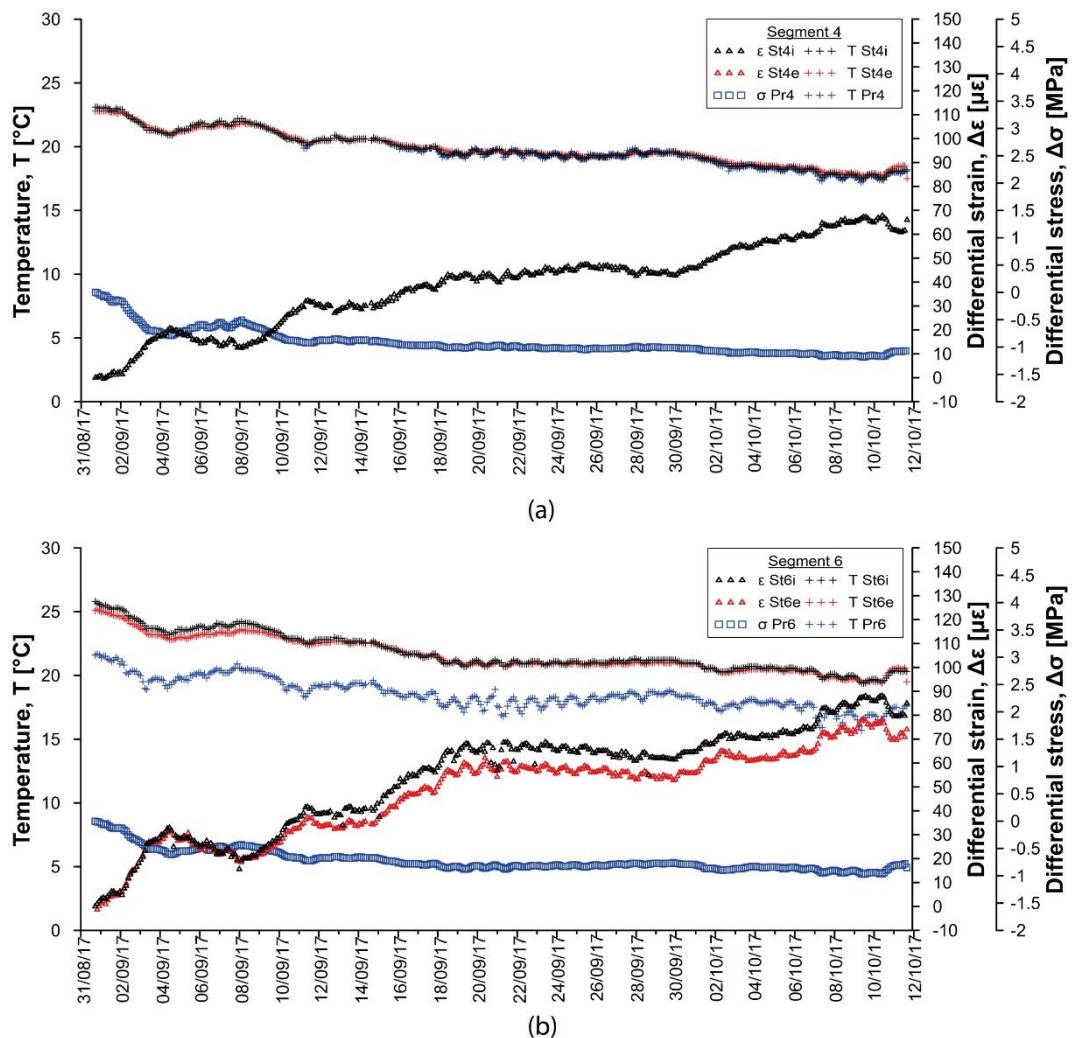


Figure 4.28: Temperatures, thermally induced strains and thermally induced stresses (a) in segment 4 and (b) in segment 6 (ring 179) during the Sep-Oct 2017 undisturbed conditions.

It can be seen that the temperature oscillation within the segments is reflected in stresses and strains, whose maximum and minimum values are summarized in Table 4.5 (see Table 4.4 for the explanation about the absence of strain value for sensor St4e). During cooling, the radial stress in the lining is reduced proportionally to temperature changes, while hoop strains increase.

Table 4.5: Maximum and minimum values of temperatures, strains and stresses during the undisturbed phase.

Segment	Sensor	Unit	Min	Max
4	St4i	[°C]	17.4	23.1
	St4i	[$\mu\epsilon$]	-1.07	68.06
	St4e	[°C]	17.5	22.9
	St4e	[$\mu\epsilon$]	-	-
	Pr4	[°C]	17.1	23.7
	Pr4	[MPa]	-1.18	0
6	St6i	[°C]	19.3	25.8
	St6i	[$\mu\epsilon$]	0	88.63
	St6e	[°C]	19.4	25.2
	St6e	[$\mu\epsilon$]	1.37	79.16
	Pr6	[°C]	15.7	21.7
	Pr6	[MPa]	-0.97	0

The reversible heat pump makes it possible to simulate summer and winter heating and cooling conditions. Depending on the fluid inlet temperature, this will be warmed or cooled by the surrounding ground. The possible types of tests that can be performed are:

- a) Ground configuration, heating mode
- b) Ground configuration, cooling mode
- c) Air configuration, tunnel cooling mode

During winter 2017/2018 type a) tests were completed with both rings operating. At the end of each test the heat pump was turned off for long enough to ensure returning to the initial undisturbed thermal and mechanical conditions. Test types b) and c) were performed during summer 2018.

For each test, the following quantities were recorded:

- inlet and outlet primary circuit temperatures measured by the heat pump probes (ENERTUN in, ENERTUN out);
- inlet and outlet secondary circuit temperatures measured by the heat pump probes (U1, U2);
- temperatures and stress-strain state in the lining (Sxny, Pxn for strains and stresses respectively, where x is the initial of the sensor orientation – longitudinal, hoop or radial -, n is the number of the sensor – 1 to 6, corresponding to each segment, and y indicates intrados or extrados);
- temperature inside the tunnel (T1);
- inlet/outlet ground temperature (T2, T3) and inlet/outlet air temperature (T4, T5) close to the energy rings;
- upstream groundwater temperature (T6);
- external air temperature close to the heat pump (T_{air}).

and the following differences of temperature were calculated:

- between primary circuit inlet and outlet close to the heat pump, considering also header pipes ($\Delta T_{\text{ENERTUN}}$);
- between primary circuit inlet and outlet close to the energy rings, without considering the header pipes (ΔT_{ground}).

The remote control of the heat pump assisted the user in setting the secondary circuit return temperature that governs the overall functioning. To guarantee a high performance of the heat pump, this temperature should not exceed the range 35-45°C in winter (Brandl, 2013). In the test type a) it was set to 45°C to bring the system to a steady-state condition and determine the maximum extractable heat flux density. The heat carrier fluid inlet temperature to the Enertun circuit and its velocity are automatically adjusted by the device. The latter depends on the circulation pumps used and on the degree of opening of asameter valves present along the circuit. For the tests performed, full turbulence was achieved (Reynolds number lays in the range 8800-14500). This is a favorable condition to increase the diffusive transfer of energy and mass. However, economical aspects should not be forgotten: higher costs for operation are needed if high heat pump performance is required to achieve turbulence (Brandl, 2006).

A number of tests were performed whose list is reported in Table 4.6. For every test the thermal power exchanged with the ground was computed and the mechanical thermally induced effects in the lining investigated. Both will be analyzed in Chapter 5 and Chapter 6 respectively. Figure 4.29 illustrates visually the effect of thermal activation on the lining temperature thanks to infrared pictures taken by using a thermal camera at three different times. During air heating mode (Figure 4.29a,b,e,f) the tunnel lining and the geothermal pipes show lower temperatures compared to the neighbouring rings. The opposite occurs in ground cooling mode (Figure 4.29c,d).

Table 4.6: List of the tests performed.

Test code	Circuit	Mode	Volumetric flow rate [m ³ /h]	Fluid velocity [m/s]	Starting time [dd/mm/aa hh:mm]	Ending time [dd/mm/aa hh:mm]	Duration [d]
GH1	Ground	Heating	1.3	0.90	15/02/2018 14:13	17/02/2018 09:57	1.82
GH2	Ground	Heating	1.3	0.90	18/02/2018 13:57	20/02/2018 09:50	1.83
GH3	Ground	Heating	1.3	0.90	22/02/2018 14:32	26/02/2018 12:50	3.93
GH5	Ground	Heating	0.8	0.55	05/03/2018 14:05	07/03/2018 14:17	2.01
GH6	Ground	Heating	1.0	0.69	09/03/2018 13:59	12/03/2018 15:47	3.07
GH8	Ground	Heating	1.3	0.90	20/03/2018 14:00	28/03/2018 11:11	7.82
GH9*	Ground	Heating	1.3	0.90	07/04/2018 10:00	16/04/2018 18:00	9.33
GH10*	Ground	Heating	1.3	0.90	08/05/2018 10:04	20/05/2018 18:00	12.33
GC1	Ground	Cooling	1.4	0.97	27/07/2018 11:29	30/07/2018 11:31	3.00
AH1	Air	Heating**	1.3	0.90	01/08/2018 10:56	03/08/2018 15:56	2.21
AH2	Air	Heating**	1.3	0.90	04/08/2018 20:00	06/08/2018 10:00	1.58
GC2	Ground	Cooling	1.4	0.97	07/08/2018 12:22	09/08/2018 07:31	1.80

*Cyclic tests with heat pump on between 10:00 and 18:00.

**In this case the heat pump heating mode corresponds to tunnel cooling.

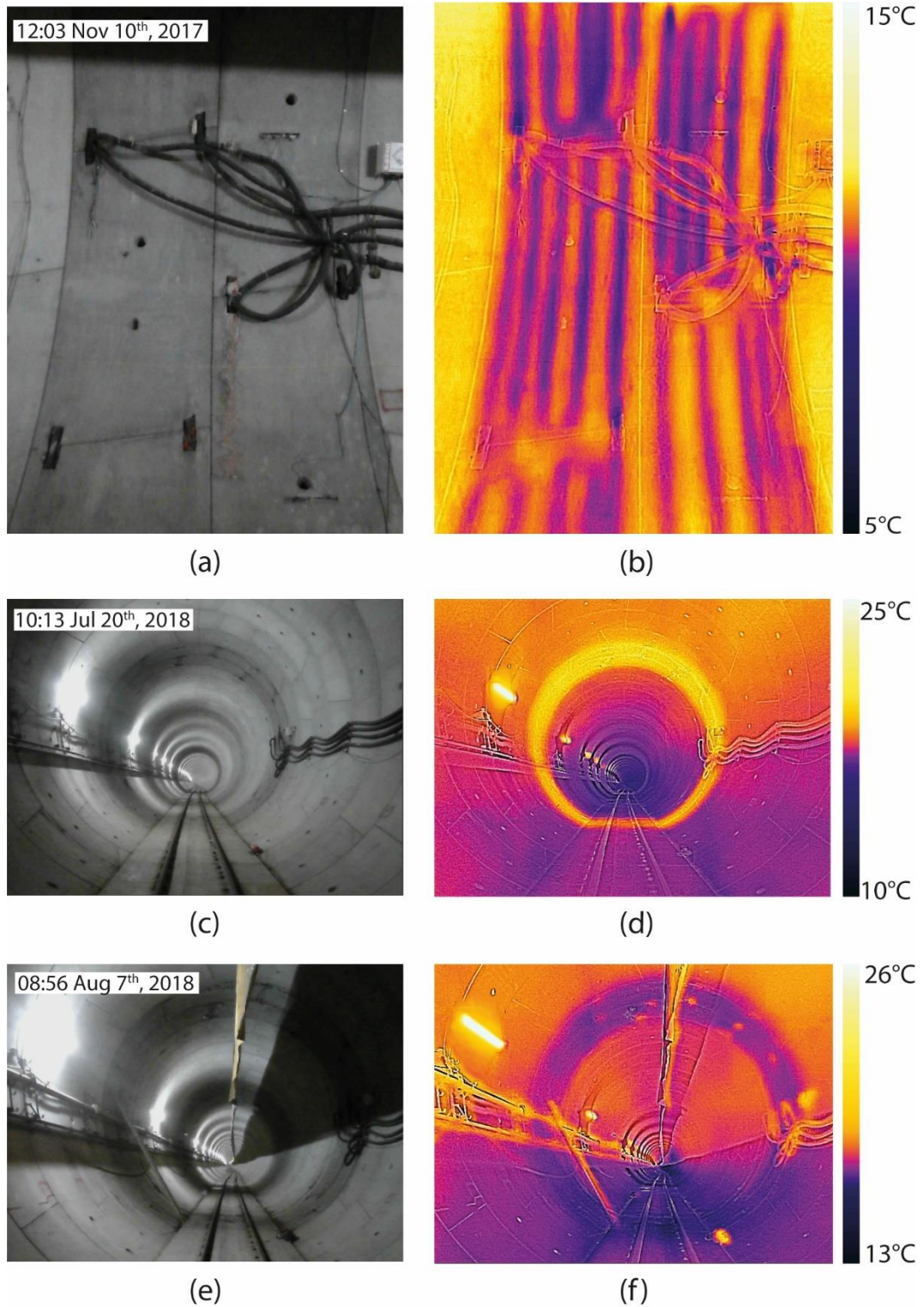


Figure 4.29: Standard view (a), (c), (e) and thermal picture (b), (d), (f) during the operation of the prototype ((a),(b) air heating; (c),(d) ground cooling; (e),(f) air heating).

4.4. Summary

The advantage of integrating thermally active systems into geotechnical structures such as tunnels is that the structures are being built anyway and the added cost is limited with respect to the overall cost. The thermal activation of tunnel linings is therefore an interesting opportunity that may allow for exploiting the energy stored in the ground with economic and environmental benefit.

The new Enertun segment is shown to provide additional improvements with respect to previous applications of similar technologies, by reducing head losses, increasing thermal exchange in the presence of groundwater flow and allowing for different configurations to better adapt to the ultimate scope of the implementation.

A real scale prototype of energy tunnel system constituted by two rings of Enertun segments was realised for the first time in Italy and underwent a complex and detailed testing campaign. The prototype is capable of reproducing real scale behaviour of an energy tunnel with both the attention posed to the thermal performance and the structural behaviour of the lining. The amount of data collected is comprehensive and of good quality and allows to push the boundaries of the understanding on the real behaviour of such systems. New design approaches could be suggested and tools tailored to allay any concern about the potential adverse impacts on safety and to open the path to such smart, economic and environmentally friendly solutions. Moreover, the construction procedures and details to implement energy segments into the tunnel construction scheme adopted are shown to be relatively simple and not matter of delays or drawbacks of the overall construction scheme. It is envisaged that improvements can be made for industrial application, e.g. to speed up segment preparation, pipes can be included in the steel cage before reaching the precast concrete plant or fiber reinforced concrete segments could be used by taking advantage of an artificial support cage then inserted within the mould; connections between segments can be done by heat sealing.

Chapter 5

Thermal design

5.1. Introduction

Few studies have dealt with the thorough investigation of the thermal performance of energy tunnels based both on a monitored, full-scale site and on numerical results. It is the scope of this Chapter to analyse the original data collected for that pertaining to the thermal performance of the Enertun prototype in both the ground and the air configuration in order to investigate the energy efficiency of thermal activation of tunnels. The experimental data from the real-scale energy tunnel prototype tested in the tunnel of the Turin Metro Line 1 South Extension described in Chapter 4 are considered, by presenting the results of the tests performed in heating and cooling mode through both the ground and air configurations of the novel Enertun layout. Thanks to the availability of the original experimental data collected, it was possible to calibrate and corroborate a thermo-hydraulic numerical model in the conditions of the site, then used to generalise the results to different ground and environmental conditions with particular reference to the still unstudied role of groundwater flow direction. Corroboration of numerical models was not possible in previous literature for the Turin case given the unavailability of a testbed (Barla et al., 2014; Barla et al., 2016). Understanding of the role of some of the most important design parameters is illustrated in the form of parametric design charts, that update to the Enertun configuration those already existing in literature. A simple method for preliminary evaluation of the potential of energy tunnels, accounting for the investigated design parameters, is formulated. Part of the work presented in this Chapter comes from Insana and Barla (2020). Detailed information about experimental tests is reported in Appendix A.

5.2. Energy performance of the prototype

The data collected from the experimental site will be here analyzed for that pertaining to the thermal performance in order to investigate the energy efficiency of thermal activation of tunnels. During winter 2017/2018 heating mode tests were completed with both rings

operating in parallel. At the end of each test the heat pump was turned off for long enough to ensure returning to the initial undisturbed thermal and mechanical conditions. Cooling mode tests were performed during summer 2018. The total list of tests performed is given in Table 4.6, with 8 tests involving the ground circuit in heating mode (both continuous and cyclic), 2 tests where the ground circuit worked in cooling mode and 2 more tests where the air circuit was used to cool the tunnel air. Different volumetric flow rates and durations were chosen in order to collect a sound database for subsequent numerical back-analysis. The fluid velocity was calculated starting from the volumetric flow rate and considering an internal diameter of the pipes within the segments of 16 mm, taking into account the fact that the two rings are connected in parallel. The volumetric flow rate user side was read in situ on the thermal energy counter and resulted to be $0.96 \text{ m}^3/\text{h}$, assumed constant for the whole duration of all tests. An illustrative test is described in the following, with the main features summarised in Table 5.1. The same applies to the other tests reported in Appendix A.

Table 5.1: Main features of the example test GH8.

Test name	-	GH8
Circuit	-	Ground
Mode	-	Heating
Target temperature	[°C]	45
Activated rings	-	Both
Starting time	[ddmmaa hh:mm]	20/03/2018 14:00
Ending time	[ddmmaa hh:mm]	28/03/2018 11:11
Duration	[d]	7.82
Volume flow rate (primary circuit)	[m ³ /h]	1.3
Fluid velocity (primary circuit)	[m/s]	0.90

The output of the test GH8 is presented in Figure 5.1, including the thermal activation phase when the heat pump was on and the thermal recovery phase. The temperatures in the two circuits are presented in Table 5.2. The daily temperature fluctuations outside the tunnel and inside the tunnel can be appreciated thanks to the probes called T_{air} and T_1 . Due to an imposed target temperature of 45°C , the heat pump regulates the inlet temperature of the heat carrier fluid directed towards the Enertun circuit, that reaches about 2.3°C if the first two-days transition step is neglected. The outlet Enertun temperature is 4.4°C , for a temperature difference between outlet and inlet of 2.1°C . The travel time needed for the water-glycol mix to enter and exit the circuit is about 1.78 min from the heat pump to the energy rings and 2.15 min within each energy ring, for a total time of 5.70 min for a speed of 0.90 m/s .

If attention is moved to what happens on the secondary circuit side, it can be noticed that U2 remains in the range $30\text{-}35^\circ\text{C}$ with some oscillations. These are due to the fact that the fan coil is immersed in an environment subject to daily temperature variations. It is expected that, if placed in a closed room, such as a building service room, the trend would be more constant. A nearly constant temperature difference between U1 and U2 is evident, meaning a nearly constant heat flux release between the secondary circuit and the heated environment. At the end of the test, the heat pump was turned off and circulation pumps kept working. ENERTUN in and ENERTUN out tended to return to the initial equilibrium temperature of about 14.2°C . Also, U1 and U2 both decrease and match, albeit with lower amplitude, external air temperature which certainly has a great influence on the secondary circuit.

It is pointed out that interestingly the in situ ground temperature measured thanks to a probe placed within a piezometer well in the area of the prototype is 18°C (Figure 5.2, constant from December 2017 to May 2018), which is somewhat higher than typical values of $14\text{-}15^\circ\text{C}$ encountered in literature that would normally be expected in Turin (Bucci et al., 2017). It is

thought that this does not represent a mean temperature of the area but is due to any kind of local anomaly, whose reason is still being investigated. It is curious to read about an analogous issue in the energy pile test at Lambeth College (Bourne-Webb et al., 2009). However, the explanation the Authors give in that case does not apply here.

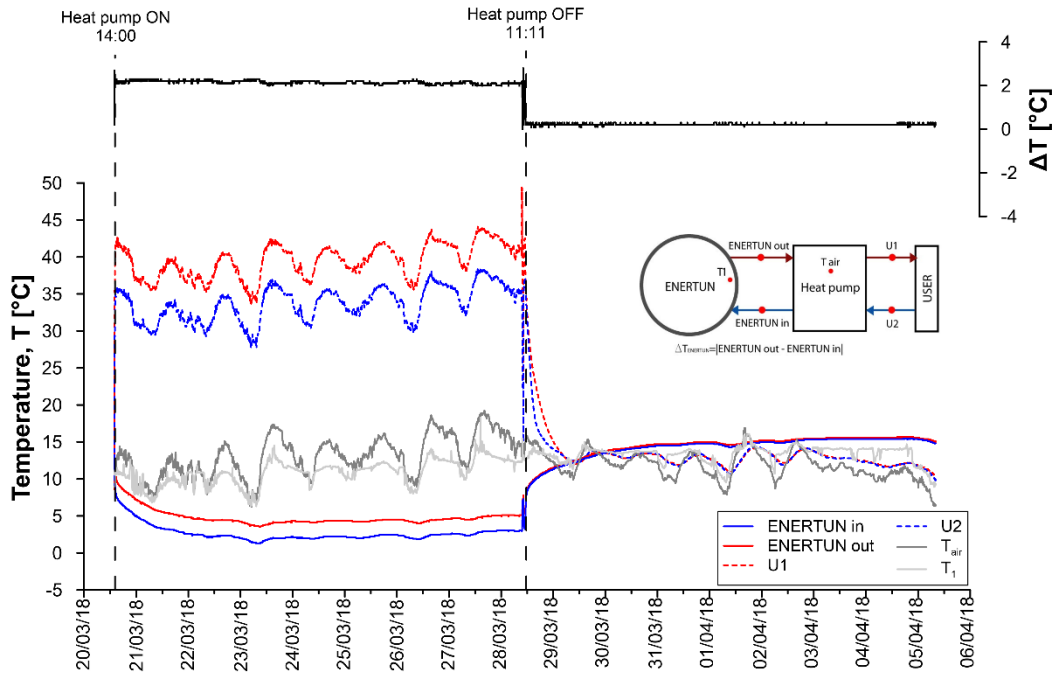


Figure 5.1: Monitored temperatures in the primary and secondary circuits during test GH8.

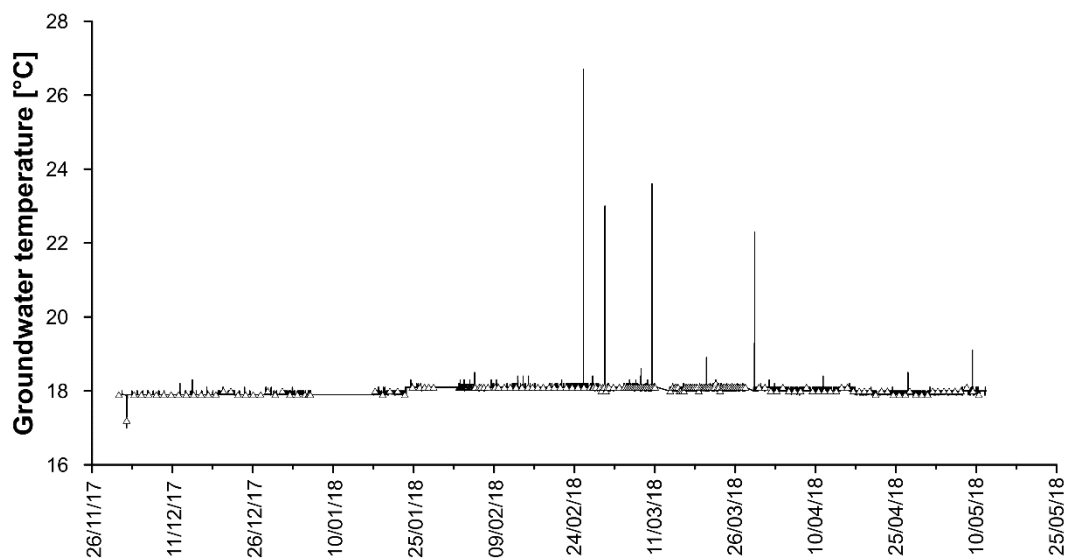


Figure 5.2: Monitored upstream groundwater temperature T6 in the area of the construction site.

Table 5.2: Temperatures during the test GH8.

ENERTUN in	[°C]	2.3
ENERTUN out	[°C]	4.4
$\Delta T_{\text{ENERTUN}}$	[°C]	2.1
U1	[°C]	35-40
U2	[°C]	30-35

When analyzing the temperature probe measurements within the tunnel, what emerges is that T1 mirrors very well the temperature fluctuations outside the tunnel. Besides, as long as the yard is operative, there is no physical boundary between the tunnel tube and the station, especially when considering that the energy rings are only 42 m from the entrance. For this reason, the thermal performance could differ in real-operating conditions, that is why we are working at making the experimental site permanent, with the scope to repeat the tests once the Metro Line will be put in service.

It was noted that temperatures recorded during the operational phase progressively increase from the starting point to the exit point of the circuit, going from segment 2 to 4 and 6 (see Figure A.107 in Appendix A). This is reasonable and consistent with the heat carrier fluid heating up during its trajectory.

The tests performed and listed in Table 4.6 allowed to investigate the energy performance of the experimental prototype of energy tunnel. The following considerations are then specifically referred to the conditions in which the prototype was tested, that is during the construction of the tunnel. Nevertheless, the data collected were particularly valuable to calibrate a thermo-hydraulic numerical model for the purpose of extending the discussion to other conditions (temperature boundary conditions, thermal ground properties, etc.), as debated in the following paragraphs.

For each test the inlet and outlet temperature over the whole duration were recorded by the heat pump. The procedure to evaluate the energy performance was as follows:

- The difference of temperature ΔT (in °C) between outlet and inlet was computed at any given time t_n when data were available

$$\Delta T(t_n) = |T_{\text{outlet}}(t_n) - T_{\text{inlet}}(t_n)| \quad \text{Eq. 5.1}$$

- The heat flow, also called thermal power, $\Delta \dot{Q}$ (in W or J/s) was derived from the first law of thermodynamics, by computing the enthalpy flow $\Delta \dot{H}$ in the case of convective heat transfer, that is the main heat transfer mechanism taking place within the pipes

$$\Delta \dot{Q}(t_n) = \Delta \dot{H} = \dot{M} c_p \Delta T(t_n) \quad \text{Eq. 5.2}$$

where \dot{M} is the mass flow rate expressed in kg/s, c_p is the specific heat capacity at constant pressure in J/(kg·°C) and ΔT is the temperature difference at the heat pump in °C;

- The thermal energy extracted or injected for each time step $\Delta Q(t_n)$ (in kWh) was computed as the trapezoidal area under the curve $\Delta \dot{Q}(t)$

$$\Delta Q(t_n) = \frac{[\Delta \dot{Q}(t_n) + \Delta \dot{Q}(t_{n-1})] \cdot [t_n - t_{n-1}]}{2} \quad \text{Eq. 5.3}$$

- The total energy extracted or injected during the test from the two energy rings was obtained by the following summation

$$Q = \sum_{t=t_{in}}^{t=t_{fin}} \Delta Q(t) \quad \text{Eq. 5.4}$$

- The average thermal power \dot{Q} was obtained by dividing the total energy extracted by the test duration. From \dot{Q} it is possible to calculate the average thermal power extracted or injected per meter of tunnel lining or per square meter of tunnel lining by using the total longitudinal length of the prototype (2.8 m, in W/m) or its total contact surface area (65.8 m² for the ground circuit and 60.5 m² for the air circuit, in W/m²).

To have a global understanding of the thermal performance of the system, Table 5.3 summarizes the energy performance expressed in terms of specific thermal power (in W/m and in W/m²) and of total thermal energy (in kWh) obtained for each of the tests listed in Table 4.6. It is pointed out that water, with 10% glycol is assumed in the computations, therefore c_p is equal to 4070 J/(kg·°C) and water density to 1009.6 kg/m³. The order of magnitude of thermal power per square meter is comparable to the one shown in Figure 2.7 for the case of groundwater flow perpendicular to the tunnel axis.

Table 5.3: Energy performance of the prototype in terms of heat flux and thermal energy for each of the tests performed.

Test code	Thermal power		Thermal energy
	[W/m]	[W/m ²]	[kWh]
GH1	1105	47.0	135.35
GH2	1198	51.0	147.25
GH3	1188	50.6	313.75
GH5	959	40.8	129.44
GH6	1076	45.8	222.34
GH8	1135	48.3	601.12
GH9*	1118	47.6	250.50
GH10*	1170	49.8	340.64
GC1	1421	60.5	286.59
AH1	1142	52.8	169.47
AH2	1179	54.6	125.48
GC2	1069	45.5	18.74

Although the total number of tests is limited and does not allow for a statistical analysis, some additional considerations can be given by observing Figure 5.3a-c. From Figure 5.3a a nearly linear relationship between the volumetric flow rate of the fluid within the pipes and the heat flux is shown, that is heat flux increases with increasing flow rates. Heat fluxes between 41 and 51 W/m² were obtained in ground heating considering both the continuous and the two cyclic tests. The energy performance is higher for ground cooling mode, especially in one case, mainly due to the higher flow rate and to the higher distance in temperature between the ground and the heat carrier fluid. When the air circuit is operated in tunnel cooling mode, heat flux values are similar to those of the ground heating and cooling tests. However, it has to be noticed that higher ranges of inlet and outlet temperatures occurred in this case, with a beneficial effect on the coefficient of performance of the heat pump.

In Figure 5.3b heat flux is plotted versus the test duration. No particular trends can be highlighted; therefore, the energy efficiency does not depend on the test duration and

comparable thermal powers were obtained also in the case of longer tests, allegedly due to the favourable groundwater thermal recharge. Figure 5.3c is intended to investigate any induced effect of the period of the year during which the test was carried out. The performance is only marginally affected leading to the conviction that it will be negligible during real operation of the tunnel, when the influence of external climatic conditions will be even lower than during the construction of the tunnel.

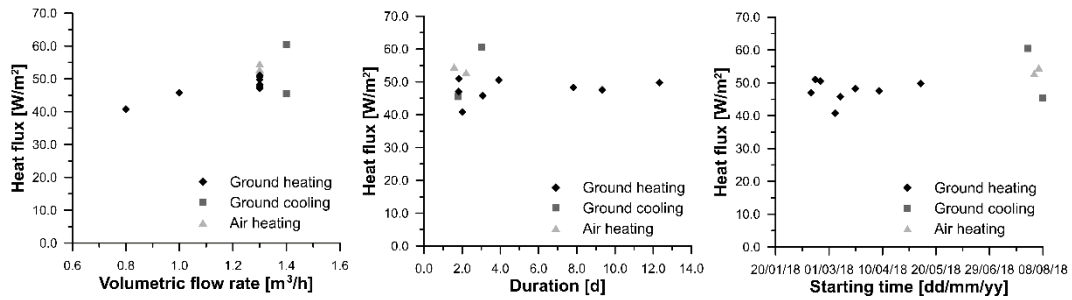


Figure 5.3: Energy tunnel thermal performance dependence on (a) heat carrier fluid volumetric flow rate, (b) test duration and (c) period of the year.

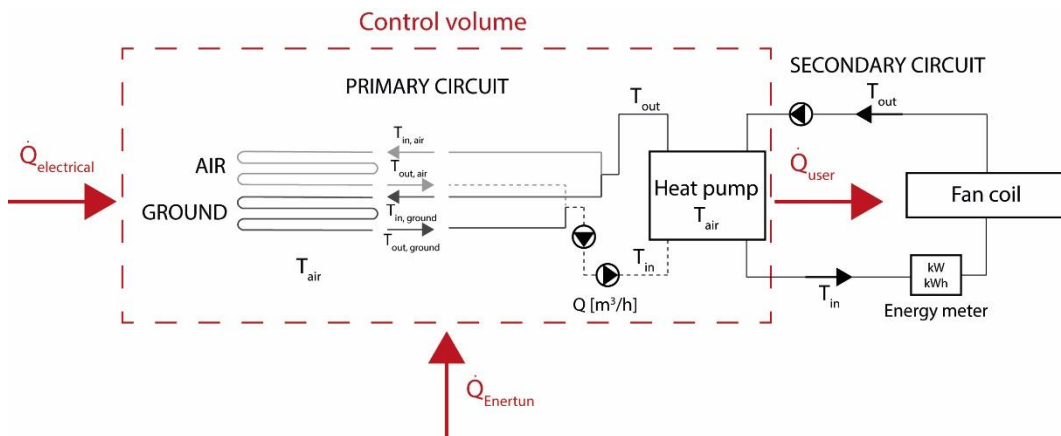


Figure 5.4: Energy balance scheme for the heat pump.

To evaluate the performance of the system, the electrical power required by the heat pump and the two circulation pumps has to be considered (sketch of the system in Figure 5.4). An electrical energy counter for the heat pump was not available, that is why an energy balance was taken into account as primary and secondary thermal powers are known. As an alternative, theoretical electrical consumption from the heat pump data sheet could be considered (see Appendix B, Figure B.2). The power consumption of the circulation pumps is 0.170 kW for DAB and 0.958 kW for Lovara. In heating mode, the COP was computed as the ratio between the useful thermal power, that is the thermal power provided to the user, and the electrical power consumed. In cooling mode, the EER presents the same formulation as the COP, but expresses the inverse process, being the effect given by cooling instead of heating. By also including the consumption of the two circulation pumps, the total COP/EER is obtained. Table 5.4 summarizes the results obtained for all the tests performed. The COP obtained from the analysis reveals rather low values. It should be noted that the accuracy of the measure of inlet and outlet temperatures is not given by the heat pump supplier, but should not exceed

1°C. Considering the total COP, the values even decrease, because of the high consumption of the circulation pumps, which aspect could be improved in a real plant by replacing the two pumps with a single one specifically designed for the plant under study.

In cooling mode, due to the poor number of tests, it is difficult to critically evaluate the results. However, the extracted thermal energy is considerable, making the cooling operation mode very interesting.

Table 5.4: COP/EER and total COP/EER calculation.

		GH1	GH2	GH3	GH5	GH6	GH8	GH9	GH10	GC1	AH1	AH2
Duration	[h]	43.74	43.89	94.30	48.20	73.80	189.18	80.00	104.00	72.03	53.00	38.00
\dot{M}_{Enertun}	[kg/s]	0.36	0.36	0.36	0.22	0.28	0.36	0.36	0.36	0.39	0.36	0.36
\dot{M}_{user}	[kg/s]	0.27	0.27	0.27	0.27	0.27	0.27	0.27	0.27	0.27	0.27	0.27
$\bar{T}_{i,\text{Enertun}}$	[°C]	3.22	2.12	0.85	1.26	2.94	2.65	8.12	10.77	36.00	14.08	11.55
$\bar{T}_{o,\text{Enertun}}$	[°C]	5.31	4.38	3.09	4.20	5.58	4.79	10.23	12.80	33.52	16.24	13.77
$\Delta T_{\text{Enertun}}$	[°C]	2.09	2.26	2.24	2.94	2.64	2.14	2.11	2.03	2.48	2.15	2.23
$\bar{T}_{i,\text{user}}$	[°C]	35.17	37.21	33.25	37.06	39.80	39.46	45.30	40.74	6.18	57.34	57.21
$\bar{T}_{o,\text{user}}$	[°C]	29.51	31.51	27.79	31.52	34.19	33.69	39.47	34.61	11.60	51.16	50.74
ΔT_{user}	[°C]	5.66	5.71	5.46	5.54	5.61	5.77	5.82	6.14	5.41	6.18	6.47
Q_{Enertun}	[kWh]	135.35	147.25	313.75	129.44	222.34	601.12	250.50	340.64	286.59	169.47	125.48
\bar{Q}_{Enertun}	[kW]	3.09	3.36	3.33	2.69	3.01	3.18	3.13	3.28	3.98	3.20	3.30
\bar{q}_{Enertun}	[W/m]	1105.27	1198.33	1188.29	959.15	1075.90	1134.83	1118.29	1169.77	1420.93	1141.99	1179.42
\bar{q}_{Enertun}	[W/m ²]	47.03	50.99	50.57	40.82	45.78	48.29	47.59	49.78	60.47	52.84	54.57
Q_{user}	[kWh]	276.00	279.24	574.11	297.83	461.92	1217.92	520.98	774.61	435.00	365.10	274.20
\bar{Q}_{user}	[kW]	6.31	6.36	6.09	6.18	6.26	6.44	6.51	7.45	6.04	6.89	7.22
$\bar{Q}_{\text{electrical}}$	[kW]	3.22	3.01	2.76	3.49	3.25	3.26	3.38	4.17	2.06	3.69	3.91
COP/EER	[-]	1.96	2.12	2.21	1.77	1.93	1.97	1.93	1.78	2.93	1.87	1.84
$\bar{Q}_{\text{electrical,tot}}$	[kW]	4.34	4.14	3.89	4.62	4.37	4.39	4.51	5.30	3.19	4.82	5.04
COP _{tot} /EER _{tot}	[-]	1.45	1.54	1.57	1.34	1.43	1.47	1.44	1.41	1.89	1.43	1.43

5.3. Numerical investigation on the thermal behaviour of the prototype

The collection of experimental data concerning the real thermal behaviour of the energy tunnel prototype was used to draw some conclusions about its thermal performance. This is of particular relevance as no such results are available in literature for Italy and for hydrogeological conditions such as those existing in Turin. However, the conditions of the experimental campaign carried out are not fully representative of the general case of an operational tunnel, mainly because of the different temperature variations of the tunnel internal air. Nevertheless, this situation can be investigated by taking advantage of a three-dimensional, time-dependent, coupled thermo-hydraulic numerical model, that was first calibrated and then validated on the experimental results. This task is described in the following and is aimed at developing some updated design charts, in the path of the ones depicted in Di Donna and Barla (2016).

A 3D numerical model was built with the FEM software Feflow (Diersch, 2009) to reproduce the combined, transient thermo-hydraulic behaviour of the two Enertun rings installed in the experimental site. The TH problem is governed by mass conservation, energy conservation equations, and Darcy's law, written in the Eulerian coordinate system for a saturated medium composed of a solid and a liquid (water) phase.

A preliminary assessment of the appropriate boundary conditions to be adopted at the intrados of the tunnel to reproduce the influence of internal air was carried out. First, a 30-cm thick air layer was included in the model by assigning moving air thermal properties. Then, this layer was deactivated and a heat transfer boundary condition was applied, by computing the corresponding heat transfer coefficient. For the subsequent analyses the second boundary condition was adopted to reduce the total number of finite elements in the model. Lateral boundary conditions were also studied. In particular, the case of temperatures fixed (i) only on top and bottom boundaries (case A), (ii) on top, bottom and left boundaries (case B) and (iii) on top, bottom, left and right boundaries (case C) were analysed. No differences were highlighted (Figure 5.5 and Figure 5.6), then the case (i) will be adopted in the following.

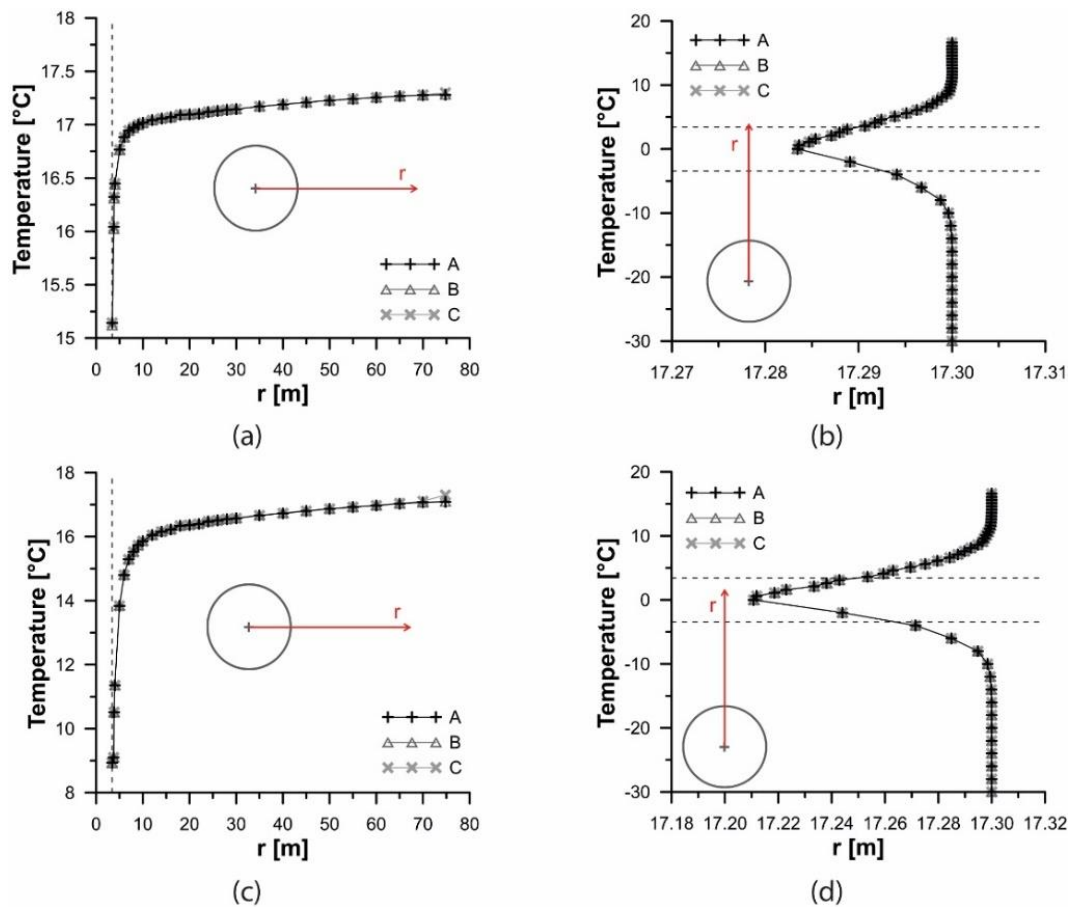


Figure 5.5: Comparison among different boundary conditions - temperature along horizontal profile (a) after 30 days and (c) after 60 days, temperature along vertical profile (b) after 30 days and (d) after 60 days.

The model, whose cross section is shown in Figure 5.7, is 74.8 m high and 149.6 m wide, with a thickness of 8.4 m, for a total of 6 rings (the two middle rings are the energy rings). The external diameter of the tunnel is 7.48 m, with a 30 cm-thick concrete lining. An 11 cm-thick layer of grout all around the lining is also reproduced. This thickness is based on visual analysis of the specimens extracted after lining installation and grout injection (an average was taken into account) as shown in Figure 5.8. The model is discretized into 2760016 triangular prismatic elements (49286 per layer) with 1420953 nodes (24929 per slice). The pipes, both ground-side and air-side, in the two equipped rings were accurately modelled reproducing the

real geometry (segments rotated from one ring to another, asymmetric pipes layout along the longitudinal direction, segments different shapes and size) with one-dimensional elements, the so called “discrete features” (shown in blue in Figure 5.9), with a cross section area of 201 mm², corresponding to an external diameter of 20 mm and a thickness of 2 mm. Note that pipes resistance is neglected in the analyses.

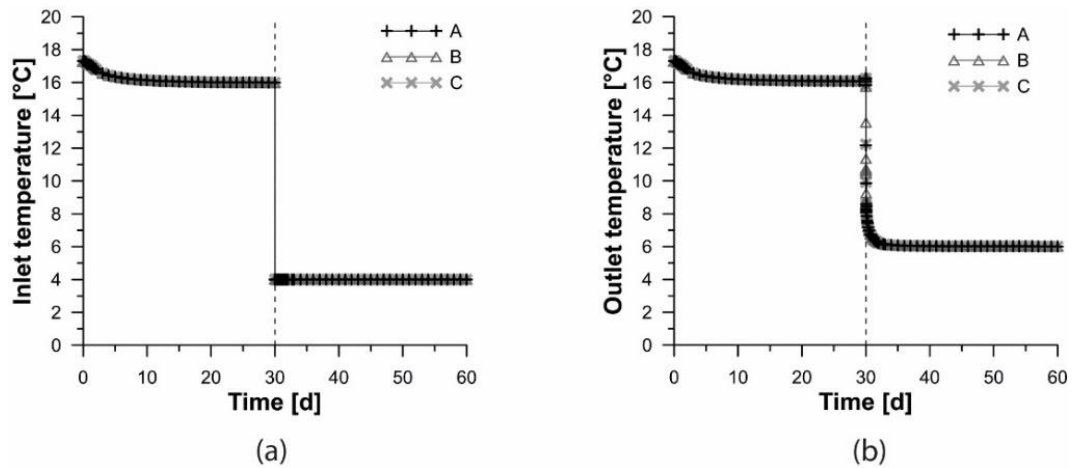


Figure 5.6: Comparison among different boundary conditions, (a) inlet and (b) outlet temperature.

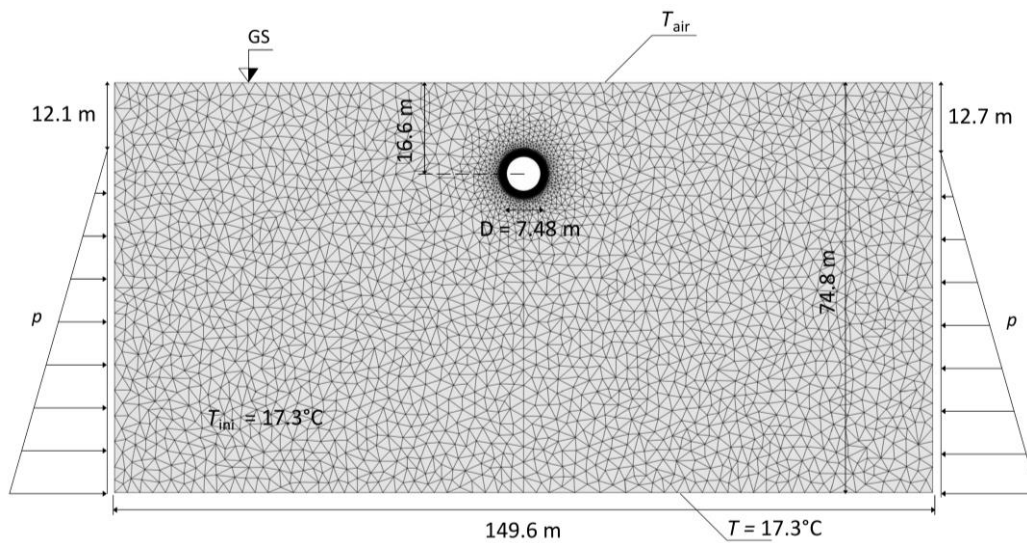


Figure 5.7: Cross section of the 3D FEM model with indication of thermal and hydraulic boundary conditions.



Specimen 1: 12 cm



Specimen 2: 12 cm



Specimen 3: 10.5 cm



Specimen 4: -



Specimen 5: 10 cm



Specimen 6: 10.5 cm



Specimen 7: -



Specimen 8: -



Specimen 9: 13 cm

Figure 5.8: Thickness of grout specimens extracted after lining installation.

Both thermal and hydraulic boundary conditions were set. As shown in Figure 5.7, the initial temperature throughout the model was set at 17.3°C, as resulting from the interpolation of three measurements in the area of the experimental site (two piezometers, whose one is shown in Figure 5.2, and an extensometer well). The time series of the external air temperature was applied on the upper boundary of the model, which represents the free surface, whereas a constant value of 17.3°C was assigned to the lower boundary. On the tunnel internal boundary, a heat transfer boundary condition was applied following the temperature coming from the monitoring system inside the tunnel T_1 . It should be remarked that the dual contact of energy tunnel linings with the ground on one side and with the air on the other side is a peculiarity typical of tunnels and diaphragm walls. This is not an issue for energy piles, for example, and adds a degree of complexity and uncertainty to the boundary conditions that should be applied at the intrados to best recreate thermal conditions existing in situ. The hydraulic boundary conditions consist of a constant hydraulic head on the left and right sides, with different values on the two sides to allow a groundwater flow of 1.5 m/day from East to West and representative of a groundwater table depth of about 12.4 m at the tunnel centerline location, as measured in situ. Above the phreatic surface, air thermal properties were assigned.

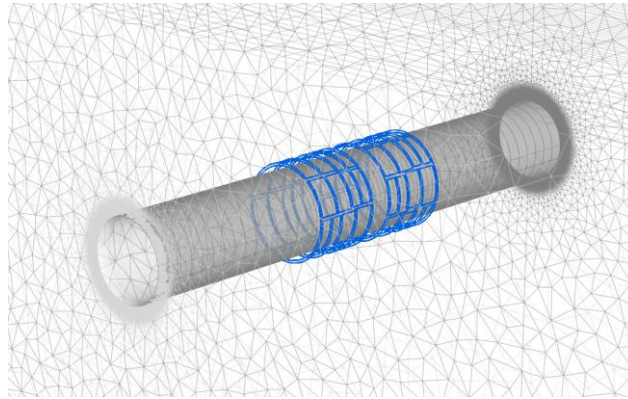


Figure 5.9: 3D view of the pipes circuit (expansion factor along longitudinal axis for a better view of the pipes network).

The numerical model was calibrated by considering the continuous ground heating mode test GH8, involving both rings working in parallel and characterized by a longer duration (see Table 4.6). To initialize the model and obtain a representative thermo-hydraulic state at the beginning of the test, a 30-days preliminary simulation was carried out with no thermal activation of the lining. At the end of this stage, a constant fluid velocity (0.9 m/s, Table 4.6) and a variable inlet temperature were imposed at the pipes inlets (velocity was also imposed at the outlets to keep it constant through the pipes), based on the monitoring data, for the whole length of the test.

First-trial hydraulic and thermal properties were obtained by previous studies (Barla et al., 2015), with the exception of the concrete thermal conductivity, which was obtained by means of heat flow meter tests. Indeed three 50x50x5 cm concrete samples were prepared by the precast concrete plant itself by using the same mix design as the one used to produce the tunnel segments (Figure 5.10a). Tests were performed thanks to the collaboration with the Energetics Department of Politecnico di Torino (DENERG). The heat flow meter is Lasercomp FOX 600 (Figure 5.10b), whose specifications are detailed in Table 5.5. The method used by the equipment to measure thermal conductivity, following the international standards ASTM C518, ISO 8301 and DIN EN 12667, is the steady state technique. The

specimen is placed between two temperature-controlled plates which establish a user-defined temperature difference (ΔT) across the sample. Two arrays of solid-state Peltier elements provide heating and cooling to each plate and maintain the necessary temperature difference through an advanced algorithm, which quickly brings the system to full thermal equilibrium.

The sample thickness (L) is directly measured by the machine to ensure an accurate measurement (Auto-Thickness Function). Indeed the flow meter is equipped with 4 optical encoders, one at each corner, driven by stepper motors for independent position control and measurement at all four plate corners. The machine automatically detects the height of the sample for each of the four points in order to level the measuring plates even for surfaces that are not perfectly parallel (Figure 5.10c). This improves thermal contact, thus avoiding accidental bias related to air bridges, and provides a representative measurement of sample thickness to within 25 μm . Table 5.6 indicates the thicknesses measured by the equipment.

The resulting heat flux (Q/A) from steady-state heat transfer through the sample is measured by two thin film heat flux transducers (<1 mm thick, Figure 5.10d) consisting of a continuous surface of sensing junctions that cover an area of 25x25 cm above and below the sample. A thermocouple is bonded in the center of each transducer within 0.1 mm of the sample surface and sealed against moisture. The design choice of the measuring devices was thus defined because, by reducing the measurement area to the most central area, the susceptibility to thermal losses or gains on the boundaries is eliminated. This ensures uniformity of temperature across the width of the sample on both surfaces of the plate and the purely linear heat flow, obtaining the most accurate measurement of thermal conductivity regardless of the thickness of the sample or the ambient temperature.

Table 5.5: Technical specifications of heat flow meter Lasercomp FOX600.

Maximum sample thickness	mm	200
Square sample width ¹	mm	610
Temperature range	°C	-15 to 65
Temperature resolution	°C	± 0.01
Accuracy	%	± 1
Reproducibility	%	± 0.5
Thermal conductivity range ²	W/mK	0.001 to 0.35
Thin film	mm	254x254
Heat flux transducer	mm	300x300

¹Guard materials may be used to test specimens that are less than the nominal width

²External thermocouple kit extends conductivity range to 2.5 W/mK

The average heat flux is used to compute thermal conductivity λ (in W/mK) and thermal resistance R (in $\text{m}^2\text{K}/\text{W}$) according to the Fourier's law:

$$\lambda = \frac{Q}{A} \cdot \frac{L}{\Delta T} \quad \text{Eq. 5.5}$$

$$R = \frac{1}{\lambda} \cdot L \quad \text{Eq. 5.6}$$

Since the tested material is a construction material that has a higher thermal conductivity than insulating materials, it is possible to use external thermocouples. The thermocouples are attached directly to the surfaces of the sample, eliminating the impact of the interface resistance and improving the measurement accuracy for higher conductivities up to 2.5 W/mK. The external thermocouples are placed in contact with the sample or placed in grooves machined in rigid specimens.

In the tests carried out on the concrete sample, 2 thermocouples were carefully arranged in the center of the upper and lower surface. However, it should be emphasized that the data obtained are affected by a certain degree of uncertainty. Indeed, the values obtained could vary by 20% since the machine is designed to typically test more insulating samples.

To further reduce the deviation of the heat flow towards the lateral areas by keeping the flow lines as vertical as possible, a layer of foam was interposed between the external doors and the material to be tested (Figure 5.10e).

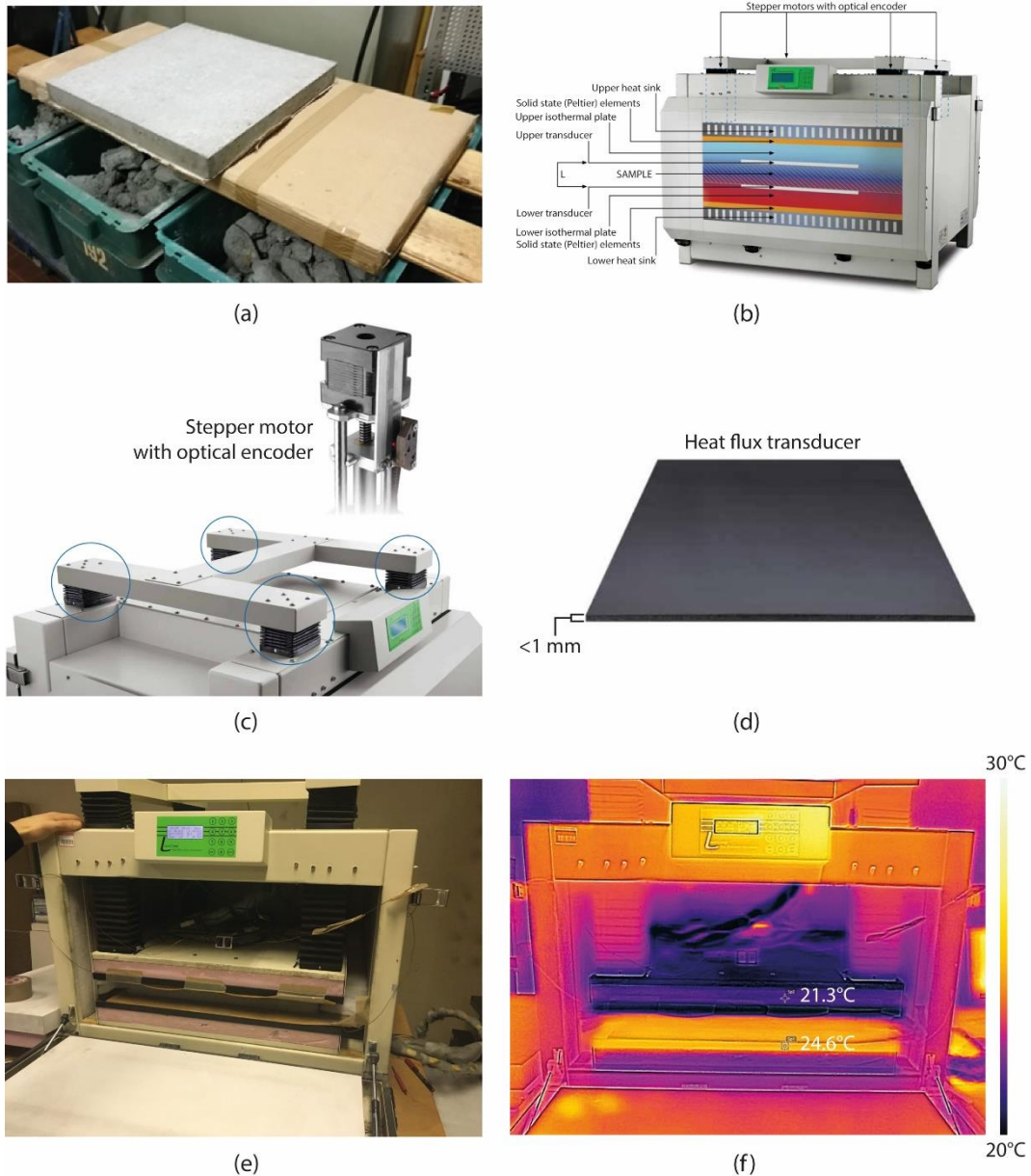


Figure 5.10: Thermal conductivity measurement: (a) Concrete sample, (b) Heat flow meter used, (c) optical encoders for automatic thickness measurement, (d) thin film heat flux transducers, (e) placement of the concrete sample, (f) thermal picture during a test.

Table 5.6: Concrete sample thickness measured by the flow meter.

Rear Left mm	Rear Right mm	Front Left mm	Front Right mm	Average mm
52.86	52.40	53.21	52.17	52.66

However, the samples presented corrugated and grooved surfaces that could have determined the formation of air pockets and contact resistances. To reduce these flows, which could lead to an alteration of the result, a layer of elastomer of known thickness and conductivity was interposed between the sample and the plate and pressed to limit contact resistances.

To obtain the thermal conductivity of the sample, three analyses were carried out modifying the thermal gradient at which the machine reached the steady heat flow (Table 5.7). The temperatures reached by the machine do not exactly correspond to the set points. It was therefore possible to define the thermal conductivity values of the materials, as shown in Table 5.8. The real temperature values were used for the conductivity calculation.

Table 5.7: Set points fixed for the heat flow meter.

	T_{upper} [°C]	T_{lower} [°C]	ΔT [°C]	$T_{upper,real}$ [°C]	$T_{lower,real}$ [°C]	T_{av} [°C]	Duration [min]
Setpoint 1	20	25	5	21.72	24.10	22.91	266
Setpoint 2	17.5	27.5	10	20.98	25.70	23.34	255
Setpoint 3	15	30	15	20.25	27.31	23.78	244

Table 5.8: Computation of concrete thermal conductivity and thermal resistance.

	Q/A_{upper} [W/m ²]	Q/A_{lower} [W/m ²]	λ_{up} [W/mK]	λ_{low} [W/mK]	λ_{av} [W/mK]	λ [W/mK]	R_{av} [m ² K/W]	R [m ² K/W]
Setpoint 1	50.28	50.35	1.114	1.115	1.114		0.04725	
Setpoint 2	100.00	100.90	1.118	1.127	1.122	1.12	0.04692	0.047
Setpoint 3	149.70	151.90	1.117	1.133	1.125		0.04682	

The calibration of the numerical model involved a number of trials. The values of a couple of thermal parameters, i.e. grout thermal conductivity and intrados heat transfer coefficient, were slightly modified, in the unavailability of any direct experimental evaluation, until reaching a good superposition of simulation and monitoring outlet temperature. In particular, grout thermal conductivity was first assumed equal to the one for concrete and then reduced to 0.655 W/mK, as found by Allan and Kavanaugh (1999) for a cement & bentonite grout (the same grout composition adopted for Turin ML1 rings), to better fit experimental data. This thermal conductivity value appears reasonable as no special mix design enhanced for thermal performance was adopted for the grout by the contractor. Material properties used in the numerical model are listed in Table 5.9 (note that blank cells mean that the same value as in Trial A was assumed), while Figure 5.11 exemplifies calibration results. The ground around the tunnel was assumed thermally isotropic and homogeneous.

In Figure 5.11a it is possible to notice that the measured outlet temperature and the computed one are highly comparable, both in trials B and C, testifying a good calibration of the numerical model. However, trial C is the one that best fits also other tests, as demonstrated in Figure 5.12a-d that analyzes the results obtained during the validation phase for four more tests (two ground heating tests with different volumetric flow rates, one ground cooling test and one air heating test). The same procedure (30 days-initialization and test simulation) was followed also for the validation analyses. It is pointed out that a number of combinations of

thermal and hydraulic parameters could yield a good match with the experimental outputs, but it stands to reason that the found set is fairly appropriate as comparison with a number of tests was undertaken.

Table 5.9: Material properties used during the calibration phase of the numerical model.

	Property	Symbol	Unit	Trial A	Trial B	Trial C
GROUND	Horizontal hydraulic conductivity	K_{xx}, K_{zz}	m/s	4.150E-03		
	Vertical hydraulic conductivity	K_{yy}	m/s	2.075E-04		
	Specific storage	S_y	1/m	1.0E-04		
	Porosity	n	-	0.25		
	Fluid-phase thermal conductivity	λ_w	W/mK	0.65		
	Solid-phase thermal conductivity	λ_s	W/mK	2.8		
	Fluid-phase volumetric thermal capacity	$\rho_w c_w$	MJ/(m ³ K)	4.2		
	Solid-phase volumetric thermal capacity	$\rho_s c_s$	MJ/(m ³ K)	2		
	Transverse aquifer thermal dispersivity	α_T	m	0.31		
	Longitudinal aquifer thermal dispersivity	α_L	m	3.1		
TUNNEL LINING	Specific storage	S_y	1/m	1.0E-04		
	Solid-phase thermal conductivity	λ_s	W/mK	1.12		
	Solid-phase volumetric thermal capacity	$\rho_s c_s$	MJ/(m ³ K)	2.19		
	Horizontal hydraulic conductivity	K_{xx}, K_{zz}	m/s	1.0E-16		
	Vertical hydraulic conductivity	K_{yy}	m/s	1.0E-16		
	Porosity	n	-	0		
	Transverse thermal dispersivity	α_T	m	0.5		
Longitudinal thermal dispersivity	α_L	m	5			
PIPES	Specific storage	S_y	1/m	1.0E-04		
	Fluid-phase thermal conductivity	λ_w	W/mK	0.542		
	Fluid-phase volumetric thermal capacity	$\rho_w c_w$	MJ/(m ³ K)	4.11		
	Longitudinal thermal dispersivity	α_L	m	5		
	Cross-sectional area	A	m ²	2.01E-04		
Hydraulic aperture	b	m	0.8			
GROUT	Specific storage	S_y	1/m	1.0E-04		
	Solid-phase thermal conductivity	λ_s	W/mK	1.12	0.655	0.655
	Solid-phase volumetric thermal capacity	$\rho_s c_s$	MJ/(m ³ K)	2.19		
	Horizontal hydraulic conductivity	K_{xx}, K_{zz}	m/s	1.0E-16		
	Vertical hydraulic conductivity	K_{yy}	m/s	1.0E-16		
	Porosity	n	-	0		
	Transverse thermal dispersivity	α_T	m	0.5		
Longitudinal thermal dispersivity	α_L	m	5			
AIR	Heat transfer coefficient	Φ	W/m ² K	1.77	1.77	5.30

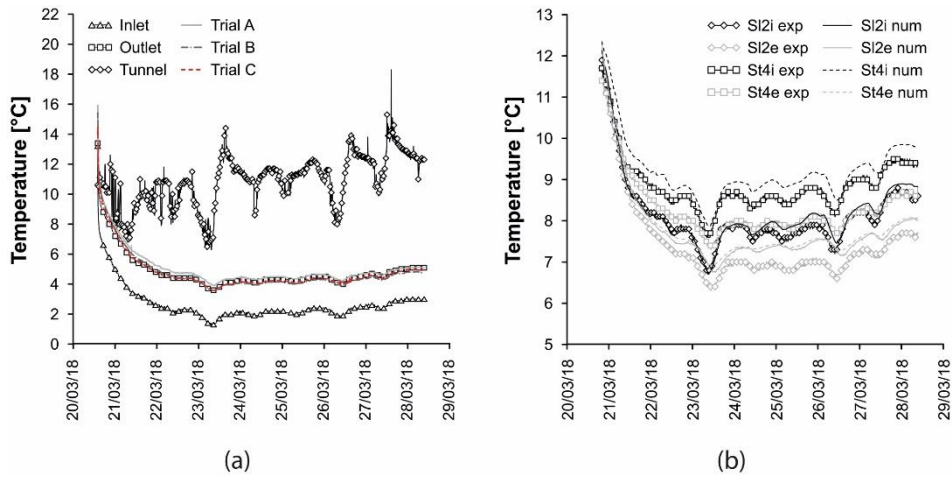


Figure 5.11: Comparison between measured and computed circuit outlet temperature: test GH8 (calibration phase).

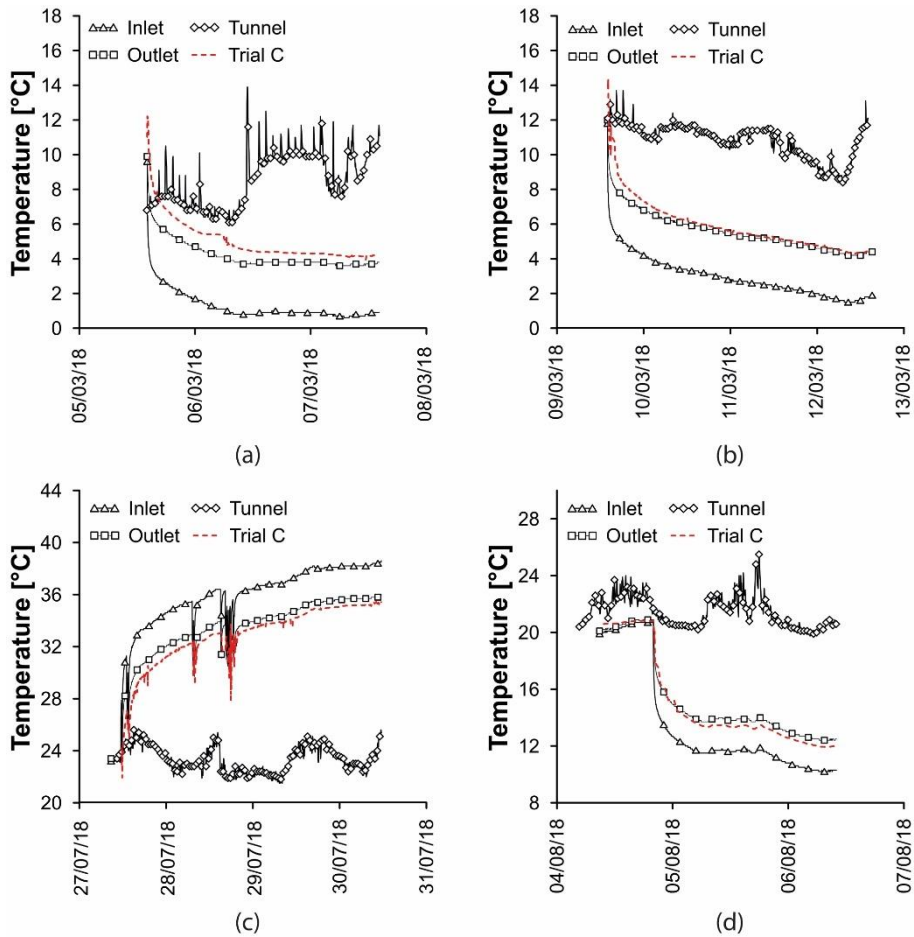


Figure 5.12: Comparison between measured and computed data: (a) test GH5, (b) test GH6, (c) test GC1 and (d) AH2 (validation phase).

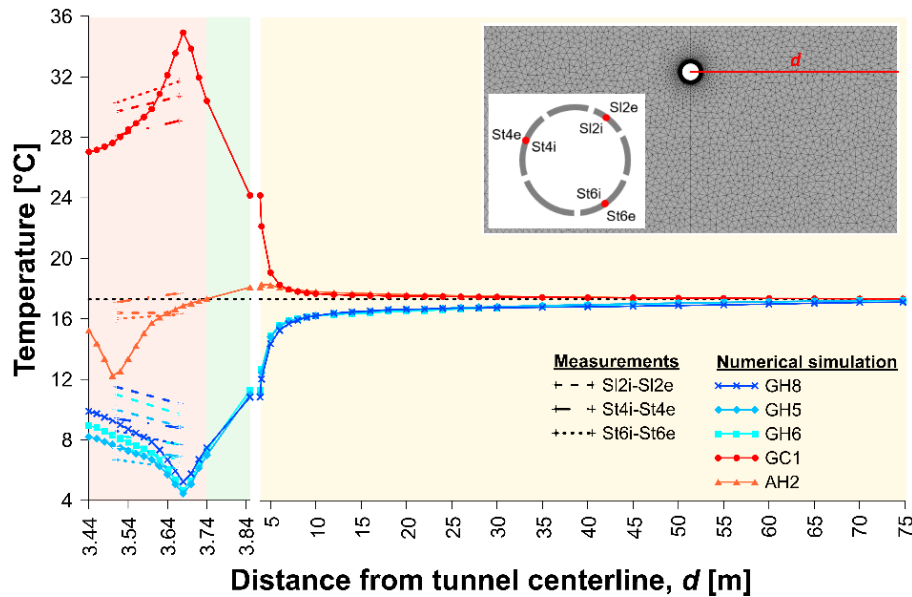


Figure 5.13: Comparison between measured and computed lining temperature at the extrados and at the intrados and computed downstream temperature at the end of the simulated tests.

This is even more true noting that the temperatures computed numerically during the calibration phase, at four different locations in the lining, well reflect those measured by vibrating wire strain gauges at the intrados and at the extrados of the lining (see Figure 5.11b), considering that the embedded thermistor accuracy is 0.5°C . Figure 5.13 depicts the computed downstream temperature from the tunnel lining intrados to the model right boundary at the end of the simulated tests, as well as the monitored temperature within the lining in correspondence of the location of three pairs of strain gauges with embedded thermistors (note that two different scales are used to better visualize the lining thermal profile and that the different background colours indicate the concrete layer, the grout layer and the ground; in SI2i, SI2e, St4i, St4e, St6i St6e i means intrados and e means extrados). A good match between computed and recorded results emerges. Moreover, it can be noted that for the test GH5 the thermal alteration is smaller than 1°C at 14 m distance, while it is even lower in the other tests. Unfortunately, monitoring data of surrounding rock temperature are not available. Indeed, during the design phase, it was ascertained that no downstream existing wells were available perpendicularly to the tunnel axis along the location of the energy tunnels. On the other hand, ad hoc wells could not be drilled for economic reasons as well as logistic constraints (the construction site is in the middle of a congested roads crossing).

According to the previous observations, the set of parameters C in Table 5.9 was adopted in the following.

5.4. Generalization to different ground and environmental conditions

5.4.1. Developing design charts

The experimental data collected during the campaign accomplished in 2017-2018 along Turin ML1 South Extension were essential to demonstrate the robustness and reliability of the

coupled numerical model. This had not been possible so far, which is why preliminary analyses had been described in literature. However, the feasibility and efficiency of energy tunnels could be legitimately argued when examining site-specific conditions different from those of the prototype described. To try to provide a comprehensive estimation of the thermal performance of the technology in a number of environmental situations, the design charts presented in Di Donna and Barla (2016), referred to previous configurations of the net of pipes, have been updated for the Enertun scenario and for three different groundwater flow directions, that is parallel, forming an angle of 45° and running perpendicular to the tunnel axis. The analysis of the groundwater flow direction is an aspect of novelty in the framework of energy tunnels in comparison to previous literature. To this aim, a new thermo-hydraulic numerical model was built, made of 15 rings all working in parallel and of six hypothetic energy segments of equal size (Figure 5.14). With special reference to the cases of parallel and oblique groundwater flow, results are pertaining to the eighth intermediate ring. The geometry of the tunnel is that of Turin ML1 SE. Of course, this could differ for other projects, but the size under study is quite representative of most typical urban tunneling situations. Further characteristics of the models are summarized in Table 5.10 (material properties not listed here can be found in Table 5.9). Different groundwater flow velocities were obtained by changing the hydraulic gradient and by keeping the permeability constant. Temperature was fixed equal to the ground value at the top and bottom boundary, without considering the influence of atmospheric temperature oscillation. Different ground temperatures and corresponding tunnel temperatures were adopted to study various climatic conditions (Table 5.10). Average winter and summer temperatures measured in an already operational section of Turin Metro Line 1, that is 13.1 and 26.7°C respectively, were related to a ground temperature of 15°C . The seasonal analyses carried out involved 30 days of thermal initialization followed by 30 days of thermal activation. A sensitivity study was also performed by varying one by one fluid inlet temperature, fluid velocity, pipes size and heat transfer coefficient at the intrados elements.

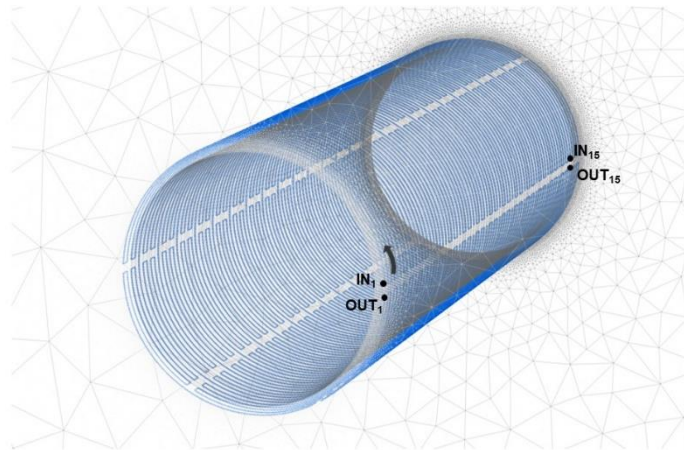


Figure 5.14: Geometry of the network of pipes embedded in the model adopted for the construction of design charts (only inlets and outlets of rings 1 and 15 are highlighted for illustrative purposes).

The resulting design charts can be seen in Figure 5.15 for winter and summer modes and for different groundwater flow directions with respect to the tunnel axis. With different colors the ranges of thermal flux in W/m^2 are indicated for each triplet of ground temperature, groundwater flow velocity and ground total thermal conductivity. The analyses were carried out for specific triplets, organized on a grid, and then interpolated by using an appropriate

polynomial law able to match satisfactorily the discrete, scattered numerical results. The charts related to the case of perpendicular flow are in line with the existing ones, although a one-to-one quantitative comparison is not possible due to different model inputs (presence of grout, different concrete thermal conductivity, pipes size, heat carrier fluid velocity, intrados boundary condition). Considerations drawn by Di Donna and Barla (2016) are confirmed here. No matter the flow direction, the highest performance is obtained with maximum ground thermal conductivity, maximum groundwater flow, due to the thermal recharge mechanism that allows the ground to return more rapidly to its undisturbed temperature, and with maximum ground temperature in winter and viceversa in summer. As groundwater flow velocity decreases, thermal conductivity starts playing a role, since the dotted and dashed lines representing boundaries between heat flux ranges move away from the continuous one. For perpendicular groundwater flow winter energy performance is in the range 10-95 W/m², while summer energy performance falls between 10-110 W/m², slightly higher than in summer. By observing the effect of groundwater flow (Figure 5.15), it is inferred that the performance is significantly increased when the flow is perpendicular to the tunnel axis as compared to an orientation of 0°, whereas little improvement is attributable to perpendicular flow in comparison to the oblique case. For this reason the configuration of prototype installed in Turin Metro is particularly advantageous.

These charts are particularly useful for the designer interested in evaluating whether it may be worth or not to invest in the feasibility study of the thermal activation of a tunnel. It is clear that a more detailed study should be conducted at the design analysis stage, as described for example in Barla and Di Donna (2018), Baralis et al. (2018) and Barla et al. (2019).

As already mentioned, numerical analyses were carried out by simulating a 30-days thermal activation timespan. Energy performance shown in the charts refers to the last day of thermal activation, which is a conservative condition for the computation of the heat exchanged through the tunnel lining because it is expected to be higher in the previous days. However, it is recognized that thermal activation may last for a longer time than 30 days. In this case, especially in absence of a strong groundwater flow, the outlet temperature is expected to keep decreasing or at least to reach an equilibrium slowly and later (instead, it will soon reach an equilibrium in presence of groundwater flow, possibly making the computation at 30 days reliable). Reminding that we are neglecting the higher power in the initial part, the estimated heat exchanged would represent an average value. It should be added that the analyses account for the most unfavourable conditions in terms of heat carrier fluid inlet temperature kept constant for the entire period of 30 days. This assumption, useful to allow the computation, clearly does not match real operational conditions, characterized by both a seasonal and a daily variation of energy demand according to external temperature. Therefore, the conservative conditions considered in the analyses are likely to occur for few hours a day and for some days of the year, not for the whole timespan.

Table 5.10: Main properties of the base and sensitivity analyses models.

Characteristic	Unit	Value
Pipes size	mm	20x2
Inlet temperature (winter)	°C	4
Inlet temperature (summer)	°C	28
Heat carrier fluid velocity	m/s	0.9
Grout thermal conductivity	W/mK	2
Concrete thermal conductivity	W/mK	1.5
Grout thickness	cm	11
Ground temperature	°C	9-12-15-18
Heat transfer coefficient	W/mK	5.3

Characteristic	Unit	Value
Tunnel temperature (winter)	°C	Variable with ground temperature 7.1-10.1-13.1-16.1
Tunnel temperature (summer)	°C	Variable with ground temperature 20.7-23.7-26.7-29.7
Ground thermal conductivity	W/mk	0.9-2.26-3.9
Groundwater flow	m/d	0-0.5-1-1.5-2

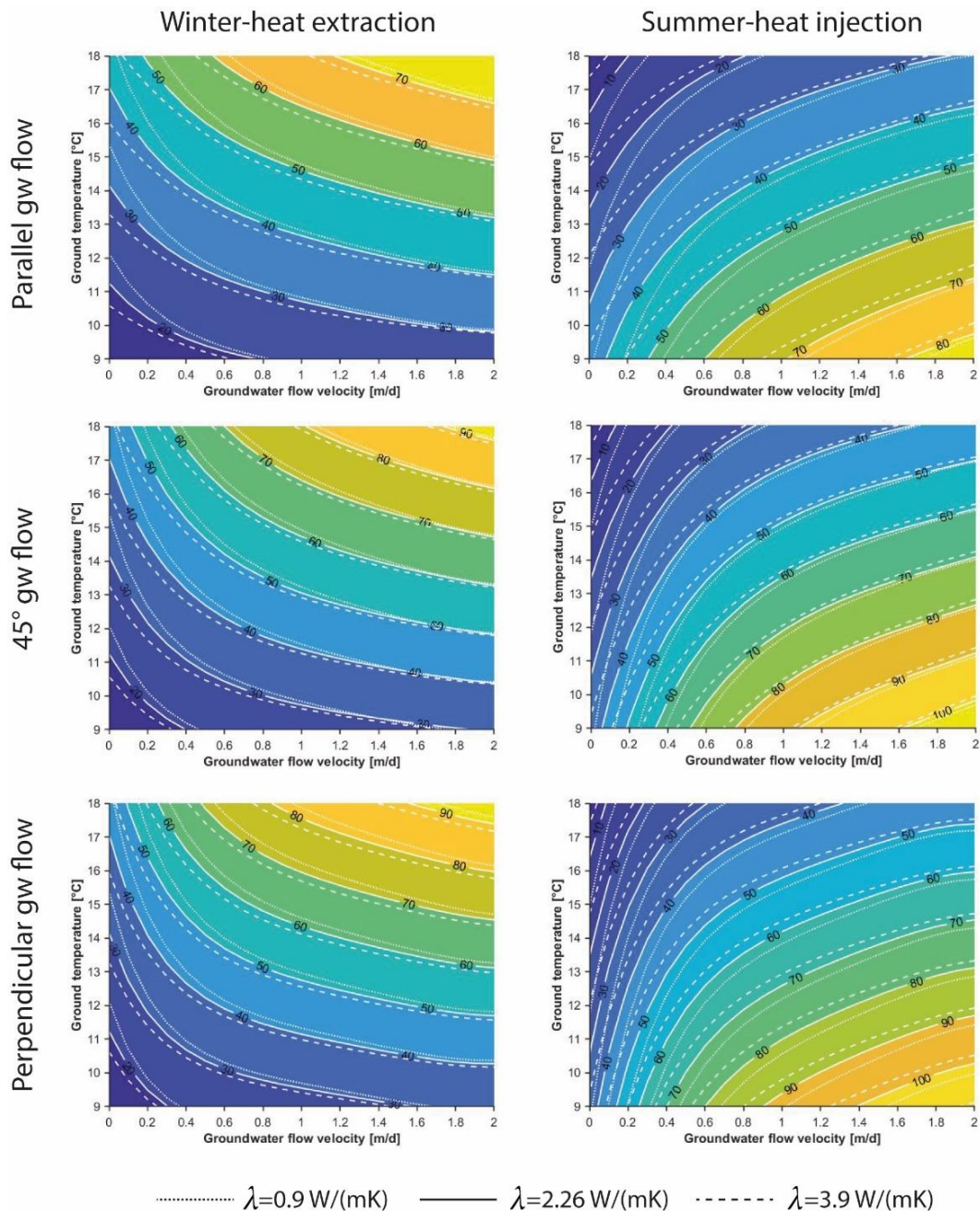


Figure 5.15: Updated preliminary design charts showing geothermal potential in W/m² for winter and summer conditions and for different groundwater flow directions with respect to the tunnel axis (0°, 45° and 90°).

5.4.2. Sensitivity analyses

To investigate the validity and range of application of the design charts, it is of interest to assess the effect of other possibly varying parameters on thermal efficiency. For this reason, some sensitivity analyses were carried out to explore the influence of different values of fluid inlet temperature T_{in} , fluid velocity v_f , pipes size d,t (diameter and thickness) and heat transfer coefficient Φ , as shown in Table 5.11.

Table 5.11: Parameters investigated in the sensitivity analyses.

Design parameter	Unit	Values	
$T_{in,winter}$	°C	1	7
$T_{in,summer}$	°C	32	36
v_f	m/s	0.4	1.4
$d \times t$	mm	16x2	25x2.3
Φ	W/m ² K	1	15

The range of variation of the heat transfer coefficient was based on the table reported in Di Donna et al. (2016). The analyses were conducted for six relevant combinations of groundwater flow velocity and ground temperature (ground thermal conductivity kept to 2.26 W/mK) so that all the chart area is spanned. In the following each aspect is explored and commented in detail.

Fluid inlet temperature. The paramount importance of fluid inlet temperature emerges clearly in Figure 5.16a in comparison to the other investigated aspects (it is highlighted that in this chart the range is two times that of the other charts) as it highly affects heat transfer, with variations of the heat flux reaching 56 W/m² in summer when using the highest inlet temperature. This parameter appears to be strictly dependent on groundwater flow velocity, as the mechanism of thermal recharge avoids heating or cooling of the surrounding ground thus improving thermal performance.

Fluid velocity and pipes size. It can be seen from Figure 5.16b that the minimum variation in the heat flux occurs when thermal exchange is minimum (low groundwater flow and low ground temperature in winter, low groundwater flow and high ground temperature in summer), whereas the maximum variation occurs in the opposite case. This last is not negligible, hence care should be taken when falling in this area (upper right and lower right corner of the design chart in winter and summer, respectively). The same goes when assessing the effect of pipes dimension (Figure 5.16c), although the maximum variations are lower than in the previous case.

Heat transfer coefficient. Quite different is the case of sensitivity analyses on the heat transfer coefficient value (Figure 5.16d). This coefficient has an effect on the amount of heat flowing from/to the tunnel environment to/from the lining. When the heat transfer coefficient is 15 W/m²K, the heat flux increases by a maximum of 14 W/m² in winter and by 8 W/m² (or decreases by 4 W/m²) in summer. When the heat transfer coefficient is 1 W/m²K, the heat flux decreases by a maximum of 19 W/m² in winter and by 10 W/m² (or increases by 5 W/m²) in summer. The overall ranges of variation are not too different from that of fluid velocity and pipes size.

The results obtained above, considering a perpendicular groundwater flow, were confirmed by running a number of relevant analyses for oblique and parallel flow.

Based on the sensitivity analyses one can conclude that fluid inlet temperature is the parameter that mostly affects heat transfer. Hence, to evaluate geothermal potential the following procedure can be followed:

- assess local groundwater flow direction and choose the appropriate chart;
- assess local groundwater flow velocity, ground undisturbed temperature and thermal conductivity;
- based on the previous inputs, evaluate the exchangeable heat \dot{q}^* from the design chart;
- if an inlet temperature different from 4°C in winter and 28°C in summer is expected, correct \dot{q}^* based on the following relationship

$$\dot{q} = \dot{q}^* + \Delta\dot{q} \quad \text{Eq. 5.7}$$

with

$$\frac{\Delta\dot{q}}{\Delta T} = 3.44 \cdot \frac{v_{\text{gw}}^{2.01}}{3.09} + 4.44 \cdot \ln(1 + v_{\text{gw}}) \quad \text{Eq. 5.8}$$

in summer, and

$$\frac{\Delta\dot{q}}{\Delta T} = - \left[3.44 \cdot \frac{v_{\text{gw}}^{2.01}}{3.09} + 4.44 \cdot \ln(1 + v_{\text{gw}}) \right] \quad \text{Eq. 5.9}$$

in winter, in the case of perpendicular and oblique groundwater and

$$\frac{\Delta\dot{q}}{\Delta T} = 3.44 \cdot \frac{v_{\text{gw}}^{0.74}}{3.05} + 2.75 \cdot \ln(1 + v_{\text{gw}}) \quad \text{Eq. 5.10}$$

in summer, and

$$\frac{\Delta\dot{q}}{\Delta T} = - \left[3.44 \cdot \frac{v_{\text{gw}}^{0.74}}{3.05} + 2.75 \cdot \ln(1 + v_{\text{gw}}) \right] \quad \text{Eq. 5.11}$$

in winter in the case of parallel groundwater, where ΔT is the difference between the actual inlet temperature and the theoretical one (4 or 28°C depending on the season) and v_{gw} is the groundwater flow velocity expressed in m/d. The equations above were obtained by direct interpolation of the computed data;

- consider a ± 10 W/m² correction to the above obtained value of W/m² to take into account different fluid velocity, pipes size and heat transfer coefficient.

Considering all the above, the design charts can be reliably adopted for a wide range of conditions. Having said this, it is clear that they cannot be considered as a general and unique indication for the evaluation of the geothermal potential of an energy tunnel and that a more detailed study should be conducted at the design analysis stage, by site-specific thermo-hydraulic numerical modelling that include detailed aspects of ground conditions, site installation and working conditions.

As an example, aspects such as the intermittent ratio (i.e. the ratio of interval time to running time as defined by Ogunleye et al. (2020) and Zhang et al. (2014)) are not explicitly taken into account in the parametric design charts, especially for the cases of slow or absent groundwater flow. For the cases with a major groundwater flow, the intermittent ratio is not expected to play a relevant role. Instead, when no groundwater flow is present at the site, it could be crucial in assessing the feasibility of an energy tunnel project. Specific thermo-hydraulic analyses should be performed at a later design stage to find an optimization strategy of the intermittent ratio so that the geothermal resource is not depleted and is properly used. Similarly, different tunnel climates arising from particular operation conditions (e.g. “hot” tunnels) should be specifically analyzed. Moreover, as winter and summer cases are considered separately, thus leading to two seasonal design charts, possible unbalanced heat situations do not emerge and cannot be caught. Long-term yearly analyses should be performed to assess this issue, both in the case of heating only, cooling only or heating and cooling (this is particularly true for unfavourable hydrogeological conditions and for single-mode operation, i.e. continuous heating only or cooling only).

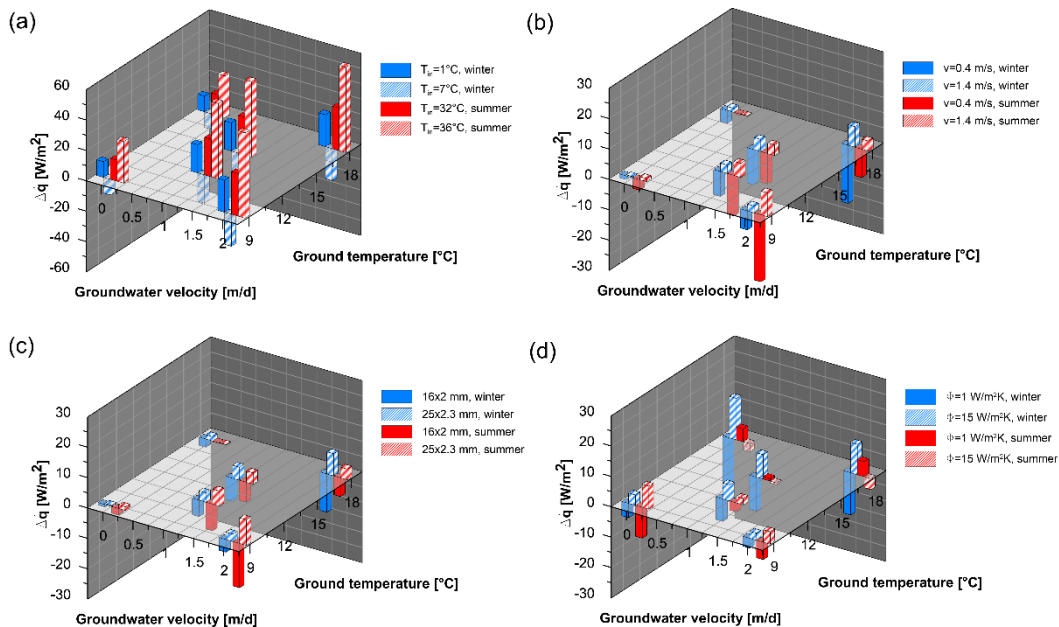


Figure 5.16: Effect of (a) fluid inlet temperature, (b) fluid velocity, (c) pipes size and (d) heat transfer coefficient on geothermal potential during winter and summer conditions expressed in terms of heat flux variations in the case perpendicular flow.

5.4.3. Validation against existing data

The design charts here presented were validated against available literature data. A summary of the obtained results can be observed in Table 5.12. A very good match is obtained in most of the cases with the actual values falling within the ranges anticipated by the design charts. This applies to cases based on numerical studies as well as to real monitored data.

Smaller values are shown for the Grand Paris Express B with respect to the computed ones. Here Cousin et al. (2019) have considered a tunnel temperature as high as 18.96°C and a heat transfer coefficient of 15.13 $\text{W/m}^2\text{K}$ which certainly has a positive effect on the heat exchange. It is noted that this also leads to substantially different results from those reported

in Bracq et al. (2017) and Fouché et al. (2018) for a similar case study. Minor difference is also shown for the case of Warsaw NE metro. However, in this case the Authors have considered adiabatic boundary conditions in the tunnel.

The case of Turin ML1 is shown to be slightly more favourable when using the design charts than in the previous study performed by Di Donna and Barla (2016) and Barla et al. (2016). The reason lies on the fact that the more efficient Enertun configuration has been used here.

Table 5.12: Validation of the design charts against available data of energy tunnels thermal power exchanged with the ground.

Case study	R/N*	v_{gw} [m/d]	T_g [°C]	λ [W/mK]	q [W/m ²]			
					Result of the study		Design charts	
					Winter	Summer	Winter	Summer
Crossrail (Nicholson et al., 2013; Nicholson et al., 2014)	N	0	14.8	1.8	10-30	-	22-42	-
Grand Paris Express A (Bracq et al., 2017; Fouché et al., 2018)	N	0	12	1.6-2.4	15-30	10-20	13-33	15-35
Grand Paris Express B – case 2.1 (Cousin et al., 2019)	N	0	13	2.1-2.3	50	-	24-44	-
Jenbach (Buhmann et al., 2016; Franzius and Pralle, 2011; Frodl et al., 2010; Mayer and Franzius, 2010; Moormann et al., 2016)	R	1	10	3.3	18-40	-	18-38	-
Katzenbergtunnel (Franzius and Pralle, 2011)	R	0	13	3	17-25	-	19-39	-
Turin ML1 SE (Barla et al., 2016; Barla and Di Donna, 2018; Barla and Di Donna, 2016; Di Donna and Barla, 2016)	N	1.5	14	2.26	53	74	53-73	58-78
Warsaw NE metro - model 1 (Baralis et al., 2018)	N	0	12	1.61	13	30	11-31	10-30
Warsaw NE metro - model 2 (Baralis et al., 2018)	N	0.09	12	2.40	15	42	17-37	19-39

*R=real case study N=numerical study

5.5. Summary

A comprehensive study on the energy performance of energy tunnels was carried out with the aim of providing quick and effective tools to designers who want to quantify heat exchange in a preliminary phase of the project. The main conclusions are as follows:

- thanks to a real scale prototype constituted by a pair of energy rings Enertun-type recently tested for the first time in Italy, an experimental campaign allowed to assess the thermal performance of tunnels in a variety of conditions (different durations and flow rates, heating case, cooling case, air circuit, ground circuit). From the processing of data collected, it was possible to infer that winter extraction thermal power amounts to 41-51 W/m², while in summer a range of 45-61 W/m² was obtained. The use of the air circuit for tunnel cooling showed exploitable heat between 53 and 55 W/m². These numbers are in line with previous numerical predictions and higher than those recorded for previous experiences. This implies that a thermal power of 1.1 MW per kilometer of thermally activated tunnel could theoretically be exploited, corresponding to 480 100 m²-apartments. A cost-benefit analysis should be carried out to identify the sections of the tunnel where the technological solution can be installed and to assess the buffer zones where potential customers can be supplied conveniently (Baralis et al., 2018; Rzyznki and Bogusz, 2016; Nicholson et al., 2014). Despite the longest test lasted more than 12 days, long-term tests are not available yet but are planned to be performed during tunnel operation;
- a 3D time-dependent thermo-hydraulic numerical model was calibrated and validated on the monitored data pertaining to the two experimental Enertun rings so that it was proven to be able to adequately simulate the conditions existing in situ. With respect to previous studies, consideration of a grout layer was included whose thermal conductivity was calibrated ad hoc. Heat transfer coefficient was also deduced by matching local temperatures measured in the lining and resulted to be slightly higher than the one used in previous models referred to the Turin case;
- the system operational behaviour was investigated in conditions different from the tested ones to generalise the results. Design charts were presented with the intention of updating to the Enertun layout those already existing in literature. In this new version, different groundwater flow directions as well as the influence of fluid inlet temperature, fluid velocity, pipes size and heat transfer coefficient were also considered. A substantial increase in performance occurs when water flow direction increases from 0° to 45°, whereas little improvement is attributable to perpendicular flow in comparison to the oblique case. The paramount importance of fluid inlet temperature emerges in comparison to the other investigated aspects;
- a new simplified procedure to calculate the exchanged thermal power by using the design charts was suggested. It can be reliably adopted for a preliminary evaluation in a wide range of conditions. It is clear, however, that a more detailed study should be conducted at the design analysis stage, which includes site-specific thermo-hydraulic numerical modelling, and that caution should be adopted when site conditions differ substantially from those considered in the sensitivity analysis herewith described.

Chapter 6

Structural design

6.1. Introduction

Energy linings are receiving great interest due to their potential to transform a tunnel into a smart energy system for enhancing thermal comfort of buildings and metro stations, as well as to absorb waste heat from the tunnel environment. Yet, besides their thermal performance, the impacts of equipping segments with a net of pipes are still challenging in the framework of energy tunnels structural design. Indeed, the thermal regime of the concrete members is altered due to heat carrier fluid circulation. Hence, the need to shed some light on the possible limit states attainment arises. In this Chapter, field monitoring of stresses and strains is presented and interpreted for the first time in relation to a full scale monitored prototype of Enertun energy tunnel lining installed in Turin, Italy. Experimental data are then compared to the results of a 2D coupled thermo-mechanical numerical model used to simulate the tests performed in situ and to extend the results to long-term operating conditions. Part of the work described in this Chapter has been published on recent articles by the Author (Insana et al., 2020; Olivero et al., 2018).

6.2. Experimental data

In the next paragraphs experimental data will be described in detail. In particular data gathered from the monitoring carried out by the construction site will be presented (designated as “Construction site measurements” in 6.2.1), as well as data strictly pertaining to the energy tunnel project coming from the monitoring system installed by the Author and described in 4.2.4 (designated as “Experimental site measurements” in 6.2.2). Additionally, the latter are distinguished among conventional sensors and optical sensors. Table 6.1 shows all data available in both rings 179 and 181. Interpretation of data is provided in 6.3.

Table 6.1: Available stress, strain and surface settlements data.

	Construction site measurements (ring 181)	Experimental site measurements (ring 179)
Strain	available	available
Stress	available	available
Surface settlements	available	not available

6.2.1. Construction site measurements

A view of ring 181 towards Lingotto station is depicted in Figure 6.1. This ring was equipped with vibrating wire strain gauges in all segments and with pressure cells in four segments, before being erected on July 3rd, 2017 at 13:01 (Figure 6.2). Table 6.2 indicates the nomenclature and the orientation of such sensors in the six segments.

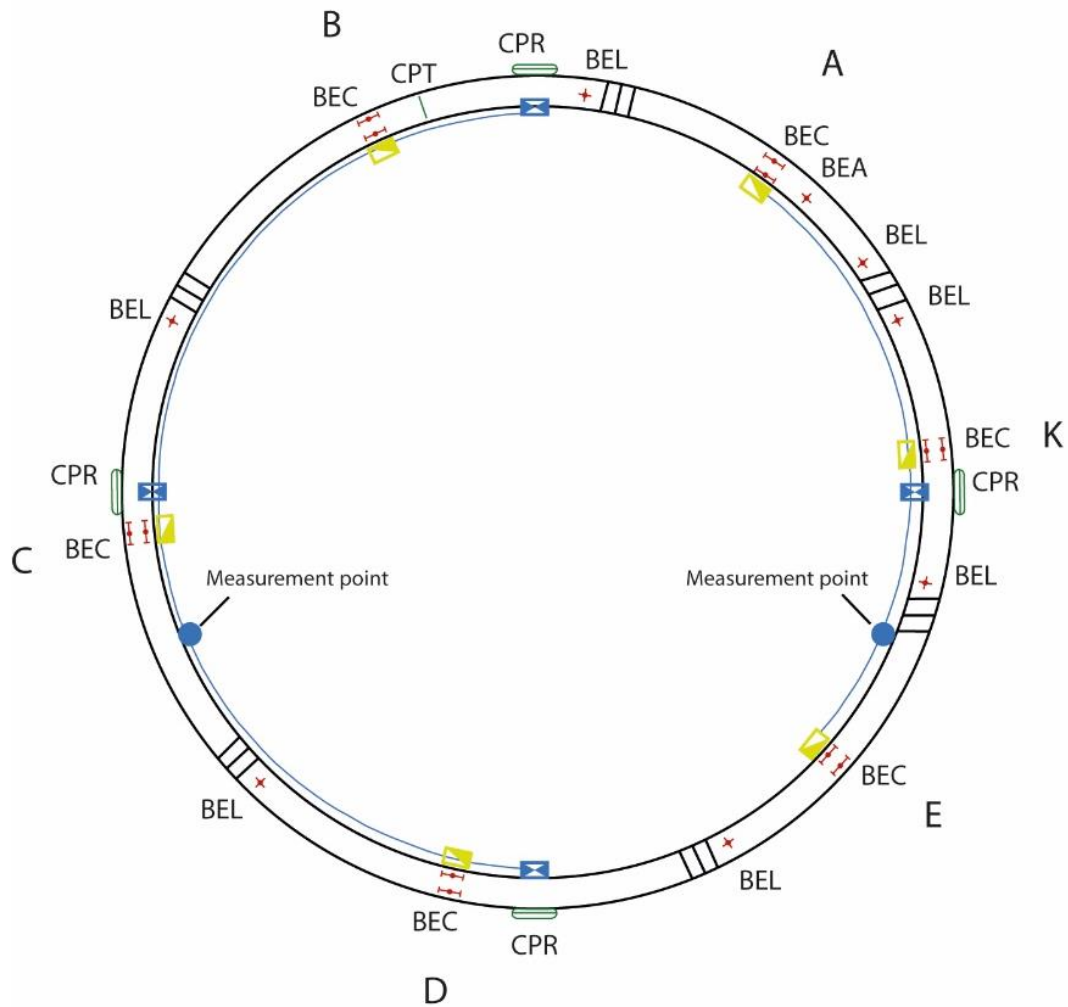


Figure 6.1: Stress and strain gauges deployed in ring 181 by the construction site.

Table 6.2: Nomenclature of the strain gauges and pressure cells in ring 181 (BEC=in hoop direction, BEL=in longitudinal direction, BEA=no stress, E=extrados, I=intrados, 1=side close to ring 182, 2=side close to ring 180, CPR=in radial direction, CPT=in hoop direction, *in MPa).

Sensors	Segment A	Segment B	Segment C	Segment D	Segment E	Segment K
Strain gauges	A-BEC-E1	B-BEC-E1	C-BEC-E1	D-BEC-E1	E-BEC-E1	K-BEC-E1
	A-BEC-I1	B-BEC-I1	C-BEC-I1	D-BEC-I1	E-BEC-I1	K-BEC-I1
	A-BEC-E2	B-BEC-E2	C-BEC-E2	D-BEC-E2	E-BEC-E2	K-BEC-E2
	A-BEC-I2	B-BEC-I2	C-BEC-I2	D-BEC-I2	E-BEC-I2	K-BEC-I2
	A-BEL	B-BEL	C-BEL	D-BEL	E-BEL	K-BEL-1
Pressure cells	A-BEA					K-BEL-2
		B-CPR B-CPT*	C-CPR	D-CPR		K-CPR

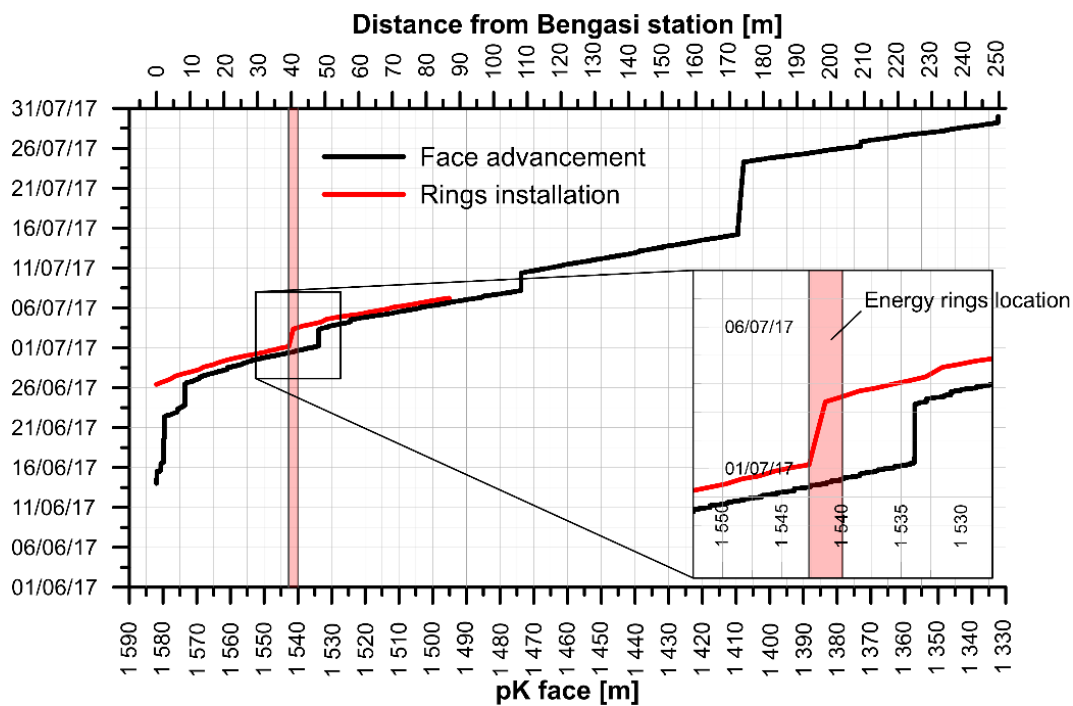


Figure 6.2: Temporal trend of face and ring installation advancement (only data available are shown).

The following readings were carried out manually for the strain gauges:

- check reading in the precast concrete plant in digit on 28/07/2016;
- pre-installation reading in digit on 03/07/2017;
- reference reading in digit on 05/07/2017;
- readings after installation in digit, until 28/06/2018 for a total of one year of readings

and for the pressure cells:

- void reading on 03/07/2017;
- zero reading on 05/07/2017;
- readings after installation, until 28/06/2018 for a total of one year of readings.

The strain gauges outputs, shown in Figure 6.3, are referred to the pre-installation reading to obtain the amount of strain due to the surrounding ground stress release. The values are obtained by multiplying the reading times the gage factor, equal to $3.304 \mu\text{e}/\text{digit}$ in this case. No particular trends with temperature (measured by Politecnico di Torino) can be highlighted. Variations are in the range $-200 \div 100 \mu\text{e}$.

The pressure cells outputs, shown in Figure 6.4, show that the measurements are included in the range 0-100 kPa for ring 181. Similar trends are obtained also for other monitored cross sections (rings 222, 322, 437) far away from the studied one. Pressure cell in segment D exhibits an anomalous behaviour, probably due to its position in invert and to the effect of overlying loads. It is unclear why all other measurements tend to zero after July 11th, 2017.

The readings of surface settlements are available from April 5th, 2017 to November 22nd, 2017. The targets are placed at a horizontal distance of -15 m, -7.5 m, 0, 7.5 m and 15 m with respect to the tunnel centerline. The first target (-15 m) was not installed because of its position within the Northern access of the construction site in Bengasi station. The maximum settlement was about 10 mm at the tunnel centerline (Figure 6.5). An asymmetric behaviour can be highlighted, as the targets SI4 and SI2 show slightly different trends. Some little time-dependent deformations are present long after the total stress release of the ground. As expected, most of the displacements occur in the vicinity of the ring installation time.

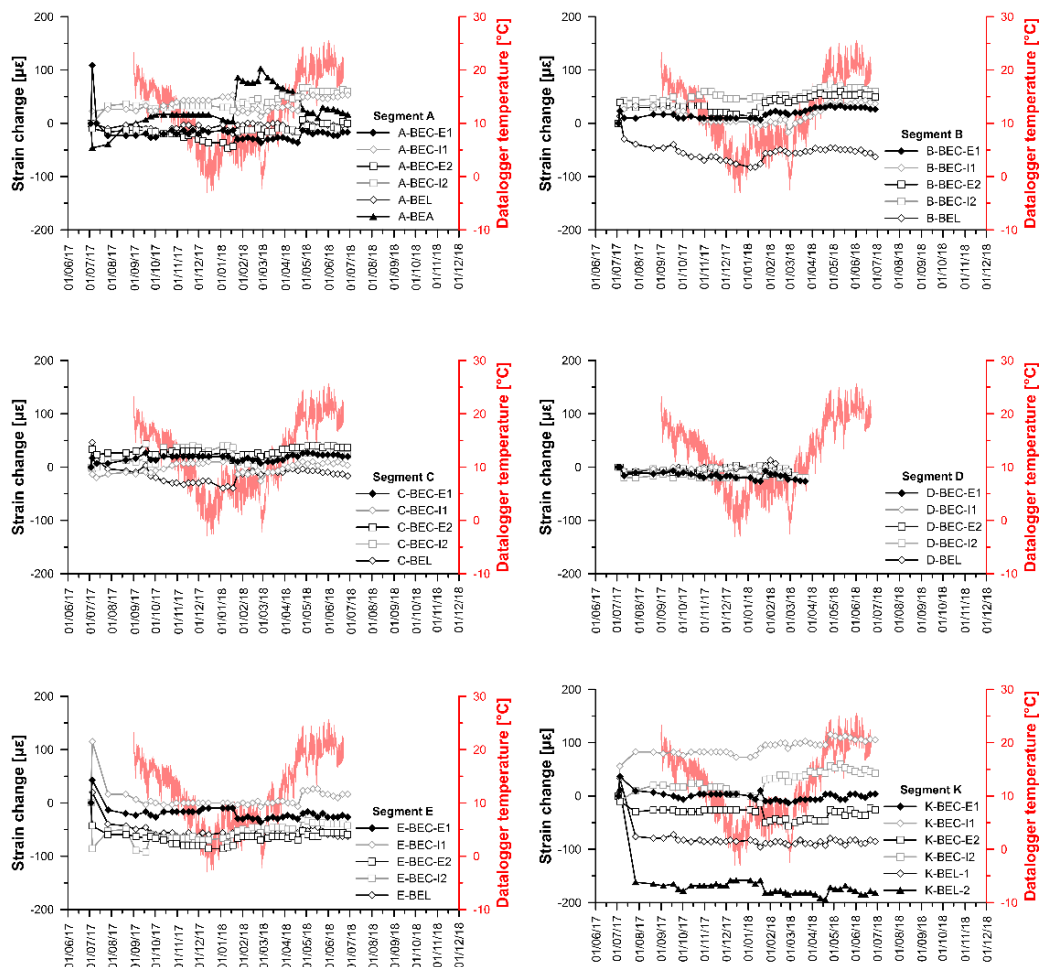


Figure 6.3: Strain outputs in ring 181 referred to the pre-installation reading.

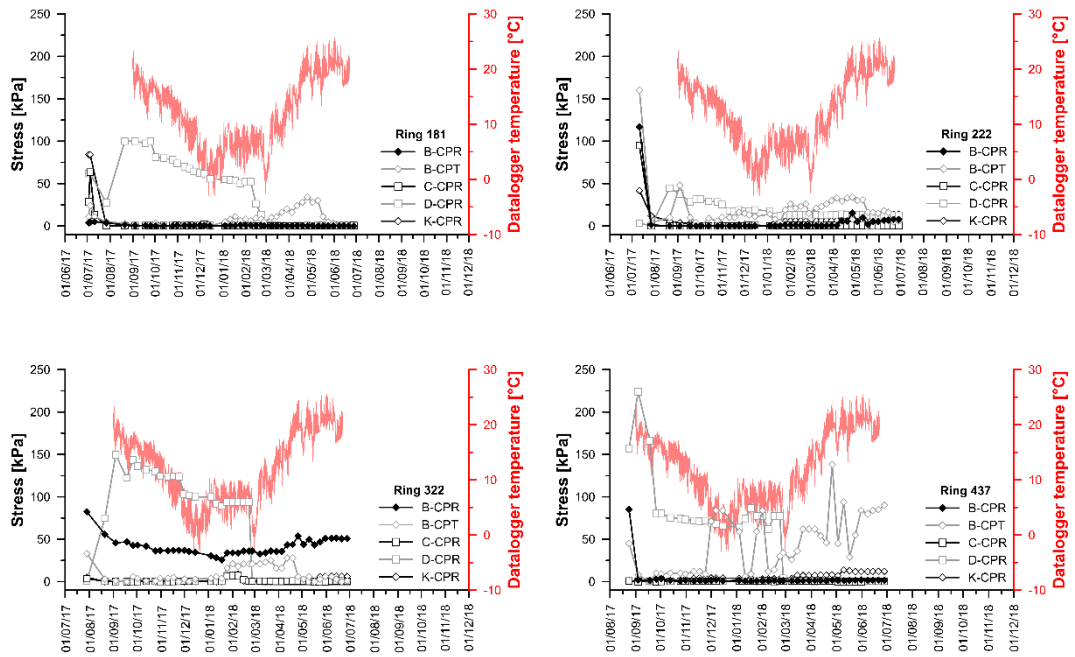


Figure 6.4: Stress outputs in ring 181, 222, 322, 437.

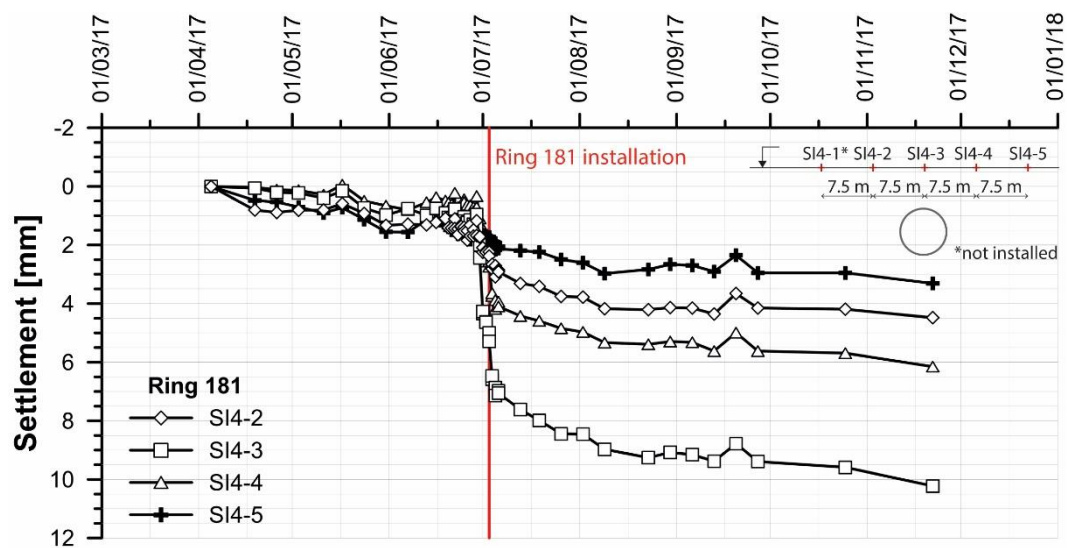


Figure 6.5: Evolution of the surface settlements profile with time.

6.2.2. Experimental site measurements

6.2.2.1. Conventional sensors

As described in Chapter 4, the experimental site involved equipping ring 179 with strain gauges and pressure cells (see Figure 6.6 for their location and orientation). In both cases a first

reading was done in the precast concrete plant on May 16th, 2017, after the steel cages setup. A second reading took place on Aug 31st, 2017 at 16:50, before pressurizing the cells to bring them within the measurement range, and later, at 17:07. Re-pressurization allows to push into the hydraulic circuit of the pressure cells a certain deaired oil quantity until obtaining again the concrete-pad contact. The strain readings at the previously mentioned times are reported in Table 6.3.

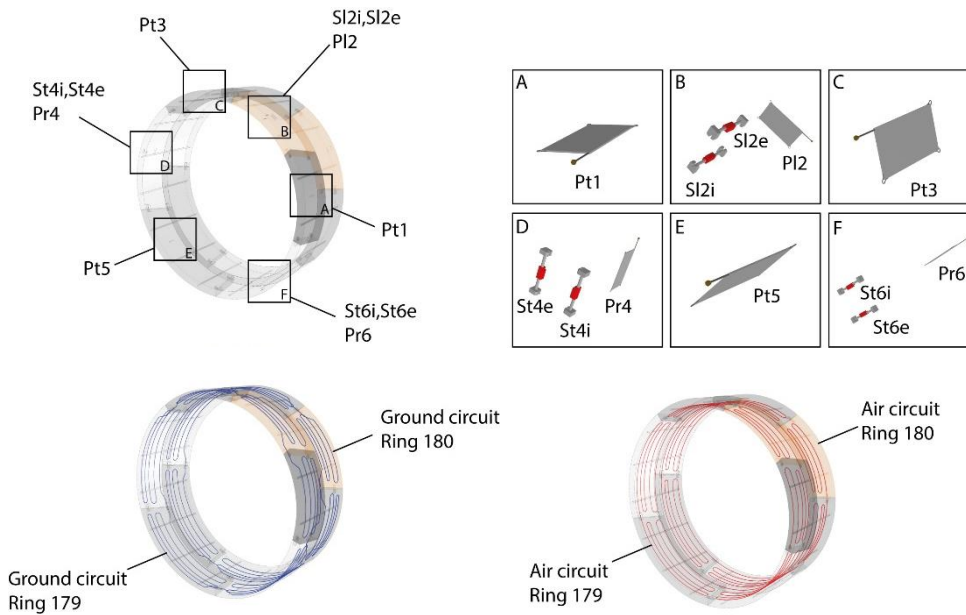


Figure 6.6: Location of the strain gauges and pressure cells in the experimental site and view of the pipes network.

Table 6.3: Strains measurements (i) in the precast concrete plant, (ii) before connecting the datalogger and (iii) after connecting the datalogger.

Segment	Sensor	(i) 16/05/2017		(ii) 31/08/2017 16:50		(iii) 31/08/2017 17:07	
		ϵ [$\cdot 10^{-6}$]	T [$^{\circ}$ C]	ϵ [digit]	T [$^{\circ}$ C]	ϵ [$\cdot 10^{-6}$]	T [$^{\circ}$ C]
B (4)	St4i	2300	24.9	519.02	23.1	1775.88	23.1
	St4e	2238	25	NAN	22.8	NAN	22.8
D (6)	St6i	2610	23.7	640.92	25.9	2193.17	25.8
	St6e	2490	23.7	533.59	25	1826.01	25
K (2)	SI2i	2225	17	101.4	23.5	346.86	23.6
	SI2e	2439	16.8	759.67	23.1	2599.57	23.1

Table 6.4: Strains differences between the second and the first reading.

Segment	Sensor	$\Delta\epsilon$ [$\cdot 10^{-6}$]
B (4)	St4i	-523.91
	St4e	NAN
D (6)	St6i	-416.77
	St6e	-664.06
K (2)	SI2i	-1878.01
	SI2e	160.59

In Table 6.4 the differences between the second and the first reading were computed. It can be seen that they all result to be negative (except one in the longitudinal direction), which

would confirm the correctness of the strains sign, that is negative in contraction (due in this case both to shrinkage following casting and to the ground load) and positive in extension. The second and third readings coincide, given that one is obtained by multiplying the other by the gage factor $3.422 \mu\epsilon/\text{digit}$ provided by the suppliers (Appendix B).

As the tests performed involve non-isothermal conditions, part of the strain is due to temperature variations. Hence, data processing is required to correct temperature change, which is why the gauges are provided with a thermistor. The output of the reading is the resonant frequency of the vibrating wire under tension, given by:

$$F = \frac{1}{2L} \sqrt{\frac{T}{\mu}} \quad \text{Eq. 6.1}$$

where L (in m) is the gauge length, T (in N) is the wire tension and μ (in kg/m) is the linear density of the steel making the wire. Knowing the Young's modulus E_w and the cross-section A of the wire, the strain can be obtained as:

$$\epsilon = \frac{T}{AE_w} \quad \text{Eq. 6.2}$$

Therefore, the strain can be related to the frequency square through a constant K depending on the sensor characteristics:

$$\epsilon = \frac{K}{1000} F^2 \quad \text{Eq. 6.3}$$

To take into account non-isothermal conditions, thermal deformation of the wire must be computed. As the linear expansion coefficient of the wire is $\alpha_w^T = 12.2 \mu\epsilon/^\circ\text{C}$, the observed thermal strain, with reference to the initial value, according to Mimouni and Laloui (2013) is:

$$\Delta\epsilon_{\text{obs}} = \Delta\epsilon_{\text{mech}} + \Delta\epsilon_{\text{th}} = \frac{K}{1000} (F_1^2 - F_0^2) + \alpha_w^T (T_1 - T_0) = L_1 - L_0 + \alpha_w^T (T_1 - T_0) \quad \text{Eq. 6.4}$$

where F_0, F_1 are the reference and current frequencies, T_0, T_1 are the reference and current temperatures, L_0, L_1 are the reference and current readings. If temperature increases, the wire expands and reduces the observed tension. The same approach is used by Mimouni and Laloui (2013).

The strain gauges' user manual suggests instead the following correction:

$$\Delta\epsilon_{\text{obs}} = L_1 - L_0 + (\alpha_w^T - \alpha_c^T) (T_1 - T_0) \quad \text{Eq. 6.5}$$

where $\alpha_c^T = 10 \mu\epsilon/^\circ\text{C}$ is the concrete's coefficient of linear thermal expansion.

In the user manual of another gauges' supplier, ROCTEST©, it can be read that the real strain is the total strain on which we add the thermal expansion of the wire, as if the strain meter was not confined:

$$\epsilon_r = \epsilon + (\alpha_w^T - \eta\alpha_c^T) (T_1 - T_0) \quad \text{Eq. 6.6}$$

where ϵ is the total strain reading, ϵ_r is the real strain and η is the freedom factor of the concrete structure in surrounding material and is between 0 and 1. The previous formulas given by Eq. 6.4 (Method 1) and Eq. 6.5 (Method 2) are particular cases of Eq. 6.6. The same manual states that $\eta\alpha_c^T$ can be estimated from a linear regression of ϵ versus T , by computing the slope of the graph.

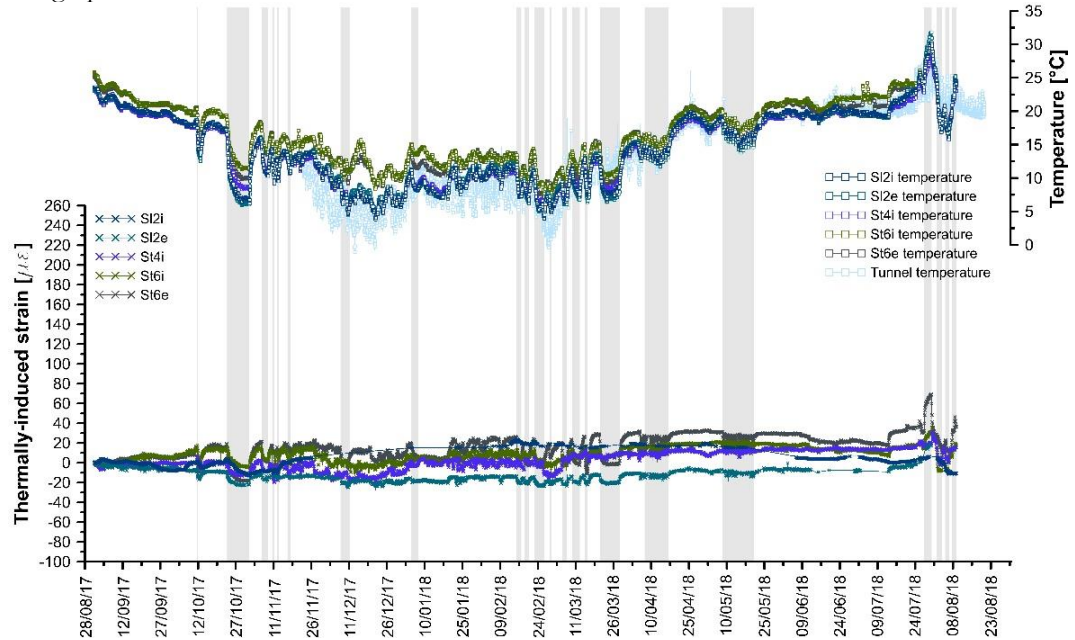


Figure 6.7: Monitored strains and temperature without compensation.

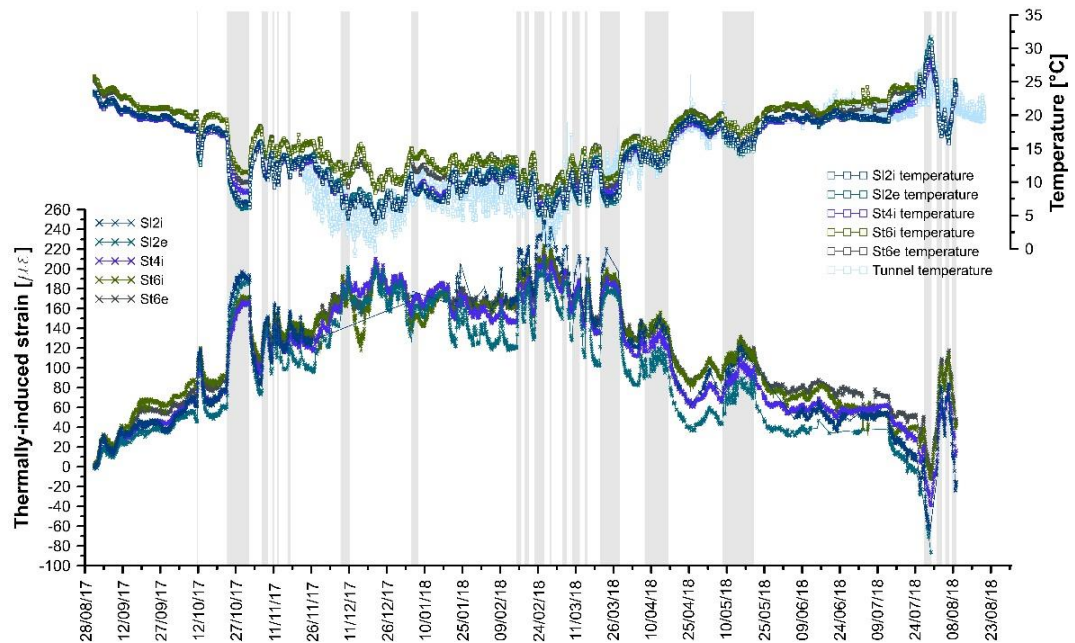


Figure 6.8: Monitored strains and temperature with compensation – Method 1.

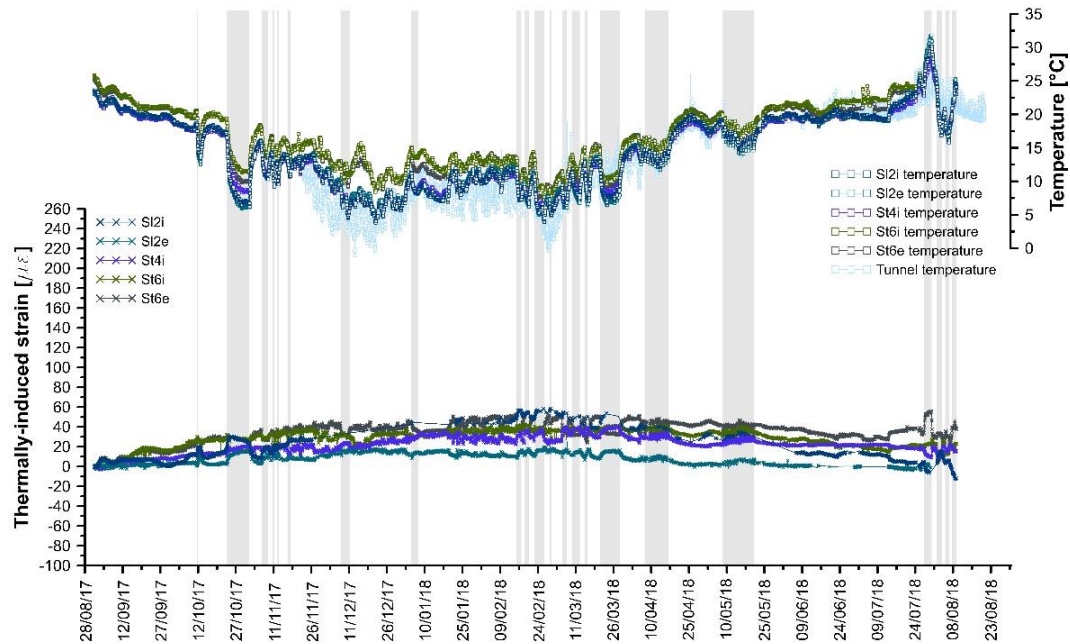


Figure 6.9: Monitored strains and temperature with compensation – Method 2.

From these evaluations, it can be noted that, beyond the reading given by the data logger, it is not straightforward to evaluate the strains when non-isothermal conditions are present. For this reason, both Eq. 6.4 and Eq. 6.5 were applied and differences evaluated, as shown in Figures 6.7-6.9, without and with compensation respectively. In these pictures, the grey bars indicate all the tests performed since the beginning of the experimental campaign.

There is a noticeable difference from the case without compensation to the extreme case of compensation using Method 1. This Method appears to be the most reliable, as upon cooling an increase in strain is recorded and viceversa. Numerical results will be useful to confirm this intuition.

As concerns the stress measurements, they can be seen in Table 6.5 for the dates (i) to (iii). The value in MPa was obtained thanks to the polynomial sensitivity factors which are reported in Appendix B (Figures B.4-B.9).

Table 6.5: Stress measurements (i) in the precast concrete plant, (ii) before connecting the datalogger and (iii) after connecting the datalogger.

Segment	Sensor	(i) 16/05/2017			(ii) 31/08/2017 16:50			(iii) 31/08/2017 17:07	
		σ [Digit]	σ [MPa]	T [°C]	σ [Digit]	σ [MPa]	T [°C]	σ [MPa]	T [°C]
A (3)	Pt3	8645	0.36	24.1	NAN	NAN	24.1	NAN	24
B (4)	Pr4	8891	-0.02	NAN	7748.78	1.72	23.5	1.71	23.4
C (5)	Pt5	9121	-0.37	24.1	7990.69	1.35	28.9	1.68	28.8
D (6)	Pr6	8849	0.04	24.5	7538.58	2.04	21.6	1.48	21.6
E (1)	Pt1	9277	-0.61	24.8	7979.06	1.37	23.8	1.98	23.7
K (2)	Pl2	8909	-0.05	24	8920.53	-0.07	23.7	-0.03	23.6

In Table 6.6 the differences between the second and the first reading were computed. It can be seen that they all result to be positive (except one in the longitudinal direction), which would confirm the correctness of the stress sign, that is positive in compression (due in this case both to shrinkage following casting and to the ground load). Of course the differences

shown in Table 6.6 do not include the sole effect of the excavation, given that they are referred to the end of August 2017 and the ring 179 was erected at the beginning of July 2017, that is almost 2 months earlier. However, the values are much higher than those in Figure 6.4 (2 MPa vs 100 kPa). Besides, in the back-analysis described by Barla (2015) the hoop stress resulted about 120 kPa, which would confirm the construction site monitoring data. Moreover, as it will be useful for the following numerical analysis, it is noted that in the same study, numerical modelling provides satisfactory results matching the in situ data (stresses and surface settlement trough) by considering a stress release rate of 80-90%.

Table 6.6: Stress differences between the second and the first reading.

Segment	Sensor	$\Delta\sigma$ [MPa]
A (3)	Pt3	NAN
B (4)	Pr4	1.74
C (5)	Pt5	1.73
D (6)	Pr6	2.00
E (1)	Pt1	1.99
K (2)	PI2	-0.02

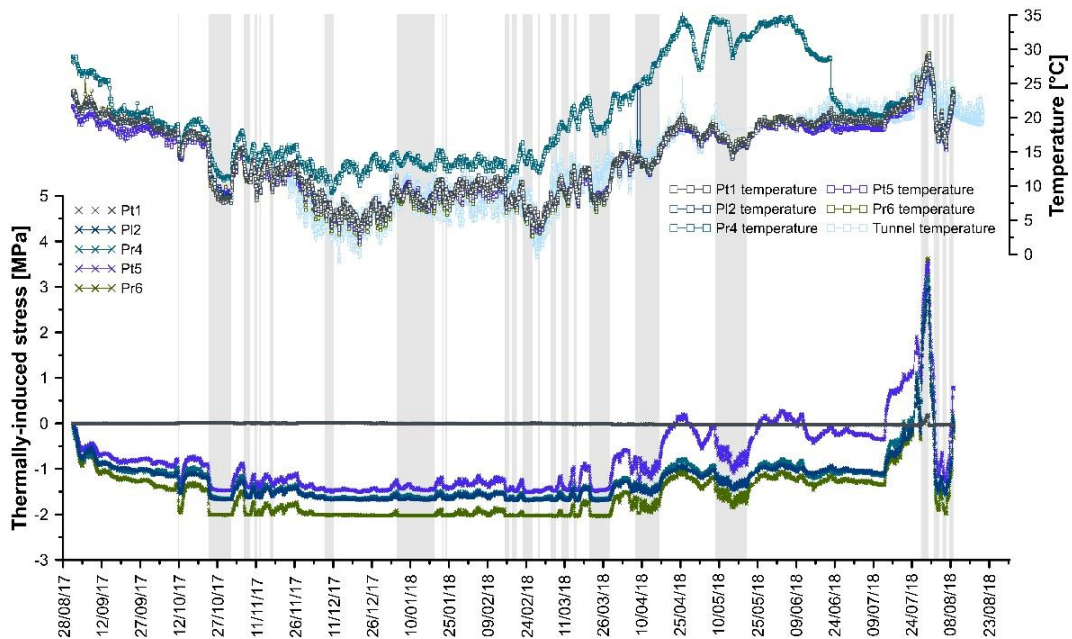


Figure 6.10: Monitored stresses and transducers temperatures.

The trend of the pressure cells measurements is shown in Figure 6.10 for which the same considerations as for Figures 6.7-6.9 apply. Based on the user manual, for vibrating wire transducers in case of non-isothermal conditions a correction should be performed because of the thermal deformation that the wire could undergo. The equation to compute the temperature correction factor is given by:

$$P_T = (T_{es} - T_0)K \quad \text{Eq. 6.7}$$

where P_T is the temperature correction, T_{es} the exercise temperature, T_0 the temperature reported on the certificate of conformity of the transducer and K the coefficient for thermal

correction reported on the same document. This correction needs to be added to the pressure found as:

$$P = L_{es} - l_0 / S \quad \text{Eq. 6.8}$$

where P is the pressure in kPa, l_0 is the reading with the cell in air before the installation, L_{es} is the reading and S is the sensitivity factor reported on the calibration certificate. This value is given automatically by the data logger. Hence, the final value of pressure is:

$$P_{\text{corr}} = L_{es} - \frac{l_0}{S} + (T_{es} - T_0)K \quad \text{Eq. 6.9}$$

where the temperature correction is the only postprocessing operation. This correction was done but given the very small values of K , in the range $-0.000496 \div 0.001361$ MPa/°C, it resulted to be negligible.

6.2.2.2. Optical sensors

The experimental site was equipped with an optical sensing system based on Fibre Bragg Grating sensors for temperature and strain, embedded in concrete ring 180 (Figure 6.11). The readings from the optical sensors were remotely recorded and compared with measurements performed with conventional electrical sensors. A comparison of the performances between the FBGs and the electric sensors is an important target, since it will support the possible future design of an all-fibre monitoring system that exploits the main advantages of optical fibre sensors: minimum invasiveness, intrinsic fire safety, electromagnetic immunity and possibility to enable remote sensing over several km, for instance by placing the interrogator hardware in a distant central office connected to the optical sensors by long fibre cables.

Two spools of standard single-mode fibre and four spools of 62.5 μm multimode fibre were also embedded during the fabrication process to enable future applications of distributed sensing by means of the most popular commercial techniques such as Optical Frequency Domain Reflectometry, phase/polarization Optical Time Domain Reflectometry, Brillouin/Raman scattering. However, measurements from these spools were not collected due to unavailability of the interrogator system.

In the field trial, the embedded optical fibre sensors have Bragg wavelengths in the range 1530-1570 nm. Each sensor contains a loosen FBG for temperature reading and an FBG for strain, in which the temperature effect can be corrected from the reading of the loosen FBG. The temperature sensitivity of the loosen FBGs K_{T1} is around 9 pm/°C, whereas the strain FBGs exhibit a sensitivity K_e of about 1.3 pm/ μe and temperature sensitivity K_{T2} around 26 pm/°C (Table 6.7 and Appendix B). The temperature and strain wavelengths variations $\lambda_{T1} - \lambda_{T0}$ and $\lambda_{\epsilon 1} - \lambda_{\epsilon 0}$ are given by the following formulations:

$$\lambda_{T1} = \lambda_{T0} + K_{T1} \cdot (T_1 - T_0) \quad \text{Eq. 6.10}$$

$$\lambda_{\epsilon 1} = \lambda_{\epsilon 0} + K_{T2} \cdot (T_1 - T_0) + K_e \cdot (\epsilon_1 - \epsilon_0) \quad \text{Eq. 6.11}$$

Hence, the temperature and the strain variation can be obtained as:

$$T_1 - T_0 = \frac{\lambda_{T1} - \lambda_{T0}}{K_{T1}} \quad \text{Eq. 6.12}$$

$$\varepsilon_1 - \varepsilon_0 = \frac{\lambda_{\varepsilon_1} - \lambda_{\varepsilon_0} - K_{T2} \cdot (T_1 - T_0)}{K_{\varepsilon}} \quad \text{Eq. 6.13}$$

Table 6.7: FBGs sensors sensitivities.

Code	Sensor name	Temperature wavelength [nm]	Strain wavelength [nm]	K_{T1} [pm/°C]	K_{T2} [pm/°C]	K_{ε} [nm/με]
170315-1	FBG3e	1539	1543	8.7	26.2	0.00127
170315-2	FBG1i	1547	1551	9.2	26.7	0.00125
170315-3	FBG5e	1555	1559	9	27.3	0.00130
170315-4	FBG3i	1541	1545	9.1	25.5	0.00126
170315-5	FBG1e	1549	1553	9	25.7	0.00127
170315-6	FBG5i	1557	1561	9	25.6	0.00130

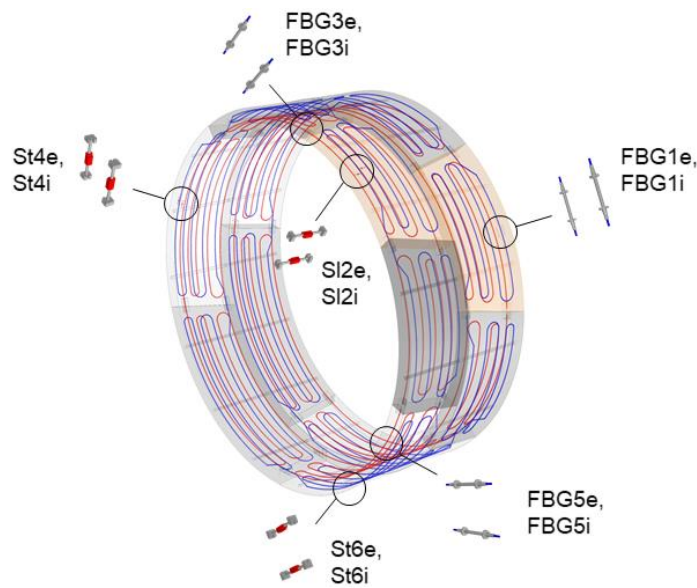


Figure 6.11: Location of FBGs and electrical strain sensors.

Remote monitoring has been performed by installing the interrogators outside the tunnel, about 70 m from the rings. The maximum interrogation distance for the electric sensors is 1 km (according to the producer user manual of the strain gauges). On the other hand, there is no practical limitation in the case of FBGs, as long as the losses of the optical link are kept at standard telecom values, since the dynamic range of the FBG interrogator is 27 dB (Smart Fibres, SmartScan datasheet). This was assessed by testing dummy FBGs connected to a 20 km fibre ring which is part of a metropolitan testbed for transmission experiments (Straullu et al., 2015). The FBG could be easily interrogated, but the propagation delay would result in a perceived static shift of the Bragg wavelength. This problem must be carefully considered in the case of a large network of sensors because FBGs with close Bragg wavelength installed at large distance from each other may yield overlapping Bragg wavelengths.

Electrical and optical sensors were embedded in the concrete lining both at the intrados and at the extrados (Figure 6.11), in order to assess temperature and strain in the cross section of the rings. Five experimental campaigns were performed, as shown in Table 6.8. As campaigns A1 and A2 lasted for very little time, only campaigns A3, B and C will be described in the following.

Table 6.8: Optical sensing experimental campaigns.

Campaign	Start [dd/mm/aa hh:mm]	End [dd/mm/aa hh:mm]	Time [d]	Time [h]	Test mode
A1	21/11/2017 11:44	21/11/2017 12:25	0.03	0.68	Ground heating
A2	07/12/2017 12:15	07/12/2017 18:15	0.25	6.00	Ground heating
A3	06/02/2018 17:57	13/02/2018 07:40	6.57	157.69	Ground heating
B	01/08/2018 17:21	04/08/2018 15:54	2.94	70.54	Air heating
C	07/08/2018 09:33	09/08/2018 07:18	1.91	45.74	Ground cooling

6.3. Interpretation of experimental data

6.3.1. Conventional sensors

Data of stress and strain pertaining to each test can be found in Appendix A. As an example, the effects produced by the 7.8-days heating test GH8 and the 3-days cooling test GC1 will be here evaluated. Figure 6.12 depicts the monitoring data recorded for these two tests respectively. Inlet and outlet temperatures are shown, as well as the tunnel temperature measured by a probe fixed close to the rings' intrados. Also illustrated are the subsequent temperatures in the lining, thermally induced strains and thermally induced stresses. It can be seen that during the heating test the heat carrier fluid circulation led to a variation of temperature in the lining of about 4-6°C and to a thermally induced contractive hoop strain of 50 $\mu\epsilon$ (Method 1 was adopted for temperature compensation). All pressure cells indicate a decrease in compression between 0.2 and 0.5 MPa. The higher reduction in compression stress in segment 6 is of unclear origin. Analogously, during the cooling test the opposite behaviour is shown. For an increase in temperature of 5-7°C expansive strains are shown, in the order of about 60 $\mu\epsilon$, despite the stress behaviour is not mirrored. Indeed, higher variations in stresses arise and it appears that an increase in compression by 2.5-3 MPa is induced. Similar considerations apply for the other tests. Based on the observed data, it can be seen that the effect of a decrease in internal air temperature is to increase the intrados and extrados strains, and to decrease the compression at mid-thickness. The same effect is related to thermal activation.

In Figures 6.13-6.18 the relationships among the thermally induced strain and the temperature variation and among the thermally induced stress and the temperature variation are illustrated. The temperature variation is the one recorded by the thermistor embedded in the strain gauges for the strains and the one recorded by the pressure transducer for the stresses. These charts, built using data from tests GH1-GH8, GC1-GC2 and AH1-AH2 (see Table 4.6), are distinguished for type of tests (ground heating, ground cooling or air heating) and include both data recorded during the tests and during the recovery phase after the tests. The six subplots in each figure are referred to a specific sensor, whose name is reported in the subplot title. Also, some reference lines are reported, corresponding to a gradient of 5, 10 and 15 $\mu\epsilon/^\circ\text{C}$ for the strains and to 0.1, 0.5 and 1 MPa/ $^\circ\text{C}$ for the stresses.

It can be seen from Figures 6.13-6.15 that almost all strain gauges record a strain variation which is around 10 $\mu\epsilon/^\circ\text{C}$, very similar to the concrete lining coefficient of thermal expansion indicating a degree of freedom DOF of segments very near to one. The range of temperature variations consequent to the tests performed is between -8 and +8°C, whereas the strains are included between -100 and 100 $\mu\epsilon$. A quasi elastic behaviour can be highlighted, as the strain difference tends to go back to the origin at the end of the tests. When no data are available, the reason is to be found in some electrical issues or in the bad connection of the sensors to the data-logger.

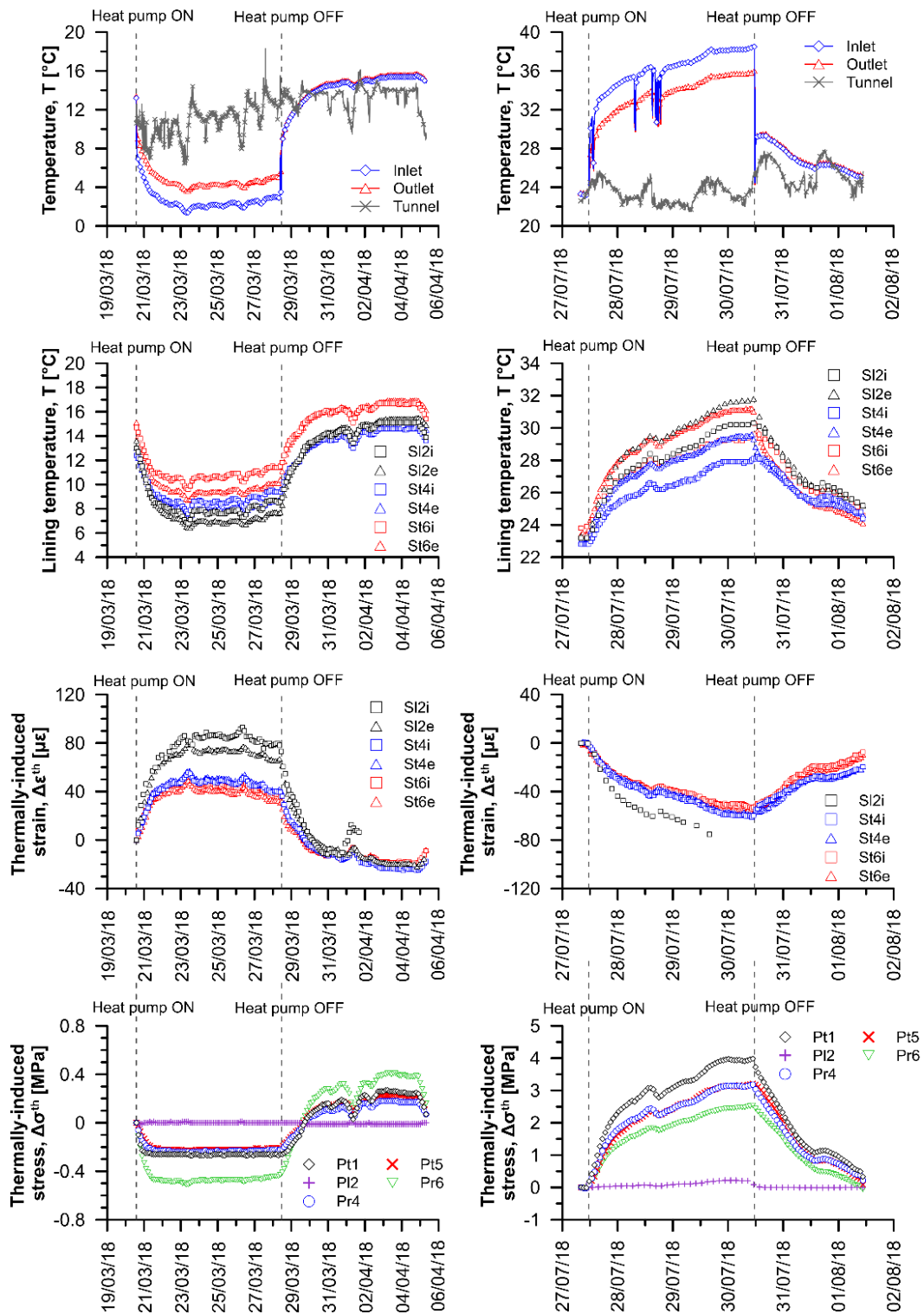


Figure 6.12: Heating test GH8 and cooling test GC1 with corresponding lining temperatures, thermally induced strains and thermally induced stresses.

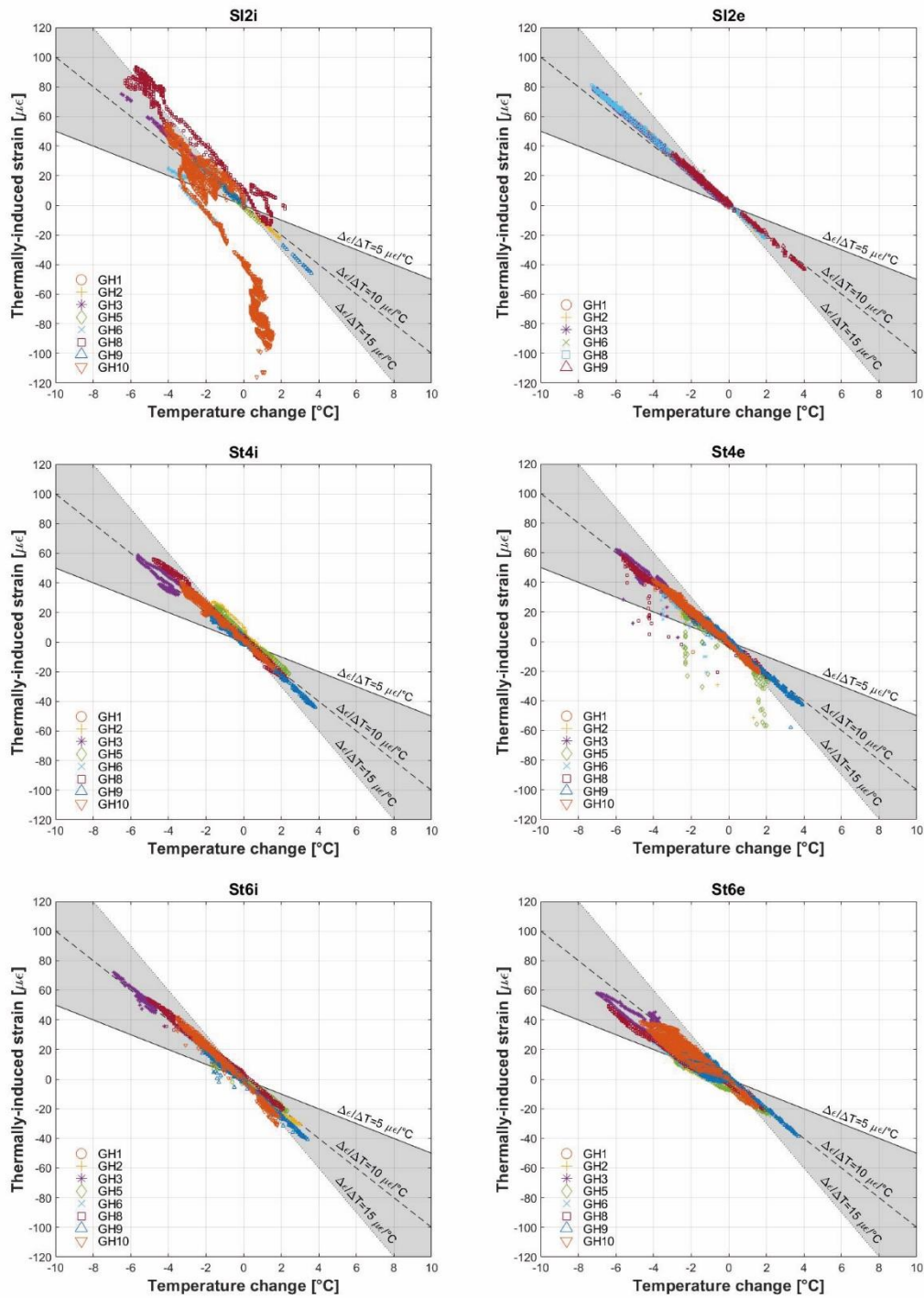


Figure 6.13: Relationship strains-temperature for the ground heating tests.

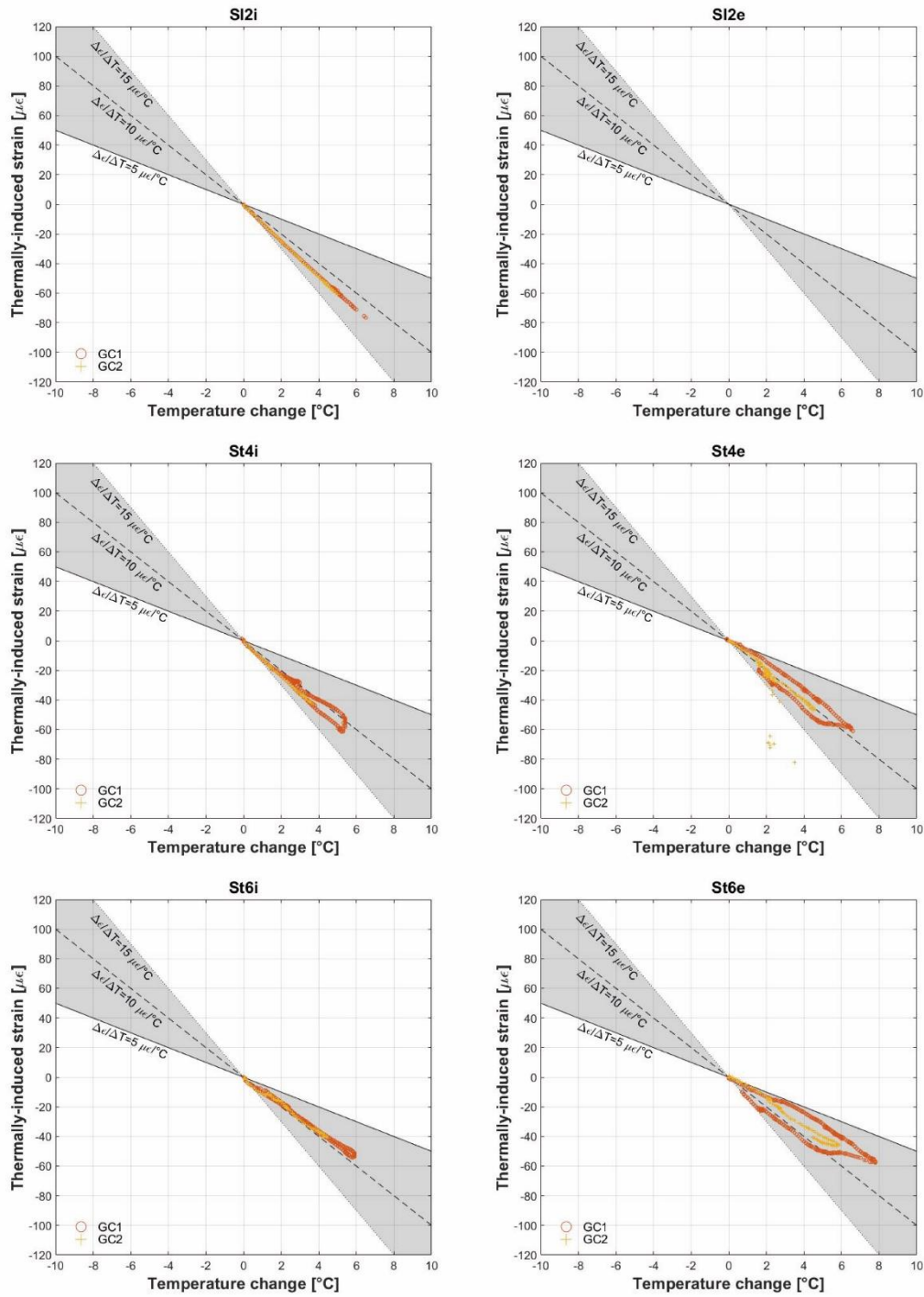


Figure 6.14: Relationship strains-temperature for the ground cooling tests.

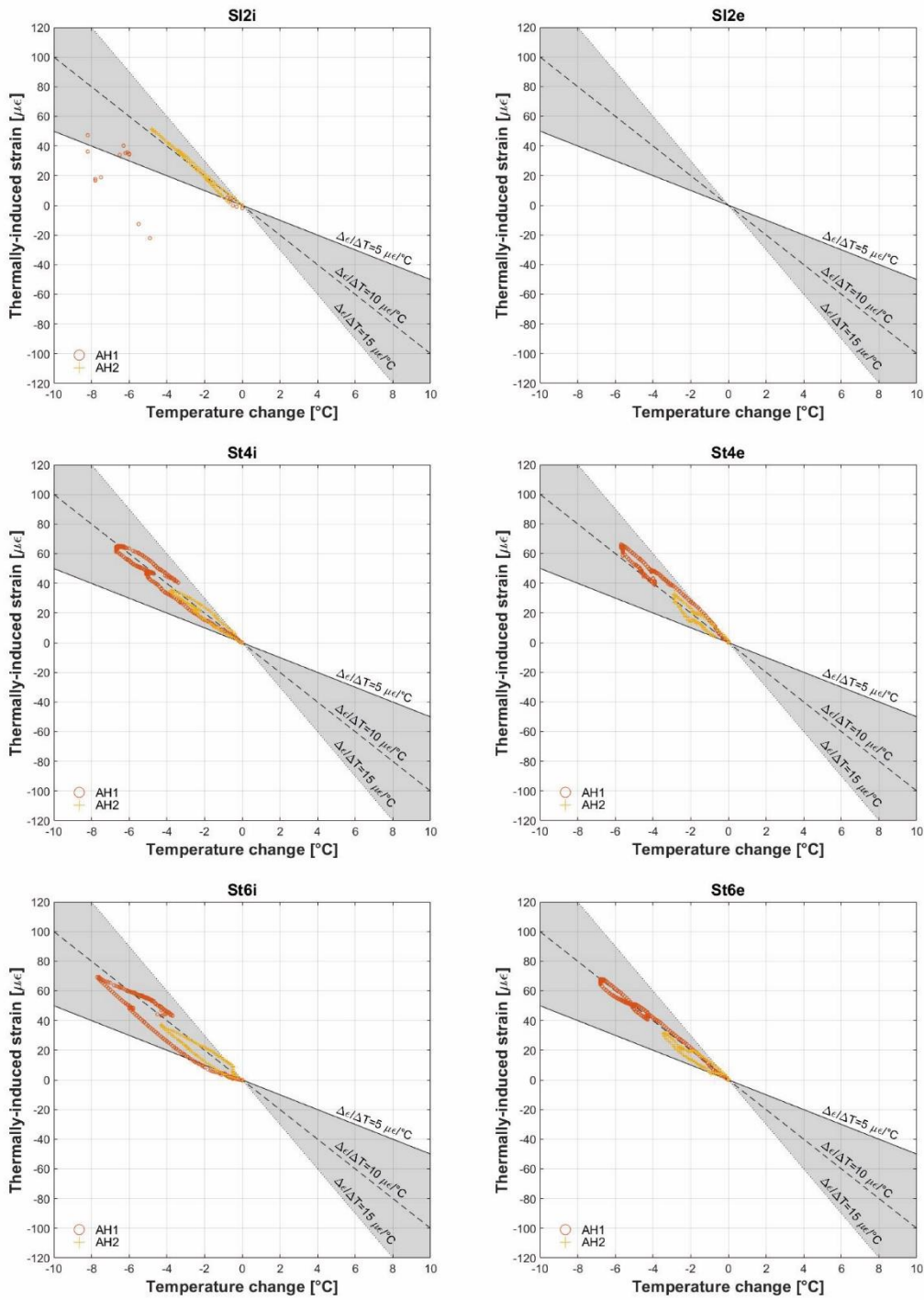


Figure 6.15: Relationship strains-temperature for the air heating tests.

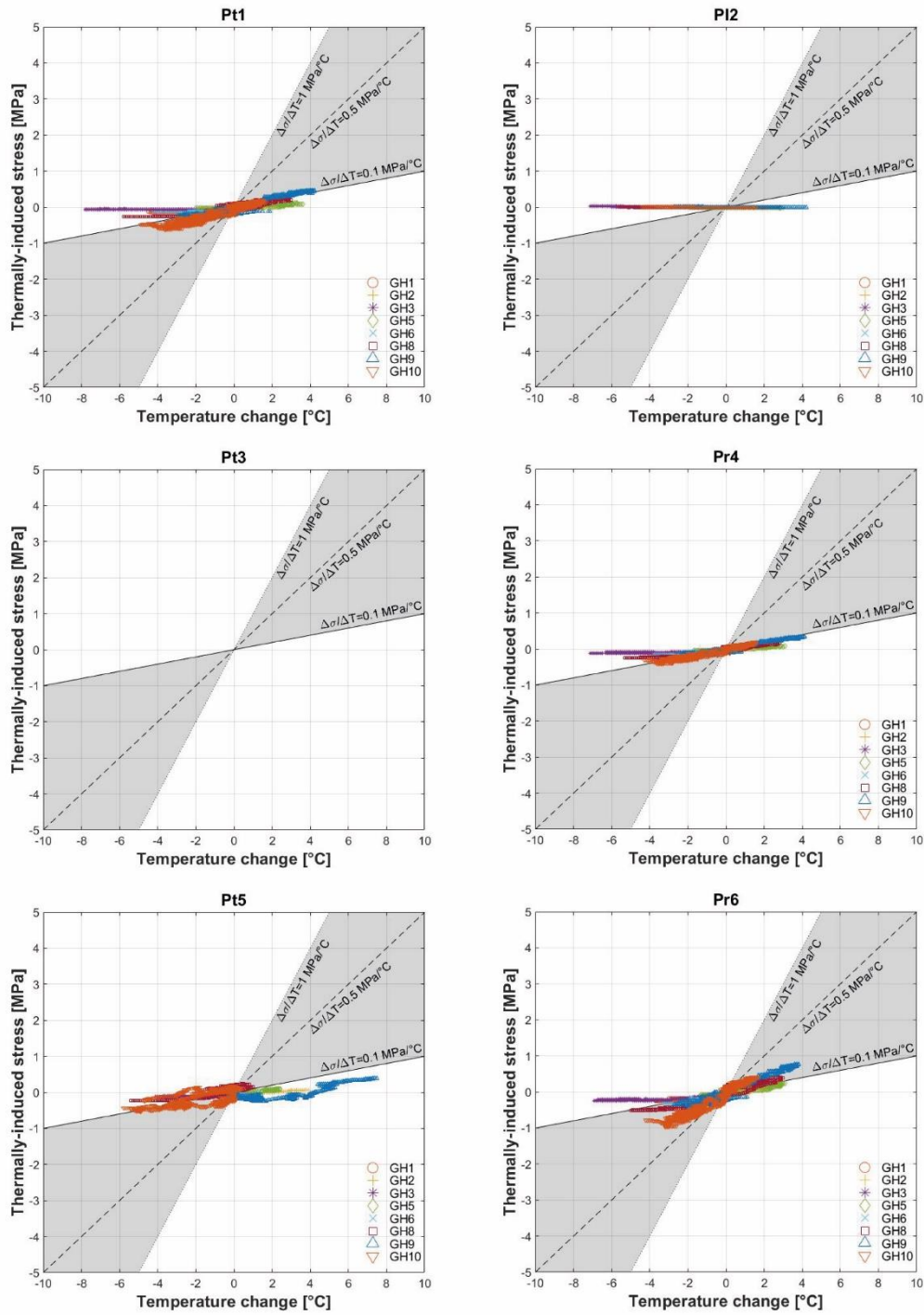


Figure 6.16: Relationship stress-temperature for the ground heating tests.

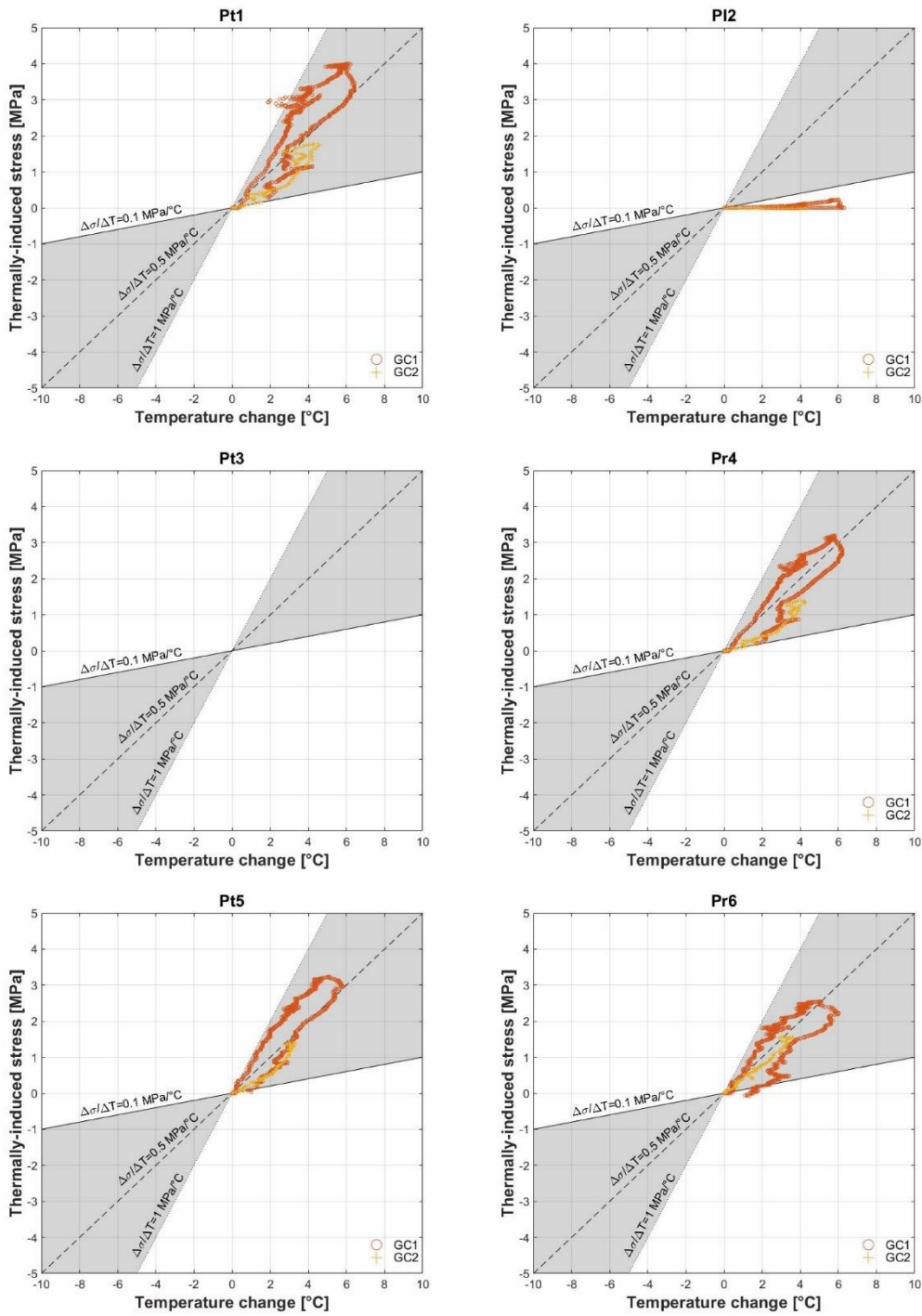


Figure 6.17: Relationship stress-temperature for the ground cooling tests.

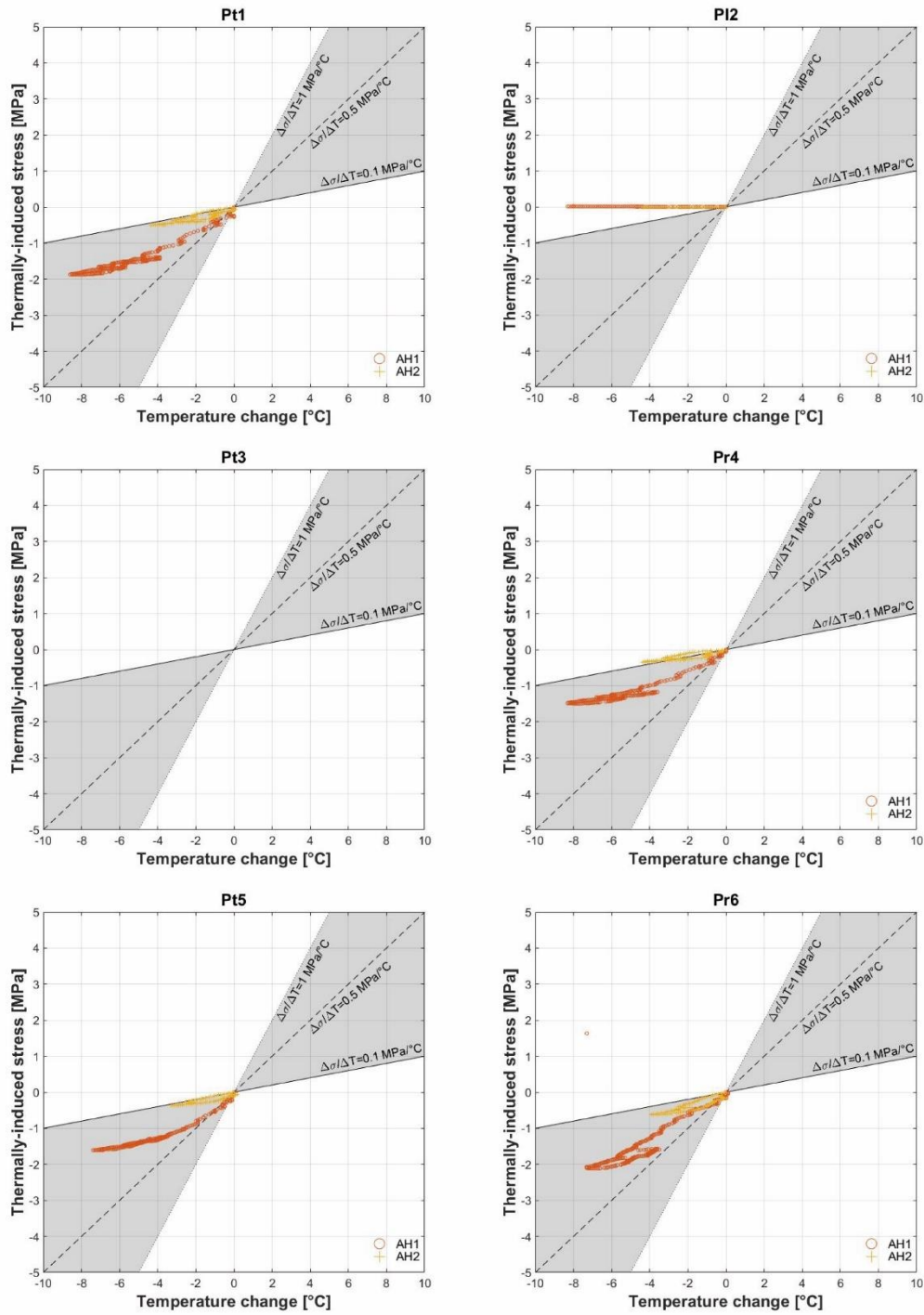


Figure 6.18: Relationship stress-temperature for the air heating tests.

Note that, as mentioned in Section 4.2.4, stress and temperature measurements are not performed precisely at the same place: stresses are measured at mid-thickness, whereas temperature is measured at the intrados (Figure 4.12). However, this difference should be small enough and is neglected here. In all tests, no induced stresses arise in the longitudinal direction (pressure cell Pl2 in Figures 6.16-6.18). For the ground heating tests the stress gradient is around 0.1 MPa/°C. For the ground cooling and air heating tests it appears to be higher and between 0.1 and 0.5 MPa/°C. However, the number of tests performed in this case is not statistically representative and further tests are to be performed to double-check these outcomes.

An example of what occurs in the lining from the mechanical point of view when the circuit is thermally activated during test GH8 is illustrated in Figure 6.19 for segment 6 of ring 179 and summarized in Table 6.9. As expected, the NTC thermistors within the vibrating wire strain gauges display a greater reduction in temperature at the extrados than at the intrados (difference of about 1.2°C) because the ground circuit which was activated is placed there. However, an effect at the intrados can also be observed. Though less pronounced, it testifies the occurrence of a conductive diffusion process across the ring concrete thickness. According to the decreasing temperature, the sensor Pr6 shows a reduction of stress of about 0.5 MPa. The strain increases both at the extrados and at the intrados by 35 and 30 $\mu\epsilon$ respectively, remaining in the elastic behaviour. After the end of the test, a new undisturbed condition is reached with time. The extrados and intrados trends reverse, extrados temperature gets over the intrados one, allegedly because of the higher surrounding ground temperature compared to tunnel air temperature.

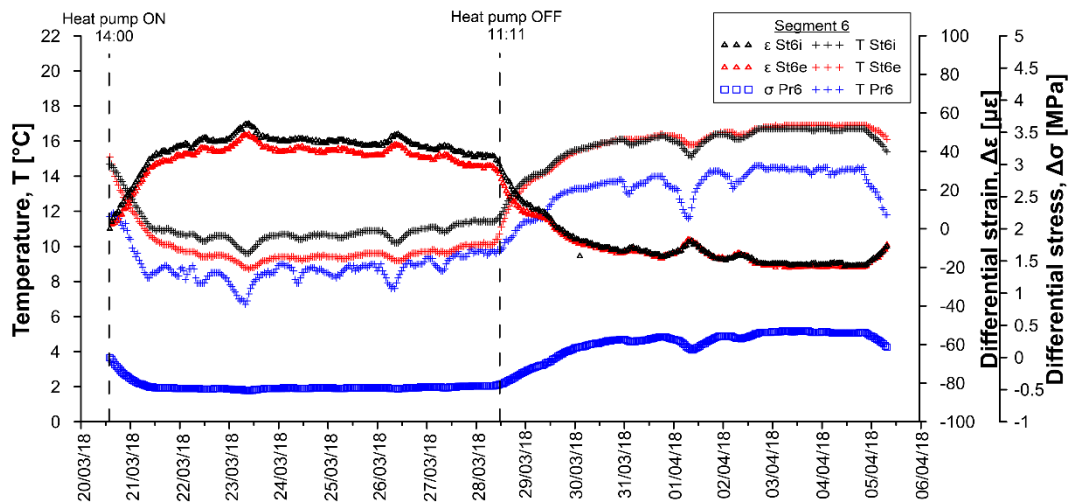


Figure 6.19: Temperatures, strains and stress in segment 6 (ring 179) during test GH8.

Table 6.9: Main segment 6 (ring 179) TM results at the end of test GH8.

St6e	[$\mu\epsilon$]	30.65
St6i	[$\mu\epsilon$]	35.55
Pr6	[MPa]	-0.43
St6e	[°C]	-4.7
St6i	[°C]	-3.2
Pr6	[°C]	-2.1

6.3.2. Optical sensors

All the temperature data obtained through electrical and optical sensors during campaign A3 are shown in Figure 6.20a (extrados) and Figure 6.20b (intrados) with reference to the left axis. The first right axis refers to the temperature spread at the heat pump and the second right axis depicts the trend of temperature within the tunnel and outside the station. The heat pump was turned on after 47.8 h and off after 72.6 h. As a general consideration, it can be said that the comparison shows a good agreement between the two monitoring technologies and a non-negligible sensitivity to the environmental temperature, especially for FBG1e given the higher variations recorded. During heat pump working the biggest drop is showed by FBG1e, followed by FBG3e and FBG5e, as expected following the path of the heat carrier fluid. The same goes for SI2e, St4e and St6e. The same sequence is fulfilled at the intrados, though with lower amplitudes as the extrados circuit was active. Similar considerations hold for campaigns B and C (Figure 6.24 and Figure 6.25).

A close-up example of temperature monitoring during the heat pump activity is reported in Figure 6.21. The graph shows that the FBGs detect the heating cycles starting at around 100 min, though they appear just above the measurement sensitivity of 0.09°C (observable as a ripple on the curves); the temperature inside the rings is initially increasing because of the influence of the temperature inside the tunnel, then it lowers over time because of heat pulling. The FBG sensor named FBG1e records a higher decrease in temperature in comparison to FBG3e. This is due to closest location of FBG1e to the circuit inlet (remember that numbering of the sensors from 1 to 6 follows the heat carrier fluid path, from the inlet segment to the outlet one) and demonstrates the progressive gain of heat from the fluid. The activity of the heat pump is depicted as the difference between the inlet and outlet temperature of the heat carrier fluid circulating in the primary circuit.

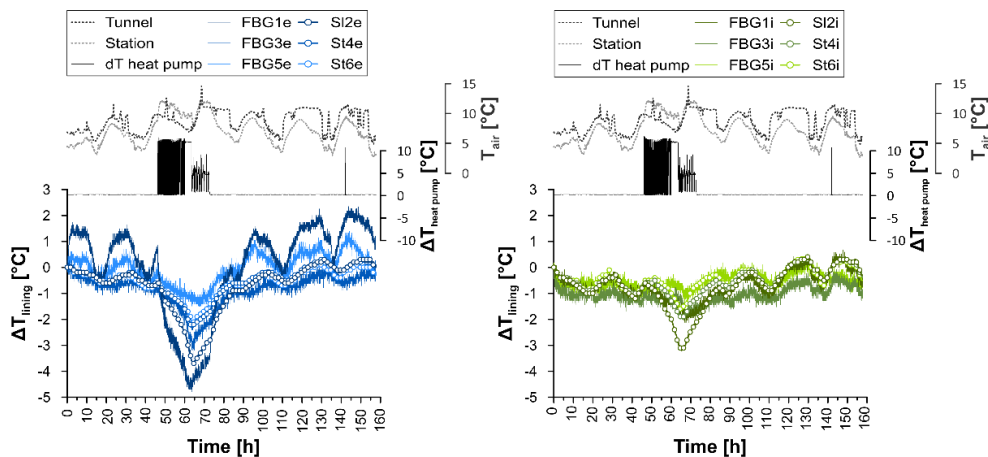


Figure 6.20: Comparison among electrical and optical fiber sensors during experimental campaign A3.

Long-term measurements have been carried out with the heat pump turned off, to evaluate the environmental temperature effect. The graphs of Figure 6.22 compare the long-term (4 days) reading from optical and correspondent electrical sensors without any energy-harvesting activity. Both graphs also report the air temperature recorded at the tunnel entrance during the tests. The FBGs and the thermistors, because of technical and economical constraints, could not be placed in the same rings, therefore the two graphs refer to temperatures measured in the two close energy rings, that is the comparison is not among perfectly homologous sensors.

This can partially explain the difference between the readings of the two types of sensor. However, both FBGs and thermistors detect the day-night variation as well as an increasing trend of the temperature of the rings during the 3-days trial. The latter may be ascribed to changes in the temperature of the ground close to the tunnel. Notice that also extrados sensors (i.e. close to the ground) are sensitive to the temperature of the tunnel. The recorded day-night variation is ~ 0.7 to 1.3 °C for a sweep of the air temperature of ~ 3 to ~ 5.6 °C. Moreover, extrados temperature is in all cases higher than intrados one, due to the warmer surrounding ground compared to internal air.

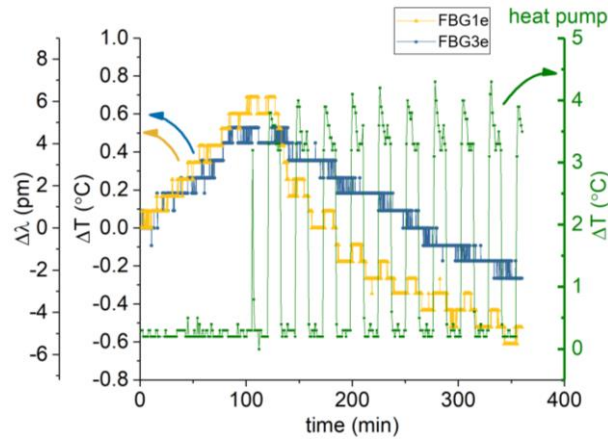


Figure 6.21: Bragg wavelength and correspondent temperature variation detected by two embedded FBGs vs time. The curve is compared to the heat pump activity (expressed as the temperature variation produced at the heat pump inlets of the primary circuit).

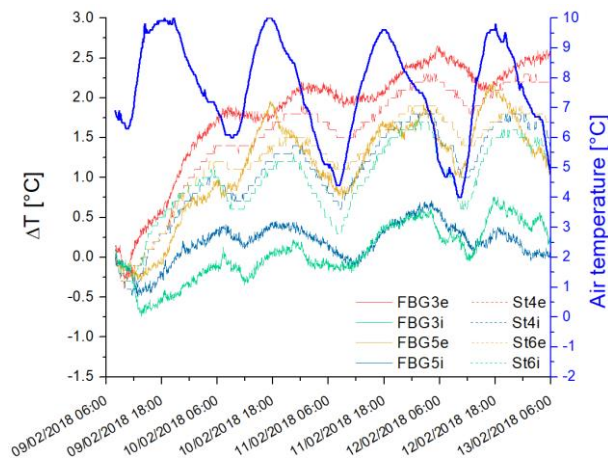


Figure 6.22: Temperature variation (with respect to the beginning of the acquisition) as recorded by comparable optical and electrical sensors. The air temperature in the tunnel is also reported.

A dependence with air temperature was also recorded by the correspondent strain sensors. An example is depicted in Figure 6.23. The wavelength shift of the strain FBG is larger, due to the larger temperature coefficient (26.2 pm/°C for the strain FBG versus 8.7 pm/°C for the temperature FBG). However, the difference is not as large as it would be for the loosen sensor, indicating a significant influence of the embedding into the concrete segments. A proper calibration should be performed in real working conditions that is, the sensors should be embedded into a concrete specimen and then calibrated for temperature variations.

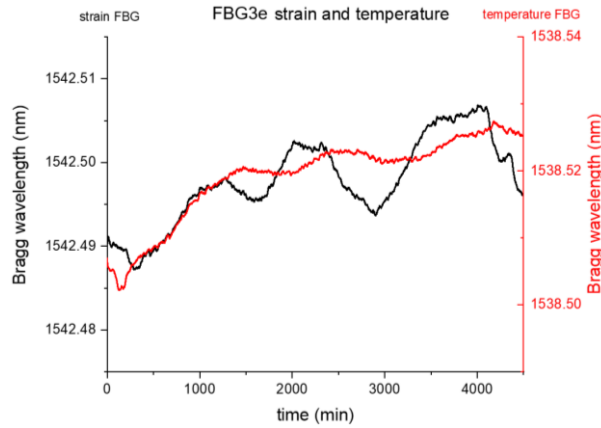


Figure 6.23: Bragg wavelengths from an optical sensor containing a strain and a temperature FBG.

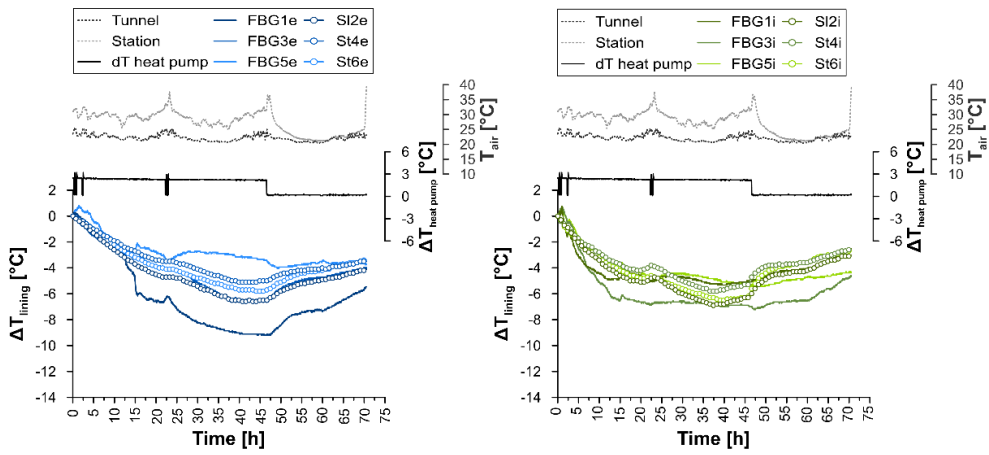


Figure 6.24: Comparison among electrical and optical fiber sensors during experimental campaign B.

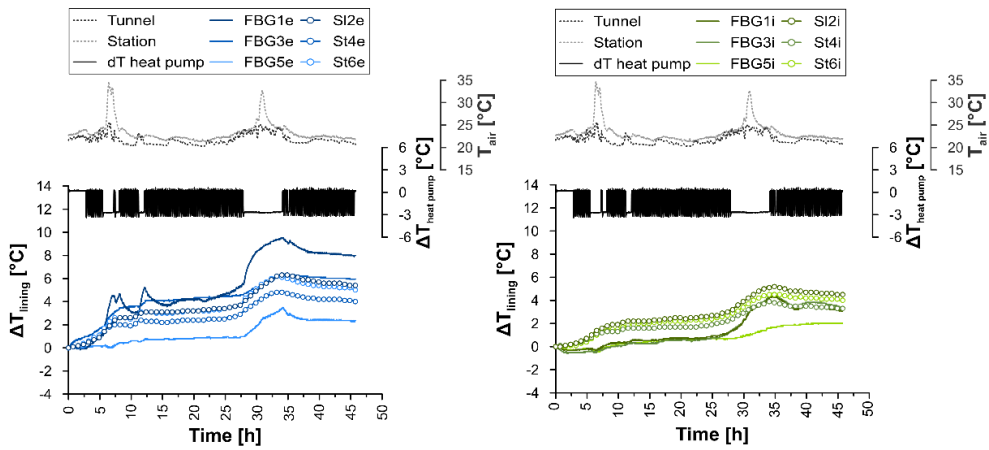


Figure 6.25: Comparison among electrical and optical fiber sensors during experimental campaign C.

6.4. Numerical investigation on the structural behaviour of the prototype

To better understand the thermo-mechanical phenomena occurring during the hydraulic flow and heat transfer process, a 2D plain strain, coupled thermo-mechanical, finite-difference numerical model was built. The reason for choosing a 2D model instead of a 3D one is related to the lower degree of complexity involved in the former case, given that a 3D TH model has already been built, and is then available, for the evaluation of the induced thermal field around the tunnel. In the following the methodology adopted is described, together with the analysis details and the results obtained.

6.4.1. Modelling procedure and input parameters

The 2D finite-difference (FD) domain was built in FLAC, Fast Lagrangian analysis of Continua (Itasca, 2016). It is 74.8 m high and 149.6 m wide and consists of 32268 elements (Figure 6.26). The mesh is refined around the tunnel. The size of the TM model coincides with that of the TH one, to be able, in a second phase, to import the temperature field from this one. The boundaries are positioned at a distance such as to minimize constraints influence on the area of interest. Horizontal displacements are prevented laterally, while vertical displacements are blocked on the lower side. As mentioned, the tunnel axis is 16.6 m deep and the tunnel diameter is 7.48 m.

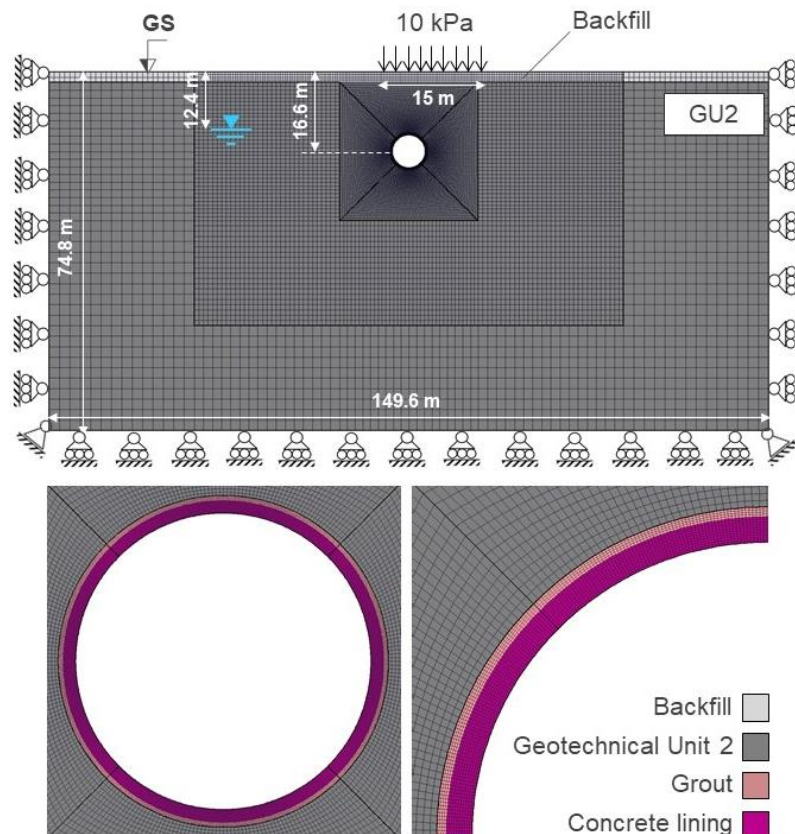


Figure 6.26: Finite difference mesh of the thermo-mechanical numerical model with stratigraphy.

Four areas were modelled: the backfill, the ground surrounding the tunnel, the grout and the concrete lining. The lining was modelled with a radial mesh, with 10 elements along the thickness in the radial direction and 576 elements in the hoop direction, so as to have nearly squared elements. The average size of an element of the lining is 3x3.9 cm (radial x hoop). The lining internal radius is 3.44 m, the external radius is 3.74 m. The injection grout was modelled with a radial mesh characterized by 4 elements in the radial direction and 576 elements in the hoop direction. The thickness of this layer was assumed equal to 11 cm, as in the TH model described in Chapter 5 (see Figure 5.8).

The model emulates the hydrogeological conditions existing in situ, characterized by a shallow 2.20 m-thick backfill layer, above a sand and gravel unit (so-called Geotechnical Unit 2, according to Barla and Barla, 2012) from loose to weakly cemented, with a percentage of cementation in the range 0-25%. The longitudinal profile with an indication of the stratigraphy can be seen in Figure 6.27. The in situ natural horizontal stress was assumed at each elevation equal to

$$\sigma'_h = (1 - \sin \varphi') \sigma'_v \quad \text{Eq. 6.14}$$

hence, the coefficient of earth pressure at rest k_0 was assumed as 0.4.

After reproducing the geostatic conditions, a drained (by virtue of the geological conditions at the site), time-independent analysis was performed to simulate tunnel construction using the convergence-confinement method (Panet, 1995). The stress release factor was determined through a back-analysis procedure with the aim to match the order of magnitude of the stresses measured in the lining and of the surface settlements (see Figure 6.4 and Figure 6.5). The mechanical properties adopted for the different materials involved are listed in Table 6.10 (these values are inferred both from Barla and Barla (2012) and from the final design report (Infratrasporti.To S.r.l., 2015)). Because during design conservative assumptions concerning strength and deformability are typically formulated, geotechnical properties deriving from the study performed by Barla and Barla (2012), reputed more realistic, are adopted here. The deformability modulus of GU2 varies according to a parabolic trend from 190 MPa at the top of the layer ($y=14.4$ m, with the origin of the reference system in correspondence of the tunnel centreline) to 240 MPa about 37.4 m below ($y=-23$ m). A simple elastic constitutive model was used for the concrete lining and grout injection, while an elastic-perfectly plastic Mohr-Coulomb model with null dilatancy was assumed for the backfill and GU2. Two sets of deformability parameters are chosen for the annular gap grout filling, related to the fresh and hardened condition. The Young's modulus of the lining was reduced by a factor f according to Muir-Wood formulation that takes into account the number of joints n_G (6), their thickness h_G (19 cm) and the ring thickness (30 cm):

$$f = \left(\frac{4}{n_G} \right)^2 + \left(\frac{h_G}{h_C} \right)^3 = 0.698 \quad \text{Eq. 6.15}$$

The unit weight was assumed as the natural soil unit weight, corresponding to the saturated one, from which, given the porosity 0.25 and assuming a saturation degree of 1, the dry unit volume was computed to be inserted among the model properties.

The calculation stages followed in the analysis are recalled in Table 6.11.

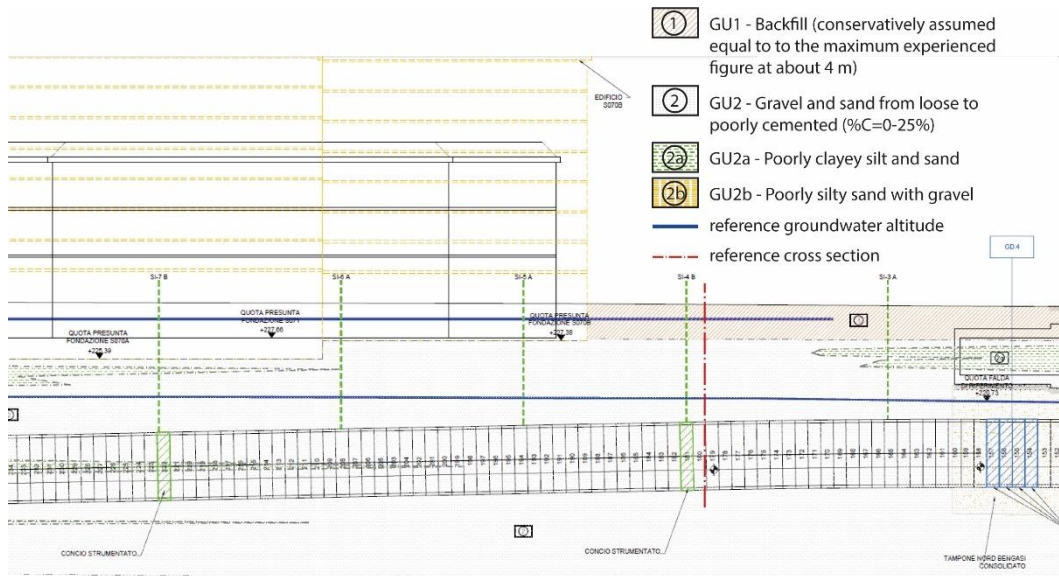


Figure 6.27: Longitudinal profile of the area of interest with indication of the stratigraphy.

Table 6.10: Mechanical and thermal material properties.

Property	Backfill			GU2			Grout	Lining
	A	B	C	A	B	C		
γ [kN/m ³]	15.5	17-19	19	17.0	18-21	19	18.5	25
E [MPa]	15	10-20	10	190-240	190-240	150	5-5000	28152
ν [-]	0.35	0.35	0.25	0.3	0.3	0.35	0.25	0.2
φ' [°]	36.5	36-37	28	38	37-39	35	-	-
c' [kPa]	1	0	0	30	0-30	0	-	-
σ_t [kPa]	1			30			-	-
λ [W/(mK)]	2.26			2.26			0.655	1.12
c_p [J/(kgK)]	1209			1209			1184	876
α_{th} [1/K]	$1 \cdot 10^{-5}$			$1 \cdot 10^{-5}$			$1 \cdot 10^{-5}$	$1 \cdot 10^{-5}$

A=This work; B=From Barla and Barla (2012); C=Design of Turin ML1 SE.

Table 6.11: Numerical modelling calculation stages.

Stage 1	Geometry creation Material properties assignment Initial geostatic stress state with groundwater table at a depth of 12.4 m and surface loads of 10 kPa (presence of the street between $x=-5$ and $x=10$ m) Reset of displacements and velocities
Stage 2	Excavation simulation by removing the elements within the excavation boundary and applying a gradually decreasing internal pressure until 20% of the initial state of stress (different trials were made, including stress release until 40% and 30%): <ul style="list-style-type: none"> ▪ Internal pressure p_i equal to $1 \cdot p_0$ (stress release factor $\lambda=0$) ▪ Internal pressure p_i equal to $0.9 \cdot p_0$ (stress release factor $\lambda=0.1$) ▪ Internal pressure p_i equal to $0.8 \cdot p_0$ (stress release factor $\lambda=0.2$) ▪ ... ▪ Internal pressure p_i equal to $0.2 \cdot p_0$ (stress release factor $\lambda=0.8$)
Stage 3	Activation of grout (fresh-state properties) and lining elements Further 10% stress release
Stage 4	Change of grout properties to its hardened state Complete stress release

Stage 5	Definition of thermal properties (Table 6.10) Assignment of initial temperatures Uncoupled thermo-mechanical simulation (nothing occurs in this stage, which is useful to define the starting thermal point)
Stage 6	Reset of displacements Assignment of temperatures corresponding to a certain timeframe Uncoupled thermo-mechanical simulation to assess the induced variation in the stress-strain state

6.4.2. Mechanical analysis

The tunnel excavation was modelled with the aim to obtain a representative initial state of stress both in the ground and in the tunnel lining. As mentioned, this was possible thanks to the convergence-confinement method (Panet, 1995). Later, this will be relevant to make a comparison between the purely thermally induced effects and the state of stress at the end of the excavation.

First, the geostatic state of stress was reproduced. The results obtained at the end of stage 1 are depicted in Figure 6.28. Then, the elements within the tunnel excavation, inside a circle of radius 3.74 m, were removed. Initially, the nodes on the boundary were fixed in both x and y directions and one step was performed to develop nodal reaction forces. These forces were then applied equal in value and opposite in sign, after freeing the nodes (stage 2). It was verified that no changes took place in this stage, as the internal pressure balances the earth pressure. Then the nodal forces were progressively reduced to 20% of their initial values. The 14 rows of elements within the excavation were activated by attributing the injection and the lining elements fresh grout and concrete properties respectively (stage 3). Afterwards, the nodal forces were reduced to 10% and the injection elements properties were modified into those pertaining to the hardened state. Finally, in stage 4, the nodal forces were reduced to zero.

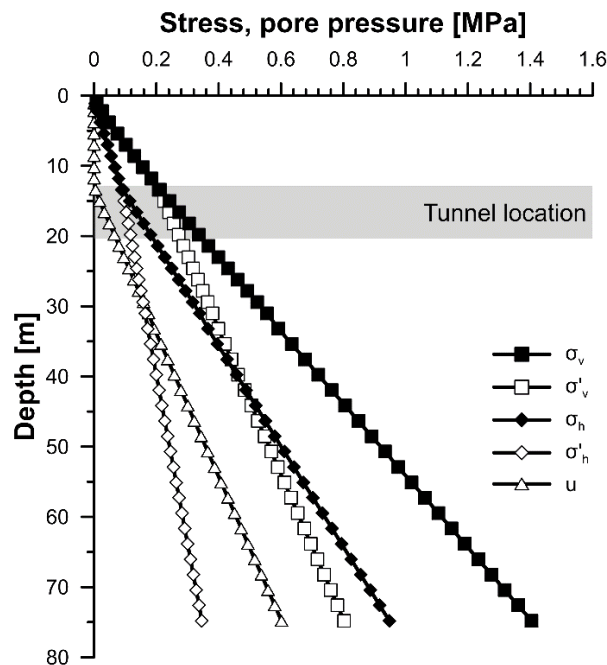


Figure 6.28: Geostatic state of stress at the end of Stage 1 along any vertical axis.

The amount of relieved excavation forces prior to lining installation was selected to match the lining axial stress and the surface settlements observed in situ (cfr. par. 6.2.1 and 6.2.2, see Figure 6.29 and Figure 6.30). As shown in Figure 6.29 at the end of the excavation the radial stresses range between -0.08 and 0.08 MPa, whereas the hoop stresses between -1.4 and 0.4 MPa (the crown intrados results slightly in tension). Figure 6.30 shows the matching between calculated and measured in situ surface settlements considering a stress release factor of 0.8.

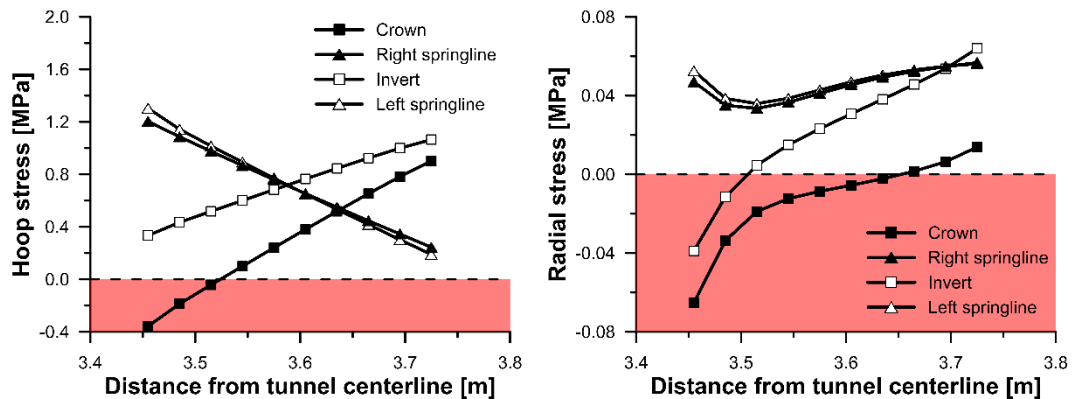


Figure 6.29: State of stress in the tunnel lining at the end of the excavation.

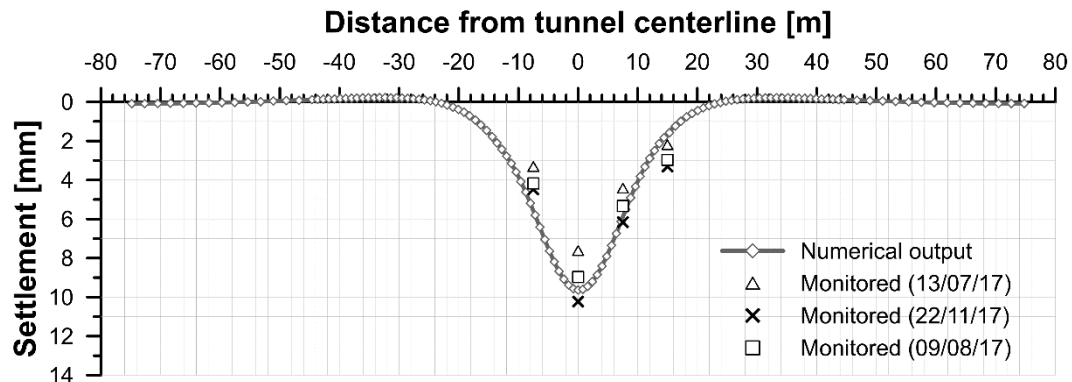


Figure 6.30: Computed and monitored surface settlements at the end of the excavation.

6.4.3. Thermo-mechanical analysis

6.4.3.1. Methodology

In this paragraph the methodology followed for the evaluation of the lining thermally induced mechanical effects is described. To this aim, the nodal temperatures obtained throughout the domain of the TH model in Chapter 5 were used. Indeed in 5.3 the construction of a 3D coupled TH model was described. Some of the prototype tests in Table 4.6, in particular GH5, GH6, GH8, GC1 and AH2, were simulated by imposing pipes inlet temperature, tunnel temperature, surface air temperature and fluid velocity equal to the measured ones. Good agreement between computed and monitored outlet temperatures from the energy tunnel prototype was obtained, as shown in Figure 5.11 and Figure 5.12. The satisfactory matching

led us to make use of the resulting temperatures throughout the domain over time with a high degree of confidence. For this reason, instead of performing a new thermo-hydraulic analysis within FLAC, the idea was to export temperature data from the FEFLOW software at specific timeframes. Under the assumption of thermoelastic behaviour of all materials this is justifiable, as the intermediate steps will not affect the stress-strain behaviour, only dependent in this case on the final temperature state and not on the path followed.

To achieve this task, a procedure to export temperatures from FEFLOW and import them within FLAC was specifically developed by the Author and repeated as many times as the number of timeframes and of vertical cross sections we were interested in. For example, for test GH5 the procedure was repeated four times: twice, at the beginning ($t=0$) and at the end of the test ($t=t_{fin}$), and again twice, in two different vertical cross sections. The cross sections, in the case of simulation of experimental tests, were the one where strain gauges were located (at a longitudinal distance of 15 cm from the adjacent non-energy ring) and the one where pressure cells were located (at mid-thickness). The procedure included several steps, that are summarized in Figure 6.31.

The first steps involved the choice of cross sections n_1, n_2, \dots and times t_1, t_2, \dots in the thermo-hydraulic model. Nodal coordinates and temperatures were exported to an Excel file for each cross section and time. On the other hand, nodal coordinates and indices were also exported from the FLAC model. All data were then converted into a .dat file.

Now that all the needed material is ready, the .dat files can be imported within an open source GIS software, which was used as a platform able to let two different softwares, from different softwarehouses, communicate with each other. The datafiles are imported as delimited text. Tables with attributes such as coordinate x and y , indices i and j and temperature are created. The temperature attribute is missing for the table pertaining to the nodes of the FLAC mesh and this is exactly what we are searching for. However, it should be reminded that the TH model discretization grid is different from the TM model one (Figure 5.7 and Figure 6.26). For this reason, an intermediate interpolation step was performed.

Given that the temperature field is known at specific points, corresponding to the TH mesh, the first thing to do is to interpolate it with the aim to create a raster map that is continuous over the domain, which has the same size for the two models. The TIN interpolation option is used, available in the GIS software.

Once the raster map is available, temperature values in correspondence of the TM nodes location can be extracted and associated as an additional attribute. A column is added to the table of FLAC nodes and indices, corresponding to temperature. This new attribute can be exported back to a datafile and can be used as a table readable by FLAC. Indeed, thanks to a user-defined routine written in the FISH language, the nodal temperatures can be imported in the TM model at the end of the mechanical-only simulation of the excavation process.

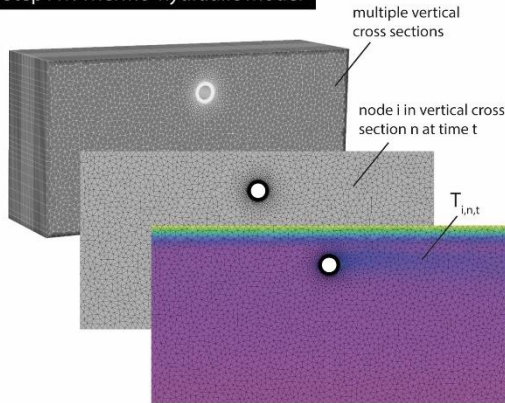
A couple of examples of the results obtained at the end of this procedure can be appreciated in Figure 6.32. It is anticipated that in the following thermally induced effects will be evaluated not only at the end of the experimental tests performed (GH5, GH6, GH8, GC1, AH2), but also at the end of the heating and cooling season for long term operation (see 6.4.3.3). Figure 6.32 refers to the latter case and shows the great level of accuracy reached thanks to the methodology described above.

Knowing the temperature field at $t=0$, for which the state of stress at the end of the excavation was considered as known, the temperature field at $t=t_{fin}$ is imported in the TM model and the corresponding induced thermal stresses can be assessed by means of an uncoupled thermo-mechanical computation until reaching mechanical equilibrium.

Beyond mechanical properties, thermal input parameters are required such as thermal conductivity, specific heat capacity and linear thermal expansion coefficient, as shown in Table

6.10. Thermal conductivity and specific heat capacity are consistent with those adopted in Chapter 5. It is reminded that heat flow meter tests were carried out on concrete specimens (see 5.3), while grout conductivity was calibrated to match the thermal performance observed in situ.

Step A1. Thermo-hydraulic model

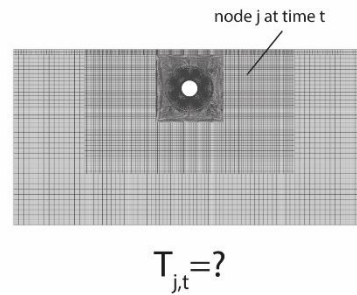


In cross sections n_1, n_2, \dots
 - export of nodal temperatures for t_1, t_2, \dots
 - export of nodes coordinates (x,y)



All data converted to a .dat file

Step A2. Thermo-mechanical model

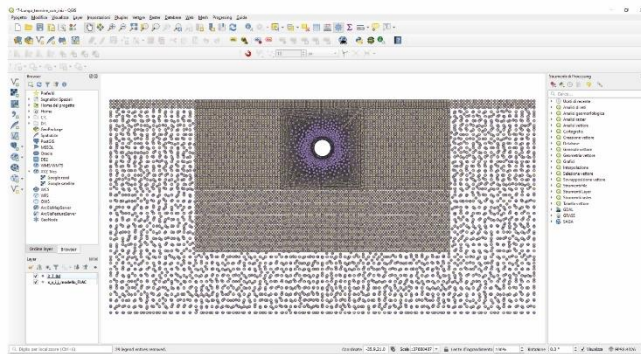


FISH routine to get nodes coordinates and indices



All data converted to a .dat file

Step B. Open source GIS software



- 1 Import of the .dat files
- 2 Linear TIN interpolation of temperatures
- 3 Raster temperature values added as an attribute to the shape given by the TM model mesh
- 4 Export of temperature as an additional attribute of the TM model mesh



$T_{j,t}$

Step C. Thermo-mechanical model



FISH routine to assign temperatures to all nodes and thermo-mechanical uncoupled simulation

```
def assign_temperature
size = table_size(1)
loop s(1,size)
i_coord=xtable(1,s)
j_coord=ytable(1,s)
temperature=xtable(2,s)
command
fix temp _temperature i i_coord j j_coord
endcommand
endloop
end
assign_temperature
```

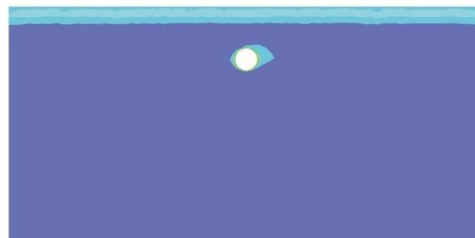


Figure 6.31: Conceptual scheme of the steps needed to import the temperature field from FEFLOW to FLAC.

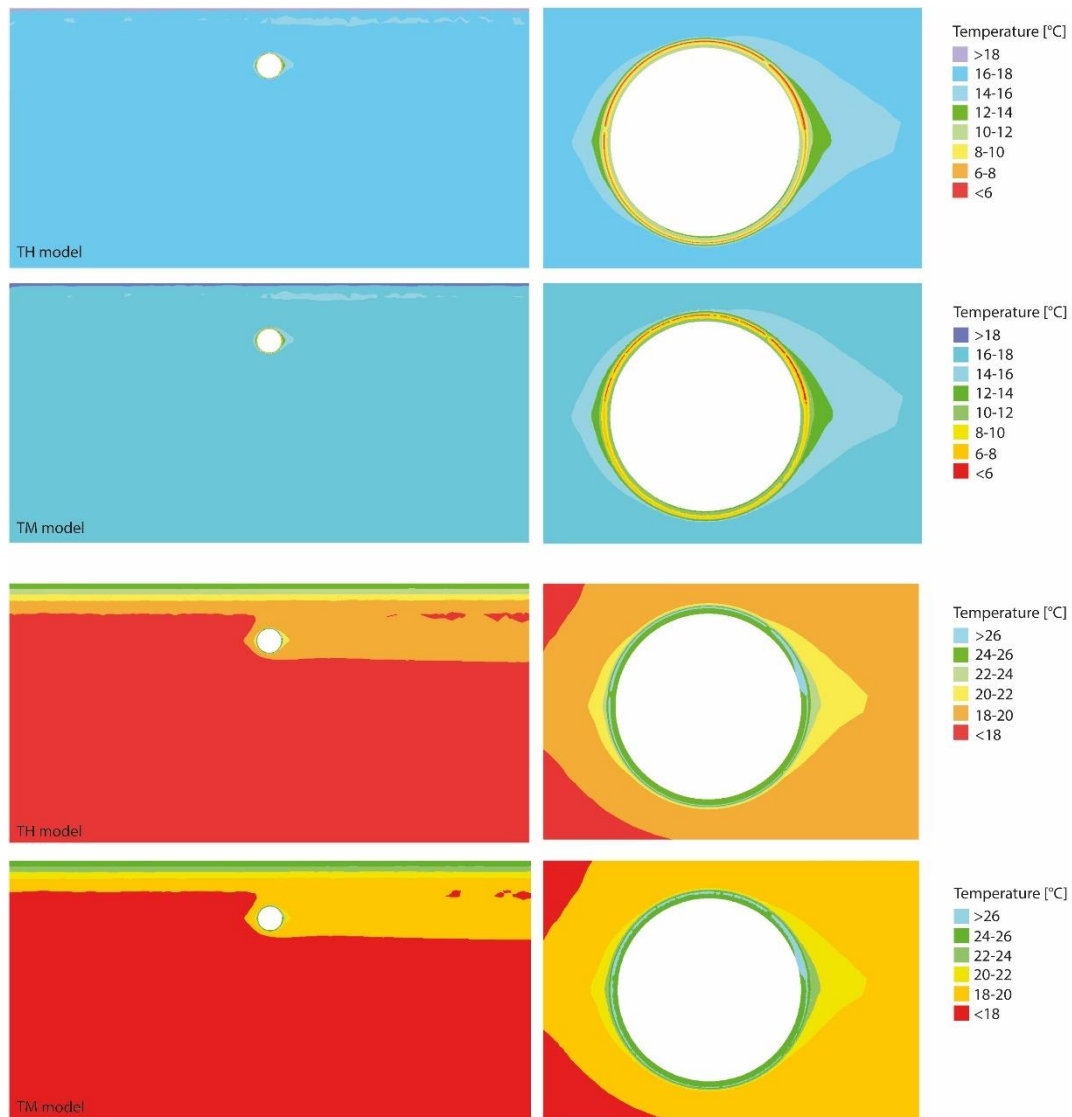


Figure 6.32: Matching of the temperature field at the end of heating and cooling season for long term operation in the TH and TM model.

6.4.3.2. Simulation of experimental tests

The computed total and thermally induced radial and hoop stresses and the thermally induced hoop strains at the end of the simulation of the heating test GH8 and the cooling test GC1 are shown in Figure 6.33 and Figure 6.34 respectively. The sign convention is the same as the one for experimental results: positive strains indicate contraction and positive stresses indicate an increase in compression. Compared to Figure 6.29, where hoop stress were characterized by a quasi linear distribution, thermal actions produce a nonlinear variation of the state of stress across the lining thickness. Table 6.12 summarizes the results for all tests and compares them to the experimental data. As it can be seen, no significant variation in radial stress occurs (<0.1 MPa) neither for heating nor cooling, which is different from what was observed experimentally. Hoop stresses at mid-thickness are compatible in the numerical

simulations and in the experiments and indicate a decrease in compression for the heating test (between 0.08 and 0.42 MPa in the numerical simulation and between 0.02 and 0.26 MPa in the experiment) and an increase in compression for the cooling test (between 0.4 and 0.58 MPa in the numerical simulation, but between 2.5 and 3.9 MPa in the experiment). The direction and amount of strains variation is also consistent, as extension is obtained upon cooling and contraction upon heating both at the extrados and at the intrados. However, strains obtained numerically result in all cases higher than the experimental outcomes, from two to peaks of six times.

Table 6.13 reports the convergences along a horizontal and a vertical axis both at the extrados and at the intrados of the concrete lining. Values in the order of 1 mm are shown, inward upon cooling (negative values, winter mode) and outward upon heating (positive values, summer mode). Inward convergences also occur upon operation of the air circuit (test AH2).

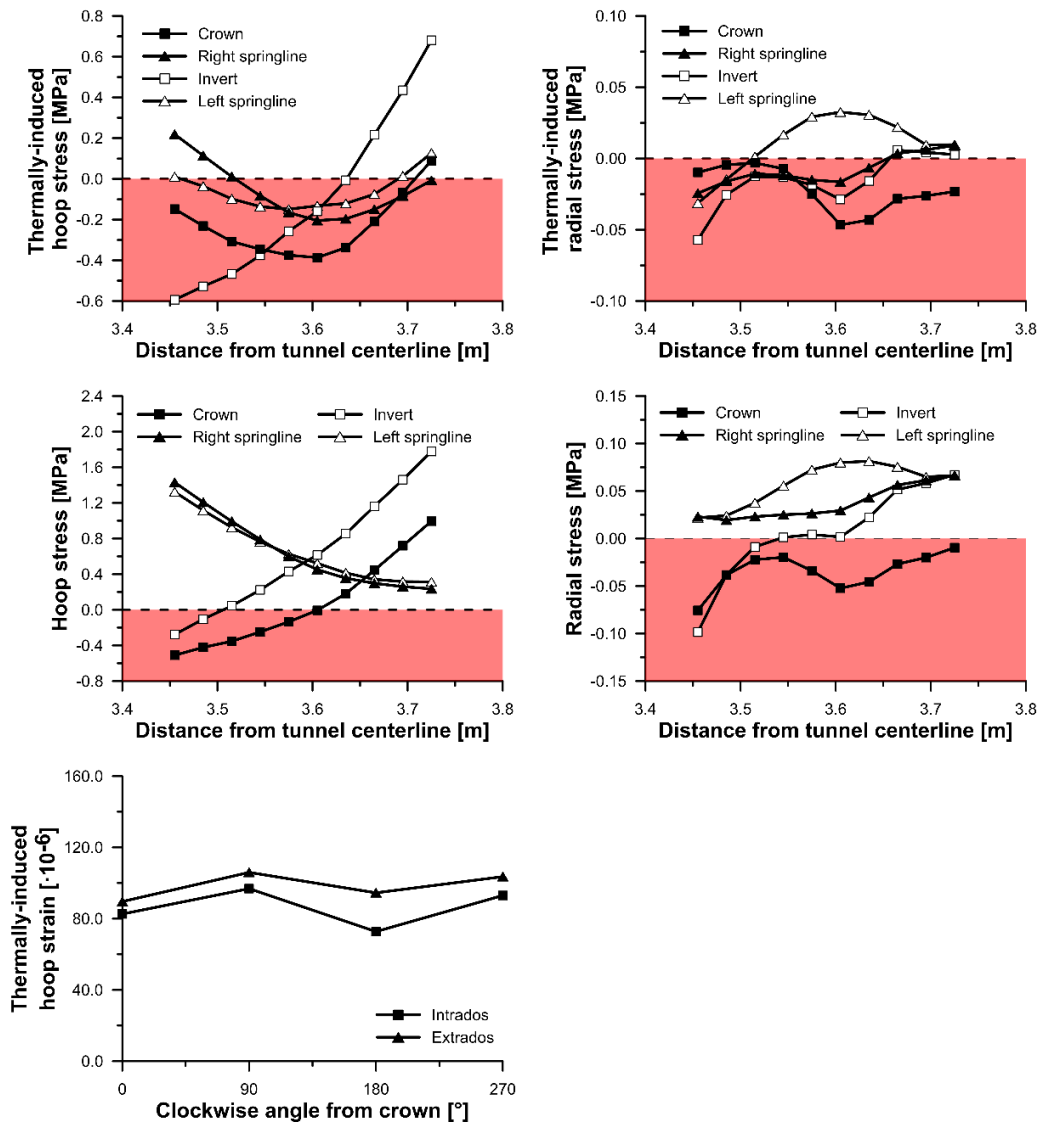


Figure 6.33: Computed hoop strains and stresses at the end of test GH8.

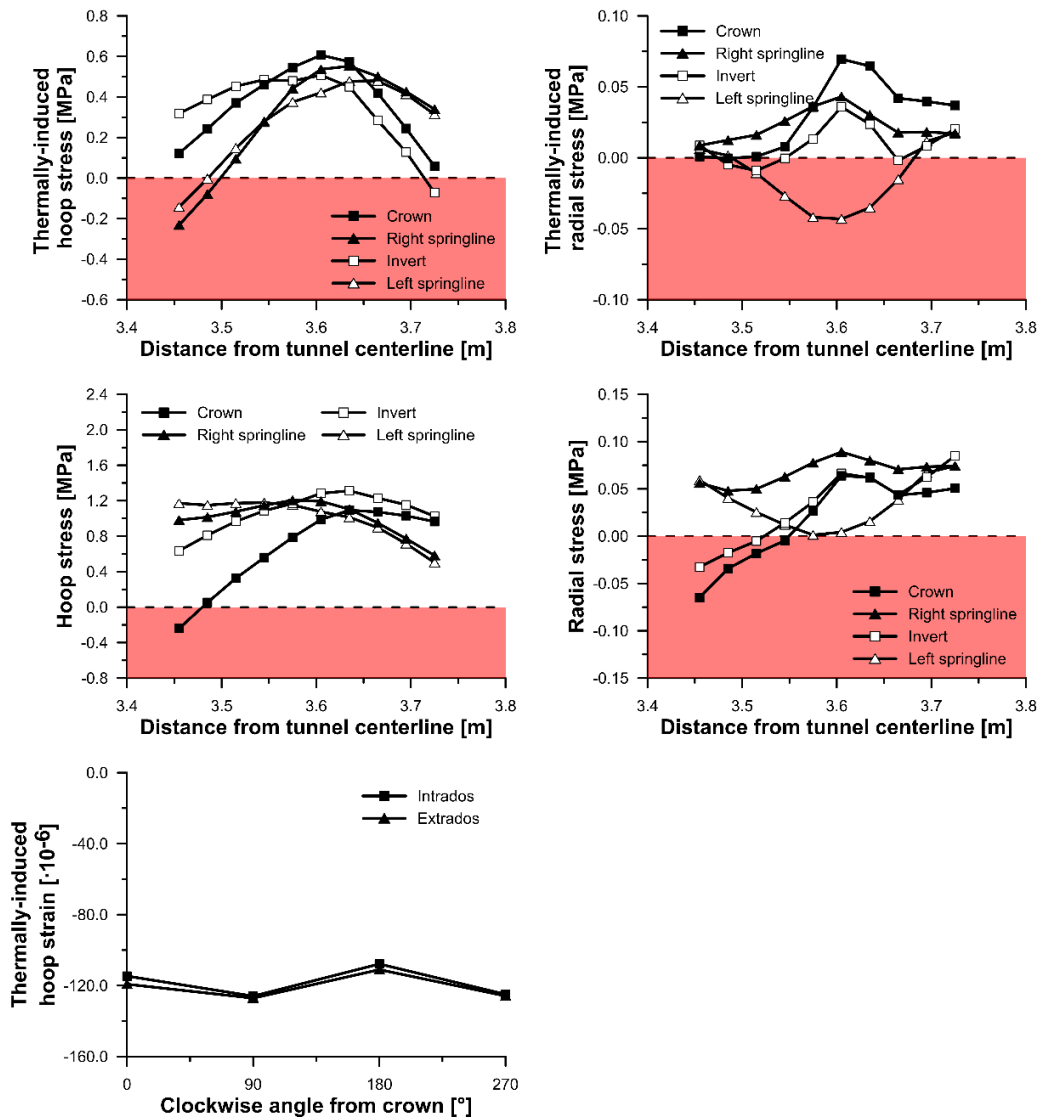


Figure 6.34: Computed hoop strains and stresses at the end of test GC1.

Table 6.12: Comparison between experimental and numerical results.

	Experimental tests			Numerical modelling		
	σ_{rad} [MPa]	σ_{hoop} [MPa]	ϵ_{hoop} [$\mu\epsilon$]	σ_{rad} [MPa]	σ_{hoop} [MPa]	ϵ_{hoop} [$\mu\epsilon$]
GH5	-0.09 \div -0.05	-0.06 \div -0.02	-21.2 \div -10.2	-0.04 \div 0.03	-0.42 \div -0.17	-128.9 \div -87.2
GH6	-0.31 \div -0.14	-0.16 \div -0.14	-33.4 \div -24.8	-0.04 \div 0.03	-0.41 \div 0.17	-118.5 \div -81.4
GH8	-0.44 \div -0.22	-0.26 \div -0.21	-40.6 \div -30.2	-0.04 \div 0.03	-0.38 \div -0.14	-106.0 \div -72.8
GC1	2.52 \div 3.14	3.20 \div 3.92	53.2 \div 59.9	-0.04 \div 0.05	0.40 \div 0.58	107.8 \div 127.1
AH2	-0.61 \div -0.33	-0.48 \div -0.35	-34.5 \div -29.6	-0.02 \div 0.10	-0.20 \div -0.08	-17.7 \div -6.3

Table 6.13: Convergences obtained numerically at the lining intrados and extrados.

	Extrados convergence		Intrados convergence	
	Crown-invert	Right-left springline	Crown-invert	Right-left springline
GH5	-1.24 mm	-0.64 mm	-1.17 mm	-0.57 mm
GH6	-1.14 mm	-0.61 mm	-1.08 mm	-0.54 mm
GH8	-1.04 mm	-0.51 mm	-0.99 mm	-0.45 mm
GC1	0.98 mm	0.82 mm	0.90 mm	0.74 mm
AH2	-0.11 mm	-0.10 mm	-0.10 mm	-0.09 mm

Based on these results, convergences, deformed lining boundaries and internal forces acting on the lining were calculated and compared to the as-constructed case. The deformed boundaries shown in Figure 6.35 demonstrate that the thermal activation of the lining provides an additional 1.24 mm convergence with respect to the as-constructed case (+0.017%), which is of the same order of magnitude of what was found by Nicholson et al. (2014). Indeed, they investigated the stress in the concrete segments and the surrounding ground by building a coupled thermo-mechanical three-dimensional FE model in London clay. The analyses were carried out for heat extraction rates from 0 (no heat extraction) to 30 W/m². In the case of heat extraction, it can be noted a further 1 mm deformation compared to the no heat extraction case, as shown in Table 6.14.

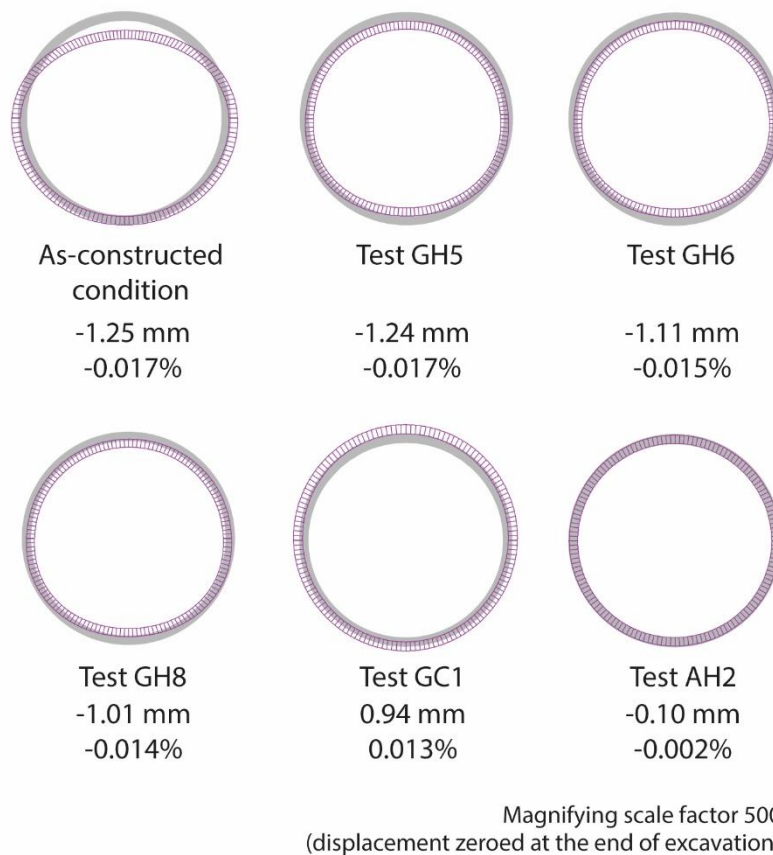


Figure 6.35: Deformed lining at the end of the excavation phase and at the end of experimental tests with indication of maximum convergences (additional convergences with respect to the end of excavation are shown for all the tests).

Table 6.14: Thermal effect on tunnel diameter change (modified from Nicholson et al. 2014).

Simulation stage	Crown-invert [mm]	Crown-invert [%]	Axis level [mm]	Axis level [%]
Summer (no heat extraction)	0.1	0.00	-1.1	-0.02
Winter (no heat extraction)	-0.5	-0.01	-1.6	-0.03
Summer (30 W/m ² heat extraction)	0.3	0.00	-1.9	-0.03
Winter (30 W/m ² heat extraction)	-0.6	-0.01	-2.6	-0.04

Internal forces were computed as the sum of the contribution at the end of excavation and of the thermo-mechanical one, multiplied by the length of the ring:

$$N_d = (1.3 \cdot N_{k,mech} + 1.5 \cdot \Delta N_{k,th-mech}) \cdot 1.4 \quad \text{Eq. 6.16}$$

$$M_d = (1.3 \cdot M_{k,mech} + 1.5 \cdot \Delta M_{k,th-mech}) \cdot 1.4 \quad \text{Eq. 6.17}$$

$$V_d = (1.3 \cdot V_{k,mech} + 1.5 \cdot \Delta V_{k,th-mech}) \cdot 1.4 \quad \text{Eq. 6.18}$$

The obtained design values are given in Table 6.15 and internal forces diagrams are shown in Figure 6.36. Thermal actions lead to an increase of axial force in summer and to a decrease in winter. Slight changes in bending moment and shear force occur in correspondence of pipes location.

Table 6.15: Triplets of internal forces at the end of excavation and of the simulated tests needed for ULS verifications.

	Condition	N _d [kN]	M _d [kNm]	T _d [kN]
As-constructed condition	N _{max}	421.2	0.3	-2.9
	M _{max +}	359.5	-22.8	-8.5
	M _{max -}	160.8	19.2	-2.8
	T _{max +}	279.6	-10.3	-23.5
	T _{max -}	300.2	-13.1	23.7
GH5	N _{max}	404.0	-15.6	-11.2
	M _{max +}	231.6	-25.2	-23.2
	M _{max -}	312.7	43.4	-11.7
	T _{max +}	227.8	-20.7	-39.2
	T _{max -}	169.6	-5.6	36.0
GH6	N _{max}	403.9	-16.9	-11.2
	M _{max +}	234.3	-27.1	-24.0
	M _{max -}	316.4	39.9	-11.9
	T _{max +}	230.3	-22.6	-39.3
	T _{max -}	173.3	-7.4	35.6
GH8	N _{max}	407.0	-20.6	-3.5
	M _{max +}	241.6	-30.5	-25.8
	M _{max -}	324.7	33.9	-11.2
	T _{max +}	237.1	-26.0	-40.4
	T _{max -}	177.5	-10.2	36.1
GC1	N _{max}	638.2	12.4	1.8
	M _{max +}	547.9	-15.3	6.6
	M _{max -}	432.6	26.6	-0.9
	T _{max +}	543.2	-2.7	-30.6
	T _{max -}	483.7	-4.4	20.1
AH2	N _{max}	404.3	1.3	3.2
	M _{max +}	333.4	-19.6	1.6
	M _{max -}	123.6	21.8	-3.7
	T _{max +}	275.0	-11.6	-35.7
	T _{max -}	208.4	6.6	31.4

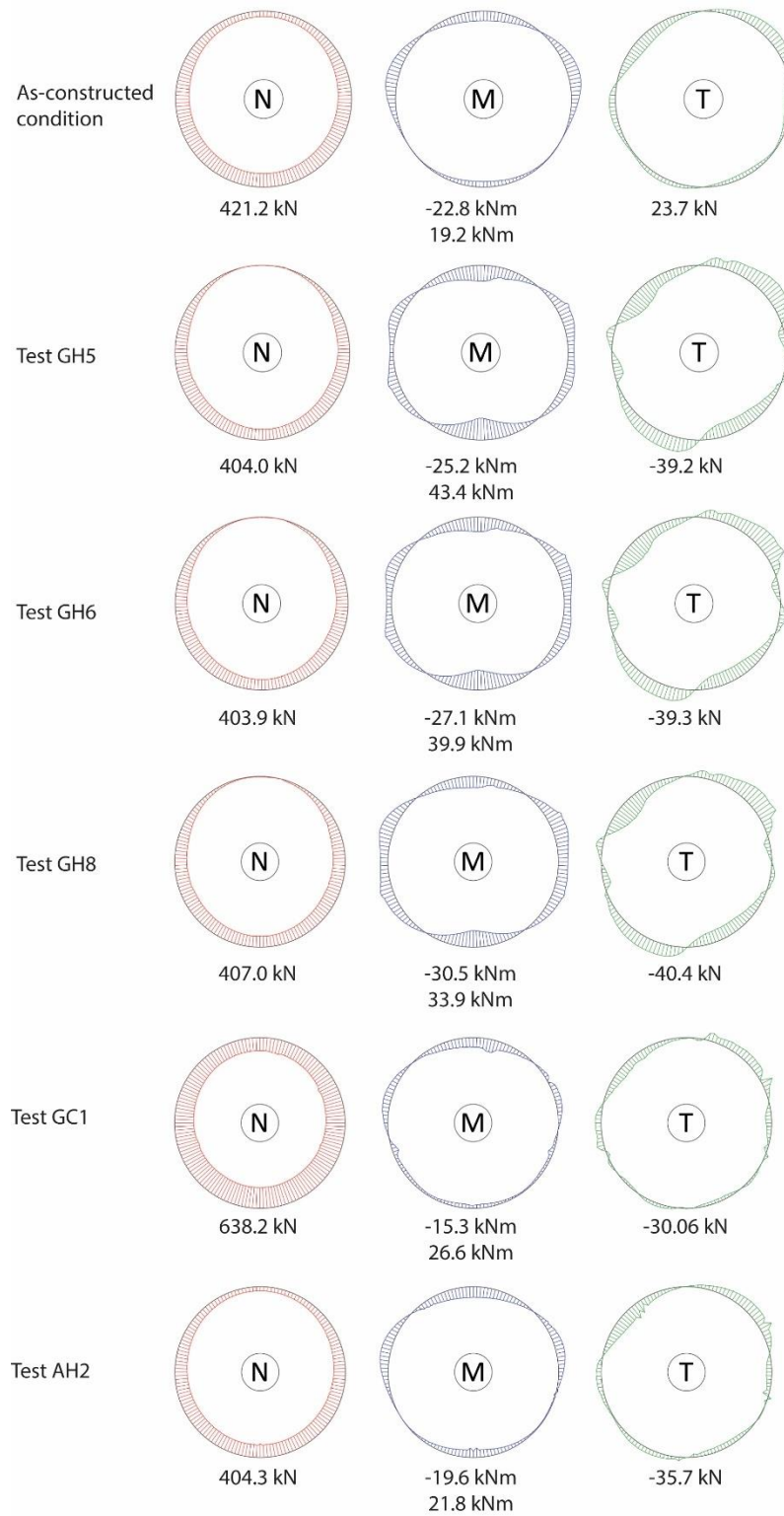


Figure 6.36: Internal actions at the end of the excavation phase and at the end of the simulated tests with indication of maximum values.

6.4.3.3. Simulation of long-term operation

Apart from thermal activation, a natural temperature oscillation can be observed within metro tunnels. This oscillation has, itself, an intrinsic effect on thermal stresses in the lining. The question one should ask is whether natural thermal stresses are or not comparable to induced thermal stresses in the case of energy tunnels in terms of additional solicitations. If yes, there will be no need to perform further limit state verifications.

The intent of this section is to try to give an answer to that question. For this reason, two numerical models will be presented, identical as geometry and thermo-hydro-mechanical properties, but one does not include thermal activation (model A) and one does (model B). Hence thermo-hydraulic boundary conditions differ for that pertaining to the geothermal circuit. Figure 6.37 depicts the external and tunnel temperature monitoring data available in a shaft close to Lingotto (existing metro tunnel, closest section to South Extension where data are available) and the corresponding sinusoidal interpolation series that were set in the numerical analyses as boundary condition in both models A and B (temperature boundary conditions for external air, heat transfer boundary condition for tunnel air with heat transfer coefficient $1.77 \text{ W}/(\text{m}^2\text{K})$). Figure 6.38 focuses on theoretical operation of the geothermal circuit referred to model B only.

The analyses consider a timespan of ten years, starting from October 15th, first day of the heating season according to the climatic classification in Turin (D.P.R. 412 del 26 Agosto 1993). The initial temperature field was obtained by initializing the model with an initial ground temperature of 17.3°C and air temperature applied at the top boundary for ten years. During the initialization stage, no boundary conditions were applied at the tunnel contour, as if the tunnel was not there and thermal activation started immediately after its construction. Groundwater flow of 1.5 m/d was taken into account in the analyses, that were performed by following the methodology described in 6.4.1.

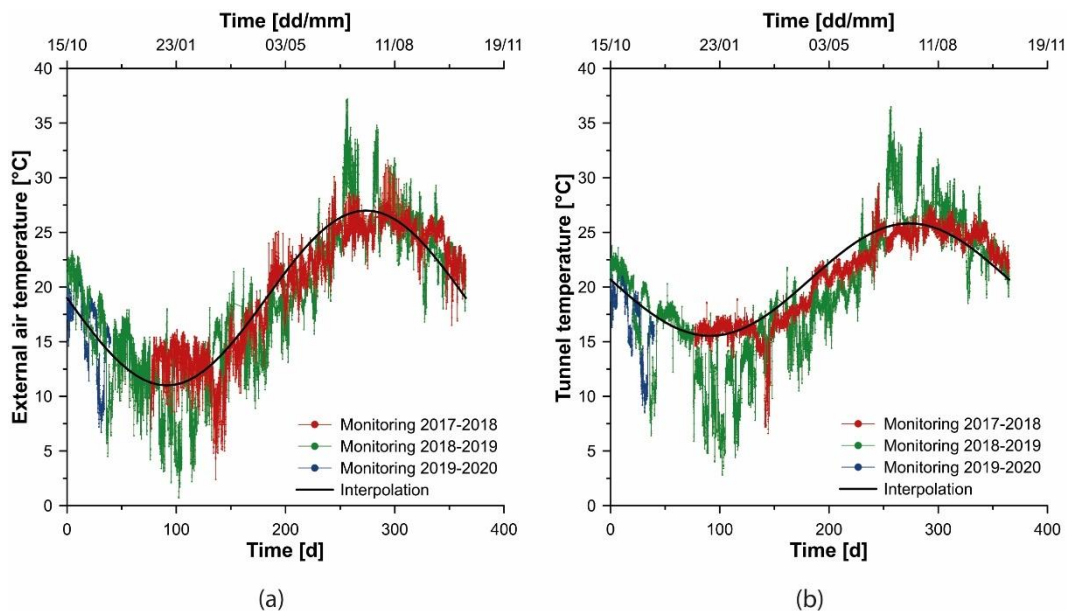


Figure 6.37: Monitoring data and sinusoidal interpolation for (a) external air and (b) tunnel air temperature.

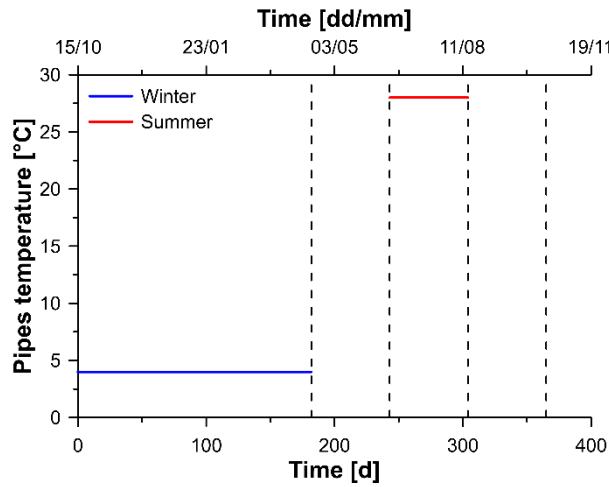


Figure 6.38: Geothermal circuit inlet temperature in model B over one year.

Thermally induced stresses and strains were evaluated at four representative timeframes, that is at the end of the heating season and at the end of the cooling season both during the first and the tenth year of operation. The reason lies in the interest to investigate heating and cooling effects and to perceive the possible differences in the short and in the long term. Of course, the presence of groundwater flow plays a favorable role, by restoring cyclically the same yearly thermal conditions.

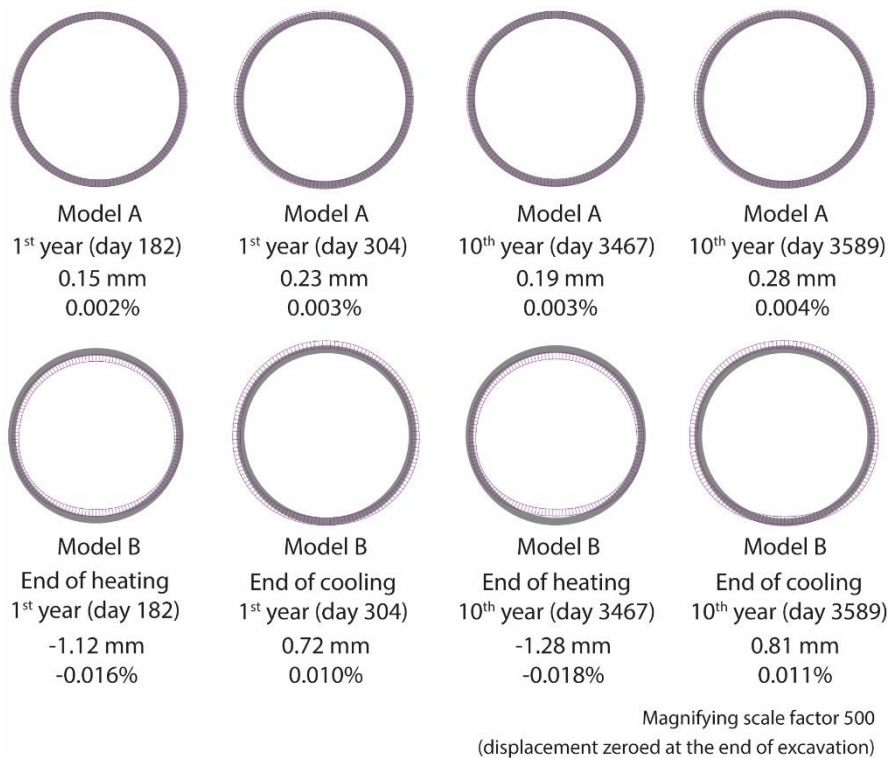


Figure 6.39: Deformed lining for models A (first row) and B (second row) at specific timeframes with indication of maximum convergences (additional convergences with respect to the end of excavation are shown).

This can be clearly seen in Figure 6.39, Figure 6.40 and Figure 6.41 where very similar convergences and internal actions are pointed out for the same model at the same time of the year, whether it is in the short or in the long term. Nevertheless, there are some quite evident differences between model A and B for equal timeframes. For instance, at the end of the winter season the sole tunnel air temperature results in negligible convergences of 0.15 mm and 0.19 mm. With thermal activation values of -1.12 and -1.28 mm are reached. Albeit very limited, they are six times those in absence of thermal activation and comparable to those obtained at the end of the excavation. In summer the amplification is even lower as the convergence in model B is only 3 times that in model A.

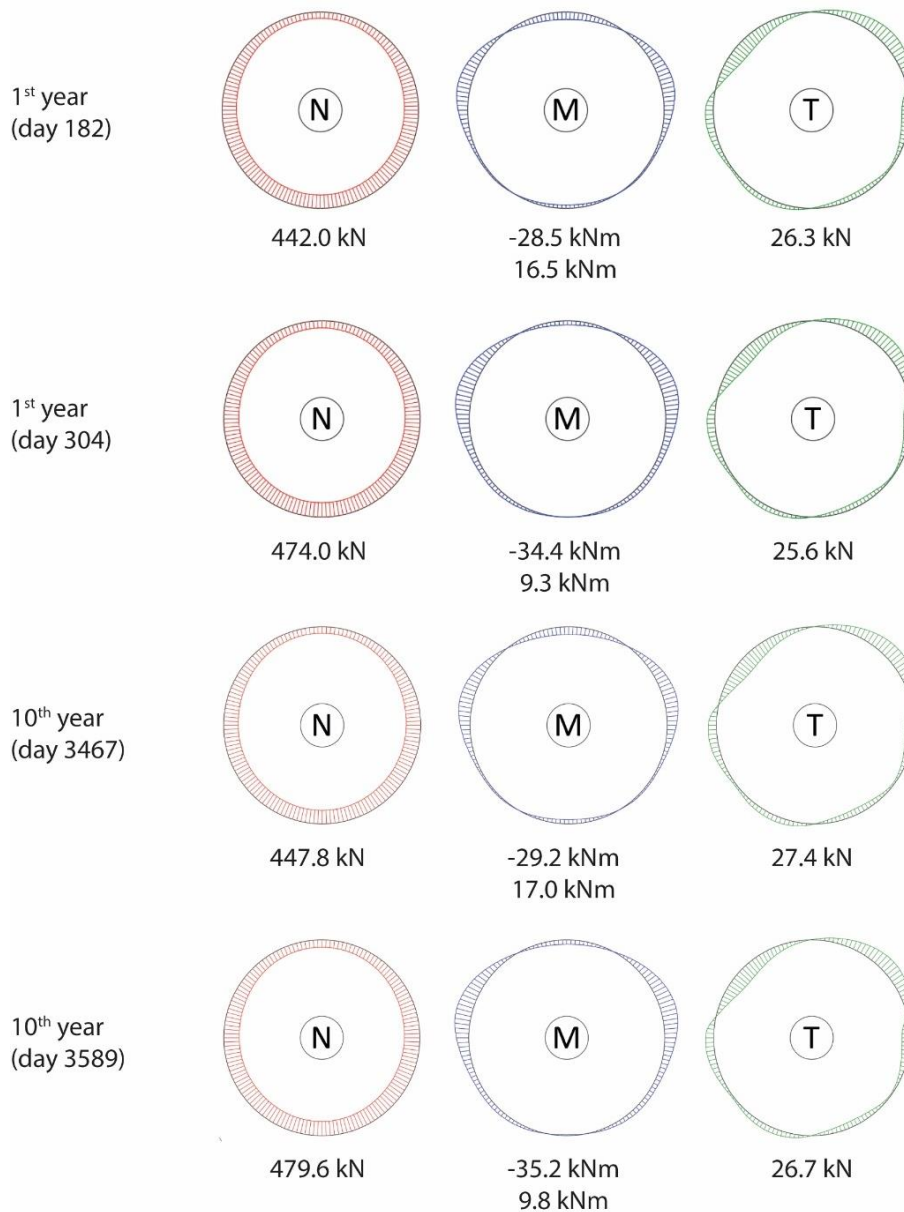


Figure 6.40: Internal actions acting within the energy lining for model A at different timeframes with indication of maximum values.

Internal actions are also different in trend and as maximum values. If in model A axial force is substantially constant all year round, oscillations are highlighted in model B, up to values of 737.8 kN in summer. The trend of both bending moment and shear force changes and becomes more irregular depending on the position of the pipes. Hence, it appears that limit state verifications cannot be neglected.

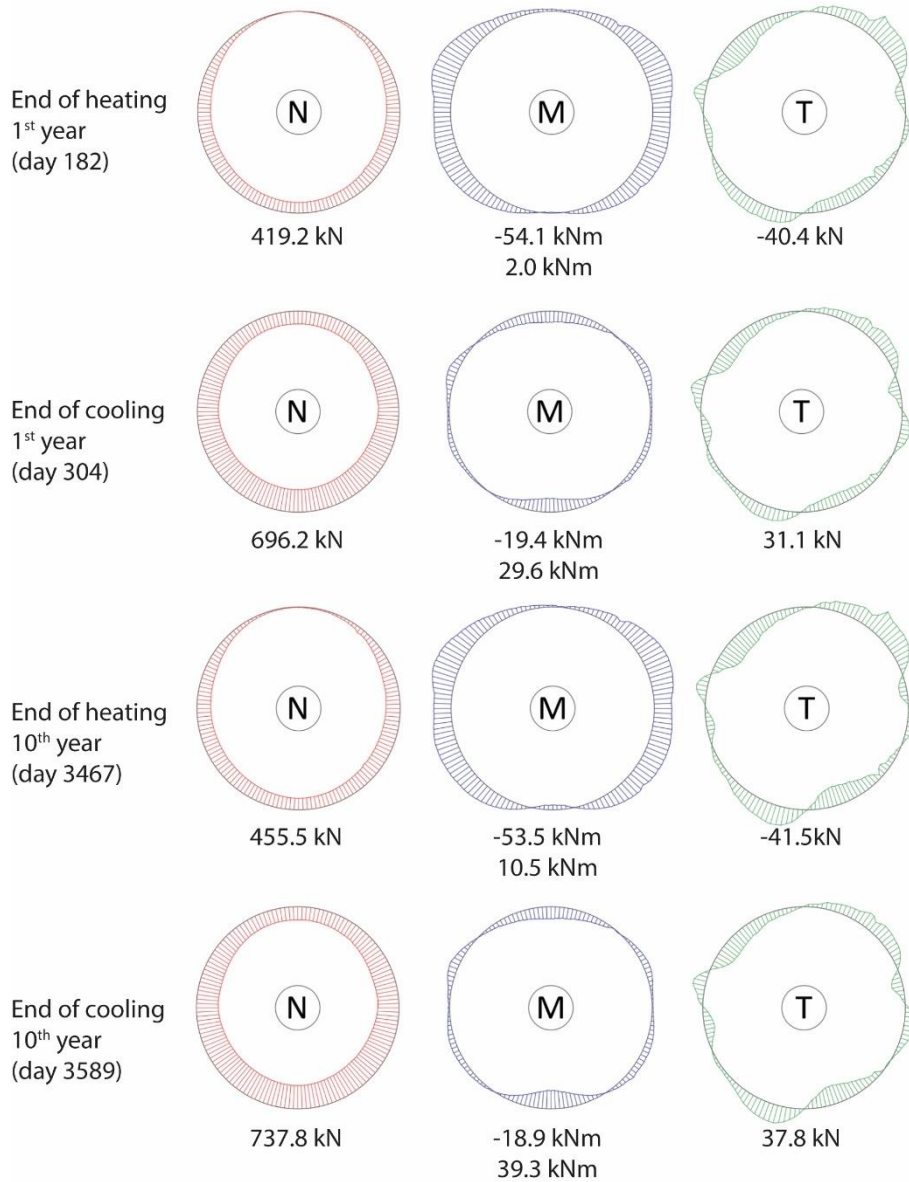


Figure 6.41: Internal actions acting within the energy lining for model B at different timeframes with indication of maximum values.

As in 6.4.3.2, the most severe combinations of axial force N , bending moment M and shear force T (expressed in terms of design values) corresponding to maximum axial force, maximum/minimum bending moment and maximum/minimum shear force are listed in Table 6.16.

Table 6.16: Triplets of internal forces at specific timeframes of model A and B for ULS verifications.

	Condition	N_k [kN]	M_k [kNm]	T_k [kN]
Model A 1 st year Day 182	N_{\max}	442.0	-3.0	3.1
	$M_{\max +}$	408.3	-28.5	-0.2
	$M_{\max -}$	186.4	16.5	-3.1
	$T_{\max +}$	317.4	-14.9	-25.8
	$T_{\max -}$	340.6	-18.3	26.3
Model A 1 st year Day 304	N_{\max}	474.0	-9.7	2.1
	$M_{\max +}$	434.6	-34.4	-0.7
	$M_{\max -}$	217.4	9.3	-3.1
	$T_{\max +}$	345.8	-21.1	-24.7
	$T_{\max -}$	368.7	-24.8	25.6
Model A 10 th year Day 3467	N_{\max}	447.8	-4.1	5.6
	$M_{\max +}$	418.9	-29.2	-0.6
	$M_{\max -}$	190.5	17.0	-3.3
	$T_{\max +}$	324.5	-14.6	-26.6
	$T_{\max -}$	329.4	-13.5	27.4
Model A 10 th year Day 3589	N_{\max}	479.6	-10.1	2.2
	$M_{\max +}$	445.6	-35.2	-1.0
	$M_{\max -}$	221.5	9.8	-3.2
	$T_{\max +}$	353.5	-20.9	-25.5
	$T_{\max -}$	358.4	-20.2	26.7
Model B 1 st year Day 182	N_{\max}	419.2	-42.4	4.7
	$M_{\max +}$	313.1	-54.1	-18.8
	$M_{\max -}$	308.6	2.0	-10.5
	$T_{\max +}$	137.7	-21.4	-40.4
	$T_{\max -}$	209.1	-41.4	35.8
Model B 1 st year Day 304	N_{\max}	696.2	-1.8	10.8
	$M_{\max +}$	587.4	-19.4	12.5
	$M_{\max -}$	657.1	29.6	2.0
	$T_{\max +}$	672.8	19.0	-26.7
	$T_{\max -}$	547.3	-10.2	31.1
Model B 10 th year Day 3467	N_{\max}	455.5	-36.5	8.2
	$M_{\max +}$	346.2	-53.5	2.9
	$M_{\max -}$	331.6	10.5	9.1
	$T_{\max +}$	152.3	-22.0	-41.5
	$T_{\max -}$	362.6	-9.2	39.3
Model B 10 th year Day 3589	N_{\max}	737.8	-7.7	11.6
	$M_{\max +}$	604.9	-18.9	3.0
	$M_{\max -}$	678.8	39.3	1.2
	$T_{\max +}$	702.3	23.5	-37.8
	$T_{\max -}$	701.4	24.4	37.8

To have a complete view of the phenomena involved by thermal activation process, the profile of surface settlements was also evaluated at specific timeframes (end of heating and end of cooling season during the first and the tenth year of operation), as shown in Figure 6.42. As highlighted in the picture, the effect on ground surface is extremely marginal given that the maximum settlement difference between model A and model B results about 0.4 mm during the winter, that is less than one tenth those induced by the excavation. Hence, consequences on the built environment is negligible. No differences can be seen after ten years of operation compared to the first year, due to the favourable groundwater flow. The existence of a settlement or slight uplift downstream is due to the higher or lower temperature of the thermal plume. The general uplift or settlement of the ground surface is mainly due to the fictitious shrinkage or swelling of the soil mass due to thermal variations applied on top.

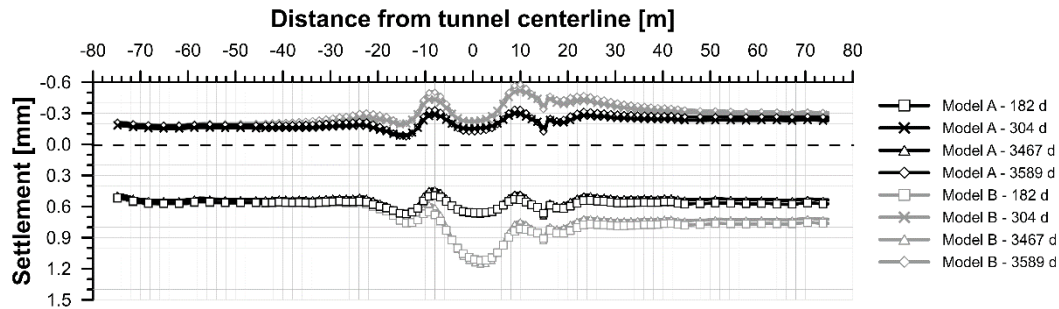


Figure 6.42: Computed surface settlements at different timeframes of model A and model B.

6.5. ULS and SLS design verifications

The aim of mechanical design is to verify that the geometrical parameters and material properties of the energy tunnel are sufficient to meet the structural requirements while allowing for shallow geothermal energy utilization. Hence, thermal loading can be treated as an additional variable action or an effect of this variable action that has to be subjected to a supplementary verification. Indeed, it has to be reminded that an action is not only a set of loads applied to a structure (direct action), but also a set of imposed deformations caused for example by temperature changes (indirect action or “coactions”, as defined by NTC2018). Indirect actions caused by imposed deformations can be either permanent or variable and should be taken into account where relevant (UNI EN 1990).

Theory of imposed deformations modifies the traditional relationship between stresses and strains, based on the hypothesis of linear elasticity, into:

$$\sigma = E(\varepsilon_{\text{tot}} - \bar{\varepsilon}) = E\varepsilon_{\text{el}} \quad \text{Eq. 6.19}$$

where ε_{tot} are the total deformations, $\bar{\varepsilon}$ is the vector of imposed deformations and ε_{el} is their difference. Imposed deformations applied to a structure can be classified, with reference to the congruence equations of a solid, as:

- congruent, that is $\bar{\varepsilon}$ fulfil the congruence equations;
- not congruent, that is $\bar{\varepsilon}$ does not fulfil the congruence equations. Given that the congruence equations include the second derivatives of the strain components, this is to say that the imposed deformations are a non-linear function. To fulfil the congruence equations, it is needed to introduce complementary elastic deformations $\varepsilon_{\text{el}} \neq 0$. Due to ε_{el} , some stresses (that are not associated to external loads) will arise.

With reference to constraints, imposed deformations can be:

- compatible, if they respect external constraints;
- incompatible, if they do not.

All the possible cases are summarized in Figure 6.43.

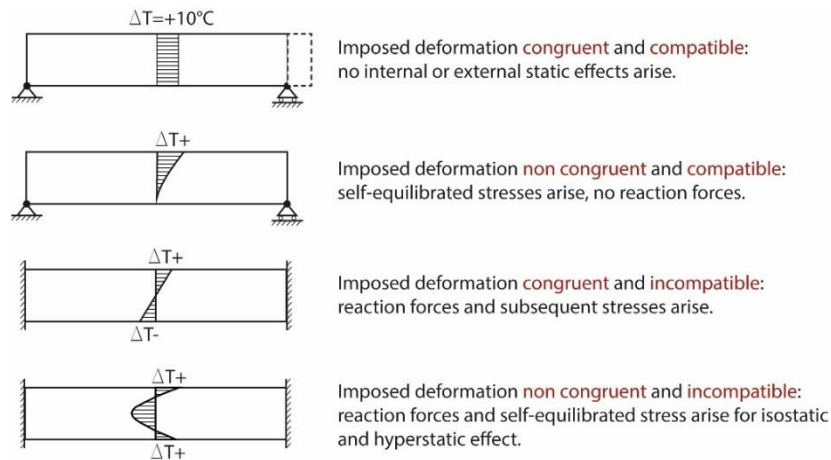


Figure 6.43: Combinations cases of congruence and compatibility in presence of thermal actions.

According to EN 1991-1-5, the temperature distribution within a structural element can be classified among (see Figure 6.44):

- a uniform temperature component;
- a linearly varying temperature difference component about the z axis;
- a linearly varying temperature difference component about the y axis;
- a non-linear temperature difference component (the case of this study, Figure 6.45 and Figure 6.46).

In the latter case, a set of self-equilibrated stresses would result, that produce no net load effect on the element. Self-equilibrated stresses are stresses that are not produced by loads, but by coactions both in isostatic and in hyperstatic structures. Thermal variation is an example of coaction, that is an external cause, different from loads, able to induce internal forces within the structure. While internal forces due to loads always have to be included in the design, those due to coactions should be considered only if their effect on the structure stress state is pejorative.

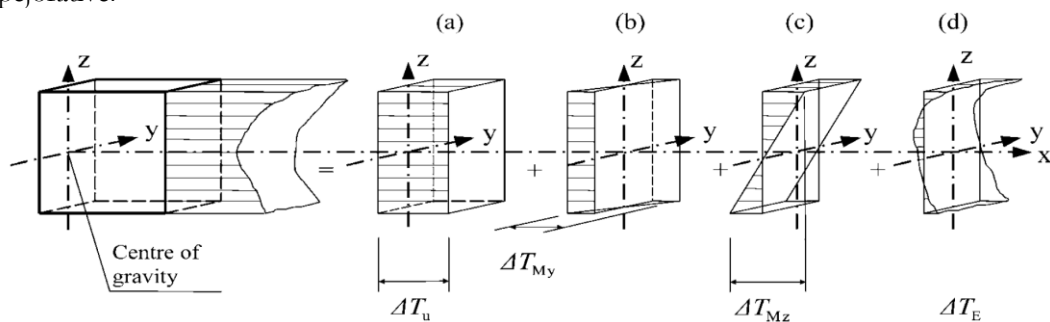


Figure 6.44: Examples of possible temperature profiles (EN 1991-1-5).

The strains and any resulting stresses depend on the geometry and boundary conditions of the element considered and on the thermophysical properties used, such as the coefficient of linear thermal expansion. The Eurocodes in Section 7 of EN 1991-1-5 consider the case of structures which are in contact with gas flow, liquids or material with different temperatures (e.g. industrial chimneys, pipelines, silos, tanks and cooling towers). Energy tunnels could be

assimilated to these special structures for simplicity, considering that they should be especially designed for effects due to the interaction between the structure and the circulation of heat carrier fluid within the lining of the tunnel during thermal activation (heating or cooling). The most relevant difference from conventional tunnels are daily and seasonal thermal variations originating within the lining. A temperature variation included between 2 and 40°C at the level of pipes could be taken into account.

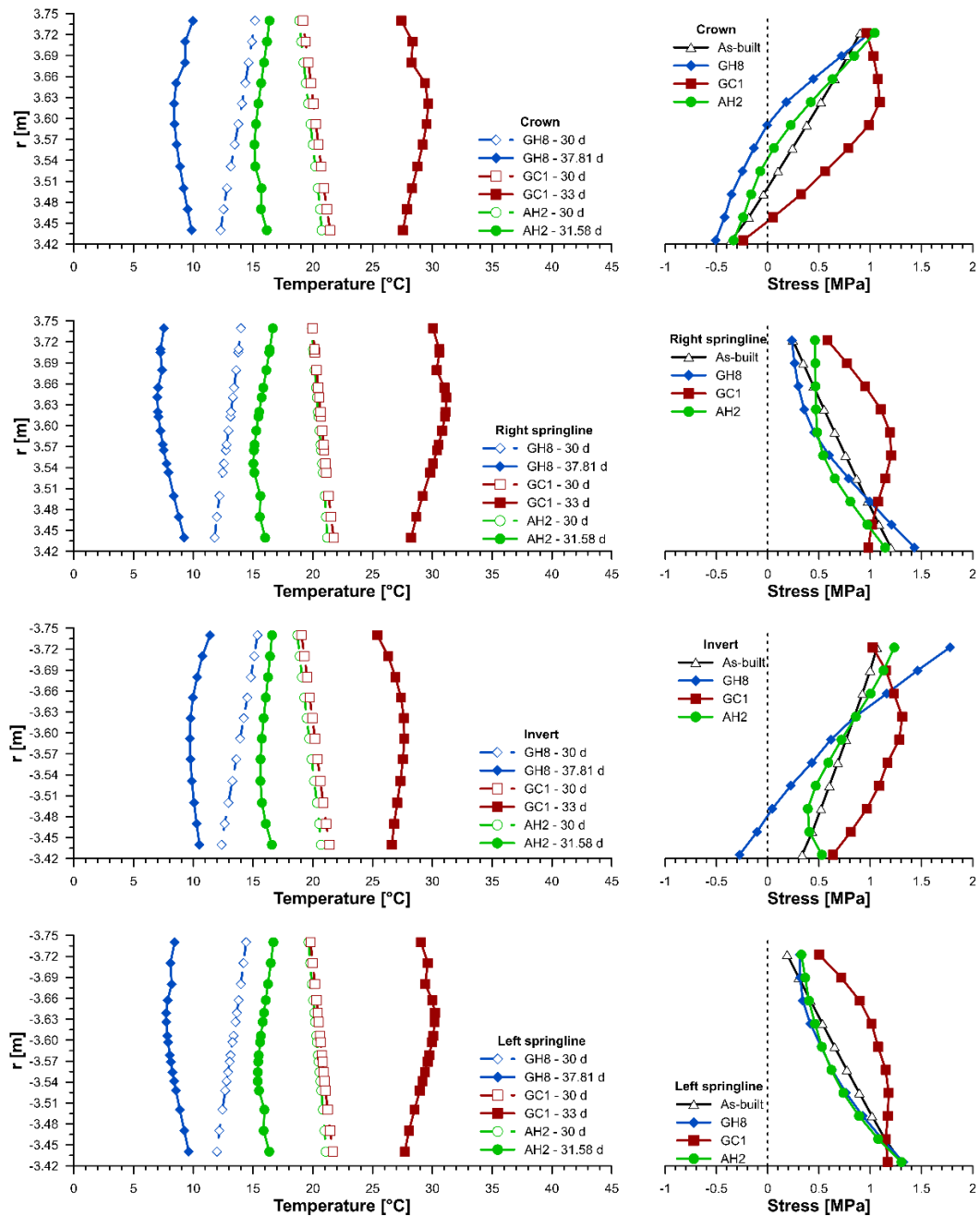


Figure 6.45: Profiles of temperature and hoop stresses computed from the numerical analyses (tests).

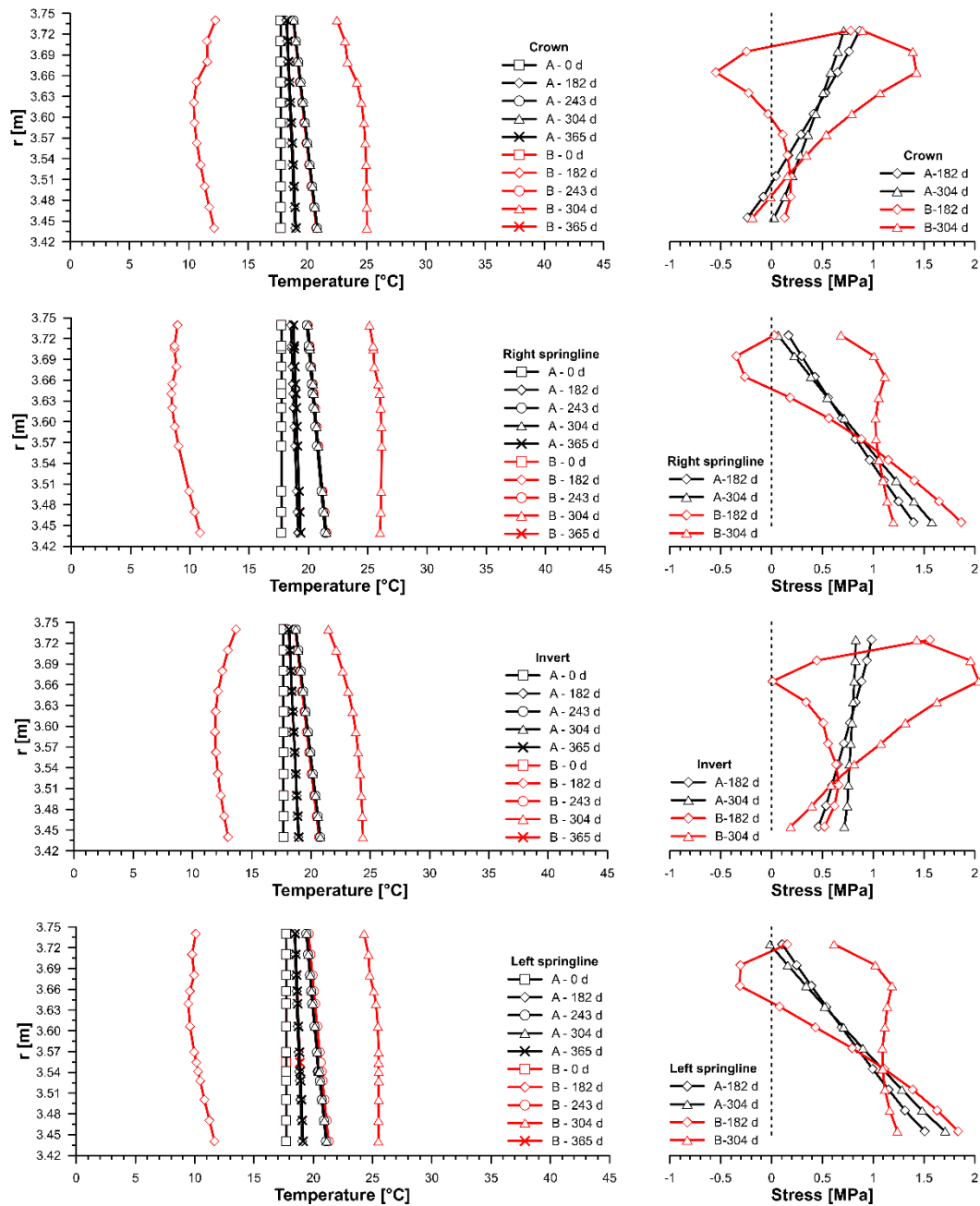


Figure 6.46: Profiles of temperature and hoop stresses computed from the numerical analyses (long-term).

The main issues associated with design of thermo-active structures are the possibility of failure as well as unsatisfactory behaviour while in service. These issues have to be verified as ultimate limit state (ULS) and serviceability limit state (SLS). The combination factors for thermal loading resulting from a heat exchanger can be assumed as in Burlon et al. (2013):

- $\Psi_0=0.6$ for ULS;
- $\Psi_1=0.5$ frequent value for SLS;
- $\Psi_2=0.2$ quasi-permanent value for SLS.

It can be seen that combination factors coincide with those defined in NTC2018 for thermal variations, with the exception of Ψ_2 , which is 0 there, meaning complete neglect of thermal actions in quasi-permanent actions combinations, but this cannot be the case.

As in conventional structural design, the verification of both ULS and SLS is required, while accounting for additional thermal action. Based on the numerical model built, an analysis can be carried out to verify whether additional stresses induced by the thermal actions do not exceed the structural resistance. Special consideration should be given to possible occurrence of tensile stresses.

For tunnels the design verifications to be achieved involve:

- ULS – bending moment with axial force;
- ULS – shear force;
- SLS – stress limitation;
- SLS – crack control.

NTC2018 establish that ULS verifications for underground earthworks should be performed using Design Approach 1, in the two combinations 1 (A1+M1+R1) and 2 (A2+M2+R2). However, as examined by Sciotti (2010), for underground earthworks, differently to other geotechnical systems, NTC2018 do not provide specific indications in relation to limit states individuation, to the choice of the design approach and to its application, despite general principles for safety and performances verifications should always hold true. For this reason, Sciotti (2010) illustrates a design approach proposal (Table 6.17) which is coherent with the prescriptions of the NTC2018. ULS verifications of structural type (STR) can be performed by applying Combination 1 of Design Approach 1 (A1+M1+R1), by applying the amplifying coefficients of group A1 to actions, while unit coefficients, belonging to groups M1 and R1, are applied to strength and global strength. In the case of thermal processes, this consideration can be extended also to thermophysical material properties, by adopting unit coefficients for these too. Hence, design internal actions at ULS are obtained by applying amplifying coefficients of actions directly to internal forces (Sciotti, 2010). In the interaction analyses to evaluate internal forces in tunnel linings, where the key factor is represented by the stiffnesses and relative soil-structure stiffness ratios, modelling with characteristic values of actions and strength provides a realistic description of the stress state in the soil and in the structural elements. Reducing soil strength parameters, as suggested by DA1C2, would provide unreliable results, by considering non congruent parameters and creating artificial plastic zones leading to an unrealistic redistribution of the lining stress state (Callisto, 2009; AFTES, 2007). Although the considerations by Sciotti (2010) were referred to the previous NTC2008, they can be considered valid for NTC2018 too, given that the two Design Approaches and the relative cited combinations are maintained in this new version.

Structural verifications will be done by considering a concrete cross section class C40/50 (Table 6.18) 30 cm-thick and 140 cm-wide, according to the geometry of Turin ML1 South Extension geometry. Design values of material strength are calculated by dividing each characteristic value by the partial safety factor referred to a specific material (Table 6.19 and Table 6.20). Figure 6.47 depicts the scheme of rebars for an illustrative segment, that presents $3i+3e\Phi 14$, $6i+6e\Phi 10$ and $3i+3e\Phi 14$ bending rebars.

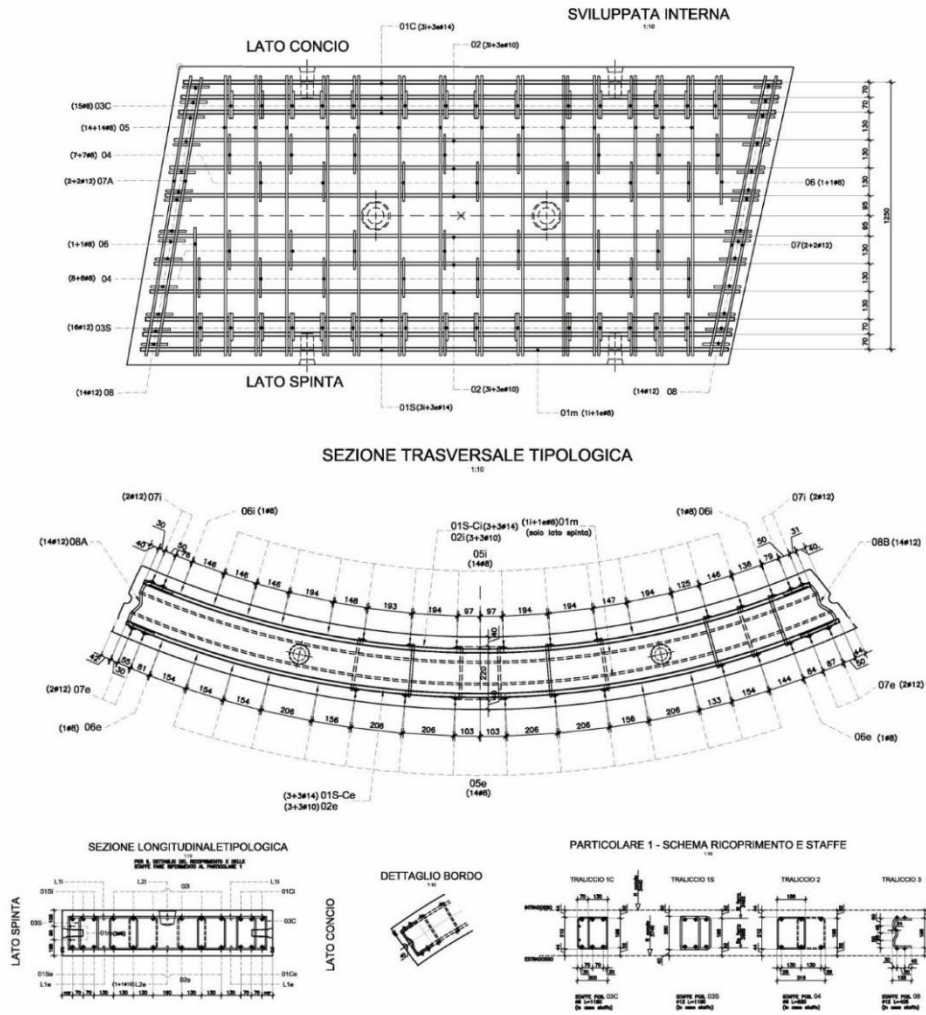


Figure 6.47: Scheme of a typical segment rebar arrangement.

Table 6.17: Design approach proposal for underground earthworks according to Sciotti (2010)

ULS	SLS
GEO: DA1C2 (A2+M2+R2)	Design values of actions, material properties and global strength are assumed equal to the characteristic ones. The design value of the effect of actions is computed and compared to limit values.
STR: DA1C1 (A1+M1+R1)	

Table 6.18: Concrete characteristics.

Strength class	Consistency class	Water/cement ratio	Max aggregates diameter [mm]	Minimum cover [mm]
C40/50	S4	≤0.5	30	40

Table 6.19: Concrete mechanical properties.

Concrete class	R _{ck} [MPa]	f _{ck} [MPa]	f _{cm} [MPa]	f _{ctm} [MPa]	f _{ctk0.05} [MPa]	α _{cc} [-]	α _{ct} [-]	γ _c [-]	f _{cd} [MPa]	f _{ctd} [MPa]
C40/50	50	41.5	49.5	3.6	2.5	0.85	1	1.5	23.5	1.7

Table 6.20: Steel mechanical properties.

Steel	f_{yk} [MPa]	γ_s [-]	f_{yd} [MPa]	E_s [MPa]
B450C	450	1.15	391.3	200000

ULS – bending moment with axial force

The first ULS verification aims to checking the validity of the following relationship:

$$M_{Rd} = M_{Rd}(N_d) \geq M_{Ed} \quad \text{Eq. 6.20}$$

Design effect of actions, reported in Table 6.15 and Table 6.16, is obtained by multiplying those at the end of excavation by an amplifying safety factor of 1.3 and the variations in internal forces by a factor of 1.5. Indeed, thermal actions are classified as a variable action and the partial safety factors are 0.0 in favorable case and 1.5 in unfavorable case. Performing the analysis in the favorable case corresponds to considering only the mechanical effects induced by excavation. The strength verification is performed by comparing design internal forces with design strength, both referred to a segment 1.4 m wide, through the construction of the support capacity plot in Figure 6.48. All the pairs M-N around the lining are reported in the strength envelope of the representative cross section of the lining. It can be noted that every pair M-N falls within the interaction domain, hence the verification is fulfilled thus showing the little influence of thermal activation on the ultimate limit state of the lining. Hence, there is no need to increase steel reinforcement area or to modify the geometry of the cross section already defined based on the traditional structural design.

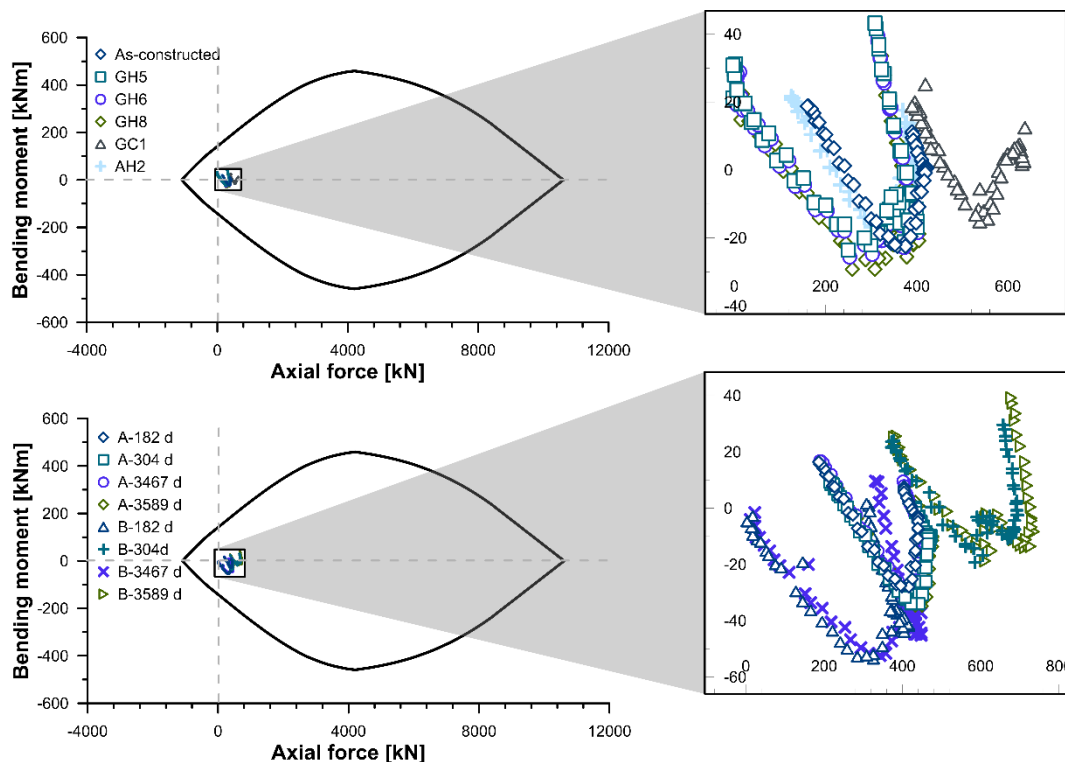


Figure 6.48: ULS - bending moment with axial force verification – tests and long term.

ULS – shear

Shear force verification is executed for the same cross section used in the previous check as it should be for reinforced concrete sections with specific reinforcing shear rebars. The validity of the following relationship must be checked for members not requiring shear reinforcement:

$$V_{Sd} \leq V_{Rd,c} \quad \text{Eq. 6.21}$$

where:

$$V_{Rd,c} = [C_{Rd,c} \cdot k \cdot (100 \cdot \rho_1 \cdot f_{ck})^{\frac{1}{3}} + k_1 \cdot \sigma_{cp}] \cdot b_w \cdot d \quad \text{Eq. 6.22}$$

with a minimum of

$$V_{Rd,c} = (v_{\min} + k_1 \cdot \sigma_{cp}) \cdot b_w \cdot d \quad \text{Eq. 6.23}$$

In Eq. 6.22 $V_{Rd,c}$ is the design shear resistance of the member without shear reinforcement. The terms $C_{Rd,c}$, k and ρ_1 represent, respectively, the base shear strength, a reduction factor of $C_{Rd,c}$ depending on the useful height d and the longitudinal rebars ratio, defined as:

$$C_{Rd,c} = 0.18 / \gamma_c \quad \text{Eq. 6.24}$$

$$k = 1 + \sqrt{200/d} \leq 2.0 \quad \text{Eq. 6.25}$$

$$\rho_1 = \frac{A_{sl}}{b_w \cdot d} \leq 0.02 \quad \text{Eq. 6.26}$$

The term A_{sl} in Eq. 6.26 represents the area of tensile reinforcement sufficiently anchored. However, for members with vertical shear reinforcement the verification is based on the compliance of the following relationship:

$$V_{Sd} < \min(V_{Rd,s}, V_{Rd,max}) \quad \text{Eq. 6.27}$$

$$V_{Rd,s} = \frac{A_{sw}}{s} \cdot z \cdot f_{ywd} \cdot \cot \theta \quad \text{Eq. 6.28}$$

$$V_{Rd,max} = \alpha_{cw} \cdot b_w \cdot z \cdot v_1 \cdot f_{cd} / (\cot \theta + \tan \theta) \quad \text{Eq. 6.29}$$

The design shear force has to be smaller than the minimum value among $V_{Rd,s}$, the design value of the shear force which can be sustained by the yielding shear reinforcement and $V_{Rd,max}$, the design value of the maximum shear force which can be sustained by the member, limited by crushing of the compression struts. In Eq. 6.28 and Eq. 6.29 A_{sw} is the cross-sectional area of the shear reinforcement, s is the spacing of the stirrups, $z=0.9d$ is the inner lever arm, f_{ywd} is the design yield strength of shear reinforcement, θ is the angle between the concrete compression strut and the beam axis perpendicular to the shear force, v_1 is a strength reduction factor for concrete cracked in shear, α_{cw} is a coefficient accounting for the state of stress in the compression chord, b_w is the minimum width between tension and compression chords. The ULS shear check is shown in Table 6.21 and Table 6.22 with largely favorable results in all cases.

Table 6.21: ULS shear verification – tests.

Condition	V _d [kN]	V _{Rd,c} [kN]	V _{Rd,s} [kN]	V _{Rd,max} [kN]	Verification
As-constructed	23.7	241.6	386.5	1872.8	$V_{Sd} \leq V_{Rd,c}$ $V_{Sd} < \min(V_{Rd,s}, V_{Rd,max})$
GH4	39.2	232.4	386.5	1872.8	$V_{Sd} \leq V_{Rd,c}$ $V_{Sd} < \min(V_{Rd,s}, V_{Rd,max})$
GH5	39.3	232.7	386.5	1872.8	$V_{Sd} \leq V_{Rd,c}$ $V_{Sd} < \min(V_{Rd,s}, V_{Rd,max})$
GH6	40.4	233.6	386.5	1872.8	$V_{Sd} \leq V_{Rd,c}$ $V_{Sd} < \min(V_{Rd,s}, V_{Rd,max})$
GC1	30.6	272.3	386.5	1872.8	$V_{Sd} \leq V_{Rd,c}$ $V_{Sd} < \min(V_{Rd,s}, V_{Rd,max})$
AH2	35.7	238.4	386.5	1872.8	$V_{Sd} \leq V_{Rd,c}$ $V_{Sd} < \min(V_{Rd,s}, V_{Rd,max})$

Table 6.22: ULS shear verification – long-term models A and B.

Condition	V _d [kN]	V _{Rd,c} [kN]	V _{Rd,s} [kN]	V _{Rd,max} [kN]	Verification
A - 1 st year, 182 d	26.3	246.7	386.5	1872.8	$V_{Sd} \leq V_{Rd,c}$ $V_{Sd} < \min(V_{Rd,s}, V_{Rd,max})$
A - 1 st year, 304 d	25.6	250.2	386.5	1872.8	$V_{Sd} \leq V_{Rd,c}$ $V_{Sd} < \min(V_{Rd,s}, V_{Rd,max})$
A - 10 th year, 3467 d	27.4	245.2	386.5	1872.8	$V_{Sd} \leq V_{Rd,c}$ $V_{Sd} < \min(V_{Rd,s}, V_{Rd,max})$
A - 10 th year, 3589 d	26.7	248.9	386.5	1872.8	$V_{Sd} \leq V_{Rd,c}$ $V_{Sd} < \min(V_{Rd,s}, V_{Rd,max})$
B - 1 st year, 182 d	40.4	221.0	386.5	1872.8	$V_{Sd} \leq V_{Rd,c}$ $V_{Sd} < \min(V_{Rd,s}, V_{Rd,max})$
B - 1 st year, 304 d	31.1	272.8	386.5	1872.8	$V_{Sd} \leq V_{Rd,c}$ $V_{Sd} < \min(V_{Rd,s}, V_{Rd,max})$
B - 10 th year, 3467 d	41.5	222.8	386.5	1872.8	$V_{Sd} \leq V_{Rd,c}$ $V_{Sd} < \min(V_{Rd,s}, V_{Rd,max})$
B - 10 th year, 3589 d	37.8	292.3	386.5	1872.8	$V_{Sd} \leq V_{Rd,c}$ $V_{Sd} < \min(V_{Rd,s}, V_{Rd,max})$

SLS – stress limitation

The SLS verification for stress limitation is based on the control of concrete and steel stresses, in order to verify the fulfilment of the limits prescribed by the NTC2018. For concrete it should be verified that the maximum compressive stress $\sigma_{c,max}$ evaluated both in characteristic and quasi permanent combination meets the following limitations:

$$\sigma_{c,max} \leq 0.60 \cdot f_{ck} = 24.9 \text{ MPa} \quad \text{for characteristic combination} \quad \text{Eq. 6.30}$$

$$\sigma_{c,max} \leq 0.45 \cdot f_{ck} = 18.7 \text{ MPa} \quad \text{for quasi-permanent combination} \quad \text{Eq. 6.31}$$

For steel the maximum stress $\sigma_{s,max}$ has to meet the following limitation:

$$\sigma_{s,max} \leq 0.80 \cdot f_{yk} = 360 \text{ MPa} \quad \text{for characteristic combination} \quad \text{Eq. 6.32}$$

Figure 6.45 and Figure 6.46 show the distribution of stresses along the thickness of the lining at the crown, springlines and invert for short and long term models, that becomes non-linear in presence of temperature effects. As well highlighted in the pictures, the circulation of a heat carrier fluid does not substantially modify the purely mechanical stresses because it induces a maximum variation of ± 1 MPa. In the present case this amount is comparable to the stresses induced by the excavation, but in general it will be a small percentage of these, and, in any case, stresses are still very low compared to the material strength. Table 6.23 and Table 6.24 report the result of the check for SLS stress limitation, where stresses are directly computed from the output of the coupled finite difference calculation. Indeed, their computation from internal forces with correct application of combination factors would not be possible in this case, as this operation would lead to a linear stress distribution different from the original one. By analysing the results, the fulfilment of the limits prescribed by the NTC2018 can be observed.

Table 6.23: SLS stress limitation verification – tests.

Condition	$\sigma_{c,max}$ [MPa]	$\sigma_{c,lim}$ [MPa]	Verification	$\sigma_{s,max}$ [MPa]	$\sigma_{s,lim}$ [MPa]	Verification
As-constructed	1.44	18.7	$\sigma_{c,max} \leq \sigma_{c,lim}$	-3.20	-360	$\sigma_{s,max} \leq \sigma_{s,lim}$
GH5	2.09	18.7	$\sigma_{c,max} \leq \sigma_{c,lim}$	-10.03	-360	$\sigma_{s,max} \leq \sigma_{s,lim}$
GH6	2.01	18.7	$\sigma_{c,max} \leq \sigma_{c,lim}$	-9.04	-360	$\sigma_{s,max} \leq \sigma_{s,lim}$
GH8	1.83	18.7	$\sigma_{c,max} \leq \sigma_{c,lim}$	-6.91	-360	$\sigma_{s,max} \leq \sigma_{s,lim}$
GC1	1.85	18.7	$\sigma_{c,max} \leq \sigma_{c,lim}$	-1.12	-360	$\sigma_{s,max} \leq \sigma_{s,lim}$
AH2	1.47	18.7	$\sigma_{c,max} \leq \sigma_{c,lim}$	-4.13	-360	$\sigma_{s,max} \leq \sigma_{s,lim}$

Table 6.24: SLS stress limitation verification – long term models A and B.

Condition	$\sigma_{c,max}$ [MPa]	$\sigma_{c,lim}$ [MPa]	Verification	$\sigma_{s,max}$ [MPa]	$\sigma_{s,lim}$ [MPa]	Verification
A - 1 st year, 182 d	1.68	18.7	$\sigma_{c,max} \leq \sigma_{c,lim}$	-1.68	-360	$\sigma_{s,max} \leq \sigma_{s,lim}$
A - 1 st year, 304 d	1.89	18.7	$\sigma_{c,max} \leq \sigma_{c,lim}$	-1.04	-360	$\sigma_{s,max} \leq \sigma_{s,lim}$
A - 10 th year, 3467 d	1.72	18.7	$\sigma_{c,max} \leq \sigma_{c,lim}$	-1.77	-360	$\sigma_{s,max} \leq \sigma_{s,lim}$
A - 10 th year, 3589 d	1.93	18.7	$\sigma_{c,max} \leq \sigma_{c,lim}$	-1.04	-360	$\sigma_{s,max} \leq \sigma_{s,lim}$
B - 1 st year, 182 d	2.30	18.7	$\sigma_{c,max} \leq \sigma_{c,lim}$	-14.06	-360	$\sigma_{s,max} \leq \sigma_{s,lim}$
B - 1 st year, 304 d	2.04	18.7	$\sigma_{c,max} \leq \sigma_{c,lim}$	-0.78	-360	$\sigma_{s,max} \leq \sigma_{s,lim}$
B - 10 th year, 3467 d	2.31	18.7	$\sigma_{c,max} \leq \sigma_{c,lim}$	-13.11	-360	$\sigma_{s,max} \leq \sigma_{s,lim}$
B - 10 th year, 3589 d	2.26	18.7	$\sigma_{c,max} \leq \sigma_{c,lim}$	-1.24	-360	$\sigma_{s,max} \leq \sigma_{s,lim}$

SLS – crack control

Cracking has to be limited so as not to jeopardize the proper functioning or the durability of the lining. A limiting value, w_{max} , for the calculated crack width, w_k , taking into account the proposed function and the nature of the structure and the costs of limiting cracking, has to be established. The NTC2018 establish the following cracking limit states:

- Decompression limit state, where for every combination of actions chosen normal stress is wherever compressive and equal to 0 as a maximum;
- Cracks formation limit stat, where for the combination of actions chosen tensile normal stress in the most stressed fiber is defined as $\sigma_t = f_{ctm}/1.2$;
- Cracks opening limit state, where for the combination of actions chosen the limit value of cracks opening computed at the considered level is equal to one of the following nominal values: $w_1=0.2$ mm, $w_2=0.3$ mm, $w_3=0.4$ mm.

The choice of the cracking limit state is performed as a function of what is defined in Table 6.25, based on the environmental conditions and on the reinforcement sensitivity to corrosion. Ordinary steel rebars are not very sensitive to corrosion.

Table 6.25: Criteria to choose the crack limit state.

Environmental conditions	Combination of actions	Reinforcement			
		Sensitive Limit state	w_k	Not very sensitive Limit state	w_k
Ordinary (X0, XC1, XC2, XC3, XF1)	Frequent	Cracks opening	$\leq w_2$	Cracks opening	$\leq w_3$
	Quasi permanent	Cracks opening	$\leq w_1$	Cracks opening	$\leq w_2$
Aggressive (XC4, XD1, XS1, XA1, XA2, XF2, XF3)	Frequent	Cracks opening	$\leq w_1$	Cracks opening	$\leq w_2$
	Quasi permanent	Decompression	-	Cracks opening	$\leq w_1$
Very aggressive (XD2, XD3, XS2, XA3, XF4)	Frequent	Cracks formation	-	Cracks opening	$\leq w_1$
	Quasi permanent	Decompression	-	Cracks opening	$\leq w_1$

The present study can be located within exposure class XC2. Hence, the fulfilment of cracks opening limits in the frequent and quasi permanent combinations has to be checked. It is highlighted that according to NTC2018 the check can be carried out following two different strategies, with a direct computation of cracks opening, or by applying an indirect method, based on the meeting of predefined geometric limits in terms of bars maximum diameters and maximum spacing. Both strategies are equally admitted by NTC2018.

By applying the direct method, it has to be ascertained that the characteristic value of cracks opening w_k does not exceed the nominal valued $w_1=0.2$ mm, $w_2=0.3$ mm, $w_3=0.4$ mm defined in Table 6.25. The characteristic opening of cracks w_k is computed as 1.7 times the product between the average strain of rebars ϵ_{sm} and the average distance among cracks Δ_{sm} :

$$w_k = 1.7 \cdot \epsilon_{sm} \cdot \Delta_{sm} \quad \text{Eq. 6.33}$$

To evaluate the crack width w_k , the approach in Eurocode 2 is adopted:

$$w_k = s_{r,max} (\epsilon_{sm} - \epsilon_{cm}) \quad \text{Eq. 6.34}$$

where $s_{r,max}$ is the maximum crack spacing (Eq. 6.35), ϵ_{sm} is the mean strain in the reinforcement under the relevant combination of loads, including the effect of imposed deformations and taking into account the effects of tension stiffening, ϵ_{cm} is the mean strain in concrete between cracks.

$$s_{r,max} = k_3 c + k_1 k_2 k_4 \phi / \sigma_{p,eff} \quad \text{Eq. 6.35}$$

where

- c is the cover to the longitudinal reinforcement
- $k_1=0.8$ (high bond bars) is a coefficient which takes into account the bond properties of reinforcement
- $k_2=0.5$ for bending, is a coefficient which accounts for the distribution of strain
- $k_3=3.4$
- $k_4=0.425$

- $\rho_{p,eff} = (A_s + \xi_1 A_p') / A_{c,eff}$ the percentage of reinforcement with reference to the effective area of concrete in tension surrounding the reinforcement.

and $\epsilon_{sm} - \epsilon_{cm}$ can be calculated from the expression:

$$\epsilon_{sm} - \epsilon_{cm} = \frac{\sigma_s - k_t \frac{f_{ct,eff}}{\rho_{p,eff}} (1 + \alpha_e \rho_{p,eff})}{E_s} \geq 0.6 \frac{\sigma_s}{E_s} \quad \text{Eq. 6.36}$$

where

- σ_s is the stress in the tension reinforcement assuming a cracked section
- $k_t = 0.4$ for long term loading
- $f_{ct,eff}$ is the mean value of the tensile strength of the concrete effective at the time when cracks may first be expected to occur (equal to f_{ctm} as cracking is expected later than 28 days)
- α_e is the ratio E_s/E_{cm}

Given the nonlinearity of the stresses in the thermomechanical cases, the verification was done for the condition existing at the end of excavation, considering that it will be valid also for the other cases. The maximum crack opening obtained being 0.012 mm, the SLS crack opening control is fulfilled.

6.6. Summary

The aim of the Chapter was to assess the mechanical effects associated to tunnel lining thermal activation which are still little studied and deserve a special attention to boost the uptake of energy tunnels around the world. The methods employed included (i) full-scale in situ testing and (ii) numerical modelling. The experimental activity presented the evidences of the thermally induced stress-strain performance of such structures. The TM numerical analyses aimed at providing a fundamental characterisation of the response of energy tunnels to thermal and mechanical loads. The knowledge gained was precious to illustrate the implications involved on the mechanical design of tunnels and of precast energy segments. This issue is the second aspect that needs to be accounted for following to thermal design.

On the basis of the work performed so far, the following conclusions can be drawn:

- the testing equipment setup adopted was shown to be effective in tracing the lining response not only in the natural state but also under the particular conditions experienced upon thermal activation;
- the strain readings required anything but a straightforward data postprocessing phase to give meaning to the trends. Overlooking this step would make data incomprehensible and the tunnel lining behaviour of very difficult interpretation. Conversely, stress data were easier to understand;
- upon cooling (winter heating mode) temperature decrease in the lining is displayed to be in the order of 4-6°C with subsequent contractive hoop strains of some tens of $\mu\epsilon$ and a decrease in compressive stresses in the order of the MPa. The opposite behaviour is exhibited upon heating (summer cooling mode) with expansive hoop strains and an increase in compressive stresses, though in this case experimental data indicate an order of

magnitude of some MPa. Further tests in summer mode are needed to confirm this result, given that only two tests were available so far;

- the correlation of strains and stresses with temperature highlights an almost reversible behaviour with ranges of strains between $\pm 100 \mu\epsilon$ and of stresses between -2 and 3 MPa when temperature changes are $\pm 8^\circ\text{C}$. Strain temperature ratio is about $10 \mu\epsilon/^\circ\text{C}$, very similar to the concrete thermal expansion coefficient, whereas stress temperature ratio goes from 0.1 up to 0.5 MPa/ $^\circ\text{C}$. Longitudinal stress is null in all cases;
- a further “experiment in the experiment” was the testing of FBG optical sensors as a possible alternative to conventional electric sensors. Good agreement between the two monitoring technologies was found, both being able to detect day-night environmental temperature and the heating cycles with slightly more sensitivity observed for the FBGs compared to the others. The progressive gain of heat is demonstrated by the progressive higher temperature logged along the circulation path. The interpretation of FBG strain data would require a proper calibration procedure in real working conditions, that is on the sensor embedded in concrete. This is among the tasks to be performed in the near future;
- a complementary thermo-mechanical numerical model allowed to have a broader view on the results. After a preliminary calibration phase to match monitored settlements and lining stresses, attention was focused on the characterization of the thermally induced effects. Numerical results confirmed the considerations coming from monitoring data. The general trends observed in situ were well replicated, despite some inconsistencies related to radial stresses and to the order of magnitude of summer stresses. However, this will require further verification and a follow-up of the experimental campaign is being envisaged in that light;
- additionally, long-term operation was simulated to investigate a condition closer to reality than the short-term tests performed in situ and compared to the case with no operation. Maximum convergences in the order of 0.02% were highlighted and stress variations of ± 1 MPa. Internal actions are also slightly different in trend and as maximum values. The effect on ground surface resulting from the system operation is extremely marginal and typically negligible;
- the framework for ULS and SLS design verification in presence of thermal actions, defined as indirect and variable actions according to European norms, was delineated with the introduction of concepts such as imposed deformations, self-equilibrated stresses and coactions. Indeed, the specific case of concrete structures embedding geothermal loops bumps into the peculiar case of nonlinear temperature distributions. A draft of the procedure that should be followed in future energy tunnels projects was outlined. Design Approach 1 with Combination 1 should be followed by applying unit coefficients not only to typical material properties but also to thermophysical properties. Amplifying coefficients of actions can be implemented directly on internal forces, by distinguishing structural and thermal effects. At ULS a coefficient of 1.3 should be applied to the former and of 1.5 to the latter in the fundamental combination. For SLS the check on maximum concrete and steel stress is recommended, though it is very likely to fulfil the prescribed limits. Cracks opening check should be verified in the as-constructed case only, as the stresses nonlinear trend would modify the traditional procedure in a way which is not coded in the available norms.

To conclude, the results illustrated that thermal loads acting on tunnels in alluvial soils involve measurable and quantifiable effects. However, these effects are not considered to threaten the structural integrity nor the serviceability of the lining. In the case analyzed in the

present work, representative of a typical case study, no need to increase steel reinforcement area or to modify the geometry of the cross section already defined based on the traditional structural design was encountered. For design purposes, numerical calculations could be performed to assess the impact of temperature variations.

Chapter 7

Summary and conclusions

7.1. Summary

This Doctoral Thesis aimed at characterising the thermal and structural performance of energy tunnels, a dual-purpose technology that integrates the role of structural support with the operation as energy supplier, with great economic, social and environmental benefits in line with the European energy roadmap targets. Since they have a twofold nature, these geostructures involve the coexistence of both mechanical and additional, seasonally cyclic thermal loads. Hence, unmatched challenges and unsolved questions related to the possible consequences from the standpoint of analysis and design are put forward, given that energy and structural behaviour are potentially affected by these actions. On one hand, the capability of a tunnel to work effectively as a geothermal heat exchanger was investigated. On the other hand, the structural implications induced by heating and cooling cycles on the lining were assessed. Both topics were considered separately in a specifically devoted chapter of this Thesis. Combining the results obtained with available norms and recommendations currently employed for the dimensioning of conventional tunnels, an extension of the latter to the special case of energy tunnel design can be included to pave the way for the development of future energy tunnel projects.

In particular, the following main tasks were undertaken.

- Given the very limited number of experimental evidences on real scale energy tunnel projects emerging from the detailed bibliographic study performed, the first experimental site of this kind in Italy was designed and accomplished in the tunnel under construction of Turin Metro Line 1 South Extension with the main objective to clarify the above mentioned aspects and to provide a sound dataset.
- A thorough and meticulous experimental campaign was scheduled and completed. Tests in ground heating, ground cooling and air heating (tunnel cooling) mode were achieved, with the collection of a large amount of stress, strain and temperature data that were specifically devoted to interpreting the lining response and the efficiency of the technology.
- A new three-dimensional, coupled thermo-hydraulic, finite element model was prepared with the objective of reproducing as realistically as possible the geometry of the pipes loop installed in the field tests as well as the thermo-hydro-geological conditions existing in situ.

The model was shown to match monitoring outcomes very satisfactorily and was further extended to different environmental and thermo-hydro-geological conditions for the assessment of thermal efficiency in these specific cases.

- A new bidimensional, thermo-mechanical model was built in a finite difference environment, the main emphasis being placed on the understanding of the lining response to thermal actions. After a preliminary back analysis step, the interest was centered on the simulation of energy tunnels operation over typical timescales of practical applications.

7.2. Conclusions

It is the purpose of the present chapter to draw some conclusions on the work performed so far that availed of both full-scale in situ testing and numerical modelling. The following aspects will be considered:

- energy tunnels thermal performance;
- energy tunnels structural performance;
- consequence of numerical and experimental results on design analyses of energy tunnels.

7.2.1. Energy tunnels thermal performance

7.2.1.1. Experimental conclusions

Based on the state-of-the-art review about the behaviour of energy tunnels, the limited number of practical energy tunnels implementations compared to numerical researches stands out. For this reason, it was decided to undergo an extensive experimental campaign to provide evidence of the larger efficiency of the Enertun layout compared to existing schemes, already claimed in literature through numerical studies, and, in general, of the remarkable benefits of tunnels thermal activation. In order to do so, a new real scale prototype of energy tunnel system constituted by two rings of Enertun segments, hydraulically connected in parallel, was designed and developed for the first time in Italy, capable of reproducing the real scale behaviour of an energy tunnel.

The results presented concerning the response under thermal cycles are almost unique in literature. The set of tests carried out led to the quantification of specific thermal power exchanged both with the ground side (mainly, for the ground circuit) and with the inner environment (mainly, for the air circuit). Figures inferred are of the same order of magnitude of those reported in literature (Barla et al., 2016), thus confirming the relevance of the assumptions and the favorable groundwater thermal recharge that avoids a progressive depletion of the geothermal reservoir over time. Indeed, they locate in the range 41-51 W/m² for ground heating, 45-61 W/m² for ground cooling and 53-55 W/m² for air heating. However, the limited number of tests in ground cooling and air heating mode would require further confirmation through additional experiments. Moreover, winter performance is likely to be underestimated due to the colder conditions recorded during construction compared to working conditions.

7.2.1.2. Numerical conclusions

The experimental data collected were essential to demonstrate the robustness and reliability of a coupled TH numerical model in three dimensional conditions. The inclusion of a grout layer and the calibration of a heat transfer coefficient added greater plausibility to the model. To try

to provide a comprehensive framework of the performance of the technology in a number of environmental conditions, the design charts presented in Di Donna and Barla (2016) were updated for the Enertun scenario and for three groundwater flow directions, which is an aspect of novelty compared to previous literature. Considerations drawn by Di Donna and Barla (2016) are confirmed here. No matter the flow direction, the highest performance is obtained with maximum ground thermal conductivity, maximum groundwater flow, due to the thermal recharge mechanism that allows the ground to return more rapidly to its undisturbed temperature, and with maximum ground temperature in winter and viceversa in summer. As groundwater flow velocity decreases, thermal conductivity starts playing a role. For perpendicular groundwater flow winter energy performance is in the range 10-95 W/m², while summer energy performance falls between 10-110 W/m², slightly higher than in winter. By observing the effect of groundwater flow, it is observed that the performance is significantly increased when the flow is perpendicular to the tunnel axis as compared to an orientation of 0°, whereas little improvement is attributable to perpendicular flow in comparison to the oblique case. For this reason the configuration of prototype installed in Turin Metro is particularly advantageous. These charts are particularly useful for the designer interested in evaluating whether it may be worth or not to invest in the feasibility study of the thermal activation of a tunnel.

The results of a sensitivity analysis on fluid inlet temperature, flow rate, pipes size and heat transfer coefficient obtained show that fluid inlet temperature is the parameter that mostly affects heat transfer. From this and the above considerations a simple procedure to estimate the geothermal potential of tunnels was developed and validated. It does not pretend to be representative of the real performance but can be considered as a screening tool. It is clear that caution should be adopted when site conditions differ substantially from those considered and that a more detailed study should be conducted at the design analysis stage. Undertaking careful, additional thermophysical characterisation of all the elements of the structure will be imperative at the feasibility stage of a project.

7.2.2. Energy tunnels structural performance

7.2.2.1. Experimental conclusions

As no experimental results were available in literature on energy tunnels thermo-mechanical behaviour, this gap was selected as the other focus of the developed experimental campaign. The testing programme accomplished had the purpose to reproduce at real scale the structural behaviour of linings undergoing thermal cycles. This main intention was studied with secondary, though not less important, and sometimes unanticipated challenges that enriched the wealth of knowledge and expertise. The interpretation of monitoring data can be mentioned, as non-isothermal conditions existing in the particular application of energy linings made stress-strain behaviour far from being easily comprehended. Indeed, temperature plays an undeniable role on thermal deformation of the vibrating wire of gauges, changing the trends completely. In this perspective, the activity of numerical modelling, as well as literature research, were essential to provide a full understanding and to forecast the expected trends.

Performances of FBGs and electric sensors measuring strains and temperatures were compared, as in future an all-fibre monitoring system could be designed to exploit the special features of optical fibre sensors. The qualitative trends of optical and electrical sensors match very well and show a remarkable influence of environmental temperature, day-night variations (also at the extrados) and heat pump activity on temperature in the rings, but from a quantitative standpoint differences up to 1°C were reported. Post-processing of FBG strain

data revealed an effect of gauge embedding on the temperature coefficient, apparently smaller than the one provided. This aspect should be further deepened in order to infer appropriate measurements.

The consequences of decreasing natural temperature on the lining are mainly:

- to increase both intrados and extrados hoop contractive strains;
- to decrease both radial and hoop compression stresses.

Most of the attention was posed on presenting experimental evidence on the impacts following thermal activation. The results obtained show:

- decrease in lining temperature (maximum of -8°C), decrease in radial and hoop compression stresses and increase in contractive strains (maximum $+100\ \mu\epsilon$) during cooling (heating mode);
- increase in lining temperature (maximum of $+8^{\circ}\text{C}$), increase in radial and hoop compressive stresses and increase in expansive strains (maximum $-100\ \mu\epsilon$) during heating (cooling mode).

The response is substantially reversible and no longitudinal stresses arise. The rates of change are:

- around $10\ \mu\epsilon/^{\circ}\text{C}$ for strains for all tests;
- around $0.1\ \text{MPa}/^{\circ}\text{C}$ for ground heating mode (in line with literature observations);
- between 0.1 and $0.5\ \text{MPa}/^{\circ}\text{C}$ for ground cooling mode and air heating mode.

The decrease or increase in temperature is more pronounced at the level of the circuit currently activated (ground or air).

Given the limited concrete tensile strength compared to compressive strength, the winter operation should be regarded carefully as some additional tensile stress could emerge. During heating (cooling mode) compressive additional stresses are induced, possibly relieving any tensile state.

7.2.2.2. Numerical conclusions

Extensive bidimensional thermo-mechanical finite difference analyses of the energy tunnel testbed were performed. This activity was essential to acquire further knowledge on the response of energy tunnels to thermal and mechanical loads and on the complex interplay with the surrounding soil, which may have been impossible to achieve otherwise. The FDM approach used was validated against the large amount of experimental data collected on the energy tunnel prototype. Despite some inaccuracies related to the order of magnitude of radial stresses, which would require further studies, numerical solutions were demonstrated to be consistent with monitoring data. Hence, thermo-mechanical numerical analyses appear to be appropriate tools for modelling the structural and energy behaviour of energy tunnels in saturated soil deposits, that is the case of this study. It is to be noted that a number of simplifications have been introduced in the research work performed, such as assuming linear thermoelasticity of all the materials involved. Nevertheless, in the specific application to Turin subsoil, this appears to be sufficiently accurate for the description of energy tunnels structural behaviour.

The main achievements obtained through the numerical simulations, referred to typical working conditions (temperature variations in the order of $\pm 10\ ^{\circ}\text{C}$) are the following:

- the profile of temperature versus lining thickness turns from quasi-linear under natural conditions to nonlinear in the case of thermal activation;
- inward convergences are shown upon cooling, outward convergences upon heating and they are in the order of $1\ \text{mm}$ in the vertical direction, about 0.02% . When the air circuit is

in operation, inward convergences are reported, whose value is one tenth of those subsequent to ground circuit activation;

- axial force decreases in heating mode (winter) and increases in cooling mode (summer);
- bending moment and shear force are slightly modified by thermal loadings and their trend around the ring reflects thermal activation and pipes location;
- the long-term analysis revealed that thermal activation produces peculiar effects compared to natural tunnel climate, modifying convergences and internal actions;
- the favorable groundwater flow does not lead to structural differences between short and long term analyses;
- the effect of thermal activation in terms of surface settlements is extremely marginal.

7.2.3. Consequences of numerical and experimental results on design analyses of energy tunnels

The prediction of energy tunnels structural behaviour and energy performance is a difficult task. The present Thesis was intended to provide some additional insights into these topics which will be of great interest in the years to come, given the energy roadmaps targeting at a decarbonised economy. Regulations should consider the specific features that characterize the phases within which the design of this innovative type of tunnel is developed, considering the interaction between mechanical and energy design. It is felt that the testing programme undertaken, described in Chapter 4, 5 and 6, was capable to reproduce effectively the behaviour of the Enertun prototype. By paying attention both to the experimental results and to those related to the activity of numerical modelling, practical implications are evident in terms of methodological approach to be adopted. In Figure 7.1 one can therefore observe that an energy tunnel project should start by an extensive and meticulous geotechnical and thermophysical characterisation of sites to avoid potential pitfalls. Using unsuitable initial and boundary thermohydrogeological conditions may be misleading in analysis and design.

The following point of interest definitely is the so-called thermal design stage. On the basis of the results of monitoring and modelling, parameters such as groundwater flow direction and velocity, pipes geometry, thermal and hydraulic properties as well as design temperature levels at the heat pump should be carefully considered. For a preliminary screening, the updated design charts described in Chapter 5 can be employed. However, in the feasibility study, bespoke thermo-hydraulic numerical analyses should be performed in a number of relevant locations, so that those that are not explicitly reproduced can be referred to these. Simulations could be devoted to analyse heating and cooling modes separately, at first, but special attention should be paid to yearly analyses involving the envisaged modes of operation according to the client's directions so that possible thermal unbalance in the surrounding ground can be highlighted and tackled. The integrity of the geothermal reservoir in the long term is, indeed, a vital prerogative. Two fundamental results at this step will be the evaluation of energy efficiency and the assessment of environmental sustainability.

The last step is structural design, aimed at identifying additional stresses and internal forces and at performing ULS and SLS design verifications to focus on possible detrimental effects of geothermal activation. Again, numerical modelling is the only available tool to address this aspect thoroughly, even if indicative orders of magnitude of thermally induced effects were shown thanks to monitoring. Keeping in mind the results mentioned in the previous paragraphs, it can be concluded that heating induces additional compressive stresses, which are normally acceptable with respect to the current norms, while cooling induces a reduction of the compressive stress with respect to that induced by the mechanical load, which might

turn into tensile stress. This aspect has to be specifically considered and accounted for in design practice. On that note, however, the effects involved by thermal loads (for cases similar to the ones analysed in this study and in normal working conditions) appeared to be negligible at ultimate limit states and at serviceability limit states and did not require an increase in steel reinforcement area or a modification in the geometry of the cross section already defined based on the traditional structural design. This consideration can streamline the design and verification of energy tunnels, especially in the first stages of the project. Conventional verifications against the action of mechanical loads only could be performed at first during the feasibility project. It is worth mentioning that the effects of thermal loads at serviceability limit state of crack control would need different procedures than what currently foreseen in the Eurocodes, given the nonlinearity of the stress profiles. Conversely, the effects of thermal loads, combined with conventional mechanical loads, in terms of compressive stress limitation and tensile stress limitation can be addressed according to the current norms' prescriptions. It is reminded that if the thermal solicitation amplitude gets more significant, the mentioned thermal-induced effects amplify too, and special care should be taken in design practice.

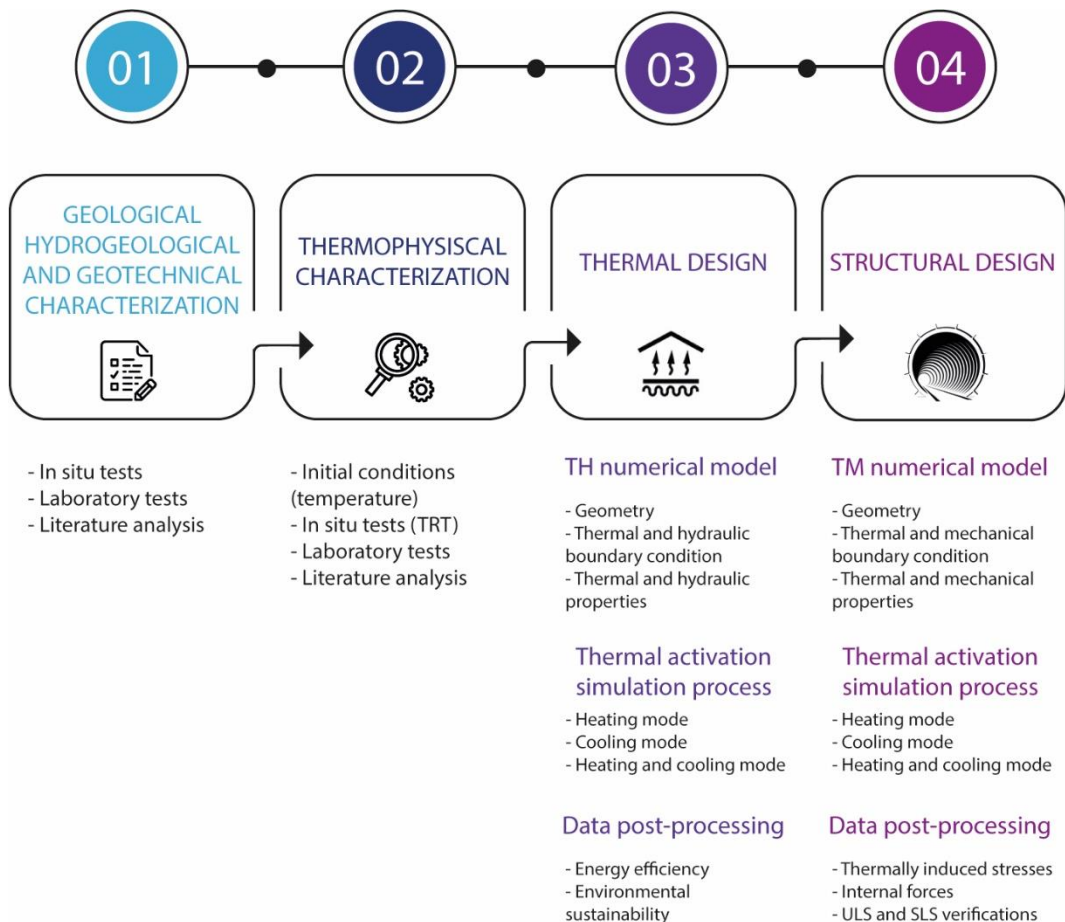


Figure 7.1: Methodology for thermal and structural design

7.3. Recommendations for further development

Energy tunnels technology is still at an early stage and there is plenty of room for further exciting research efforts, that do not certainly limit to the topics discussed in this Doctoral Thesis. Broad perspectives and opportunities for development are still clearly offered to clarify the issues which could not be solved completely. The final objective should be kept in mind, which is to provide the design engineer with better and effective tools and methodologies than presently available to deal with the design of energy tunnels. The following main aspects are to be considered.

- Typically, in numerical models, thermal boundary condition at the intrados of the tunnel is assumed as Cauchy-type, but questions could arise about the interaction between the tunnel environment and the heat exchanger system. If the tunnel climate has a not negligible role on the heat exchanged, one may ask what would happen if temperature at that boundary was not prescribed to vary according to a certain fashion but was free to change. The implications of this new assumptions on the geothermal potential could be investigated.
- The experimental site and subsequent numerical analyses in the present work were characterized by a specific hydraulic configuration, that is all-in-parallel rings. The choice at the numerical level simply mirrored that at the experimental one that was defined by costs constrains (only two rings were installed) and based on literature evidence, where this case was generally studied (see for example Barla et al., 2016). However, this is not necessarily the best solution from the cost-analysis point of view. It is expected to be the most effective in terms of thermal performance, as heat carrier fluid temperature trend is not linear with the distance covered, that is the length of the loop, which is why specific thermal power is likely to be higher for all-in-parallel rings. Nevertheless, energy rings basically involve a hydraulic network that needs moving a fluid spending energy. Pressure drops should be estimated. Searching for the configuration that optimizes both the hydraulic costs and the energetic benefits is therefore essential. Analysis for future energy tunnels projects should account for the identified optimal configuration(s).
- An important issue would be the distance between the rings equipped with heat exchangers and the buildings with their own thermal needs (both cooling and heating) given that heat losses might occur. Their amount depends on a number of aspects: type of insulation, temperature within the tunnel, temperature outside the tunnel and in the first few meters of the ground, location of the heat pump (in the station, close to the buildings...), distance of the buildings to be served. Based on this, buffer zones should be defined. Nicholson et al. (2014) considered circles of 250 m radius around shafts and cross-passages. In Turin Metro Line 2 feasibility study buffers have an extension of 100 m (Barla et al., 2020). In Baralis et al. (2018) buffer areas with extension of 25 m were selected. Specific insulation should be designed and numerical simulations involving also the distribution network could be carried out to understand which technological solution works best and up to what distance the system could be driven.
- Additional tests are to be performed for investigating the structural behaviour in ground cooling and air heating mode in order to confirm the order of magnitude of stresses and strains.
- Further experimental analyses are needed under working conditions to check any differences from the results under construction conditions. This would be valuable to go a step forward into the comprehension of interplay with tunnel environmental conditions. Additionally, long-term tests would allow gaining insight into possible unbalanced situations.

- The need for an appropriate calibration of strain FBG measurements emerged from the observation of strain wavelength shifts. Suitable experimental testing in a climatic chamber should therefore be performed both on a sensor embedded within a concrete sample and on a free sensor at the same time to evaluate the differences in wavelength change and validate or refute the provided calibration temperature coefficients.
- Further attention needs be paid to the thermo-mechanical implications under different in situ stresses (k_0) and hydro-geological conditions.
- It is recognized that the strategy of resorting to data transfers from one software to the other, used in the present work for understanding and analysis purposes, might result unfeasible and too complicated in practice, as well as the adoption of fully coupled THM analyses. For this reason, simplified tools should be devised, such as design charts for thermo-mechanical actions or user-friendly apps in order to help practitioners in dealing with energy tunnels structural design for predicting the thermo-mechanical consequences of thermal loads applied.

Selected list of publications

Journal papers

- Barla, M., Di Donna, A. Insana A. (2019). A novel real scale experimental prototype of energy tunnel. *Tunnelling and Underground Space Technology* 87, 1-14.
- Epting, J., Baralis, M., Künze, R., Mueller, M.H., Insana, A., Barla, M., Huggenberger, P. (2020). Geothermal potential of tunnel infrastructures – development of tools at the city-scale of Basel, Switzerland. *Geothermics* 83, 101734, 1-12.
- Insana, A., Barla, M. (2020). Experimental and numerical investigations on the energy performance of a thermo-active tunnel. *Renewable Energy* 152, 781-792.
- Olivero, M., Insana, A., Vallan, A., Gaudino, R., Barla, M., Perrone, G. (**in preparation**). Structural and thermal monitoring of an energy tunnel by fiber Bragg gratings.

Conference papers

- Barla, M., Di Donna, A. Insana, A. (2017). Energy tunnel experimental site in Turin metro. In: Proceedings of 15th IACMAG, Wuhan (China) October 19-23, 2017.
- Barla, M. Insana A. (2018). Energy Tunnel Segmental Lining: an Experimental Site in Turin Metro. In: Proceedings of World Tunnel Congress, Dubai (United Arab Emirates) April 21-26, 2018.
- Olivero, M., Insana, A., Vallan, A., Gaudino, R., Barla, M. Perrone, G. (2018). Fibre Bragg Gratings Monitoring in a Pilot Project of an Energy Tunnel. In: Proceedings of 20a edizione del Convegno Italiano delle Tecnologie Fotoniche, Lecce, May 23-25, 2018.
- Insana, A., Barla, M., Pereira, J.M. Sulem, J. (2018). Analisi del comportamento termo-meccanico di gallerie energetiche in conci prefabbricati. In: Proceedings of Incontro Annuale dei Ricercatori di Geotecnica (IARG), Genova, July 4-6, 2018.
- Barla, M., Insana, A. Zacco, F., Testing of an Enertun segment prototype in Turin metro line 1. In: Proceedings of World Tunnel Congress, Napoli, May 3-9, 2019.
- Barla, M., Baralis, M., Insana, A., Zacco, F., Aiassa, S., Antolini, F., Azzarone, F. Marchetti, P. (2019). Feasibility study for the thermal activation of Turin metro line 2. In: Proceedings of World Tunnel Congress, Napoli, May 3-9, 2019.
- Epting, J., Baralis, M., Künze, R., Mueller, M.H., Insana, A., Barla, M., Huggenberger, P. (**in print**). Thermal activation of tunnel infrastructures: city-scale solutions for Basel, Switzerland. In: Proceedings of 16th IACMAG, Torino (Italy) July 1-4, 2020.
- Baralis, M., Insana, A., Barla, M. (**in print**). Energy tunnels for deicing of a bridge deck in Alpine region. In: Proceedings of 16th IACMAG, Torino (Italy) 1-4 July 2020.
- Barla, M., Baralis, M., Insana, A., Aiassa, S., Antolini, F., Vigna, F., Azzarone, F. Marchetti, P. (**in print**). On the thermal activation of Turin metro Line 2 tunnels. In: Proceedings of 16th IACMAG, Torino (Italy) July 1-4, 2020.
- Insana, A., Barla, M., Sulem, J. (**accepted**). Energy tunnel linings thermo-mechanical performance: comparison between field observations and numerical modelling, In:

Proceedings of 2nd International Conference on Energy Geotechnics, La Jolla, California (USA) September 20-23, 2020.

Guidelines

- Barla, M., Insana, A. (**under preparation**). Valorizzazione del calore del terreno. In: Linee guida per la gestione sostenibile delle acque e del calore nelle gallerie/Guidelines for sustainable water and heat management in tunnels, Chapter 6. Gruppo di Lavoro: studio della gestione sostenibile delle acque nelle gallerie (GESTAG). Coordinated by da Antonio Dematteis e Alessandro Gargini.
- Bogusz, W., Habert, J., Insana, A., Josifsovski, J., Li, Z., Mroueh, H., Sterpi, D. (**under preparation**). Geotechnical design. In: Energy geostructures guidelines, Chapter 5. Working Group 5 of Cost Action TU1405.

Presentations at international events

- Insana, A., Di Donna, A., Barla, M. (2017). An experimental site of energy tunnel lining. 4th Working Group Meeting of COST Action TU1405 Geothermal Applications for Buildings and Infrastructure GABI, Turin, December 6-7, 2016.
- Insana, A., Di Donna, A., Barla, M. (2017). Energy tunnels – Experimental site in Torino. 6th Working Group Meeting of COST Action TU1405 Geothermal Applications for Buildings and Infrastructure GABI, Sofia (Bulgaria) September 25-26, 2017.
- Insana, A., Barla, M., Di Donna, A., Baralis, M., Zacco, F. (2018). Enertun: energy segmental lining. International Symposium on Energy Geotechnics SEG-2018, Innovation Hub, Lausanne, September 25-26, 2018.
- Insana, A. (2018). Gallerie energetiche: un'opportunità di sviluppo per le aree urbane. VII Edizione dell'Incontro delle Commissioni di Ingegneria Geotecnica, Seminario d'aggiornamento Ingegneria geotecnica: scoperta, applicazione, impatto, diffusione, Bolzano, November 22, 2018.
- Barla, M., Insana, A., Zacco, F. (2019). Thermal performance of an energy tunnel prototype. In: Proceedings of 1st Computational & Geoenvironmental Geomechanics for Underground and Subsurface Structures, Nancy (France) February 12-14, 2019.
- Insana, A., Barla, M. (2019). Recupero del calore nelle gallerie. GEAM course “La gestione sostenibile delle acque e del calore negli scavi in sotterraneo”, Politecnico di Torino, Torino, November 4th, 2019.

References

- Abuel-Naga, H.M., Bergado, D.T., Ramana, G.V., Grino, L., Rujivipat, P., Thet, Y. (2006). Experimental evaluation of engineering behavior of soft Bangkok clay under elevated temperature. *Journal of Geotechnical and Geoenvironmental Engineering* 132(7), 902-910.
- Abuel-Naga, H.M., Bergado, D.T., Bouazza, A. (2007a). Thermally induced volume change and excess pore water pressure of soft Bangkok clay. *Engineering Geology* 89(1-2), 144-154.
- Abuel-Naga, H.M., Bergado, D.T., Lim, B.F. (2007b). Effect of temperature on shear strength and yielding behavior of soft Bangkok clay. *Soils and foundations* 47(3), 423-436.
- Adam, D., Markiewicz, R. (2009). Energy from earth-coupled structures, foundations, tunnels and sewers. *Géotechnique* 59(3), 229-236.
- Adinolfi M., Maiorano R.M.S., Mauro, A., Massarotti, N., Aversa S. (2018). On the influence of thermal cycles on the yearly performance of an energy pile. *Geomechanics for Energy and the Environment* 16, 32-44.
- AFTES, 1997. Recommandations relatives à la conception, le dimensionnement et l'exécution des revêtements en voussoirs préfabriqués en béton armé installés à l'arrière d'un tunnelier.
- AFTES, 2007. Compatibilité des recommandations AFTES relatives aux revêtements des tunnels en béton avec les Eurocodes. Tunnels et Ouvrages Souterrains, 204.
- Ahmad, S., Rizvi, Z., Khan, M.A., Ahmad, J., Wuttke, F. (2019). Experimental study of thermal performance of the backfill material around underground power cable under steady and cyclic thermal loading. *Materials Today: Proceedings* 17(1), 85-95.
- Alberdi-Pagola, M. (2018). Design and performance of energy pile foundations. PhD Thesis, Aalborg University, Aalborg, Denmark.
- Allan, M.L., Kavanaugh, S.P. (1999). Thermal conductivity of cementitious grouts and impact on heat exchanger length design for ground source heat pumps thermal conductivity of cementitious grouts and impact in heat exchanger length design for ground source heat pumps. *HVAC&R Res.*, 85-96.
- Amis, T., Loveridge, F. (2014). Energy piles and other thermal foundations for GSHP – developments in UK practice and research. *REHVA JOURNAL*, 32-35.
- Aversa, S., Evangelista, A. (1993). Thermal expansion of Neapolitan yellow tuff. *Rock Mechanics and Rock Engineering* 26(4), 281-306.
- Baldi, G., Hueckel, T., Pellegrini, R. (1988). Thermal volume changes of mineral-water system in low-porosity clay soils. *Canadian Geotechnical Journal* 25, 807-825.
- Baldi, G., Hueckel, T., Peano, A., Pellegrini, R. (1991). Developments in modelling of thermohydro-mechanical behaviour of Boom clay and clay-based buffer materials. ISBN: 92-826-0582-2.
- Banks, D. (2012). The subsurface as a heat storage reservoir. In *An introduction to thermogeology: ground source heating and cooling*, Banks, D. John Wiley & Sons, Ltd, 40-78.
- Baralis, M., Barla, M., Bogusz, W., Di Donna, A., Ryzynski, G., Zerun, M. (2018). Geothermal potential of the NE extension Warsaw (Poland) metro tunnels. *Environmental Geotechnics*, 1-13.
- Barla, G., Barla, M., Bonini, D.M., Debernardi, D., Perino, A., Antolini, F., Gilardi, M. (2015). 3D thermo-hydro modeling and real-time monitoring for a geothermal system in Torino, Italy. In: *Proceedings of the 16th ECSMGE, Geotechnical Engineering for Infrastructure and Development* ICE Publishing, Edinburgh 13-17 September 2015, 2481-2486.
- Barla, M., Barla, G. (2012). Torino subsoil characterization by combining site investigations and numerical modelling. *Geomechanics and Tunneling* 5(3), 214-231.

- Barla, M., Perino, A. (2014). Geothermal heat from the Turin metro south extension tunnels. In: World Tunnel Congress 2014, Iguassu falls, Brazil, May 9-15, 1-8.
- Barla, M., Perino, A. (2015). Energy from geo-structures: a topic of growing interest. *Environmental Geotechnics* 2(1), 3-7.
- Barla, M., Di Donna, A. (2016). Conci energetici per il rivestimento delle gallerie. *Strade & Autostrade* 5, 2-5.
- Barla, M., Di Donna, A. (2018). Energy tunnels: concept and design aspects. *Underground Space* 3(4), 268-276.
- Barla, M., Di Donna, A., Perino, A. (2016). Application of energy tunnels to an urban environment. *Geothermics* 61, 104-113.
- Barla, M., Di Donna, A., Santi, A. (2018). Energy and mechanical aspects on the thermal activation of diaphragm walls for heating and cooling. *Renewable Energy* (in press).
- Barla, M., Di Donna, A., Insana, A. (2019). A novel real-scale experimental prototype of energy tunnel. *Tunnelling and Underground Space Technology* 87, 1-14.
- Barla, M., Baralis, M., Insana, A., Zacco, F., Aiassa, S., Antolini, F., Azzarone, F., Marchetti, P. (2019). Feasibility study for the thermal activation of Turin metro line 2. In: Proceedings of World Tunnel Congress, Napoli, May 3-9, 2019.
- Barla, M., Baralis, M., Insana, A., Aiassa, S., Antolini, F., Vigna, F., Azzarone, F., Marchetti, P. (in print). On the thermal activation of Turin metro Line 2 tunnels. In: Proceedings of 16th IACMAG, Torino (Italy) July 1-4, 2020.
- Berg, A., Grimm, M., Stergiaropoulos, K. (2017). Geothermal usage in inner city tunnels - A study of the Fasanenhof subway tunnel in Stuttgart Germany. In: 12th IEA Heat Pump Conference, 1-11.
- Bergado, D.T., Abuel-Naga, H., Bouazza, A. (2007). Temperature effects on engineering behaviour of soft Bangkok clay. In: Proceedings of the 4th International Conference on Soft Soil Engineering, Vancouver, Canada, 4-6 October 2006, 373-379.
- Bidarmaghz, A., Narsilio, G.A., Buhmann, P., Moormann, C., Westrich, B. (2017). Thermal interaction between tunnel ground heat exchangers and borehole heat exchangers. *Geomechanics for Energy and the Environment* 10, 29-41.
- Bidarmaghz, A., Narsilio, G.A. (2018). Heat exchange mechanisms in energy tunnel systems. *Geomechanics for Energy and the Environment* 16, 83-95.
- Bouazza, A., Adam, D., Rao Singh, M., Ranjith, P.G. (2011). Direct geothermal energy from geostructures. In: Australian Geothermal Energy Conference 2011, 21-24.
- Boudali, M., Leroueil, S., Srinivasa Murthy, B. R. (1994). Viscous behaviour of natural clays. In: Proceedings of the 13th International Conference on Soil Mechanics and Foundation engineering, 1, 411-416.
- Bourne-Webb, P.J., Amatya, B., Soga, K., Amis, T., Davidson, C., Payne, P. (2009). Energy pile test at Lambeth College, London: geotechnical and thermodynamic aspects of pile response to heat cycles. *Géotechnique* 59, 237-248.
- Bourne-Webb, P., Amis, T., Bernard, J.-B., Friedemann, W., von der Hude, N., Pralle, N., Uotinen, V.M., Widerin, B. (2013). Delivery of energy geostructures. In: Laloui, L., Di Donna, A. (Eds.), *Energy Geostructures: Innovation in Underground Engineering*, Wiley-ISTE, 229-263.
- Bourne-Webb, P.J., da Costa Goncalves, R.A., Bodas Freitas, T.M. (2015). Retaining walls as heat exchangers: a numerical study. In: Proceedings of the 16th ECSMGE, Geotechnical Engineering for Infrastructure and development, 2499-2504.
- Bowers, G.A., Olgun, C.G. (2013). Systèmes géothermiques de dégivrage des tabliers de ponts basés sur les fondations énergétiques. In: Laloui, L., Di Donna, A. (Eds.), *Géostrucures énergétiques*, ISTE Ltd. and John Wiley & Sons Inc, 239-256.
- Bracq, G., Soussi, C., Fouché, O., Minec, S. (2017). Utilisation de l'énergie géothermique en tunnel/Capturing geothermal energy using tunnel lining. In: Congrès International de l'AFITES - L'espace Souterrain Notre Richesse, 1-8.

- Brandl, H. (2006). Energy foundations and other thermo-active ground structures. *Géotechnique* 56(2), 81–122.
- Brandl, H. (2013). Thermo-active ground-source structures for heating and cooling. *Procedia Engineering* 57, 9–18.
- Browne, R.D. (1968). Properties of Concrete in Reactor Vessels. In: Conference on Prestressed Concrete Pressure Vessels at Church House, Westminster, The Institute of Civil Engineers, London, 131-151.
- Bucci, A., Barbero, D., Lasagna, M., Forno, M.G., De Luca, D.A. (2017). Shallow groundwater temperature in the Turin area (NW Italy): vertical distribution and anthropogenic effects. *Environmental Earth Sciences* 76(221).
- Buhmann, P., Moormann, C., Westrich, B., Pralle, N., Friedemann, W. (2016). Tunnel geothermics—A German experience with renewable energy concepts in tunnel projects. *Geomechanics for Energy and the Environment* 8, 1-7.
- Burghignoli A., Desideri A., Miliziano S. (1992). Deformability of clays under non isothermal conditions. *Rivista Italiana di Geotecnica* 4/92, 227-236.
- Burghignoli A., Desideri A., Miliziano S. (2000). A laboratory study on the thermomechanical behaviour of clayey soils. *Canadian Geotechnical Journal* 37, 764-780.
- Burlon, S., Habert, J., Szymkiewicz, F., Suryatriyastuti, M., Mroueh, H. (2013). Towards a design approach of bearing capacity of thermo-active piles. European Geothermal Congress, Pisa, Italy.
- Cairo, S., Prodan, I.C., Barla, M. (2018). Assesment of input parameters in designing energy tunnels. In: C65 International Conference Tradition and Innovation - 65 Years of Constructions in Transilvania, Universitatea Tehnică din Cluj-Napoca, 1-2.
- Callisto, L. (2009). Analisi agli stati limite di sistemi geotecnici. Incontro Annuale dei Ricercatori di Geotecnica.
- Campanella, R.G., Mitchell, J.K. (1968). Influence of the temperature variations on soil behaviour. *Journal of the Soil Mechanics and Foundation Engineering Division* 94(SM3), 709-734.
- Carslaw, H.S., Jaeger, J.C. (1959). Conduction of Heat in Solids. Oxford University Press, Oxford.
- Cekerevac, C., Laloui, L. (2004). Experimental study of thermal effects on the mechanical behaviour of a clay. *Int. J. Numer. Anal. Meth. Geomech.*, 28: 209-228.
- Cekerevac, C., Laloui, L. (2010). Experimental analysis of the cyclic behaviour of kaolin at high temperature. *Géotechnique* 60(8), 651-655.
- CFMS/SYNTEC INGENIERIE/SOFFONS-FNTP (2016). Recommandations pour la conception, le dimensionnement et la mise en oeuvre des géostructures thermiques. *Rev. Fr. Geotech.* 149(1), 1-120.
- Chiu, J.P.S. (1996). Behavior of normally consolidated clay at elevated temperature, Ph.D. thesis, University of Sydney, Australia.
- Cobo, A., Martinez, I., Prieto, M.I., Moreno, E. (2015). Mechanical behaviour of thermally activated building structures. *Magazine of Concrete Research* 67(6), 271-281.
- Cousin, B., Rotta Loria, A.F., Bourget, A., Rognon, F., Laloui, L. (2019). Energy performance and economic feasibility of energy segmental linings for subway tunnels. *Tunnelling and Underground Space Technology* 91.
- Cui, Y.J., Sultan, N., Delage, P. (2000). A thermomechanical model for saturated clays. *Canadian Geotechnical Journal* 37, 607-620.
- DAUB (2013). Recommendations for the design, production and installation of segmental rings. German Tunnelling Committee (DAUB), Köln, Germany.
- Delage, P., Cui, Y.J., Tang, A.-M. (2010). Clays in radioactive waste disposal. *Journal of Rock Mechanics and Geotechnical Engineering* 2(2), 111-123.
- Delage, P. (2013). On the thermal impact on the excavation damaged zone around deep radioactivewaste disposal. *Journal of Rock Mechanics and Geotechnical Engineering* 5, 179-190.
- Delerablée, Y., Rammal, D., Mroueh, H., Burlon, S., Habert, J., Froitier, C. (2018). Integration of thermoactive metro stations in a smart energy system: feedbacks from the Grand Paris Project. *Infrastructures* 3(56), 1-15.

- Delerablée, Y., Burlon, S., Reiffsteck, P. (2019). Long-term assessment of thermal sustainability of thermoactive geostructures. *Environmental Geotechnics* 0 0:0, 1-17.
- Di Donna, A. (2014). Constructive recommendations for optimized and reliable heat exchanger pile systems. PhD Thesis, EPFL, Lausanne, Switzerland.
- Di Donna, A., Barla, M. (2016). The role of ground conditions on energy tunnels' heat exchange. *Environmental Geotechnics* 3.
- Di Donna, A., Barla, M., Amis, T. (2017). Energy geostructures: a collection of data from real applications. In: 15th IACMAG, 19-23 October 2017, Wuhan, China, 1-9.
- Di Donna, A., Cecinato, F., Loveridge, F., Barla, M. (2016). Energy performance of diaphragm walls used as heat exchangers. *Proceedings of the Institution of Civil Engineers - Geotechnical Engineering* 170(3), 232–245.
- Di Donna, A., Ferrari, A., Laloui, L. (2016). Experimental investigation of the soil-concrete interface: physical mechanisms, cyclic mobilization, and behaviour at different temperatures. *Canadian Geotechnical Journal* 53, 659-672.
- Di Donna, A., Laloui, L. (2015). Response of soil subjected to thermal cyclic loading: Experimental and constitutive study. *Engineering Geology* 190, 65-76.
- Diersch, H.J.G. (2009). DHI Wasy Software—Feflow 6.1—Finite Element Subsurface Flow & Transport Simulation System: Reference Manual.
- Directive 2009/28/EC (2009). Directive 2009/28/EC of the European Parliament and of the Council of 23 April 2009 on the promotion of the use of energy from renewable sources. *Official Journal of the European Union* 140, 16–62.
- Dixon, D.A., Gray, M.N., Lingnau, B.E., Graham, J., Campbell, S.L. (1993). Thermal expansion testing to determine the influence of pore water structure on water flow through dense clays. In: Proceedings of the 46th Canadian Geotechnical Conference, Saskatoon, 177-183.
- D.P.R. 26 agosto 1993, n. 412. Regolamento recante norme per la progettazione, l'installazione, l'esercizio e la manutenzione degli impianti termici degli edifici ai fini del contenimento dei consumi di energia, in attuazione dell'art. 4, comma 4, della L. 9 gennaio 1991, n. 10.
- Dupray, F., Mimouni, T., Laloui, L. (2013). Alternative uses of heat-exchanger geostructures. In: Laloui, L., Di Donna, A. (Eds.), *Energy Geostructures: Innovation in Underground Engineering*, ISTE Ltd. and John Wiley & Sons Inc, 119-138.
- EN 1992-1-2 (2004). Eurocode 2: Design of concrete structures - Part 1-2: General rules - Structural fire design.
- Epting, J., Handel, F., Huggenberger, P. (2013). Thermal management of an unconsolidated shallow urban groundwater body. *Hydrology and Earth System Sciences* 17, 1851-1869.
- Epting, J., Huggenberger, P. (2013). Unraveling the heat island effect observed in urban groundwater bodies – Definition of a potential natural state. *Journal of Hydrology* 501, 193–204.
- Eriksson, L.G. (1989). Temperature effects on consolidation properties of sulphide clays. In: Proceedings of the 12th International Conference on Soil Mechanics and Foundation Engineering, Rio de Janeiro, 1989, 2087–2090.
- European Commission (2012). Commission Recommendation of 17 July 2012 on access to and preservation of scientific information (2012/417/EU). Official Journal of the European Union.
- European Commission (2016). Overview of support activities and projects of the European Union on energy efficiency and renewable energy in the heating & cooling sector. Publications Office of the European Union, Luxembourg.
- Eurostat (2017). Smarter, greener, more inclusive? - Indicators to support the Europe 2020 strategy. Publications Office of the European Union, Luxembourg.
- Favero, V., Ferrari, A., Laloui, L. (2016). An insight on the thermo-mechanical behaviour of a shale. In: 5th EAGE Shale Workshop.
- Fei, Y. (1995). Thermal expansion. In: Thomas JA, editor. *Mineral Physics and Crystal-lography: A Handbook of Physical Constants*. Washington, D.C., American Geophysical Union, 29–44.

- Fouché, O., Soussi, C., Bracq, G., Minec, S. (2018). Seasonal storage of sensible heat in tunnel-surrounding rocks. In: Proceedings of the First International Conference on Advances in Rock Mechanics, TUNIROCK 2018, Hammamet, Tunisia, 29-31 March 2018, 63–68.
- François, B., Laloui, L. (2008). ACMEG-TS: a constitutive model for unsaturated soils under non-isothermal conditions. *International Journal for Numerical and Analytical Methods in Geomechanics* 32, 1955-1988.
- Franzius, J.N., Pralle, N. (2011). Turning segmental tunnels into sources of renewable energy. Proceedings of the ICE - Civil Engineering 164, 35–40.
- Frodl, S., Franzius, J.N., Bartl, T. (2010). Design and construction of the tunnel geothermal system in Jenbach. *Geomechanik Tunnelbau* 3, 658-668.
- Geimer, C. (2013). Metro tunnels enable geothermal-air conditioning. BINE information service, Projektinfo 09/2013, FIZ Karlsruhe – Leibniz Institute for Information Infrastructure, Germany (ISSN 0937-8367).
- Gens, A., Vaunat, J., Garitte, B., Wileveau, Y. (2007). In situ behaviour of a stiff layered clay subjected to thermal loading: observations and interpretation. *Géotechnique* 57, 207-228.
- Ghazebloo, S., Sulem, J. (2009). Stress dependent thermal pressurization of a fluid-saturated rock. *J. Rock Mechanics and Rock Engineering* 42(1), 1-24.
- Graham, J., Tanaka, N., Crilly, T., Alfaro, M. (2001). Modified Cam-Clay modelling of temperature effects in clay. *Canadian Geotechnical Journal* 38, 608-621.
- GSHPA, 2012. Thermal pile design, installation and materials standards. Issue 1.0, Ground Source Heat Pump Association, Milton Keynes, UK.
- Habert, J., Mroueh, H., Josifovski, J., Bogusz, W., Sterpi, D., Georgiadis, K. (2018). Synthesis of a benchmark exercise for geotechnical analysis of a thermoactive pile. *ICE Environmental Geotechnics*.
- Horseman, S.T., McEwen, T.J. (1996). Thermal constraints on disposal of heat-emitting waste in argillaceous rocks. *Engng Geol.* 41, 5–16.
- Hueckel, T., Baldi, G. (1990). Thermoplasticity of saturated clays: experimental constitutive study. *Journal of Geotechnical Engineering* 116(12), 1768–1796.
- Hueckel, T., Borsetto, M. (1990). Thermoplasticity of saturated soils and shales: constitutive equations. *Journal of Geotechnical Engineering* 112(16), 1765-1777.
- Hueckel, T., Pellegrini, R. (1992). Effective stress and water pressure in saturated clays during heating-cooling cycles. *Canadian Geotechnical Journal* 29, 1095-1102.
- Hueckel, T., Pellegrini, R., Del Olmo, C. (1998). A constitutive study of thermo-elastoplasticity of deep carbonatic clays. *International Journal for Numerical and Analytical Methods in Geomechanics* 22(7), 549-574.
- Hueckel, T., François, C., Laloui, L. (2009). Explaining thermal failure in saturated clays. *International Géotechnique* 59(3), 197-212.
- IEA, World Bank (2015). Sustainable Energy for All 2015—Progress Toward Sustainable Energy. Washington, DC.
- Infratrasporti.To S.r.l. (2015). Metropolitana automatica di Torino Linea 1 Prolungamento Sud – Tratta 4 Lingotto/Bengasi. Appalto integrato per la progettazione esecutiva ed esecuzione dei lavori, ai sensi dell'art. 232 D.Lgs. 163/20. Progetto esecutivo di dettaglio. Progetto strutturale galleria a foro cieco. Scavo meccanizzato. Relazione di dimensionamento dei conci prefabbricati. MIL1T4A0CSTRGN1R000101. Appaltatore: Consorzio Cooperative Costruzioni. Progettista dell'Appaltatore: AK Ingegneria Geotecnica S.r.l., Studio Corona S.r.l., Prof. Ing. Sebastiano Pelizza.
- Insana, A., Barla, M. (2020). Experimental and numerical investigations on the energy performance of a thermo-active tunnel. *Renewable Energy* 152, 781-792.
- Insana, A., Barla, M., Sulem, J. (**accepted**). Energy tunnel linings thermo-mechanical performance: comparison between field observations and numerical modelling, In: Proceedings of 2nd International Conference on Energy Geotechnics, La Jolla, California (USA) September 20-23, 2020.

- Islam, S., Fukuhara, T., Watanabe, H., Nakamura, A. (2006). Horizontal U-Tube road heating system using tunnel ground heat. *Journal of Snow Engineering of Japan* 22(3), 229-234.
- ITA (2000). Guidelines for the Design of Shield Tunnel Lining. *Tunnelling and Underground Space Technology* 15(3), 303-331.
- Itasca (2016). Flac ver.7.0 user's manual.
- Kassir, M.K., Bandyopadhyay, K.K., Reich, M. (1996). Thermal degradation of concrete in the temperature range from ambient to 315°C. Report, Department of Advanced Technology, Brookhaven National Laboratory, New York.
- Khalili, N., Uchaipichat, A., Javadi, A.A. (2010). Skeletal thermal expansion coefficient and thermo-hydro-mechanical constitutive relations for saturated homogeneous porous media. *Mechanics of Materials* 42, 593-598.
- Knellwolf, C., Peron, H., Laloui, L. (2011). Geotechnical analysis of heat exchanger piles. *Journal of Geotechnical and Geoenvironmental Engineering* 137(10), 890-902.
- Knödler, P. (2019). Thermo-mechanical investigations of packed beds for high temperature heat storage: uniaxial compression test experiments and particle discrete simulations. *Applied Sciences* 9(8), 1600, 1-11.
- Kürten, S., Mottaghy, D., Ziegler, M. (2015). A new model for the description of the heat transfer for plane thermo-active geotechnical systems based on thermal resistances. *Acta Geotechnica* 10, 219-229.
- Laloui, L. (2001). Thermo-mechanical behaviour of soils. *Revue Française de Génie Civil* 5(6), 809-843.
- Laloui, L., Cekerevac, C. (2003). Thermo-plasticity of clays: an isotropic yield mechanism. *Computers and Geotechnics* 30, 649-660.
- Laloui, L., Moreni, M., Vulliet, L. (2003). Comportement d'un pieu bi-fonction, fondation et échangeur de chaleur. *Canadian Geotechnical Journal* 40(2), 388-402.
- Laloui, L., Di Donna, A. (2011). Understanding the behaviour of energy geo-structures. Proceedings of the *Institution of Civil Engineers - Civil Engineering* 164(4), 184-191.
- Laloui, L., Di Donna, A. (2013). Energy Geostructures: Innovation in Underground Engineering. ISTE Ltd and John Wiley & Sons Inc.
- Laloui, L., François, B. (2009). ACMEG-T: Soil thermoplasticity model. *Journal of Engineering Mechanics* 135(9), 932-944.
- Laloui, L., Nuth, M., Vuillet, L. (2006). Experimental and numerical investigations of the behaviour of a heat exchanger pile. *International Journal for Numerical and Analytical Methods in Geomechanics* 30, 763-781.
- Laloui, L., Olgun, C.G., Sutman, M., McCartney, J.S., Coccia, C.J., Abuel-Naga, H.M., Bowers, G.A. (2014). Issues involved with thermo-active geotechnical systems: characterization of thermo-mechanical soil behavior and soil-structure interface behavior. *DFI Journal – The Journal of the Deep Found Institute* 8(2), 108-120.
- Lee, C., Park, S., Won, J., Jeoung, J., Sohn, B., Choi, H. (2012). Evaluation of thermal performance of energy textile installed in Tunnel. *Renewable Energy* 42, 11-22.
- Lee, C., Park, S., Choi, H.-J., Lee, I.-M., Choi, H. (2016). Development of energy textile to use geothermal energy in tunnels. *Tunnelling and Underground Space Technology*, 59, 105-113.
- Lee, K.S. (2013). Underground Thermal Energy Storage. In: *Underground Thermal Energy Storage. Green Energy and Technology*. Springer, London.
- Loveridge, F., Low, J., Powrie, W. (2017). Site investigation for energy geostructures. *Quarterly Journal of Engineering Geology and Hydrogeology* 50, 158-168.
- Loveridge, F., Powrie, W. (2013). Pile heat exchangers: thermal behaviour and interactions. *Proceedings of the Institution of Civil Engineers - Geotechnical Engineering* 166(GE2), 178-196.
- Lund, J.W. Freeston, D.H., Boyd, T.L. (2011). Direct utilization of geothermal energy 2010 worldwide review. *Geothermics* 40: 159-180.
- Markiewicz, R. (2004). Numerische und Experimentelle Untersuchungen zur Nutzung von geothermischer Energie Mittels erdberührter Bauteile und Neuentwicklungen für den

- Tunnelbau Doctoral Thesis. Institute for Soil Mechanics and Geotechnical Eng., Technical Univ. of Vienna, Germany.
- Markiewicz, R., Adam, D. (2003). Utilisation of Geothermal Energy using Earthcoupled Structure - Theoretical and Experimental Investigations, Case Histories. In: Geotechnical Problems With Man-Made And Man Influenced Grounds, XIII European Conference on Soil Mechanics and Geotechnical Engineering, 25-28 August 2003, Prague.
- Markiewicz, R., Adam, D., Hofinger, J., Unterberger, W. (2005). Extraction of geothermal energy from tunnels. In: Proceedings of the 16th International Conference on Soil Mechanics and Geotechnical Engineering, 1629-1632.
- Maruyama, I., Kontani, O., Sawada, S., Sato, O., Takizawa, M. (2013). Evaluation of Irradiation Effects on Concrete Structure: Background and Preparation of Neutron Irradiation Test. In: Proceedings of the ASME 2013 Power Conference POWER2013, July 29-August 1, 2013, Boston, Massachusetts, USA.
- Mayer, P.-M., Franzius, J.N. (2010). Thermische Berechnungen im Tunnelbau. *Geotechnik* 33, 145–151.
- McKinstry H.A. (1965). Thermal expansion of clay minerals. *The American Mineralogist* 50(1-2), 212-222.
- McTigue, D.F. (1986). Thermoelastic response of fluid-saturated porous rock. *Journal of Geo-physical Research* 91, 9533–42 (B9).
- Mimouni, T. (2014). Thermomechanical Characterization of Energy Geostructures with Emphasis on Energy Piles. PhD Thesis, EPFL, Lausanne, Switzerland.
- Mimouni, T., Dupray, F., Minon, S., Laloui, L. (2013). Heat exchanger anchors for thermo-active tunnels. Report, EPFL, Lausanne, Switzerland.
- Mimouni, T., Laloui, L. (2013). Full-scale in situ testing of energy piles. In Energy Geostructures: Innovation in Underground Engineering, Laloui, L., Di Donna, A. (eds). ISTE, London, UK and Wiley, Hoboken, NJ, USA, 23–43.
- Modaressi, H., Laloui, L. (1997). A thermo-viscoplastic constitutive model for clays. *International Journal of Numerical and Analytical methods in Geomechanics* 21, 313-335.
- Monfared, M., Sulem, J., Delage, P., Mohajerani, M. (2011). A laboratory investigation on thermal properties of the Opalinus claystone. *Int J Rock Mech Min Sci* 44(6), 735-747.
- Moormann, C., Buhmann, P., Friedemann, W., Homuth, S., Pralle, N. (2016). Tunnel geothermics – International experience with renewable energy concepts in tunnelling. *Geomechanik Tunnelbau* 9, 467-480.
- Moormann, C., Buhmann, P., Westrich, B. (2018). Web-based application for the investigation of thermally activated tunnels. *Tunnel* 6, 46-56.
- Moritz, L. (1995). Geotechnical properties of clay at elevated temperatures. Report, vol. 47, Linköping: Swedish Geotechnical Institute.
- Mroueh, H., Habert, J., Rammal, D. (2018). Design charts for geothermal piles under various thermo-mechanical conditions. *ce/papers* 2, 181-190.
- NHBC (2010). Efficient Design of Piled Foundations for Low Rise Housing, Design Guide. NHBC Foundation, Milton Keynes, UK.
- Nicholson, D.P., Chen, Q., Pillai, A., Chendorain, M. (2013). Developments in thermal pile and thermal tunnel linings for city scale GSHP systems. In: Proceedings of the 38th Workshop on Geothermal Reservoir Engineering, Stanford University, Stanford, California, February 11-13.
- Nicholson, D.P., Chen, Q., De Silva, M., Winter, A., Winterling, R. (2014). The design of thermal tunnel energy segments for Crossrail, UK. *Engineering Sustainability* 167 (3), 118–134.
- NTC2018 (2018). D.M. 17-01-2018: Aggiornamento delle «Norme tecniche per le costruzioni».
- Ogunleye, O., Singh, R.M., Cecinato, F., Chan Choi, J. (2019). Effect of intermittent operation on the thermal efficiency of energy tunnels under varying tunnel air temperature. *Renewable Energy* 146, 2646-2658.
- Olivero, M., Insana, A., Vallan, A., Gaudino, R., Barla, M. Perrone, G. (2018). Fibre Bragg Gratings Monitoring in a Pilot Project of an Energy Tunnel. In: Proceedings of 20a edizione del Convegno Italiano delle Tecnologie Fotoniche, Lecce, May 23-25, 2018.

- Pahud, D. (2013). A case study: the Dock Midfield of zurich Airport. In: Laloui, L., Di Donna, A. (Eds.), *Energy Geostructures: Innovation in Underground Engineering*, ISTE Ltd and John Wiley & Sons Inc, 281–295.
- Palciauskas, V.V., Domenico, P.A. (1982). Characterization of drained and undrained response of thermally loaded repository rocks. *Water Resources Research* 18(2), 281–90.
- Peltier, M., Rotta Loria, A.F., Lepage, L., Garin, E., Laloui, L. (2019). Numerical investigation of the convection heat transfer driven by airflows in underground tunnels. *Applied Thermal Engineering* 159.
- Plum, R.L., Estrig, M.I. (1969). Some temperature effects on soil compressibility and pore water pressure. Effect of temperature and heat on engineering behaviour of soils. *Highway Research Board Special Report* 103, 231-242.
- Preene, M., Powrie, W. (2009). Ground energy systems: from analysis to geotechnical design. *Géotechnique* 59(3), 261-271.
- Rammal, D., Mroueh, H., Burlon, S. (2018a). Impact of thermal solicitations on the design of energy piles. *Renewable and Sustainable Energy Reviews* 92, 111-120.
- Rammal, D., Mroueh, H., Burlon, S. (2018b). Thermal behaviour of geothermal diaphragm walls: evaluation of exchanged thermal power. *Renewable Energy* 92, 111-120.
- REN21 (2017). *Renewables Global Futures Report: Great debates towards 100% renewable energy*. Paris.
- Ronchi, F., Salciarini, D., Cavalagli, N., Tamagnini, C. (2018). Thermal response prediction of a prototype of Energy Micro-Pile. *Geomechanics for Energy and the Environment* 16, 64-82.
- Rotta Loria, A.F. (2017). On the geo-structural behaviour of thermo-active pile groups under mechanical and thermal cyclic actions. PhD Thesis, EPFL, Lausanne, Switzerland.
- Rybach, L. (1995). Thermal waters in deep Alpine tunnels. *Geothermics* 24(5–6), 631-637.
- Ryzynski, G., Bogusz, W. (2016). City-scale perspective for thermoactive structures in Warsaw. *Environmental Geotechnics* 3(4), 280–290.
- Sakurai, S., Akutagawa, S., Takeuchi, K., Shinji, M., Shimizu, N. (2003). Back analysis for tunnel engineering as a modern observational method. *Tunnelling and Underground Space Technology* 18, 185–196.
- Sanner, B. (2001). Shallow geothermal energy. *GHC Bulletin*. June Issue, 19–25.
- Shafagh, I., Rees, S. (2018). A foundation wall heat exchanger model and validation study. In: IGSHPA Research Track, Stockholm, 18-20 September 2018.
- Schetty, R., Singh, D.N., Ferrari, A. (2019). Volume change characteristics of fine-grained soils due to sequential thermo-mechanical stresses. *Engineering Geology* 253, 47-54.
- Schlosser, T., Schmidt, M., Schneider, M., Vermeer, P. (2007). Potenzial der Tunnelbaustrecke des Bahnprojektes Stuttgart 21 zur Wärme- und Kältenutzung, Final Report, IGE-07-07.
- Schofield, A.N., Wroth, C.P. (1968). *Critical state soil mechanics*. McGraw-Hill, London, United Kingdom.
- Schneider, M., Moormann, C. (2010). GeoTU6 – a geothermal Research Project for Tunnels. *Tunnel* 29, 14-21.
- SIA (2005). *Utilisation de la chaleur du sol par des ouvrages de fondation et de soutènement en béton, guide pour la conception, la réalisation et la maintenance*. Swiss Society of Engineers and Architects, Geneva, Switzerland.
- Documentation D 0190 (in French).
- Sciotti, A. (2010). Applicazione delle nuove norme tecniche per le costruzioni (DM 14/1/2008) alle opere in sotterraneo. *Gallerie e grandi opere sotterranee* 93, 61–69. Patron.
- Smart Fibres, SmartScan datasheet. Available: <https://www.smartfibres.com/products/smartsan>.
- Soga, K., Rui, Y. (2016). Energy geostructures, in: Rees, S.J. (Ed.), *Advances in Ground-Source Heat Pump Systems*. Woodhead Publishing, 185–221.

- Sterpi, D., Coletto, A., Mauri, L. (2017). Investigation on the behaviour of a thermo-active diaphragm wall by thermo-mechanical analyses. *Geomechanics for Energy and the Environment* 9, 1-20.
- Sterpi, D., Angelotti, A., Habibzadeh-Bigdarvish, O., Jalili, D. (2018). Assessment of thermal behaviour of thermoactive diaphragm walls based on monitoring data. *Journal of Rock Mechanics and Geotechnical Engineering* 10, 1145-1153.
- Sterpi, D., Tomaselli, G., Angelotti, A. (2019). Energy performance of ground heat exchangers embedded in diaphragm walls: Field observations and optimization by numerical modelling. *Renewable Energy* (in press).
- Straullu, S., Savio, P., Chang, J., Ferrero, V., Nespola, A., Gaudino, R. (2015). Optimization of Reflective FDMA-PON Architecture to Achieve 32 Gb/s Per Upstream Wavelength Over 31 dB ODN Loss. *J. Light. Technol.*, 33(2), 474-480.
- Suryatriyastuti, M., Mroueh, H., Burlon, S. (2012). Understanding the temperature-induced mechanical behaviour of energy pile foundations. *Renewable and Sustainable Energy Reviews* 16(5), 3344-3354.
- Tang, A.-M., Cui, Y.-J., Barnel, N. (2008). Thermomechanical behaviour of a compacted swelling clay. *Géotechnique* 58(1), 45-54.
- Tidfors, M., Sallfors, S. (1989). Temperature effect on preconsolidation pressure. *Geotechnical Testing Journal* 12(1), 93-97.
- Tinti, F., Boldini, D., Ferrari, M., Lanconelli, M., Kasmae, S., Bruno, R., Egger, H., Voza, A., Zurlo, R. (2017). Exploitation of geothermal energy using tunnel lining technology in a mountain environment. A feasibility study for the Brenner Base tunnel – BBT. *Tunnelling and Underground Space Technology* 70, 182-203.
- Towhata, I., Kuntiwattanaku, P., Seko, I., Ohishi, K. (1993). Volume change of clays induced by heating as observed in consolidation tests. *Soils and Foundations* 33(4), 170-1993.
- Tsagarakis, K., Efthymiou, L., Michopoulos, A., Mavragani, A., Andjelkovic, A., Antolini, F., Bacic, M., Bajare, D., Baralis, M., Bogusz, W., Burlon, S., Figueira, J., Serdar Genç, M., Javed, S., Jurelionis, A., Koca, K., Ryżyński, G., Urchueguia, J., Zlender, B. (2020). A review of the legal framework in shallow geothermal energy in selected European countries: Need for guidelines. *Renewable Energy* 147, 2556-2571.
- Tsagarakis, K. (2020). Shallow geothermal energy under the microscope: social, economic and institutional aspects. *Renewable Energy* 147, 2801-2808.
- UNI 11104 (2004). Calcestruzzo - Specificazione, prestazione, produzione e conformità - Istruzioni complementari per l'applicazione della EN 206-1.
- UNI EN 206-1 (2006). Calcestruzzo - Parte 1: Specificazione, prestazione, produzione e conformità.
- UNI EN 14511-1:2018 (2018). Air conditioners, liquid chilling packages and heat pumps for space heating and cooling and process chillers, with electrically driven compressors - Part 1: Terms and definitions.
- UNI EN 1990 (2006). Eurocode 0 - Basis of structural design.
- UNI EN 1991 (2004). Eurocode 1 - Actions on structures.
- UNI EN 1992 (2008). Eurocode 2 - Design of concrete structures.
- UNI EN 1997 (2009). Eurocode 7 - Geotechnical Design.
- Unterberger, W., Hofinger, H., Grünstäudl, T., Adam, D., Markiewicz, R. (2004). Utilization of Tunnels as Source of Ground Heat and Cooling – Practical Applications in Austria. In: Proceedings of the ISRM International Symposium 3rd ARMS, Kyoto, 2004, 421-426.
- Vieira, A., Alberdi-Pagola, M., Christodoulides, P., Javed, S., Loveridge, P., Nguyen, F., Cecinato F. et al. (2017). Characterisation of ground thermal and thermo-mechanical behaviour for shallow geothermal energy applications. *Energies* MDPI 10(12).
- Wilhelm, J., Rybach, L. (2003). The geothermal potential of Swiss Alpine tunnels. *Geothermics*, 32, 557-568.
- Woodside, W., Messmer, J.M. (1961). Thermal conductivity of porous media. *Journal of Applied Physics*, 32, 1688-1706.

- Yavari, N., Tang, A.M., Pereira, J.M., Hassen, G. (2016). Effect of temperature on the shear strength of soils and the soil-structure interface. *Canadian Geotechnical Journal* 53, 1186–1194.
- Zhang, G., Xia, C., Sun, M., Zou, Y., Xiao, S. (2013). A new model and analytical solution for the heat conduction of tunnel lining ground heat exchangers. *Cold Regions Science and Technology* 88, 59-66.
- Zhang, G., Xia, C., Yang, Y., Sun, M., Zou, Y. (2014). Experimental study on the thermal performance of tunnel lining ground heat exchangers. *Energy and Buildings* 77, 149-157.
- Zhang, G., Guo, Y., Zhou, Y., Ye, M., Chen, R., Zhang, H., Yang, J., Chen, J., Zhang, M., Lian, Y., Liu, C. (2016). Experimental study on the thermal performance of tunnel lining GHE under groundwater flow. *Applied Thermal Engineering* 106, 784-795.

Appendix A

Experimental data

A.1 Contents

The present Appendix is to collect the data of the experimental programme carried out in this Thesis and described in Chapter 4. For each test, in chronological order, after a short description, a table is given by reporting the circuit in operation, mode (heating, cooling or ventilation), secondary temperature set, working rings, flow rate, flow velocity, starting/ending time and duration. Next, figures depicting the following records are provided, when available:

- temperatures measured by the heat pump (primary circuit, secondary circuit and air);
- temperatures measured by probes T1-T5;
- thermally induced strains in the lining;
- thermally induced stresses in the lining;
- temperatures measured in correspondence of the strain gauges location;
- temperatures measured in correspondence of pressure cells transducer;
- air temperature;
- temperatures, thermally induced strains and thermally induced stresses in segments 2, 4 and 6 of ring 179;
- temperatures and thermally induced stresses in segments 1, 3 and 5 of ring 179.

It is pointed out that if anyone of the above-mentioned figures or quantities does not appear, this is due to missing data or unavailability of the monitoring system. Records of undisturbed phases (that is subjected only to natural thermal conditions) are added to the tests. Also given are complete data sets obtained. All data are organised in three tables, listing:

- strains and related temperatures;
- stresses and related temperatures;
- temperatures measured by sensors T1-T5 and by the heat pump embedded sensors.

In the last table of each test a summary of initial, final, differential and average quantities is shown, useful for comparisons between tests conditions and results. A complete list of the tests performed is reported in Table 4.6. Clarification about the sensors coding is given in Table A.1.

Table A.1: Meaning of sensors coding

Coding	Meaning
ENERTUN IN or IN	Supply primary temperature (from the heat pump) measured by the heat pump
ENERTUN OUT or OUT	Back primary temperature (to the heat pump) measured by the heat pump
Pt1	Hoop pressure cell located at mid-thickness of segment 1
Pl2	Longitudinal pressure cell located at mid-thickness of segment 2
Pt3	Hoop pressure cell located at mid-thickness of segment 3
Pr4	Radial pressure cell located at mid-thickness of segment 4
Pt5	Hoop pressure cell located at mid-thickness of segment 5
Pr6	Radial pressure cell located at mid-thickness of segment 6
Sl2e	Longitudinal strain gauge located at the extrados of segment 2
Sl2i	Longitudinal strain gauge located at the intrados of segment 2
St4e	Hoop strain gauge located at the extrados of segment 4
St4i	Hoop strain gauge located at the intrados of segment 4
St6e	Hoop strain gauge located at the extrados of segment 6
St6i	Hoop strain gauge located at the intrados of segment 6
T _{air}	Temperature measured by the heat pump gauge on top of it
T ₁	Temperature in the tunnel close to the prototype
T ₂	Supply temperature immediately before segment 1 inlet in ground circuit
T ₃	Back temperature immediately after segment 6 outlet in ground circuit
T ₄	Supply temperature immediately before segment 1 inlet in air circuit
T ₅	Back temperature immediately after segment 6 outlet in air circuit
T _{DL} or T _{DATALOGGER}	Temperature measured by the datalogger to check possible overheating
T _{thermoigrometer}	Temperature measured by a portable thermoigrometer inside the tunnel
U1	Supply secondary temperature (from the heat pump) measured by the heat pump
U2	Back secondary temperature (to the heat pump) measured by the heat pump
ΔT_{air}	$T_5 - T_4$
$\Delta T_{ENERTUN}$	IN-OUT
ΔT_{ground}	$T_3 - T_2$

Undisturbed phase (winter 2017)

Before the execution of the tests, natural conditions were investigated with the aim to verify the correct functioning of the monitoring system. In this phase, the heat pump was not present as it was not available yet, hence the heat carrier fluid did not circulate in the pipes. The very first test was performed in the afternoon of October 11th, 2017. The temperature probes T1-T5 were installed later too, on November 23rd, 2017.

Starting time t_0 :	31/08/2017 17:22
Ending time t_1 :	11/10/2017 15:01
Duration:	40.9 days

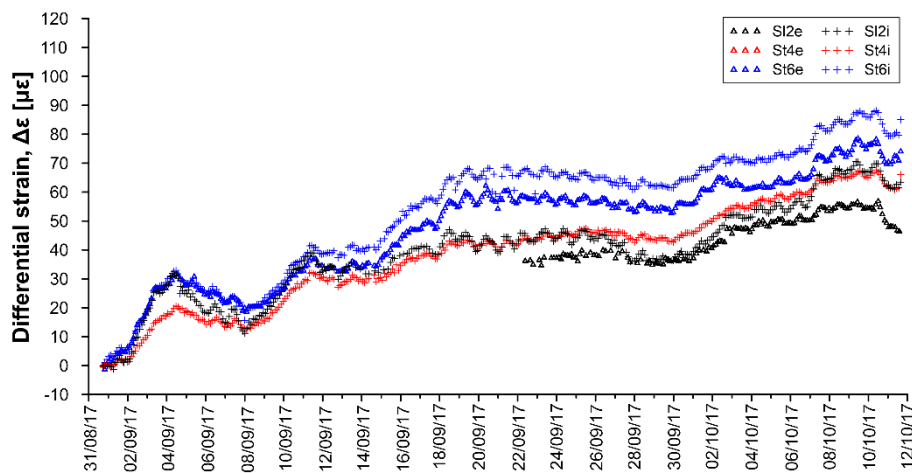


Figure A.1: Differential strains for the undisturbed phase (winter 2017).

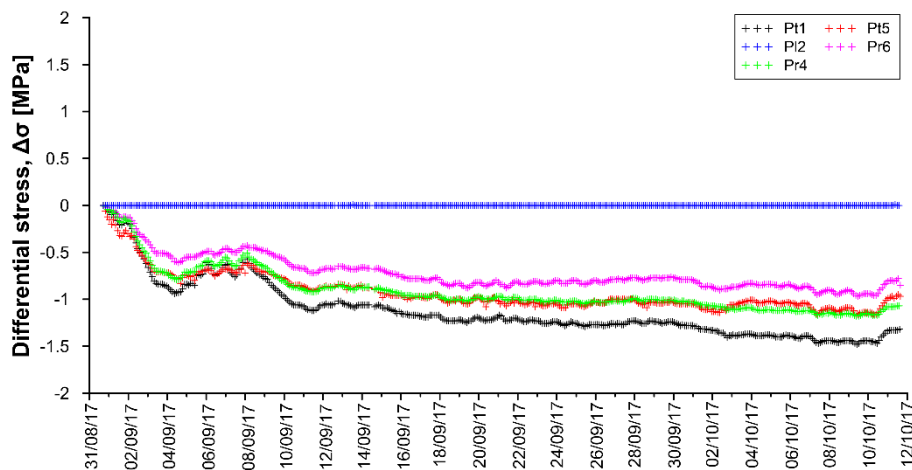


Figure A.2: Differential stresses for the undisturbed phase (winter 2017).

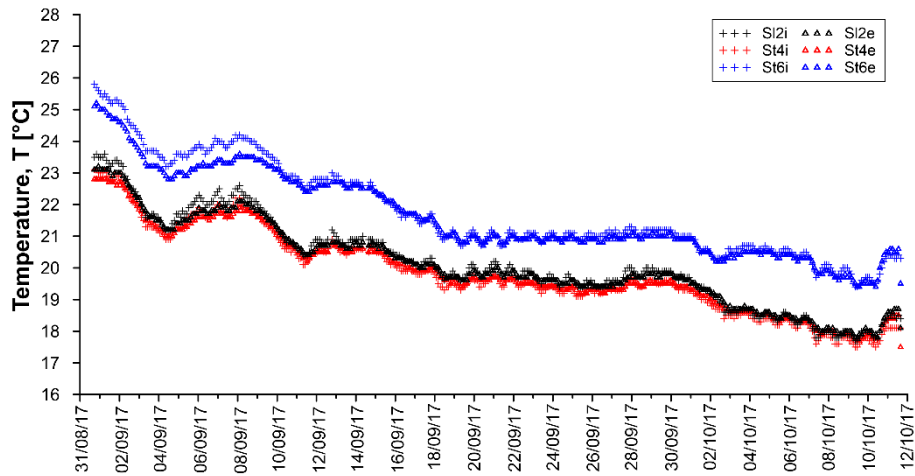


Figure A.3: Temperatures measured by VWSG for the undisturbed phase (winter 2017).

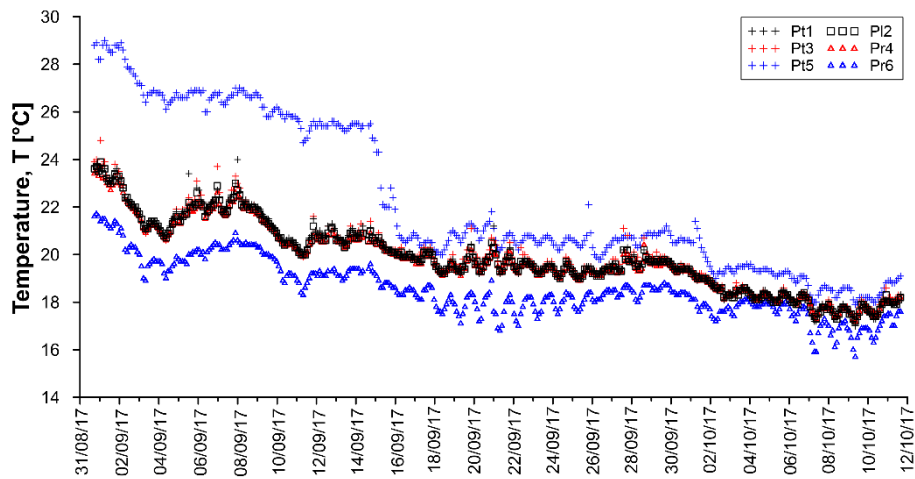


Figure A.4: Temperatures measured by PC for the undisturbed phase (winter 2017).

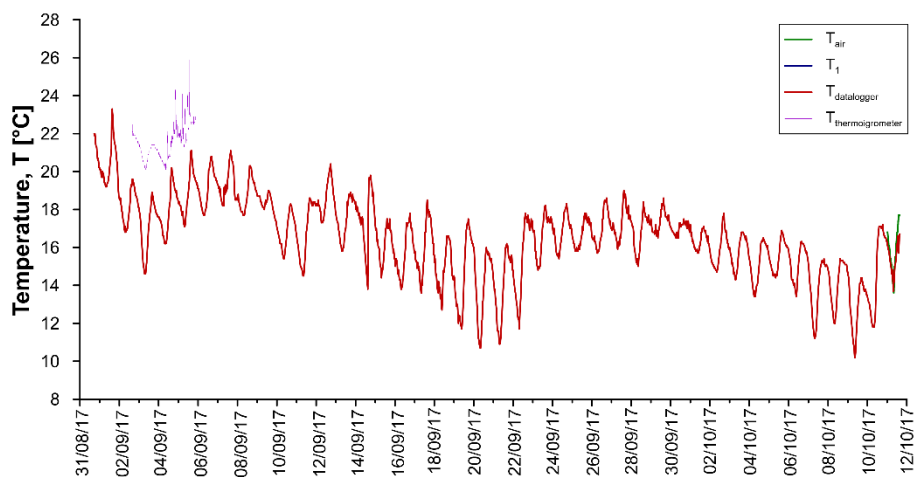


Figure A.5: Air temperatures for the undisturbed phase (winter 2017).

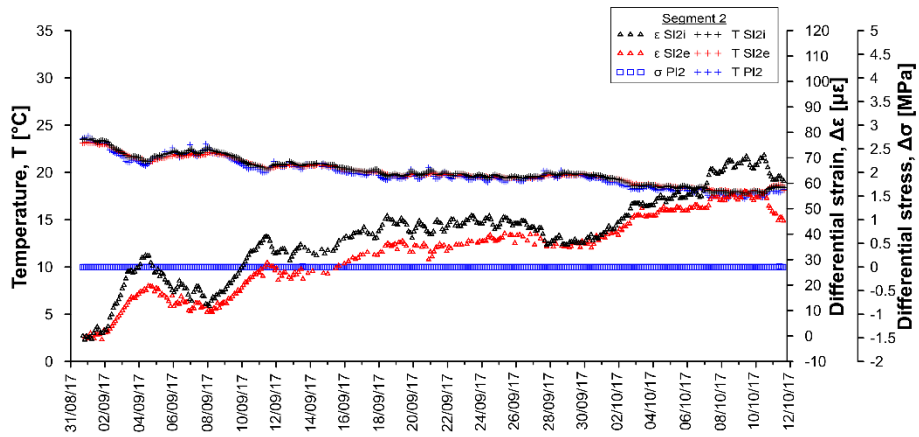


Figure A.6: Temperatures, differential strains and differential stresses in segment 2, ring 179 for the undisturbed phase (winter 2017).

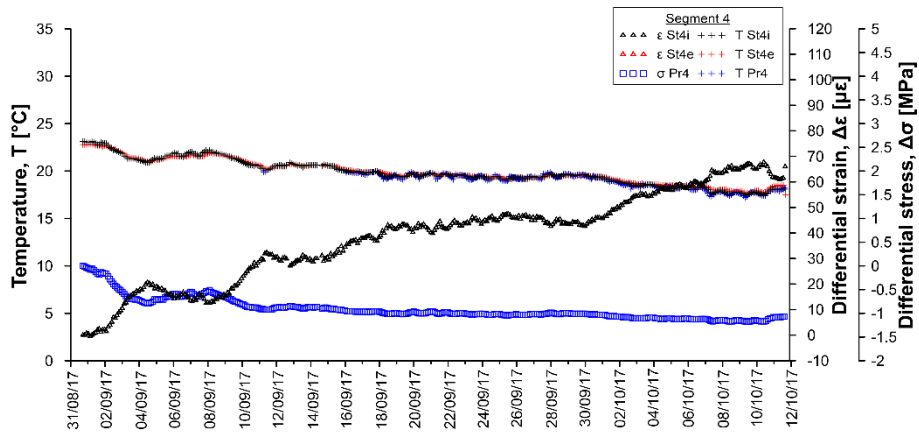


Figure A.7: Temperatures, differential strains and differential stresses in segment 4, ring 179 for the undisturbed phase (winter 2017).

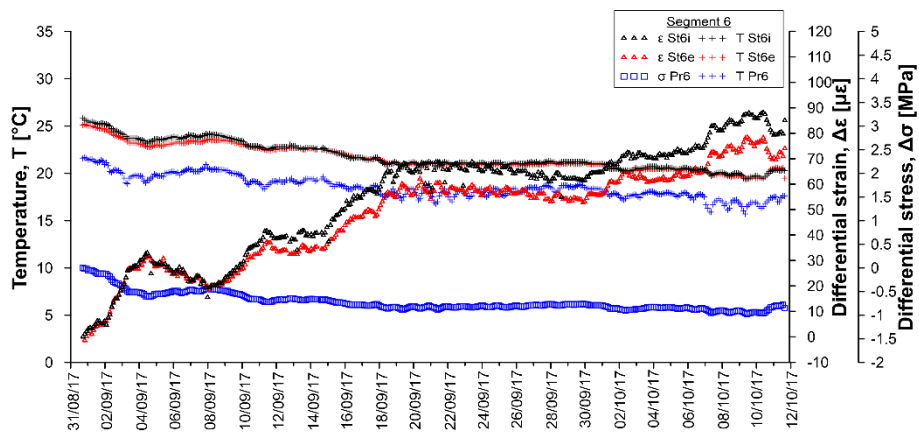


Figure A.8: Temperatures, differential strains and differential stresses in segment 6, ring 179 for the undisturbed phase (winter 2017).

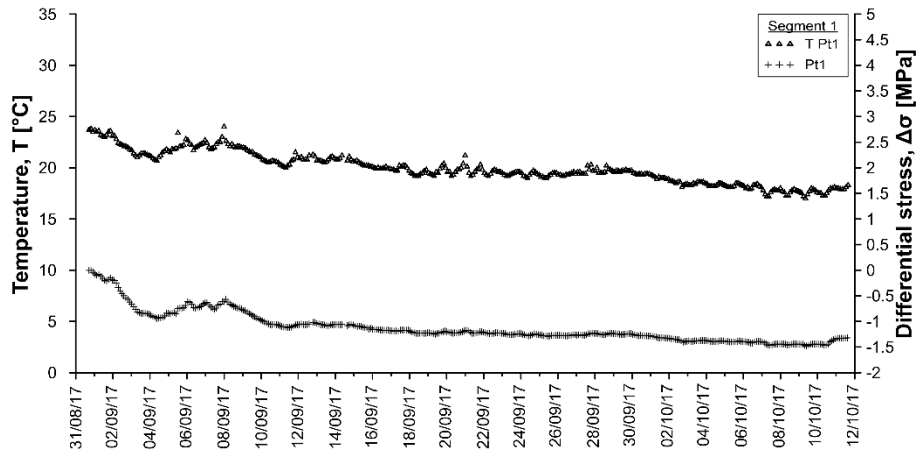


Figure A.9: Temperatures and differential stresses in segment 1, ring 179 for the undisturbed phase (winter 2017).

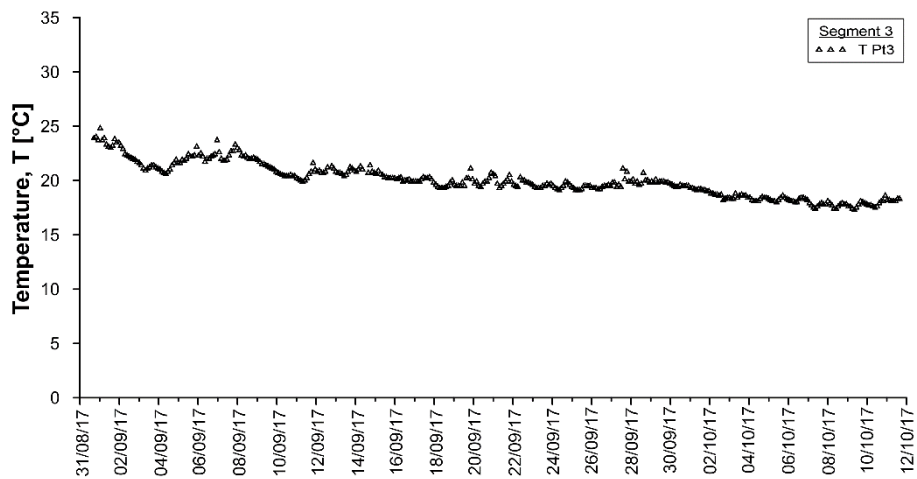


Figure A.10: Temperatures and differential stresses in segment 3, ring 179 for the undisturbed phase (winter 2017).

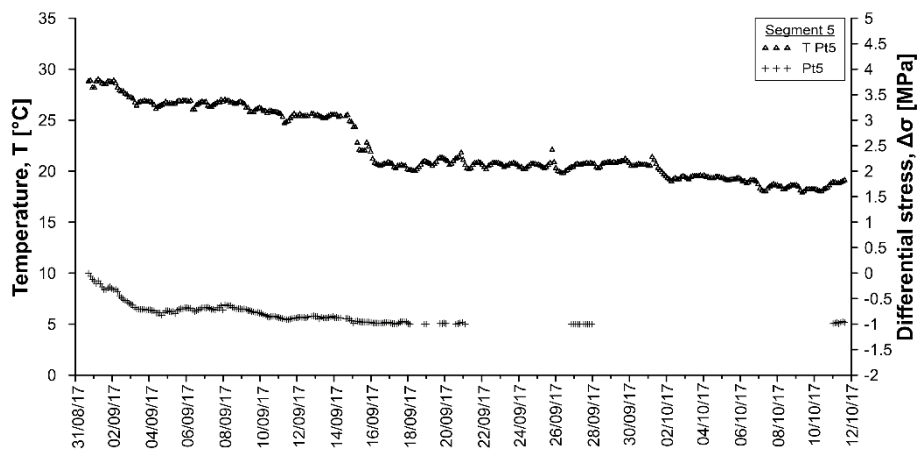


Figure A.11: Temperatures and differential stresses in segment 5, ring 179 for the undisturbed phase (winter 2017).

Table A.2: Data sheet for the undisturbed phase (winter 2017) – strains and temperatures.

Date	T _{Dl} [°C]	SI2i [με]	SI2i [°C]	SI2e [με]	SI2e [°C]	St4i [με]	St4i [°C]	St4e [με]	St4e [°C]	St6i [με]	St6i [°C]	St6e [με]	St6e [°C]
31/08/2017 17:22	22.0	0.00	23.5	0.00	23.1	0.00	23.1	-	22.8	0.00	25.8	0.00	25.1
01/09/2017 01:22	20.1	-0.01	23.5	-0.83	23.1	-0.10	23.1	-	22.8	-0.66	25.5	0.31	25.0
01/09/2017 09:22	19.4	-0.06	23.4	-0.65	23.1	-1.01	22.9	-	22.8	-0.98	25.4	0.24	24.9
01/09/2017 17:22	21.9	-0.16	23.3	-1.74	23.0	-0.61	22.9	-	22.7	-1.79	25.2	0.11	24.7
02/09/2017 01:22	18.6	-0.35	23.3	-1.14	22.9	-1.23	22.8	-	22.7	-2.70	25.2	0.14	24.6
02/09/2017 09:22	17.0	-0.06	22.8	-0.71	22.7	-3.39	22.4	-	22.5	-1.49	24.7	1.82	24.3
02/09/2017 17:22	19.4	0.62	22.4	-1.46	22.4	-4.39	22.1	-	22.1	-0.77	24.4	1.93	23.9
03/09/2017 01:22	17.6	1.59	22.1	-2.10	22.1	-5.57	21.7	-	21.9	0.12	24.2	2.65	23.7
03/09/2017 09:22	15.2	2.19	21.6	-2.62	21.7	-7.27	21.3	-	21.5	0.52	23.6	4.11	23.3
03/09/2017 17:22	18.5	3.19	21.7	-3.49	21.6	-5.71	21.3	-	21.4	2.03	23.7	3.39	23.2
04/09/2017 01:22	17.5	3.67	21.5	-3.28	21.5	-6.44	21.1	-	21.2	1.93	23.5	3.64	23.1
04/09/2017 09:22	16.3	3.25	21.2	-3.32	21.3	-7.38	20.9	-	21.1	-3.25	23.2	4.86	22.9
04/09/2017 17:22	19.7	3.26	21.5	-4.49	21.2	-3.11	21.2	-	21.0	1.41	23.4	2.45	22.9
05/09/2017 01:22	18.3	2.96	21.6	-3.10	21.4	-3.51	21.3	-	21.2	1.66	23.6	2.19	23.0
05/09/2017 09:22	17.8	2.73	21.7	-4.15	21.5	-3.44	21.3	-	21.3	1.47	23.6	2.43	23.0
05/09/2017 17:22	20.3	2.46	22.0	-3.43	21.7	-1.38	21.7	-	21.5	1.74	23.7	1.68	23.1
06/09/2017 01:22	18.9	2.44	22.2	-2.32	21.9	-0.69	21.8	-	21.6	1.66	23.9	1.40	23.2
06/09/2017 09:22	18.0	1.91	21.9	-2.10	21.8	-2.75	21.6	-	21.6	0.53	23.6	2.31	23.2
06/09/2017 17:22	20.5	1.54	22.1	-2.97	21.8	-0.94	21.7	-	21.6	0.74	23.8	1.11	23.2
07/09/2017 01:22	19.1	1.45	22.5	-2.83	21.9	0.11	22.0	-	21.7	0.42	24.0	0.99	23.4
07/09/2017 08:57	18.8	1.27	22.0	-2.35	21.9	-2.48	21.7	-	21.6	-0.38	23.8	1.57	23.3
07/09/2017 16:51	20.8	0.82	22.3	-3.46	21.9	0.54	22.0	-	21.7	-0.16	24.0	0.38	23.4
08/09/2017 00:51	18.8	0.83	22.6	-2.45	22.1	1.14	22.2	-	21.8	-0.19	24.2	-0.05	23.6
08/09/2017 08:51	17.8	0.43	22.3	-2.46	22.0	-0.36	21.9	-	21.8	-0.45	24.1	0.70	23.5
08/09/2017 16:51	20.2	0.30	22.1	-2.59	21.9	-1.20	21.8	-	21.7	-0.72	24.0	1.07	23.5
09/09/2017 00:51	18.7	0.00	22.0	-2.39	21.8	-1.67	21.7	-	21.6	-0.94	23.8	1.01	23.4
09/09/2017 08:51	18.0	-0.36	21.8	-3.59	21.7	-2.53	21.4	-	21.5	-0.88	23.7	1.77	23.3
09/09/2017 16:51	18.6	0.09	21.5	-3.05	21.5	-2.74	21.3	-	21.3	-0.89	23.5	1.72	23.2
10/09/2017 00:51	16.9	-0.16	21.2	-3.23	21.2	-3.59	20.9	-	21.1	-0.90	23.3	2.36	23.1
10/09/2017 08:51	15.4	0.06	20.9	-3.45	21.0	-4.47	20.6	-	20.9	-0.90	22.9	3.39	22.9
10/09/2017 16:51	18.3	0.55	20.8	-3.89	20.8	-3.43	20.5	-	20.7	0.39	22.9	3.05	22.7
11/09/2017 00:51	16.3	0.94	20.6	-4.18	20.7	-4.02	20.4	-	20.6	0.99	22.8	3.55	22.7
11/09/2017 08:51	14.5	1.01	20.4	-	20.4	-4.72	20.1	-	20.3	1.15	22.5	4.55	22.5
11/09/2017 16:51	18.5	0.46	20.6	-5.53	20.4	-2.85	20.3	-	20.3	1.93	22.7	3.18	22.4
12/09/2017 00:51	18.3	0.98	20.9	-4.15	20.7	-1.12	20.5	-	20.5	1.97	22.8	3.01	22.5
12/09/2017 08:51	17.4	1.14	20.8	-4.10	20.7	-1.46	20.5	-	20.5	2.38	22.8	3.48	22.6
12/09/2017 19:29	19.6	1.80	21.2	-4.13	20.9	0.23	20.8	-	20.7	3.21	23.0	3.19	22.7
13/09/2017 03:29	16.9	1.56	20.9	-5.34	20.8	-1.62	20.6	-	20.6	2.84	22.8	3.87	22.7
13/09/2017 11:29	17.0	-	20.7	-4.05	20.6	-1.80	20.4	-	20.5	2.75	22.7	4.32	22.6
13/09/2017 19:29	18.6	-	20.9	-	20.7	-0.30	20.6	-	20.5	2.39	22.7	3.23	22.5
14/09/2017 03:29	17.7	-	20.9	-3.89	20.7	-1.88	20.6	-	20.6	1.67	22.7	3.63	22.6
14/09/2017 15:52	18.6	1.02	20.8	-	20.7	-1.99	20.5	-	20.5	2.17	22.6	3.01	22.5
14/09/2017 23:52	17.3	0.37	20.8	-4.05	20.7	-1.57	20.5	-	20.5	1.34	22.4	3.67	22.4
15/09/2017 07:52	14.6	0.52	20.8	-4.14	20.7	-1.98	20.5	-	20.5	1.75	22.3	4.29	22.3
15/09/2017 15:52	17.0	0.78	20.5	-3.88	20.5	-1.97	20.2	-	20.3	3.69	22.1	4.93	22.1
15/09/2017 23:52	15.4	0.25	20.4	-4.50	20.3	-2.15	20.1	-	20.2	2.67	21.9	5.96	22.0
16/09/2017 07:52	13.8	-0.35	20.3	-	20.3	-1.80	20.0	-	20.1	3.79	21.7	5.07	21.8
16/09/2017 15:52	17.3	0.21	20.2	-4.87	20.2	-1.78	19.9	-	20.0	4.54	21.7	5.34	21.7
16/09/2017 23:52	15.7	-0.10	20.1	-4.72	20.1	-2.88	19.8	-	19.9	4.69	21.6	6.27	21.7
17/09/2017 07:52	13.6	-0.88	20.1	-4.81	20.0	-2.31	19.8	-	19.8	1.97	21.4	6.28	21.5
17/09/2017 15:52	18.2	-0.69	20.2	-4.86	20.1	-1.32	19.9	-	19.9	6.07	21.6	4.94	21.5
17/09/2017 23:52	15.6	-	20.1	-	20.1	-2.11	19.8	-	19.9	4.19	21.4	6.16	21.5
18/09/2017 07:52	13.5	-	19.8	-	19.8	-3.01	19.5	-	19.7	5.51	21.0	6.61	21.1
18/09/2017 15:52	16.5	-0.82	19.7	-7.30	19.7	-2.64	19.4	-	19.6	6.55	21.0	6.12	21.0
18/09/2017 23:52	14.5	-1.16	19.8	-4.51	19.7	-2.06	19.5	-	19.6	6.36	21.1	6.31	21.1
19/09/2017 07:52	12.0	-1.50	19.6	-5.34	19.6	-2.99	19.3	-	19.4	5.18	20.7	7.62	20.8
19/09/2017 15:52	17.2	-1.84	19.8	-4.73	19.7	-1.11	19.5	-	19.5	7.72	21.0	5.53	20.8
19/09/2017 23:52	16.0	-1.74	20.1	-4.62	19.9	-0.36	19.7	-	19.7	8.15	21.1	6.01	21.0
20/09/2017 07:52	10.7	-1.20	19.8	-5.30	19.8	-1.37	19.5	-	19.5	6.65	20.7	7.69	20.8
20/09/2017 15:52	15.8	-1.09	19.9	-5.13	19.8	-0.30	19.6	-	19.6	8.59	21.0	6.08	20.9
20/09/2017 23:52	14.4	-1.33	20.2	-5.91	19.9	-0.09	19.8	-	19.7	-0.48	21.1	5.43	21.1
21/09/2017 07:52	10.9	-0.46	19.8	-5.50	19.8	-2.00	19.4	-	19.6	6.34	20.7	8.05	20.8
21/09/2017 15:52	16.1	-0.83	19.9	-5.08	19.8	-0.26	19.6	-	19.5	8.10	21.0	6.13	20.8

Date	T _{Di} [°C]	SI _{2i} [μϵ]	SI _{2i} [°C]	SI _{2e} [μϵ]	SI _{2e} [°C]	SI _{4i} [μϵ]	SI _{4i} [°C]	SI _{4e} [μϵ]	SI _{4e} [°C]	SI _{6i} [μϵ]	SI _{6i} [°C]	SI _{6e} [μϵ]	SI _{6e} [°C]
21/09/2017 23:52	14.8	-0.49	20.0	-5.12	19.9	-0.39	19.6	-	19.7	8.21	21.1	6.50	21.0
22/09/2017 08:30	12.6	-1.89	19.6	-	19.7	-2.07	19.4	-	19.5	-0.42	20.8	7.79	20.9
22/09/2017 16:30	17.5	-0.74	19.9	-5.59	19.7	0.17	19.6	-	19.6	8.85	21.1	6.24	20.9
23/09/2017 00:30	16.8	-1.03	19.8	-	19.7	-0.50	19.5	-	19.6	8.24	21.1	6.38	21.0
23/09/2017 08:30	15.0	-1.83	19.5	-5.38	19.6	-1.65	19.2	-	19.4	7.52	20.8	7.29	20.9
23/09/2017 16:30	17.8	-1.93	19.6	-4.89	19.5	-0.61	19.3	-	19.3	8.34	21.0	5.97	20.9
24/09/2017 00:30	16.9	-2.39	19.7	-5.48	19.6	-0.64	19.4	-	19.4	7.74	21.1	5.87	21.0
24/09/2017 08:31	15.6	-2.67	19.4	-5.17	19.5	-1.94	19.2	-	19.3	6.90	20.9	6.68	20.9
24/09/2017 16:31	18.1	-3.35	19.7	-5.84	19.5	-0.18	19.4	-	19.3	7.48	21.1	5.15	20.9
25/09/2017 00:31	16.5	-3.70	19.6	-5.26	19.5	-1.08	19.3	-	19.4	7.13	21.0	5.63	21.0
25/09/2017 08:31	15.9	-3.82	19.4	-	19.4	-1.65	19.1	-	19.2	6.92	20.9	6.30	20.8
25/09/2017 16:31	17.5	-3.91	19.5	-5.23	19.4	-0.23	19.3	-	19.2	7.17	21.0	4.99	20.9
26/09/2017 00:31	16.5	-4.66	19.5	-5.19	19.4	-0.71	19.3	-	19.3	6.53	21.0	5.16	20.9
26/09/2017 08:31	15.8	-4.74	19.4	-	19.4	-1.02	19.2	-	19.2	6.48	20.9	5.31	20.8
26/09/2017 16:31	18.5	-6.00	19.5	-4.36	19.4	-0.31	19.3	-	19.3	6.22	21.1	4.40	20.9
27/09/2017 00:31	16.9	-5.48	19.6	-6.84	19.5	-0.36	19.3	-	19.3	6.00	21.1	4.61	20.9
27/09/2017 08:31	16.3	-6.23	19.5	-	19.5	-1.35	19.2	-	19.3	-0.77	21.0	5.54	20.9
27/09/2017 16:31	18.6	-6.40	19.9	-5.75	19.6	1.10	19.6	-	19.4	6.09	21.2	3.98	21.0
28/09/2017 00:31	17.3	-6.87	20.0	-	19.8	0.86	19.6	-	19.5	4.18	21.3	4.57	21.1
28/09/2017 08:31	15.0	-6.70	19.8	-	19.7	-0.15	19.4	-	19.4	5.65	21.0	5.55	21.0
28/09/2017 16:31	17.8	-6.72	20.0	-4.23	19.7	1.46	19.6	-	19.5	6.38	21.2	4.17	21.0
29/09/2017 00:31	17.2	-6.84	20.0	-5.49	19.7	0.88	19.6	-	19.5	5.93	21.3	4.24	21.1
29/09/2017 08:31	16.5	-7.16	19.9	-	19.8	0.12	19.5	-	19.5	6.24	21.2	4.77	21.0
29/09/2017 16:31	18.1	-7.30	19.9	-5.00	19.8	0.39	19.6	-	19.5	5.46	21.2	3.94	21.0
30/09/2017 00:31	17.0	-7.58	19.8	-5.24	19.7	-0.16	19.5	-	19.5	5.41	21.2	4.34	21.0
30/09/2017 08:31	16.5	-7.93	19.6	-4.53	19.7	-0.93	19.3	-	19.4	5.71	21.0	4.95	20.9
30/09/2017 16:31	17.4	-7.90	19.7	-3.40	19.6	-0.51	19.3	-	19.4	5.87	21.0	4.44	20.9
01/10/2017 00:31	17.1	-8.00	19.6	-6.82	19.5	-0.72	19.3	-	19.3	6.08	21.0	4.86	20.9
01/10/2017 08:31	15.9	-7.98	19.4	-6.39	19.4	-1.19	19.1	-	19.2	4.69	20.7	5.53	20.7
01/10/2017 16:31	17.1	-7.97	19.3	-5.68	19.4	-0.99	19.0	-	19.1	4.25	20.6	4.45	20.5
02/10/2017 00:31	15.6	-7.76	19.2	-5.87	19.2	-1.50	18.9	-	19.0	3.80	20.4	5.07	20.4
02/10/2017 08:31	14.7	-7.69	19.0	-5.50	19.1	-1.82	18.6	-	18.9	4.37	20.3	5.12	20.2
02/10/2017 16:31	17.7	-8.57	18.6	-5.56	18.9	-3.83	18.4	-	18.7	2.85	20.3	5.01	20.2
03/10/2017 00:31	15.9	-7.69	18.6	-	18.7	-1.73	18.5	-	18.7	7.30	20.6	4.78	20.4
03/10/2017 08:31	14.6	-7.61	18.6	-4.60	18.6	-1.18	18.5	-	18.6	7.77	20.6	4.89	20.4
03/10/2017 16:31	16.8	-7.50	18.7	-6.16	18.7	-0.57	18.6	-	18.6	8.02	20.7	4.74	20.5
04/10/2017 00:31	15.3	-7.22	18.7	-6.48	18.7	-0.83	18.5	-	18.6	7.88	20.7	5.09	20.6
04/10/2017 08:31	13.9	-7.00	18.5	-6.68	18.6	-1.47	18.3	-	18.5	7.21	20.5	5.68	20.5
04/10/2017 16:31	16.4	-6.90	18.6	-7.09	18.5	-0.30	18.4	-	18.5	8.08	20.7	5.32	20.5
05/10/2017 00:31	15.4	-7.15	18.5	-6.70	18.5	-0.55	18.4	-	18.5	7.98	20.6	5.55	20.5
05/10/2017 08:31	14.5	-7.02	18.4	-6.78	18.4	-1.07	18.2	-	18.4	7.85	20.5	6.18	20.4
05/10/2017 16:31	16.8	-6.75	18.5	-6.99	18.5	0.56	18.4	-	18.4	8.62	20.6	5.50	20.4
06/10/2017 00:31	15.6	-6.82	18.5	-6.98	18.5	-0.16	18.3	-	18.4	8.35	20.5	5.83	20.4
06/10/2017 08:31	13.6	-6.76	18.2	-6.76	18.4	-1.10	18.1	-	18.3	7.84	20.4	6.64	20.3
06/10/2017 16:31	16.2	-6.58	18.4	-7.10	18.4	0.53	18.3	-	18.3	9.24	20.5	5.73	20.3
07/10/2017 00:31	14.9	-5.45	18.3	-7.17	18.4	-0.07	18.2	-	18.3	9.38	20.4	7.02	20.3
07/10/2017 08:31	11.3	-4.19	17.8	-7.31	18.1	-2.69	17.7	-	18.0	8.14	19.7	9.02	19.9
07/10/2017 16:31	15.3	-3.05	18.0	-7.68	18.0	-0.15	17.9	-	17.9	11.22	20.0	7.22	19.8
08/10/2017 00:31	14.7	-2.31	18.0	-7.86	18.0	0.17	17.9	-	18.0	11.60	20.1	7.58	19.9
08/10/2017 08:31	12.0	-1.48	17.8	-5.40	18.0	-1.68	17.6	-	17.9	10.57	19.7	8.90	19.7
08/10/2017 16:31	15.3	-0.98	17.9	-7.64	17.9	0.36	17.8	-	17.9	12.65	20.0	7.51	19.7
09/10/2017 00:31	14.5	-0.57	17.9	-7.82	18.0	-0.25	17.7	-	17.9	12.42	19.9	8.15	19.7
09/10/2017 08:31	10.2	-0.22	17.7	-7.80	17.8	-1.83	17.5	-	17.7	9.30	19.4	9.65	19.5
09/10/2017 16:31	14.3	-0.09	18.0	-8.04	17.9	0.84	17.8	-	17.8	11.54	19.6	7.83	19.5
10/10/2017 00:31	13.3	-0.04	18.0	-7.80	18.0	0.14	17.7	-	17.9	11.50	19.7	7.90	19.6
10/10/2017 08:31	11.9	0.09	17.8	-7.78	17.9	-0.74	17.6	-	17.8	11.19	19.5	8.68	19.4
10/10/2017 16:31	17.1	0.37	18.1	-7.40	18.1	0.64	17.8	-	18.1	12.63	20.0	12.50	20.1
11/10/2017 00:31	16.1	0.32	18.4	-7.66	18.6	0.67	18.1	-	18.4	13.54	20.4	14.23	20.5
11/10/2017 08:31	14.2	0.46	18.4	-6.87	18.6	-0.05	18.0	-	18.4	13.08	20.3	16.37	20.5

Table A.3: Data sheet for the undisturbed phase (winter 2017) – stresses and temperatures.

Date	Pt1 [MPa]	Pt1 [°C]	PI2 [MPa]	PI2 [°C]	Pt3 [MPa]	Pt3 [°C]	Pr4 [MPa]	Pr4 [°C]	Pt5 [MPa]	Pt5 [°C]	Pr6 [MPa]	Pr6 [°C]
31/08/2017 17:22	0.00	23.7	0.00	23.6	-	23.9	0.00	23.4	0.00	28.8	0.00	21.6
01/09/2017 01:22	-0.08	23.5	0.00	23.7	-	24.2	-0.05	23.4	-0.16	28.4	-0.05	21.4
01/09/2017 09:22	-0.14	23.1	0.00	23.1	-	23.1	-0.11	22.9	-0.24	28.6	-0.08	21.3
01/09/2017 17:22	-0.20	23.3	0.00	23.2	-	23.5	-0.17	23.0	-0.33	28.8	-0.12	21.4
02/09/2017 01:22	-0.19	23.2	0.00	23.2	-	23.4	-0.17	22.9	-0.33	28.7	-0.13	20.9
02/09/2017 09:22	-0.40	22.3	0.00	22.4	-	22.3	-0.33	22.2	-0.44	27.9	-0.25	20.1
02/09/2017 17:22	-0.55	22.0	0.00	22.1	-	22.0	-0.46	21.9	-0.54	27.6	-0.33	20.3
03/09/2017 01:22	-0.68	21.6	0.00	21.6	-	21.5	-0.56	21.5	-0.62	27.3	-0.40	20.0
03/09/2017 09:22	-0.83	21.1	0.00	21.1	-	21.0	-0.69	21.0	-0.72	26.7	-0.50	19.2
03/09/2017 17:22	-0.84	21.4	0.00	21.4	-	21.4	-0.71	21.2	-0.71	26.9	-0.51	19.8
04/09/2017 01:22	-0.88	21.1	0.00	21.0	-	21.0	-0.74	21.0	-0.72	26.8	-0.53	19.7
04/09/2017 09:22	-0.94	21.5	0.00	20.8	-	20.7	-0.79	20.7	-0.83	26.2	-0.60	19.2
04/09/2017 17:22	-0.89	21.6	0.00	21.4	-	21.7	-0.76	21.3	-0.77	26.5	-0.59	19.6
05/09/2017 01:22	-0.85	21.5	0.00	21.4	-	21.5	-0.72	21.3	-0.75	26.7	-0.55	19.7
05/09/2017 09:22	-0.84	21.6	0.00	21.4	-	21.4	-0.71	21.3	-0.77	26.6	-0.55	19.7
05/09/2017 17:22	-0.74	22.1	0.00	22.0	-	22.2	-0.65	21.8	-0.70	26.8	-0.52	20.1
06/09/2017 01:22	-0.61	22.5	0.00	22.1	-	22.2	-0.59	21.9	-0.68	26.9	-0.49	20.2
06/09/2017 09:22	-0.74	21.8	0.00	21.7	-	21.8	-0.65	21.6	-0.75	25.9	-0.52	19.9
06/09/2017 17:22	-0.71	22.3	0.00	22.1	-	22.3	-0.62	21.9	-0.71	26.7	-0.50	20.3
07/09/2017 01:22	-0.63	22.8	0.00	22.6	-	23.2	-0.56	22.3	-0.68	26.8	-0.46	20.5
07/09/2017 08:57	-0.74	21.9	0.00	21.7	-	21.8	-0.64	21.6	-0.71	26.3	-0.50	20.2
07/09/2017 16:51	-0.68	22.5	0.00	22.4	-	22.6	-0.59	22.2	-0.68	26.8	-0.48	20.6
08/09/2017 00:51	-0.57	22.8	0.00	22.6	-	22.8	-0.53	22.3	-0.63	27.0	-0.43	20.7
08/09/2017 08:51	-0.67	22.1	0.00	22.1	-	22.2	-0.58	21.9	-0.63	27.1	-0.45	20.4
08/09/2017 16:51	-0.73	22.0	0.00	21.9	-	22.0	-0.63	21.7	-0.70	26.6	-0.47	20.3
09/09/2017 00:51	-0.78	22.0	0.00	21.8	-	21.9	-0.66	21.7	-0.71	26.7	-0.49	20.3
09/09/2017 08:51	-0.85	21.6	0.00	21.5	-	21.7	-0.72	21.4	-0.73	26.1	-0.52	19.9
09/09/2017 16:51	-0.92	21.3	0.00	21.2	-	21.2	-0.77	21.1	-0.76	25.9	-0.55	19.9
10/09/2017 00:51	-0.99	20.8	0.00	20.8	-	20.8	-0.82	20.8	-0.79	26.1	-0.59	19.6
10/09/2017 08:51	-1.04	20.5	0.00	20.4	-	20.3	-0.87	20.4	-0.85	25.8	-0.65	18.8
10/09/2017 16:51	-1.06	20.6	0.00	20.5	-	20.5	-0.88	20.5	-0.85	25.8	-0.66	19.2
11/09/2017 00:51	-1.08	20.3	0.00	20.2	-	20.1	-0.90	20.2	-0.87	25.7	-0.68	18.9
11/09/2017 08:51	-1.12	20.0	0.00	19.9	-	19.8	-0.92	19.9	-0.91	24.7	-0.72	18.4
11/09/2017 16:51	-1.10	20.9	0.00	20.6	-	20.7	-0.91	20.6	-0.89	25.4	-0.71	19.1
12/09/2017 00:51	-1.06	20.9	0.00	20.7	-	20.9	-0.88	20.6	-0.88	25.4	-0.68	19.1
12/09/2017 08:51	-1.06	20.8	0.00	20.6	-	20.7	-0.88	20.5	-0.87	25.4	-0.67	19.1
12/09/2017 19:29	-1.02	21.2	0.00	21.0	-	21.2	-0.85	20.9	-0.84	25.6	-0.65	19.4
13/09/2017 03:29	-1.05	20.7	0.00	20.6	-	20.7	-0.87	20.5	-0.85	25.5	-0.66	19.2
13/09/2017 11:29	-1.08	20.6	0.00	20.4	-	20.5	-0.90	20.4	-0.88	25.2	-0.68	19.1
13/09/2017 19:29	-1.06	20.9	0.00	20.8	-	21.0	-0.87	20.7	-0.86	25.4	-0.67	19.4
14/09/2017 03:29	-1.06	20.8	0.00	20.7	-	21.0	-0.88	20.6	-0.87	25.5	-0.66	19.4
14/09/2017 15:52	-1.08	20.7	0.00	20.6	-	20.7	-0.90	20.5	-0.89	25.4	-0.68	19.4
14/09/2017 23:52	-1.08	20.6	0.00	20.5	-	20.6	-0.90	20.4	-0.93	24.7	-0.68	19.2
15/09/2017 07:52	-1.09	20.6	0.00	20.6	-	20.9	-0.90	20.4	-0.94	22.5	-0.72	18.8
15/09/2017 15:52	-1.13	20.2	0.00	20.2	-	20.2	-0.93	20.0	-0.96	22.0	-0.74	18.8
15/09/2017 23:52	-1.15	20.1	0.00	20.1	-	20.2	-0.94	20.0	-0.96	21.9	-0.76	18.6
16/09/2017 07:52	-1.16	20.2	0.00	20.3	-	20.5	-0.96	20.0	-0.98	20.7	-0.78	18.5
16/09/2017 15:52	-1.17	20.0	0.00	19.9	-	20.0	-0.97	19.8	-0.98	20.7	-0.78	18.6
16/09/2017 23:52	-1.18	19.9	0.00	19.8	-	19.9	-0.97	19.7	-0.97	20.8	-0.78	18.4
17/09/2017 07:52	-	19.9	0.00	19.9	-	20.3	-0.97	19.8	-1.01	20.5	-0.81	18.3
17/09/2017 15:52	-1.17	20.2	0.00	20.0	-	20.2	-0.96	20.0	-0.95	20.6	-0.78	18.7
17/09/2017 23:52	-1.18	19.7	-0.02	19.7	-	19.8	-0.97	19.6	-0.98	20.2	-0.80	18.1
18/09/2017 07:52	-1.22	19.3	0.00	19.4	-	19.5	9.65	19.3	-1.03	20.1	-0.85	17.6
18/09/2017 15:52	-1.23	19.6	0.00	19.4	-	19.6	-1.01	19.4	-1.01	20.6	-0.84	18.1
18/09/2017 23:52	-1.22	19.5	0.00	19.5	-	19.6	-1.00	19.4	-1.00	21.0	-0.83	17.9
19/09/2017 07:52	-1.24	19.2	0.00	19.3	-	19.5	-1.02	19.1	-1.05	20.5	-0.88	17.1
19/09/2017 15:52	-1.22	19.8	0.00	19.7	-	20.0	-1.00	19.6	-1.00	21.2	-0.84	18.3
19/09/2017 23:52	-1.19	19.9	0.00	19.8	-	20.0	-0.97	19.7	-0.98	21.2	-0.82	18.3
20/09/2017 07:52	-1.23	19.2	0.00	19.4	-	19.5	-1.00	19.2	-1.03	20.7	-0.85	17.3
20/09/2017 15:52	-1.22	19.8	0.00	19.8	-	19.9	-0.99	19.6	-1.00	21.3	-0.83	18.3
20/09/2017 23:52	-1.19	21.2	0.00	20.3	-	20.6	-0.97	20.0	-1.02	21.1	-0.82	17.6
21/09/2017 07:52	-1.22	19.1	0.00	19.2	-	19.3	-1.00	19.1	-1.06	19.9	-0.87	16.5
21/09/2017 15:52	-1.22	19.7	0.00	19.7	-	19.9	-1.00	19.6	-1.01	20.8	-0.84	18.0

Date	Pt1 [MPa]	Pt1 [°C]	Pl2 [MPa]	Pl2 [°C]	Pt3 [MPa]	Pt3 [°C]	Pr4 [MPa]	Pr4 [°C]	Pt5 [MPa]	Pt5 [°C]	Pr6 [MPa]	Pr6 [°C]
21/09/2017 23:52	-1.21	19.5	0.00	19.6	-	19.7	-0.98	19.5	-1.02	20.6	-0.82	17.6
22/09/2017 08:30	-1.25	19.6	0.00	19.7	-	21.0	-1.01	19.6	-1.10	20.5	-0.84	17.8
22/09/2017 16:30	-1.22	19.7	0.00	19.7	-	19.8	-1.00	19.6	-1.03	20.8	-0.82	18.2
23/09/2017 00:30	-1.23	19.5	0.00	19.4	-	19.6	-1.01	19.4	-1.04	20.7	-0.81	18.0
23/09/2017 08:30	-1.26	19.1	0.00	19.2	-	19.3	-1.03	19.1	-1.07	20.4	-0.84	17.2
23/09/2017 16:30	-1.25	19.5	0.00	19.5	-	19.6	-1.02	19.3	-1.05	20.7	-0.82	18.2
24/09/2017 00:30	-1.24	19.5	0.00	19.4	-	19.5	-1.01	19.3	-1.05	20.4	-0.80	18.1
24/09/2017 08:31	-1.27	19.0	0.00	19.0	-	19.1	-1.03	19.0	-1.09	20.2	-0.83	17.7
24/09/2017 16:31	-1.26	19.6	0.00	19.6	-	19.8	-1.02	19.5	-1.05	20.7	-0.81	18.3
25/09/2017 00:31	-1.26	19.3	0.00	19.3	-	19.4	-1.02	19.2	-1.05	20.6	-0.80	18.0
25/09/2017 08:31	-1.28	19.1	0.00	19.1	-	19.3	-1.04	19.0	-1.08	20.4	-0.83	17.6
25/09/2017 16:31	-1.27	19.6	0.00	19.4	-	19.7	-1.03	19.3	-1.05	20.8	-0.82	18.3
26/09/2017 00:31	-1.27	19.3	0.00	19.2	-	19.3	-1.03	19.2	-1.03	20.3	-0.80	18.1
26/09/2017 08:31	-1.28	19.2	0.00	19.1	-	19.2	-1.03	19.1	-1.04	19.8	-0.82	18.1
26/09/2017 16:31	-1.27	19.7	0.00	19.5	-	19.7	-1.03	19.5	-1.01	20.2	-0.79	18.5
27/09/2017 00:31	-1.27	19.4	0.00	19.3	-	19.5	-1.02	19.3	-1.00	20.5	-0.79	18.4
27/09/2017 08:31	-1.28	19.3	0.00	19.2	-	19.3	-1.03	19.2	-1.05	20.6	-0.80	18.2
27/09/2017 16:31	-1.24	19.8	0.00	19.8	-	20.1	-1.01	19.7	-1.00	20.8	-0.78	18.7
28/09/2017 00:31	-1.23	19.9	0.00	19.8	-	20.0	-0.99	19.6	-1.02	20.7	-0.77	18.5
28/09/2017 08:31	-1.26	19.4	0.00	19.5	-	19.6	-1.02	19.3	-1.06	20.3	-0.80	18.0
28/09/2017 16:31	-1.24	19.9	0.00	19.9	-	20.1	-1.00	19.8	-1.04	20.8	-0.78	18.7
29/09/2017 00:31	-1.23	19.7	0.00	19.9	-	20.1	-1.00	19.7	-1.03	20.8	-0.77	18.6
29/09/2017 08:31	-1.25	19.6	0.00	19.7	-	19.8	-1.01	19.5	-1.04	20.9	-0.78	18.5
29/09/2017 16:31	-1.25	19.7	0.00	19.7	-	19.8	-1.01	19.6	-1.03	21.0	-0.77	18.8
30/09/2017 00:31	-1.25	19.6	0.00	19.6	-	19.7	-1.01	19.5	-1.03	20.7	-0.77	18.5
30/09/2017 08:31	-1.28	19.3	0.00	19.3	-	19.4	-1.03	19.2	-1.05	20.5	-0.79	18.3
30/09/2017 16:31	-1.28	19.4	0.00	19.4	-	19.5	-1.03	19.3	-1.05	20.6	-0.79	18.5
01/10/2017 00:31	-1.28	19.3	0.00	19.2	-	19.3	-1.03	19.2	-1.05	20.5	-0.80	18.1
01/10/2017 08:31	-1.31	19.0	0.00	19.0	-	19.1	-1.05	18.9	-1.08	21.1	-0.83	17.8
01/10/2017 16:31	-1.32	19.0	0.00	19.0	-	19.1	-1.06	18.9	-1.11	20.0	-0.86	17.9
02/10/2017 00:31	-1.33	18.8	0.00	18.8	-	18.9	-1.07	18.7	-1.13	19.4	-0.88	17.5
02/10/2017 08:31	-1.35	18.6	0.00	18.6	-	18.6	-1.08	18.5	-1.14	19.1	-0.90	17.3
02/10/2017 16:31	-1.41	18.1	0.00	18.2	-	18.2	-1.11	18.1	-1.12	19.2	-0.89	17.6
03/10/2017 00:31	-1.38	18.4	0.00	18.3	-	18.4	-1.10	18.4	-1.05	19.4	-0.87	17.7
03/10/2017 08:31	-1.38	18.4	0.00	18.3	-	18.4	-1.10	18.4	-1.05	19.5	-0.87	17.8
03/10/2017 16:31	-1.37	18.6	0.00	18.5	-	18.6	-1.09	18.5	-1.02	19.5	-0.84	18.1
04/10/2017 00:31	-1.37	18.4	0.00	18.3	-	18.4	-1.09	18.4	-1.01	19.6	-0.83	18.0
04/10/2017 08:31	-1.39	18.2	0.00	18.1	-	18.1	-1.12	18.2	-1.04	19.3	-0.85	17.8
04/10/2017 16:31	-1.39	18.5	0.00	18.3	-	18.5	-1.11	18.4	-1.03	19.4	-0.84	18.0
05/10/2017 00:31	-1.39	18.3	0.00	18.2	-	18.2	-1.11	18.2	-1.03	19.3	-0.84	17.9
05/10/2017 08:31	-1.40	18.1	0.00	18.0	-	18.1	-1.12	18.1	-1.05	19.0	-0.86	17.4
05/10/2017 16:31	-1.39	18.6	0.00	18.4	-	18.5	-1.11	18.4	-1.04	19.3	-0.85	17.9
06/10/2017 00:31	-1.39	18.2	0.00	18.1	-	18.2	-1.12	18.2	-1.04	19.2	-0.85	17.7
06/10/2017 08:31	-1.42	17.9	0.00	17.9	-	17.9	-1.13	17.9	-1.06	18.7	-0.88	17.1
06/10/2017 16:31	-1.39	18.4	0.00	18.3	-	18.4	-1.12	18.3	-1.04	19.2	-0.87	17.8
07/10/2017 00:31	-1.40	18.0	0.00	18.0	-	18.1	-1.12	18.0	-1.07	18.4	-0.88	16.9
07/10/2017 08:31	-1.46	17.2	0.00	17.3	-	17.4	-1.16	17.3	-1.15	18.0	-0.94	15.9
07/10/2017 16:31	-1.44	17.9	0.00	17.8	-	17.9	-1.15	17.8	-1.11	18.6	-0.92	17.1
08/10/2017 00:31	-1.44	17.9	0.00	17.8	-	18.1	-1.14	17.8	-1.09	18.6	-0.90	16.8
08/10/2017 08:31	-1.46	17.3	0.00	17.3	-	17.4	-1.17	17.4	-1.13	18.2	-0.94	16.1
08/10/2017 16:31	-1.44	17.9	0.00	17.8	-	17.9	-1.16	17.8	-1.10	18.6	-0.92	17.1
09/10/2017 00:31	-1.44	17.5	0.00	17.5	-	17.6	-1.15	17.6	-1.09	18.5	-0.91	16.7
09/10/2017 08:31	-1.48	17.0	0.00	17.2	-	17.3	-1.18	17.2	-1.16	17.9	-0.96	15.7
09/10/2017 16:31	-1.44	17.9	0.00	17.9	-	18.1	-1.16	17.8	-1.15	18.2	-0.95	16.9
10/10/2017 00:31	-1.44	17.6	0.00	17.7	-	17.8	-1.16	17.6	-1.14	18.2	-0.94	16.9
10/10/2017 08:31	-1.46	17.4	0.00	17.4	-	17.5	-1.17	17.4	-1.16	18.0	-0.96	16.4
10/10/2017 16:31	-1.39	18.0	0.00	17.9	-	18.0	-1.12	17.9	-1.08	18.4	-0.88	17.1
11/10/2017 00:31	-1.34	18.0	0.00	18.0	-	18.2	-1.08	18.0	-0.99	18.9	-0.81	17.5
11/10/2017 08:31	-1.33	17.9	0.00	17.9	-	18.1	-1.08	17.9	-0.99	18.8	-0.81	17.0

Table A.4: Summary of the undisturbed phase (winter 2017) records.

Quantity	Unit	$x(t_0)$	$x(t_1)$	$x(t_1) - x(t_0)$	$\bar{x}(t_0, t_1)$
T_{bl}	[°C]	22.0	16.7	-5.3	16.5
SI2i	[$\mu\epsilon$]	-346.84	-345.69	1.15	20.1
	[$\mu\epsilon$] _{comp}	0	60.9	60.9	
	[°C]	23.5	18.6	-4.9	
SI2e	[$\mu\epsilon$]	-2598.81	-2609.1	-10.33	20.1
	[$\mu\epsilon$] _{comp}	0	45.8	45.8	
	[°C]	23.1	18.5	-4.6	
St4i	[$\mu\epsilon$]	-1775.93	-1771.9	4.01	19.8
	[$\mu\epsilon$] _{comp}	0	63.8	63.8	
	[°C]	23.1	18.2	-4.9	
St4e	[$\mu\epsilon$]	-	-	-	19.9
	[$\mu\epsilon$] _{comp}	-	-	-	
	[°C]	22.8	17.9	-4.9	
St6i	[$\mu\epsilon$]	-2193.13	-2175.9	17.27	21.8
	[$\mu\epsilon$] _{comp}	0	83.2	83.2	
	[°C]	25.8	20.4	-5.4	
St6e	[$\mu\epsilon$]	-1825.99	-1816.6	9.36	21.6
	[$\mu\epsilon$] _{comp}	0	74.0	74.0	
	[°C]	25.1	20.0	-5.1	
Pt1	[MPa]	1.97	0.6	-1.35	19.9
	[°C]	23.7	18.3	-5.4	
Pl2	[MPa]	-0.03	0.0	0.00	19.9
	[°C]	23.6	18.2	-5.4	
Pt3	[MPa]	-	-	-	20.0
	[°C]	23.9	18.4	-5.5	
Pr4	[MPa]	1.70	0.6	-1.11	19.8
	[°C]	23.4	18.2	-5.2	
Pt5	[MPa]	1.67	0.7	-0.95	22.3
	[°C]	28.8	19.1	-9.7	
Pr6	[MPa]	1.48	0.7	-0.82	18.5
	[°C]	21.6	17.7	-3.9	

Test GH1

After dealing with a number of difficulties, such as a bottleneck along the circuit and some heat pump low-pressure issues, this was the first successful test performed to simulate the extraction of heat from the ground.

Circuit:	Ground
Mode:	Heating
Secondary circuit temperature:	45°C
Activated rings:	179+180
Volumetric flow rate:	1.3 m ³ /h
Fluid velocity in primary circuit:	0.9 m/s
Starting time t_0 :	15/02/2018 14:13
Ending time t_1 :	17/02/2018 09:57
Duration:	1.82 days
Note:	Weird shift in response on February 16 th , 2018 right in correspondence of asameters manipulation.

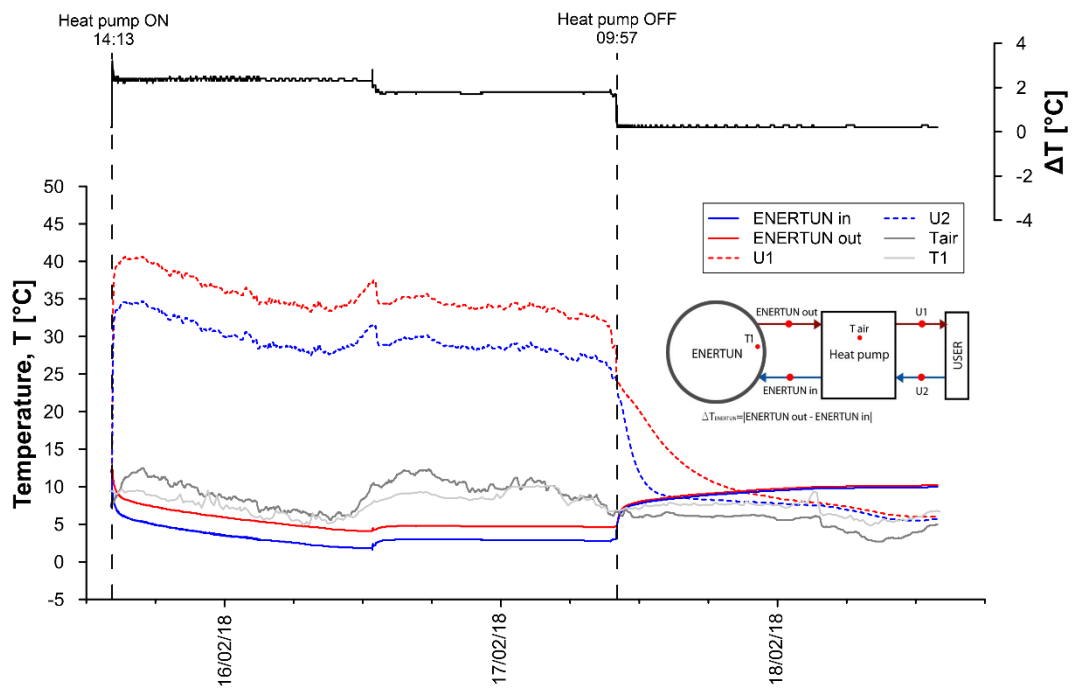


Figure A.12: Primary circuit, secondary circuit and air temperatures for test GH1.

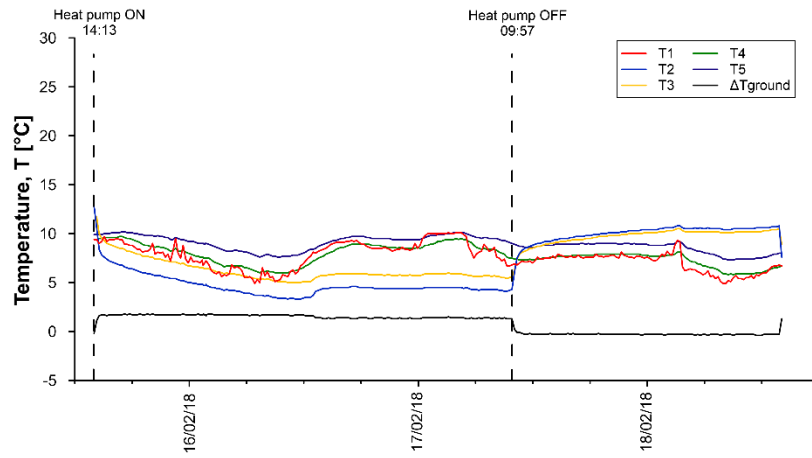


Figure A.13: Temperatures T1-T5 for test GH1

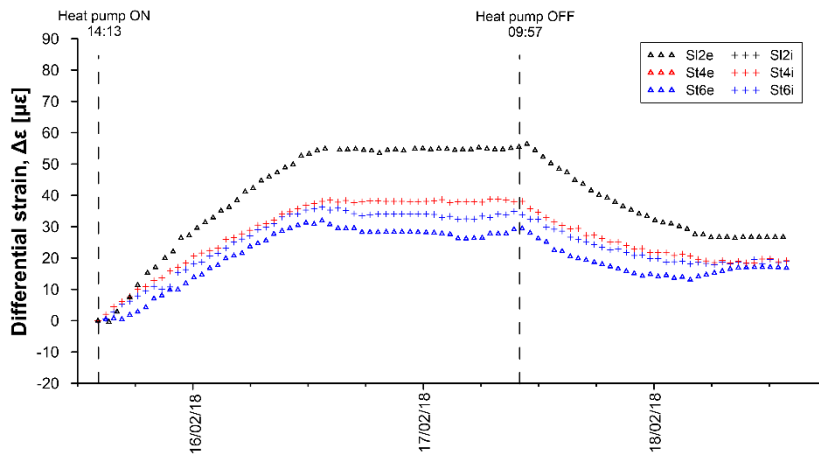


Figure A.14: Differential strains for test GH1

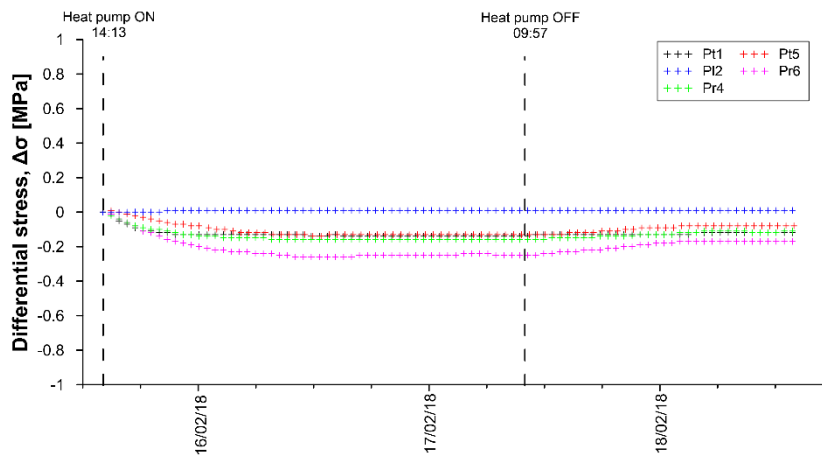


Figure A.15: Differential stresses for test GH1

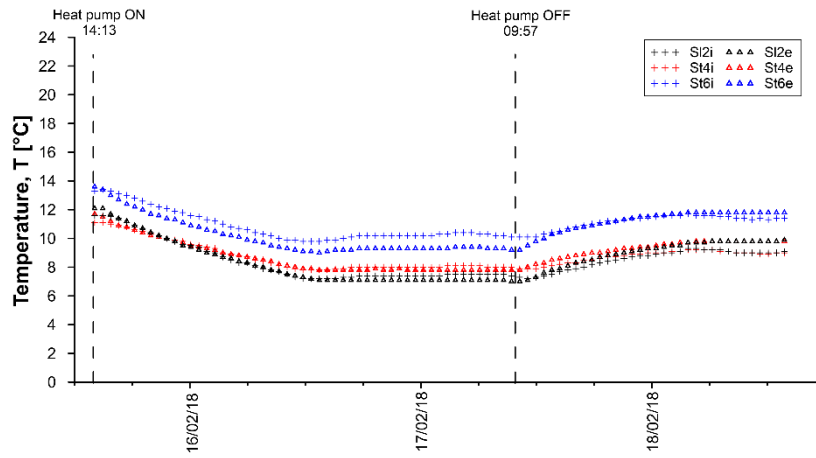


Figure A.16: Temperatures measured by VWSG for test GH1

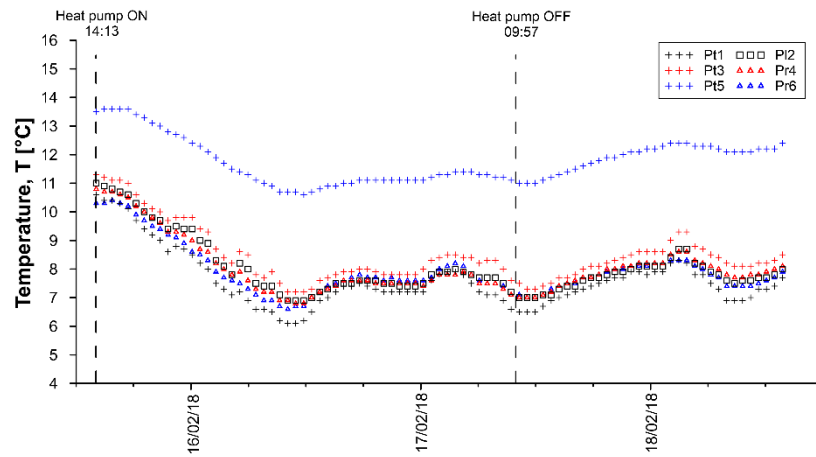


Figure A.17: Temperatures measured by PC for test GH1

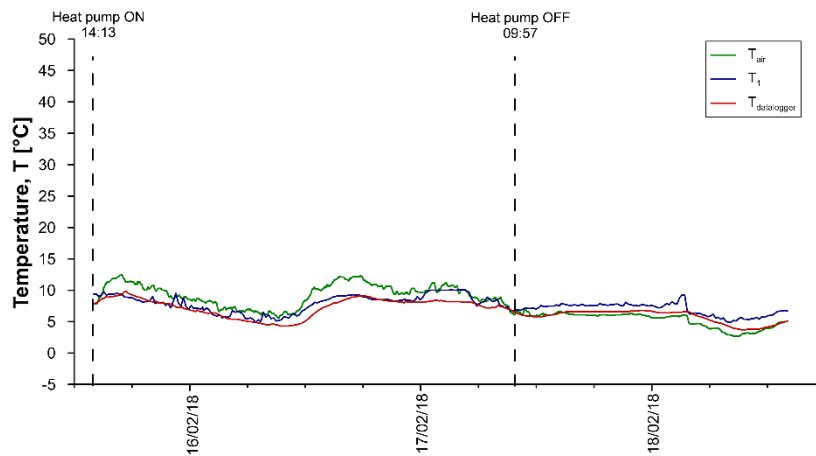


Figure A.18: Air temperatures for test GH1

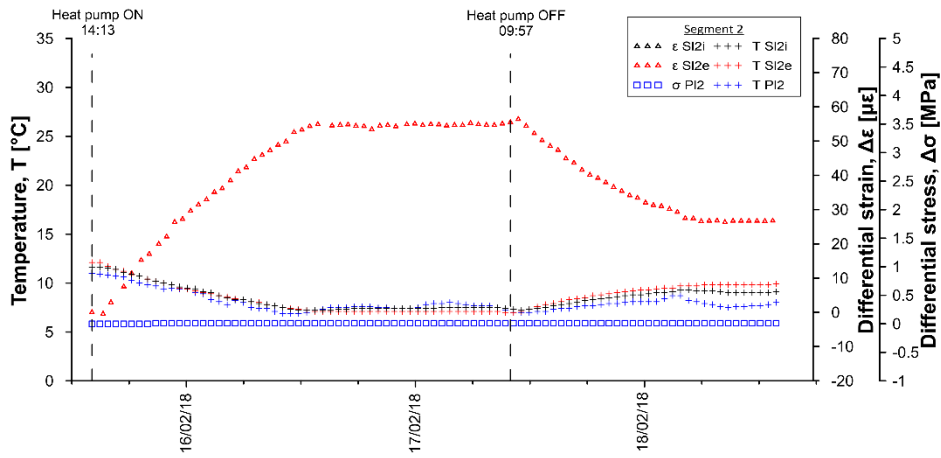


Figure A.19: Temperatures, differential strains and differential stresses in segment 2, ring 179 for test GH1

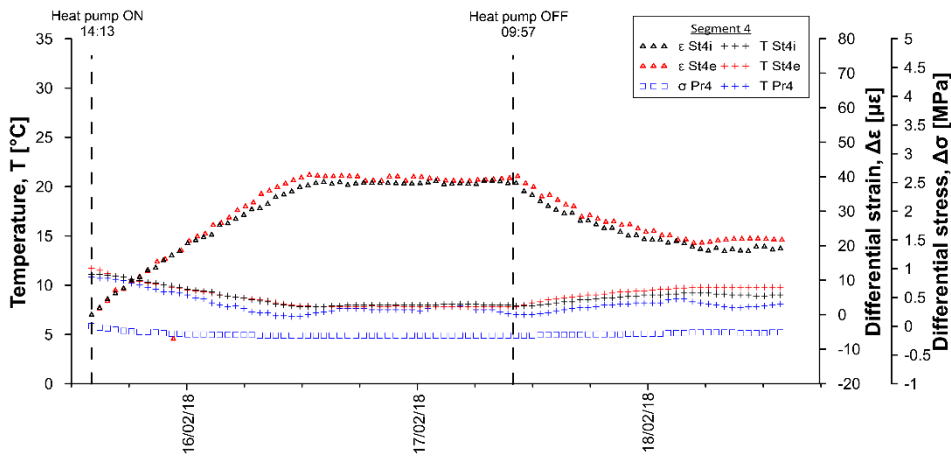


Figure A.20: Temperatures, differential strains and differential stresses in segment 4, ring 179 for test GH1

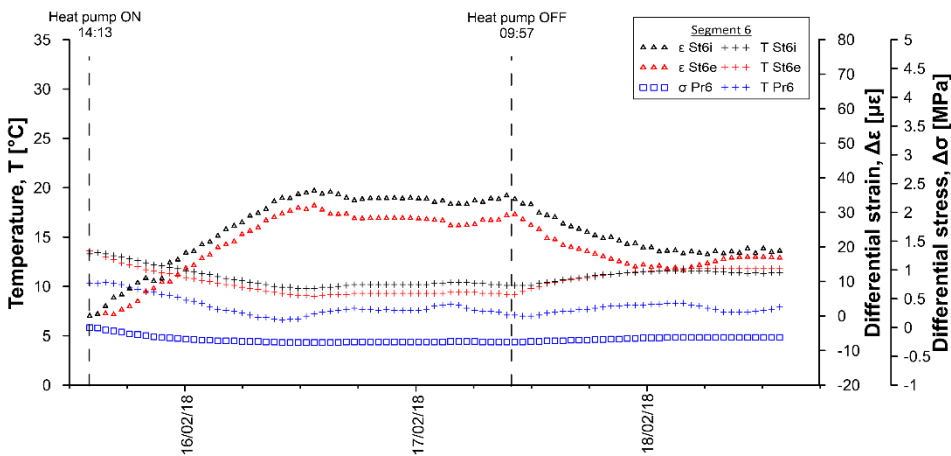


Figure A.21: Temperatures, differential strains and differential stresses in segment 6, ring 179 for test GH1

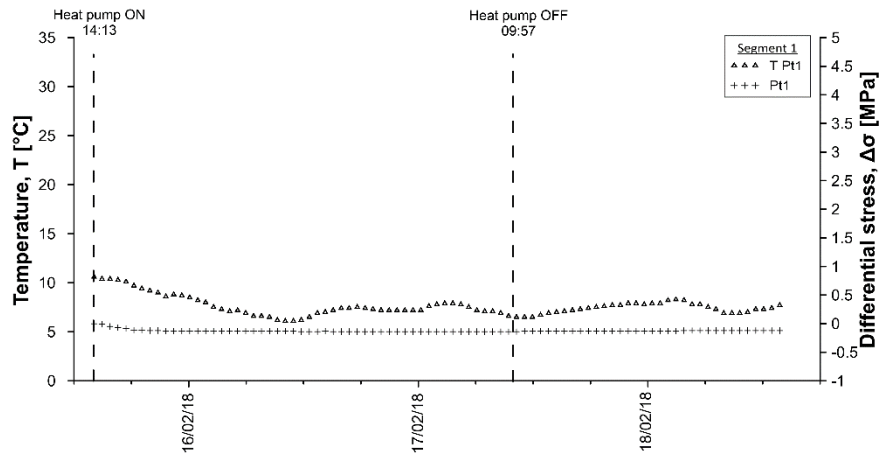


Figure A.22: Temperatures and differential stresses in segment 1, ring 179 for test GH1

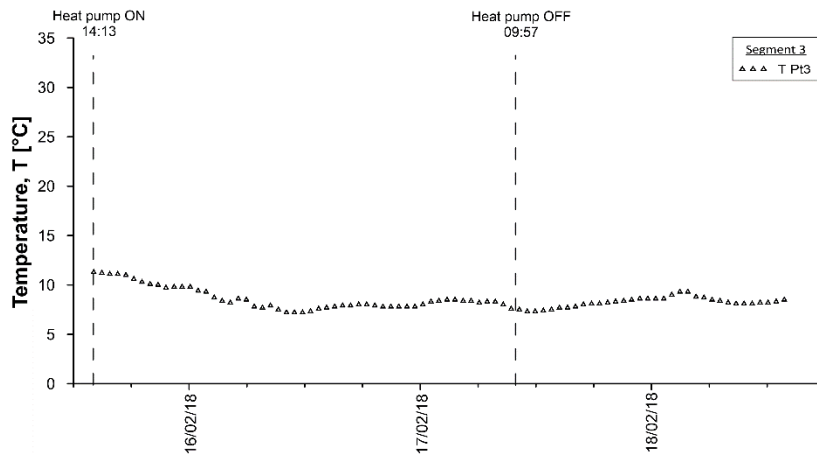


Figure A.23: Temperatures and differential stresses in segment 3, ring 179 for test GH1

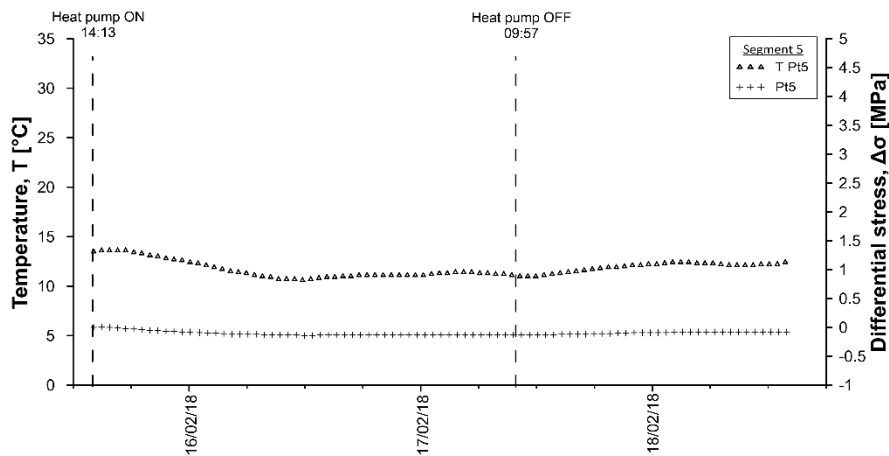


Figure A.24: Temperatures and differential stresses in segment 5, ring 179 for test GH1

Date	T _{Di} [°C]	SI _{2i} [με]	SI _{2i} [°C]	SI _{2e} [με]	SI _{2e} [°C]	SI _{4i} [με]	SI _{4i} [°C]	SI _{4e} [με]	SI _{4e} [°C]	SI _{6i} [με]	SI _{6i} [°C]	SI _{6e} [με]	SI _{6e} [°C]
18/02/2018 05:06	5.8	-2.88	9.2	-1.83	9.7	-3.92	9.2	-2.30	9.8	-2.24	11.6	-7.47	11.8
18/02/2018 06:06	5.2	-2.95	9.2	-1.77	9.8	-4.46	9.1	-2.20	9.8	-2.71	11.6	-6.77	11.8
18/02/2018 07:06	4.8	-3.02	9.2	-1.39	9.8	-5.10	9.1	-1.90	9.8	-3.24	11.5	-6.18	11.8
18/02/2018 08:06	4.2	-2.94	9.1	-1.41	9.8	-6.17	9.1	-1.50	9.8	-3.99	11.5	-5.41	11.8
18/02/2018 09:06	3.8	-3.16	9.0	-1.19	9.8	-6.85	9.0	-1.10	9.8	-4.68	11.4	-4.98	11.8
18/02/2018 10:06	3.8	-3.35	9.0	-1.34	9.8	-7.15	8.9	-1.00	9.8	-4.95	11.4	-4.90	11.8
18/02/2018 11:06	3.8	-3.42	9.0	-1.60	9.8	-7.12	8.9	-1.10	9.8	-4.97	11.4	-4.89	11.8
18/02/2018 12:06	4.2	-3.44	9.0	-1.56	9.8	-7.06	8.9	-1.30	9.8	-4.86	11.3	-4.90	11.8
18/02/2018 13:06	4.6	-3.47	9.0	-1.32	9.8	-6.76	8.9	-1.40	9.8	-4.56	11.4	-5.01	11.8
18/02/2018 14:06	5.1	-3.50	9.1	-1.47	9.8	-5.99	9.0	-1.40	9.8	-3.88	11.5	-5.05	11.8

Table A.6: Data sheet for test GH1 – stresses and temperatures

Date	Pt1 [MPa]	Pt1 [°C]	PI2 [MPa]	PI2 [°C]	Pt3 [MPa]	Pt3 [°C]	Pr4 [MPa]	Pr4 [°C]	Pt5 [MPa]	Pt5 [°C]	Pr6 [MPa]	Pr6 [°C]
15/02/2018 14:06	0.00	10.6	0.00	11.0	-	11.3	0.00	10.8	0.00	13.5	0.00	10.3
15/02/2018 15:06	-0.02	10.6	0.00	10.9	-	11.3	-0.03	10.8	0.01	13.7	-0.01	10.4
15/02/2018 16:06	-0.06	10.3	0.00	10.8	-	11	-0.05	10.7	-0.01	13.6	-0.05	10.3
15/02/2018 17:06	-0.08	10.2	0.00	10.7	-	11	-0.07	10.6	-0.02	13.6	-0.07	10.3
15/02/2018 18:06	-0.10	9.7	0.00	10.4	-	10.7	-0.09	10.3	-0.03	13.4	-0.10	10.0
15/02/2018 19:06	-0.11	9.4	0.00	10.0	-	10.3	-0.10	10.0	-0.04	13.3	-0.12	9.7
15/02/2018 20:06	-0.12	9.1	0.00	9.8	-	10	-0.11	9.7	-0.05	13.1	-0.15	9.5
15/02/2018 21:06	-0.13	8.9	0.01	9.5	-	9.8	-0.12	9.4	-0.07	12.9	-0.16	9.4
15/02/2018 22:06	-0.13	8.6	0.01	9.4	-	9.6	-0.13	9.2	-0.07	12.8	-0.17	9.1
15/02/2018 23:06	-0.13	8.7	0.01	9.5	-	9.8	-0.13	9.2	-0.08	12.6	-0.19	8.9
16/02/2018 00:06	-0.13	8.5	0.01	9.4	-	9.8	-0.14	9.0	-0.08	12.4	-0.20	8.6
16/02/2018 01:06	-0.13	8.2	0.01	9.0	-	9.3	-0.14	8.7	-0.09	12.2	-0.21	8.4
16/02/2018 02:06	-0.13	7.8	0.01	8.6	-	9.1	-0.14	8.5	-0.10	12.0	-0.22	8.2
16/02/2018 03:06	-0.13	7.3	0.01	8.1	-	8.5	-0.15	8.0	-0.11	11.7	-0.22	7.7
16/02/2018 04:06	-0.13	7.2	0.01	7.9	-	8.2	-0.15	7.8	-0.11	11.6	-0.23	7.6
16/02/2018 05:06	-0.13	7.2	0.01	8.2	-	8.6	-0.15	7.9	-0.12	11.4	-0.23	7.5
16/02/2018 06:06	-0.13	6.8	0.01	7.8	-	8.3	-0.15	7.5	-0.12	11.2	-0.24	7.2
16/02/2018 07:06	-0.13	6.5	0.01	7.3	-	7.7	-0.16	7.2	-0.13	11.0	-0.24	7.0
16/02/2018 08:06	-0.13	6.6	0.01	7.6	-	8.1	-0.16	7.3	-0.13	11.0	-0.25	6.9
16/02/2018 09:06	-0.13	6.2	0.01	7.2	-	7.6	-0.16	6.9	-0.13	10.7	-0.25	6.7
16/02/2018 10:06	-0.13	6.1	0.01	6.9	-	7.2	-0.16	6.9	-0.13	10.7	-0.26	6.6
16/02/2018 11:06	-0.13	6.1	0.01	6.9	-	7.2	-0.16	6.8	-0.13	10.7	-0.26	6.7
16/02/2018 12:06	-0.14	6.3	0.01	7.0	-	7.2	-0.16	6.9	-0.14	10.6	-0.26	6.8
16/02/2018 13:06	-0.14	6.7	0.01	7.2	-	7.5	-0.16	7.1	-0.13	10.8	-0.26	7.1
16/02/2018 14:06	-0.14	7.0	0.01	7.3	-	7.7	-0.16	7.3	-0.13	10.8	-0.26	7.3
16/02/2018 15:06	-0.14	7.2	0.01	7.5	-	7.8	-0.16	7.4	-0.13	10.9	-0.26	7.5
16/02/2018 16:06	-0.14	7.3	0.01	7.5	-	7.9	-0.16	7.5	-0.13	11.0	-0.26	7.6
16/02/2018 17:06	-0.14	7.5	0.01	7.6	-	7.9	-0.16	7.6	-0.13	11.1	-0.25	7.7
16/02/2018 18:06	-0.14	7.5	0.01	7.6	-	8	-0.16	7.6	-0.13	11.1	-0.25	7.8
16/02/2018 19:06	-0.14	7.3	0.01	7.6	-	7.9	-0.16	7.6	-0.13	11.1	-0.25	7.7
16/02/2018 20:06	-0.14	7.2	0.01	7.5	-	7.8	-0.16	7.5	-0.13	11.1	-0.25	7.6
16/02/2018 21:06	-0.14	7.2	0.01	7.5	-	7.9	-0.16	7.5	-0.13	11.1	-0.25	7.6
16/02/2018 22:06	-0.14	7.2	0.01	7.5	-	7.8	-0.16	7.5	-0.13	11.1	-0.25	7.6
16/02/2018 23:06	-0.14	7.2	0.01	7.4	-	7.8	-0.16	7.5	-0.13	11.1	-0.25	7.6
17/02/2018 00:06	-0.14	7.2	0.01	7.5	-	7.9	-0.16	7.4	-0.13	11.1	-0.25	7.6
17/02/2018 01:06	-0.14	7.6	0.01	7.8	-	8.3	-0.16	7.6	-0.13	11.2	-0.25	7.7
17/02/2018 02:06	-0.14	7.8	0.01	7.9	-	8.5	-0.16	7.8	-0.13	11.3	-0.25	8.0
17/02/2018 03:06	-0.14	7.9	0.01	7.9	-	8.6	-0.16	7.8	-0.13	11.3	-0.24	8.1
17/02/2018 04:06	-0.14	7.8	0.01	8.0	-	8.5	-0.16	7.9	-0.13	11.4	-0.24	8.2
17/02/2018 05:06	-0.14	7.5	0.01	7.9	-	8.4	-0.16	7.8	-0.13	11.4	-0.24	7.8
17/02/2018 06:06	-0.14	7.2	0.01	7.7	-	8.2	-0.16	7.5	-0.13	11.3	-0.24	7.6
17/02/2018 07:06	-0.14	7.2	0.01	7.7	-	8.3	-0.16	7.5	-0.13	11.3	-0.25	7.5
17/02/2018 08:06	-0.14	7.2	0.01	7.7	-	8.3	-0.16	7.5	-0.13	11.3	-0.25	7.5
17/02/2018 09:06	-0.14	6.8	0.01	7.3	-	7.8	-0.16	7.3	-0.13	11.1	-0.25	7.3
17/02/2018 10:06	-0.14	6.5	0.01	7.1	-	7.5	-0.16	7.0	-0.13	11.0	-0.25	7.0
17/02/2018 11:06	-0.13	6.5	0.01	7.0	-	7.3	-0.16	7.0	-0.13	11.0	-0.25	7.0
17/02/2018 12:06	-0.13	6.6	0.01	7.0	-	7.3	-0.16	7.0	-0.13	11.0	-0.24	7.0
17/02/2018 13:06	-0.13	6.7	0.01	7.1	-	7.5	-0.15	7.2	-0.13	11.1	-0.24	7.2
17/02/2018 14:06	-0.13	6.9	0.01	7.2	-	7.6	-0.15	7.3	-0.13	11.3	-0.23	7.4
17/02/2018 15:06	-0.13	7.1	0.01	7.4	-	7.7	-0.15	7.5	-0.12	11.4	-0.23	7.5
17/02/2018 16:06	-0.13	7.2	0.01	7.4	-	7.8	-0.15	7.6	-0.12	11.5	-0.22	7.5
17/02/2018 17:06	-0.13	7.4	0.01	7.6	-	8	-0.15	7.7	-0.12	11.6	-0.22	7.7
17/02/2018 18:06	-0.13	7.5	0.01	7.6	-	8.1	-0.14	7.8	-0.11	11.8	-0.22	7.8
17/02/2018 19:06	-0.13	7.6	0.01	7.8	-	8.2	-0.14	7.9	-0.11	11.8	-0.21	7.9
17/02/2018 20:06	-0.13	7.6	0.01	7.9	-	8.3	-0.14	8.0	-0.10	11.9	-0.20	7.9
17/02/2018 21:06	-0.13	7.7	0.01	7.9	-	8.4	-0.14	8.1	-0.10	12.0	-0.20	8.0
17/02/2018 22:06	-0.13	7.8	0.01	8.0	-	8.5	-0.13	8.2	-0.09	12.1	-0.19	8.1
17/02/2018 23:06	-0.13	7.9	0.01	8.1	-	8.6	-0.13	8.2	-0.09	12.2	-0.19	8.1
18/02/2018 00:06	-0.13	7.9	0.01	8.1	-	8.5	-0.13	8.2	-0.09	12.2	-0.18	8.1
18/02/2018 01:06	-0.13	7.9	0.01	8.1	-	8.6	-0.13	8.3	-0.09	12.3	-0.18	8.2
18/02/2018 02:06	-0.13	8.2	0.01	8.4	-	9	-0.12	8.5	-0.08	12.4	-0.17	8.3
18/02/2018 03:06	-0.13	8.4	0.01	8.7	-	9.3	-0.12	8.7	-0.08	12.4	-0.17	8.4
18/02/2018 04:06	-0.12	7.8	0.01	8.4	-	9	-0.11	8.4	-0.08	12.3	-0.17	8.1

Date	Pt1 [MPa]	Pt1 [°C]	Pl2 [MPa]	Pl2 [°C]	Pt3 [MPa]	Pt3 [°C]	Pr4 [MPa]	Pr4 [°C]	Pt5 [MPa]	Pt5 [°C]	Pr6 [MPa]	Pr6 [°C]
18/02/2018 05:06	-0.12	7.7	0.01	8.1	-	8.6	-0.11	8.2	-0.08	12.3	-0.17	8.0
18/02/2018 06:06	-0.12	7.5	0.01	8.0	-	8.5	-0.11	8.1	-0.08	12.2	-0.17	7.8
18/02/2018 07:06	-0.12	7.3	0.01	7.8	-	8.4	-0.11	8.0	-0.08	12.2	-0.17	7.7
18/02/2018 08:06	-0.12	6.9	0.01	7.5	-	8.2	-0.11	7.7	-0.08	12.1	-0.17	7.4
18/02/2018 09:06	-0.12	6.8	0.01	7.5	-	8	-0.11	7.6	-0.08	12.0	-0.17	7.3
18/02/2018 10:06	-0.12	7.0	0.01	7.6	-	8.1	-0.12	7.7	-0.08	12.1	-0.17	7.4
18/02/2018 11:06	-0.12	7.2	0.01	7.6	-	8.1	-0.12	7.8	-0.08	12.1	-0.17	7.5
18/02/2018 12:06	-0.12	7.3	0.01	7.7	-	8.2	-0.12	7.9	-0.08	12.2	-0.17	7.6
18/02/2018 13:06	-0.12	7.5	0.01	7.8	-	8.3	-0.11	8.0	-0.08	12.2	-0.17	7.7
18/02/2018 14:06	-0.12	7.9	0.01	8.0	-	8.6	-0.11	8.2	-0.08	12.4	-0.17	8.0

Date	T1 [°C]	T2 [°C]	T3 [°C]	T4 [°C]	T5 [°C]	Date	Tair [°C]	IN [°C]	OUT [°C]	U1 [°C]	U2 [°C]
18/02/2018 01:49	7.7	10.6	10.2	7.7	8.8	18/02/2018 04:56	4.7	9.8	10	7.6	7.3
18/02/2018 02:53	8.8	10.7	10.4	7.9	9	18/02/2018 05:56	3.9	9.8	10	7.3	7
18/02/2018 03:57	6.2	10.5	10.2	7.6	8.7	18/02/2018 06:56	3.9	9.9	10.1	7.1	6.7
18/02/2018 05:01	6.3	10.6	10.2	7.1	8.3	18/02/2018 07:56	2.9	9.9	10.1	6.8	6.3
18/02/2018 06:05	5.9	10.5	10.2	6.7	8	18/02/2018 08:56	2.7	9.9	10.1	6.5	6
18/02/2018 07:09	5.4	10.5	10.2	6.4	7.8	18/02/2018 09:56	3.2	9.9	10.1	6.3	5.7
18/02/2018 08:13	4.9	10.4	10.1	5.9	7.4	18/02/2018 10:56	3.3	9.9	10.1	6.1	5.5
18/02/2018 09:17	5.7	10.5	10.2	5.9	7.4	18/02/2018 11:56	3.9	9.9	10.1	6	5.5
18/02/2018 10:21	5.5	10.5	10.2	5.9	7.4	18/02/2018 12:56	4.6	9.9	10.2	6	5.6
18/02/2018 11:25	5.8	10.6	10.2	6	7.5						
18/02/2018 12:29	6	10.6	10.3	6.2	7.6						
18/02/2018 13:33	6.7	10.7	10.4	6.5	7.9						

Table A.8: Summary of test GH1 records

Quantity	Unit	$x(t_0)$	$x(t_1)$	$x(t_1) - x(t_0)$	$\bar{x}(t_0, t_1)$
T _{DL}	[°C]	8.0	6.4	-1.6	7.3
Sl2i	[με]	-324.43	-326.08	-1.65	8.4
	[με] _{comp}	0.17	51.0	50.8	
Sl2e	[°C]	11.6	7.3	-4.3	8.2
	[με]	-2613.06	-2619.77	-6.71	
St4i	[με] _{comp}	-1.25	55.5	56.8	8.7
	[°C]	12.2	7.0	-5.2	
St4e	[με]	-1776.30	-1776.64	-0.34	8.6
	[με] _{comp}	0.1	38.8	38.7	
St6i	[°C]	11.1	7.9	-3.2	10.8
	[με]	-1505.78	-1513.24	-7.46	
St6e	[με] _{comp}	-0.25	41.1	41.4	10.1
	[°C]	11.7	7.7	-4.0	
Pt1	[με]	-2182.45	-2187.15	-4.70	7.7
	[με] _{comp}	0.1	34.4	34.3	
Pl2	[°C]	13.3	10.1	-3.2	8.2
	[με] _{comp}	-1800.75	-1825.21	-24.46	
Pr4	[με] _{comp}	0.05	29.3	29.2	8.1
	[°C]	13.6	9.2	-4.4	
Pt3	[MPa]	0.08	-0.06	-0.14	8.0
	[°C]	10.5	6.5	-4.0	
Pr6	[MPa]	-0.04	-0.03	0.01	8.0
	[°C]	11.0	7.1	-3.9	
T1	[MPa]	-	-	-	8.0
	[°C]	11.4	7.5	-3.9	
T2	[MPa]	0.18	0.02	-0.16	8.1
	[°C]	10.8	7.1	-3.7	
T3	[MPa]	0.15	0.02	-0.13	11.6
	[°C]	13.6	11.0	-2.6	
T4	[MPa]	0.25	0.00	-0.25	8.0
	[°C]	10.3	7.1	-3.2	
T5	[°C]	9.4	6.8	-2.6	8.0
	[°C]	10.6	4.3	-6.3	
Air	[°C]	11.7	5.6	-6.1	6.2
	[°C]	9.4	7.5	-1.9	
IN	[°C]	9.9	9.0	-0.9	9.2
	[°C]	7.8	6.6	-1.2	
OUT	[°C]	11.9	3.0	-8.9	3.2
	[°C]	12.2	4.7	-7.5	
U1	[°C]	7.7	28.6	20.9	35.2
	[°C]	7.9	24.5	16.6	
U2	[°C]	7.9	24.5	16.6	29.5
	[°C]	7.9	24.5	16.6	

Test GH2

This test was repeated identical to GH1 to investigate the influence of external temperature on the primary circuit temperatures.

Circuit:	Ground
Mode:	Heating
Secondary circuit temperature:	45°C
Activated rings:	179+180
Volumetric flow rate:	1.3 m ³ /h
Fluid velocity in primary circuit:	0.9 m/s
Starting time t_0 :	18/02/2018 13:57
Ending time t_1 :	20/02/2018 09:50
Duration:	1.83 days
Note:	Heat pump turned on for a mistake at the end of the test, then immediately turned off.

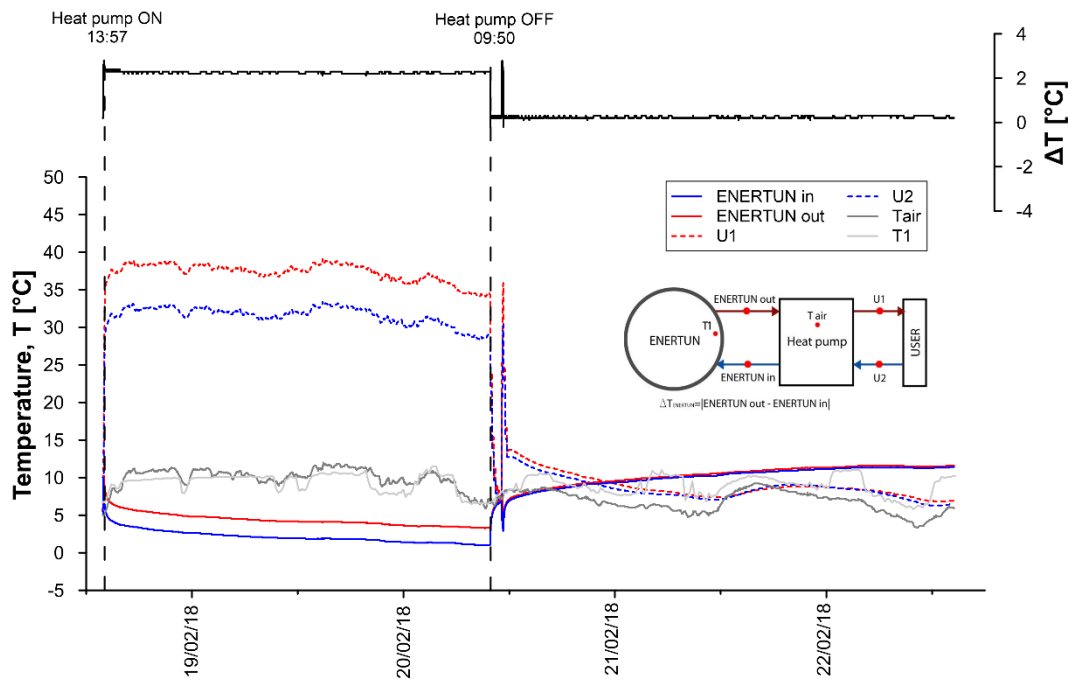


Figure A.25: Primary circuit, secondary circuit and air temperatures for test GH2

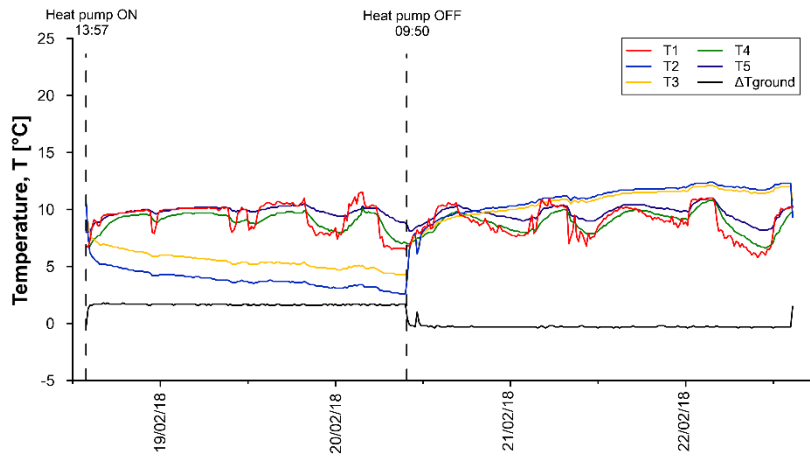


Figure A.26: Temperatures T1-T5 for test GH2

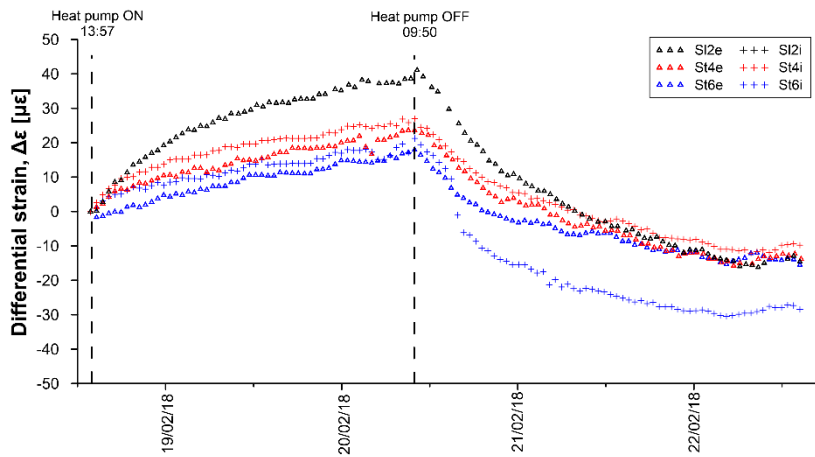


Figure A.27: Differential strains for test GH2

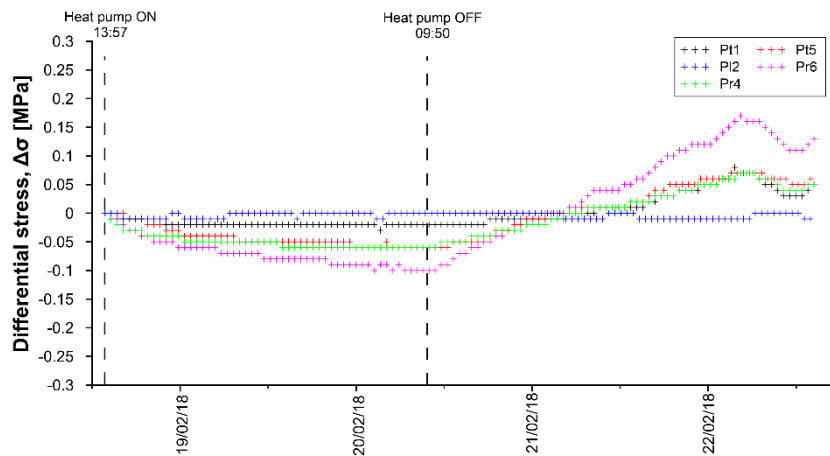


Figure A.28: Differential stresses for test GH2

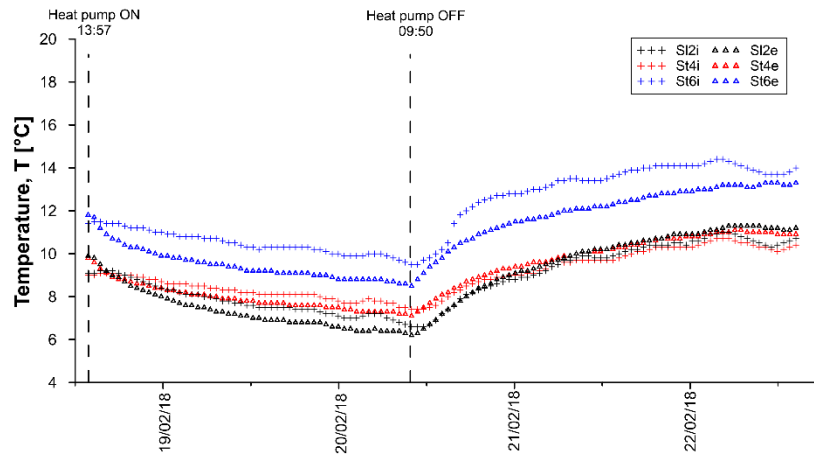


Figure A.29: Temperatures measured by VWSG for test GH2

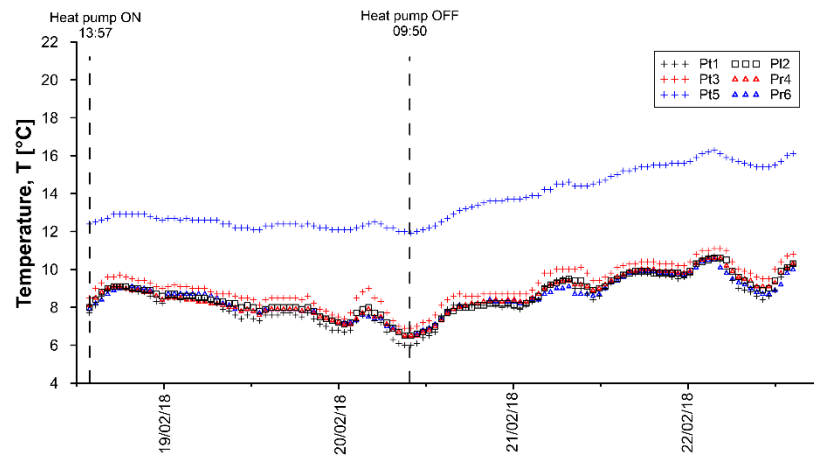


Figure A.30: Temperatures measured by PC for test GH2

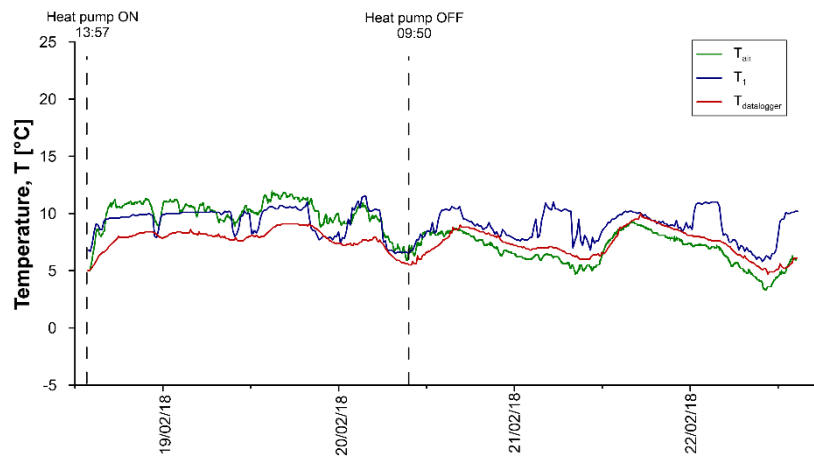


Figure A.31: Air temperatures for test GH2

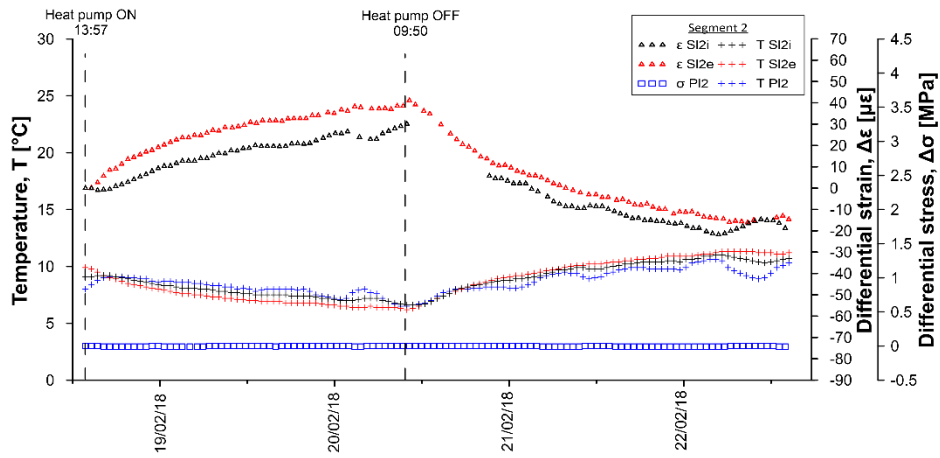


Figure A.32: Temperatures, differential strains and differential stresses in segment 2, ring 179 for test GH2

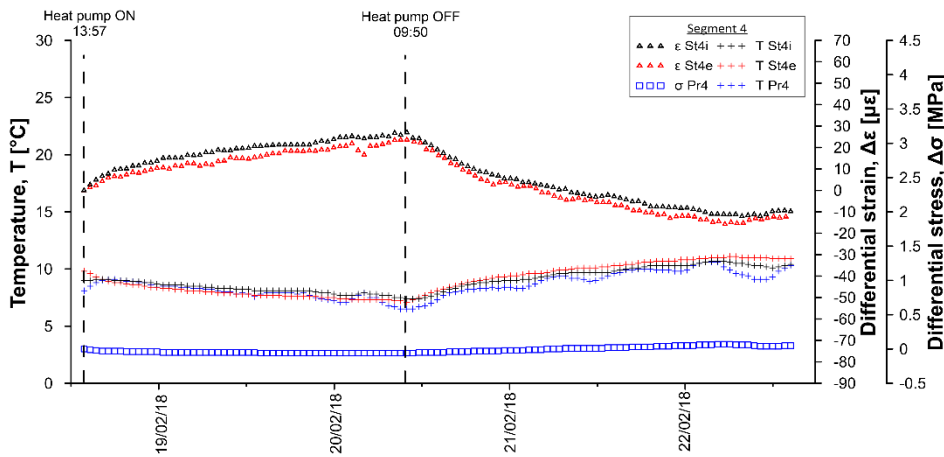


Figure A.33: Temperatures, differential strains and differential stresses in segment 4, ring 179 for test GH2

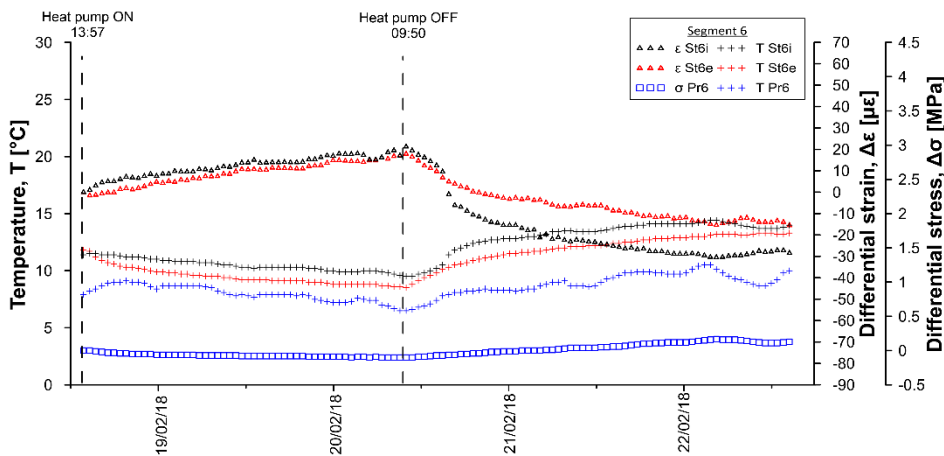


Figure A.34: Temperatures, differential strains and differential stresses in segment 6, ring 179 for test GH2

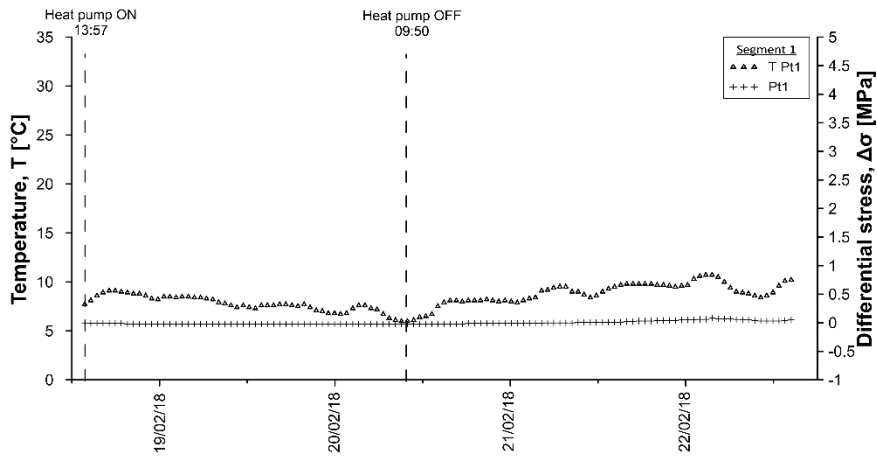


Figure A.35: Temperatures and differential stresses in segment 1, ring 179 for test GH2

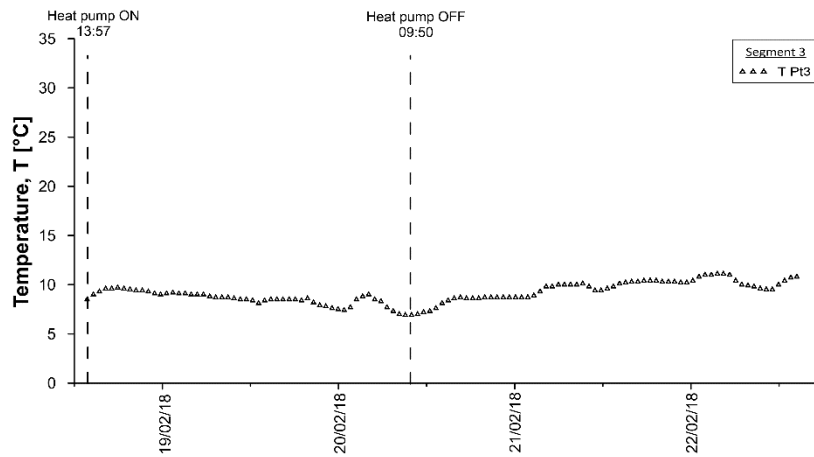


Figure A.36: Temperatures and differential stresses in segment 3, ring 179 for test GH2

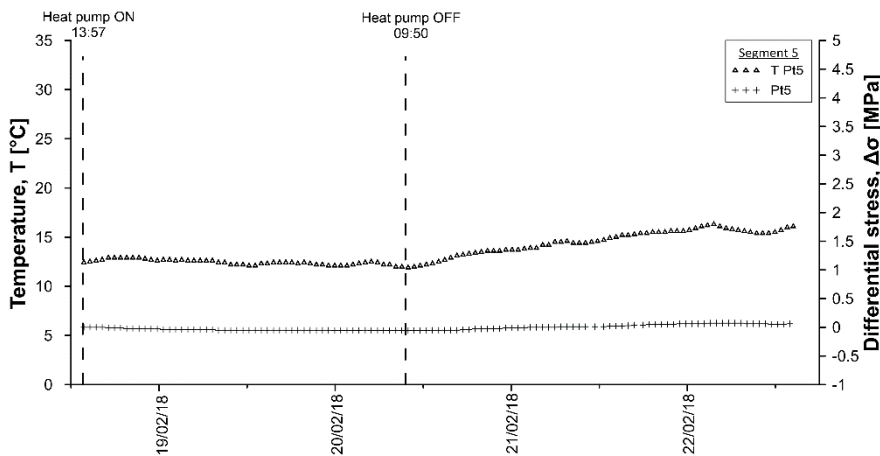


Figure A.37: Temperatures and differential stresses in segment 5, ring 179 for test GH2

Date	T _{bl} [°C]	SI2i [με]	SI2i [°C]	SI2e [με]	SI2e [°C]	St4i [με]	St4i [°C]	St4e [με]	St4e [°C]	St6i [με]	St6i [°C]	St6e [με]	St6e [°C]
21/02/2018 04:46	7.1	-0.33	9.4	-0.30	9.5	6.75	9.3	-2.46	9.7	1.94	13.2	-5.03	11.8
21/02/2018 05:46	7.0	-0.25	9.5	-0.04	9.7	7.36	9.5	-3.31	9.8	2.40	13.3	-4.58	11.9
21/02/2018 06:46	6.7	-0.14	9.7	-0.08	9.8	7.71	9.6	-2.24	9.9	3.24	13.4	-4.21	12.0
21/02/2018 07:46	6.4	-0.05	9.8	0.14	9.9	7.90	9.7	-1.99	10.0	3.24	13.5	-4.01	12.0
21/02/2018 08:46	6.1	0.03	9.8	0.27	10.0	7.32	9.7	-1.66	10.0	2.23	13.5	-2.90	12.1
21/02/2018 09:46	6.0	0.21	9.9	0.37	10.1	6.81	9.7	-1.12	10.1	1.73	13.4	-2.33	12.1
21/02/2018 10:46	6.4	0.32	9.8	-	10.2	5.84	9.7	-0.78	10.1	1.27	13.4	-1.67	12.1
21/02/2018 11:46	6.3	-0.01	9.8	-	10.2	5.49	9.7	-0.66	10.1	1.01	13.4	-1.38	12.2
21/02/2018 12:46	7.0	0.02	9.8	0.61	10.3	5.94	9.7	-0.62	10.2	1.66	13.5	-1.18	12.3
21/02/2018 13:46	7.9	0.02	9.9	0.73	10.3	6.61	9.8	-0.83	10.2	2.69	13.6	-1.29	12.3
21/02/2018 14:46	8.8	0.22	10.0	0.52	10.4	7.20	9.9	-0.78	10.3	3.20	13.7	-1.24	12.4
21/02/2018 15:46	9.2	0.35	10.2	0.64	10.4	7.74	10.0	-0.81	10.3	4.04	13.8	-1.21	12.5
21/02/2018 16:46	9.5	0.52	10.2	0.88	10.5	8.15	10.1	-0.82	10.4	4.58	13.9	-0.97	12.5
21/02/2018 17:46	9.6	0.66	10.3	0.73	10.6	8.34	10.2	-0.82	10.5	5.08	14.0	-0.62	12.6
21/02/2018 18:46	9.4	0.80	10.4	0.67	10.7	8.41	10.2	-0.65	10.6	5.29	14.1	-0.18	12.7
21/02/2018 19:46	9.1	0.35	10.4	1.00	10.7	8.30	10.3	-0.50	10.7	5.28	14.1	0.27	12.8
21/02/2018 20:46	8.9	0.39	10.4	0.87	10.8	8.18	10.3	-0.38	10.7	5.23	14.1	0.68	12.8
21/02/2018 21:46	8.6	1.19	10.5	0.96	10.9	7.89	10.3	-0.29	10.7	4.50	14.1	0.96	12.8
21/02/2018 22:46	8.4	0.48	10.5	0.92	10.9	7.81	10.3	0.00	10.8	4.08	14.1	1.16	12.9
21/02/2018 23:46	8.1	0.89	10.5	1.09	10.9	7.69	10.3	0.20	10.8	4.02	14.1	1.43	12.9
22/02/2018 00:46	8.0	0.73	10.6	1.46	10.9	7.92	10.4	0.00	10.8	4.05	14.1	1.42	12.9
22/02/2018 01:46	7.9	0.86	10.7	1.19	11.0	8.89	10.5	-0.30	10.9	4.99	14.2	1.07	13.0
22/02/2018 02:46	7.7	0.45	10.9	1.20	11.1	9.41	10.6	-0.09	10.9	5.78	14.3	0.84	13.0
22/02/2018 03:46	7.6	0.51	10.9	0.99	11.1	9.75	10.7	-0.15	11.0	6.38	14.4	1.15	13.1
22/02/2018 04:46	7.4	1.44	11.0	1.88	11.2	9.60	10.7	0.30	11.1	5.85	14.4	2.00	13.2
22/02/2018 05:46	6.8	2.02	11.0	1.43	11.3	8.64	10.7	0.60	11.1	4.60	14.2	2.88	13.2
22/02/2018 06:46	6.4	1.94	10.9	1.43	11.3	7.36	10.6	1.20	11.1	3.60	14.1	3.48	13.2
22/02/2018 07:46	6.0	1.75	10.7	1.39	11.3	6.22	10.5	0.90	11.0	2.14	14.0	3.68	13.1
22/02/2018 08:46	5.6	1.74	10.6	0.88	11.3	5.39	10.4	0.80	11.0	1.28	13.9	3.90	13.0
22/02/2018 09:46	5.1	1.50	10.5	2.07	11.2	4.36	10.3	1.30	11.0	0.53	13.8	4.14	13.3
22/02/2018 10:46	4.9	1.27	10.4	-	11.2	3.62	10.2	1.50	11.0	0.22	13.6	4.34	13.3
22/02/2018 11:46	5.1	0.83	10.4	-	11.2	3.54	10.2	0.50	10.9	0.08	13.6	4.21	13.2
22/02/2018 12:46	5.2	0.58	10.5	0.88	11.1	5.03	10.2	0.50	10.9	0.96	13.7	3.76	13.2
22/02/2018 13:46	5.6	0.79	10.6	1.16	11.1	6.65	10.4	1.10	10.9	2.28	13.8	2.97	13.2

Table A.10: Data sheet for test GH2 – stresses and temperatures

Date	Pt1 [MPa]	Pt1 [°C]	Pt2 [MPa]	Pt2 [°C]	Pt3 [MPa]	Pt3 [°C]	Pr4 [MPa]	Pr4 [°C]	Pt5 [MPa]	Pt5 [°C]	Pr6 [MPa]	Pr6 [°C]
18/02/2018 13:46	0	7.7	0	8	-	8.5	0	8.1	0	12.4	0	7.9
18/02/2018 14:46	-0.01	8.3	0	8.5	-	9.1	-0.01	8.6	0	12.6	0	8.3
18/02/2018 15:46	-0.01	8.6	0	8.9	-	9.4	-0.02	8.9	0	12.6	-0.01	8.4
18/02/2018 16:46	-0.01	9	-0.01	9.1	-	9.6	-0.03	9.1	-0.01	12.8	-0.02	8.9
18/02/2018 17:46	-0.01	9.1	-0.01	9.1	-	9.6	-0.03	9.1	-0.01	12.9	-0.03	9
18/02/2018 18:46	-0.01	9	-0.01	9.1	-	9.6	-0.03	9	-0.01	12.9	-0.04	9
18/02/2018 19:46	-0.02	8.8	-0.01	9.1	-	9.5	-0.04	8.9	-0.02	12.9	-0.04	9
18/02/2018 20:46	-0.02	8.8	-0.01	9	-	9.4	-0.04	8.9	-0.02	12.9	-0.05	9
18/02/2018 21:46	-0.02	8.7	-0.01	8.9	-	9.4	-0.04	8.8	-0.03	12.8	-0.05	9
18/02/2018 22:46	-0.02	8.4	-0.01	8.8	-	9.2	-0.04	8.7	-0.03	12.7	-0.05	8.6
18/02/2018 23:46	-0.02	8.2	0	8.6	-	9	-0.04	8.4	-0.03	12.6	-0.06	8.4
19/02/2018 00:46	-0.02	8.5	-0.01	8.7	-	9.2	-0.05	8.5	-0.04	12.7	-0.06	8.7
19/02/2018 01:46	-0.02	8.5	-0.01	8.7	-	9.2	-0.05	8.5	-0.04	12.7	-0.06	8.8
19/02/2018 02:46	-0.02	8.5	-0.01	8.6	-	9.1	-0.05	8.4	-0.04	12.6	-0.06	8.8
19/02/2018 03:46	-0.02	8.4	-0.01	8.6	-	9	-0.05	8.4	-0.04	12.7	-0.06	8.7
19/02/2018 04:46	-0.02	8.4	-	8.5	-	9	-0.05	8.3	-0.04	12.6	-0.06	8.7
19/02/2018 05:46	-0.02	8.4	0	8.5	-	8.9	-0.05	8.3	-0.04	12.6	-0.07	8.6
19/02/2018 06:46	-0.02	8.3	0	8.4	-	8.8	-0.05	8.3	-0.04	12.6	-0.07	8.6
19/02/2018 07:46	-0.02	8	0	8.3	-	8.7	-0.05	8.2	-0.04	12.5	-0.07	8.3
19/02/2018 08:46	-0.02	7.9	0	8.3	-	8.7	-0.05	8.1	-0.05	12.4	-0.07	8.1
19/02/2018 09:46	-0.02	7.6	0	8.2	-	8.6	-0.05	8	-0.05	12.2	-0.07	7.9
19/02/2018 10:46	-0.02	7.4	0	8	-	8.5	-0.05	7.8	-0.05	12.2	-0.07	7.9
19/02/2018 11:46	-0.02	7.6	0	8.1	-	8.5	-0.05	7.9	-0.05	12.2	-0.08	7.9
19/02/2018 12:46	-0.02	7.3	0	7.8	-	8.2	-0.05	7.7	-0.05	12.1	-0.08	7.7
19/02/2018 13:46	-0.02	7.6	0	7.9	-	8.4	-0.06	7.7	-0.05	12.2	-0.08	7.9
19/02/2018 14:46	-0.02	7.6	-0.01	8	-	8.5	-0.06	7.9	-0.05	12.3	-0.08	7.9
19/02/2018 15:46	-0.02	7.6	0	8	-	8.5	-0.06	7.9	-0.05	12.3	-0.08	7.9
19/02/2018 16:46	-0.02	7.7	0	8	-	8.5	-0.06	7.9	-0.05	12.4	-0.08	8
19/02/2018 17:46	-0.02	7.6	0	8	-	8.4	-0.06	7.9	-0.05	12.4	-0.08	7.9
19/02/2018 18:46	-0.02	7.5	0	7.9	-	8.4	-0.06	7.8	-0.05	12.3	-0.08	7.8
19/02/2018 19:46	-0.02	7.7	0	8	-	8.6	-0.06	7.9	-0.05	12.4	-0.08	7.9
19/02/2018 20:46	-0.02	7.3	0	7.7	-	8.1	-0.06	7.7	-0.05	12.3	-0.09	7.7
19/02/2018 21:46	-0.02	7	0	7.4	-	7.8	-0.06	7.4	-0.05	12.1	-0.09	7.5
19/02/2018 22:46	-0.02	6.9	0	7.3	-	7.7	-0.06	7.3	-0.05	12.2	-0.09	7.4
19/02/2018 23:46	-0.02	6.8	0	7.2	-	7.5	-0.06	7.2	-0.05	12.1	-0.09	7.3
20/02/2018 00:46	-0.02	6.7	0	7.1	-	7.4	-0.06	7.1	-0.06	12.1	-0.09	7.2
20/02/2018 01:46	-0.02	6.9	0	7.3	-	8	-0.06	7.2	-0.06	12.2	-0.1	7.2
20/02/2018 02:46	-0.02	7.5	-0.01	7.9	-	8.9	-0.06	7.6	-0.06	12.3	-0.1	7.4
20/02/2018 03:46	-0.02	8	-0.01	8.2	-	9.4	-0.06	8.1	-0.06	12.4	-0.1	7.6
20/02/2018 04:46	-0.02	7.3	0	7.8	-	8.5	-0.06	7.6	-0.06	12.4	-0.09	7.4
20/02/2018 05:46	-0.02	7.2	0	7.6	-	8.3	-0.06	7.5	-0.06	12.4	-0.09	7.4
20/02/2018 06:46	-0.02	6.6	0	7.1	-	7.6	-0.06	7	-0.06	12.2	-0.1	7
20/02/2018 07:46	-0.02	6.2	0	6.8	-	7.2	-0.06	6.7	-0.06	12.1	-0.1	6.7
20/02/2018 08:46	-0.02	6	0	6.6	-	7	-0.06	6.5	-0.06	12	-0.1	6.6
20/02/2018 09:46	-0.02	6	0	6.5	-	6.9	-0.06	6.5	-0.06	11.9	-0.1	6.5
20/02/2018 10:46	-0.02	6.1	0	6.6	-	7	-0.06	6.5	-0.06	12	-0.1	6.6
20/02/2018 11:46	-0.02	6.4	0	6.7	-	7.2	-0.05	6.7	-0.06	12.1	-0.09	6.8
20/02/2018 12:46	-0.02	6.6	0	6.8	-	7.6	-0.05	6.9	-0.06	12.2	-0.08	6.9
20/02/2018 13:46	-0.02	7.2	0	7.2	-	7.9	-0.05	7.1	-0.05	12.4	-0.08	7.2
20/02/2018 14:46	-0.02	7.9	0	7.7	-	8.4	-0.05	7.6	-0.05	12.7	-0.07	7.8
20/02/2018 15:46	-0.02	8.1	0	7.8	-	8.6	-0.04	7.9	-0.05	12.9	-0.06	7.9
20/02/2018 16:46	-0.02	8.1	0	8	-	8.7	-0.04	8	-0.04	13.1	-0.06	8
20/02/2018 17:46	-0.01	8	0	8	-	8.6	-0.04	8.1	-0.04	13.2	-0.05	8.2
20/02/2018 18:46	-0.01	8	0	8.1	-	8.6	-0.04	8.2	-0.04	13.3	-0.04	8.2
20/02/2018 19:46	-0.01	8.1	0	8.1	-	8.6	-0.03	8.2	-0.03	13.4	-0.04	8.3
20/02/2018 20:46	-0.01	8.2	0	8.2	-	8.7	-0.03	8.3	-0.03	13.6	-0.03	8.4
20/02/2018 21:46	-0.01	8.1	0	8.2	-	8.7	-0.03	8.3	-0.02	13.6	-0.02	8.3
20/02/2018 22:46	-0.01	8.1	0	8.2	-	8.7	-0.02	8.3	-0.01	13.7	-0.01	8.3
20/02/2018 23:46	-0.01	8	0	8.2	-	8.7	-0.02	8.3	-0.01	13.7	-0.01	8.3
21/02/2018 00:46	-0.01	7.9	0	8.2	-	8.8	-0.02	8.4	-0.01	13.8	-0.01	8.3
21/02/2018 01:46	-0.01	8.1	0	8.2	-	8.7	-0.02	8.3	-0.01	13.8	0	8.3
21/02/2018 02:46	-0.01	8.3	0	8.5	-	9	-0.01	8.5	-0.01	13.9	0	8.4
21/02/2018 03:46	-0.01	8.6	0	8.8	-	9.5	-0.01	8.8	0	14.1	0	8.5

Date	Pt1 [MPa]	Pt1 [°C]	PI2 [MPa]	PI2 [°C]	Pt3 [MPa]	Pt3 [°C]	Pr4 [MPa]	Pr4 [°C]	Pt5 [MPa]	Pt5 [°C]	Pr6 [MPa]	Pr6 [°C]
21/02/2018 04:46	-0.01	9.2	-0.01	9.1	-	9.9	-0.01	9.1	0	14.3	0.01	8.8
21/02/2018 05:46	0	9.4	-0.01	9.3	-	10	0	9.3	0	14.4	0.01	8.9
21/02/2018 06:46	0	9.5	-0.01	9.4	-	10	0	9.4	0.01	14.5	0.02	9
21/02/2018 07:46	0	9.5	-0.01	9.4	-	10	0.01	9.5	0.01	14.6	0.03	9
21/02/2018 08:46	0	9	-0.01	9.4	-	10	0.01	9.3	0.01	14.4	0.04	8.7
21/02/2018 09:46	0.01	8.8	0	9.3	-	9.9	0.01	9.1	0.01	14.4	0.04	8.7
21/02/2018 10:46	0.01	8.4	0	8.9	-	9.5	0.01	8.9	-29.84	14.5	0.04	8.6
21/02/2018 11:46	0.01	8.6	0	9	-	9.4	0.01	9	-	14.6	0.04	8.7
21/02/2018 12:46	0.01	9.1	0	9.2	-	9.7	0.01	9.2	0.01	14.8	0.05	9.1
21/02/2018 13:46	0.01	9.3	0	9.5	-	10	0.02	9.5	0.02	14.9	0.05	9.3
21/02/2018 14:46	0.01	9.6	-0.01	9.6	-	10.1	0.02	9.7	0.02	15.1	0.06	9.6
21/02/2018 15:46	0.02	9.8	-0.01	9.8	-	10.3	0.02	9.8	0.03	15.2	0.07	9.7
21/02/2018 16:46	0.02	9.8	-0.01	9.9	-	10.3	0.03	9.9	0.04	15.3	0.08	9.8
21/02/2018 17:46	0.03	9.8	-0.01	9.9	-	10.4	0.03	10	0.04	15.4	0.09	9.9
21/02/2018 18:46	0.03	9.8	-0.01	9.9	-	10.4	0.03	10	0.05	15.4	0.1	9.8
21/02/2018 19:46	0.04	9.7	-0.01	9.9	-	10.3	0.04	9.9	0.05	15.5	0.11	9.8
21/02/2018 20:46	0.04	9.7	-0.01	9.8	-	10.3	0.04	9.9	0.05	15.5	0.11	9.8
21/02/2018 21:46	0.04	9.6	-0.01	9.8	-	10.3	0.04	9.9	0.05	15.6	0.12	9.7
21/02/2018 22:46	0.04	9.6	-0.01	9.8	-	10.2	0.05	9.9	0.06	15.6	0.12	9.8
21/02/2018 23:46	0.05	9.7	-0.01	9.9	-	10.4	0.05	10	0.06	15.7	0.12	9.8
22/02/2018 00:46	0.05	10.1	-0.01	10.1	-	10.6	0.05	10.1	0.06	15.9	0.12	10
22/02/2018 01:46	0.06	10.5	-0.01	10.4	-	10.9	0.06	10.5	0.06	16	0.13	10.3
22/02/2018 02:46	0.06	10.7	-0.01	10.5	-	11	0.06	10.6	0.07	16.2	0.15	10.5
22/02/2018 03:46	0.07	10.7	-0.01	10.6	-	11.1	0.07	10.6	0.07	16.2	0.16	10.4
22/02/2018 04:46	0.07	10.2	-0.01	10.5	-	11.1	0.07	10.4	0.07	16	0.17	9.9
22/02/2018 05:46	0.07	9.7	-0.01	10.1	-	10.7	0.07	10	0.07	15.8	0.16	9.6
22/02/2018 06:46	0.06	9	0	9.6	-	10.1	0.06	9.7	0.07	15.7	0.16	9.3
22/02/2018 07:46	0.05	8.9	0	9.4	-	9.9	0.06	9.5	0.06	15.6	0.15	9.2
22/02/2018 08:46	0.05	8.6	0	9.2	-	9.8	0.05	9.4	0.06	15.5	0.13	8.9
22/02/2018 09:46	0.04	8.6	0	9	-	9.6	0.05	9.2	0.06	15.4	0.12	8.8
22/02/2018 10:46	0.03	8.5	0	9	-	9.4	0.04	9	0.05	15.4	0.12	8.7
22/02/2018 11:46	0.03	8.8	0	9.3	-	9.8	0.04	9.3	0.05	15.5	0.11	8.9
22/02/2018 12:46	0.03	9.6	-0.01	9.9	-	10.4	0.04	9.8	0.05	15.7	0.11	9.2
22/02/2018 13:46	0.05	10.1	-0.01	10.2	-	10.7	0.05	10.2	0.05	16	0.12	9.9

Table A.11: Data sheet for test GH2 - sensors T1-T5 and heat pump

Date	T1 [°C]	T2 [°C]	T3 [°C]	T4 [°C]	T5 [°C]	Date	Tair [°C]	IN [°C]	OUT [°C]	U1 [°C]	U2 [°C]
18/02/2018 13:49	6.8	10.8	10.5	6.6	8	18/02/2018 13:53	5	10	10.2	6	5.7
18/02/2018 14:53	9.1	5.7	7.4	7.4	8.7	18/02/2018 14:00	5	7.4	10.2	20.4	16.1
18/02/2018 15:57	9.3	5.2	6.9	8	9	18/02/2018 15:59	8.4	3.7	6	37.5	31.7
18/02/2018 17:01	9.6	5.1	6.8	8.8	9.5	18/02/2018 17:59	10.6	3.3	5.6	38	32.2
18/02/2018 18:05	9.6	5	6.7	9.2	9.6	18/02/2018 19:59	10.9	3	5.3	38.2	32.4
18/02/2018 19:09	9.7	4.8	6.5	9.4	9.7	18/02/2018 21:59	11.2	2.8	5.1	38.7	32.8
18/02/2018 20:13	9.8	4.7	6.4	9.5	9.8	18/02/2018 23:59	10.6	2.6	4.8	38	32.2
18/02/2018 21:17	9.9	4.6	6.3	9.6	9.9	19/02/2018 01:59	11.1	2.5	4.7	38.2	32.4
18/02/2018 22:21	9.9	4.5	6.1	9.5	10	19/02/2018 03:59	10.6	2.3	4.6	37.8	32
18/02/2018 23:25	8.6	4.2	5.9	8.9	9.6	19/02/2018 05:59	10.4	2.2	4.5	37.7	32
19/02/2018 00:29	10	4.3	6	9.2	9.9	19/02/2018 07:58	9.4	2.1	4.3	36.8	31.1
19/02/2018 01:33	10	4.3	6	9.5	10	19/02/2018 09:58	9.2	1.9	4.2	36.9	31.2
19/02/2018 02:37	10.1	4.2	5.9	9.6	10.1	19/02/2018 11:58	10.3	1.9	4.2	37.7	32
19/02/2018 03:41	10.1	4.1	5.8	9.7	10.1	19/02/2018 13:58	11.6	1.8	4.1	38.5	32.8
19/02/2018 04:45	10.1	4.1	5.8	9.7	10.2	19/02/2018 15:58	11.3	1.8	4.1	38.4	32.8
19/02/2018 05:49	10.1	4	5.7	9.7	10.2	19/02/2018 17:58	11.3	1.8	4	38.3	32.6
19/02/2018 06:53	10.1	4	5.6	9.7	10.2	19/02/2018 19:58	11	1.7	3.9	37.9	32.2
19/02/2018 07:57	9.9	3.8	5.5	9.5	10.1	19/02/2018 21:58	9.2	1.5	3.8	36.9	31.3
19/02/2018 09:01	10.2	3.8	5.5	9.5	10.2	19/02/2018 23:57	9.9	1.4	3.7	35.9	30.2
19/02/2018 10:05	8.2	3.6	5.2	8.9	9.9	20/02/2018 01:57	9.8	1.3	3.6	36.4	30.8
19/02/2018 11:09	10.2	3.8	5.4	9	10	20/02/2018 03:57	10.3	1.3	3.6	36.7	31
19/02/2018 11:57	9.2	3.7	5.3	9	9.9	20/02/2018 05:57	8.8	1.2	3.5	34.9	29.2
19/02/2018 12:17	8.4	3.6	5.2	8.8	9.8	20/02/2018 07:57	6.9	1.1	3.3	34.3	28.7
19/02/2018 12:24	8.3	3.6	5.2	8.8	9.8	20/02/2018 09:50	6.6	1	3.3	34.2	28.8
19/02/2018 12:28	8.5	3.6	5.2	8.8	9.8	20/02/2018 10:50	7.4	6.6	6.8	8.3	7.6
19/02/2018 12:47	8.3	3.5	5.2	8.8	9.8	20/02/2018 11:50	8.3	6.7	6.9	13.4	12.7
19/02/2018 13:51	10.3	3.7	5.4	9	10	20/02/2018 12:50	8.3	7.4	7.6	13.3	12.5
19/02/2018 14:55	10.6	3.8	5.4	9.4	10.1	20/02/2018 13:49	8.2	7.7	7.9	12.6	11.8
19/02/2018 15:59	10.7	3.7	5.4	9.7	10.2	20/02/2018 14:49	8.4	8	8.2	12	11.2
19/02/2018 17:03	10.5	3.7	5.3	9.7	10.3	20/02/2018 15:49	8.7	8.2	8.4	11.6	10.8
19/02/2018 18:07	10.6	3.7	5.3	9.8	10.4	20/02/2018 16:49	8.5	8.4	8.6	11.2	10.5
19/02/2018 19:11	10.5	3.6	5.2	9.7	10.4	20/02/2018 17:49	8.1	8.6	8.8	10.9	10.3
19/02/2018 20:15	8.7	3.5	5.1	9.6	10.3	20/02/2018 18:49	7.6	8.7	8.9	10.6	10
19/02/2018 21:19	7.7	3.3	4.9	8.8	9.9	20/02/2018 19:49	7.3	8.9	9.1	10.3	9.7
19/02/2018 22:23	7.8	3.2	4.9	8.4	9.8	20/02/2018 20:49	7.4	9.1	9.3	10	9.4
19/02/2018 23:27	8	3.1	4.8	8.2	9.6	20/02/2018 21:49	6.7	9.1	9.4	9.8	9.1
20/02/2018 00:31	7.9	3.1	4.7	8	9.4	20/02/2018 22:49	6.8	9.2	9.4	9.5	8.8
20/02/2018 01:35	9	3.1	4.8	8.2	9.4	20/02/2018 23:49	6.5	9.3	9.5	9.2	8.6
20/02/2018 02:39	11.1	3.4	5.1	9.1	9.9	21/02/2018 00:49	6.2	9.4	9.6	9	8.3
20/02/2018 03:43	11.5	3.4	5.1	10	10.3	21/02/2018 01:49	6	9.5	9.7	8.7	8.1
20/02/2018 04:47	10.3	3.2	4.9	9.7	10.1	21/02/2018 02:49	6.3	9.6	9.8	8.5	8
20/02/2018 05:51	9.2	3.1	4.7	9.5	10.1	21/02/2018 03:49	6.1	9.7	9.9	8.4	7.9
20/02/2018 06:55	6.8	2.8	4.4	8.1	9.5	21/02/2018 04:49	6.4	9.8	10	8.3	7.8
20/02/2018 07:59	6.6	2.7	4.4	7.4	9.2	21/02/2018 05:48	6.2	9.9	10.1	8.2	7.8
20/02/2018 09:03	6.6	2.6	4.3	7	8.9	21/02/2018 06:48	5.6	10	10.2	8	7.7
20/02/2018 10:07	6.8	6.5	6.4	7	8.1	21/02/2018 07:48	5.4	10.1	10.3	7.9	7.6
20/02/2018 11:11	8.2	6.1	7.1	7.5	8.5	21/02/2018 08:48	5.2	10.1	10.3	7.7	7.4
20/02/2018 12:15	8.5	8.3	8.1	7.8	8.8	21/02/2018 09:48	5.4	10.2	10.4	7.5	7.2
20/02/2018 13:19	8.4	8.7	8.4	8	9.2	21/02/2018 10:48	5.3	10.2	10.5	7.4	7.1
20/02/2018 14:23	10.3	9.2	8.9	8.9	9.8	21/02/2018 11:48	6	10.3	10.5	7.4	7.1
20/02/2018 15:27	10.6	9.4	9.2	9.5	10.1	21/02/2018 12:48	7.6	10.4	10.7	7.5	7.3
20/02/2018 16:31	10.6	9.7	9.4	9.8	10.3	21/02/2018 13:48	8.2	10.5	10.8	7.7	7.7
20/02/2018 17:35	9.4	9.7	9.4	9.6	10.1	21/02/2018 14:48	8.6	10.6	10.8	8	8
20/02/2018 18:39	8.9	9.8	9.6	9.4	9.9	21/02/2018 15:48	9.2	10.7	10.9	8.2	8.4
20/02/2018 19:43	8.6	9.9	9.6	9.1	9.8	21/02/2018 16:48	9	10.7	11	8.5	8.7
20/02/2018 20:47	8.8	10.1	9.8	9	9.7	21/02/2018 17:48	8.8	10.8	11	8.6	8.9
20/02/2018 21:51	8	10.1	9.8	8.7	9.5	21/02/2018 18:48	8.4	10.9	11.1	8.7	9
20/02/2018 22:55	8.1	10.2	9.9	8.5	9.4	21/02/2018 19:48	8.1	10.9	11.1	8.8	9
20/02/2018 23:59	7.8	10.3	10	8.2	9.3	21/02/2018 20:48	7.9	11	11.2	8.8	9
21/02/2018 01:03	7.8	10.4	10.1	8.1	9.1	21/02/2018 21:47	7.7	11	11.3	8.8	9
21/02/2018 02:07	7.9	10.5	10.2	8	9.1	21/02/2018 22:47	7.6	11.1	11.3	8.8	8.9
21/02/2018 03:11	7.9	10.6	10.3	8.2	9.3	21/02/2018 23:47	7.4	11.1	11.3	8.7	8.8
21/02/2018 04:15	10.9	10.9	10.7	8.9	9.9	22/02/2018 00:47	7.2	11.1	11.4	8.7	8.7

Date	T1 [°C]	T2 [°C]	T3 [°C]	T4 [°C]	T5 [°C]	Date	Tair [°C]	IN [°C]	OUT [°C]	U1 [°C]	U2 [°C]
21/02/2018 05:19	11	11	10.8	9.5	10.2	22/02/2018 01:47	7.2	11.2	11.4	8.6	8.6
21/02/2018 06:23	10.2	11.1	10.8	9.8	10.3	22/02/2018 02:47	7	11.3	11.5	8.6	8.5
21/02/2018 07:27	10.2	11.2	10.9	10	10.3	22/02/2018 03:47	7.1	11.3	11.6	8.4	8.4
21/02/2018 08:31	8.1	11	10.7	8.9	9.4	22/02/2018 04:47	6.3	11.3	11.6	8.4	8.3
21/02/2018 09:35	8.1	11	10.8	8.3	9.2	22/02/2018 05:47	5.4	11.3	11.6	8.2	8
21/02/2018 10:39	7.9	11	10.7	7.9	9	22/02/2018 06:47	5.3	11.3	11.6	8	7.8
21/02/2018 11:43	8.1	11.2	10.9	8	9.1	22/02/2018 07:47	4.8	11.3	11.6	7.8	7.5
21/02/2018 12:47	9.2	11.4	11.1	8.6	9.6	22/02/2018 08:47	4.5	11.3	11.5	7.6	7.2
21/02/2018 13:51	9.6	11.5	11.2	9	9.9	22/02/2018 09:47	4	11.3	11.5	7.4	6.9
21/02/2018 14:55	10.1	11.7	11.3	9.4	10.2	22/02/2018 10:47	3.6	11.2	11.5	7.1	6.5
21/02/2018 15:59	10.2	11.7	11.4	9.8	10.4	22/02/2018 11:47	4.4	11.2	11.5	6.9	6.3
21/02/2018 17:03	10.1	11.8	11.5	10	10.4	22/02/2018 12:46	4.8	11.3	11.5	6.8	6.3
21/02/2018 18:07	9.7	11.8	11.5	9.9	10.4	22/02/2018 13:46	6	11.3	11.6	6.8	6.4
21/02/2018 19:11	9.4	11.8	11.5	9.8	10.2						
21/02/2018 20:15	9.3	11.8	11.6	9.6	10.1						
21/02/2018 21:19	9	11.9	11.6	9.4	10.1						
21/02/2018 22:23	8.7	11.9	11.6	9.3	10						
21/02/2018 23:27	9.2	11.9	11.6	9.1	9.8						
22/02/2018 00:31	10.1	12.1	11.8	9.4	9.9						
22/02/2018 01:35	10.8	12.3	12	10	10.7						
22/02/2018 02:39	10.9	12.3	12	11	10.9						
22/02/2018 03:43	11	12.4	12.1	11	11						
22/02/2018 04:47	8.2	12.1	11.8	9.7	10.1						
22/02/2018 05:51	7.7	12	11.7	8.7	9.5						
22/02/2018 06:55	7.2	12	11.7	8	9.1						
22/02/2018 07:59	6.7	12	11.7	7.7	8.9						
22/02/2018 09:03	6	11.8	11.4	7.1	8.5						
22/02/2018 10:07	6	11.7	11.4	6.8	8.2						
22/02/2018 11:11	6.5	11.8	11.5	6.7	8.2						
22/02/2018 12:15	9.3	12.2	11.9	7.7	9						
22/02/2018 13:19	10	12.3	12	8.7	9.9						
22/02/2018 14:23	10.2	12.3	12	9.7	10.2						

Table A.12: Summary of test GH2 records

Quantity	Unit	$x(t_0)$	$x(t_1)$	$x(t_1) - x(t_0)$	$\bar{x}(t_0, t_1)$
T _{DL}	[°C]	5.0	5.5	0.5	7.8
Sl2i	[με]	-328.12	-328.43	-0.31	7.8
	[με] _{comp} [°C]	-0.04 9.1	30.15 6.6	30.19 -2.5	
Sl2e	[με]	-2614.43	-2620.32	-5.89	7.4
	[με] _{comp} [°C]	1.52 9.8	39.55 6.2	38.03 -3.6	
St4i	[με]	-1782.78	-1775.24	7.54	8.3
	[με] _{comp} [°C]	0.09 9.0	27.15 7.4	27.06 -1.6	
St4e	[με]	-1507.04	-1515.42	-8.38	8.0
	[με] _{comp} [°C]	0.03 9.8	23.37 7.2	23.34 -2.6	
St6i	[με]	-2186.78	-2188.63	-1.85	10.5
	[με] _{comp} [°C]	0.1 11.4	20.21 9.6	20.11 -1.8	
St6e	[με]	-1806.00	-1828.13	-22.13	9.5
	[με] _{comp} [°C]	-0.08 11.8	18.05 8.5	18.13 -3.3	
Pt1	[MPa]	-0.04	-0.06	-0.02	7.8
	[°C]	7.7	6.0	-1.7	
Pl2	[MPa]	-0.03	-0.03	0.00	8.1
	[°C]	8.0	6.5	-1.5	
Pt3	[MPa]	-	-	-	8.6
	[°C]	8.5	6.9	-1.6	
Pr4	[MPa]	0.07	0.01	-0.06	8.0
	[°C]	8.2	6.5	-1.7	
Pt5	[MPa]	0.07	0.01	-0.06	12.4
	[°C]	12.4	11.9	-0.5	
Pr6	[MPa]	0.08	-0.02	-0.10	8.0
	[°C]	8.0	6.5	-1.5	
T1	[°C]	6.8	6.5	-0.3	9.3
T2	[°C]	10.8	2.6	-8.2	3.9
T3	[°C]	10.5	4.3	-6.2	5.5
T4	[°C]	6.6	7.1	0.5	9.0
T5	[°C]	8.0	8.8	0.8	9.8
Air	[°C]	5.0	6.6	1.6	10.0
IN	[°C]	10.0	1.0	-9.0	2.1
OUT	[°C]	10.2	3.3	-6.9	4.4
U1	[°C]	4.9	34.2	29.3	37.2
U2	[°C]	5.2	28.8	23.6	31.5

Test GH3

Again, this test was carried out identical to GH1 and GH2 for repeatability reasons.

Circuit:	Ground
Mode:	Heating
Secondary circuit temperature:	45°C
Activated rings:	179+180
Volumetric flow rate:	1.3 m ³ /h
Fluid velocity in primary circuit:	0.9 m/s
Starting time t_0 :	22/02/2018 14:32
Ending time t_1 :	26/02/2018 12:50
Duration:	3.93 days
Note:	The test actually stopped at 11:29 and 12:03 for low-pressure causes (primary temperature below 0°C).

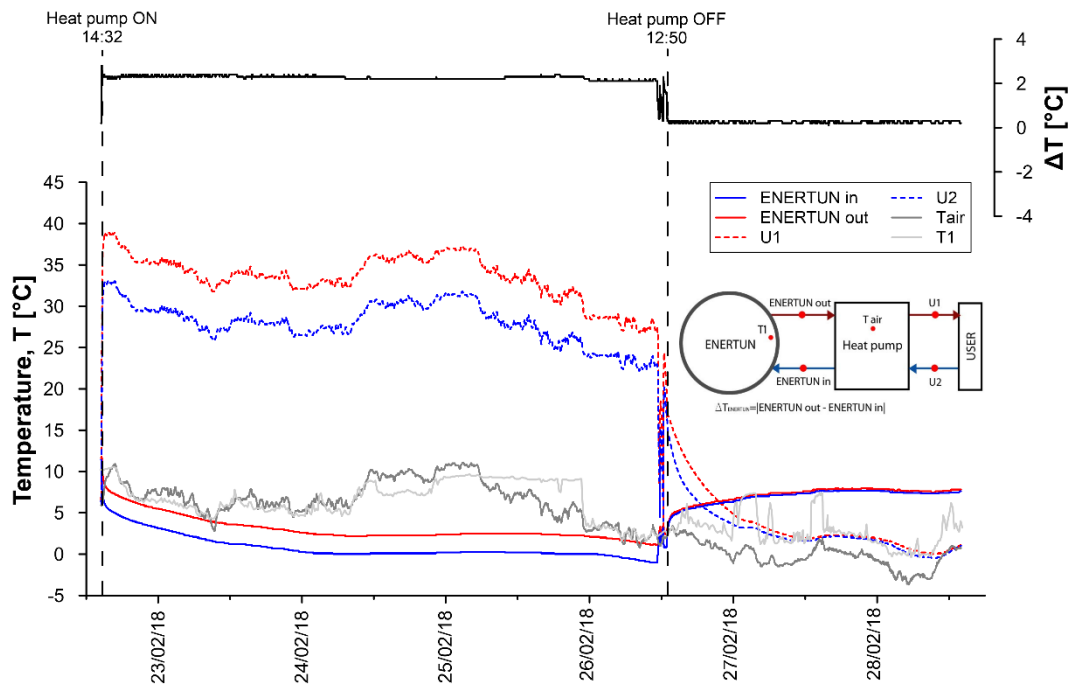


Figure A.38: Primary circuit, secondary circuit and air temperatures for test GH3.

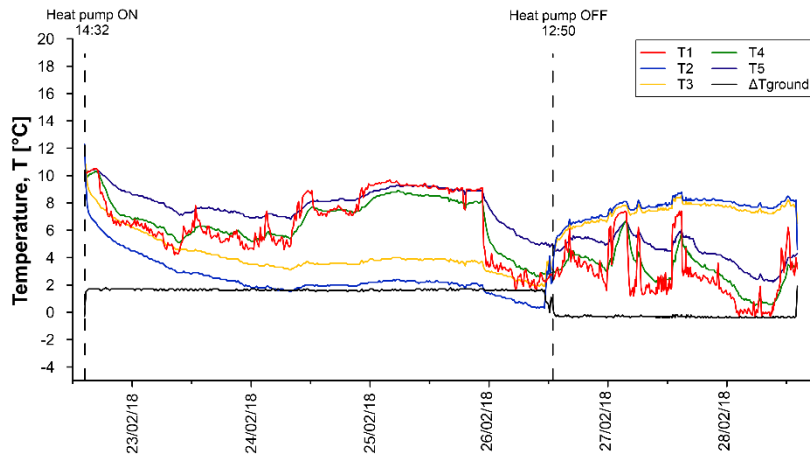


Figure A.39: Temperatures T1-T5 for test GH3.

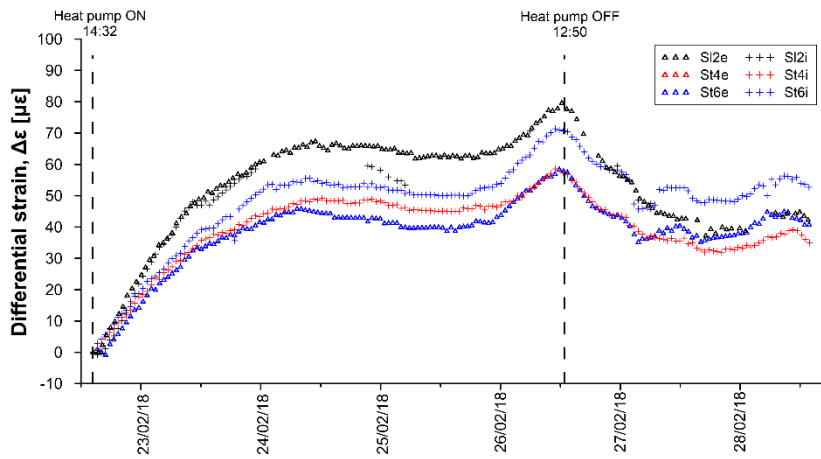


Figure A.40: Differential strains for test GH3.

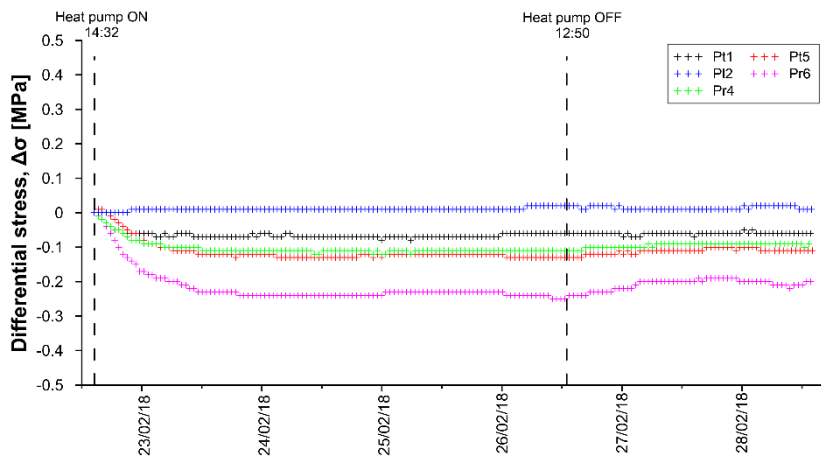


Figure A.41: Differential stresses for test GH3.

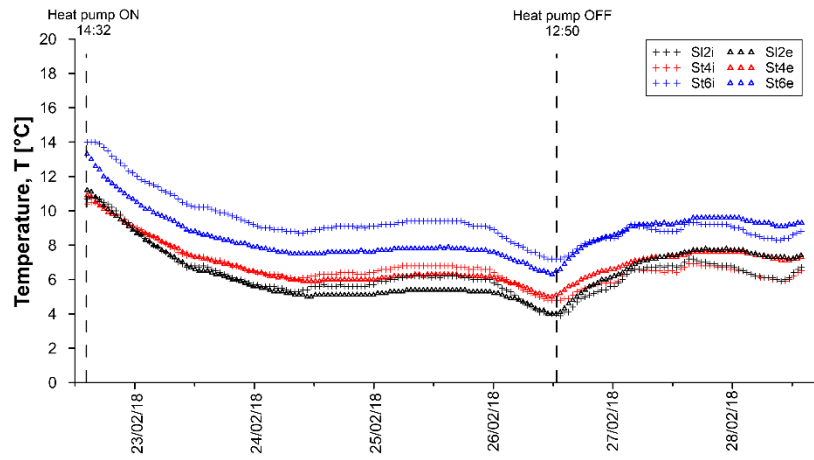


Figure A.42: Temperatures measured by VWSG for test GH3.

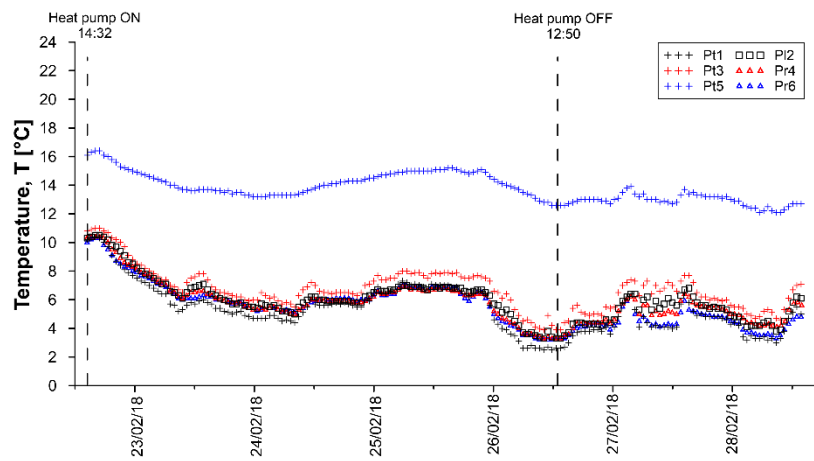


Figure A.43: Temperatures measured by PC for test GH3.

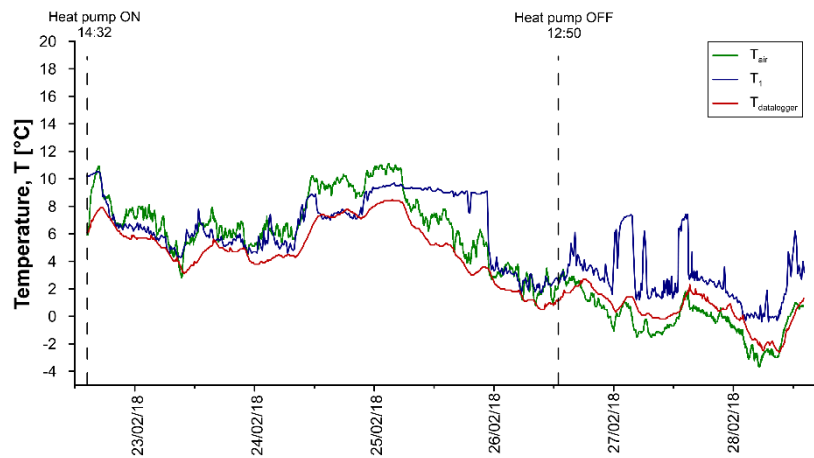


Figure A.44: Air temperatures for test GH3.

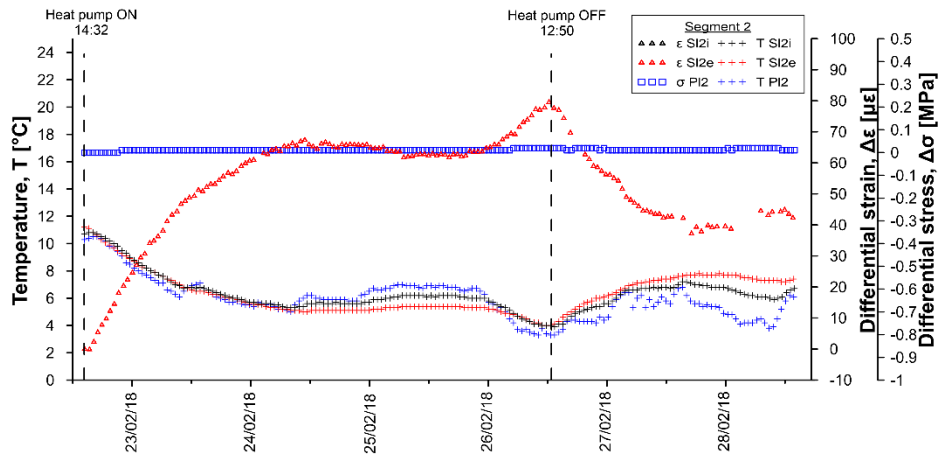


Figure A.45: Temperatures, differential strains and differential stresses in segment 2, ring 179 for test GH3.

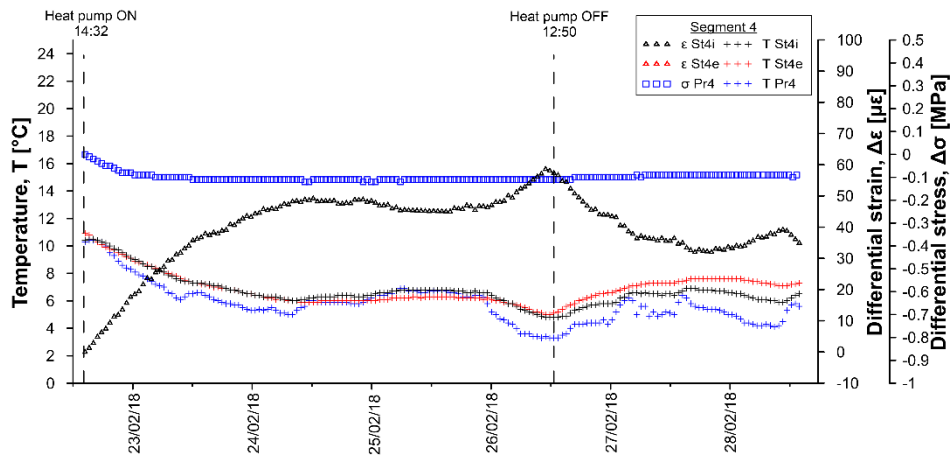


Figure A.46: Temperatures, differential strains and differential stresses in segment 4, ring 179 for test GH3.

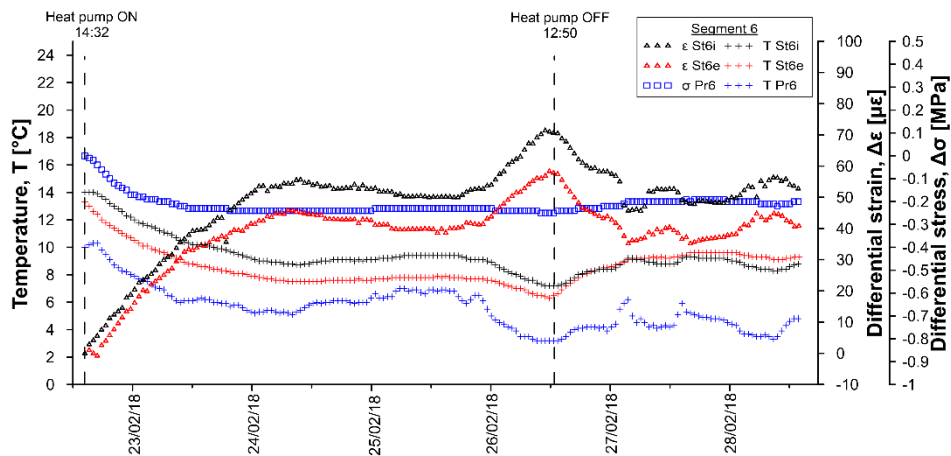


Figure A.47: Temperatures, differential strains and differential stresses in segment 6, ring 179 for test GH3.

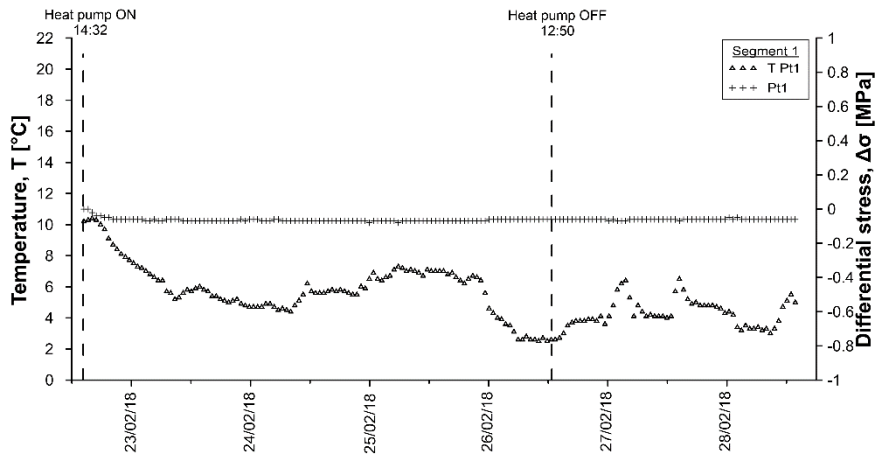


Figure A.48: Temperatures and differential stresses in segment 1, ring 179 for test GH3.

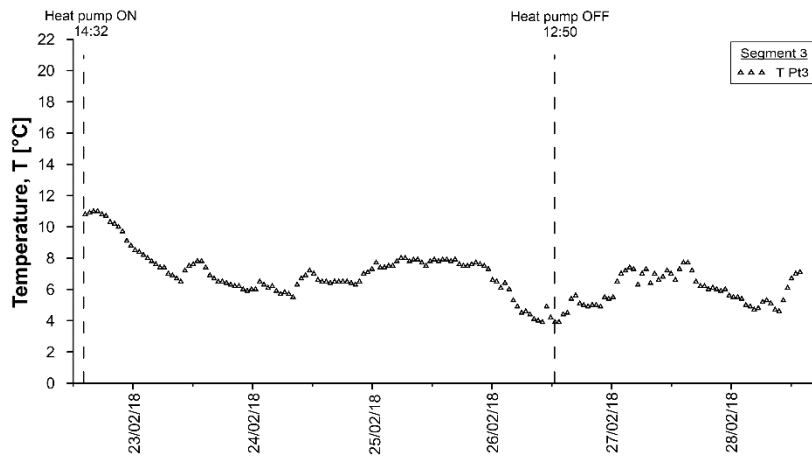


Figure A.49: Temperatures and differential stresses in segment 3, ring 179 for test GH3.

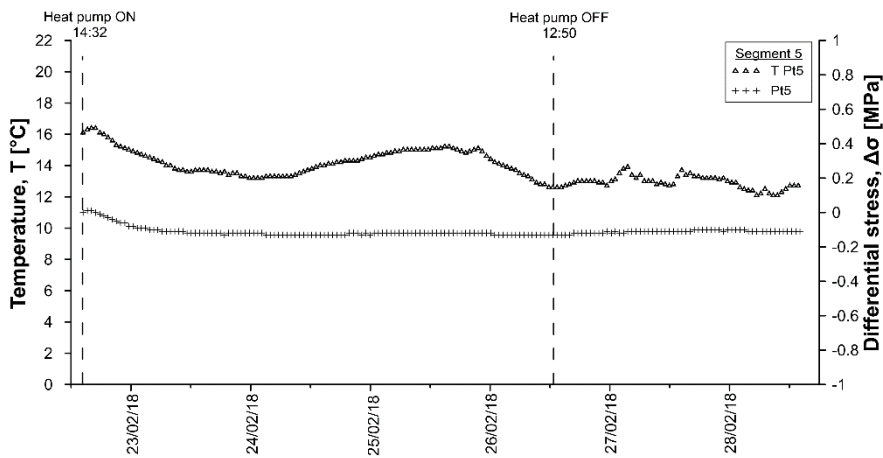


Figure A.50: Temperatures and differential stresses in segment 5, ring 179 for test GH3.

Table A.13: Data sheet for test GH3 – strains and temperatures.

Date	T _{DL} [°C]	SI2i [µε]	SI2i [°C]	SI2e [µε]	SI2e [°C]	St4i [µε]	St4i [°C]	St4e [µε]	St4e [°C]	St6i [µε]	St6i [°C]	St6e [µε]	St6e [°C]
22/02/2018 14:26	6.1	0.00	10.7	0.00	11.2	0.00	10.4	0.00	10.9	0.00	14.0	0.00	-13.3
22/02/2018 16:26	7.6	1.05	10.7	-2.63	10.7	4.43	10.5	-4.48	10.4	4.32	14.0	10.12	-12.5
22/02/2018 18:26	7.4	1.53	10.4	-2.98	10.2	4.99	10.2	-4.78	10.0	2.99	13.5	14.10	-11.8
22/02/2018 20:26	6.3	1.59	9.9	-3.80	9.7	3.87	9.8	-4.80	9.7	-0.13	12.9	15.69	-11.4
22/02/2018 22:26	5.7	1.67	9.3	-3.89	9.2	2.46	9.4	-4.73	9.3	-2.63	12.5	16.84	-11.0
23/02/2018 00:26	5.6	1.16	8.8	-4.92	8.7	1.40	9.0	-4.81	8.9	-3.98	12.0	17.99	-10.5
23/02/2018 02:26	5.7	0.84	8.3	-5.21	8.3	0.69	8.6	-5.17	8.6	-4.61	11.7	18.96	-10.1
23/02/2018 04:26	5.4	0.61	7.9	-5.41	7.9	-0.05	8.3	-5.49	8.4	-5.09	11.4	19.52	-9.8
23/02/2018 06:26	4.8	-0.38	7.5	-5.38	7.5	-0.81	8.1	-5.91	8.1	-5.42	11.1	20.13	-9.6
23/02/2018 08:26	4.3	-0.07	7.1	-5.70	7.2	-2.54	7.7	-6.12	7.8	-6.40	10.7	20.50	-9.3
23/02/2018 10:26	3.3	-0.76	6.7	-6.07	6.8	-3.48	7.4	-6.61	7.5	-7.31	10.4	21.17	-8.9
23/02/2018 12:26	3.9	-0.59	6.8	-6.35	6.6	-1.90	7.3	-7.34	7.3	-7.12	10.2	22.11	-8.7
23/02/2018 14:26	4.9	-0.24	6.7	-6.32	6.5	-1.13	7.3	-8.18	7.2	-6.60	10.2	22.85	-8.6
23/02/2018 16:26	5.3	-0.45	6.5	-6.55	6.3	-2.02	7.1	-8.00	7.0	-6.55	10.0	23.18	-8.5
23/02/2018 18:26	4.8	-0.79	6.2	-6.63	6.1	-2.93	6.9	-8.34	6.9	-6.77	9.8	23.51	-8.3
23/02/2018 20:26	4.7	-1.08	6.0	-6.77	6.0	-3.31	6.8	-8.18	6.8	-6.87	9.6	23.92	-8.1
23/02/2018 22:26	4.6	-1.18	5.8	-7.38	5.8	-3.68	6.6	-9.27	6.6	-7.01	9.3	24.20	-8.0
24/02/2018 00:26	3.8	-	5.7	-7.51	5.6	-4.52	6.4	-8.68	6.4	-7.61	9.1	24.54	-7.9
24/02/2018 02:26	4.0	-	5.6	-	5.4	-4.70	6.3	-9.29	6.3	-9.07	9.0	24.21	-7.7
24/02/2018 04:26	4.4	-	5.6	-7.63	5.3	-4.18	6.3	-10.06	6.2	-8.84	9.0	24.78	-7.7
24/02/2018 06:26	4.4	-	5.4	-7.57	5.2	-5.03	6.1	-9.88	6.1	-9.03	8.8	24.94	-7.6
24/02/2018 08:26	4.4	-	5.2	-8.12	5.1	-5.53	6.0	-10.31	6.0	-9.24	8.7	25.18	-7.5
24/02/2018 10:26	5.6	-	5.4	-8.60	5.0	-3.85	6.1	-11.40	5.9	-8.92	8.8	25.81	-7.5
24/02/2018 12:26	7.1	-	5.6	-8.18	5.1	-1.99	6.2	-12.01	5.9	-8.32	8.9	26.39	-7.5
24/02/2018 14:26	7.3	-	5.7	-8.55	5.1	-1.69	6.3	-11.92	6.0	-7.53	9.0	26.52	-7.6
24/02/2018 16:26	7.3	-	5.6	-7.85	5.1	-1.54	6.3	-11.86	6.0	-7.18	9.1	26.57	-7.6
24/02/2018 18:26	7.8	-	5.6	-8.50	5.1	-1.21	6.4	-16.16	6.0	-6.98	9.1	26.70	-7.6
24/02/2018 20:26	7.4	-	5.6	-8.44	5.1	-1.27	6.3	-11.86	6.0	-6.94	9.1	26.61	-7.6
24/02/2018 22:26	7.4	-2.96	5.6	-7.97	5.1	-1.09	6.4	-12.34	6.1	-7.20	9.1	26.74	-7.6
25/02/2018 00:26	8.1	-	5.8	-8.53	5.1	0.01	6.5	-12.32	6.0	-7.07	9.1	27.11	-7.7
25/02/2018 02:26	8.4	-	5.9	-8.50	5.2	0.55	6.6	-14.71	6.1	-6.83	9.2	27.10	-7.7
25/02/2018 04:26	8.4	-2.67	6.0	-8.30	5.3	0.94	6.7	-16.57	6.2	-6.84	9.3	27.21	-7.8
25/02/2018 06:26	7.6	-2.44	6.2	-8.53	5.4	1.62	6.7	-13.78	6.2	-5.96	9.4	27.48	-7.8
25/02/2018 08:26	6.4	-	6.2	-8.34	5.4	1.41	6.8	-17.34	6.3	-5.88	9.4	27.41	-7.8
25/02/2018 10:26	5.6	-	6.1	-8.15	5.4	1.20	6.8	-14.34	6.3	-5.92	9.4	27.24	-7.8
25/02/2018 12:26	5.3	-	6.2	-8.30	5.4	1.24	6.8	-14.35	6.3	-5.99	9.4	27.33	-7.8
25/02/2018 14:26	5.3	-	6.2	-8.02	5.4	1.13	6.8	-12.35	6.3	-5.96	9.4	27.24	-7.8
25/02/2018 16:26	4.4	-	6.1	-8.24	5.4	0.82	6.7	-13.65	6.3	-6.23	9.4	27.04	-7.8
25/02/2018 18:26	3.5	-	6.1	-8.14	5.4	0.57	6.7	-12.71	6.2	-6.79	9.2	26.68	-7.8
25/02/2018 20:26	3.2	-	6.0	-8.30	5.3	0.28	6.6	-12.77	6.2	-7.36	9.1	26.82	-7.7
25/02/2018 22:26	3.5	-	6.0	-8.15	5.3	0.26	6.6	-12.63	6.1	-7.10	9.1	26.86	-7.7
26/02/2018 00:26	2.3	-	5.7	-8.19	5.2	-2.50	6.3	-11.33	6.1	-8.66	8.8	25.62	-7.5
26/02/2018 02:26	1.9	-	5.4	-8.27	5.0	-5.22	6.0	-10.73	5.9	-9.98	8.4	25.25	-7.3
26/02/2018 04:26	1.8	-	5.1	-8.41	4.8	-6.84	5.7	-10.48	5.7	-10.74	8.1	25.34	-7.1
26/02/2018 06:26	1.1	-2.68	4.6	-8.51	4.6	-9.06	5.3	-9.98	5.5	-11.61	7.8	25.22	-6.9
26/02/2018 08:26	0.9	-	4.3	-9.17	4.3	-9.48	5.1	-10.45	5.2	-10.86	7.6	26.56	-6.6
26/02/2018 10:26	0.7	-	4.0	-9.62	4.1	-9.99	4.8	-11.01	5.0	-11.69	7.3	27.10	-6.4
26/02/2018 12:26	1.1	-	3.9	-	4.0	-11.05	4.8	-11.82	5.1	-12.37	7.2	25.39	-6.5
26/02/2018 14:26	1.7	-	4.1	-7.35	4.4	-12.51	4.8	-8.04	5.4	-12.90	7.3	22.18	-7.0
26/02/2018 16:26	2.2	-	4.6	-6.11	4.9	-12.22	5.2	-7.84	5.8	-11.72	7.8	19.73	-7.6
26/02/2018 18:26	2.7	-	5.0	-	5.4	-11.67	5.5	-6.91	6.1	-10.96	8.1	18.10	-8.0
26/02/2018 20:26	1.8	-	5.2	-4.76	5.8	-11.88	5.7	-6.62	6.3	-10.28	8.3	16.70	-8.2
26/02/2018 22:26	1.3	-	5.4	-4.67	6.0	-12.19	5.8	-5.90	6.5	-10.12	8.4	15.37	-8.4
27/02/2018 00:26	0.3	-	5.6	-4.95	6.2	-12.53	5.8	-5.80	6.6	-10.76	8.5	14.59	-8.6
27/02/2018 02:26	1.3	-	6.2	-4.96	6.5	-10.13	6.3	-6.48	6.8	-13.99	8.9	15.94	-8.9
27/02/2018 04:26	0.9	-	6.6	-4.64	6.9	-8.55	6.6	-6.42	7.1	-12.67	9.2	15.07	-9.1
27/02/2018 06:26	0.1	-2.55	6.7	-4.05	7.1	-10.10	6.5	-5.38	7.2	-14.04	9.0	13.42	-9.2
27/02/2018 08:26	-0.1	-	6.7	-4.01	7.2	-11.48	6.5	-4.63	7.3	-10.53	8.9	10.89	-9.3
27/02/2018 10:26	-0.2	-	6.7	-3.82	7.3	-12.34	6.4	-5.58	7.3	-10.97	8.8	10.00	-9.3
27/02/2018 12:26	0.2	-	6.8	-4.32	7.4	-12.28	6.4	-4.43	7.3	-10.95	8.8	9.54	-9.2
27/02/2018 14:26	1.5	-	7.0	-	7.6	-10.16	6.7	-5.29	7.4	-9.48	9.2	11.02	-9.4
27/02/2018 16:26	2.0	-	7.2	-3.57	7.7	-10.27	6.9	-10.02	7.6	-9.59	9.3	9.64	-9.6
27/02/2018 18:26	1.2	-	7.0	-3.87	7.8	-11.40	6.8	-3.52	7.6	-9.83	9.2	8.80	-9.6

Date	T _{bl} [°C]	SI2i [με]	SI2i [°C]	SI2e [με]	SI2e [°C]	St4i [με]	St4i [°C]	St4e [με]	St4e [°C]	St6i [με]	St6i [°C]	St6e [με]	St6e [°C]
27/02/2018 20:26	0.6	-	6.9	-2.82	7.7	-11.99	6.7	-3.49	7.6	-10.20	9.2	8.25	-9.6
27/02/2018 22:26	0.5	-	6.8	-3.11	7.7	-12.33	6.7	-3.75	7.6	-10.59	9.2	7.86	-9.6
28/02/2018 00:26	0.0	-	6.7	-3.53	7.7	-13.10	6.6	-2.92	7.6	-11.02	9.0	7.14	-9.6
28/02/2018 02:26	-0.6	-	6.5	-	7.6	-14.13	6.4	-3.03	7.5	-11.75	8.8	6.05	-9.5
28/02/2018 04:26	-1.7	-	6.3	-	7.5	-15.27	6.2	-3.02	7.4	-12.67	8.5	6.19	-9.3
28/02/2018 06:26	-2.1	-	6.1	-	7.4	-15.82	6.1	-2.26	7.3	-14.82	8.4	5.27	-9.3
28/02/2018 08:26	-2.3	-	6.1	-3.51	7.3	-15.88	6.0	-2.58	7.2	-13.20	8.4	6.41	-9.2
28/02/2018 10:26	-1.4	-	6.0	-	7.3	-15.92	5.9	-2.93	7.2	-13.12	8.4	7.14	-9.2
28/02/2018 12:26	0.3	-	6.4	-4.02	7.3	-13.48	6.3	-4.83	7.2	-11.50	8.6	8.16	-9.2

Table A.14: Data sheet for test GH3 – stresses and temperatures.

Date	Pt1 [MPa]	Pt1 [°C]	PI2 [MPa]	PI2 [°C]	Pt3 [MPa]	Pt3 [°C]	Pr4 [MPa]	Pr4 [°C]	Pt5 [MPa]	Pt5 [°C]	Pr6 [MPa]	Pr6 [°C]
22/02/2018 14:26	0	10.2	0	10.3	-	10.8	0	10.3	0	16.1	0	10
22/02/2018 16:26	-0.03	10.4	0	10.5	-	10.9	-0.03	10.4	0	16.4	-0.03	10.3
22/02/2018 18:26	-0.05	9.7	0	10.3	-	10.8	-0.04	10	-0.01	16	-0.07	9.6
22/02/2018 20:26	-0.06	8.6	0	9.7	-	10.3	-0.07	9.2	-0.05	15.5	-0.12	8.7
22/02/2018 22:26	-0.06	8.1	0.01	8.8	-	9.4	-0.08	8.6	-0.06	15.2	-0.15	8.3
23/02/2018 00:26	-0.06	7.5	0.01	8.2	-	8.5	-0.09	8.1	-0.08	14.9	-0.17	7.9
23/02/2018 02:26	-0.06	7	0.01	7.8	-	8.1	-0.09	7.7	-0.09	14.6	-0.19	7.6
23/02/2018 04:26	-0.06	6.6	0.01	7.4	-	7.7	-0.1	7.3	-0.1	14.4	-0.19	7.2
23/02/2018 06:26	-0.06	6.3	0.01	7	-	7.4	-0.1	7	-0.11	14.2	-0.2	6.9
23/02/2018 08:26	-0.06	5.5	0.01	6.4	-	6.8	-0.1	6.4	-0.11	13.9	-0.21	6.3
23/02/2018 10:26	-0.07	5.6	0.01	6.5	-	7.2	-0.1	6.3	-0.11	13.7	-0.22	6.1
23/02/2018 12:26	-0.07	5.9	0.01	7	-	7.7	-0.11	6.5	-0.12	13.7	-0.23	6.2
23/02/2018 14:26	-0.07	5.8	0.01	6.9	-	7.5	-0.11	6.4	-0.12	13.7	-0.23	6.2
23/02/2018 16:26	-0.07	5.4	0.01	6.2	-	6.7	-0.11	6.1	-0.12	13.6	-0.23	6
23/02/2018 18:26	-0.07	5.1	0.01	5.8	-	6.4	-0.11	5.8	-0.12	13.4	-0.23	5.8
23/02/2018 20:26	-0.07	5.1	0.01	5.7	-	6.2	-0.11	5.7	-0.12	13.5	-0.24	5.8
23/02/2018 22:26	-0.06	4.9	0.01	5.6	-	6	-0.11	5.5	-0.12	13.3	-0.24	5.6
24/02/2018 00:26	-0.06	4.7	0.01	5.3	-	5.8	-0.11	5.3	-0.12	13.2	-0.24	5.2
24/02/2018 02:26	-0.07	4.7	0.01	5.5	-	6.2	-0.11	5.3	-0.13	13.3	-0.24	5.3
24/02/2018 04:26	-0.07	4.8	0.01	5.4	-	6.1	-0.11	5.4	-0.13	13.3	-0.24	5.4
24/02/2018 06:26	-0.07	4.6	0.01	5.2	-	5.8	-0.11	5.1	-0.13	13.3	-0.24	5.3
24/02/2018 08:26	-0.07	4.5	0.01	5.2	-	5.8	-0.11	5.1	-0.13	13.3	-0.24	5.2
24/02/2018 10:26	-0.07	5.4	0.01	5.9	-	6.8	-0.12	5.6	-0.13	13.5	-0.24	5.5
24/02/2018 12:26	-0.07	5.7	0.01	6.2	-	7	-0.11	6	-0.13	13.8	-0.24	5.9
24/02/2018 14:26	-0.07	5.6	0.01	5.9	-	6.5	-0.11	5.9	-0.13	14	-0.24	6
24/02/2018 16:26	-0.07	5.8	0.01	5.9	-	6.5	-0.11	5.9	-0.13	14.1	-0.24	6.1
24/02/2018 18:26	-0.07	5.8	0.01	5.9	-	6.5	-0.11	6	-0.13	14.3	-0.24	6.1
24/02/2018 20:26	-0.07	5.5	0.01	5.8	-	6.3	-0.11	5.8	-0.12	14.3	-0.24	5.9
24/02/2018 22:26	-0.07	6.2	0.01	6.2	-	7.1	-0.12	6	-0.12	14.4	-0.24	6.1
25/02/2018 00:26	-0.08	6.9	0.01	6.7	-	7.6	-0.12	6.5	-0.12	14.6	-0.23	6.5
25/02/2018 02:26	-0.07	6.4	0.01	6.6	-	7.4	-0.11	6.4	-0.12	14.7	-0.23	6.3
25/02/2018 04:26	-0.07	6.9	0.01	6.8	-	7.6	-0.11	6.6	-0.12	14.8	-0.23	6.6
25/02/2018 06:26	-0.07	7.2	0.01	7	-	8	-0.11	6.9	-0.12	14.9	-0.23	7
25/02/2018 08:26	-0.07	7	0.01	6.9	-	7.9	-0.11	6.7	-0.12	15	-0.23	6.9
25/02/2018 10:26	-0.07	6.8	0.01	6.8	-	7.6	-0.11	6.6	-0.12	15.1	-0.23	6.7
25/02/2018 12:26	-0.07	7	0.01	6.9	-	7.9	-0.11	6.7	-0.12	15.1	-0.23	6.9
25/02/2018 14:26	-0.07	7	0.01	6.9	-	7.9	-0.11	6.7	-0.12	15.1	-0.23	6.9
25/02/2018 16:26	-0.07	6.9	0.01	6.8	-	7.8	-0.11	6.6	-0.12	15.1	-0.23	6.8
25/02/2018 18:26	-0.07	6.5	0.01	6.6	-	7.5	-0.11	6.4	-0.12	14.9	-0.23	6.2
25/02/2018 20:26	-0.07	6.6	0.01	6.6	-	7.6	-0.11	6.4	-0.12	14.9	-0.23	6.4
25/02/2018 22:26	-0.07	6.4	0.01	6.5	-	7.5	-0.11	6.3	-0.12	14.9	-0.23	6.1
26/02/2018 00:26	-0.06	4.4	0.01	5.4	-	6.3	-0.11	5.1	-0.12	14.3	-0.24	4.8
26/02/2018 02:26	-0.06	3.9	0.01	5.3	-	6.4	-0.11	4.6	-0.13	14	-0.24	4.4
26/02/2018 04:26	-0.06	3.5	0.01	4.4	-	5.2	-0.11	4.2	-0.13	13.8	-0.24	4.1
26/02/2018 06:26	-0.06	2.7	0.02	3.7	-	4.6	-0.11	3.6	-0.13	13.5	-0.24	3.5
26/02/2018 08:26	-0.06	2.6	0.02	3.5	-	4.1	-0.11	3.4	-0.13	13.1	-0.24	3.3
26/02/2018 10:26	-0.06	2.6	0.02	3.3	-	4	-0.11	3.3	-0.13	12.9	-0.25	3.2
26/02/2018 12:26	-0.06	2.5	0.02	3.3	-	4	-0.11	3.3	-0.13	12.6	-0.25	3.2
26/02/2018 14:26	-0.06	2.7	0.02	3.4	-	4.2	-0.11	3.4	-0.13	12.5	-0.24	3.3
26/02/2018 16:26	-0.06	4	0.01	4.7	-	6	-0.11	4.5	-0.12	12.9	-0.24	4.1
26/02/2018 18:26	-0.06	3.8	0.02	4.3	-	5	-0.1	4.3	-0.12	13	-0.23	4.1
26/02/2018 20:26	-0.06	3.8	0.02	4.3	-	4.9	-0.1	4.4	-0.12	12.9	-0.23	4.2
26/02/2018 22:26	-0.06	3.9	0.02	4.3	-	5.1	-0.1	4.4	-0.12	12.8	-0.22	4.1
27/02/2018 00:26	-0.06	4.5	0.01	4.9	-	5.8	-0.1	4.8	-0.12	13.2	-0.22	4.5
27/02/2018 02:26	-0.07	6	0.01	6.1	-	7.1	-0.1	5.9	-0.12	13.7	-0.21	5.7
27/02/2018 04:26	-0.06	5.3	0.01	6.4	-	7.3	-0.1	6	-0.11	13.4	-0.2	5
27/02/2018 06:26	-0.06	5.3	0.01	6.2	-	7.2	-0.1	5.8	-0.11	13.3	-0.2	4.9
27/02/2018 08:26	-0.06	4.2	0.01	5.9	-	6.9	-0.09	5.1	-0.11	13	-0.2	4.3
27/02/2018 10:26	-0.06	4.1	0.01	5.8	-	6.8	-0.09	5.1	-0.11	12.8	-0.2	4.2
27/02/2018 12:26	-0.06	4.1	0.01	5.3	-	6.4	-0.09	5	-0.11	12.8	-0.2	4.3
27/02/2018 14:26	-0.07	6.5	0.01	6.7	-	7.7	-0.09	6.4	-0.11	13.7	-0.2	5.9
27/02/2018 16:26	-0.06	4.9	0.01	5.8	-	6.7	-0.09	5.7	-0.1	13.4	-0.19	5.1
27/02/2018 18:26	-0.06	4.9	0.01	5.6	-	6.3	-0.09	5.4	-0.1	13.2	-0.19	4.9

Date	Pt1 [MPa]	Pt1 [°C]	Pl2 [MPa]	Pl2 [°C]	Pt3 [MPa]	Pt3 [°C]	Pr4 [MPa]	Pr4 [°C]	Pt5 [MPa]	Pt5 [°C]	Pr6 [MPa]	Pr6 [°C]
27/02/2018 20:26	-0.06	4.8	0.01	5.5	-	6.1	-0.09	5.4	-0.1	13.2	-0.19	4.9
27/02/2018 22:26	-0.06	4.8	0.01	5.5	-	6.1	-0.09	5.4	-0.1	13.2	-0.19	4.8
28/02/2018 00:26	-0.05	4.4	0.02	4.8	-	5.5	-0.09	5	-0.1	12.9	-0.2	4.4
28/02/2018 02:26	-0.06	3	0.02	4.3	-	5.1	-0.09	4.5	-0.1	12.5	-0.2	3.6
28/02/2018 04:26	-0.06	3.3	0.02	4.2	-	4.8	-0.09	4.3	-0.11	12.4	-0.2	3.6
28/02/2018 06:26	-0.06	3.5	0.02	4.3	-	5.2	-0.09	4.2	-0.11	12.2	-0.21	3.5
28/02/2018 08:26	-0.06	3.1	0.02	3.9	-	4.8	-0.09	4.1	-0.11	12.1	-0.21	3.4
28/02/2018 10:26	-0.06	3.8	0.02	4.5	-	5.3	-0.09	4.5	-0.11	12.3	-0.21	3.9
28/02/2018 12:26	-0.06	5.5	0.01	6	-	6.9	-0.1	5.8	-0.11	12.8	-0.21	4.9

Table A.15: Data sheet for test GH3 - sensors T1-T5 and heat pump .

Date	T1 [°C]	T2 [°C]	T3 [°C]	T4 [°C]	T5 [°C]	Date	T _{air} [°C]	IN [°C]	OUT [°C]	U1 [°C]	U2 [°C]
22/02/2018 14:23	10.2	12.3	12	9.7	10.2	22/02/2018 14:28	5.9	11.4	11.6	6.9	6.5
22/02/2018 16:31	10.5	6.6	8.3	10.3	10.5	22/02/2018 15:32	9.4	5.6	7.9	38.7	32.8
22/02/2018 18:39	8.1	5.7	7.5	9	9.9	22/02/2018 17:32	9.2	4.7	7	37.5	31.6
22/02/2018 20:47	6.4	5.1	6.8	7.4	9.2	22/02/2018 19:32	7.3	4.1	6.4	35.9	30
22/02/2018 22:55	6.7	4.7	6.4	7	8.8	22/02/2018 21:32	6.6	3.6	5.9	35.4	29.5
23/02/2018 01:03	6.7	4.4	6.1	6.9	8.6	22/02/2018 23:32	7.9	3.2	5.6	35.2	29.3
23/02/2018 03:11	6.2	4	5.7	6.6	8.3	23/02/2018 01:32	8	2.9	5.2	35.6	29.8
23/02/2018 05:19	5.9	3.7	5.3	6.2	8	23/02/2018 03:32	6.9	2.6	4.9	34.6	28.9
23/02/2018 07:27	4.9	3.2	4.9	5.7	7.7	23/02/2018 05:31	7.1	2.2	4.5	34.5	28.7
23/02/2018 09:35	4.6	2.9	4.5	5.1	7.1	23/02/2018 07:31	4.6	1.8	4.2	32.8	27
23/02/2018 11:43	5.8	2.8	4.5	5.7	7.3	23/02/2018 09:31	3	1.5	3.8	31.8	26
23/02/2018 13:51	6.2	2.8	4.5	6.3	7.7	23/02/2018 11:31	5.7	1.3	3.6	32.7	27
23/02/2018 15:59	5.4	2.6	4.2	6.2	7.6	23/02/2018 13:31	6.7	1.2	3.5	34	28.3
23/02/2018 18:07	5.1	2.4	4	5.9	7.4	23/02/2018 15:31	7.9	1.1	3.4	34.5	28.8
23/02/2018 20:15	5.5	2.3	3.9	5.7	7.3	23/02/2018 17:31	6	0.9	3.2	33.7	28
23/02/2018 22:23	4.7	2	3.6	5.6	7.2	23/02/2018 19:31	5.7	0.7	3	33.5	27.8
24/02/2018 00:31	4.6	1.8	3.5	5.2	6.9	23/02/2018 21:30	6.8	0.6	2.9	34	28.3
24/02/2018 02:39	5.3	1.8	3.4	5.4	7	23/02/2018 23:30	5.2	0.3	2.7	32.2	26.6
24/02/2018 04:47	5.1	1.7	3.3	5.7	7.1	24/02/2018 01:30	6	0.2	2.5	32.3	26.6
24/02/2018 06:55	5	1.6	3.2	5.6	7	24/02/2018 03:30	6	0.1	2.4	33.3	27.6
24/02/2018 09:03	6.7	1.7	3.3	5.9	7.2	24/02/2018 05:30	5.3	0	2.3	32.5	26.9
24/02/2018 11:11	8.8	2	3.7	7.2	7.9	24/02/2018 07:30	6.1	0	2.2	32.5	26.9
24/02/2018 13:19	7.4	2	3.6	7.6	8.2	24/02/2018 09:30	7.1	0	2.2	34	28.5
24/02/2018 15:27	7.4	2	3.5	7.4	8.1	24/02/2018 11:29	10.2	0.1	2.3	36.1	30.5
24/02/2018 17:35	7.8	2	3.6	7.5	8.2	24/02/2018 13:29	9.8	0.1	2.3	36.1	30.6
24/02/2018 19:43	7.1	1.9	3.5	7.4	8.2	24/02/2018 15:29	8.9	0.1	2.3	35.7	30.1
24/02/2018 21:51	8.3	2	3.5	7.4	8.3	24/02/2018 17:29	10	0.1	2.3	36.4	30.9
24/02/2018 23:59	9.3	2.2	3.9	8.1	8.8	24/02/2018 19:29	9.5	0.1	2.3	35.8	30.2
25/02/2018 02:07	9.4	2.2	3.8	8.6	9	24/02/2018 21:29	8.8	0.1	2.3	35.8	30.2
25/02/2018 04:15	9.5	2.3	3.9	8.8	9.2	24/02/2018 23:29	10.2	0.2	2.4	36.7	31.1
25/02/2018 06:23	9.3	2.3	3.9	8.8	9.2	25/02/2018 01:29	11	0.2	2.4	37	31.5
25/02/2018 08:31	9.3	2.3	3.9	8.6	9.2	25/02/2018 03:28	10.8	0.3	2.5	36.9	31.4
25/02/2018 10:39	9.2	2.2	3.8	8.5	9.3	25/02/2018 05:28	10.4	0.3	2.5	36.4	30.8
25/02/2018 12:47	9.3	2.2	3.8	8.5	9.2	25/02/2018 07:28	7.7	0.3	2.5	34.2	28.7
25/02/2018 14:55	9	2.2	3.9	8.4	9.1	25/02/2018 09:28	7.3	0.3	2.5	33.6	28
25/02/2018 17:03	8.9	2.1	3.7	8.2	9	25/02/2018 11:28	7.4	0.2	2.5	34	28.4
25/02/2018 19:11	7.5	1.7	3.4	7.5	8.6	25/02/2018 13:28	7	0.2	2.5	33.5	28
25/02/2018 21:19	8.9	2.1	3.7	8.1	8.9	25/02/2018 15:28	6.7	0.2	2.5	32.4	26.8
25/02/2018 23:27	3.4	1.4	3	6.2	8.1	25/02/2018 17:28	5.2	0.1	2.4	31.6	26
26/02/2018 01:35	3.5	1.2	2.8	4.4	6.8	25/02/2018 19:27	4.4	0	2.3	31.4	25.8
26/02/2018 03:43	3.1	1	2.6	3.9	6.2	25/02/2018 21:27	6.1	0	2.3	31.9	26.3
26/02/2018 05:51	2.6	0.7	2.3	3.3	5.6	25/02/2018 23:27	2.8	0	2.2	28.5	23.9
26/02/2018 07:59	2.2	0.5	2.1	3	5.3	26/02/2018 01:27	2.9	-0.1	2.1	28.6	24
26/02/2018 09:51	2.2	0.4	2	2.7	5	26/02/2018 03:27	3.6	-0.2	1.9	28.6	24
26/02/2018 11:59	2.5	2.8	3.4	2.8	5	26/02/2018 05:27	1.6	-0.5	1.7	27.1	22.5
26/02/2018 14:07	2.6	5.6	5.3	3.1	4.5	26/02/2018 07:27	3	-0.6	1.5	28.1	23.5
26/02/2018 16:15	6.1	6.8	6.5	4.6	5.6	26/02/2018 09:27	1.6	-0.9	1.2	27	22.4
26/02/2018 18:23	3.4	6.6	6.3	4.1	5.5	26/02/2018 11:26	1.6	0.2	1.5	24.2	20.3
26/02/2018 20:31	3.5	6.8	6.6	3.8	5.4	26/02/2018 12:50	2.1	0.8	2.4	19.7	17
26/02/2018 22:39	3	7.1	6.8	3.6	5.2	26/02/2018 14:26	2.3	4.8	5.1	14.1	10.7
27/02/2018 00:47	3.5	7.3	7	3.4	5.1	26/02/2018 16:26	2.3	5.4	5.7	11.1	7.8
27/02/2018 02:55	7.3	8	7.8	6.2	6.4	26/02/2018 18:26	1.2	5.7	6	8.9	6.1
27/02/2018 05:03	1.8	7.5	7.2	4.1	5.7	26/02/2018 20:26	0.7	6	6.3	7.2	5
27/02/2018 05:43	2.1	7.6	7.3	3.7	5.5	26/02/2018 22:26	0.5	6.2	6.5	5.8	4.2
27/02/2018 05:52	4.4	7.8	7.5	3.8	5.6	27/02/2018 00:26	0	6.5	6.7	4.6	3.4
27/02/2018 07:45	2	7.7	7.4	2.9	5.1	27/02/2018 02:25	1	6.8	7	4	3.2
27/02/2018 09:39	1.3	7.7	7.4	2.2	4.6	27/02/2018 04:25	-1.1	7	7.2	3.5	2.9
27/02/2018 09:55	1.4	7.7	7.4	2.2	4.6	27/02/2018 06:25	-0.2	7.1	7.4	2.9	2.3
27/02/2018 10:11	2.2	7.9	7.5	2.3	4.6	27/02/2018 08:25	-1.2	7.2	7.4	2.4	1.9
27/02/2018 10:27	2.3	7.8	7.5	2.3	4.6	27/02/2018 10:25	-0.9	7.2	7.5	2.1	1.6
27/02/2018 10:43	2.7	7.9	7.6	2.4	4.6	27/02/2018 12:25	-0.4	7.3	7.6	2	1.6
27/02/2018 10:59	2.1	7.9	7.5	2.3	4.6	27/02/2018 14:25	1.7	7.7	7.9	2.1	1.9
27/02/2018 11:15	1.7	7.9	7.5	2.4	4.6	27/02/2018 16:25	0.6	7.6	7.9	2.3	2.2

Date	T1 [°C]	T2 [°C]	T3 [°C]	T4 [°C]	T5 [°C]	Date	Tair [°C]	IN [°C]	OUT [°C]	U1 [°C]	U2 [°C]
27/02/2018 11:31	2.5	7.9	7.6	2.4	4.6	27/02/2018 18:24	0.2	7.7	7.9	2.3	2.1
27/02/2018 11:47	1.7	7.9	7.5	2.4	4.6	27/02/2018 20:24	-0.5	7.7	7.9	2.2	1.9
27/02/2018 12:03	1.8	7.8	7.5	2.4	4.5	27/02/2018 22:24	0	7.7	7.9	2	1.8
27/02/2018 12:19	2.2	7.9	7.6	2.4	4.5	28/02/2018 00:24	-0.9	7.7	7.9	1.9	1.6
27/02/2018 12:35	1.8	7.9	7.6	2.4	4.5	28/02/2018 02:24	-2.3	7.5	7.8	1.5	1.1
27/02/2018 12:51	1.8	7.9	7.6	2.4	4.5	28/02/2018 04:24	-2.9	7.5	7.7	0.9	0.4
27/02/2018 13:07	6.4	8.5	8.2	3.6	5	28/02/2018 06:24	-2.6	7.4	7.7	0.4	-0.2
27/02/2018 13:23	6.4	8.5	8.2	3.8	5.2	28/02/2018 08:24	-3	7.3	7.6	0.2	-0.4
27/02/2018 13:39	6.9	8.5	8.3	4	5.3	28/02/2018 10:23	-0.8	7.4	7.6	0.1	-0.4
27/02/2018 13:55	7	8.6	8.4	4.5	5.6	28/02/2018 12:23	1	7.5	7.8	0.6	0.4
27/02/2018 14:11	7.1	8.7	8.4	4.9	5.7						
27/02/2018 14:27	7.3	8.7	8.4	5.2	5.9						
27/02/2018 14:43	7.3	8.7	8.4	5.6	5.9						
27/02/2018 14:59	3.3	8.5	8.2	5.4	5.8						
27/02/2018 15:15	2.8	8.2	7.9	4.9	5.5						
27/02/2018 15:31	3	8.2	7.9	4.7	5.5						
27/02/2018 15:47	3.3	8.4	8.1	4.8	5.6						
27/02/2018 16:03	3.2	8.2	7.9	4.4	5.5						
27/02/2018 16:19	2.8	8.2	7.9	4.2	5.5						
27/02/2018 16:35	2.8	8.2	7.9	4.2	5.4						
27/02/2018 16:51	2.8	8.2	7.9	4	5.4						
27/02/2018 18:45	2.3	8.2	7.8	3.4	4.4						
27/02/2018 20:53	2.3	8.2	7.9	3.1	4.3						
27/02/2018 23:01	1.5	8.2	7.8	2.7	4.1						
28/02/2018 01:09	1.1	8	7.6	1.9	3.7						
28/02/2018 03:17	-0.1	7.8	7.4	1	3						
28/02/2018 05:25	0.8	7.7	7.3	0.6	2.5						
28/02/2018 07:33	-0.1	7.7	7.3	0.7	2.3						
28/02/2018 09:05	0.1	7.6	7.2	0.6	2.3						
28/02/2018 09:22	0.3	7.6	7.3	0.7	2.3						
28/02/2018 09:30	0.6	7.7	7.3	0.7	2.3						
28/02/2018 09:38	0.7	7.7	7.3	0.7	2.3						
28/02/2018 11:01	4.7	8.1	7.8	1.9	3						
28/02/2018 13:09	3.7	8.2	7.8	3.3	4						

Table A.16: Summary of test GH3 records.

Quantity	Unit	$x(t_0)$	$x(t_1)$	$x(t_1) - x(t_0)$	$\bar{x}(t_0, t_1)$
T _{DL}	[°C]	6.1	1.1	-5.0	5.0
Sl2i	[με]	-327.29	-3207.85	-	
	[με] _{comp}	0.02	-2797.58	-	
	[°C]	10.7	3.9	-6.8	6.4
Sl2e	[με]	-2613.48	-2622.2	-8.70	
	[με] _{comp}	1.19	77.89	76.7	
	[°C]	11.1	4.1	-7.0	6.1
St4i	[με]	-1775.38	-1786.6	-11.20	
	[με] _{comp}	-1.02	57.32	58.34	
	[°C]	10.5	4.8	-5.7	7.0
St4e	[με]	-1506.21	-1517.93	-11.72	
	[με] _{comp}	-1.25	59.01	60.26	
	[°C]	11.0	5.1	-5.9	6.8
St6i	[με]	-2183.37	-2195.84	-12.47	
	[με] _{comp}	0.24	70.73	70.49	
	[°C]	14.0	7.2	-6.8	9.7
St6e	[με]	-1803.13	-1828.2	-25.07	
	[με] _{comp}	0.04	57.93	57.89	
	[°C]	13.3	6.5	-6.8	8.3
Pt1	[MPa]	0.01	-0.1	-0.06	
	[°C]	10.2	2.6	-7.6	5.9
Pl2	[MPa]	-0.04	0.0	0.02	
	[°C]	10.3	3.3	-7.0	6.4
Pt3	[MPa]	-	-	-	
	[°C]	10.8	3.9	-6.9	7.1
Pr4	[MPa]	0.13	0.0	-0.12	
	[°C]	10.3	3.3	-7.0	6.2
Pt5	[MPa]	0.13	0.0	-0.13	
	[°C]	16.2	12.6	-3.6	14.2
Pr6	[MPa]	0.21	0.0	-0.25	
	[°C]	10.0	3.2	-6.8	6.2
T1	[°C]	10.2	2.7	-7.5	6.6
T2	[°C]	9.3	2.2	-7.1	2.5
T3	[°C]	10.8	3.1	-7.7	4.1
T4	[°C]	9.8	2.9	-6.9	6.7
T5	[°C]	10.3	5.0	-5.3	7.9
Air	[°C]	5.9	2.1	-3.8	6.7
IN	[°C]	11.0	0.8	-10.2	0.8
OUT	[°C]	11.6	2.4	-9.2	3.1
U1	[°C]	6.1	19.7	13.6	33.2
U2	[°C]	6.3	17.0	10.7	27.8

Test GH4

In this test the flow rate was reduced to 0.8 m³/h to study its role on thermal performance. The flow rate was reduced on February 27th, 2018 at 17:00.

Circuit:	Ground
Mode:	Heating
Secondary circuit temperature:	45°C
Activated rings:	179+180
Volumetric flow rate:	0.8 m ³ /h
Fluid velocity in primary circuit:	0.55 m/s
Starting time t_0 :	28/02/2018 14:04
Ending time t_1 :	01/03/2018 08:23
Duration:	0.76 days
Note:	The test was stopped because of the primary low temperatures causing low-pressure issues.

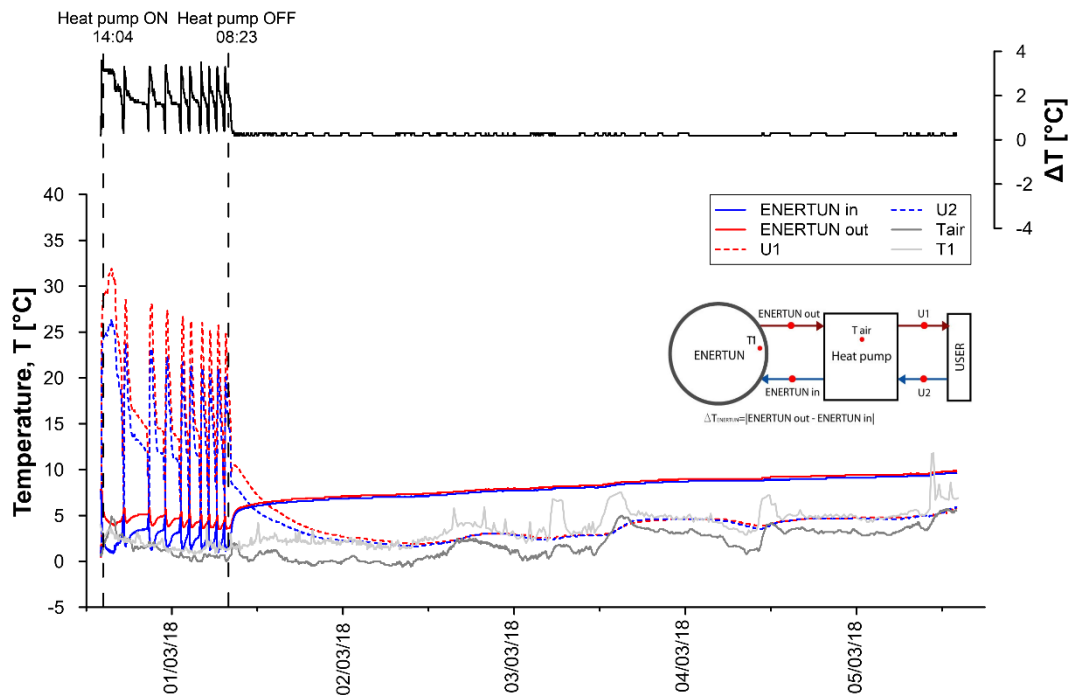


Figure A.51: Primary circuit, secondary circuit and air temperatures for test GH4.

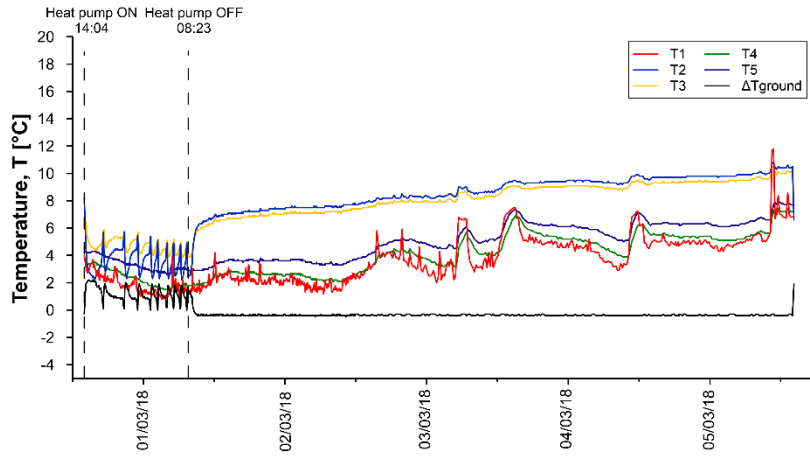


Figure A.52: Temperatures T1-T5 for test GH4.

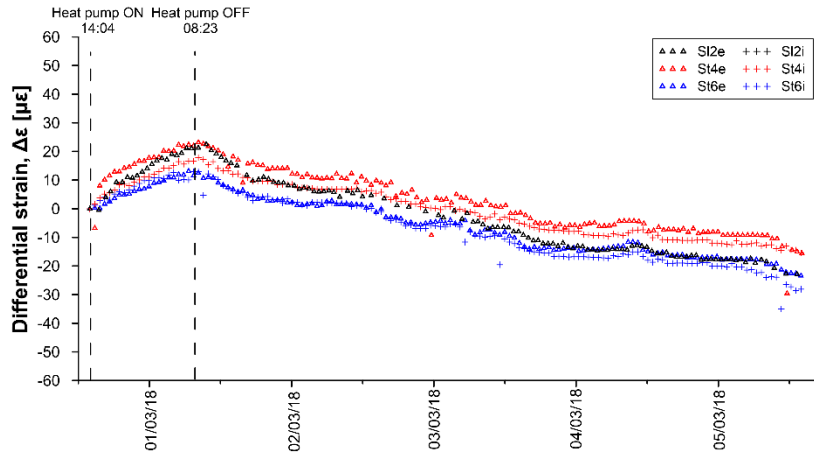


Figure A.53: Differential strains for test GH4.

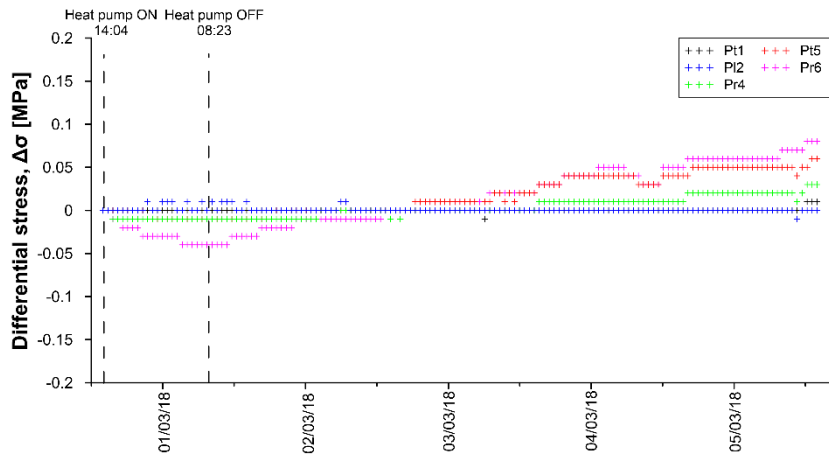


Figure A.54: Differential stresses for test GH4.

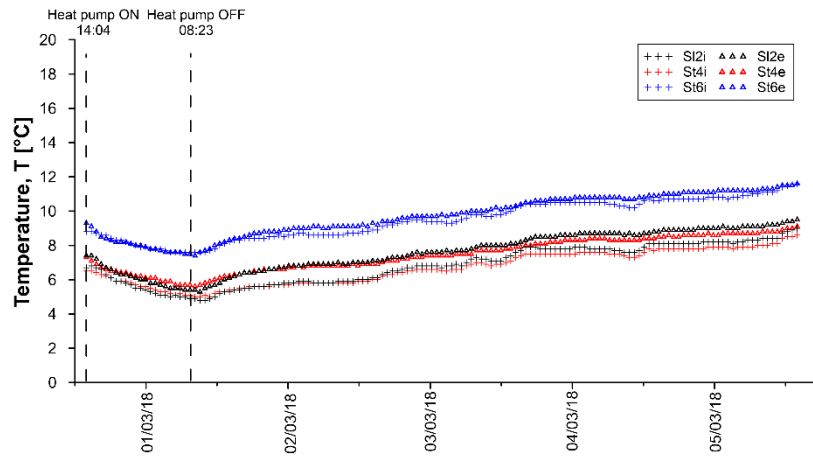


Figure A.55: Temperatures measured by VWSG for test GH4.

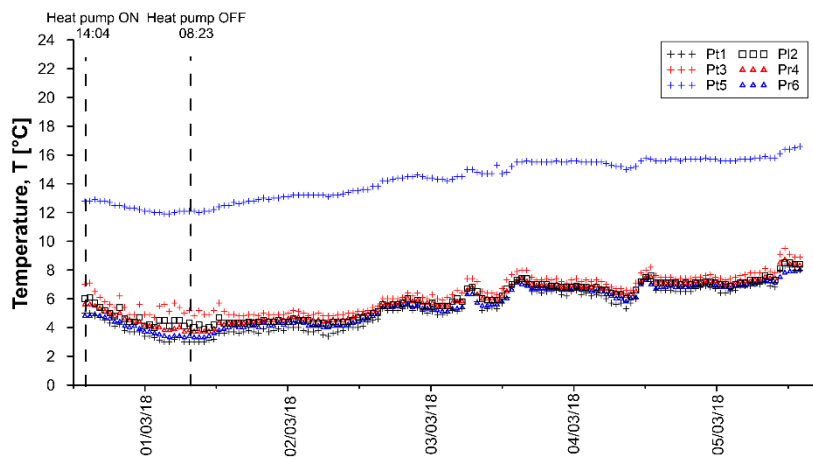


Figure A.56: Temperatures measured by PC for test GH4.

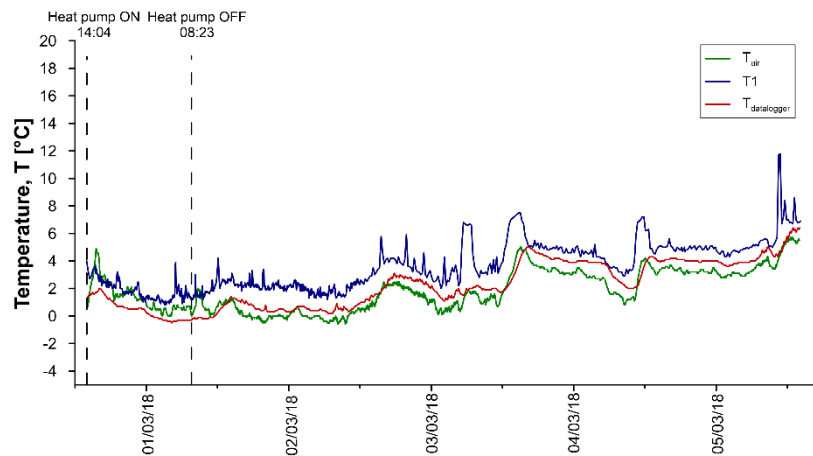


Figure A.57: Air temperatures for test GH4.

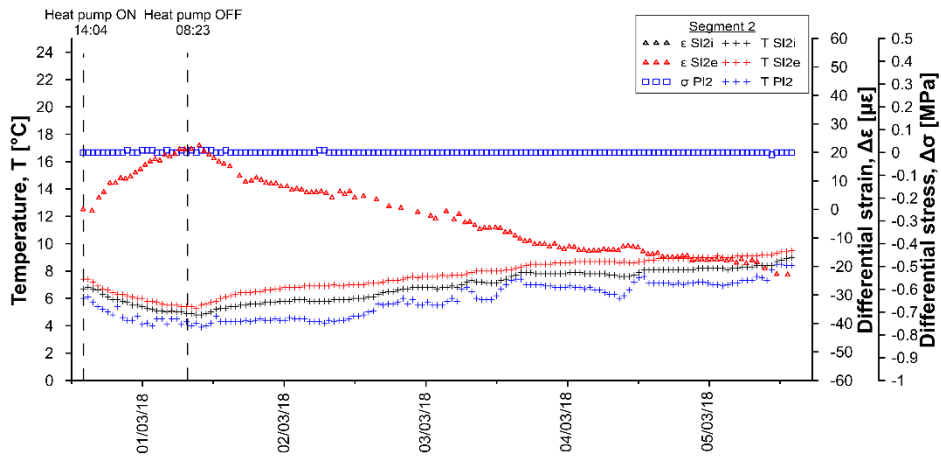


Figure A.58: Temperatures, differential strains and differential stresses in segment 2, ring 179 for test GH4.

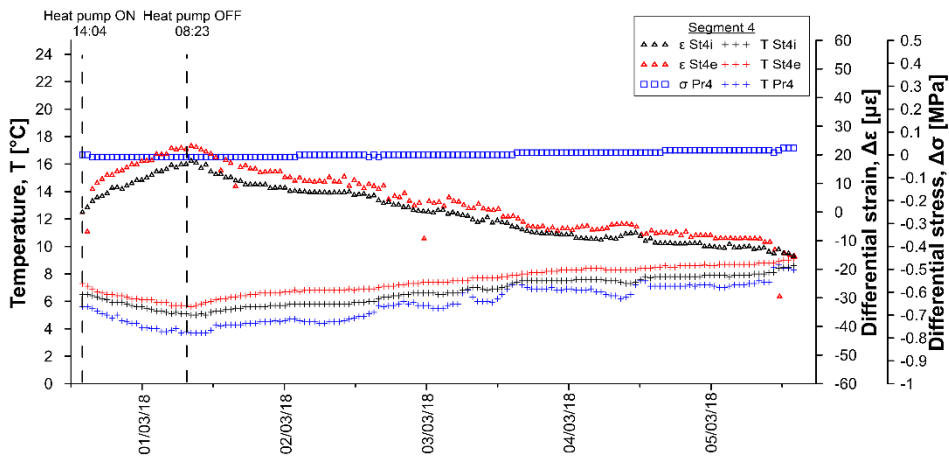


Figure A.59: Temperatures, differential strains and differential stresses in segment 4, ring 179 for test GH4.

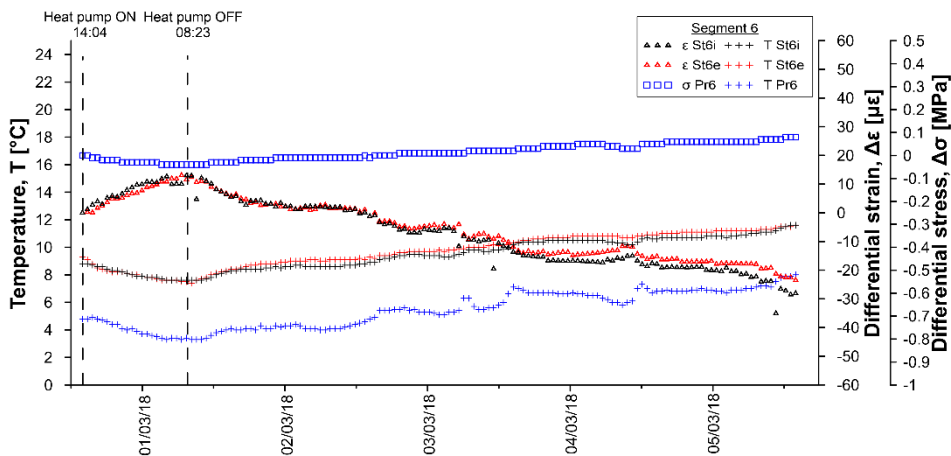


Figure A.60: Temperatures, differential strains and differential stresses in segment 6, ring 179 for test GH4.

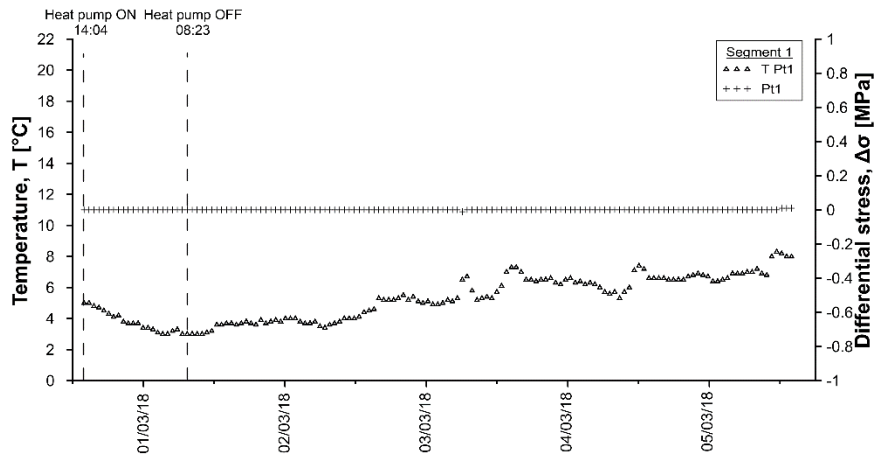


Figure A.61: Temperatures and differential stresses in segment 1, ring 179 for test GH4.

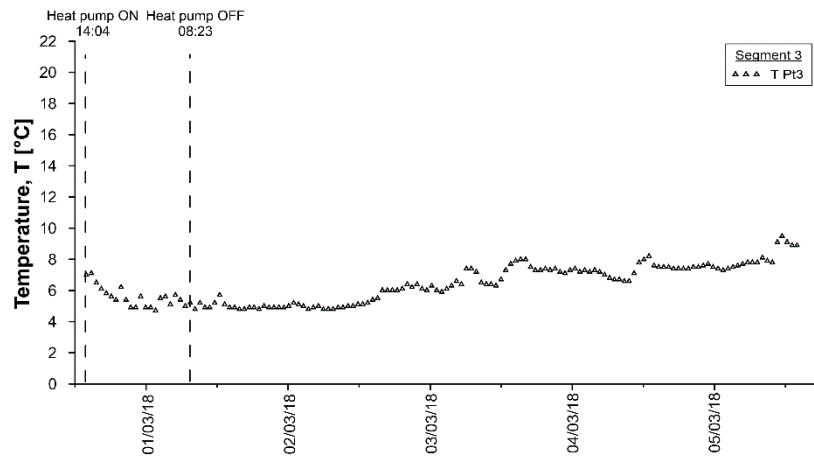


Figure A.62: Temperatures and differential stresses in segment 3, ring 179 for test GH4.

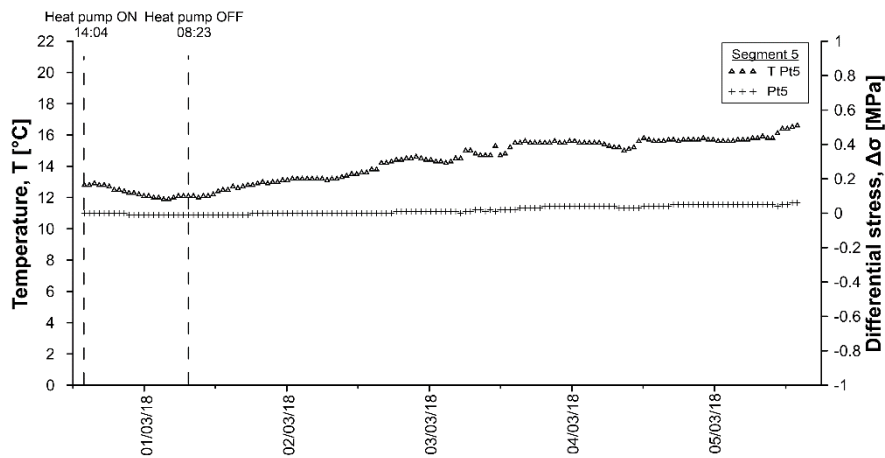


Figure A.63: Temperatures and differential stresses in segment 5, ring 179 for test GH4.

Table A.17: Data sheet for test GH4 – strains and temperatures.

Date	T _{DL} [°C]	SI2i [με]	SI2i [°C]	SI2e [με]	SI2e [°C]	St4i [με]	St4i [°C]	St4e [με]	St4e [°C]	St6i [με]	St6i [°C]	St6e [με]	St6e [°C]
28/02/2018 13:56	1.1	0.00	6.7	0.00	7.4	0.00	6.5	0.00	7.3	0.00	8.8	0.00	9.3
28/02/2018 15:06	1.6	-	6.8	-	7.3	1.72	6.5	-23.03	7.0	1.30	8.9	-3.89	9.0
28/02/2018 17:06	1.5	-	6.4	-2.69	6.7	2.21	6.2	2.93	6.6	0.84	8.6	-8.47	8.4
28/02/2018 19:06	0.7	-	5.9	-2.70	6.4	1.05	5.9	3.21	6.4	-0.30	8.3	-8.57	8.2
28/02/2018 21:06	0.5	2.67	5.7	-2.65	6.3	0.51	5.8	3.76	6.4	-0.83	8.1	-8.02	8.2
28/02/2018 23:06	0.6	-	5.5	-2.27	6.0	0.14	5.6	3.24	6.2	-1.20	7.9	-8.92	8.0
01/03/2018 01:06	0.0	-	5.2	-3.28	5.8	-0.38	5.4	3.28	6.1	-1.51	7.8	-9.26	7.8
01/03/2018 03:06	-0.3	-1.87	5.1	-3.57	5.7	-0.40	5.3	3.04	5.9	-1.57	7.7	-9.76	7.7
01/03/2018 05:06	-0.4	-2.74	5.0	-3.22	5.5	-0.72	5.2	2.47	5.8	-4.73	7.6	-8.88	7.6
01/03/2018 07:06	-0.3	-1.20	5.0	-3.30	5.4	-0.43	5.1	2.18	5.7	-4.52	7.6	-9.34	7.5
01/03/2018 09:06	-0.1	-4.10	4.8	-3.81	5.3	-1.09	5.0	3.14	5.7	-9.92	7.6	-10.05	7.6
01/03/2018 11:06	-0.1	-5.90	4.9	-1.43	5.6	-1.84	5.0	4.41	5.9	-2.25	7.7	-7.21	7.9
01/03/2018 13:06	0.8	-2.97	5.2	-1.08	5.9	-1.38	5.3	4.47	6.1	-1.33	8.0	-5.94	8.2
01/03/2018 15:06	1.2	-3.06	5.4	-1.02	6.2	-1.26	5.5	4.85	6.3	-0.54	8.3	-5.03	8.4
01/03/2018 17:06	0.9	-3.40	5.5	-0.98	6.4	-1.32	5.6	5.25	6.5	-0.85	8.4	-4.39	8.6
01/03/2018 19:06	0.5	-2.37	5.6	-0.75	6.5	-1.34	5.6	5.37	6.5	-0.74	8.4	-3.66	8.7
01/03/2018 21:06	0.3	-1.75	5.7	-0.19	6.6	-1.36	5.7	5.56	6.6	-0.54	8.5	-3.21	8.8
01/03/2018 23:06	0.5	-1.51	5.8	-0.68	6.7	-1.27	5.7	5.58	6.7	-0.28	8.6	-2.84	8.9
02/03/2018 01:06	0.5	-1.32	5.8	-0.21	6.8	-1.20	5.8	5.03	6.7	-0.12	8.6	-2.48	9.0
02/03/2018 03:06	0.5	-0.43	5.9	0.14	6.8	-1.42	5.8	4.43	6.8	-0.11	8.6	-1.86	9.0
02/03/2018 05:06	0.4	-1.17	5.8	-0.12	6.9	-1.64	5.8	4.41	6.8	-0.33	8.6	-1.30	9.1
02/03/2018 07:06	0.2	-1.82	5.8	-0.32	6.9	-1.80	5.8	6.37	6.8	-0.49	8.6	-0.93	9.1
02/03/2018 09:06	0.4	-1.26	5.8	-	7.0	-1.73	5.8	-18.20	6.8	-0.48	8.6	-0.82	9.1
02/03/2018 11:06	0.7	-2.15	5.9	0.33	6.9	-1.47	5.9	4.92	6.8	-0.22	8.7	-0.99	9.1
02/03/2018 13:06	1.2	-2.12	6.0	-	7.0	-1.05	5.9	-1.66	6.8	-0.19	8.8	-1.45	9.2
02/03/2018 15:06	1.6	-2.07	6.1	0.14	7.1	-0.34	6.0	4.15	6.9	0.28	8.9	-1.32	9.2
02/03/2018 17:06	2.7	-0.75	6.4	-	7.2	0.79	6.3	2.13	7.0	1.12	9.2	-1.60	9.4
02/03/2018 19:06	2.9	-0.10	6.6	-0.47	7.4	1.36	6.4	-0.71	7.1	1.54	9.3	-1.31	9.5
02/03/2018 21:06	2.5	-	6.7	-	7.6	1.67	6.6	3.89	7.3	1.68	9.5	-0.65	9.7
02/03/2018 23:06	2.5	-	6.8	-	7.6	1.11	6.6	-3.65	7.4	1.36	9.5	-0.12	9.7
03/03/2018 01:06	1.6	-	6.8	-0.29	7.6	0.95	6.6	5.99	7.4	1.11	9.4	0.62	9.7
03/03/2018 03:06	1.4	-	6.8	-	7.7	0.61	6.5	4.46	7.4	0.76	9.3	0.87	9.8
03/03/2018 05:06	1.6	-	6.8	0.54	7.7	0.80	6.6	6.37	7.4	0.74	9.4	1.20	9.8
03/03/2018 07:06	2.1	0.00	7.2	0.38	7.8	3.66	6.9	4.95	7.6	2.73	9.8	-0.55	10.0
03/03/2018 09:06	1.9	-	7.2	0.39	8.0	2.12	6.9	5.97	7.7	1.79	9.7	1.38	10.0
03/03/2018 11:06	1.9	-	7.1	0.89	8.0	1.11	6.9	4.25	7.7	-7.31	9.8	1.88	10.2
03/03/2018 13:06	2.3	-1.86	7.4	0.84	8.1	2.82	7.0	4.80	7.8	1.99	9.9	1.30	10.2
03/03/2018 15:06	4.3	-	7.7	0.56	8.2	5.51	7.4	5.65	7.9	4.22	10.3	0.08	10.4
03/03/2018 17:06	4.8	-	7.9	0.96	8.4	5.48	7.5	4.84	8.1	4.41	10.4	1.39	10.5
03/03/2018 19:06	4.4	-	7.8	1.30	8.5	4.77	7.5	5.70	8.2	4.13	10.4	2.28	10.6
03/03/2018 21:06	4.2	-	7.8	1.06	8.5	4.71	7.5	6.12	8.2	4.14	10.5	2.72	10.7
03/03/2018 23:06	3.9	-	7.8	1.27	8.6	4.25	7.5	6.47	8.3	3.88	10.5	3.36	10.7
04/03/2018 01:06	4.0	-	7.9	1.41	8.6	4.37	7.6	6.26	8.3	3.99	10.5	3.58	10.8
04/03/2018 03:06	3.9	-	7.9	1.30	8.7	4.07	7.6	7.26	8.3	3.71	10.5	4.01	10.8
04/03/2018 05:06	3.8	-	7.8	1.69	8.7	3.77	7.5	7.33	8.4	3.45	10.5	4.42	10.8
04/03/2018 07:06	2.7	-	7.7	1.50	8.7	3.06	7.5	7.82	8.3	2.82	10.4	5.14	10.8
04/03/2018 09:06	2.0	-	7.6	1.52	8.6	2.24	7.4	8.04	8.3	2.09	10.2	5.51	10.7
04/03/2018 11:06	2.6	-3.99	7.8	1.50	8.6	3.31	7.5	7.36	8.3	2.60	10.4	4.19	10.8
04/03/2018 13:06	4.3	-	8.1	1.35	8.7	5.76	7.7	5.74	8.4	4.52	10.6	3.53	10.9
04/03/2018 15:06	4.0	-	8.1	1.47	8.8	4.99	7.8	7.31	8.5	4.12	10.6	4.32	11.0
04/03/2018 17:06	4.2	-	8.1	2.27	8.9	4.93	7.8	7.24	8.5	4.24	10.7	4.60	11.0
04/03/2018 19:06	4.0	-	8.1	1.71	8.9	4.79	7.8	7.24	8.6	4.11	10.7	4.84	11.1
04/03/2018 21:06	3.9	-0.44	8.1	1.62	9.0	4.91	7.8	7.70	8.6	4.24	10.7	4.93	11.1
04/03/2018 23:06	4.0	-	8.2	1.83	9.0	5.06	7.9	7.77	8.6	4.41	10.8	5.03	11.1
05/03/2018 01:06	3.8	-	8.2	1.85	9.1	4.73	7.9	7.87	8.7	4.10	10.8	5.43	11.2
05/03/2018 03:06	3.8	-	8.1	1.85	9.0	4.59	7.8	7.90	8.7	3.97	10.8	5.56	11.2
05/03/2018 05:06	3.9	-0.42	8.2	1.89	9.1	4.72	7.9	7.84	8.7	4.23	10.9	5.38	11.2
05/03/2018 07:06	4.2	-0.46	8.3	-	9.1	5.32	7.9	7.35	8.7	4.51	11.0	5.28	11.2
05/03/2018 09:06	4.8	-	8.4	2.08	9.1	5.78	8.0	7.80	8.8	4.32	11.1	5.06	11.2
05/03/2018 11:06	4.7	-4.56	8.6	-	9.2	9.75	8.3	5.68	8.8	4.59	11.3	4.58	11.4
05/03/2018 13:06	6.2	-	8.9	3.27	9.4	9.95	8.5	5.79	9.0	5.64	11.6	4.24	11.5

Table A.18: Data sheet for test GH4 – stresses and temperatures.

Date	Pt1 [MPa]	Pt1 [°C]	PI2 [MPa]	PI2 [°C]	Pt3 [MPa]	Pt3 [°C]	Pr4 [MPa]	Pr4 [°C]	Pt5 [MPa]	Pt5 [°C]	Pr6 [MPa]	Pr6 [°C]
28/02/2018 13:56	0	5	0	6	-	7	0	5.6	0	12.8	0	4.8
28/02/2018 15:06	0	4.9	0	6	-	7	0	5.6	0	12.8	-0.01	4.9
28/02/2018 17:06	0	4.5	0	5.2	-	5.8	-0.01	5.2	0	12.8	-0.02	4.7
28/02/2018 19:06	0	4.2	0	4.9	-	5.6	-0.01	4.8	0	12.6	-0.02	4.5
28/02/2018 21:06	0	3.7	0.01	4.5	-	5.1	-0.01	4.5	0	12.4	-0.03	4
28/02/2018 23:06	0	3.7	0	4.7	-	5.6	-0.01	4.4	-0.01	12.2	-0.03	3.9
01/03/2018 01:06	0	3.4	0.01	4.1	-	4.8	-0.01	4	-0.01	12.1	-0.03	3.6
01/03/2018 03:06	0	3.1	0	4.5	-	5.6	-0.01	3.9	-0.01	11.9	-0.03	3.4
01/03/2018 05:06	0	3.3	0	4.6	-	5.7	-0.01	4.1	-0.01	12.1	-0.04	3.4
01/03/2018 07:06	0	3.1	0	4.3	-	5.2	-0.01	3.8	-0.01	12.1	-0.04	3.4
01/03/2018 09:06	0	3	0	4.2	-	5.2	-0.01	3.7	-0.01	12	-0.04	3.3
01/03/2018 11:06	0	3.2	0	4.2	-	5.2	-0.01	3.8	-0.01	12.2	-0.03	3.5
01/03/2018 13:06	0	3.6	0	4.4	-	5.1	-0.01	4.1	-0.01	12.5	-0.03	3.8
01/03/2018 15:06	0	3.7	0	4.3	-	4.9	-0.01	4.3	-0.01	12.7	-0.03	4
01/03/2018 17:06	0	3.8	0	4.3	-	4.8	-0.01	4.4	-0.01	12.8	-0.02	4.1
01/03/2018 19:06	0	3.6	0	4.4	-	4.8	-0.01	4.4	0	12.9	-0.02	4
01/03/2018 21:06	0	3.7	0	4.4	-	4.9	-0.01	4.4	0	12.9	-0.02	4.1
01/03/2018 23:06	0	3.8	0	4.4	-	4.9	-0.01	4.5	0	13.1	-0.01	4.2
02/03/2018 01:06	0	4.1	0	4.6	-	5.1	-0.01	4.7	0	13.2	-0.01	4.3
02/03/2018 03:06	0	3.6	0	4.4	-	4.9	0	4.5	0	13.2	-0.01	4.2
02/03/2018 05:06	0	3.8	0	4.3	-	5	0	4.5	0	13.2	-0.01	4.1
02/03/2018 07:06	0	3.6	0	4.4	-	4.8	0	4.5	0	13.2	-0.01	4.1
02/03/2018 09:06	0	3.7	0	4.3	-	4.8	0	4.5	0	13.2	-0.01	4.1
02/03/2018 11:06	0	4.1	0	4.6	-	5.1	0	4.8	0	13.5	-0.01	4.4
02/03/2018 13:06	0	4.3	0	4.8	-	5.3	0	4.9	0	13.6	0	4.6
02/03/2018 15:06	0	4.6	0	5.1	-	5.5	0	5.2	0	13.8	0	4.9
02/03/2018 17:06	0	5.1	0	5.5	-	6	0	5.6	0	14.2	0	5.3
02/03/2018 19:06	0	5.3	0	5.7	-	6.1	0	5.7	0.01	14.4	0.01	5.5
02/03/2018 21:06	0	5.2	0	5.7	-	6.2	0	5.8	0.01	14.5	0.01	5.5
02/03/2018 23:06	0	5.1	0	5.6	-	6.2	0	5.8	0.01	14.5	0.01	5.4
03/03/2018 01:06	0	4.9	0	5.5	-	6	0	5.5	0.01	14.3	0.01	5.2
03/03/2018 03:06	0	5	0	5.6	-	6.1	0	5.5	0.01	14.2	0.01	5.1
03/03/2018 05:06	0	4.9	0	5.5	-	6.2	0	5.6	0.01	14.3	0.01	5.1
03/03/2018 07:06	0	6.5	0	6.8	-	7.4	0	6.7	0.01	15	0.02	6.2
03/03/2018 09:06	0	5.3	0	5.8	-	6.4	0	5.9	0.02	14.6	0.02	5.5
03/03/2018 11:06	0	5.3	0	5.9	-	6.3	0	5.9	0.01	15.3	0.02	5.6
03/03/2018 13:06	0	6.4	0	6.8	-	7.4	0	6.7	0.02	14.9	0.02	6.2
03/03/2018 15:06	0	7.4	0	7.4	-	7.9	0	7.3	0.02	15.6	0.03	7.1
03/03/2018 17:06	0	6.4	0	6.9	-	7.4	0.01	7	0.03	15.5	0.03	6.6
03/03/2018 19:06	0	6.5	0	7	-	7.3	0.01	6.9	0.03	15.5	0.04	6.7
03/03/2018 21:06	0	6.6	0	6.9	-	7.4	0.01	7	0.04	15.6	0.04	6.7
03/03/2018 23:06	0	6.3	0	6.8	-	7.2	0.01	6.8	0.04	15.5	0.04	6.6
04/03/2018 01:06	0	6.3	0	6.8	-	7.3	0.01	6.9	0.04	15.5	0.04	6.6
04/03/2018 03:06	0	6.3	0	6.7	-	7.1	0.01	6.8	0.04	15.6	0.05	6.5
04/03/2018 05:06	0	6.1	0	6.6	-	7.1	0.01	6.7	0.04	15.5	0.05	6.4
04/03/2018 07:06	0	5.6	0	6.3	-	6.7	0.01	6.4	0.04	15.2	0.04	6
04/03/2018 09:06	0	5.3	0	6.1	-	6.5	0.01	6.2	0.03	15.1	0.03	5.8
04/03/2018 11:06	0	7	0	7.2	-	7.7	0.01	7.2	0.03	15.6	0.03	6.9
04/03/2018 13:06	0	7.1	0	7.6	-	8.1	0.01	7.4	0.04	15.6	0.05	6.9
04/03/2018 15:06	0	6.5	0	7	-	7.4	0.02	7.1	0.04	15.6	0.05	6.8
04/03/2018 17:06	0	6.5	0	7.1	-	7.4	0.02	7.1	0.05	15.7	0.06	6.8
04/03/2018 19:06	0	6.6	0	7.1	-	7.4	0.02	7.1	0.05	15.7	0.06	6.9
04/03/2018 21:06	0	6.8	0	7.1	-	7.5	0.02	7.2	0.05	15.7	0.06	6.9
04/03/2018 23:06	0	6.7	0	7.2	-	7.6	0.02	7.2	0.05	15.7	0.06	6.9
05/03/2018 01:06	0	6.4	0	7	-	7.3	0.02	7.1	0.05	15.7	0.06	6.7
05/03/2018 03:06	0	6.6	0	7	-	7.5	0.02	7.1	0.05	15.6	0.06	6.9
05/03/2018 05:06	0	7	0	7.2	-	7.7	0.02	7.2	0.05	15.7	0.06	7
05/03/2018 07:06	0	7.1	0	7.3	-	7.8	0.02	7.4	0.05	15.8	0.06	7.1
05/03/2018 09:06	0	6.8	0	7.4	-	7.9	0.02	7.4	0.05	15.8	0.07	7.1
05/03/2018 11:06	0	8.5	-0.01	8.7	-	10	0.02	9.1	0.05	16.3	0.07	7.8
05/03/2018 13:06	0.01	8	0	8.4	-	8.9	0.03	8.4	0.06	16.5	0.08	7.9

Table A.19: Data sheet for test GH4 - sensors T1-T5 and heat pump.

Date	T1 [°C]	T2 [°C]	T3 [°C]	T4 [°C]	T5 [°C]	Date	Tair [°C]	IN [°C]	OUT [°C]	U1 [°C]	U2 [°C]
28/02/2018 13:57	4	8.2	7.9	3.4	4.2	28/02/2018 13:59	0.7	7.6	7.8	1.1	1
28/02/2018 16:01	2.5	2.5	4.5	3.4	4.2	28/02/2018 15:04	3.1	1.3	4.3	29.9	25.3
28/02/2018 17:05	2.5	4.9	5.3	3.2	4.1	28/02/2018 17:04	2.8	3.9	4.7	12	11.2
28/02/2018 18:09	2.3	3.9	5	3	3.8	28/02/2018 19:04	1.6	3.3	5	15.9	13.2
28/02/2018 19:13	3.1	4.4	5.4	3	3.7	28/02/2018 21:04	1.8	1.3	4.2	27.6	23
28/02/2018 20:17	1.6	4.4	5.3	2.6	3.6	28/02/2018 23:04	1.4	5	5.3	3.9	3.8
28/02/2018 21:21	1.8	2.8	4.3	2.4	3.3	01/03/2018 01:03	0.5	3.5	4.7	8.5	8.2
28/02/2018 22:25	2.1	4.3	5.1	2.3	3.3	01/03/2018 03:03	0.6	2	3.9	17.7	14.5
28/02/2018 23:29	1	2.6	4.2	2.1	3.1	01/03/2018 05:03	0.5	3.8	4.3	9.5	8.1
01/03/2018 00:33	1.3	4	4.9	2	3	01/03/2018 07:03	0.7	2.4	3.9	14.8	12.2
01/03/2018 01:37	1.1	2.5	4	1.7	2.8	01/03/2018 08:23	1	3.5	4	10	8.5
01/03/2018 02:41	1.1	2.3	4	1.7	2.7	01/03/2018 10:03	0.4	5.7	6	9.3	7
01/03/2018 03:45	1.1	3.7	4.5	1.5	2.7	01/03/2018 12:03	0.7	6.1	6.3	7.2	5.4
01/03/2018 04:49	1.8	3.5	4.4	1.6	2.8	01/03/2018 14:03	1	6.3	6.6	5.8	4.5
01/03/2018 05:53	2	3.3	4.3	1.8	3	01/03/2018 16:02	0.3	6.4	6.7	4.8	3.9
01/03/2018 06:57	1.3	3.1	4.1	1.9	3.1	01/03/2018 18:02	-0.1	6.6	6.8	4	3.2
01/03/2018 08:01	1.3	2.9	4	1.8	2.9	01/03/2018 20:02	-0.4	6.7	6.9	3.3	2.7
01/03/2018 09:05	1.7	6.1	5.7	1.9	2.9	01/03/2018 22:02	0	6.8	7	3	2.5
01/03/2018 10:09	1.8	6.4	6.1	1.9	2.9	02/03/2018 00:02	0	6.8	7.1	2.7	2.2
01/03/2018 11:13	1.8	6.7	6.3	2.2	3.1	02/03/2018 02:02	0.1	6.9	7.1	2.6	2.2
01/03/2018 12:17	2.7	6.9	6.6	2.6	3.5	02/03/2018 04:02	-0.1	6.9	7.2	2.4	2
01/03/2018 13:21	2.3	6.9	6.6	2.6	3.5	02/03/2018 06:02	-0.4	7	7.2	2.2	1.9
01/03/2018 14:25	3.1	7.1	6.7	2.8	3.7	02/03/2018 08:01	-0.1	7	7.3	2	1.7
01/03/2018 15:29	2.1	7	6.7	2.8	3.6	02/03/2018 10:01	0	7.1	7.3	1.9	1.6
01/03/2018 16:33	2.2	7.1	6.8	2.7	3.6	02/03/2018 12:01	0.4	7.1	7.4	2	1.8
01/03/2018 17:37	2.1	7.2	6.8	2.7	3.6	02/03/2018 14:01	1	7.2	7.5	2.2	2
01/03/2018 18:41	2.3	7.2	6.8	2.8	3.6	02/03/2018 16:01	2.5	7.4	7.6	2.4	2.3
01/03/2018 19:45	3.4	7.4	7	2.9	3.7	02/03/2018 18:01	2.3	7.5	7.7	2.8	2.8
01/03/2018 20:49	2	7.3	6.9	2.6	3.6	02/03/2018 20:01	2.1	7.6	7.8	3	3
01/03/2018 21:53	2.3	7.4	7.1	2.7	3.7	02/03/2018 22:01	1.7	7.7	7.9	3	3
01/03/2018 22:57	2	7.4	7	2.6	3.6	03/03/2018 00:00	1	7.7	7.9	3	2.9
02/03/2018 00:01	2.2	7.4	7.1	2.5	3.6	03/03/2018 02:00	0.2	7.7	7.9	2.8	2.6
02/03/2018 01:05	2.5	7.6	7.2	2.7	3.7	03/03/2018 04:00	0.9	7.8	8.1	2.6	2.4
02/03/2018 02:09	2.1	7.5	7.1	2.7	3.7	03/03/2018 06:00	1.7	8	8.2	2.7	2.5
02/03/2018 03:13	1.8	7.5	7.1	2.5	3.6	03/03/2018 08:00	1.3	8	8.2	2.8	2.7
02/03/2018 04:17	1.7	7.5	7.1	2.4	3.5	03/03/2018 10:00	1.5	8.1	8.3	2.9	2.8
02/03/2018 05:21	1.8	7.6	7.2	2.3	3.5	03/03/2018 12:00	1.6	8.1	8.3	2.9	2.8
02/03/2018 06:25	1.4	7.5	7.1	2.2	3.3	03/03/2018 14:00	3.7	8.3	8.5	3.3	3.2
02/03/2018 07:29	2.1	7.6	7.2	2.2	3.4	03/03/2018 15:59	4.7	8.5	8.7	4	4.2
02/03/2018 08:33	1.6	7.6	7.2	2.2	3.4	03/03/2018 17:59	3.6	8.5	8.8	4.4	4.6
02/03/2018 09:37	1.5	7.6	7.2	2.1	3.3	03/03/2018 19:59	3.2	8.6	8.8	4.5	4.6
02/03/2018 10:41	2.1	7.7	7.3	2.3	3.5	03/03/2018 21:59	3.1	8.7	8.9	4.6	4.6
02/03/2018 11:45	2.5	7.7	7.4	2.6	3.7	03/03/2018 23:59	3.2	8.7	9	4.6	4.6
02/03/2018 15:01	3.4	8	7.6	3.3	4.2	04/03/2018 01:59	3	8.8	9	4.6	4.6
02/03/2018 19:17	3.7	8.2	7.9	4.3	5.1	04/03/2018 03:59	2.7	8.8	9	4.6	4.5
02/03/2018 23:33	3.1	8.3	8	3.8	4.9	04/03/2018 05:58	1.7	8.8	9	4.5	4.4
03/03/2018 03:49	3.2	8.5	8.1	3.5	4.8	04/03/2018 07:58	1.4	8.8	9	4.2	4
03/03/2018 08:05	2.8	8.5	8.1	4.5	5.2	04/03/2018 09:58	1.4	8.8	9	3.9	3.6
03/03/2018 12:21	4.8	8.9	8.5	4.3	5.3	04/03/2018 11:58	4.1	8.9	9.2	4.1	3.9
03/03/2018 16:37	5.1	9.2	8.9	6.1	6.6	04/03/2018 13:58	3	8.9	9.2	4.4	4.4
03/03/2018 20:53	4.9	9.4	9	5.4	6.2	04/03/2018 15:58	3.5	9	9.2	4.6	4.6
04/03/2018 01:09	4.3	9.4	9.1	5.2	6.1	04/03/2018 17:58	3.5	9	9.3	4.7	4.7
04/03/2018 05:25	3.8	9.4	9	4.7	5.7	04/03/2018 19:58	3.2	9.1	9.3	4.7	4.7
04/03/2018 09:41	3.3	9.3	8.9	3.9	5.1	04/03/2018 21:57	3.2	9.1	9.3	4.7	4.7
04/03/2018 13:57	4.8	9.6	9.2	5.5	6.2	04/03/2018 23:57	3.3	9.1	9.4	4.8	4.7
04/03/2018 18:05	4.8	9.7	9.3	5.4	6.3	05/03/2018 01:57	3	9.1	9.4	4.8	4.7
04/03/2018 18:47	4.8	9.7	9.3	5.3	6.2	05/03/2018 03:57	3	9.2	9.4	4.8	4.6
04/03/2018 23:03	5.1	9.8	9.4	5.4	6.3	05/03/2018 05:57	3.3	9.2	9.4	4.8	4.6
05/03/2018 03:19	4.7	9.8	9.5	5.1	6.1	05/03/2018 07:57	3.9	9.3	9.5	4.9	4.8
05/03/2018 07:35	5.5	10	9.6	5.5	6.5	05/03/2018 09:57	3.4	9.3	9.5	5	4.9
05/03/2018 11:51	7	10.4	10	7.2	7.9	05/03/2018 11:57	5.5	9.5	9.8	5.3	5.3
						05/03/2018 13:56	5.5	9.6	9.8	5.8	5.9

Table A.20: Summary of test GH4 records.

Quantity	Unit	$x(t_0)$	$x(t_1)$	$x(t_1) - x(t_0)$	$\bar{x}(t_0, t_1)$
T _{DL}	[°C]	1.3	-0.2	-1.5	0.4
Sl2i	[με]	-3181.13	-3182.20	-1.07	5.6
	[με] _{comp} [°C]	-1.36 6.7	20.75 4.8	22.11 -1.9	
Sl2e	[με]	-	-2621.12	-	6.1
	[με] _{comp} [°C]	- 7.5	21.84 5.3	- -2.2	
St4i	[με]	-1788.12	-1788.77	-0.65	5.7
	[με] _{comp} [°C]	0.15 6.5	17.8 5.0	17.65 -1.5	
St4e	[με]	-1515.57	-1513.86	1.71	6.2
	[με] _{comp} [°C]	0.61 7.3	23.06 5.6	22.45 -1.7	
St6i	[με]	-2194.33	-2196.00	-1.67	8.0
	[με] _{comp} [°C]	-0.06 8.8	12.91 7.6	12.97 -1.2	
St6e	[με]	-1811.25	-1821.85	-10.60	8.0
	[με] _{comp} [°C]	-0.03 9.3	12.55 7.4	12.58 -1.9	
Pt1	[MPa]	-0.05	-0.05	0.00	3.7
	[°C]	5.2	3.1	-2.1	
Pl2	[MPa]	-0.03	-0.03	0.00	4.7
	[°C]	6.1	4.1	-2.0	
Pt3	[MPa]	-	-	-	5.5
	[°C]	7.0	4.9	-2.1	
Pr4	[MPa]	0.03	0.02	-0.01	4.5
	[°C]	5.7	3.8	-1.9	
Pt5	[MPa]	0.02	0.01	-0.01	12.3
	[°C]	12.9	12.2	-0.7	
Pr6	[MPa]	0.01	-0.03	-0.04	4.0
	[°C]	4.9	3.4	-1.5	
T1	[°C]	3.2	1.8	-1.4	1.8
T2	[°C]	4.6	4.3	-0.3	3.5
T3	[°C]	6.5	4.6	-1.9	4.7
T4	[°C]	3.6	2.0	-1.6	2.3
T5	[°C]	4.3	3.0	-1.3	3.3
Air	[°C]	0.8	1.0	0.2	1.3
IN	[°C]	7.3	3.5	-3.8	2.5
OUT	[°C]	7.8	4.0	-3.8	4.5
U1	[°C]	0.6	10.0	9.4	18.6
U2	[°C]	0.8	8.5	7.7	15.3

Test GH5

Given the problems faced during test GH4, this test was repeated identical.

Circuit:	Ground
Mode:	Heating
Secondary circuit temperature:	45°C
Activated rings:	179+180
Volumetric flow rate:	0.8 m ³ /h
Fluid velocity in primary circuit:	0.55 m/s
Starting time t_0 :	05/03/2018 14:05
Ending time t_1 :	07/03/2018 14:17
Duration:	2.01 days
Note:	Test stop was forced by low-pressure issue. The heat pump was turned on for 9 minutes for a mistake on March 8 th , 2018.

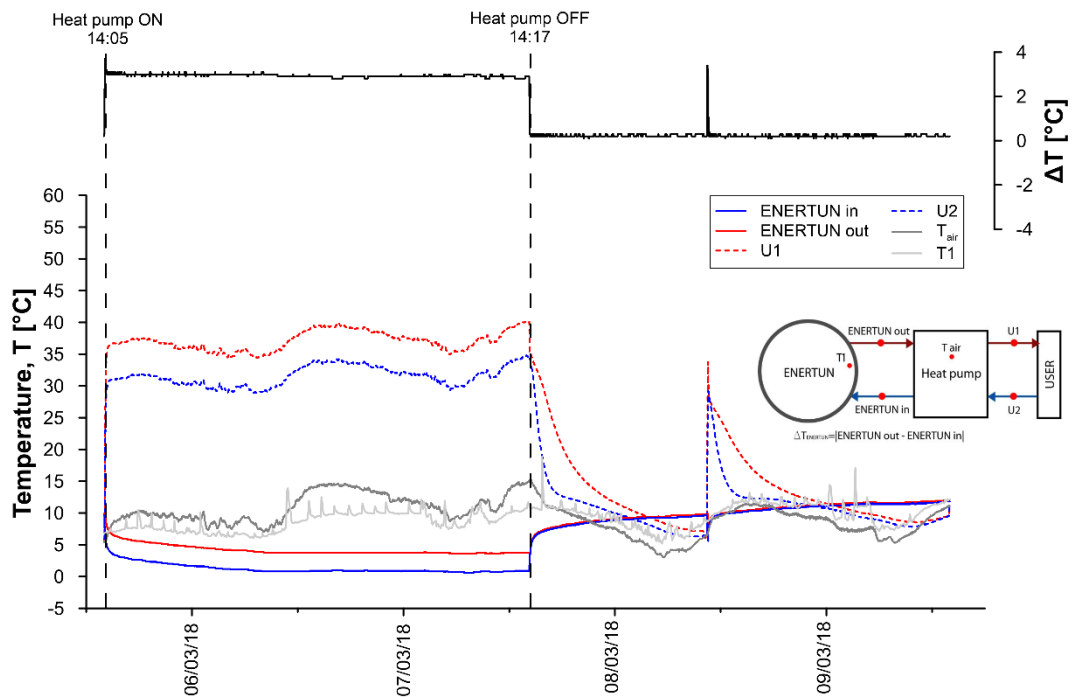


Figure A.64: Primary circuit, secondary circuit and air temperatures for test GH5.

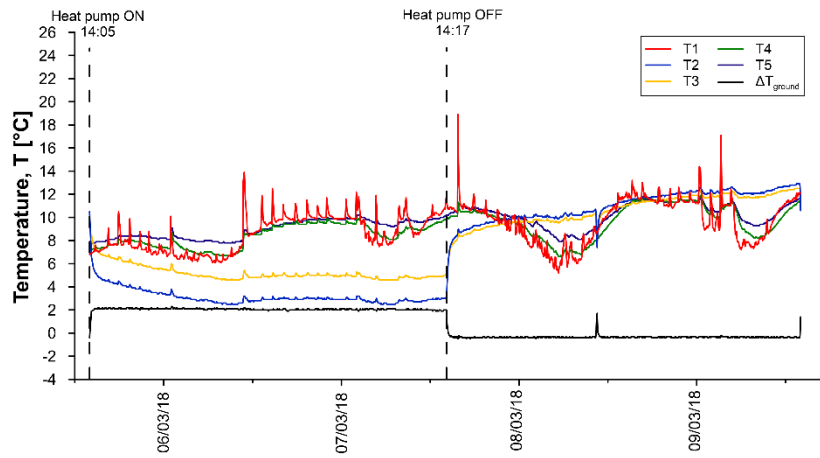


Figure A.65: Temperatures T1-T5 for test GH5.

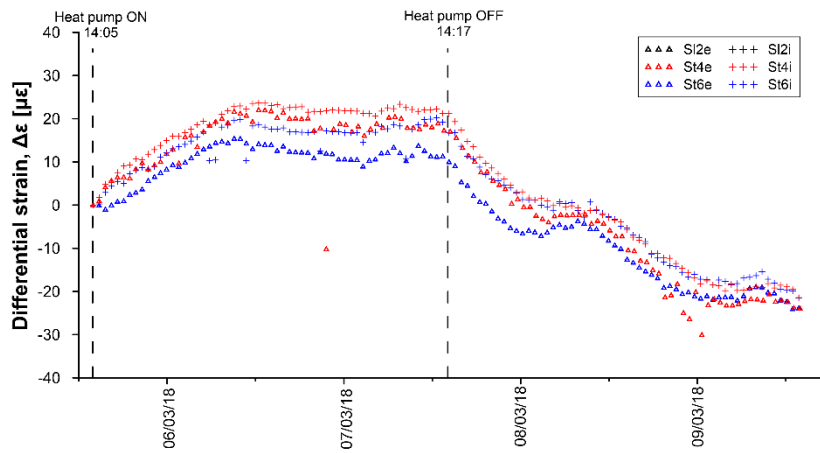


Figure A.66: Differential strains for test GH5.

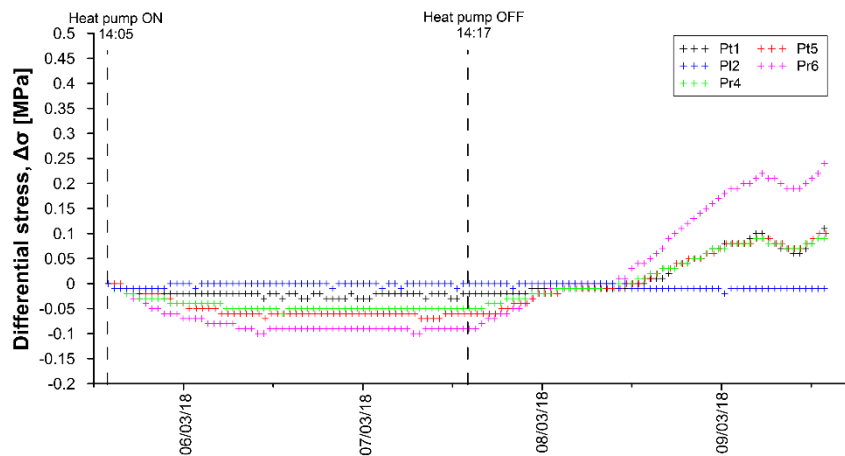


Figure A.67: Differential stresses for test GH5.

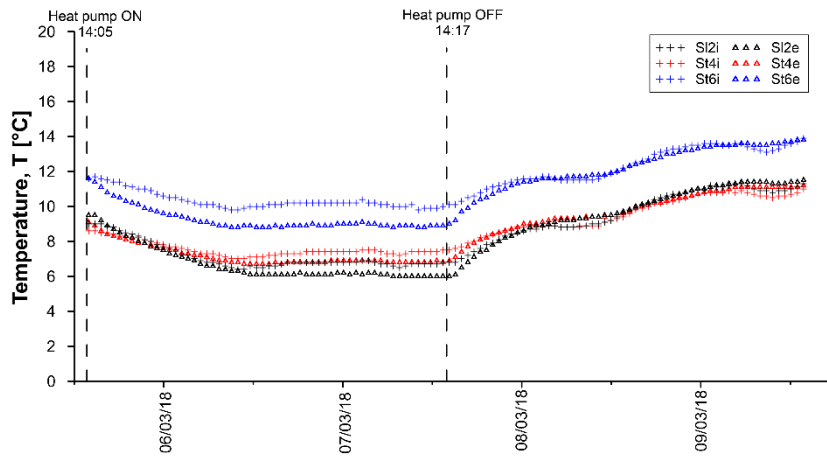


Figure A.68: Temperatures measured by VWSG for test GH5.

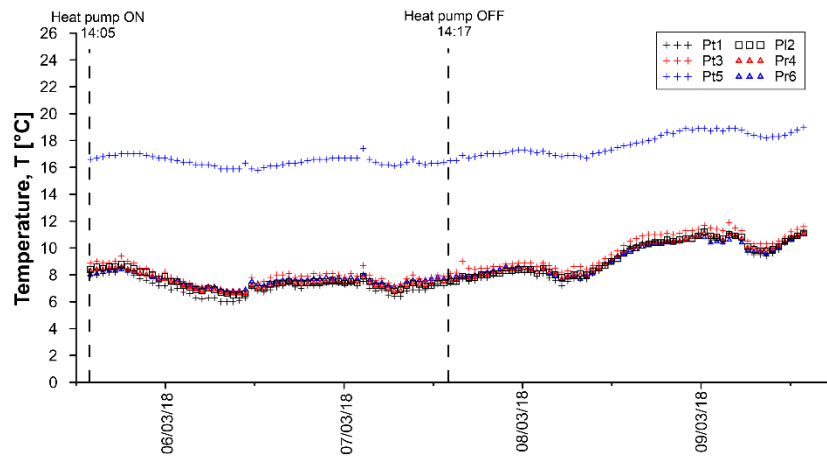


Figure A.69: Temperatures measured by PC for test GH5.

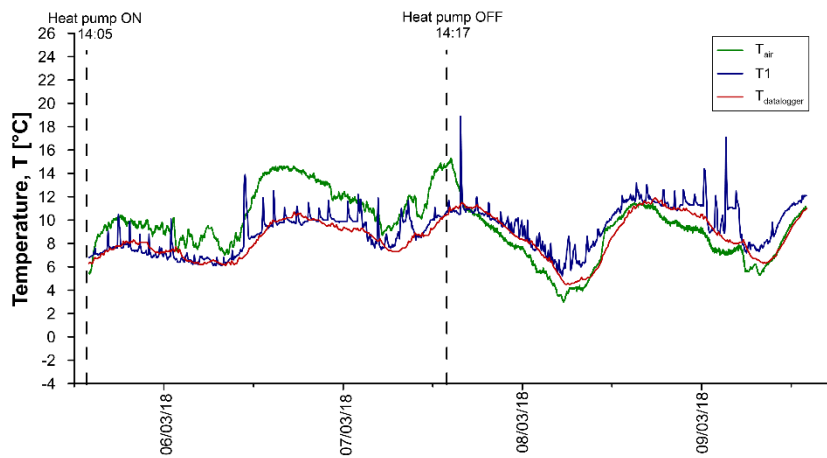


Figure A.70: Air temperatures for test GH5.

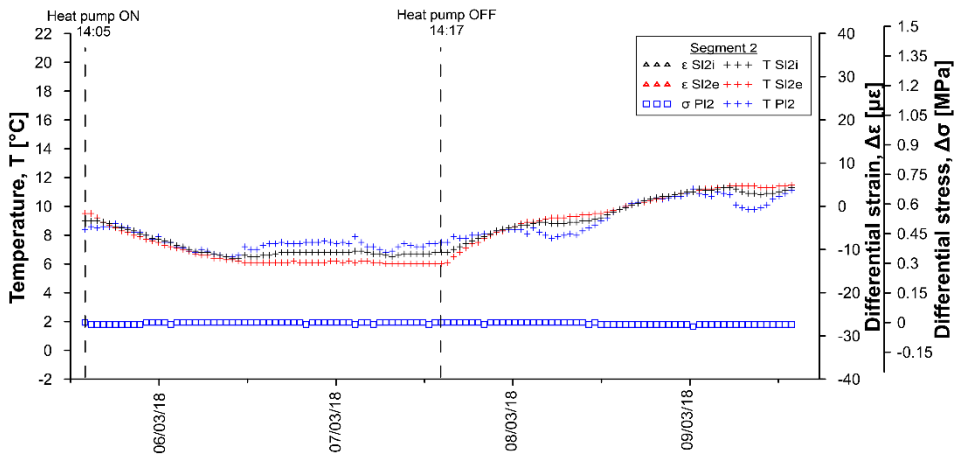


Figure A.71: Temperatures, differential strains and differential stresses in segment 2, ring 179 for test GH5.

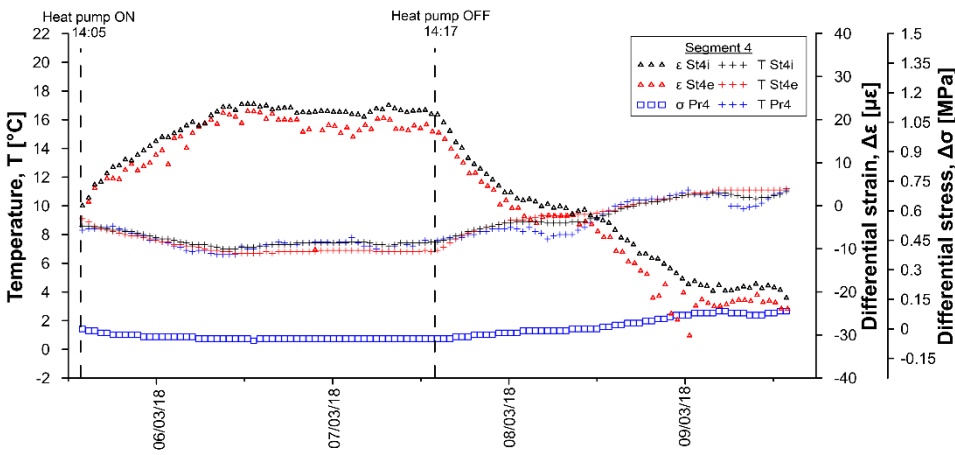


Figure A.72: Temperatures, differential strains and differential stresses in segment 4, ring 179 for test GH5.

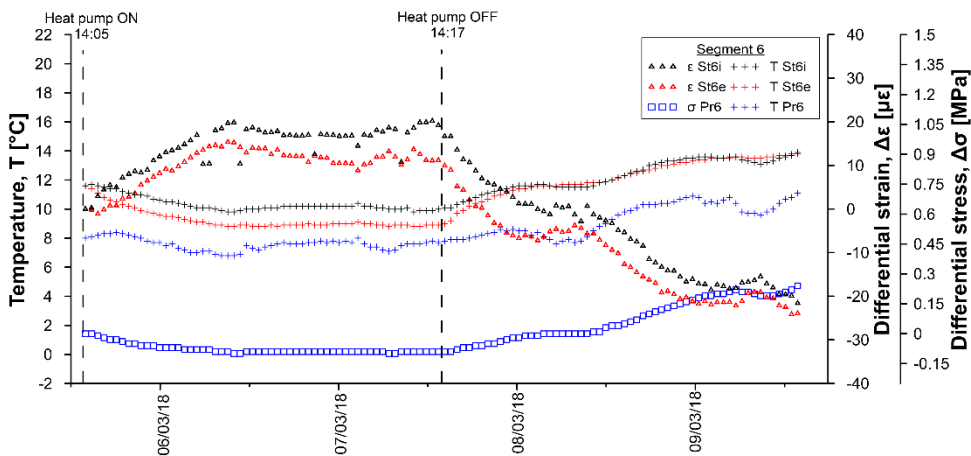


Figure A.73: Temperatures, differential strains and differential stresses in segment 6, ring 179 for test GH5.

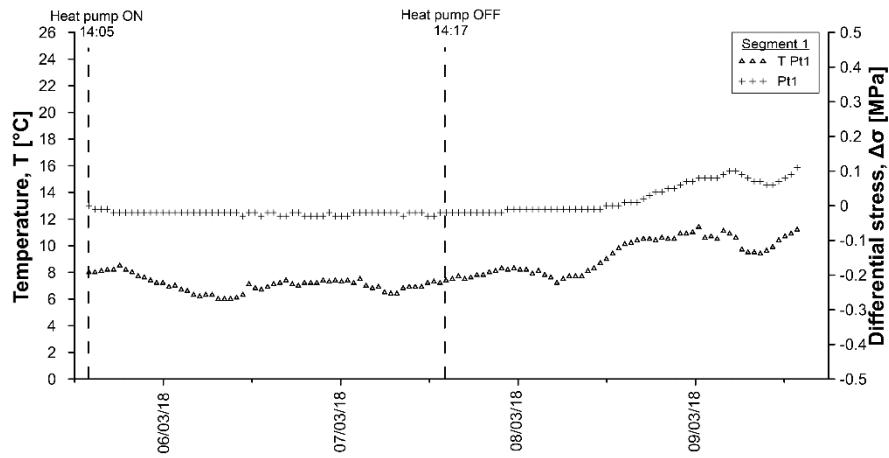


Figure A.74: Temperatures and differential stresses in segment 1, ring 179 for test GH5.

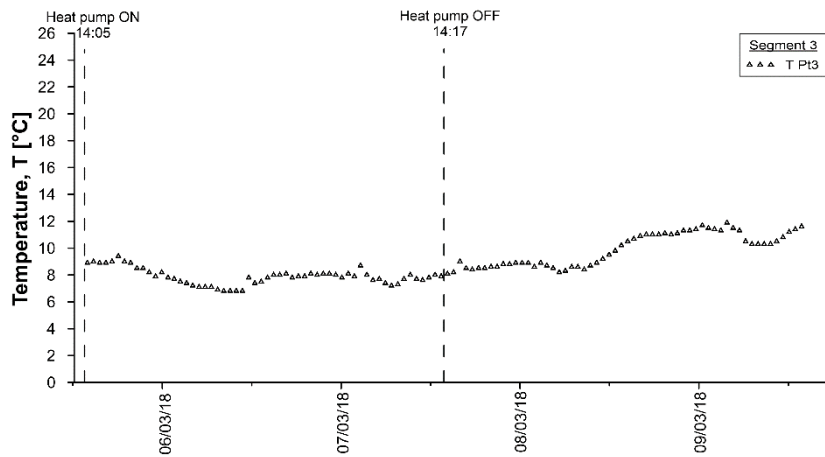


Figure A.75: Temperatures and differential stresses in segment 3, ring 179 for test GH5.

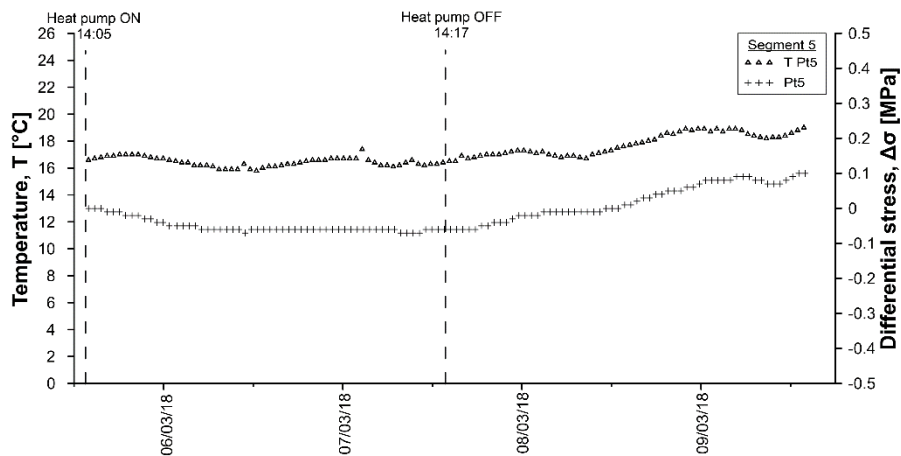


Figure A.76: Temperatures and differential stresses in segment 5, ring 179 for test GH5.

Date	T _{bl} [°C]	SI2i [μ€]	SI2i [°C]	SI2e [μ€]	SI2e [°C]	St4i [μ€]	St4i [°C]	St4e [μ€]	St4e [°C]	St6i [μ€]	St6i [°C]	St6e [μ€]	St6e [°C]
08/03/2018 04:06	6.1	-1.50	8.9	-	9.1	4.18	9.0	-1.19	9.2	0.60	11.6	-5.73	11.6
08/03/2018 05:06	5.1	-1.36	8.8	-	9.2	2.99	8.9	-1.31	9.3	-0.42	11.6	-4.84	11.6
08/03/2018 06:06	4.6	-1.71	8.8	-	9.2	1.93	8.8	-0.86	9.3	-0.92	11.5	-4.08	11.7
08/03/2018 07:06	4.7	-1.75	8.9	-	9.2	2.27	8.8	0.10	9.3	-0.63	11.5	-3.85	11.7
08/03/2018 08:06	4.9	-	8.9	-	9.3	1.70	8.8	0.17	9.3	-2.63	11.5	-2.32	11.7
08/03/2018 09:06	5.1	-	8.9	-	9.3	2.23	8.9	-1.05	9.4	-0.75	11.5	-3.09	11.7
08/03/2018 10:06	5.9	-1.69	9.0	-	9.4	2.70	8.9	0.16	9.4	-0.30	11.6	-4.52	11.8
08/03/2018 11:06	7.4	-	9.1	-	9.5	3.82	9.1	-0.70	9.4	0.49	11.8	-4.67	11.8
08/03/2018 12:06	8.6	-	9.2	-	9.5	4.52	9.2	-1.06	9.5	1.18	11.9	-4.57	11.9
08/03/2018 13:06	9.5	-	9.5	-	9.6	5.52	9.3	-3.85	9.6	2.18	12.1	-4.31	12.0
08/03/2018 14:06	10.4	-1.47	9.7	-	9.8	6.45	9.5	-1.04	9.7	2.95	12.3	-4.15	12.2
08/03/2018 15:06	11.0	-	9.9	-	9.9	7.12	9.7	-1.89	9.9	4.00	12.4	-3.86	12.3
08/03/2018 16:06	11.3	-	10.1	-	10.1	7.75	9.9	-1.10	10.0	4.73	12.6	-3.54	12.5
08/03/2018 17:06	11.4	-	10.3	-	10.2	8.13	10.1	-1.09	10.1	5.19	12.8	-3.24	12.6
08/03/2018 18:06	11.7	-	10.4	-	10.3	8.45	10.1	-1.26	10.2	5.81	13.0	-2.57	12.8
08/03/2018 19:06	11.4	-	10.5	-	10.5	8.36	10.3	-2.24	10.3	5.98	13.1	-2.36	12.9
08/03/2018 20:06	10.9	-	10.6	-	10.6	8.44	10.4	-1.23	10.4	6.49	13.2	-1.73	13.0
08/03/2018 21:06	10.9	-	10.7	-	10.7	8.44	10.4	-0.36	10.5	6.56	13.3	-1.22	13.1
08/03/2018 22:06	10.8	-	10.8	-	10.8	8.69	10.5	-6.73	10.6	6.44	13.5	-1.22	13.2
08/03/2018 23:06	10.6	-	10.9	-	10.9	8.76	10.6	-0.03	10.7	6.93	13.5	-0.44	13.2
09/03/2018 00:06	10.5	-	11.0	-	11.0	8.80	10.7	0.18	10.8	7.14	13.6	-0.22	13.3
09/03/2018 01:06	9.6	-	11.2	-	11.1	9.48	10.8	-23.67	10.9	7.12	13.6	0.58	13.4
09/03/2018 02:06	8.7	-	11.1	-	11.2	8.38	10.8	-0.08	10.9	5.90	13.6	1.24	13.5
09/03/2018 03:06	8.3	-	11.1	-	11.2	8.07	10.8	0.61	11.0	5.75	13.5	1.89	13.5
09/03/2018 04:06	8.1	-	11.2	-	11.3	8.33	10.8	-25.99	11.0	5.62	13.5	1.81	13.5
09/03/2018 05:06	8.1	-	11.3	-	11.3	8.51	10.9	-2.42	11.1	6.16	13.6	1.78	13.6
09/03/2018 06:06	7.5	-	11.2	-	11.4	7.40	10.8	1.84	11.1	5.41	13.4	3.04	13.5
09/03/2018 07:06	6.7	-	11.0	-	11.4	6.32	10.7	2.48	11.1	4.00	13.3	3.85	13.5
09/03/2018 08:06	6.4	-	10.9	-	11.4	-5.51	10.6	-2.5	11.1	-3.09	13.2	-4.18	13.5
09/03/2018 09:06	6.5	-	10.9	-	11.4	-5.18	10.5	-2.55	11.1	-2.74	13.1	-4.3	13.5
09/03/2018 10:06	7.3	-	10.8	-	11.4	-5.08	10.6	-2.46	11.1	-2.54	13.2	-4.14	13.6
09/03/2018 11:06	8.2	-	10.9	-	11.3	-5.7	10.6	-2.46	11.1	-3.48	13.4	-3.65	13.7
09/03/2018 12:06	9.4	-	11	-	11.4	-6.66	10.7	-2.06	11.1	-4.79	13.6	-3.16	13.7
09/03/2018 13:06	10.2	-	11.2	-	11.5	-7.44	10.9	-1.73	11.2	-5.85	13.8	-2.98	13.8
09/03/2018 14:06	11	-	11.3	-	11.5	-8.2	11	-1.78	11.2	-6.94	13.9	-2.97	13.8

Table A.22: Data sheet for test GH5 – stresses and temperatures.

Date	Pt1 [MPa]	Pt1 [°C]	PI2 [MPa]	PI2 [°C]	Pt3 [MPa]	Pt3 [°C]	Pr4 [MPa]	Pr4 [°C]	Pt5 [MPa]	Pt5 [°C]	Pr6 [MPa]	Pr6 [°C]
05/03/2018 13:56	0	8	0	8.4	-	8.9	0	8.3	0	16.6	0	8
05/03/2018 14:06	0	8	0	8.4	-	8.9	0	8.4	0	16.6	0	8
05/03/2018 15:06	-0.01	8.1	-0.01	8.6	-	9	-0.01	8.4	0	16.8	-0.01	8.1
05/03/2018 16:06	-0.01	8.2	-0.01	8.5	-	8.9	-0.02	8.4	0	16.9	-0.02	8.2
05/03/2018 17:06	-0.01	8.2	-0.01	8.6	-	9	-0.02	8.5	-0.01	16.9	-0.02	8.3
05/03/2018 18:06	-0.02	8.5	-0.01	8.8	-	9.4	-0.03	8.6	-0.01	17	-0.03	8.4
05/03/2018 19:06	-0.02	8.1	-0.01	8.5	-	8.9	-0.03	8.4	-0.02	17	-0.04	8.3
05/03/2018 20:06	-0.02	7.9	-0.01	8.4	-	8.8	-0.03	8.2	-0.02	17	-0.05	8.1
05/03/2018 21:06	-0.02	7.8	-0.01	8.4	-	8.7	-0.03	8.2	-0.03	17	-0.06	8.1
05/03/2018 22:06	-0.02	7.4	0	8	-	8.2	-0.04	7.8	-0.03	16.8	-0.06	7.9
05/03/2018 23:06	-0.02	7.2	0	7.7	-	7.9	-0.04	7.6	-0.04	16.7	-0.06	7.7
06/03/2018 00:06	-0.02	7	-0.01	7.8	-	8.1	-0.04	7.6	-0.04	16.7	-0.07	7.6
06/03/2018 01:06	-0.02	7.3	0	7.6	-	7.8	-0.04	7.5	-0.05	16.6	-0.07	7.7
06/03/2018 02:06	-0.02	6.7	0	7.3	-	7.6	-0.04	7.2	-0.05	16.5	-0.07	7.4
06/03/2018 03:06	-0.02	6.6	0	7.1	-	7.4	-0.04	7.1	-0.05	16.4	-0.08	7.2
06/03/2018 04:06	-0.02	6.3	0	6.9	-	7.2	-0.04	6.9	-0.05	16.2	-0.08	7
06/03/2018 05:06	-0.02	6.3	0	6.8	-	7.1	-0.04	6.8	-0.06	16.2	-0.08	7
06/03/2018 06:06	-0.02	6.4	0	7	-	7.2	-0.05	7	-0.06	16.2	-0.08	7.2
06/03/2018 07:06	-0.02	6.1	0	6.8	-	6.9	-0.05	6.7	-0.06	16	-0.08	7
06/03/2018 08:06	-0.02	6	0	6.5	-	6.8	-0.05	6.6	-0.07	15.9	-0.09	6.8
06/03/2018 09:06	-0.02	6	0	6.5	-	6.8	-0.05	6.6	-0.06	15.9	-0.09	6.8
06/03/2018 10:06	-0.02	6.1	0	6.5	-	6.8	-0.05	6.6	-0.06	15.9	-0.09	6.8
06/03/2018 11:06	-0.03	7.4	-0.01	7.5	-	8.2	-0.05	7.3	-0.07	16.8	-0.09	7.5
06/03/2018 12:06	-0.02	6.9	0	7	-	7.5	-0.05	7.1	-0.06	15.8	-0.09	7.4
06/03/2018 13:06	-0.02	6.6	0	7	-	7.3	-0.05	7	-0.06	15.9	-0.09	7.2
06/03/2018 14:06	-0.02	6.9	0	7.3	-	7.8	-0.05	7.2	-0.06	16.1	-0.09	7.4
06/03/2018 15:06	-0.02	7.1	0	7.4	-	7.9	-0.05	7.3	-0.06	16.1	-0.09	7.5
06/03/2018 16:06	-0.03	7.4	0	7.5	-	8	-0.05	7.3	-0.06	16.3	-0.09	7.7
06/03/2018 17:06	-0.02	7.3	0	7.4	-	7.9	-0.05	7.4	-0.06	16.3	-0.09	7.6
06/03/2018 18:06	-0.02	7.1	0	7.5	-	7.9	-0.05	7.4	-0.06	16.5	-0.09	7.6
06/03/2018 19:06	-0.03	7.2	0	7.4	-	7.9	-0.05	7.3	-0.06	16.5	-0.09	7.6
06/03/2018 20:06	-0.03	7.2	0	7.5	-	8	-0.05	7.4	-0.06	16.6	-0.09	7.7
06/03/2018 21:06	-0.03	7.4	0	7.6	-	8.2	-0.05	7.5	-0.06	16.6	-0.09	7.8
06/03/2018 22:06	-0.03	7.4	-0.01	7.5	-	8	-0.05	7.6	-0.06	16.6	-0.09	7.8
06/03/2018 23:06	-0.03	7.3	0	7.5	-	8	-0.05	7.5	-0.06	16.7	-0.09	7.8
07/03/2018 00:06	-0.03	7.3	0	7.4	-	7.8	-0.05	7.4	-0.06	16.7	-0.09	7.7
07/03/2018 01:06	-0.03	7.4	0	7.5	-	8.1	-0.05	7.5	-0.06	16.7	-0.09	7.8
07/03/2018 02:06	-0.03	7.4	-0.01	7.5	-	7.9	-0.05	7.6	-0.06	17.2	-0.09	7.8
07/03/2018 03:06	-0.02	7.2	0	7.6	-	8.3	-0.05	7.5	-0.06	16.8	-0.09	7.7
07/03/2018 04:06	-0.02	6.9	0	7.2	-	7.7	-0.05	7.2	-0.06	16.4	-0.09	7.5
07/03/2018 05:06	-0.02	6.9	-0.01	7.2	-	7.7	-0.05	7.2	-0.06	16.2	-0.09	7.4
07/03/2018 06:06	-0.02	6.5	0	7	-	7.4	-0.05	7	-0.06	16.2	-0.09	7.2
07/03/2018 07:06	-0.02	6.4	0	6.9	-	7.2	-0.05	6.8	-0.06	16.1	-0.1	7.1
07/03/2018 08:06	-0.02	6.7	0	7.2	-	7.6	-0.05	7.1	-0.07	16.3	-0.1	7.4
07/03/2018 09:06	-0.02	7	0	7.5	-	8.1	-0.05	7.5	-0.06	16.6	-0.09	7.6
07/03/2018 10:06	-0.02	6.9	0	7.3	-	7.7	-0.05	7.3	-0.07	16.3	-0.09	7.6
07/03/2018 11:06	-0.02	7	0	7.2	-	7.6	-0.05	7.2	-0.06	16.3	-0.09	7.6
07/03/2018 12:06	-0.03	7.3	0	7.3	-	7.9	-0.05	7.5	-0.06	16.3	-0.09	7.8
07/03/2018 13:06	-0.02	7.4	0	7.4	-	8	-0.05	7.6	-0.06	16.4	-0.09	7.8
07/03/2018 14:06	-0.03	7.4	-0.01	7.4	-	8	-0.05	7.6	-0.07	16.4	-0.09	7.8
07/03/2018 15:06	-0.02	7.5	0	7.5	-	8.2	-0.05	7.7	-0.06	16.5	-0.09	7.9
07/03/2018 16:06	-0.02	7.7	-0.01	7.9	-	9	-0.05	7.8	-0.06	16.8	-0.08	7.9
07/03/2018 17:06	-0.02	7.6	0	7.8	-	8.5	-0.04	7.8	-0.06	16.7	-0.07	8
07/03/2018 18:06	-0.02	7.9	0	8	-	8.6	-0.04	8.1	-0.06	16.8	-0.07	8.1
07/03/2018 19:06	-0.02	7.8	0	8	-	8.5	-0.03	8	-0.05	16.9	-0.06	8.2
07/03/2018 20:06	-0.02	8	-0.01	8.1	-	8.6	-0.03	8.2	-0.05	17	-0.05	8.3
07/03/2018 21:06	-0.02	8.2	0	8.2	-	8.7	-0.03	8.3	-0.04	17.1	-0.05	8.5
07/03/2018 22:06	-0.02	8.2	0	8.3	-	8.8	-0.03	8.4	-0.03	17.2	-0.03	8.5
07/03/2018 23:06	-0.01	8.2	0	8.3	-	8.8	-0.02	8.4	-0.03	17.2	-0.02	8.5
08/03/2018 00:06	-0.01	8.2	0	8.4	-	8.9	-0.02	8.4	-0.02	17.3	-0.02	8.6
08/03/2018 01:06	-0.01	8.2	0	8.4	-	8.9	-0.02	8.4	-0.02	17.2	-0.01	8.5
08/03/2018 02:06	-0.01	8.1	0	8.4	-	8.9	-0.01	8.4	-0.02	17.3	-0.01	8.4
08/03/2018 03:06	-0.01	8	0	8.3	-	8.8	-0.01	8.4	-0.01	17.1	-0.01	8.3

Date	Pt1 [MPa]	Pt1 [°C]	PI2 [MPa]	PI2 [°C]	Pt3 [MPa]	Pt3 [°C]	Pr4 [MPa]	Pr4 [°C]	Pt5 [MPa]	Pt5 [°C]	Pr6 [MPa]	Pr6 [°C]
08/03/2018 04:06	-0.01	7.7	0	8.2	-	8.7	-0.01	8.2	-0.01	17	0	8
08/03/2018 05:06	-0.01	7.2	0	7.8	-	8.2	-0.01	7.8	-0.01	16.9	0	7.7
08/03/2018 06:06	-0.01	7.5	0	7.9	-	8.3	-0.01	7.9	-0.01	16.9	0	7.8
08/03/2018 07:06	-0.01	7.8	0	8.1	-	8.6	-0.01	8.1	-0.01	16.9	0	7.9
08/03/2018 08:06	-0.01	7.7	0	8	-	8.5	0	8	-0.01	16.7	0	7.7
08/03/2018 09:06	-0.01	8	0	8.2	-	8.6	0	8.2	-0.01	16.9	0	8.1
08/03/2018 10:06	-0.01	8.1	0	8.4	-	8.8	0	8.4	-0.01	17	0.01	8.4
08/03/2018 11:06	-0.01	8.7	0	8.7	-	9.2	0	8.8	0	17.2	0.01	8.8
08/03/2018 12:06	0	9.1	-0.01	9	-	9.5	0	9.1	0	17.3	0.03	9.1
08/03/2018 13:06	0	9.5	-0.01	9.4	-	10	0.01	9.5	0	17.5	0.04	9.4
08/03/2018 14:06	0	10	-0.01	9.7	-	10.4	0.01	9.8	0.01	17.7	0.05	9.7
08/03/2018 15:06	0.01	10.2	-0.01	9.9	-	10.7	0.02	10.1	0.02	17.7	0.06	9.9
08/03/2018 16:06	0.01	10.4	-0.01	10.2	-	10.9	0.03	10.3	0.02	17.9	0.07	10.1
08/03/2018 17:06	0.02	10.5	-0.01	10.3	-	11	0.03	10.4	0.03	18	0.09	10.3
08/03/2018 18:06	0.03	10.4	-0.01	10.4	-	11	0.04	10.4	0.04	18.3	0.1	10.3
08/03/2018 19:06	0.04	10.5	-0.01	10.5	-	11.1	0.04	10.5	0.04	18.5	0.11	10.4
08/03/2018 20:06	0.05	10.5	-0.01	10.5	-	11	0.05	10.5	0.05	18.6	0.13	10.5
08/03/2018 21:06	0.05	10.5	-0.01	10.6	-	11.1	0.05	10.5	0.05	18.7	0.14	10.5
08/03/2018 22:06	0.06	10.9	-0.01	10.8	-	11.3	0.06	10.7	0.06	18.8	0.16	10.8
08/03/2018 23:06	0.07	11	-0.01	10.8	-	11.2	0.07	10.8	0.07	18.9	0.17	10.8
09/03/2018 00:06	0.07	10.9	-0.01	10.9	-	11.3	0.07	10.8	0.08	18.9	0.18	10.8
09/03/2018 01:06	0.08	10.8	-0.01	11.1	-	11.8	0.08	11	0.08	18.8	0.19	10.6
09/03/2018 02:06	0.08	10.7	-0.01	10.8	-	11.4	0.08	10.8	0.08	18.9	0.19	10.5
09/03/2018 03:06	0.08	10.5	-0.01	10.7	-	11.3	0.08	10.6	0.08	18.7	0.2	10.3
09/03/2018 04:06	0.09	11	-0.01	11	-	11.7	0.08	10.9	0.08	18.9	0.21	10.7
09/03/2018 05:06	0.1	11	-0.01	11	-	11.5	0.09	11	0.09	19	0.22	10.8
09/03/2018 06:06	0.09	9.8	-0.01	10.2	-	10.6	0.09	10.1	0.09	18.6	0.22	9.9
09/03/2018 07:06	0.08	9.5	-0.01	9.9	-	10.3	0.08	10	0.08	18.4	0.21	9.7
09/03/2018 08:06	0.07	9.6	-0.01	9.8	-	10.2	0.08	9.8	0.08	18.3	0.2	9.7
09/03/2018 09:06	0.06	9.4	-0.01	9.8	-	10.2	0.07	9.9	0.07	18.2	0.19	9.6
09/03/2018 10:06	0.06	9.7	-0.01	10.1	-	10.4	0.07	10	0.07	18.3	0.19	9.9
09/03/2018 11:06	0.07	10.3	-0.01	10.4	-	10.7	0.08	10.4	0.08	18.4	0.2	10.4
09/03/2018 12:06	0.08	10.7	-0.01	10.7	-	11.2	0.08	10.8	0.09	18.6	0.21	10.7
09/03/2018 13:06	0.1	11	-0.01	11	-	11.4	0.09	11	0.1	18.9	0.23	10.9
09/03/2018 14:06	0.11	11.3	-0.01	11.2	-	11.7	0.1	11.2	0.1	19	0.24	11.1

Table A.23: Data sheet for test GH5 - sensors T1-T5 and heat pump.

Date	T1 [°C]	T2 [°C]	T3 [°C]	T4 [°C]	T5 [°C]	Date	Tair [°C]	IN [°C]	OUT [°C]	U1 [°C]	U2 [°C]
05/03/2018 13:59	6.8	10.5	10.1	7.2	7.7	05/03/2018 14:00	5.5	9.6	9.8	5.8	5.9
05/03/2018 15:43	7.2	4.6	6.8	7.4	7.9	05/03/2018 14:05	5.5	7.8	9.9	8.2	5.9
05/03/2018 17:03	7.6	4.4	6.5	7.6	8.1	05/03/2018 15:05	8.6	3.5	6.5	36.8	31.1
05/03/2018 18:23	7.6	4.2	6.3	7.9	8.4	05/03/2018 16:05	9.4	3	6	37	31.3
05/03/2018 19:43	7.4	3.9	6.1	8	8.4	05/03/2018 17:05	10	2.8	5.8	37.3	31.7
05/03/2018 21:03	7.2	3.8	5.9	7.9	8.4	05/03/2018 18:05	10.3	2.6	5.6	37.5	31.9
05/03/2018 22:21	6.8	3.5	5.7	7.6	8.2	05/03/2018 19:05	9.8	2.4	5.4	37.4	31.7
05/03/2018 23:41	7.6	3.5	5.6	7.4	8.2	05/03/2018 20:05	9.8	2.2	5.2	37	31.3
06/03/2018 01:01	8.3	3.8	6	8.6	8.9	05/03/2018 21:05	9.3	2.1	5.1	36.7	31.1
06/03/2018 02:21	6.7	3.1	5.2	7.5	8.2	06/03/2018 22:05	9.2	1.9	4.9	36.1	30.5
06/03/2018 03:41	6.3	2.9	5	7.1	8	05/03/2018 23:05	9.5	1.8	4.8	36	30.4
06/03/2018 05:01	6.8	2.9	5	7	7.9	06/03/2018 00:05	9.1	1.7	4.7	36	30.5
06/03/2018 06:21	6.5	2.8	4.9	7	8	06/03/2018 01:05	9.2	1.6	4.6	36.4	30.8
06/03/2018 07:41	6.1	2.6	4.7	6.7	7.8	06/03/2018 02:05	8.2	1.4	4.4	35.3	29.7
06/03/2018 09:01	6.7	2.5	4.6	6.7	7.8	06/03/2018 03:05	8.1	1.3	4.3	35.5	29.9
06/03/2018 10:21	7.4	2.6	4.7	7.1	7.9	06/03/2018 04:05	7.7	1.2	4.2	34.6	29
06/03/2018 11:41	8.5	2.7	4.8	8.5	8.6	06/03/2018 05:04	8.6	1.1	4.1	35.4	29.9
06/03/2018 13:01	8.9	2.8	4.8	8.5	8.8	06/03/2018 06:04	9.3	1.1	4.1	35.8	30.3
06/03/2018 14:21	9.5	2.9	4.9	8.9	9	06/03/2018 07:04	8.2	0.9	3.9	34.5	28.9
06/03/2018 15:41	9.8	3	5	9.2	9.3	06/03/2018 08:04	7.1	0.8	3.9	34.7	29.1
06/03/2018 17:01	9.9	2.9	4.9	9.4	9.5	06/03/2018 09:04	8.1	0.8	3.8	35.2	29.6
06/03/2018 18:21	9.6	2.9	4.9	9.4	9.7	06/03/2018 10:04	8.2	0.8	3.7	35.6	30.1
06/03/2018 19:41	10.2	3	5	9.6	9.8	06/03/2018 11:04	10.5	0.8	3.7	37.2	31.7
06/03/2018 21:01	10.2	3	5	9.7	9.9	06/03/2018 12:04	11.9	0.8	3.7	38	32.5
06/03/2018 22:21	10.2	3	5	9.7	9.9	06/03/2018 13:04	13.6	0.8	3.7	38.7	33.2
06/03/2018 23:41	9.9	2.9	4.9	9.5	9.8	06/03/2018 14:04	14.1	0.9	3.8	39.2	33.7
07/03/2018 01:01	10.1	2.9	5	9.5	9.9	06/03/2018 15:04	14.4	0.9	3.8	39.5	34
07/03/2018 02:21	11.8	3.2	5.1	9.8	10.2	06/03/2018 16:04	14.4	1	3.8	39.2	33.7
07/03/2018 03:41	8.8	2.8	4.8	9.2	9.8	06/03/2018 17:04	14.3	1	3.8	39.4	33.9
07/03/2018 05:01	7.7	2.6	4.7	8.6	9.5	06/03/2018 18:04	14.2	0.9	3.8	39.1	33.6
07/03/2018 06:21	7.6	2.5	4.6	8.2	9.3	06/03/2018 19:04	13.9	0.9	3.8	39	33.5
07/03/2018 07:41	10.2	2.7	4.7	8.4	9.4	06/03/2018 20:04	13.9	0.9	3.8	38.7	33.3
07/03/2018 09:01	10	2.8	4.9	9.1	9.7	06/03/2018 21:03	13.2	0.9	3.8	38.4	32.9
07/03/2018 10:21	8.7	2.7	4.7	8.9	9.6	06/03/2018 22:03	13.1	0.9	3.8	38.1	32.6
07/03/2018 11:41	10	2.9	4.9	9.1	9.7	06/03/2018 23:03	11.9	0.9	3.8	37.6	32.1
07/03/2018 13:01	10.3	3	4.9	9.6	9.9	07/03/2018 00:03	12.3	0.9	3.8	37.7	32.2
07/03/2018 14:21	10.8	5.2	5.7	10	10.2	07/03/2018 01:03	11.6	0.9	3.8	37.2	31.7
07/03/2018 15:41	10.5	8.5	8.1	10.1	10.5	07/03/2018 02:03	11.8	0.9	3.8	37.3	31.9
07/03/2018 17:01	10.9	9	8.6	10.5	10.8	07/03/2018 03:03	11.1	0.8	3.8	36.9	31.5
07/03/2018 18:21	10.6	9.3	8.9	10.4	10.8	07/03/2018 04:03	11	0.8	3.7	36.6	31
07/03/2018 19:41	10.1	9.5	9.2	10.3	10.7	07/03/2018 05:03	9.5	0.7	3.7	35.5	29.9
07/03/2018 21:01	9.8	9.7	9.3	10	10.4	07/03/2018 06:03	9.5	0.7	3.6	35.4	29.9
07/03/2018 22:21	8.9	9.8	9.5	9.7	10.2	07/03/2018 07:03	9.7	0.6	3.6	35.5	30
07/03/2018 23:41	9	9.9	9.6	9.4	10	07/03/2018 08:03	10.5	0.7	3.6	36.9	31.4
08/03/2018 01:01	8.2	10	9.7	9	9.8	07/03/2018 09:03	12	0.8	3.7	37.5	32
08/03/2018 02:21	8.4	10.2	9.8	8.6	9.7	07/03/2018 10:03	10.5	0.7	3.7	37.1	31.6
08/03/2018 03:41	6.5	10	9.7	7.7	8.8	07/03/2018 11:03	11.3	0.7	3.7	37.8	32.3
08/03/2018 05:01	5.5	10	9.6	7	8.2	07/03/2018 12:02	13.5	0.8	3.7	39.2	33.8
08/03/2018 06:21	7.9	10.3	10	7.2	8.5	07/03/2018 13:02	14.8	0.9	3.7	39.8	34.3
08/03/2018 07:41	6.3	10.2	9.8	7	8.2	07/03/2018 14:02	14.8	0.9	3.8	40.2	34.7
08/03/2018 09:01	7.5	10.4	10.1	7.2	8.5	07/03/2018 14:17	15	2.4	3.8	37.8	34.7
08/03/2018 10:21	8.7	10.7	10.3	8	9.2	07/03/2018 15:02	13.7	6.5	6.7	32.8	27
08/03/2018 11:41	10.1	10.9	10.5	9	9.8	07/03/2018 16:02	11.3	7.2	7.4	28.9	16.9
08/03/2018 13:01	10.8	11.1	10.8	10	10.5	07/03/2018 17:02	10.9	7.6	7.8	24.1	13.5
08/03/2018 14:21	11.8	11.4	11	10.9	11.1	07/03/2018 18:02	10.4	7.8	8.1	20.4	12.6
08/03/2018 15:41	11.8	11.6	11.2	11.4	11.5	07/03/2018 19:02	9.8	8.1	8.3	17.8	12.2
08/03/2018 17:01	12.1	11.7	11.3	11.6	11.5	07/03/2018 20:02	9.3	8.3	8.5	15.9	11.8
08/03/2018 18:21	11.4	11.8	11.4	11.5	11.3	07/03/2018 21:02	8.8	8.5	8.6	14.5	11.4
08/03/2018 19:41	11	11.8	11.5	11.4	11.3	07/03/2018 22:02	8.1	8.6	8.8	13.3	10.9
08/03/2018 21:01	11.1	12	11.6	11.3	11.3	07/03/2018 23:02	7.7	8.7	9	12.4	10.4
08/03/2018 22:21	11.4	12.1	11.8	11.5	11.5	08/03/2018 00:02	7.6	8.9	9.1	11.6	9.9
08/03/2018 23:41	11.3	12.2	11.9	11.5	11.5	08/03/2018 01:02	7	9	9.2	11	9.5
09/03/2018 01:01	9	12.1	11.7	11	11.2	08/03/2018 02:02	5.6	9	9.3	10.3	9.1

Date	T1 [°C]	T2 [°C]	T3 [°C]	T4 [°C]	T5 [°C]	Date	Tair [°C]	IN [°C]	OUT [°C]	U1 [°C]	U2 [°C]
09/03/2018 02:21	8.9	12.1	11.8	10.1	10.6	08/03/2018 03:02	5.5	9.1	9.4	9.8	8.6
09/03/2018 03:41	11	12.4	12.1	10.8	11	08/03/2018 04:01	4.5	9.2	9.4	9.2	8.1
09/03/2018 05:01	11	12.5	12.2	11.1	11.3	08/03/2018 05:01	3.6	9.2	9.4	8.7	7.5
09/03/2018 06:21	8.1	12.1	11.8	9	9.7	08/03/2018 06:01	3.7	9.3	9.5	8.1	6.9
09/03/2018 07:41	7.3	12	11.7	8.3	9.3	08/03/2018 07:01	4.2	9.3	9.6	7.7	6.6
09/03/2018 09:01	8.2	12.1	11.8	8.4	9.4	08/03/2018 08:01	4	9.4	9.6	7.4	6.4
09/03/2018 10:21	9.7	12.4	12	9.1	10	08/03/2018 09:01	5.1	9.5	9.7	7.2	6.3
09/03/2018 11:41	10.9	12.7	12.3	10.1	10.9	08/03/2018 10:03	6.2	9.5	9.8	7.1	6.5
09/03/2018 13:01	11.6	12.8	12.4	11	11.3	08/03/2018 11:03	9.1	9.3	9.6	26.9	25.3
						08/03/2018 12:03	9.5	9.8	10	24.6	17.3
						08/03/2018 13:03	10.3	9.9	10.2	21.9	13.9
						08/03/2018 14:03	10.9	10.1	10.3	19.6	12.7
						08/03/2018 15:03	11.4	10.2	10.5	17.8	12.4
						08/03/2018 16:03	11.4	10.4	10.6	16.3	12.3
						08/03/2018 17:02	11.2	10.5	10.7	15.2	12.3
						08/03/2018 18:02	10.9	10.6	10.8	14.3	12.1
						08/03/2018 19:02	10	10.7	10.9	13.6	11.9
						08/03/2018 20:02	9.8	10.8	11	13	11.7
						08/03/2018 21:02	9.6	10.9	11.1	12.6	11.4
						08/03/2018 22:02	9.3	11	11.2	12.1	11.2
						08/03/2018 23:02	9.3	11.1	11.3	11.8	10.9
						09/03/2018 00:02	9	11.1	11.4	11.4	10.7
						09/03/2018 01:02	8	11.2	11.4	11.1	10.5
						09/03/2018 02:02	7.5	11.2	11.5	10.7	10.1
						09/03/2018 03:02	7.3	11.3	11.5	10.3	9.6
						09/03/2018 04:02	7.3	11.3	11.6	10	9.3
						09/03/2018 05:02	7.7	11.4	11.7	9.8	9.1
						09/03/2018 06:02	5.6	11.4	11.6	9.6	8.9
						09/03/2018 07:02	6.1	11.4	11.6	9.2	8.5
						09/03/2018 08:02	5.5	11.4	11.6	8.9	8.1
						09/03/2018 09:01	6.3	11.4	11.6	8.6	7.9
						09/03/2018 10:01	7	11.4	11.7	8.5	7.9
						09/03/2018 11:01	8.6	11.5	11.8	8.6	8.1
						09/03/2018 12:01	9.6	11.6	11.8	8.9	8.6
						09/03/2018 13:01	10.5	11.7	11.9	9.2	9.1

Table A.24: Summary of test GH5 records.

Quantity	Unit	$x(t_0)$	$x(t_1)$	$x(t_1) - x(t_0)$	$\bar{x}(t_0, t_1)$
T _{DL}	[°C]	6.4	11.1	4.7	8.2
Sl2i	[με]	-328.42	-3198.49	-	
	[με] _{comp}	0.0	-2843.23	-	
	[°C]	9.0	6.8	-2.2	7.1
Sl2e	[με]	-	-2620.53	-	
	[με] _{comp}	-	-	-	
	[°C]	9.5	6.0	-3.5	6.7
St4i	[με]	-1778.24	-1770.32	7.92	
	[με] _{comp}	-0.16	21.18	21.34	
	[°C]	8.6	7.5	-1.1	7.5
St4e	[με]	-1509.80	-1518.80	-9.00	
	[με] _{comp}	-0.25	17.59	17.84	
	[°C]	9.1	6.9	-2.2	7.2
St6i	[με]	-2188.19	-2189.77	-1.58	
	[με] _{comp}	0.0	16.72	16.72	
	[°C]	11.6	10.1	-1.5	10.3
St6e	[με]	-1806.56	-1828.36	-21.80	
	[με] _{comp}	-0.01	9.91	9.92	
	[°C]	11.6	9.0	-2.6	9.3
Pt1	[MPa]	-0.04	-0.06	-0.02	
	[°C]	8.0	7.4	-0.6	7.1
Pl2	[MPa]	-0.03	-0.03	0.00	
	[°C]	8.4	7.5	-0.9	7.5
Pt3	[MPa]	-	-	-	
	[°C]	8.9	8.1	-0.8	7.9
Pr4	[MPa]	0.06	0.01	-0.05	
	[°C]	8.4	7.6	-0.8	7.4
Pt5	[MPa]	0.08	0.02	-0.06	
	[°C]	16.6	16.5	-0.1	16.5
Pr6	[MPa]	0.09	0.00	-0.09	
	[°C]	8.0	7.8	-0.2	7.6
T1	[°C]	6.9	11.4	4.5	8.6
T2	[°C]	6.6	3.1	-3.5	3.1
T3	[°C]	8.5	5.1	-3.4	5.2
T4	[°C]	7.2	10.0	2.8	8.4
T5	[°C]	7.7	10.2	2.5	9.0
Air	[°C]	5.5	14.9	9.4	10.9
IN	[°C]	7.8	0.9	-6.9	1.3
OUT	[°C]	9.9	3.8	-6.1	4.2
U1	[°C]	8.2	40.1	31.9	37.1
U2	[°C]	5.9	34.7	28.8	31.5

Test GH6

In this test the flow rate was set at 1.0 m³/h to study its role on thermal performance. The flow rate was modified on March 8th, 2018 at 10:27.

Circuit:	Ground
Mode:	Heating
Secondary circuit temperature:	45°C
Activated rings:	179+180
Volumetric flow rate:	1.0 m ³ /h
Fluid velocity in primary circuit:	0.69 m/s
Starting time t ₀ :	09/03/2018 13:59
Ending time t ₁ :	12/03/2018 15:47
Duration:	3.07 days

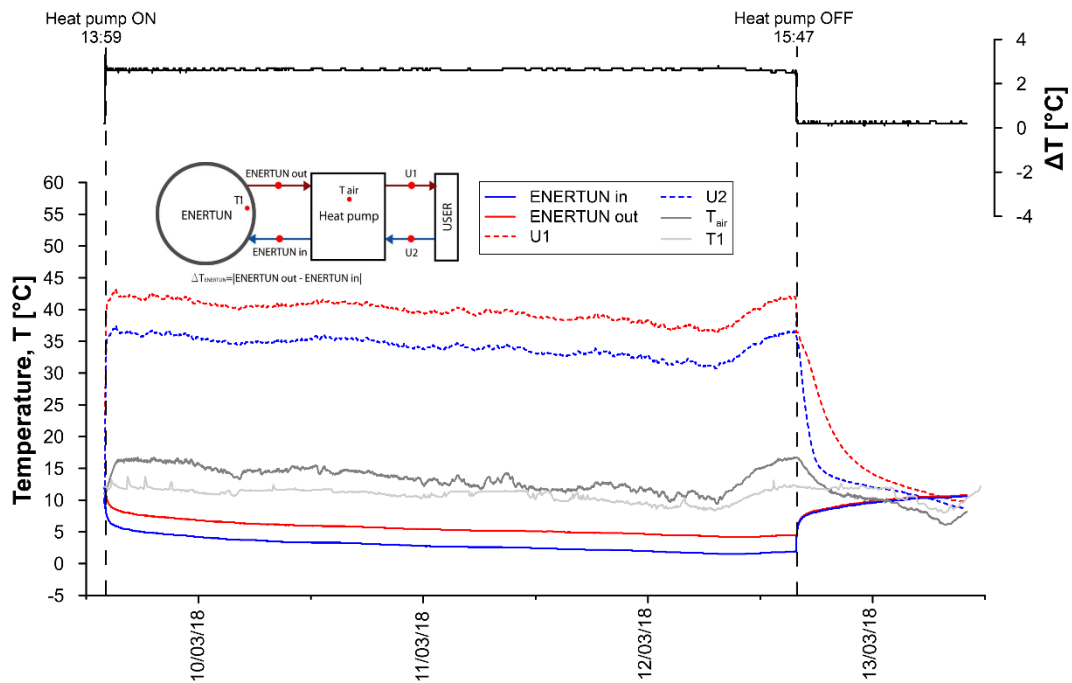


Figure A.77: Primary circuit, secondary circuit and air temperatures for test GH6.

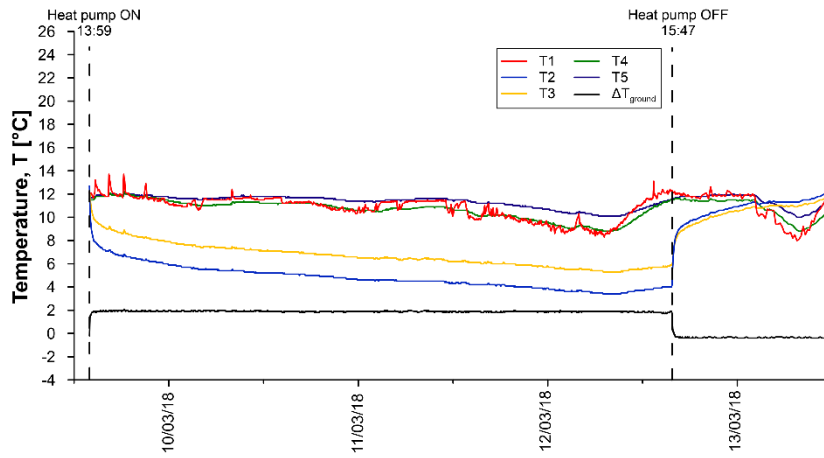


Figure A.78: Temperatures T1-T5 for test GH6.

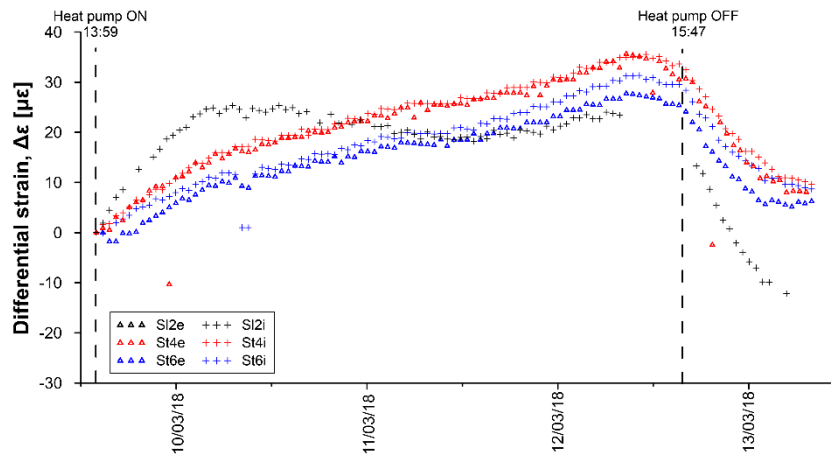


Figure A.79: Differential strains for test GH6.

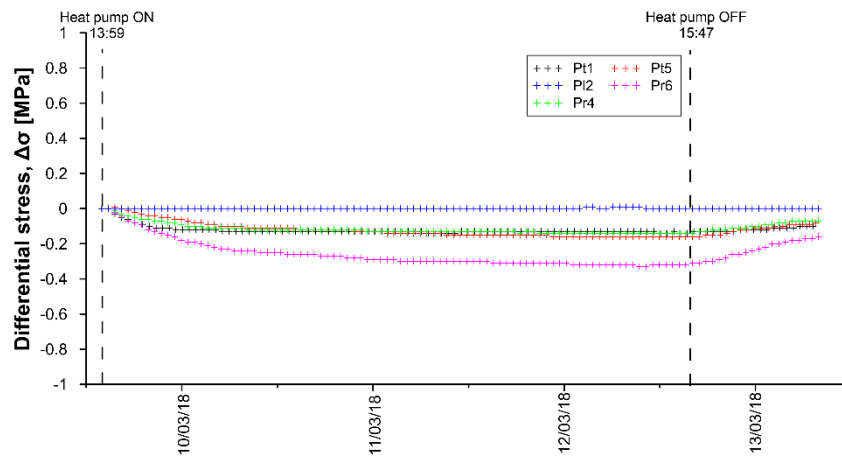


Figure A.80: Differential stresses for test GH6.

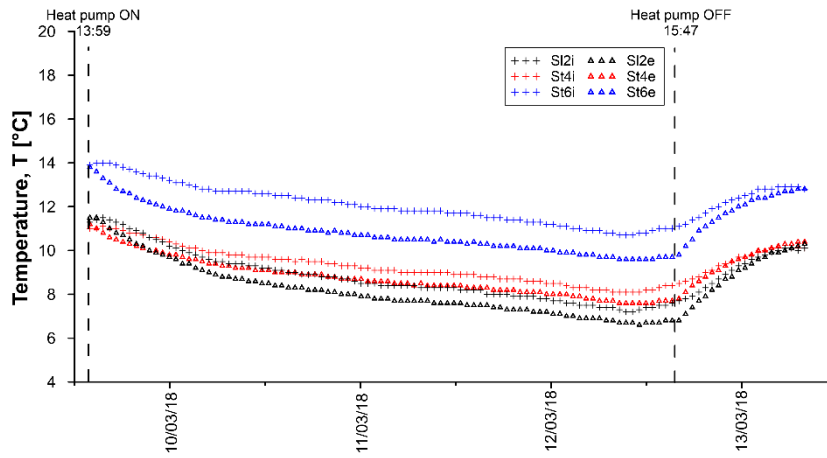


Figure A.81: Temperatures measured by VWSG for test GH6.

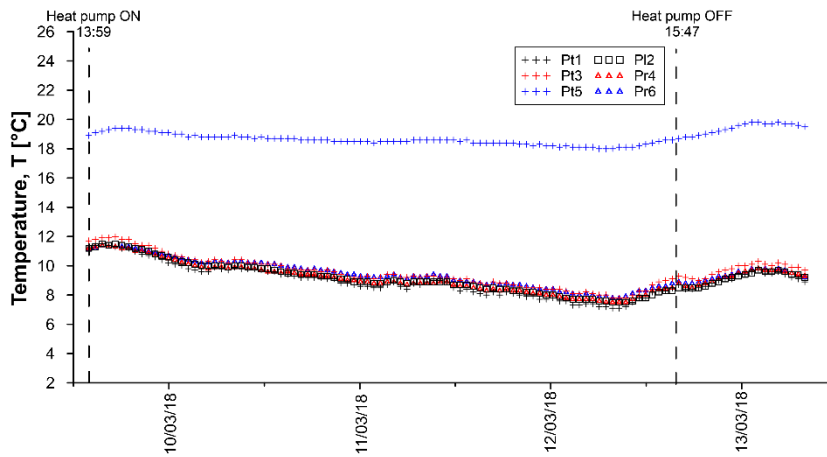


Figure A.82: Temperatures measured by PC for test GH6.

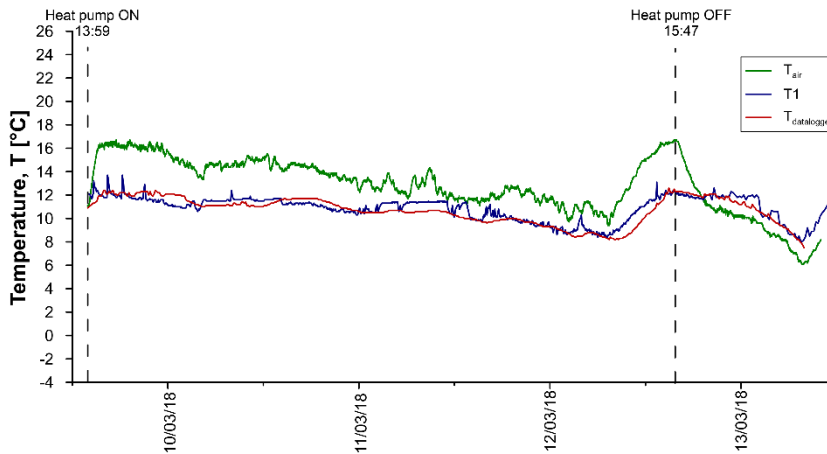


Figure A.83: Air temperatures for test GH6.

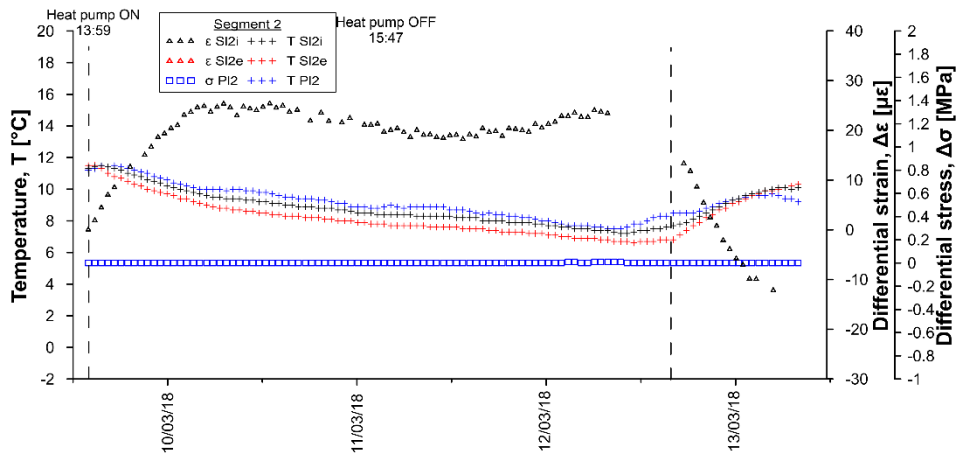


Figure A.84: Temperatures, differential strains and differential stresses in segment 2, ring 179 for test GH6.

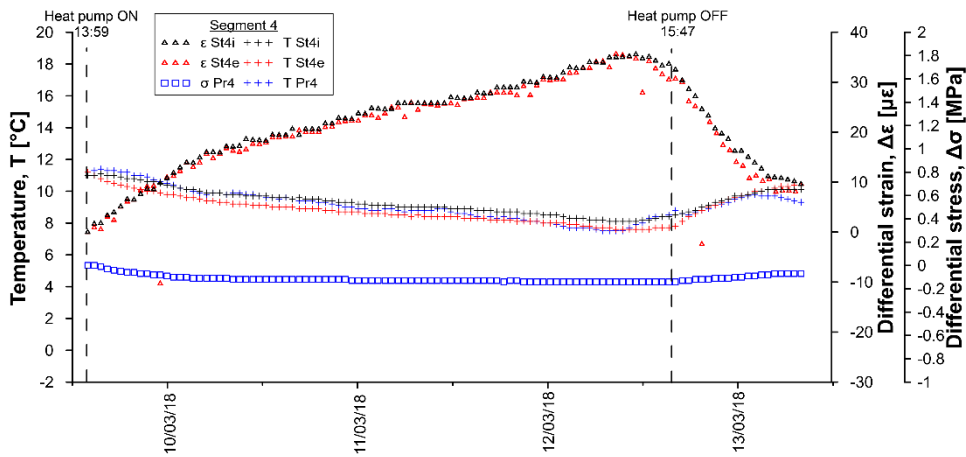


Figure A.85: Temperatures, differential strains and differential stresses in segment 4, ring 179 for test GH6.

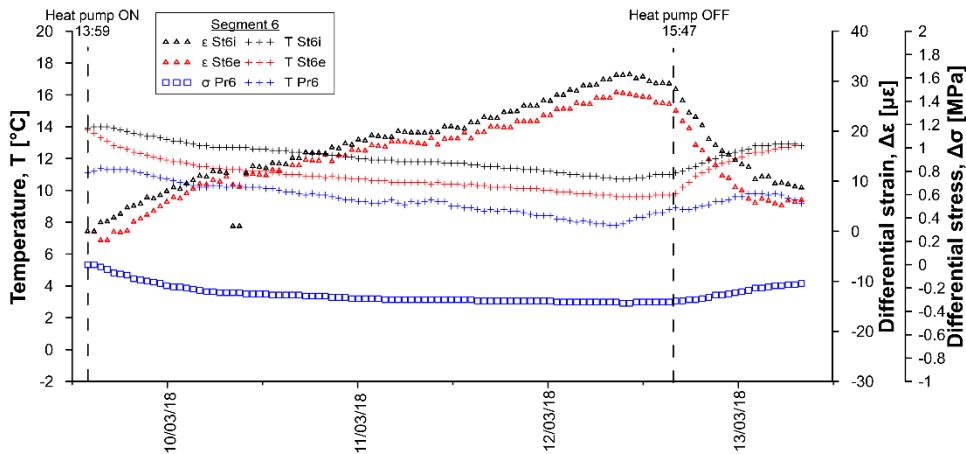


Figure A.86: Temperatures, differential strains and differential stresses in segment 6, ring 179 for test GH6.

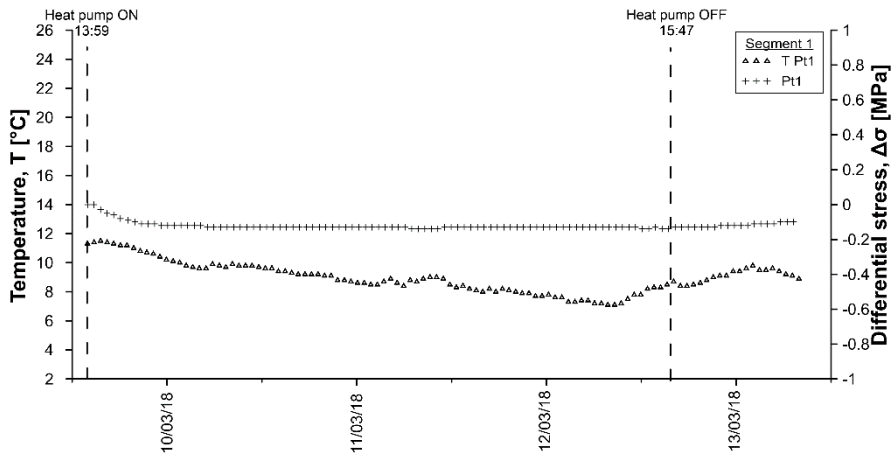


Figure A.87: Temperatures and differential stresses in segment 1, ring 179 for test GH6.

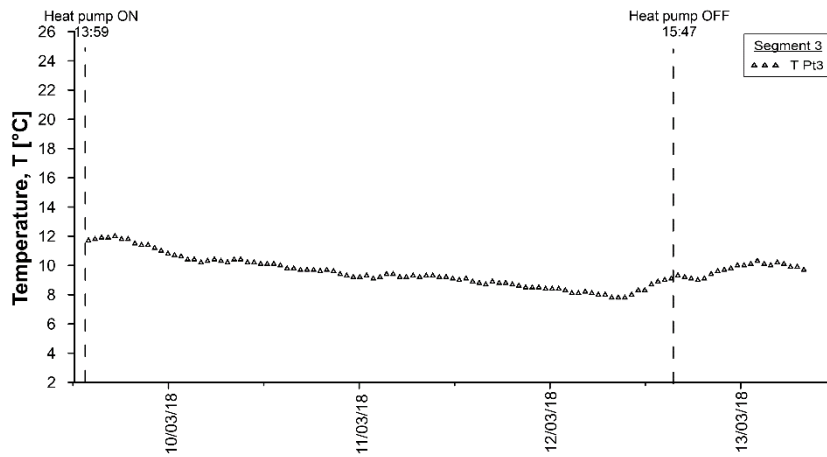


Figure A.88: Temperatures and differential stresses in segment 3, ring 179 for test GH6.

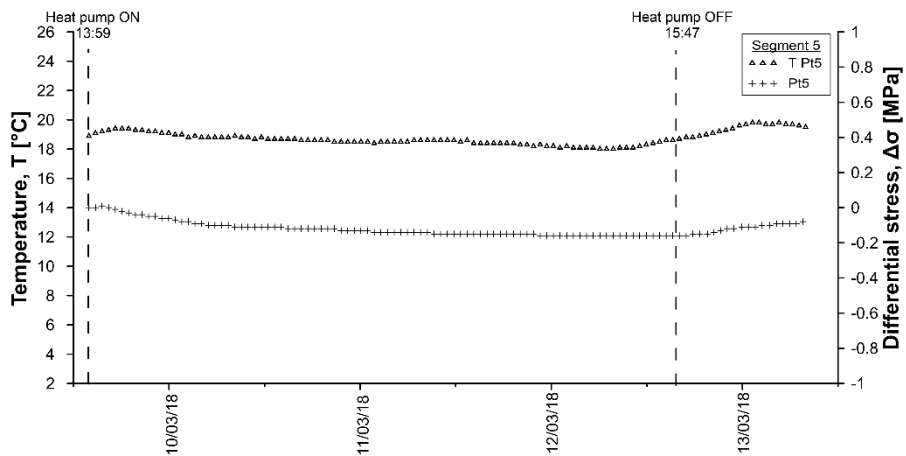


Figure A.89: Temperatures and differential stresses in segment 5, ring 179 for test GH6.

Date	T _{bl} [°C]	SI2i [μ€]	SI2i [°C]	SI2e [μ€]	SI2e [°C]	St4i [μ€]	St4i [°C]	St4e [μ€]	St4e [°C]	St6i [μ€]	St6i [°C]	St6e [μ€]	St6e [°C]
12/03/2018 04:56	8.8	-23.53	7.5	-	6.9	-0.18	8.2	-10.70	7.8	-7.44	10.9	-23.36	9.8
12/03/2018 05:56	8.6	-23.42	7.4	-	6.9	-0.27	8.2	-10.70	7.8	-7.38	10.9	-23.34	9.7
12/03/2018 06:56	8.4	-23.82	7.4	-	6.8	-0.28	8.2	-8.56	7.7	-7.50	10.8	-23.33	9.7
12/03/2018 07:56	8.3	-24.04	7.3	18.00	6.8	-0.41	8.1	-9.33	7.7	-7.82	10.8	-23.37	9.6
12/03/2018 08:56	8.3	-	7.3	-	6.7	-0.42	8.1	-10.20	7.6	-7.83	10.7	-23.53	9.6
12/03/2018 09:56	8.7	-	7.2	-	6.7	-0.32	8.0	-8.70	7.6	-7.79	10.7	-23.76	9.6
12/03/2018 10:56	9.3	-	7.3	-	6.7	0.08	8.1	-9.16	7.6	-7.40	10.8	-24.09	9.6
12/03/2018 11:56	10.1	-	7.4	-	6.7	0.56	8.2	-16.00	7.6	-6.94	10.8	-24.35	9.6
12/03/2018 12:56	10.7	-	7.4	-	6.7	1.05	8.2	-9.88	7.6	-6.54	10.9	-24.54	9.6
12/03/2018 13:56	11.4	-	7.5	-	6.7	1.54	8.3	-10.70	7.7	-5.79	11.0	-24.38	9.7
12/03/2018 14:56	12.6	-	7.6	-	6.7	1.79	8.4	-23.90	7.7	-5.96	11.0	-24.53	9.7
12/03/2018 15:56	12.3	-	7.7	-	6.8	2.13	8.5	-11.00	7.7	-5.53	11.1	-24.81	9.7
12/03/2018 16:56	12.2	-	7.8	-	7.1	1.07	8.6	-7.88	8.1	-6.83	11.2	-21.90	10.2
12/03/2018 17:56	12.1	-28.65	8.0	-	7.4	0.49	8.7	-8.06	8.5	-6.76	11.4	-19.31	10.6
12/03/2018 18:56	11.9	-29.39	8.2	-	7.8	0.25	8.9	-5.70	8.7	-6.15	11.6	-17.62	10.9
12/03/2018 19:56	12.0	-29.95	8.4	-	8.2	0.07	9.1	-5.01	8.9	-5.65	11.8	-16.43	11.2
12/03/2018 20:56	11.9	-30.31	8.7	-	8.4	0.07	9.2	-4.73	9.1	-5.52	12.0	-15.53	11.4
12/03/2018 21:56	11.6	-29.18	8.9	-	8.7	0.21	9.4	-7.76	9.3	-4.72	12.2	-14.49	11.7
12/03/2018 22:56	11.4	-29.71	9.1	-	8.9	0.20	9.5	-4.39	9.5	-4.15	12.4	-13.62	11.9
12/03/2018 23:56	11.2	-29.20	9.3	-	9.2	0.36	9.7	-4.22	9.6	-3.50	12.5	-12.86	12.0
13/03/2018 00:56	11.0	-29.01	9.5	-	9.3	0.36	9.8	-4.32	9.8	-3.36	12.6	-12.19	12.2
13/03/2018 01:56	10.7	-29.43	9.7	-	9.5	0.42	9.9	-3.63	9.9	-3.20	12.7	-11.52	12.3
13/03/2018 02:56	10.3	-	9.8	-	9.7	0.45	10.0	-3.26	10.0	-2.53	12.8	-10.61	12.4
13/03/2018 03:56	9.9	-	9.9	-	9.9	0.14	10.1	-2.92	10.1	-2.53	12.8	-9.69	12.6
13/03/2018 04:56	9.4	-	10.0	-	10.0	-0.07	10.1	-2.90	10.2	-2.50	13.0	-8.82	12.7
13/03/2018 05:56	9.1	-	10.0	-	10.1	-0.35	10.1	-2.68	10.3	-2.66	12.9	-7.72	12.7
13/03/2018 06:56	8.3	-	10.0	-	10.2	-0.81	10.1	-2.93	10.4	-3.26	12.9	-6.61	12.8
13/03/2018 07:56	7.5	-	10.1	-	10.3	-1.38	10.1	-2.66	10.4	-4.70	12.8	-5.93	12.8

Table A.26: Data sheet for test GH6 – stresses and temperatures.

Date	Pt1 [MPa]	Pt1 [°C]	Pl2 [MPa]	Pl2 [°C]	Pt3 [MPa]	Pt3 [°C]	Pr4 [MPa]	Pr4 [°C]	Pt5 [MPa]	Pt5 [°C]	Pr6 [MPa]	Pr6 [°C]
09/03/2018 13:56	0	11.3	0	11.2	-	11.7	0	11.2	0	18.9	0	11.1
09/03/2018 14:56	-0.01	11.5	0	11.4	-	11.9	0	11.4	0.01	19.2	-0.01	11.3
09/03/2018 15:56	-0.04	11.4	0	11.4	-	11.9	-0.02	11.4	0.01	19.2	-0.03	11.3
09/03/2018 16:56	-0.06	11.4	0	11.6	-	12.1	-0.04	11.4	0	19.4	-0.06	11.4
09/03/2018 17:56	-0.08	11.2	0	11.4	-	11.8	-0.05	11.3	-0.01	19.4	-0.08	11.3
09/03/2018 18:56	-0.09	11.2	0	11.3	-	11.8	-0.06	11.2	-0.03	19.4	-0.09	11.3
09/03/2018 19:56	-0.1	10.9	0	11.1	-	11.5	-0.07	11	-0.04	19.3	-0.12	11.1
09/03/2018 20:56	-0.11	10.8	0	11	-	11.4	-0.07	10.9	-0.05	19.2	-0.13	11.1
09/03/2018 21:56	-0.11	10.7	0	10.9	-	11.3	-0.08	10.8	-0.05	19.2	-0.15	11
09/03/2018 22:56	-0.11	10.4	0	10.7	-	11	-0.08	10.6	-0.06	19.1	-0.16	10.8
09/03/2018 23:56	-0.12	10.2	0	10.6	-	10.8	-0.09	10.5	-0.06	19.1	-0.18	10.7
10/03/2018 00:56	-0.12	10.1	0	10.4	-	10.7	-0.1	10.3	-0.07	19	-0.19	10.5
10/03/2018 01:56	-0.12	9.9	0	10.3	-	10.5	-0.1	10.2	-0.08	18.9	-0.2	10.4
10/03/2018 02:56	-0.12	9.8	0	10.2	-	10.4	-0.1	10	-0.09	18.9	-0.2	10.4
10/03/2018 03:56	-0.12	9.6	0	10	-	10.3	-0.11	9.9	-0.09	18.8	-0.22	10.2
10/03/2018 04:56	-0.13	9.6	0	10	-	10.3	-0.11	9.8	-0.1	18.8	-0.23	10.2
10/03/2018 05:56	-0.13	9.9	0	10	-	10.4	-0.11	9.9	-0.1	18.8	-0.23	10.3
10/03/2018 06:56	-0.13	9.8	0	9.9	-	10.3	-0.11	9.9	-0.1	18.8	-0.24	10.3
10/03/2018 07:56	-0.13	9.8	0	9.9	-	10.2	-0.11	9.8	-0.1	18.8	-0.24	10.2
10/03/2018 08:56	-0.13	9.9	0	10	-	10.4	-0.12	9.9	-0.11	18.9	-0.24	10.4
10/03/2018 09:56	-0.13	9.8	0	9.9	-	10.2	-0.12	9.8	-0.11	18.8	-0.25	10.2
10/03/2018 10:56	-0.13	9.7	0	9.8	-	10.2	-0.12	9.8	-0.11	18.8	-0.25	10.2
10/03/2018 11:56	-0.13	9.6	0	9.7	-	10	-0.12	9.6	-0.11	18.7	-0.25	10.1
10/03/2018 12:56	-0.13	9.5	0	9.7	-	10	-0.12	9.6	-0.11	18.7	-0.25	10.1
10/03/2018 13:56	-0.13	9.4	0	9.7	-	10	-0.12	9.6	-0.11	18.7	-0.26	10
10/03/2018 14:56	-0.13	9.4	0	9.5	-	9.8	-0.12	9.6	-0.12	18.7	-0.26	9.9
10/03/2018 15:56	-0.13	9.3	0	9.5	-	9.7	-0.12	9.4	-0.12	18.7	-0.26	9.8
10/03/2018 16:56	-0.13	9.2	0	9.4	-	9.7	-0.12	9.4	-0.12	18.6	-0.27	9.8
10/03/2018 17:56	-0.13	9.2	0	9.4	-	9.6	-0.12	9.4	-0.12	18.6	-0.27	9.8
10/03/2018 18:56	-0.13	9.2	0	9.3	-	9.7	-0.12	9.4	-0.12	18.6	-0.27	9.7
10/03/2018 19:56	-0.13	9.1	0	9.3	-	9.7	-0.12	9.3	-0.12	18.6	-0.27	9.7
10/03/2018 20:56	-0.13	9	0	9.2	-	9.6	-0.12	9.2	-0.13	18.5	-0.28	9.5
10/03/2018 21:56	-0.13	8.8	0	9.1	-	9.4	-0.12	9.1	-0.13	18.5	-0.28	9.5
10/03/2018 22:56	-0.13	8.7	0	9	-	9.3	-0.13	9	-0.13	18.5	-0.28	9.3
10/03/2018 23:56	-0.13	8.6	0	8.9	-	9.2	-0.13	8.9	-0.13	18.4	-0.29	9.3
11/03/2018 00:56	-0.13	8.6	0	8.9	-	9.3	-0.13	8.9	-0.13	18.5	-0.29	9.3
11/03/2018 01:56	-0.13	8.5	0	8.8	-	9.1	-0.13	8.8	-0.14	18.4	-0.29	9.2
11/03/2018 02:56	-0.13	8.5	0	8.9	-	9.2	-0.13	8.8	-0.14	18.5	-0.3	9.2
11/03/2018 03:56	-0.13	8.9	0	8.9	-	9.4	-0.13	8.9	-0.14	18.5	-0.3	9.4
11/03/2018 04:56	-0.13	8.6	0	8.9	-	9.2	-0.13	8.9	-0.14	18.5	-0.3	9.2
11/03/2018 05:56	-0.13	8.4	0	8.8	-	9.2	-0.13	8.7	-0.14	18.5	-0.3	9.1
11/03/2018 06:56	-0.14	8.9	0	8.9	-	9.2	-0.13	8.8	-0.14	18.6	-0.3	9.3
11/03/2018 07:56	-0.14	8.8	0	8.9	-	9.3	-0.13	8.8	-0.14	18.5	-0.3	9.3
11/03/2018 08:56	-0.14	9	0	9	-	9.3	-0.13	8.9	-0.15	18.6	-0.3	9.4
11/03/2018 09:56	-0.14	9	0	8.9	-	9.2	-0.13	8.9	-0.15	18.6	-0.3	9.3
11/03/2018 10:56	-0.14	8.9	0	8.9	-	9.2	-0.13	8.9	-0.15	18.6	-0.3	9.3
11/03/2018 11:56	-0.13	8.5	0	8.7	-	9.1	-0.13	8.7	-0.15	18.5	-0.3	9.1
11/03/2018 12:56	-0.13	8.3	0	8.7	-	9.1	-0.13	8.5	-0.15	18.5	-0.3	8.9
11/03/2018 13:56	-0.13	8.3	0	8.7	-	9.1	-0.13	8.6	-0.15	18.5	-0.3	9
11/03/2018 14:56	-0.13	8.1	0	8.5	-	8.8	-0.13	8.4	-0.15	18.4	-0.31	8.8
11/03/2018 15:56	-0.13	8	0	8.4	-	8.7	-0.13	8.3	-0.15	18.4	-0.31	8.7
11/03/2018 16:56	-0.13	8.1	0	8.5	-	8.9	-0.13	8.4	-0.15	18.4	-0.31	8.8
11/03/2018 17:56	-0.13	8	0	8.4	-	8.8	-0.13	8.3	-0.15	18.4	-0.31	8.7
11/03/2018 18:56	-0.13	8.1	0	8.4	-	8.7	-0.13	8.4	-0.15	18.4	-0.31	8.7
11/03/2018 19:56	-0.13	8	0	8.3	-	8.6	-0.13	8.3	-0.15	18.4	-0.31	8.7
11/03/2018 20:56	-0.13	7.9	0	8.2	-	8.5	-0.14	8.2	-0.15	18.3	-0.31	8.6
11/03/2018 21:56	-0.13	8	0	8.1	-	8.6	-0.14	8.1	-0.15	18.3	-0.31	8.5
11/03/2018 22:56	-0.13	7.7	0	8	-	8.4	-0.14	8	-0.16	18.3	-0.31	8.4
11/03/2018 23:56	-0.13	7.7	0	8	-	8.4	-0.14	8	-0.16	18.2	-0.31	8.4
12/03/2018 00:56	-0.13	7.6	0	7.9	-	8.4	-0.14	7.9	-0.16	18.2	-0.32	8.3
12/03/2018 01:56	-0.13	7.6	0	7.8	-	8.3	-0.14	7.8	-0.16	18.2	-0.32	8.2
12/03/2018 02:56	-0.13	7.4	0	7.7	-	8.1	-0.14	7.7	-0.16	18.1	-0.32	8.1
12/03/2018 03:56	-0.13	7.4	0	7.8	-	8.2	-0.14	7.7	-0.16	18.1	-0.32	8.1

Date	Pt1 [MPa]	Pt1 [°C]	Pl2 [MPa]	Pl2 [°C]	Pt3 [MPa]	Pt3 [°C]	Pr4 [MPa]	Pr4 [°C]	Pt5 [MPa]	Pt5 [°C]	Pr6 [MPa]	Pr6 [°C]
12/03/2018 04:56	-0.13	7.4	0	7.7	-	8.1	-0.14	7.7	-0.16	18.1	-0.32	8
12/03/2018 05:56	-0.13	7.3	0.01	7.6	-	8	-0.14	7.6	-0.16	18	-0.32	8
12/03/2018 06:56	-0.13	7.2	0.01	7.6	-	8	-0.14	7.5	-0.16	18	-0.32	7.9
12/03/2018 07:56	-0.13	7.1	0.01	7.5	-	7.8	-0.14	7.5	-0.16	18	-0.32	7.8
12/03/2018 08:56	-0.13	7.2	0.01	7.5	-	7.8	-0.14	7.5	-0.16	18	-0.32	7.8
12/03/2018 09:56	-0.13	7.3	0.01	7.5	-	7.8	-0.14	7.6	-0.16	18.1	-0.33	8
12/03/2018 10:56	-0.14	7.8	0	7.7	-	8.2	-0.14	7.9	-0.16	18.2	-0.33	8.3
12/03/2018 11:56	-0.13	7.8	0	7.8	-	8.3	-0.14	8	-0.16	18.3	-0.32	8.3
12/03/2018 12:56	-0.14	8.2	0	8.1	-	8.8	-0.14	8.4	-0.16	18.4	-0.32	8.5
12/03/2018 13:56	-0.13	8.1	0	8.2	-	8.9	-0.14	8.3	-0.16	18.5	-0.32	8.5
12/03/2018 14:56	-0.14	8.4	0	8.3	-	9.1	-0.14	8.5	-0.16	18.6	-0.32	8.7
12/03/2018 15:56	-0.14	8.7	0	8.5	-	9.3	-0.14	8.8	-0.16	18.6	-0.31	9
12/03/2018 16:56	-0.13	8.4	0	8.5	-	9.2	-0.13	8.6	-0.16	18.8	-0.31	8.8
12/03/2018 17:56	-0.13	8.4	0	8.5	-	9.1	-0.13	8.6	-0.15	18.8	-0.3	8.8
12/03/2018 18:56	-0.13	8.5	0	8.5	-	9	-0.12	8.7	-0.15	18.9	-0.29	9
12/03/2018 19:56	-0.13	8.7	0	8.7	-	9.3	-0.12	8.9	-0.14	19	-0.28	9.1
12/03/2018 20:56	-0.13	8.9	0	8.9	-	9.6	-0.12	9	-0.14	19.2	-0.27	9.3
12/03/2018 21:56	-0.12	9.1	0	9.1	-	9.7	-0.11	9.2	-0.13	19.3	-0.26	9.3
12/03/2018 22:56	-0.12	9.3	0	9.2	-	9.9	-0.11	9.4	-0.12	19.5	-0.25	9.5
12/03/2018 23:56	-0.12	9.4	0	9.4	-	10	-0.1	9.5	-0.11	19.6	-0.24	9.6
13/03/2018 00:56	-0.12	9.5	0	9.5	-	10.1	-0.1	9.6	-0.11	19.7	-0.22	9.7
13/03/2018 01:56	-0.12	9.8	0	9.7	-	10.3	-0.09	9.7	-0.1	19.8	-0.21	9.8
13/03/2018 02:56	-0.11	9.5	0	9.6	-	10.1	-0.08	9.7	-0.1	19.7	-0.2	9.8
13/03/2018 03:56	-0.11	9.5	0	9.6	-	10.1	-0.08	9.6	-0.1	19.8	-0.19	9.8
13/03/2018 04:56	-0.11	9.6	0	9.7	-	10.3	-0.07	9.7	-0.09	19.7	-0.18	9.8
13/03/2018 05:56	-0.1	9.3	0	9.5	-	10	-0.07	9.6	-0.09	19.6	-0.17	9.6
13/03/2018 06:56	-0.1	9.2	0	9.4	-	9.9	-0.07	9.4	-0.09	19.6	-0.17	9.4
13/03/2018 07:56	-0.1	8.9	0	9.2	-	9.7	-0.07	9.3	-0.08	19.5	-0.16	9.2

Table A.27: Data sheet for test GH6 - sensors T1-T5 and heat pump.

Date	T1 [°C]	T2 [°C]	T3 [°C]	T4 [°C]	T5 [°C]	Date	T _{air} [°C]	IN [°C]	OUT [°C]	U1 [°C]	U2 [°C]
09/03/2018 13:57	12.1	12.7	12.5	11.4	11.6	09/03/2018 13:55	11.1	11.8	12	9.5	9.6
09/03/2018 14:57	12.6	7.7	9.6	11.8	11.9	09/03/2018 14:39	13.9	6.3	9	41.9	36.3
09/03/2018 15:57	11.8	7.2	9.1	11.8	11.8	09/03/2018 15:39	16.2	5.7	8.3	42.1	36.4
09/03/2018 16:57	12.1	6.9	8.9	11.9	12	09/03/2018 16:39	16.3	5.3	7.9	42.2	36.5
09/03/2018 17:57	11.9	6.7	8.7	11.8	11.9	09/03/2018 17:39	16.2	5.1	7.7	41.7	36
09/03/2018 18:57	11.9	6.6	8.5	12	12	09/03/2018 18:39	16.2	4.9	7.5	42	36.3
09/03/2018 19:57	11.7	6.4	8.4	11.8	11.9	09/03/2018 19:39	16.3	4.7	7.4	42.1	36.4
09/03/2018 20:57	12.2	6.3	8.2	11.8	11.9	09/03/2018 20:39	16.1	4.6	7.2	42.1	36.3
09/03/2018 21:57	11.6	6.2	8.1	11.7	11.8	09/03/2018 21:39	16.2	4.5	7.1	41.7	36
09/03/2018 22:57	11.4	6.1	8	11.6	11.8	09/03/2018 22:39	16.4	4.4	6.9	42	36.3
09/03/2018 23:57	11.2	5.9	7.9	11.4	11.7	09/03/2018 23:39	15.4	4.2	6.9	41	35.4
10/03/2018 00:57	11	5.8	7.7	11.3	11.6	10/03/2018 00:38	15	4.1	6.8	40.9	35.2
10/03/2018 01:57	10.9	5.7	7.6	11.2	11.6	10/03/2018 01:38	14.9	4	6.6	40.8	35.1
10/03/2018 02:57	11.3	5.6	7.6	11.1	11.6	10/03/2018 02:38	14.5	3.9	6.5	40.7	35
10/03/2018 03:57	10.7	5.5	7.5	11	11.5	10/03/2018 03:38	13.8	3.8	6.5	40.2	34.5
10/03/2018 04:57	11.5	5.5	7.5	11	11.6	10/03/2018 04:38	14.1	3.7	6.4	40.3	34.7
10/03/2018 05:57	11.5	5.5	7.4	11	11.6	10/03/2018 05:38	14.7	3.7	6.3	40.6	34.9
10/03/2018 06:57	11.5	5.4	7.4	11.1	11.7	10/03/2018 06:38	14.5	3.6	6.2	40.5	34.8
10/03/2018 07:57	12.1	5.4	7.3	11.1	11.7	10/03/2018 07:38	14.4	3.5	6.2	40.5	34.8
10/03/2018 08:57	11.6	5.4	7.3	11.3	11.8	10/03/2018 08:38	14.6	3.5	6.1	40.6	34.9
10/03/2018 09:57	11.7	5.3	7.2	11.3	11.8	10/03/2018 09:38	14.6	3.4	6.1	40.5	34.9
10/03/2018 10:57	11.5	5.2	7.2	11.3	11.8	10/03/2018 10:38	15	3.4	6	40.8	35.1
10/03/2018 11:57	11.5	5.2	7.1	11.2	11.8	10/03/2018 11:38	15	3.4	6	40.9	35.3
10/03/2018 12:57	11.6	5.2	7.1	11.2	11.8	10/03/2018 12:38	15.4	3.3	6	41.4	35.7
10/03/2018 13:57	11.7	5.2	7.1	11.2	11.8	10/03/2018 13:38	14.8	3.3	5.9	41.2	35.6
10/03/2018 14:57	11.2	5.1	7	11.2	11.7	10/03/2018 14:38	14.1	3.3	5.9	41	35.4
10/03/2018 15:57	11.2	5.1	7	11.2	11.7	10/03/2018 15:37	14.7	3.2	5.9	41.3	35.6
10/03/2018 16:57	11.3	5.1	6.9	11.2	11.7	10/03/2018 16:37	14.6	3.2	5.8	40.9	35.3
10/03/2018 17:57	11.3	5	6.9	11.2	11.7	10/03/2018 17:37	14.3	3.1	5.7	40.9	35.3
10/03/2018 18:57	11	5	6.8	11.1	11.7	10/03/2018 18:37	14.3	3.1	5.7	40.8	35.2
10/03/2018 19:57	10.9	4.9	6.8	11	11.6	10/03/2018 19:37	14	3	5.7	40.6	35
10/03/2018 20:57	10.7	4.8	6.7	10.9	11.6	10/03/2018 20:37	13.9	3	5.6	40.3	34.7
10/03/2018 21:57	10.9	4.8	6.7	10.8	11.5	10/03/2018 21:37	13.4	2.9	5.6	39.8	34.2
10/03/2018 22:57	10.6	4.7	6.6	10.7	11.4	10/03/2018 22:37	13.3	2.9	5.5	39.7	34.1
10/03/2018 23:57	10.6	4.6	6.5	10.6	11.4	10/03/2018 23:37	13.4	2.8	5.5	39.6	34
11/03/2018 00:57	10.9	4.6	6.5	10.6	11.4	11/03/2018 00:37	13.2	2.8	5.4	39.7	34
11/03/2018 01:57	10.5	4.6	6.5	10.6	11.3	11/03/2018 01:37	12.8	2.7	5.4	39.6	33.9
11/03/2018 02:57	11.3	4.6	6.5	10.5	11.4	11/03/2018 02:37	12.4	2.7	5.3	39.4	33.8
11/03/2018 03:57	11.3	4.6	6.5	10.7	11.5	11/03/2018 03:37	13.8	2.7	5.3	40.3	34.7
11/03/2018 04:57	10.8	4.5	6.4	10.8	11.5	11/03/2018 04:37	12.5	2.7	5.3	39.6	34
11/03/2018 05:57	11.3	4.5	6.4	10.7	11.5	11/03/2018 05:37	12.2	2.6	5.2	39.1	33.5
11/03/2018 08:37	11.4	4.5	6.4	10.9	11.6	11/03/2018 06:37	12.8	2.6	5.2	39.8	34.2
11/03/2018 09:37	11.4	4.5	6.3	10.9	11.6	11/03/2018 07:36	12.8	2.6	5.2	39.6	34
11/03/2018 10:37	11.4	4.5	6.4	10.9	11.6	11/03/2018 08:36	13.9	2.5	5.2	39.7	34.1
11/03/2018 11:37	10.5	4.3	6.2	10.8	11.5	11/03/2018 09:36	12.9	2.5	5.2	39.5	33.9
11/03/2018 12:37	10.8	4.4	6.2	10.6	11.5	11/03/2018 10:36	12	2.5	5.2	39.4	33.8
11/03/2018 13:37	11.1	4.4	6.2	10.6	11.5	11/03/2018 11:36	12.1	2.4	5.1	38.9	33.3
11/03/2018 14:37	9.9	4.2	6.1	10.3	11.3	11/03/2018 12:36	11.7	2.4	5.1	38.8	33.2
11/03/2018 15:37	10.1	4.2	6	10.1	11.2	11/03/2018 13:36	11.3	2.4	5.1	38.7	33.1
11/03/2018 16:37	10.2	4.2	6.1	10.2	11.2	11/03/2018 14:36	11.6	2.3	5	38.5	32.9
11/03/2018 17:37	10.5	4.2	6	10.2	11.2	11/03/2018 15:36	11.5	2.3	4.9	38.4	32.8
11/03/2018 18:37	9.9	4.1	6	10.2	11.1	11/03/2018 16:36	12	2.3	4.9	39	33.3
11/03/2018 19:37	9.9	4.1	6	10.1	11	11/03/2018 17:36	11.8	2.2	4.9	38.7	33.1
11/03/2018 20:37	9.8	4	5.9	9.9	10.9	11/03/2018 18:36	12.8	2.2	4.9	39.2	33.6
11/03/2018 21:37	9.5	4	5.9	9.8	10.9	11/03/2018 19:36	12.6	2.2	4.8	39.1	33.5
11/03/2018 22:37	9.4	3.9	5.8	9.7	10.8	11/03/2018 20:36	12.1	2.1	4.8	38.2	32.6
11/03/2018 23:37	9.4	3.9	5.7	9.6	10.7	11/03/2018 21:36	12.3	2.1	4.7	38.4	32.8
12/03/2018 00:37	9.3	3.8	5.7	9.4	10.6	11/03/2018 22:35	11.5	2	4.7	37.8	32.2
12/03/2018 01:37	9	3.7	5.7	9.3	10.5	11/03/2018 23:35	11.6	2	4.7	38.1	32.5
12/03/2018 02:37	8.8	3.6	5.5	9	10.3	12/03/2018 00:35	11.3	1.9	4.6	37.3	31.8
12/03/2018 03:37	9.6	3.6	5.5	9.2	10.4	12/03/2018 01:35	11.3	1.9	4.5	37.7	32.1
12/03/2018 04:37	9	3.6	5.5	9.2	10.4	12/03/2018 02:35	9.9	1.8	4.4	36.9	31.3
12/03/2018 05:37	8.7	3.5	5.4	9.1	10.2	12/03/2018 03:35	10.9	1.7	4.4	37.1	31.5

Date	T1 [°C]	T2 [°C]	T3 [°C]	T4 [°C]	T5 [°C]	Date	Tair [°C]	IN [°C]	OUT [°C]	U1 [°C]	U2 [°C]
12/03/2018 06:37	8.7	3.5	5.4	8.9	10.1	12/03/2018 04:35	11.4	1.7	4.4	37.4	31.9
12/03/2018 07:37	8.6	3.4	5.3	8.8	10.1	12/03/2018 05:35	10.4	1.7	4.4	36.8	31.3
12/03/2018 08:37	8.9	3.4	5.3	8.9	10.1	12/03/2018 06:35	10.5	1.6	4.3	36.8	31.2
12/03/2018 09:37	9.7	3.5	5.4	9.2	10.2	12/03/2018 07:35	10	1.5	4.2	36.8	31.3
12/03/2018 10:37	10.5	3.6	5.5	9.6	10.4	12/03/2018 08:35	11.4	1.5	4.2	37.4	31.9
12/03/2018 11:37	11	3.7	5.5	10.1	10.7	12/03/2018 09:35	12.5	1.5	4.2	38.2	32.6
12/03/2018 12:37	11.6	3.8	5.6	10.5	10.9	12/03/2018 10:35	13.6	1.6	4.2	39.4	33.8
12/03/2018 13:37	11.9	3.9	5.7	11	11.1	12/03/2018 11:35	14.9	1.6	4.2	40.2	34.6
12/03/2018 14:37	12.3	4	5.8	11.3	11.3	12/03/2018 12:35	15.3	1.7	4.3	41	35.4
12/03/2018 15:37	12.3	4	5.9	11.5	11.5	12/03/2018 13:35	16	1.8	4.3	41.5	36
12/03/2018 16:37	12.1	9	8.6	11.6	11.7	12/03/2018 14:34	16.5	1.8	4.4	41.6	36.1
12/03/2018 17:37	11.8	9.5	9.1	11.5	11.8	12/03/2018 15:34	16.7	1.9	4.4	42.1	36.6
12/03/2018 18:37	11.8	9.8	9.4	11.4	11.8	12/03/2018 16:14	16.3	6.7	6.9	35.3	32.4
12/03/2018 22:13	11.9	10.6	10.3	11.4	11.9	12/03/2018 17:14	14.1	7.8	8	31.5	20.3
13/03/2018 02:13	11.8	11.3	10.9	11.5	11.9	12/03/2018 18:14	12.6	8.2	8.4	26.4	15.4
13/03/2018 06:13	8.6	11.3	11	9.6	10.5	12/03/2018 19:14	11.7	8.6	8.7	22.3	14.1
13/03/2018 10:13	10.5	11.8	11.4	9.7	10.7	12/03/2018 20:14	11	8.8	9	19.5	13.4
						12/03/2018 21:14	10.8	9	9.3	17.4	13
						12/03/2018 22:14	10.6	9.3	9.5	15.9	12.6
						12/03/2018 23:14	10.1	9.5	9.7	14.8	12.3
						13/03/2018 00:14	10.2	9.6	9.8	13.9	12
						13/03/2018 01:14	9.9	9.8	10	13.3	11.8
						13/03/2018 02:14	9.6	9.9	10.2	12.7	11.5
						13/03/2018 03:14	8.9	10	10.2	12.2	11.2
						13/03/2018 04:14	8.6	10.2	10.4	11.8	10.9
						13/03/2018 05:14	8.2	10.3	10.5	11.4	10.5
						13/03/2018 06:13	7.2	10.3	10.6	11	10.2
						13/03/2018 07:13	6.5	10.4	10.6	10.6	9.7
						13/03/2018 08:13	6.3	10.4	10.6	10.1	9.2
						13/03/2018 09:13	7.3	10.5	10.7	9.8	8.9

Table A.28: Summary of test GH6 records.

Quantity	Unit	$x(t_0)$	$x(t_1)$	$x(t_1) - x(t_0)$	$\bar{x}(t_0, t_1)$
T _{DL}	[°C]	10.9	12.3	1.4	10.6
Sl2i	[με]	-3188.67	-331.49	-	
	[με] _{comp}	0.0	2901.10	-	
	[°C]	11.3	7.7	-3.6	8.8
Sl2e	[με]	-48666.89	-2618.44	-	
	[με] _{comp}	0.0	46105.79	-	
	[°C]	11.5	6.8	-4.7	8.1
St4i	[με]	-1770.11	-1768.00	2.11	
	[με] _{comp}	0.0	32.61	32.61	
	[°C]	11.0	8.5	-2.5	9.3
St4e	[με]	-1507.90	-1519.08	-11.18	
	[με] _{comp}	0.0	31.52	31.52	
	[°C]	11.2	7.7	-3.5	8.8
St6i	[με]	-2181.45	-2187.02	-5.57	
	[με] _{comp}	0.0	28.59	25.32	
	[°C]	13.9	11.1	-2.8	12.1
St6e	[με]	-1803.82	-1828.52	-24.70	
	[με] _{comp}	0.0	25.32	25.32	
	[°C]	13.8	9.7	-4.1	10.8
Pt1	[MPa]	0.07	-0.07	-0.14	
	[°C]	11.3	8.7	-2.6	8.9
Pl2	[MPa]	-0.04	-0.04	0.00	
	[°C]	11.2	8.5	-2.7	9.2
Pt3	[MPa]	-	-	-	
	[°C]	11.7	9.3	-2.4	9.5
Pr4	[MPa]	0.15	0.01	-0.14	
	[°C]	11.2	8.8	-2.4	9.1
Pt5	[MPa]	0.18	0.02	-0.16	
	[°C]	18.9	18.6	-0.3	18.6
Pr6	[MPa]	0.33	0.01	-0.32	
	[°C]	11.1	9.0	-2.1	9.4
T1	[°C]	12.1	12.3	0.2	10.8
T2	[°C]	10.6	4.2	-6.4	4.8
T3	[°C]	12.0	5.9	-6.1	6.7
T4	[°C]	11.4	11.5	0.1	10.7
T5	[°C]	11.7	11.6	-0.1	11.3
Air	[°C]	11.0	16.7	5.7	13.5
IN	[°C]	8.9	1.9	-7.0	2.9
OUT	[°C]	12.0	4.5	-7.5	5.6
U1	[°C]	16.4	41.5	25.1	39.8
U2	[°C]	13.0	36.2	23.2	34.2

Test GH7

In this test the valve located on the ground circuit of ring 180 was closed so as to perform the test with the sole ring 179. The air circuit was also closed.

Circuit:	Ground
Mode:	Heating
Secondary circuit temperature:	45°C
Activated rings:	179
Volumetric flow rate:	0.7 m ³ /h
Fluid velocity in primary circuit:	0.97 m/s
Starting time t_0 :	14/03/2018 14:00
Ending time t_1 :	15/03/2018 18:59
Duration:	1.21 days
Note:	The test exhibited low-pressure issues because of the primary low temperatures.

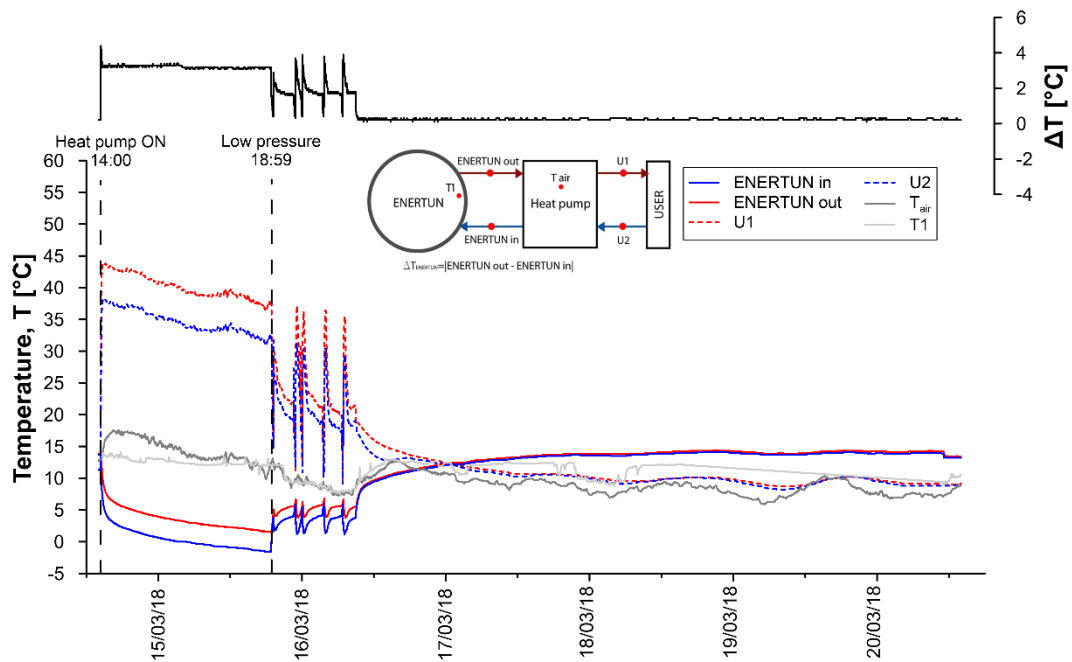


Figure A.90: Primary circuit, secondary circuit and air temperatures for test GH7.

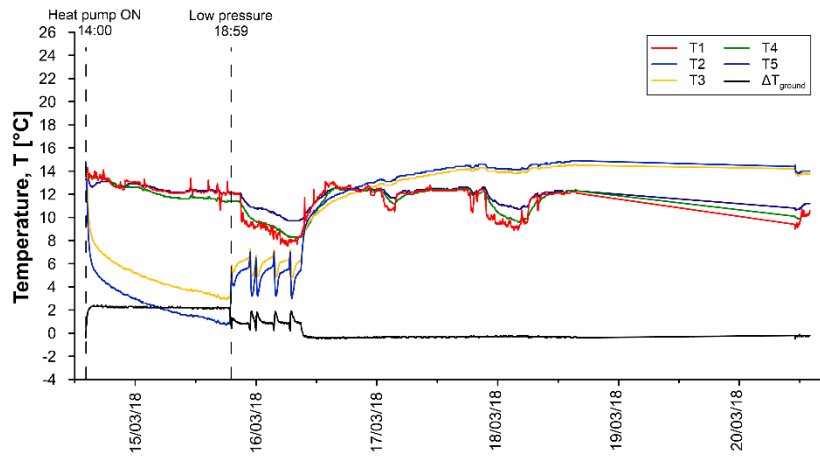


Figure A.91: Temperatures T1-T5 for test GH7.

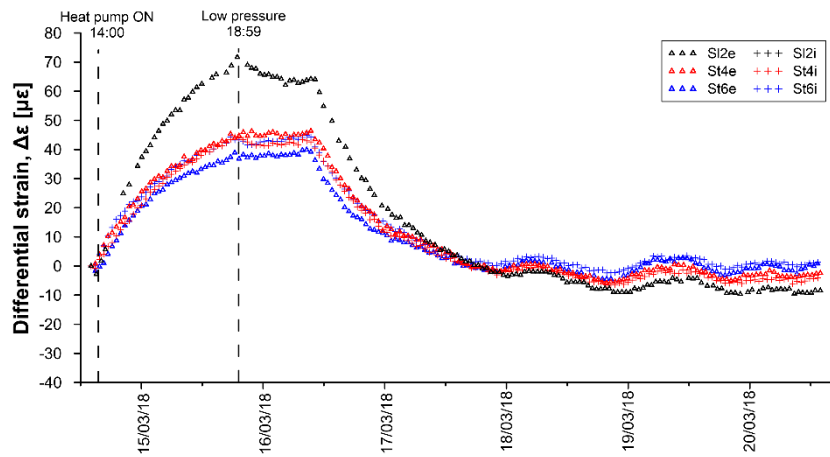


Figure A.92: Differential strains for test GH7.

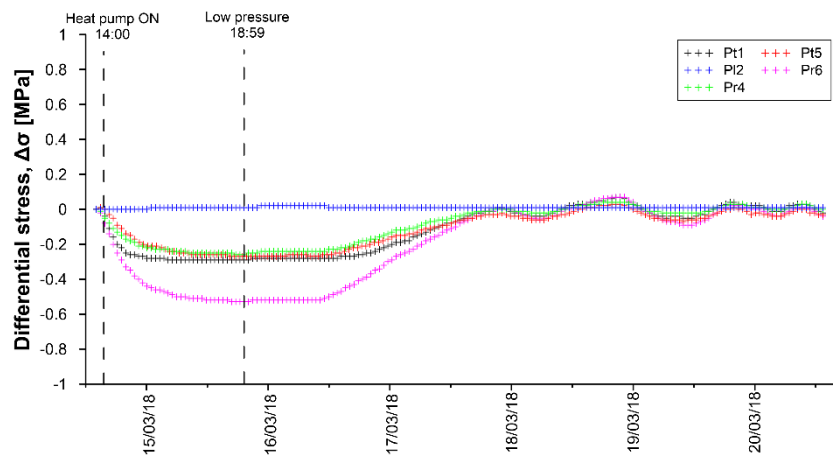


Figure A.93: Differential stresses for test GH7.

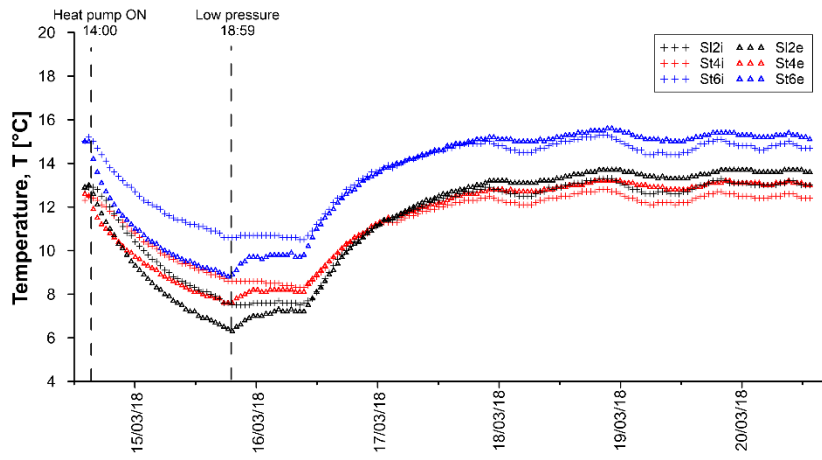


Figure A.94: Temperatures measured by VWSG for test GH7.

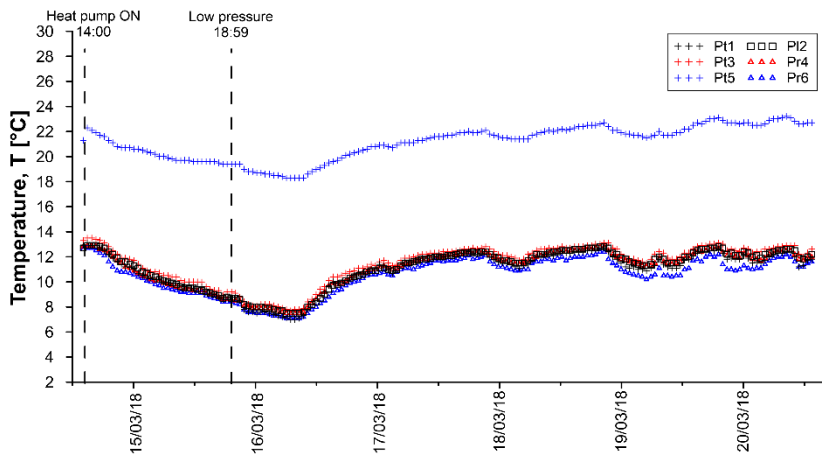


Figure A.95: Temperatures measured by PC for test GH7.

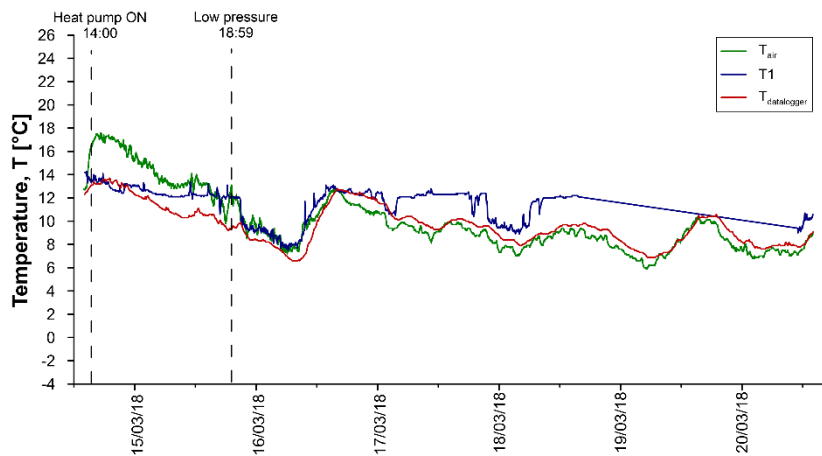


Figure A.96: Air temperatures for test GH7.

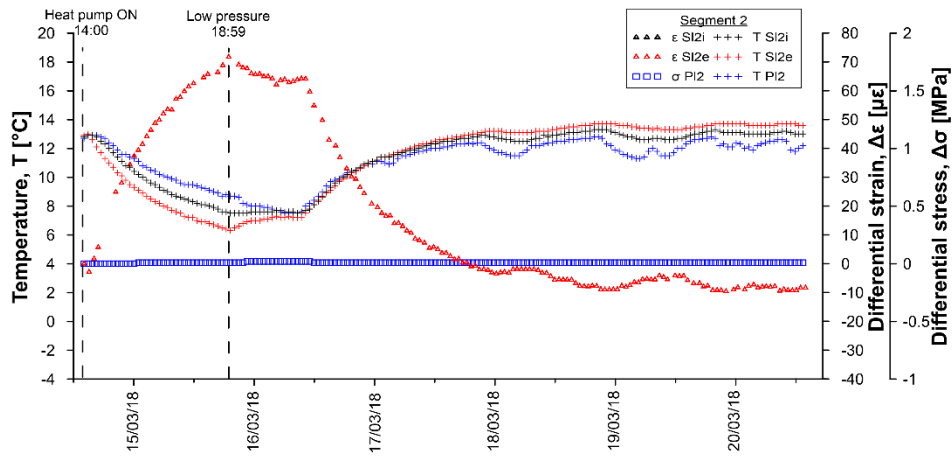


Figure A.97: Temperatures, differential strains and differential stresses in segment 2, ring 179 for test GH7.

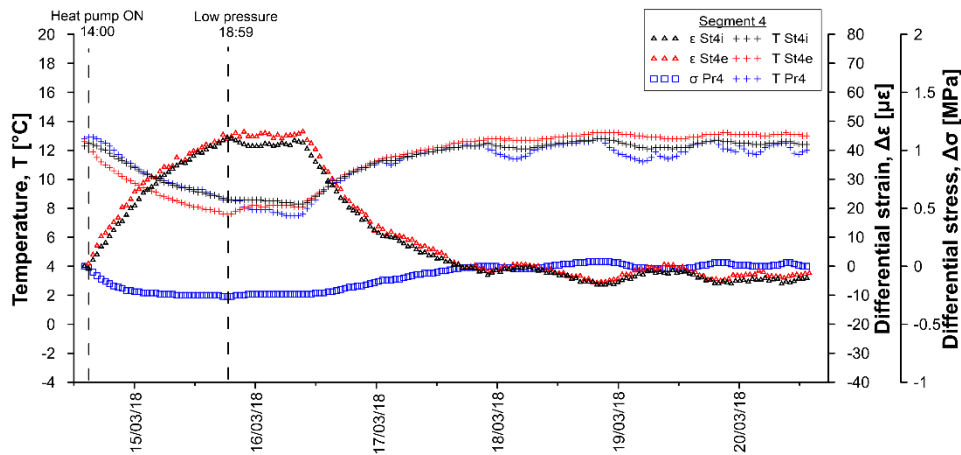


Figure A.98: Temperatures, differential strains and differential stresses in segment 4, ring 179 for test GH7.

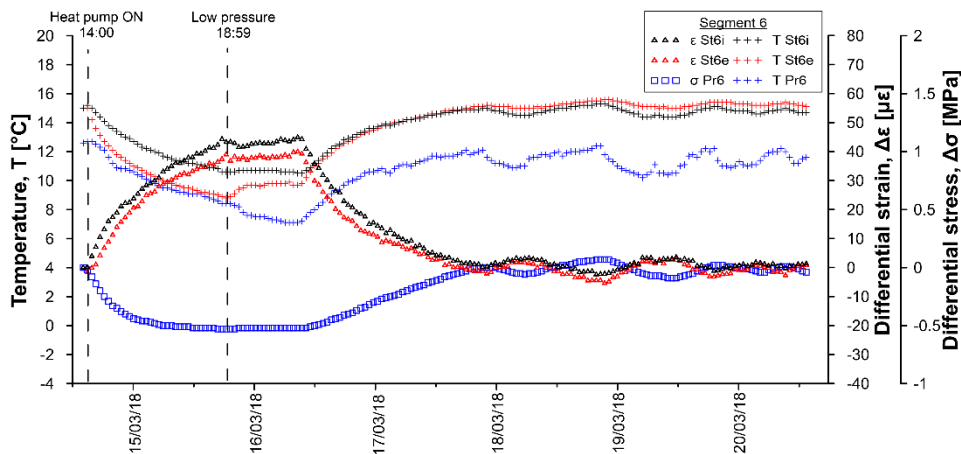


Figure A.99: Temperatures, differential strains and differential stresses in segment 6, ring 179 for test GH7.

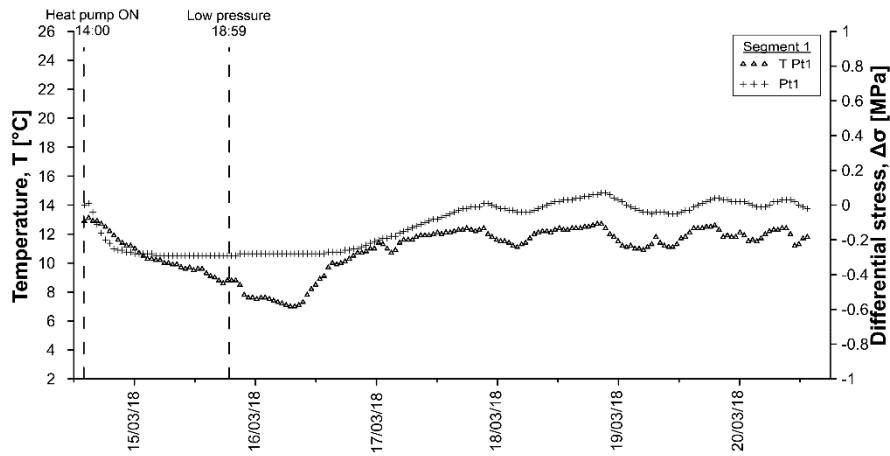


Figure A.100: Temperatures and differential stresses in segment 1, ring 179 for test GH7.

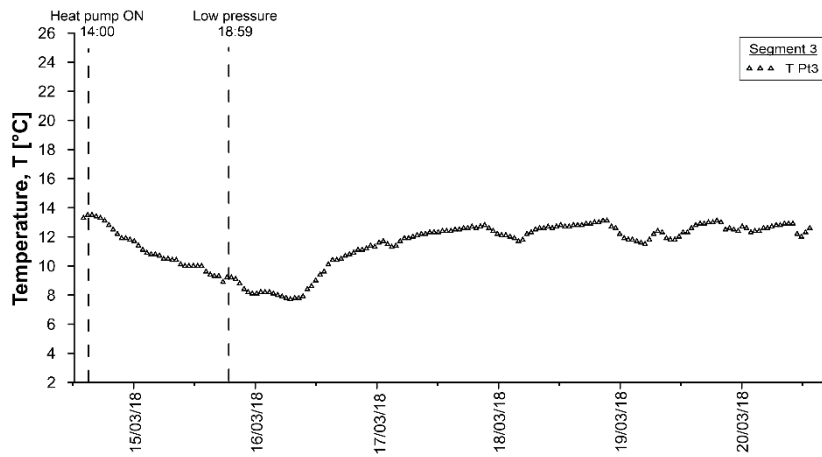


Figure A.101: Temperatures and differential stresses in segment 3, ring 179 for test GH7.

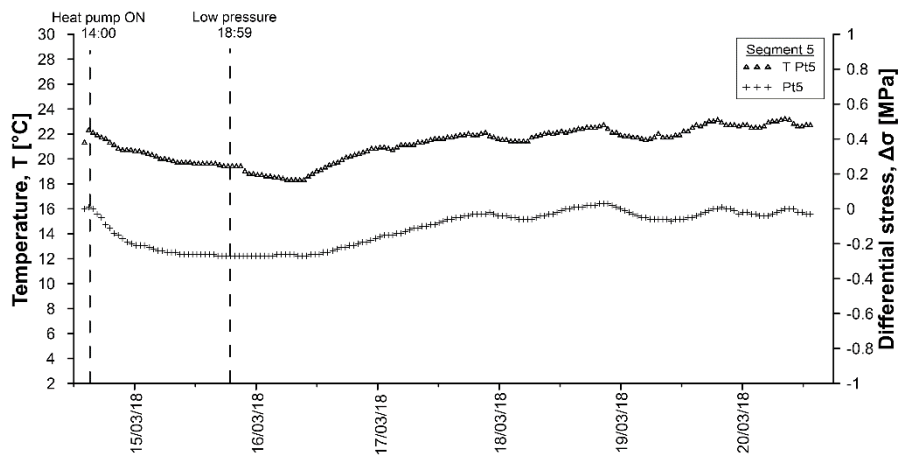


Figure A.102: Temperatures and differential stresses in segment 5, ring 179 for test GH7.

Date	T _{Di} [°C]	SI _{2i} [με]	SI _{2i} [°C]	SI _{2e} [με]	SI _{2e} [°C]	SI _{4i} [με]	SI _{4i} [°C]	SI _{4e} [με]	SI _{4e} [°C]	SI _{6i} [με]	SI _{6i} [°C]	SI _{6e} [με]	SI _{6e} [°C]
19/03/2018 20:06	9.9	-3.20	13.3	0.54	13.7	-1.20	12.7	2.30	13.1	0.09	15.1	2.19	15.4
19/03/2018 22:06	9.1	-3.55	13.1	0.16	13.7	-2.19	12.6	3.00	13.1	-1.23	14.9	2.80	15.4
20/03/2018 00:06	8.2	-6.03	13.1	0.89	13.7	-2.55	12.5	2.80	13.1	-1.72	14.8	2.76	15.3
20/03/2018 02:06	8.0	-2.55	13.0	0.67	13.7	-3.03	12.4	3.30	13.1	-2.33	14.7	3.02	15.3
20/03/2018 04:06	7.6	-4.44	12.9	0.66	13.6	-3.49	12.4	3.20	13.1	-3.25	14.6	2.97	15.2
20/03/2018 06:06	7.9	-4.38	13.0	0.68	13.6	-2.49	12.5	2.30	13.0	-1.68	14.8	2.22	15.2
20/03/2018 08:06	7.9	-3.91	13.1	0.40	13.6	-1.86	12.6	2.50	13.1	-0.75	14.9	2.12	15.3
20/03/2018 10:06	8.0	-0.89	13.2	0.55	13.7	-1.97	12.6	2.70	13.1	-0.80	14.9	2.59	15.3
20/03/2018 12:06	8.0	-0.88	13.0	0.55	13.7	-3.16	12.4	3.10	13.1	-2.64	14.7	2.76	15.2
20/03/2018 14:06	9.1	-0.29	13.0	0.03	13.6	-2.91	12.4	2.20	13.0	-2.45	14.7	1.78	15.1

Table A.30: Data sheet for test GH7 – stresses and temperatures.

Date	Pt1 [MPa]	Pt1 [°C]	Pl2 [MPa]	Pl2 [°C]	Pt3 [MPa]	Pt3 [°C]	Pr4 [MPa]	Pr4 [°C]	Pt5 [MPa]	Pt5 [°C]	Pr6 [MPa]	Pr6 [°C]
14/03/2018 14:06	0.00	12.9	0.00	12.7	-	13.3	0.00	12.8	0.00	21.3	0.00	12.6
14/03/2018 16:06	-0.07	13	0.00	12.9	-	13.4	-0.06	12.9	-0.01	22	-0.10	12.6
14/03/2018 18:06	-0.19	12.6	0.00	12.7	-	13.2	-0.12	12.5	-0.09	21.6	-0.23	12.1
14/03/2018 20:06	-0.25	11.8	0.00	12.1	-	12.4	-0.17	11.9	-0.14	21	-0.33	11.1
14/03/2018 22:06	-0.27	11.2	0.00	11.6	-	11.9	-0.20	11.3	-0.18	20.7	-0.39	10.8
15/03/2018 00:06	-0.28	11	0.00	11.3	-	11.7	-0.22	10.9	-0.20	20.6	-0.44	10.6
15/03/2018 02:06	-0.28	10.5	0.01	10.8	-	11.1	-0.23	10.5	-0.21	20.4	-0.46	10.2
15/03/2018 04:06	-0.29	10.3	0.01	10.4	-	10.8	-0.23	10.2	-0.23	20.2	-0.48	9.9
15/03/2018 06:06	-0.29	10	0.01	10.1	-	10.4	-0.24	9.8	-	19.9	-0.50	9.5
15/03/2018 08:06	-0.29	9.9	0.01	9.8	-	10.4	-0.24	9.7	-0.25	19.7	-0.51	9.4
15/03/2018 10:06	-0.29	9.6	0.01	9.5	-	10	-0.25	9.4	-0.26	19.7	-0.51	9.2
15/03/2018 12:06	-0.29	9.6	0.01	9.5	-	10	-0.25	9.3	-0.26	19.6	-0.52	9.1
15/03/2018 14:06	-0.29	9.3	0.01	9.2	-	9.7	-0.25	9.1	-0.26	19.6	-0.52	8.9
15/03/2018 16:06	-0.29	8.9	0.01	8.9	-	9.3	-0.25	8.8	-0.26	19.5	-0.53	8.7
15/03/2018 18:06	-0.29	8.5	0.01	8.7	-	8.9	-0.26	8.5	-0.27	19.4	-0.53	8.3
15/03/2018 20:06	-0.29	8.8	0.01	8.7	-	9.1	-0.25	8.5	-0.27	19.4	-0.53	8.3
15/03/2018 22:06	-0.28	7.8	0.01	8.2	-	8.3	-0.25	8.1	-0.27	18.9	-0.52	7.7
16/03/2018 00:06	-0.28	7.5	0.02	7.9	-	8.1	-0.24	7.9	-0.27	18.7	-0.52	7.5
16/03/2018 02:06	-0.28	7.6	0.02	7.9	-	8.2	-0.24	7.9	-0.27	18.6	-0.52	7.5
16/03/2018 04:06	-0.28	7.4	0.02	7.8	-	8	-0.24	7.7	-0.26	18.5	-0.52	7.4
16/03/2018 06:06	-0.28	7.1	0.02	7.5	-	7.8	-0.24	7.5	-0.26	18.3	-0.52	7.1
16/03/2018 08:06	-0.28	7.1	0.02	7.5	-	7.8	-0.24	7.5	-0.26	18.3	-0.52	7.1
16/03/2018 10:06	-0.28	7.7	0.02	7.9	-	8.4	-0.24	7.9	-0.26	18.6	-0.52	7.4
16/03/2018 12:06	-0.28	8.5	0.01	8.5	-	9	-0.23	8.6	-0.26	19	-0.50	8.1
16/03/2018 14:06	-0.28	9.6	0.01	9.2	-	10	-0.22	9.5	-0.25	19.4	-0.47	8.7
16/03/2018 16:06	-0.27	9.9	0.01	9.8	-	10.4	-0.21	9.8	-0.23	19.7	-0.44	9.3
16/03/2018 18:06	-0.26	10.2	0.01	10.2	-	10.7	-0.19	10.2	-0.21	20.1	-0.41	9.7
16/03/2018 20:06	-0.25	10.7	0.01	10.5	-	11.1	-0.17	10.7	-0.20	20.3	-0.38	10.1
16/03/2018 22:06	-0.23	10.8	0.01	10.8	-	11.3	-0.16	10.9	-0.19	20.6	-0.33	10.5
17/03/2018 00:06	-0.20	11.1	0.01	11	-	11.4	-0.13	11.1	-0.16	20.9	-0.29	10.7
17/03/2018 02:06	-0.19	11	0.01	11	-	11.5	-0.12	11.1	-0.15	20.8	-0.26	10.6
17/03/2018 04:06	-0.17	11.2	0.01	11.1	-	11.5	-0.11	11.2	-0.14	21	-0.23	10.9
17/03/2018 06:06	-0.14	11.6	0.01	11.5	-	11.9	-0.09	11.6	-0.12	21.1	-0.20	11.1
17/03/2018 08:06	-0.12	11.8	0.01	11.7	-	12.2	-0.07	11.7	-0.10	21.3	-0.17	11.3
17/03/2018 10:06	-0.10	11.9	0.01	11.9	-	12.3	-0.06	11.8	-0.09	21.4	-0.14	11.4
17/03/2018 12:06	-0.08	12.1	0.01	12	-	12.3	-0.05	12	-0.08	21.6	-0.11	11.7
17/03/2018 14:06	-0.05	12.1	0.01	12.1	-	12.4	-0.03	12.1	-0.06	21.7	-0.08	11.7
17/03/2018 16:06	-0.03	12.2	0.01	12.2	-	12.5	-0.02	12.2	-0.05	21.9	-0.05	11.9
17/03/2018 18:06	-0.02	12.4	0.01	12.3	-	12.7	-0.01	12.3	-0.04	22	-0.02	12
17/03/2018 20:06	-0.01	12.2	0.01	12.3	-	12.7	0.00	12.3	-0.03	21.8	-0.01	11.8
17/03/2018 22:06	0.01	12	0.01	12.2	-	12.6	0.00	12.1	-0.02	21.8	0.00	11.6
18/03/2018 00:06	-0.01	11.6	0.01	11.8	-	12.1	0.00	11.7	-0.04	21.5	-0.01	11.2
18/03/2018 02:06	-0.03	11.4	0.01	11.6	-	12	-0.01	11.6	-0.05	21.4	-0.03	10.9
18/03/2018 04:06	-0.04	11.1	0.01	11.5	-	11.7	-0.02	11.4	-0.06	21.3	-0.05	10.8
18/03/2018 06:06	-0.04	11.5	0.01	11.8	-	12.2	-0.02	11.6	-0.06	21.5	-0.06	11.1
18/03/2018 08:06	-0.02	12.1	0.01	12.2	-	12.6	-0.01	12.1	-0.04	21.9	-0.04	11.6
18/03/2018 10:06	0.00	12.2	0.01	12.3	-	12.6	0.00	12.3	-0.03	22	-0.01	11.7
18/03/2018 12:06	0.02	12.4	0.01	12.5	-	12.8	0.01	12.4	-0.01	22.2	0.01	12
18/03/2018 14:06	0.03	12.3	0.01	12.5	-	12.7	0.02	12.4	0.00	22.2	0.03	11.9
18/03/2018 16:06	0.04	12.4	0.01	12.6	-	12.8	0.03	12.5	0.01	22.3	0.05	12
18/03/2018 18:06	0.05	12.5	0.01	12.7	-	12.9	0.04	12.6	0.02	22.5	0.06	12.1
18/03/2018 20:06	0.06	12.7	0.01	12.8	-	13.1	0.04	12.7	0.03	22.6	0.07	12.4
18/03/2018 22:06	0.06	12.1	0.01	12.4	-	12.8	0.04	12.3	0.02	22.2	0.07	11.6
19/03/2018 00:06	0.03	11.5	0.01	11.9	-	12.1	0.02	11.8	0.00	21.9	0.03	11
19/03/2018 02:06	-0.01	11.2	0.01	11.6	-	11.8	0.00	11.5	-0.03	21.8	0.00	10.7
19/03/2018 04:06	-0.03	11	0.01	11.3	-	11.6	-0.01	11.3	-0.05	21.6	-0.04	10.4
19/03/2018 06:06	-0.05	11.2	0.01	11.6	-	12	-0.02	11.4	-0.06	21.6	-0.06	10.5
19/03/2018 08:06	-0.04	11.5	0.01	12	-	12.4	-0.02	11.7	-0.06	21.8	-0.07	10.6
19/03/2018 10:06	-0.05	11.1	0.01	11.5	-	11.8	-0.02	11.4	-0.07	21.8	-0.09	10.4
19/03/2018 12:06	-0.04	11.6	0.01	11.8	-	12.2	-0.02	11.8	-0.06	22.2	-0.08	11.2
19/03/2018 14:06	-0.03	12.1	0.01	12.3	-	12.6	-0.01	12.2	-0.05	22.5	-0.06	11.7
19/03/2018 16:06	0.01	12.3	0.00	12.5	-	12.8	0.00	12.4	-0.03	22.7	-0.03	11.6
19/03/2018 18:06	0.03	12.5	0.01	12.7	-	13	0.02	12.5	0.00	22.9	0.00	11.8

Date	Pt1 [MPa]	Pt1 [°C]	Pl2 [MPa]	Pl2 [°C]	Pt3 [MPa]	Pt3 [°C]	Pr4 [MPa]	Pr4 [°C]	Pt5 [MPa]	Pt5 [°C]	Pr6 [MPa]	Pr6 [°C]
19/03/2018 20:06	0.04	12.1	0.01	12.5	-	13	0.03	12.3	0.01	22.8	0.02	11.2
19/03/2018 22:06	0.03	11.7	0.01	12.1	-	12.4	0.02	12	-0.01	22.7	0.01	11
20/03/2018 00:06	0.02	12.1	0.01	12.4	-	12.7	0.01	12.3	-0.02	22.7	0.00	11.3
20/03/2018 02:06	0.01	11.6	0.01	11.9	-	12.2	0.01	11.7	-0.03	22.6	-0.01	11.1
20/03/2018 04:06	-0.01	11.7	0.01	12.1	-	12.5	0.00	11.9	-0.04	22.6	-0.04	11.2
20/03/2018 06:06	0.01	12.2	0.01	12.4	-	12.7	0.00	12.3	-0.03	23	-0.02	12
20/03/2018 08:06	0.02	12.4	0.01	12.6	-	12.9	0.02	12.5	0.00	23.1	0.00	12.1
20/03/2018 10:06	0.03	12	0.01	12.5	-	12.9	0.03	12.2	0.00	22.8	0.01	11.6
20/03/2018 12:06	-0.01	11.4	0.01	11.8	-	12	0.00	11.7	-0.03	22.6	-0.02	11.3
20/03/2018 14:06	-0.02	11.9	0.01	12.2	-	12.5	-0.01	12	-0.04	22.7	-0.04	11.7

Table A.31: Data sheet for test GH7 - sensors T1-T5 and heat pump.

Date	T1 [°C]	T2 [°C]	T3 [°C]	T4 [°C]	T5 [°C]	Date	Tair [°C]	IN [°C]	OUT [°C]	U1 [°C]	U2 [°C]
14/03/2018 14:09	14.2	14.8	14.4	13.5	13.3	14/03/2018 14:00	12.7	13.7	13.9	11.3	11.3
14/03/2018 15:47	13.6	5.5	7.9	13.4	12.7	14/03/2018 16:00	17	3.4	6.7	43.4	37.8
14/03/2018 17:15	13.5	4.7	7.1	13.4	13.1	14/03/2018 18:00	17.2	2.2	5.6	42.6	37
14/03/2018 18:43	13.4	4.2	6.5	13.2	13.1	14/03/2018 20:00	17.1	1.7	4.9	42.6	37
14/03/2018 20:11	12.6	3.8	6	12.9	12.8	14/03/2018 22:00	16.2	1.1	4.3	41.4	35.8
14/03/2018 21:39	12.4	3.4	5.6	12.6	12.7	15/03/2018 00:00	15.3	0.6	3.9	40.7	35.2
14/03/2018 23:07	13.1	3.1	5.4	12.6	12.9	15/03/2018 02:00	15.2	0.2	3.6	40.5	35
15/03/2018 00:35	13	2.9	5.1	12.6	12.9	15/03/2018 04:00	13.9	0	3.2	39.6	34.2
15/03/2018 02:03	12.7	2.6	4.9	12.4	12.8	15/03/2018 05:59	13.7	-0.2	2.9	39.4	34
15/03/2018 03:31	12.4	2.4	4.6	12.2	12.6	15/03/2018 07:59	12.9	-0.5	2.7	38.8	33.3
15/03/2018 04:59	12.3	2.2	4.4	12	12.4	15/03/2018 09:59	13.3	-0.7	2.4	39.2	33.7
15/03/2018 06:27	12.2	2	4.2	11.8	12.3	15/03/2018 11:59	13.5	-0.9	2.3	39.6	34.1
15/03/2018 07:55	12.1	1.8	4	11.7	12.2	15/03/2018 13:59	13.2	-1	2.1	38.7	33.3
15/03/2018 09:23	12.1	1.6	3.8	11.6	12.2	15/03/2018 15:59	12.3	-1.3	1.8	37.5	32.1
15/03/2018 10:51	12.5	1.5	3.7	11.7	12.3	15/03/2018 17:59	9.9	-1.6	1.6	36.3	30.9
15/03/2018 12:19	12.2	1.5	3.7	11.7	12.3	15/03/2018 19:59	12	2.6	4.5	25.2	22.6
15/03/2018 13:47	12.2	1.3	3.4	11.6	12.3	15/03/2018 21:58	9.3	3.8	5.5	22	19.6
15/03/2018 15:15	12.3	1.1	3.3	11.6	12.3	15/03/2018 23:58	9.8	4.8	5.3	18.5	16.8
15/03/2018 16:43	12.2	0.9	3.1	11.6	12.3	16/03/2018 01:58	9.2	3.6	5.4	22.8	20.3
15/03/2018 18:11	12.1	0.8	3	11.3	12.1	16/03/2018 03:58	8.8	1.6	4.2	35.8	30
15/03/2018 19:39	12	4.1	5.3	11.4	12.1	16/03/2018 05:58	7.4	3.8	5.6	20.4	17.9
15/03/2018 21:07	9.7	5.4	6.2	11.1	11.9	16/03/2018 07:58	7.7	3.2	5	21.2	18.6
15/03/2018 22:35	9.2	5.7	6.5	10.1	11	16/03/2018 09:58	9.4	8.2	8.4	18	16
16/03/2018 00:03	9.2	5.2	6.7	9.6	10.8	16/03/2018 11:57	10.5	9.4	9.6	16	13.6
16/03/2018 01:31	9.5	5.2	6.1	9.5	10.7	16/03/2018 13:57	11.6	10.1	10.3	14.9	12.8
16/03/2018 02:59	9.1	5.7	6.5	9.3	10.4	16/03/2018 15:57	12.7	10.7	10.9	14.3	13
16/03/2018 04:27	8.7	4.7	5.7	9	10.2	16/03/2018 17:57	11.7	11.1	11.3	13.7	13.1
16/03/2018 05:55	8	5.4	6.3	8.5	9.8	16/03/2018 19:57	11.4	11.4	11.6	13.2	12.8
16/03/2018 07:23	8	3.6	5	8.3	9.7	16/03/2018 21:57	10.8	11.7	11.9	12.8	12.5
16/03/2018 08:51	8.3	5.4	6.3	8.4	9.8	16/03/2018 23:57	10.8	12	12.2	12.5	12.1
16/03/2018 10:19	10.3	9.8	9.4	9.3	10.6	17/03/2018 01:57	9.6	12.2	12.4	12.2	11.9
16/03/2018 11:47	11.3	10.6	10.2	10.4	11.3	17/03/2018 03:56	9.5	12.4	12.6	11.7	11.3
16/03/2018 13:15	12.2	11.1	10.7	11.4	11.8	17/03/2018 05:56	9.7	12.6	12.8	11.5	11.1
16/03/2018 14:43	12.9	11.7	11.2	12.2	12.4	17/03/2018 07:56	9.1	12.8	13	11.2	10.9
16/03/2018 16:11	12.6	12	11.6	12.5	12.5	17/03/2018 09:56	8.9	12.9	13.2	11	10.6
16/03/2018 17:39	12.5	12.2	11.8	12.4	12.4	17/03/2018 11:56	9.1	13.1	13.3	10.7	10.3
16/03/2018 19:07	12.4	12.5	12.1	12.4	12.5	17/03/2018 13:56	9.9	13.3	13.5	10.7	10.4
16/03/2018 20:35	12.3	12.7	12.3	12.3	12.4	17/03/2018 15:56	9.9	13.4	13.6	10.7	10.6
16/03/2018 22:03	12.6	12.9	12.5	12.3	12.5	17/03/2018 17:56	9.4	13.5	13.7	10.7	10.6
16/03/2018 23:31	12	13	12.7	12.2	12.3	17/03/2018 19:55	8.8	13.6	13.8	10.5	10.4
17/03/2018 00:59	11.8	13.3	12.9	12.2	12.4	17/03/2018 21:55	8.6	13.7	13.9	10.5	10.3
17/03/2018 02:27	10.6	13.1	12.8	11.5	11.8	17/03/2018 23:55	7.5	13.6	13.8	10.2	10
17/03/2018 03:55	11.9	13.4	13.1	11.4	11.8	18/03/2018 01:55	7.8	13.6	13.8	9.9	9.6
17/03/2018 05:23	12.1	13.6	13.3	11.9	12.3	18/03/2018 03:55	7	13.5	13.8	9.7	9.3
17/03/2018 06:51	12	13.7	13.4	12	12.2	18/03/2018 05:55	7.9	13.5	13.8	9.5	9.1
17/03/2018 08:19	12.2	13.8	13.5	12.2	12.4	18/03/2018 07:55	8.7	13.7	13.9	9.5	9.3
17/03/2018 09:47	12.5	14	13.6	12.3	12.4	18/03/2018 09:55	8.7	13.8	14	9.6	9.5
17/03/2018 11:15	12.3	14	13.7	12.4	12.5	18/03/2018 11:54	9.1	13.9	14.1	9.8	9.7
17/03/2018 12:43	12.3	14.1	13.8	12.4	12.4	18/03/2018 13:54	9.1	13.9	14.1	9.9	9.9
17/03/2018 14:11	12.3	14.3	13.9	12.4	12.4	18/03/2018 15:54	9.2	14	14.2	10.1	10.1
17/03/2018 15:39	12.3	14.4	14	12.4	12.5	18/03/2018 17:54	8.5	14	14.3	10.1	10.1
17/03/2018 17:07	12.4	14.4	14.1	12.5	12.6	18/03/2018 19:54	8.6	14.1	14.3	10.1	10
17/03/2018 18:35	11.8	14.4	14.1	12.4	12.5	18/03/2018 21:54	7.8	14.1	14.3	10	9.9
17/03/2018 20:03	11.9	14.4	14.1	11.9	12.2	18/03/2018 23:54	7.6	14	14.2	9.8	9.6
17/03/2018 21:31	11.5	14.6	14.3	12.1	12.5	19/03/2018 01:53	6.9	13.9	14.1	9.5	9.2
17/03/2018 22:59	9.8	14.3	14	11	11.5	19/03/2018 03:53	6.6	13.8	14	9.2	8.8
18/03/2018 00:27	9.6	14.2	13.9	10.3	11.1	19/03/2018 05:53	6.2	13.7	13.9	8.9	8.4
18/03/2018 01:53	9.4	14.2	13.9	10	11	19/03/2018 07:53	7.1	13.7	14	8.7	8.2
18/03/2018 03:21	9	14.1	13.8	9.7	10.8	19/03/2018 09:53	7.4	13.7	13.9	8.7	8.3
18/03/2018 04:49	10.6	14.3	14	9.9	10.9	19/03/2018 11:53	8.3	13.7	14	8.9	8.7
18/03/2018 06:13	11.2	14.4	14.1	10.2	11.2	19/03/2018 13:53	9.4	13.8	14.1	9.3	9.2
18/03/2018 07:41	11.8	14.6	14.3	11.4	12	19/03/2018 15:53	9.9	14	14.2	9.9	9.8
18/03/2018 09:09	12	14.6	14.3	11.7	12.1	19/03/2018 17:52	9.9	14	14.3	10.1	10.2

Date	T1 [°C]	T2 [°C]	T3 [°C]	T4 [°C]	T5 [°C]	Date	Tair [°C]	IN [°C]	OUT [°C]	U1 [°C]	U2 [°C]
18/03/2018 09:52	12	14.6	14.3	11.9	12.2	19/03/2018 19:52	8.7	14.1	14.3	10.2	10.3
18/03/2018 11:02	12	14.7	14.4	12.1	12.2	19/03/2018 21:52	7.9	14	14.2	10.1	10
18/03/2018 11:24	12.1	14.7	14.4	12.1	12.3	19/03/2018 23:52	7.7	14	14.2	9.8	9.5
18/03/2018 12:25	12.1	14.8	14.5	12.2	12.3	20/03/2018 01:52	7	13.9	14.1	9.5	9.2
18/03/2018 13:53	12.1	14.8	14.5	12.3	12.3	20/03/2018 03:52	7	13.9	14.1	9.3	8.9
20/03/2018 11:11	9.2	14	13.7	10	10.6	20/03/2018 05:52	7.7	14	14.2	9.2	8.8
20/03/2018 11:55	9.4	13.9	13.7	9.9	10.7	20/03/2018 07:52	7.4	14	14.2	9.1	8.8
20/03/2018 12:39	10.4	14	13.8	10.2	11	20/03/2018 09:51	7.1	14	14.2	9.1	8.8
20/03/2018 13:23	10.1	14	13.7	10.2	11.2	20/03/2018 11:51	7.6	13.2	13.4	9	8.8
						20/03/2018 13:51	8.8	13.2	13.4	9.1	9

Table A.32: Summary of test GH7 records.

Quantity	Unit	$x(t_0)$	$x(t_1)$	$x(t_1) - x(t_0)$	$\bar{x}(t_0, t_1)$
T _{DL}	[°C]	12.3	9.3	-3.0	11.6
Sl2i	[με]	-3206.46	-331.46	-	9.8
	[με] _{comp}	0.0	2939.7	-	
	[°C]	12.8	7.5	-5.3	
Sl2e	[με]	-2611.63	-2620.48	-8.85	8.8
	[με] _{comp}	0.0	71.67	71.67	
	[°C]	12.9	6.3	-6.6	
St4i	[με]	-1767.45	-1768.08	-0.63	10.3
	[με] _{comp}	0.0	44.51	44.51	
	[°C]	12.3	8.6	-3.7	
St4e	[με]	-1507.46	-1524.20	-16.74	9.3
	[με] _{comp}	0.0	45.48	45.48	
	[°C]	12.6	7.5	-5.1	
St6i	[με]	-2179.61	-2189.14	-9.53	12.3
	[με] _{comp}	0.0	44.15	44.15	
	[°C]	15.0	10.6	-4.4	
St6e	[με]	-1799.99	-1837.88	-37.89	10.7
	[με] _{comp}	0.0	37.75	37.75	
	[°C]	15.0	8.8	-6.2	
Pt1	[MPa]	0.22	-0.07	-0.29	10.6
	[°C]	12.9	8.9	-4.0	
Pl2	[MPa]	-0.05	-0.04	0.01	10.6
	[°C]	12.7	8.8	-3.9	
Pt3	[MPa]	-	-	-	11.1
	[°C]	13.3	9.3	-4.0	
Pr4	[MPa]	0.26	0.00	-0.26	10.5
	[°C]	12.8	8.6	-4.2	
Pt5	[MPa]	0.28	0.01	-0.27	20.3
	[°C]	21.3	19.4	-1.9	
Pr6	[MPa]	0.53	-0.01	-0.54	10.1
	[°C]	12.6	8.4	-4.2	
T1	[°C]	14.1	12.1	-2.0	12.6
T2	[°C]	12.1	3.3	-8.8	2.6
T3	[°C]	13.6	4.3	-9.3	4.9
T4	[°C]	13.6	11.4	-2.2	12.2
T5	[°C]	13.4	12.2	-1.2	12.6
Air	[°C]	12.9	12.7	-0.2	14.4
IN	[°C]	9.8	1.1	-8.7	0.4
OUT	[°C]	13.9	2.2	-11.7	3.6
U1	[°C]	17.9	31.5	13.6	40.0
U2	[°C]	13.9	27.7	13.8	34.5

Test GH8

In this test the flow rate was set at $1.3 \text{ m}^3/\text{h}$, as in GH1, GH2 and GH3. However, in this case the test was prolonged for nearly 8 days.

Circuit:	Ground
Mode:	Heating
Secondary circuit temperature:	45°C
Activated rings:	179+180
Volumetric flow rate:	$1.3 \text{ m}^3/\text{h}$
Fluid velocity in primary circuit:	0.9 m/s
Starting time t_0 :	20/03/2018 14:00
Ending time t_1 :	28/03/2018 11:11
Duration:	7.82 days

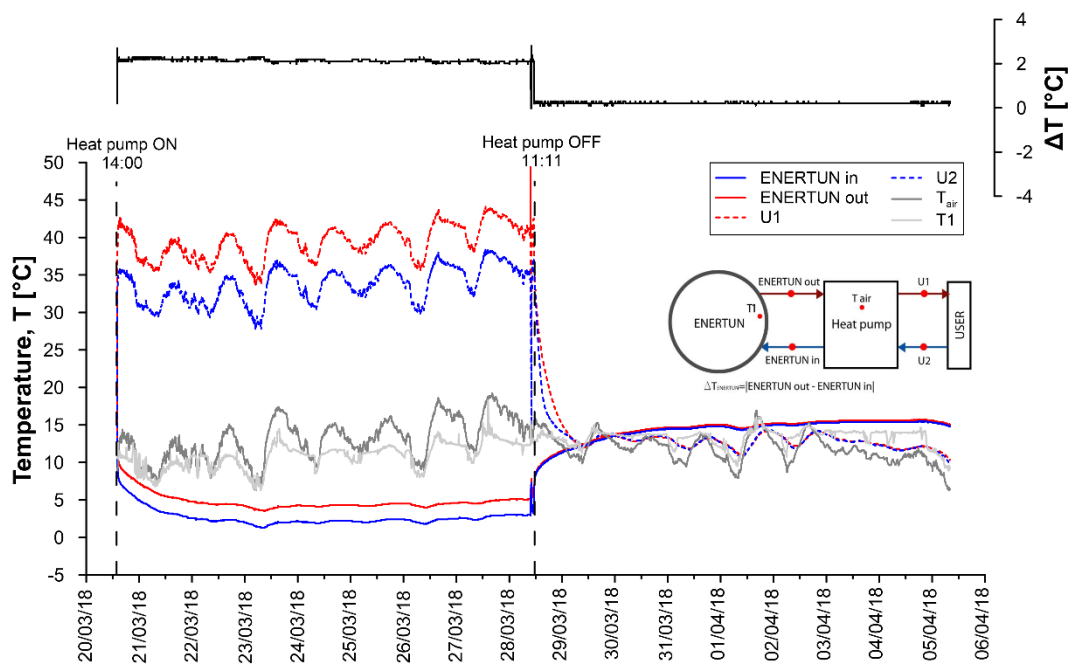


Figure A.103: Primary circuit, secondary circuit and air temperatures for test GH8.

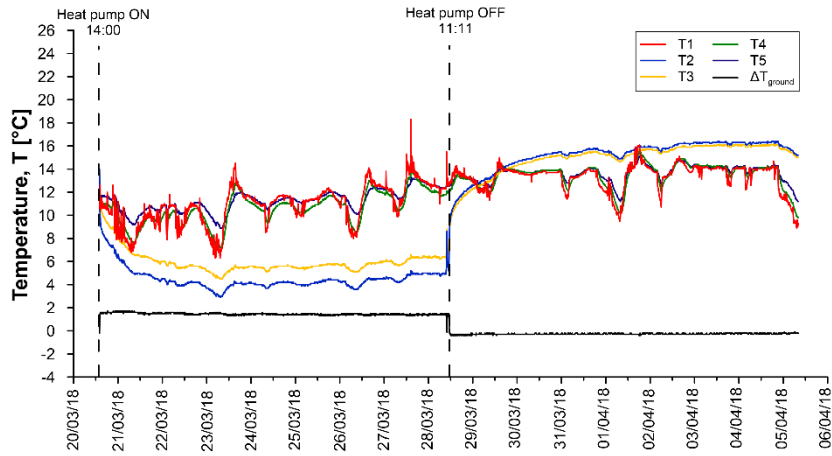


Figure A.104: Temperatures T1-T5 for test GH8.

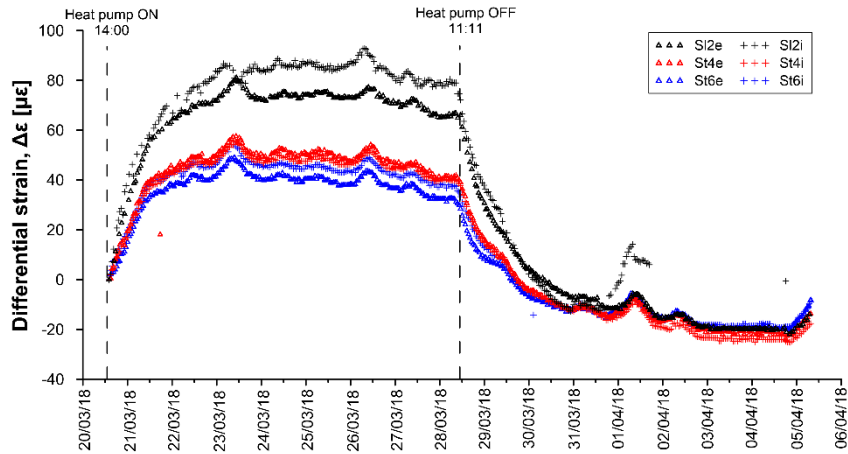


Figure A.105: Differential strains for test GH8.

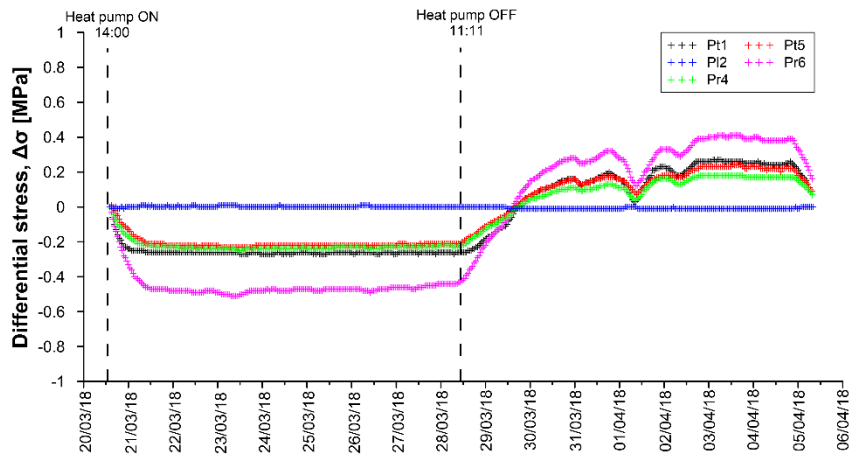


Figure A.106: Differential stresses for test GH8.

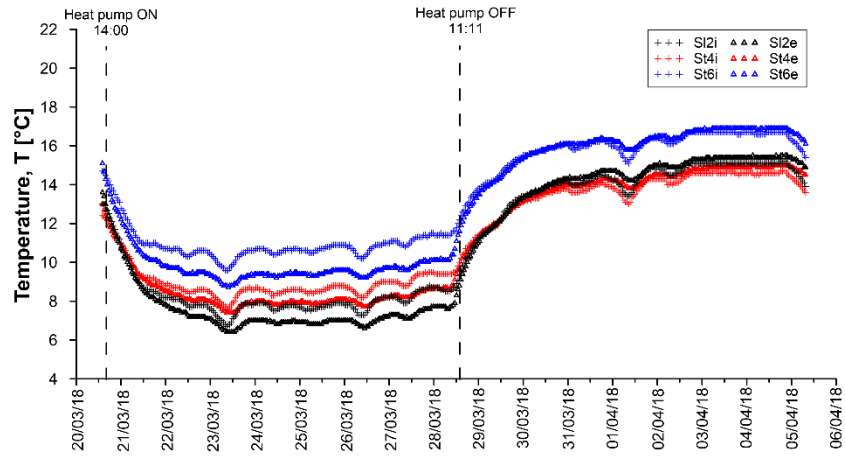


Figure A.107: Temperatures measured by VWSG for test GH8.

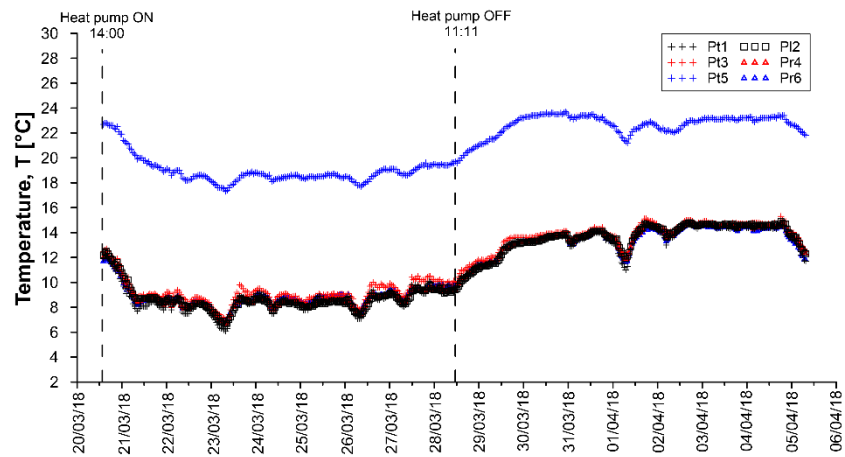


Figure A.108: Temperatures measured by PC for test GH8.

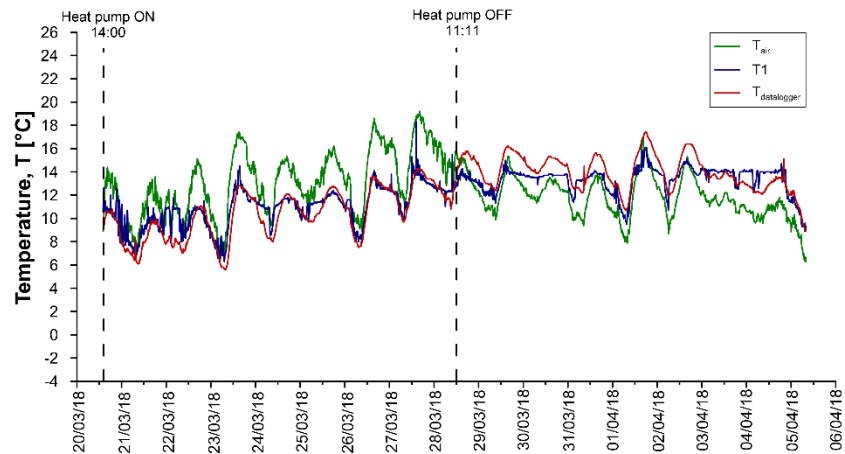


Figure A.109: Air temperatures for test GH8.

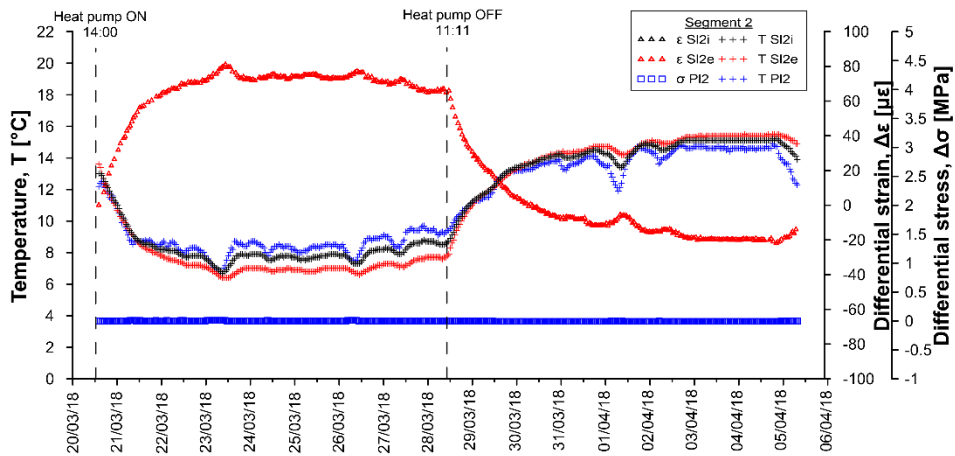


Figure A.110: Temperatures, differential strains and differential stresses in segment 2, ring 179 for test GH8.

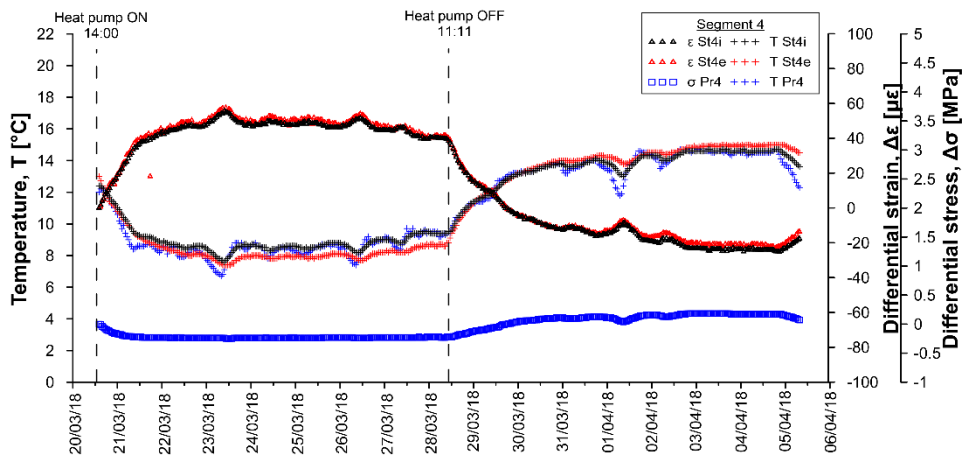


Figure A.111: Temperatures, differential strains and differential stresses in segment 4, ring 179 for test GH8.

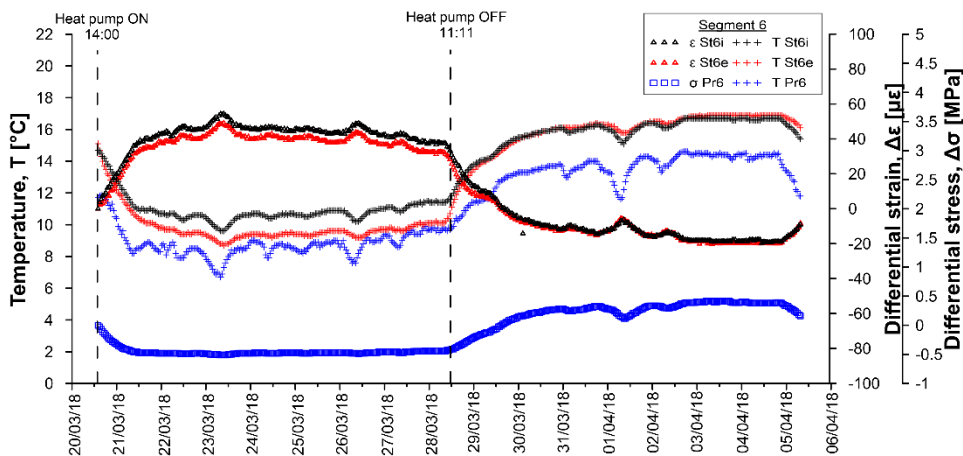


Figure A.112: Temperatures, differential strains and differential stresses in segment 6, ring 179 for test GH8.

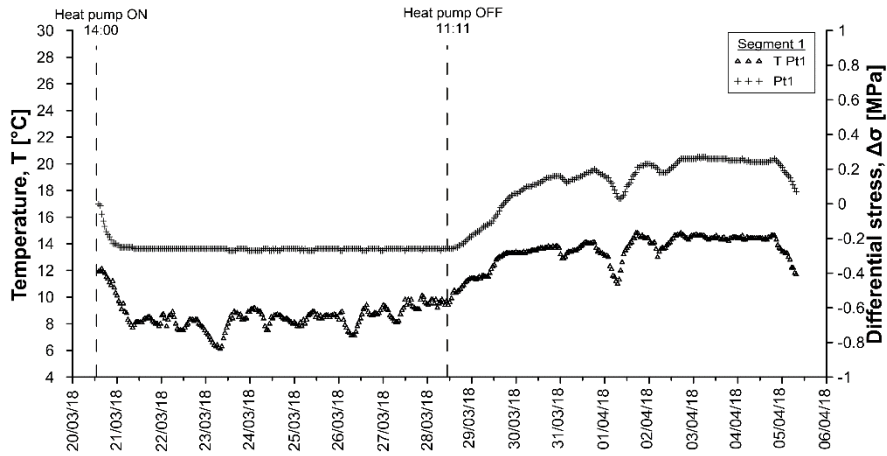


Figure A.113: Temperatures and differential stresses in segment 1, ring 179 for test GH8.

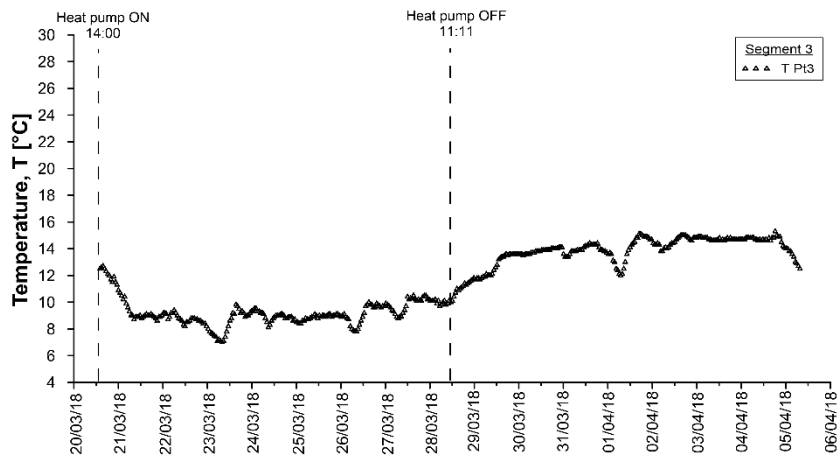


Figure A.114: Temperatures and differential stresses in segment 3, ring 179 for test GH8.

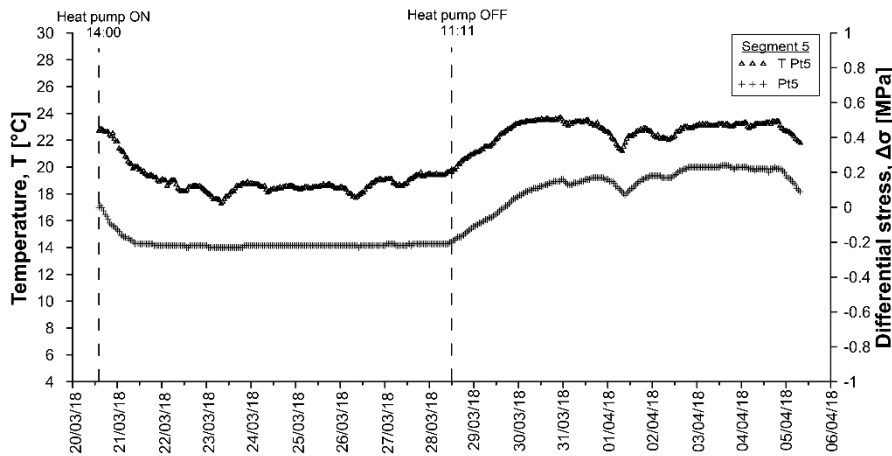


Figure A.115: Temperatures and differential stresses in segment 5, ring 179 for test GH8 .

Date	T _{DL} [°C]	SI2i [μ€]	SI2i [°C]	SI2e [μ€]	SI2e [°C]	St4i [μ€]	St4i [°C]	St4e [μ€]	St4e [°C]	St6i [μ€]	St6i [°C]	St6e [μ€]	St6e [°C]
31/03/2018 02:06	12.9	4.20	14.0	1.84	14.4	3.30	13.6	1.00	14.0	3.79	15.9	0.62	16.1
31/03/2018 06:06	12.5	2.95	14.0	1.46	14.3	3.63	13.6	0.60	13.9	4.25	15.9	0.29	16.0
31/03/2018 10:06	13.5	2.93	14.2	1.57	14.4	3.94	13.7	0.60	14.0	4.27	16.0	0.22	16.1
31/03/2018 14:06	15.4	4.21	14.4	1.57	14.6	4.46	13.9	0.20	14.2	4.99	16.2	0.06	16.3
31/03/2018 18:06	15.2	7.89	14.5	1.40	14.7	4.41	14.0	0.60	14.3	5.04	16.3	0.48	16.4
31/03/2018 22:06	13.4	12.90	14.3	1.84	14.7	3.26	13.9	1.50	14.3	3.99	16.1	1.29	16.3
01/04/2018 02:06	13.0	17.40	14.2	1.92	14.6	2.51	13.8	1.80	14.2	3.33	16.0	1.61	16.2
01/04/2018 06:06	10.9	19.90	13.6	2.05	14.4	-0.75	13.2	3.30	14.0	-0.10	15.4	2.84	15.9
01/04/2018 10:06	13.0	15.40	13.6	1.10	14.2	0.85	13.2	1.70	13.8	0.12	15.4	1.28	15.8
01/04/2018 14:06	15.8	23.10	14.2	0.93	14.4	3.67	13.8	0.60	14.0	3.58	15.9	0.48	16.0
01/04/2018 18:06	17.4	-	14.7	1.44	14.8	4.83	14.2	0.40	14.3	4.94	16.3	0.41	16.3
01/04/2018 22:06	15.9	-	14.9	1.78	15.0	4.31	14.3	1.20	14.5	5.04	16.4	0.88	16.5
02/04/2018 02:06	14.4	-	14.8	2.03	15.0	3.45	14.3	2.10	14.5	4.18	16.3	1.57	16.5
02/04/2018 06:06	12.0	-	14.5	1.29	15.0	1.99	14.0	2.80	14.5	2.83	16.1	2.11	16.4
02/04/2018 10:06	13.4	-	14.6	1.59	14.9	2.47	14.1	2.30	14.4	4.40	16.2	1.92	16.4
02/04/2018 14:06	15.9	-	14.9	1.58	15.1	3.57	14.3	1.50	14.5	5.84	16.5	1.41	16.5
02/04/2018 18:06	16.4	-	15.1	1.58	15.2	4.04	14.6	1.50	14.7	6.53	16.7	1.45	16.7
02/04/2018 22:06	15.0	-	15.1	2.05	15.3	3.47	14.6	2.00	14.8	6.10	16.7	1.91	16.8
03/04/2018 02:06	13.9	-	15.1	2.02	15.3	3.52	14.6	2.10	14.9	6.30	16.7	1.94	16.8
03/04/2018 06:06	13.7	-	15.1	2.32	15.3	3.44	14.6	2.10	14.9	6.27	16.7	1.99	16.8
03/04/2018 10:06	13.5	-	15.1	1.95	15.4	3.21	14.6	2.30	14.9	5.60	16.7	2.12	16.9
03/04/2018 14:06	13.8	-	15.1	1.99	15.4	3.25	14.7	2.30	14.9	5.72	16.8	2.15	16.9
03/04/2018 18:06	13.0	-	15.1	2.12	15.4	2.93	14.6	2.50	14.9	5.52	16.7	2.38	16.9
03/04/2018 22:06	13.1	-	15.1	2.12	15.4	3.01	14.6	2.30	15.0	5.73	16.7	2.13	16.9
04/04/2018 02:06	12.7	-	15.1	2.00	15.4	2.98	14.6	2.20	15.0	5.89	16.7	2.05	16.9
04/04/2018 06:06	12.3	-	15.1	2.08	15.4	2.63	14.6	2.40	14.9	5.07	16.6	2.35	16.9
04/04/2018 10:06	12.4	-	15.1	-	15.4	2.81	14.6	0.90	15.0	5.37	16.7	2.10	16.9
04/04/2018 14:06	13.1	-	15.1	1.54	15.4	2.81	14.6	2.30	15.0	5.20	16.7	2.13	16.9
04/04/2018 18:06	13.5	-24.7	15.2	-	15.5	-3.07	14.7	-1.9	15	-5.34	16.8	-1.93	16.9
04/04/2018 22:06	12.4	-	15.1	-2.25	15.5	-1.92	14.5	-2.9	15	-4.33	16.6	-2.7	16.8
05/04/2018 02:06	11.8	-	14.7	-1.74	15.2	-0.31	14.2	-3.5	14.8	-2.7	16.2	-3.16	16.7
05/04/2018 06:06	9.7	-	14.2	-1.65	15	1.96	13.7	-4.5	14.5	-0.5	15.6	-3.87	16.3

Table A.34: Data sheet for test GH8 – stresses and temperatures.

Date	Pt1 [MPa]	Pt1 [°C]	Pl2 [MPa]	Pl2 [°C]	Pt3 [MPa]	Pt3 [°C]	Pr4 [MPa]	Pr4 [°C]	Pt5 [MPa]	Pt5 [°C]	Pr6 [MPa]	Pr6 [°C]
20/03/2018 14:06	0	11.9	0	12.2	-	12.5	0	12	0	22.7	0	11.7
20/03/2018 18:06	-0.15	11.5	0	11.9	-	12.1	-0.1	11.8	-0.05	22.5	-0.17	11.5
20/03/2018 22:06	-0.23	11.1	0	11.5	-	11.7	-0.16	11.3	-0.11	22.4	-0.29	11.3
21/03/2018 02:06	-0.25	9.4	0	10.4	-	10.6	-0.19	10	-0.15	21.2	-0.37	9.7
21/03/2018 06:06	-0.25	8.3	0	9	-	9.2	-0.21	8.9	-0.18	20.4	-0.42	8.7
21/03/2018 10:06	-0.26	8.1	0	8.7	-	8.9	-0.22	8.5	-0.2	20	-0.46	8.4
21/03/2018 14:06	-0.26	8.3	0	8.7	-	9	-0.23	8.6	-0.21	19.6	-0.47	8.7
21/03/2018 18:06	-0.26	8.5	0	8.7	-	9	-0.23	8.7	-0.21	19.5	-0.47	8.8
21/03/2018 22:06	-0.26	7.9	0	8.5	-	8.9	-0.23	8.3	-0.22	19	-0.48	8.4
22/03/2018 02:06	-0.26	8.3	0	8.6	-	9	-0.23	8.5	-0.22	19	-0.48	8.5
22/03/2018 06:06	-0.26	8.9	0	8.7	-	9.4	-0.24	8.6	-0.22	19	-0.48	8.9
22/03/2018 10:06	-0.26	7.5	0.01	8.1	-	8.6	-0.23	7.9	-0.22	18.2	-0.49	7.9
22/03/2018 14:06	-0.26	8.2	0	8.2	-	8.6	-0.24	8.2	-0.23	18.4	-0.49	8.4
22/03/2018 18:06	-0.26	8.2	0	8.2	-	8.6	-0.24	8.3	-0.22	18.6	-0.48	8.5
22/03/2018 22:06	-0.26	7.8	0	8	-	8.4	-0.24	8	-0.22	18.4	-0.48	8.2
23/03/2018 02:06	-0.26	7	0.01	7.4	-	7.7	-0.24	7.4	-0.23	17.9	-0.5	7.5
23/03/2018 06:06	-0.26	6.4	0.01	6.9	-	7.2	-0.24	6.9	-0.23	17.5	-0.5	7
23/03/2018 10:06	-0.26	7.1	0.01	7.1	-	7.6	-0.24	7.2	-0.23	17.7	-0.51	7.4
23/03/2018 14:06	-0.26	8.5	0	8.3	-	9.2	-0.24	8.5	-0.23	18.2	-0.49	8.3
23/03/2018 18:06	-0.26	8.6	0	8.6	-	9.3	-0.24	8.6	-0.23	18.6	-0.48	8.5
23/03/2018 22:06	-0.26	8.4	0	8.4	-	9	-0.24	8.4	-0.22	18.9	-0.48	8.5
24/03/2018 02:06	-0.27	9.1	0	8.6	-	9.4	-0.24	8.7	-0.22	18.7	-0.48	9
24/03/2018 06:06	-0.27	8.8	0	8.4	-	9.1	-0.24	8.5	-0.22	18.5	-0.47	8.8
24/03/2018 10:06	-0.26	7.6	0	7.9	-	8.4	-0.24	7.8	-0.22	18.4	-0.48	7.9
24/03/2018 14:06	-0.26	8.5	0	8.4	-	9	-0.24	8.4	-0.22	18.4	-0.48	8.7
24/03/2018 18:06	-0.26	8.4	0	8.3	-	8.8	-0.24	8.4	-0.22	18.5	-0.47	8.6
24/03/2018 22:06	-0.26	8.2	0	8.3	-	8.7	-0.23	8.3	-0.22	18.5	-0.47	8.5
25/03/2018 02:06	-0.26	7.8	0	8	-	8.4	-0.24	8.1	-0.22	18.3	-0.47	8.3
25/03/2018 06:06	-0.27	8.1	0	8.1	-	8.7	-0.24	8.1	-0.22	18.5	-0.48	8.3
25/03/2018 10:06	-0.27	8.9	0	8.4	-	9.1	-0.24	8.5	-0.22	18.5	-0.47	8.9
25/03/2018 14:06	-0.26	8.6	0	8.4	-	9	-0.24	8.7	-0.22	18.6	-0.47	8.8
25/03/2018 18:06	-0.26	8.6	0	8.5	-	9.1	-0.23	8.8	-0.22	18.6	-0.47	8.9
25/03/2018 22:06	-0.26	8.7	0	8.5	-	9.1	-0.23	8.7	-0.22	18.4	-0.47	9
26/03/2018 02:06	-0.26	8.7	0	8.4	-	9	-0.23	8.6	-0.22	18.5	-0.47	8.9
26/03/2018 06:06	-0.26	7.3	0.01	7.6	-	8	-0.23	7.7	-0.22	17.9	-0.48	7.9
26/03/2018 10:06	-0.26	7.8	0	7.7	-	8.3	-0.24	7.8	-0.23	17.9	-0.49	8.2
26/03/2018 14:06	-0.27	9.1	0	8.7	-	9.7	-0.24	8.9	-0.22	18.5	-0.48	8.9
26/03/2018 18:06	-0.26	8.7	0	8.8	-	9.5	-0.23	8.8	-0.22	18.8	-0.47	8.9
26/03/2018 22:06	-0.26	8.7	0	8.9	-	9.5	-0.23	8.9	-0.22	19.1	-0.46	8.9
27/03/2018 02:06	-0.26	9.1	0	9	-	9.7	-0.23	9.1	-0.21	19.1	-0.46	9.3
27/03/2018 06:06	-0.26	8.2	0	8.4	-	8.9	-0.23	8.5	-0.22	18.7	-0.46	8.7
27/03/2018 10:06	-0.27	8.9	0	8.7	-	9.3	-0.24	8.8	-0.22	18.7	-0.47	9.1
27/03/2018 14:06	-0.26	9.4	0	9.3	-	10.2	-0.23	9.4	-0.21	19.2	-0.46	9.4
27/03/2018 18:06	-0.26	9.1	0	9.4	-	10.1	-0.23	9.2	-0.21	19.4	-0.45	9.4
27/03/2018 22:06	-0.26	9.8	0	9.6	-	10.4	-0.22	9.6	-0.21	19.4	-0.45	9.8
28/03/2018 02:06	-0.26	9.8	0	9.4	-	10.1	-0.22	9.5	-0.21	19.4	-0.44	9.8
28/03/2018 06:06	-0.26	9.4	0	9.2	-	9.7	-0.23	9.2	-0.21	19.4	-0.44	9.5
28/03/2018 10:06	-0.26	9.8	0	9.4	-	10.2	-0.22	9.5	-0.21	19.8	-0.43	9.9
28/03/2018 14:06	-0.25	10.3	0	9.9	-	10.8	-0.2	10.2	-0.18	19.9	-0.39	10.2
28/03/2018 18:06	-0.24	10.6	0	10.5	-	11.2	-0.17	10.6	-0.16	20.5	-0.32	10.7
28/03/2018 22:06	-0.2	11.3	0	11	-	11.6	-0.14	11.2	-0.12	20.9	-0.24	11.2
29/03/2018 02:06	-0.17	11.4	0	11.2	-	11.8	-0.11	11.4	-0.1	21.1	-0.18	11.4
29/03/2018 06:06	-0.14	11.6	0	11.5	-	12	-0.09	11.6	-0.07	21.5	-0.13	11.6
29/03/2018 10:06	-0.11	11.9	0	11.7	-	12.2	-0.07	11.9	-0.05	21.8	-0.09	11.9
29/03/2018 14:06	-0.05	12.9	-0.01	12.6	-	13.3	-0.03	12.7	-0.02	22.3	-0.01	12.7
29/03/2018 18:06	0.01	13.2	-0.01	13	-	13.5	0	13	0.01	22.8	0.06	13
29/03/2018 22:06	0.05	13.4	-0.01	13.2	-	13.6	0.03	13.2	0.05	23.2	0.12	13.2
30/03/2018 02:06	0.07	13.3	-0.01	13.2	-	13.6	0.05	13.2	0.08	23.3	0.16	13.3
30/03/2018 06:06	0.1	13.4	-0.01	13.3	-	13.6	0.06	13.3	0.1	23.4	0.19	13.3
30/03/2018 10:06	0.11	13.5	-0.01	13.5	-	13.8	0.07	13.5	0.11	23.6	0.22	13.5
30/03/2018 14:06	0.13	13.7	-0.01	13.7	-	13.9	0.09	13.6	0.13	23.5	0.24	13.6
30/03/2018 18:06	0.15	13.7	-0.01	13.7	-	14	0.1	13.7	0.14	23.5	0.26	13.7
30/03/2018 22:06	0.16	13.8	-0.01	13.9	-	14.1	0.11	13.8	0.15	23.6	0.28	13.8

Date	Pt1 [MPa]	Pt1 [°C]	PI2 [MPa]	PI2 [°C]	Pt3 [MPa]	Pt3 [°C]	Pr4 [MPa]	Pr4 [°C]	Pt5 [MPa]	Pt5 [°C]	Pr6 [MPa]	Pr6 [°C]
31/03/2018 02:06	0.13	13	-0.01	13.2	-	13.4	0.1	13.2	0.14	23.3	0.26	13
31/03/2018 06:06	0.14	13.4	-0.01	13.6	-	13.8	0.1	13.5	0.14	23.3	0.26	13.4
31/03/2018 10:06	0.15	13.7	-0.01	13.8	-	13.9	0.11	13.7	0.15	23.3	0.27	13.6
31/03/2018 14:06	0.18	14.1	-0.01	14.1	-	14.4	0.12	14.1	0.16	23.4	0.3	14.1
31/03/2018 18:06	0.19	14	-0.01	14.1	-	14.3	0.13	14.1	0.17	23.2	0.32	14
31/03/2018 22:06	0.17	13.2	-0.01	13.6	-	13.7	0.12	13.5	0.16	22.7	0.3	13.4
01/04/2018 02:06	0.15	12.9	-0.01	13.4	-	13.5	0.11	13.3	0.15	22.2	0.27	13.1
01/04/2018 06:06	0.06	11.2	0	12.1	-	12.1	0.06	11.9	0.1	21.4	0.17	11.7
01/04/2018 10:06	0.05	13.2	-0.01	13.3	-	13.5	0.05	13.2	0.08	22	0.13	13.1
01/04/2018 14:06	0.14	14	-0.01	14.1	-	14.5	0.1	13.9	0.12	22.4	0.21	13.8
01/04/2018 18:06	0.21	14.7	-0.01	14.7	-	15.1	0.14	14.6	0.16	22.8	0.28	14.3
01/04/2018 22:06	0.23	14.4	-0.01	14.5	-	14.8	0.16	14.5	0.18	22.8	0.33	14.3
02/04/2018 02:06	0.22	14	-0.01	14.3	-	14.3	0.16	14.1	0.18	22.2	0.33	14
02/04/2018 06:06	0.18	13.7	-0.01	13.9	-	14.1	0.13	13.8	0.17	22.2	0.3	13.7
02/04/2018 10:06	0.19	14	-0.01	14.2	-	14.3	0.14	14.1	0.17	22.3	0.3	13.9
02/04/2018 14:06	0.23	14.6	-0.01	14.7	-	14.9	0.16	14.6	0.2	22.6	0.34	14.5
02/04/2018 18:06	0.26	14.7	-0.01	14.8	-	15	0.18	14.7	0.22	23	0.39	14.6
02/04/2018 22:06	0.26	14.5	-0.01	14.6	-	14.8	0.18	14.6	0.23	23	0.39	14.4
03/04/2018 02:06	0.27	14.6	-0.01	14.7	-	14.9	0.18	14.6	0.23	23.2	0.4	14.5
03/04/2018 06:06	0.27	14.6	-0.01	14.7	-	14.8	0.18	14.6	0.23	23.1	0.41	14.5
03/04/2018 10:06	0.26	14.4	-0.01	14.6	-	14.7	0.18	14.5	0.23	23.1	0.4	14.4
03/04/2018 14:06	0.26	14.4	-0.01	14.6	-	14.6	0.18	14.6	0.24	23.2	0.41	14.4
03/04/2018 18:06	0.26	14.3	-0.01	14.6	-	14.8	0.18	14.4	0.23	23	0.4	14.2
03/04/2018 22:06	0.25	14.5	-0.01	14.6	-	14.8	0.17	14.6	0.23	23.3	0.39	14.5
04/04/2018 02:06	0.26	14.5	-0.01	14.7	-	14.8	0.17	14.6	0.23	23.3	0.4	14.5
04/04/2018 06:06	0.24	14.4	-0.01	14.6	-	14.8	0.17	14.4	0.22	23	0.38	14.1
04/04/2018 10:06	0.24	14.4	-0.01	14.6	-	14.7	0.17	14.5	0.22	23.2	0.38	14.4
04/04/2018 14:06	0.24	14.3	-0.01	14.6	-	14.6	0.17	14.5	0.22	23.3	0.38	14.4
04/04/2018 18:06	0.25	14.7	-0.01	15	-	15.3	0.17	14.8	0.23	23.5	0.39	14.5
04/04/2018 22:06	0.23	13.7	-0.01	14	-	14.3	0.16	13.9	0.21	22.8	0.37	13.6
05/04/2018 02:06	0.17	13.2	0	13.5	-	13.7	0.13	13.4	0.16	22.5	0.29	13.1
05/04/2018 06:06	0.11	12.1	0	12.6	-	12.9	0.09	12.6	0.11	21.9	0.2	12

Table A.35: Data sheet for test GH8 - sensors T1-T5 and heat pump.

Date	T1 [°C]	T2 [°C]	T3 [°C]	T4 [°C]	T5 [°C]	Date	Tair [°C]	IN [°C]	OUT [°C]	U1 [°C]	U2 [°C]
20/03/2018 13:59	10.6	14	13.8	10.4	11.2	20/03/2018 14:00	8.9	13.2	13.4	9.00	9
20/03/2018 16:07	10.9	8.3	9.9	10.9	11.7	20/03/2018 18:00	13.3	6.4	8.6	40.90	34.9
20/03/2018 18:15	12	7.9	9.4	11.2	11.7	20/03/2018 22:00	12.3	5.5	7.7	39.50	33.5
20/03/2018 20:23	10.1	7.3	8.9	10.6	11.4	21/03/2018 01:59	8.7	4.6	6.8	36.40	30.3
20/03/2018 22:31	11.5	7	8.6	11	11.4	21/03/2018 05:59	8.1	4	6.2	36.20	30.1
21/03/2018 00:39	8.4	6.2	7.9	9.6	10.6	21/03/2018 09:59	8.9	3.4	5.6	36.70	30.7
21/03/2018 02:35	8.5	5.9	7.6	8.9	10	21/03/2018 13:59	12.3	3.2	5.4	39.50	33.7
21/03/2018 04:43	7.7	5.6	7.2	8.5	9.8	21/03/2018 17:58	13.2	3	5.2	39.90	34.1
21/03/2018 06:51	7.3	5.2	6.8	7.9	9.4	21/03/2018 21:58	10.1	2.7	4.9	37.10	31.2
21/03/2018 08:59	7.6	5	6.6	7.7	9.2	22/03/2018 01:58	9.5	2.5	4.7	36.40	30.5
21/03/2018 11:39	8.8	5	6.5	8.6	10	22/03/2018 05:58	10.8	2.4	4.6	36.70	30.8
21/03/2018 13:47	9.8	5	6.5	9.2	10.3	22/03/2018 09:57	9.3	2.2	4.4	36.50	30.7
21/03/2018 15:55	10.1	4.9	6.4	9.7	10.6	22/03/2018 13:57	13.6	2.3	4.4	39.60	33.9
21/03/2018 18:03	10.1	4.8	6.3	10	10.8	22/03/2018 17:57	14.5	2.3	4.4	40.30	34.6
21/03/2018 20:11	8.9	4.5	6	9.5	10.4	22/03/2018 21:57	11.3	2.1	4.3	38.00	32.2
21/03/2018 22:19	8.9	4.4	5.9	9.4	10.4	23/03/2018 01:56	9.4	1.8	4	35.80	30
22/03/2018 00:27	10.9	4.5	6	10	10.8	23/03/2018 05:56	8	1.4	3.7	34.60	28.7
22/03/2018 02:35	8	4	5.6	9.5	10.4	23/03/2018 09:56	12.9	1.4	3.6	38.70	33
22/03/2018 04:39	10.9	4.3	5.8	10.1	10.9	23/03/2018 13:56	16.8	1.9	4	42.30	36.6
22/03/2018 06:47	10.9	4.3	5.8	10.4	11	23/03/2018 17:55	16.7	2	4.1	41.50	35.9
22/03/2018 08:55	10	4	5.5	9.3	10.4	23/03/2018 21:55	14.3	2.1	4.2	40.70	35
22/03/2018 11:03	9	4	5.5	9	10.2	23/03/2018 01:55	11.9	2.1	4.2	38.10	32.4
22/03/2018 13:11	10.2	4.1	5.6	9.5	10.5	24/03/2018 05:55	10.4	2	4.2	36.80	31
22/03/2018 15:19	10.8	4.2	5.7	10.3	10.8	24/03/2018 09:54	10.6	1.9	4.1	38.00	32.2
22/03/2018 17:27	10.9	4.2	5.6	10.6	11	24/03/2018 13:54	14.6	2.1	4.2	41.00	35.3
22/03/2018 19:35	10.5	4.2	5.6	10.5	11.1	24/03/2018 17:54	14.4	2.2	4.3	40.70	35.1
22/03/2018 21:43	9.4	3.9	5.4	9.9	10.8	24/03/2018 21:54	13.3	2.2	4.3	39.70	34
22/03/2018 23:51	8.4	3.7	5.2	9.3	10.4	25/03/2018 01:53	11.9	2.1	4.3	38.40	32.7
23/03/2018 01:59	7.8	3.5	5	8.5	9.9	25/03/2018 06:53	11.8	2	4.2	37.90	32.1
23/03/2018 04:07	6.7	3.3	4.8	7.8	9.5	25/03/2018 10:53	12.9	2.1	4.2	39.40	33.7
23/03/2018 06:15	6.8	3.1	4.6	7.4	9.3	25/03/2018 14:52	15.2	2.3	4.4	41.70	36
23/03/2018 08:23	7.5	3	4.5	7.3	8.9	25/03/2018 18:52	15.5	2.4	4.5	41.70	36.1
23/03/2018 10:29	10.7	3.6	5	9.2	9.8	25/03/2018 22:52	14	2.4	4.5	40.70	34.9
23/03/2018 12:33	12.6	3.9	5.2	11.1	10.7	26/03/2018 02:52	13.4	2.3	4.5	39.60	33.9
23/03/2018 14:41	14.1	4.1	5.4	12.1	11.4	26/03/2018 06:51	10.2	2	4.2	36.60	30.8
23/03/2018 16:49	12.7	4.1	5.5	12.5	11.9	26/03/2018 10:51	12.3	1.9	4	39.00	33.3
23/03/2018 18:57	12.3	4.1	5.5	12	12	26/03/2018 14:51	17.5	2.3	4.4	43.20	37.5
23/03/2018 21:05	11.5	4.1	5.5	11.4	11.8	26/03/2018 18:51	16.9	2.4	4.5	42.40	36.7
23/03/2018 23:13	11.6	4.2	5.6	11.2	11.6	26/03/2018 22:50	16.2	2.5	4.6	41.80	36.1
24/03/2018 01:21	11.2	4.1	5.5	10.9	11.5	27/03/2018 02:50	16	2.6	4.7	41.30	35.6
24/03/2018 03:29	11	4	5.5	10.7	11.3	27/03/2018 06:50	12.3	2.4	4.6	39.00	33.2
24/03/2018 05:37	10.8	4	5.5	10.4	11	27/03/2018 10:50	14.5	2.4	4.5	41.30	35.6
24/03/2018 07:45	8.8	3.8	5.3	10.1	10.9	27/03/2018 14:49	18.6	2.8	4.8	43.70	38
24/03/2018 09:51	10.4	3.8	5.2	9.5	10.6	27/03/2018 18:49	17.7	2.9	4.9	43.10	37.4
24/03/2018 11:59	11.1	4	5.5	10.4	11	27/03/2018 22:49	17.3	3	5	42.80	37.1
24/03/2018 14:07	11.5	4.1	5.5	10.8	11.2	28/03/2018 02:49	16.5	3	5.1	41.80	36.1
24/03/2018 16:15	11.7	4.2	5.6	11	11.4	28/03/2018 06:48	13.3	2.9	5	40.10	34.4
24/03/2018 18:23	11.6	4.2	5.6	11.1	11.5	28/03/2018 10:08	14.8	7.3	7.5	17.40	17.1
24/03/2018 20:31	11.6	4.2	5.6	11	11.5	28/03/2018 14:08	14.8	9.4	9.6	25.90	22
24/03/2018 22:39	11.5	4.2	5.6	10.9	11.5	28/03/2018 18:07	14.1	10.4	10.6	19.80	16
25/03/2018 00:47	9.9	4	5.4	10.3	11.2	28/03/2018 22:07	12.6	11.1	11.3	16.20	14.5
25/03/2018 04:15	11.2	4	5.5	10.3	11.2	29/03/2018 02:07	11.6	11.6	11.8	14.10	13.7
25/03/2018 06:23	11.2	4	5.5	10.4	11.2	29/03/2018 06:07	10.8	11.9	12.1	12.70	12.9
25/03/2018 08:31	11.3	4.1	5.5	10.7	11.3	29/03/2018 10:06	10.8	12.2	12.5	12.10	12.3
25/03/2018 10:39	11.4	4.2	5.6	10.8	11.4	29/03/2018 14:06	14.1	12.7	12.9	12.60	12.8
25/03/2018 12:47	11.4	4.2	5.6	11	11.5	29/03/2018 18:06	14.1	13.1	13.3	13.50	13.8
25/03/2018 14:55	12.1	4.3	5.7	11.4	11.7	29/03/2018 22:06	13.2	13.4	13.6	13.60	13.8
25/03/2018 17:03	12.2	4.4	5.7	11.6	11.9	30/03/2018 02:05	11.9	13.6	13.8	13.40	13.5
25/03/2018 19:11	12.2	4.4	5.7	11.7	12	30/03/2018 06:05	11.8	13.8	14	13.00	13.1
25/03/2018 21:19	11.6	4.4	5.8	11.5	12	30/03/2018 10:05	12.4	14	14.2	12.80	12.9
25/03/2018 23:27	11	4.3	5.7	11.2	11.8	30/03/2018 14:05	13.4	14.2	14.4	13.10	13.3
26/03/2018 01:35	11.6	4.3	5.7	10.9	11.7	30/03/2018 18:04	13	14.3	14.5	13.40	13.6
26/03/2018 03:43	9.3	4	5.5	10.5	11.3	30/03/2018 22:04	12.4	14.4	14.6	13.30	13.4

Date	T1 [°C]	T2 [°C]	T3 [°C]	T4 [°C]	T5 [°C]	Date	Tair [°C]	IN [°C]	OUT [°C]	U1 [°C]	U2 [°C]
26/03/2018 05:51	8.6	3.8	5.2	9.4	10.8	31/03/2018 02:04	10.7	14.5	14.7	13.00	13
26/03/2018 07:59	8.4	3.6	5.1	8.7	10.2	31/03/2018 06:04	10.3	14.5	14.7	12.30	12.1
26/03/2018 10:07	9.4	3.7	5.2	8.8	10.2	31/03/2018 10:03	11.2	14.5	14.7	11.90	11.8
26/03/2018 12:15	11.5	4.1	5.5	10.4	10.8	31/03/2018 14:03	13.2	14.7	14.9	12.60	12.6
26/03/2018 14:23	13.3	4.4	5.8	12.2	11.6	31/03/2018 18:03	13.3	14.8	15	13.20	13.4
26/03/2018 16:31	13.5	4.5	5.9	13	12.3	31/03/2018 22:03	10.9	14.8	15	13.00	13
26/03/2018 18:39	13	4.5	5.9	12.5	12.4	01/04/2018 02:02	10.3	14.8	15	12.40	12.2
26/03/2018 20:47	12.6	4.5	5.9	12.1	12.3	01/04/2018 06:02	8.5	14.5	14.8	11.70	11.5
26/03/2018 22:55	12.5	4.5	6	12	12.3	01/04/2018 10:02	10.6	14.3	14.6	11.00	10.8
27/03/2018 01:01	13.8	4.7	6.1	12.2	12.5	01/04/2018 14:01	14.1	14.5	14.7	12.30	12.4
27/03/2018 03:09	12.3	4.6	6	11.7	12.2	01/04/2018 18:01	15.9	14.8	15	13.80	14
27/03/2018 05:17	10.3	4.4	5.8	11.2	11.9	01/04/2018 22:01	13.5	14.9	15.1	14.20	14.4
27/03/2018 07:25	10.1	4.2	5.7	10.5	11.5	02/04/2018 02:01	12.2	15	15.2	13.80	13.8
27/03/2018 09:33	10.9	4.3	5.7	10.6	11.5	02/04/2018 06:01	9.2	14.9	15.1	12.90	12.8
27/03/2018 11:41	12.9	4.6	6	11.6	11.9	02/04/2018 10:00	11.2	14.9	15.1	12.20	11.9
27/03/2018 13:49	14.1	4.9	6.2	13.2	12.7	02/04/2018 14:00	14.3	15.1	15.3	12.90	12.9
27/03/2018 15:57	14.2	5	6.3	13.7	13.1	02/04/2018 18:00	14.2	15.2	15.4	13.90	14
27/03/2018 18:05	13.7	5	6.3	13.1	13.1	02/04/2018 22:00	12.7	15.3	15.5	14.00	14.1
27/03/2018 20:11	13.1	4.9	6.3	12.7	13	03/04/2018 01:59	11.7	15.3	15.5	13.60	13.5
27/03/2018 22:19	12.9	5	6.4	12.5	12.8	03/04/2018 05:59	11.5	15.4	15.6	13.10	12.9
28/03/2018 00:27	12.7	4.9	6.4	12.2	12.7	03/04/2018 09:59	11.2	15.4	15.6	12.80	12.8
28/03/2018 02:35	12.6	5	6.4	12	12.6	03/04/2018 13:58	11.8	15.4	15.6	12.80	12.9
28/03/2018 04:43	12.4	4.9	6.3	12	12.5	03/04/2018 17:58	11.3	15.4	15.6	12.80	12.7
28/03/2018 06:51	12.3	4.8	6.3	11.7	12.3	03/04/2018 21:58	11.1	15.4	15.6	12.50	12.3
28/03/2018 08:59	12.3	5	6.4	11.8	12.3	04/04/2018 01:58	10.6	15.4	15.6	12.30	12.2
28/03/2018 11:07	12.6	5.2	6.6	12.1	12.6	04/04/2018 05:57	10.3	15.4	15.6	11.90	11.8
28/03/2018 13:15	13.4	10.6	10.3	12.6	13	04/04/2018 09:57	10.4	15.4	15.6	11.70	11.6
28/03/2018 15:23	14.1	11.3	11	13.5	13.5	04/04/2018 13:57	10.8	15.4	15.6	11.90	11.8
28/03/2018 17:31	13.5	11.7	11.3	13.2	13.2	04/04/2018 17:57	11.6	15.5	15.7	12.10	12.1
28/03/2018 19:37	13.6	12.1	11.7	13.3	13.4	04/04/2018 21:56	10	15.4	15.6	12.00	12
28/03/2018 21:45	13.2	12.3	12	13.1	13.2	05/04/2018 01:56	10	15.3	15.5	11.60	11.4
28/03/2018 23:53	13	12.6	12.3	13	13.1	05/04/2018 05:56	7.4	15	15.2	11.00	10.6
29/03/2018 02:01	13	12.8	12.5	12.8	13						
29/03/2018 04:09	12	12.9	12.6	12.3	12.7						
29/03/2018 06:17	12.2	13.1	12.8	12.2	12.6						
29/03/2018 08:25	12.2	13.2	12.9	12.2	12.7						
29/03/2018 10:33	12.6	13.4	13.1	12.2	12.7						
29/03/2018 17:41	13.9	14.2	13.9	14.1	13.8						
30/03/2018 02:13	13.6	14.7	14.4	13.7	13.7						
30/03/2018 10:45	13.6	15.1	14.8	13.8	13.8						
30/03/2018 19:17	13.7	15.3	15.1	13.9	13.9						
31/03/2018 03:49	11.8	15.2	15	12.1	12.8						
31/03/2018 12:21	13.8	15.6	15.4	13.8	13.9						
31/03/2018 20:53	12.6	15.6	15.3	13.2	13.5						
01/04/2018 05:25	10.5	15.1	14.9	11	11.9						
01/04/2018 13:57	14	15.6	15.3	14	14						
01/04/2018 22:29	14.2	15.9	15.7	14.6	14.3						
02/04/2018 07:01	13.3	15.8	15.5	12.7	13.3						
02/04/2018 15:33	14.8	16.2	15.9	14.8	14.7						
03/04/2018 00:05	14.2	16.3	16	14.3	14.4						
03/04/2018 08:37	14	16.2	16	14.3	14.1						
03/04/2018 17:09	13.3	16.3	16.1	14.2	14.3						
04/04/2018 01:41	14.1	16.3	16.1	14.2	14.2						
04/04/2018 10:13	14	16.2	16	14	14.1						
04/04/2018 18:45	14.7	16.4	16.2	14.3	14.4						
05/04/2018 03:17	11.1	15.8	15.6	11.6	12.5						

Table A.36: Summary of test GH8 records.

Quantity	Unit	$x(t_0)$	$x(t_1)$	$x(t_1) - x(t_0)$	$\bar{x}(t_0, t_1)$
T _{DL}	[°C]	9.1	11.2	2.1	10.3
Sl2i	[με]	-3206.75	-3185.80	20.95	8.2
	[με] _{comp}	0.0	74.63	74.63	
	[°C]	13.0	8.6	-4.4	
Sl2e	[με]	-2611.60	-2617.63	-6.03	7.6
	[με] _{comp}	0.0	65.95	65.95	
	[°C]	13.6	7.7	-5.9	
St4i	[με]	-1770.36	-1767.52	2.84	8.9
	[με] _{comp}	0.0	39.44	39.44	
	[°C]	12.4	9.4	-3	
St4e	[με]	-1505.23	-1515.75	-10.52	8.4
	[με] _{comp}	0.0	40.72	40.72	
	[°C]	13.0	8.8	-4.2	
St6i	[με]	-2182.06	-2185.55	-3.49	10.9
	[με] _{comp}	0.0	35.55	35.55	
	[°C]	14.7	11.5	-3.2	
St6e	[με]	-1798.21	-1824.90	-26.69	9.9
	[με] _{comp}	0.0	30.65	30.65	
	[°C]	15.1	10.4	-4.7	
Pt1	[MPa]	0.20	-0.06	-0.26	8.6
	[°C]	11.9	9.4	-2.5	
Pl2	[MPa]	-0.04	-0.04	0	8.7
	[°C]	12.2	9.3	-2.9	
Pt3	[MPa]	-	-	-	9.2
	[°C]	12.5	9.9	-2.6	
Pr4	[MPa]	0.25	0.03	-0.22	8.7
	[°C]	12.0	9.4	-2.6	
Pt5	[MPa]	0.24	0.03	-0.21	19.0
	[°C]	22.7	19.6	-3.1	
Pr6	[MPa]	0.49	0.06	-0.43	8.8
	[°C]	11.7	9.6	-2.1	
T1	[°C]	10.8	12.3	1.5	10.9
T2	[°C]	12.6	5.0	-7.6	4.5
T3	[°C]	13.6	6.4	-7.2	6.0
T4	[°C]	10.4	11.8	1.4	10.6
T5	[°C]	11.3	12.4	1.1	11.2
Air	[°C]	8.9	13.0	4.1	13.1
IN	[°C]	13.2	3.0	-10.2	2.6
OUT	[°C]	13.4	5.1	-8.3	4.8
U1	[°C]	9.0	40.1	31.1	39.5
U2	[°C]	9.0	34.4	25.4	33.7

Test GH9 – cyclic test

This test was inspired by the trials described in Moormann et al. (2016) characterized by an intermittent operation mode. The heat pump was turned on from 10:00 to 18:00 every day.

Circuit:	Ground
Mode:	Heating
Secondary circuit temperature:	45°C
Activated rings:	179+180
Volumetric flow rate:	1.3 m ³ /h
Fluid velocity in primary circuit:	0.9 m/s
Starting time t_0 :	07/04/2018 10:00
Ending time t_1 :	16/04/2018 18:00
Duration:	9.33 days

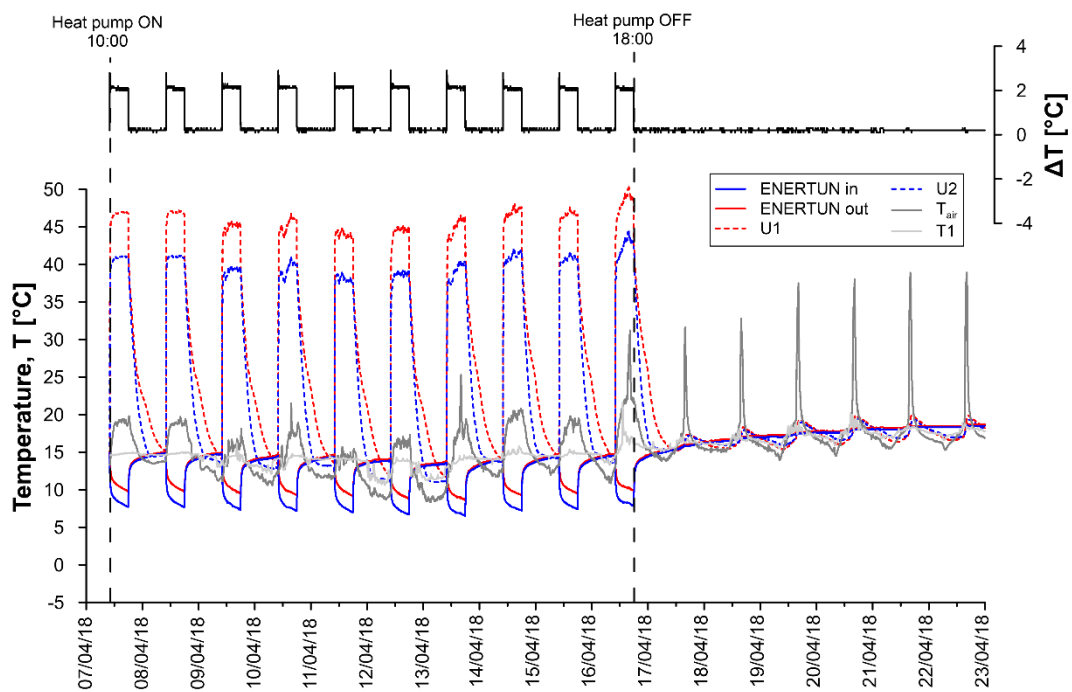


Figure A.116: Primary circuit, secondary circuit and air temperatures for test GH9.

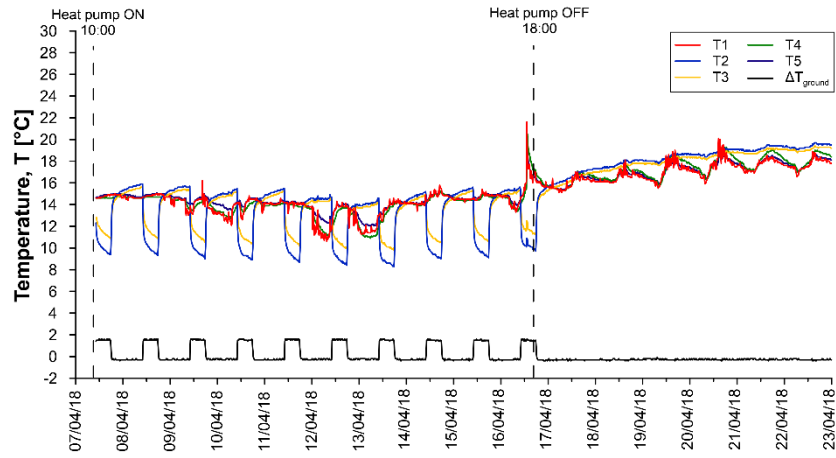


Figure A.117: Temperatures T1-T5 for test GH9.

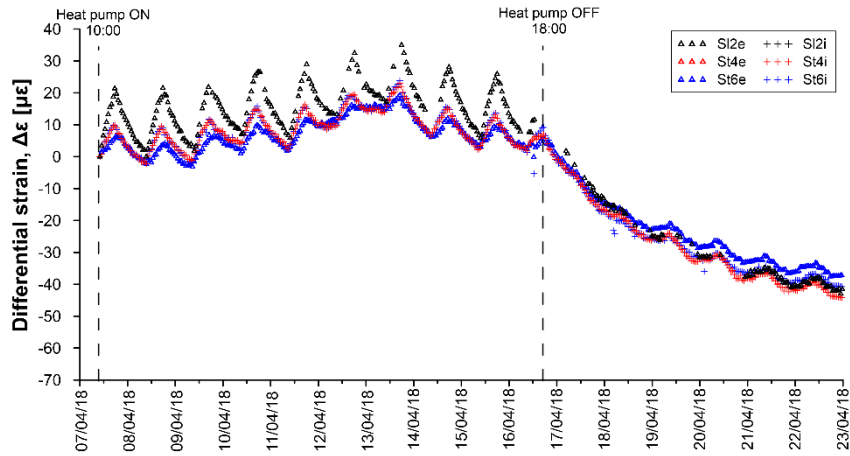


Figure A.118: Differential strains for test GH9.

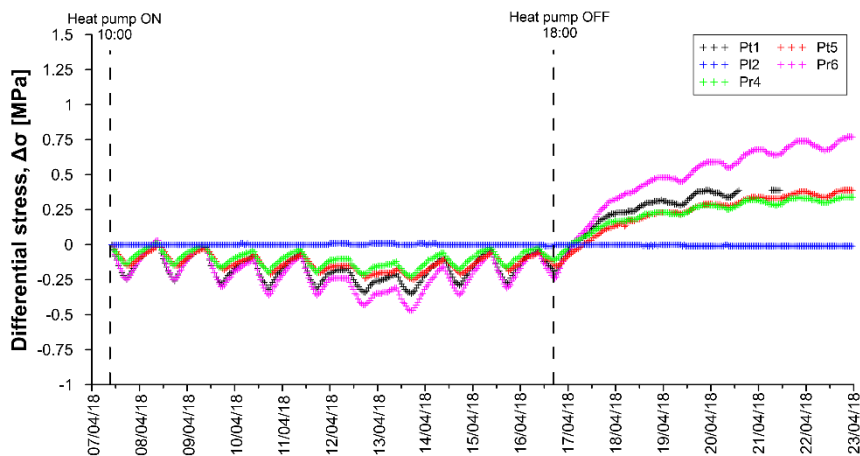


Figure A.119: Differential stresses for test GH9.

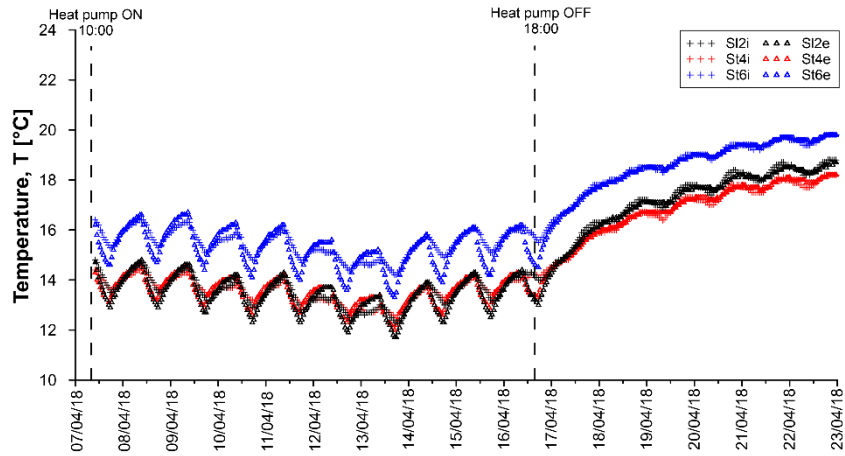


Figure A.120: Temperatures measured by VWSG for test GH9.

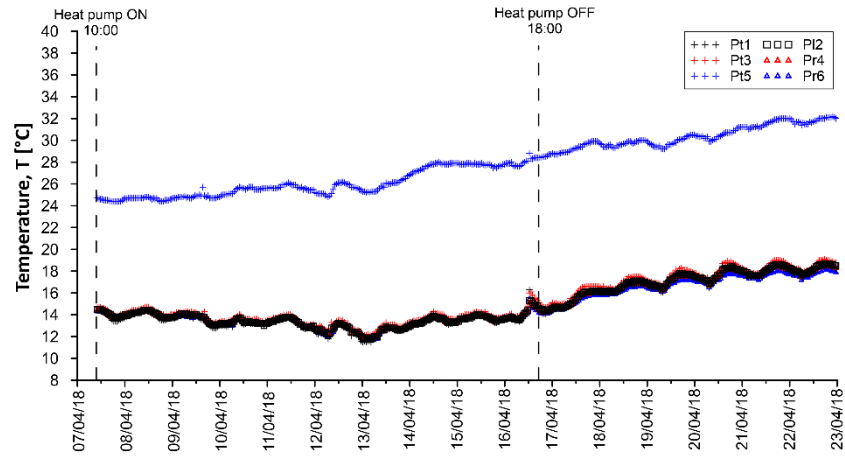


Figure A.121: Temperatures measured by PC for test GH9.

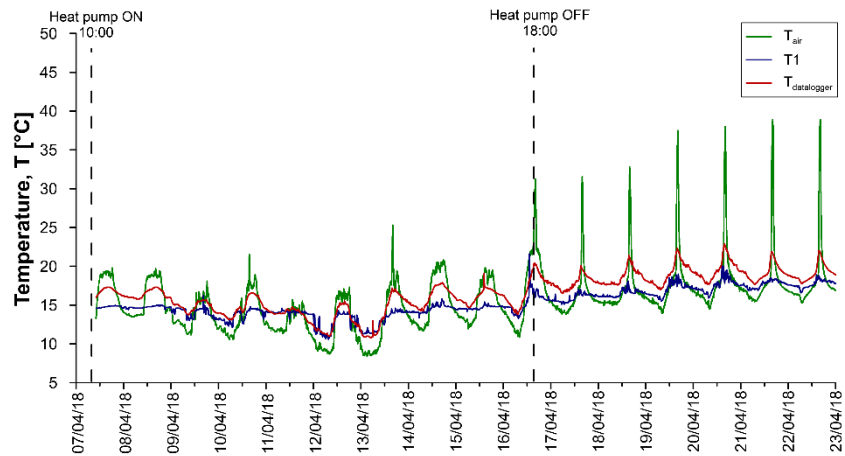


Figure A.122: Air temperatures for test GH9.

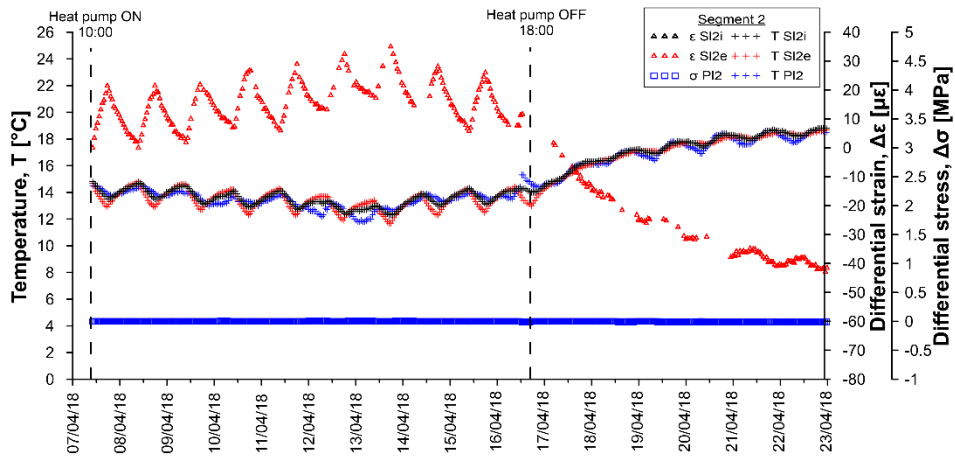


Figure A.123: Temperatures, differential strains and differential stresses in segment 2, ring 179 for test GH9.

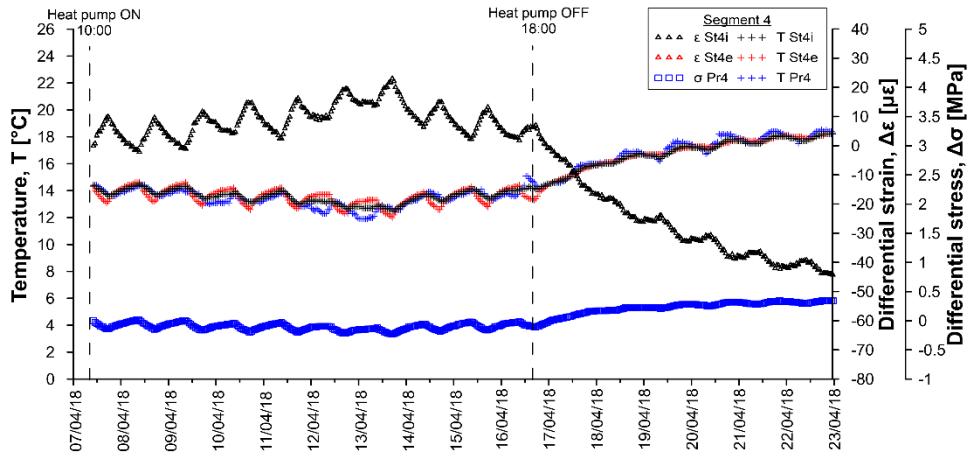


Figure A.124: Temperatures, differential strains and differential stresses in segment 4, ring 179 for test GH9.

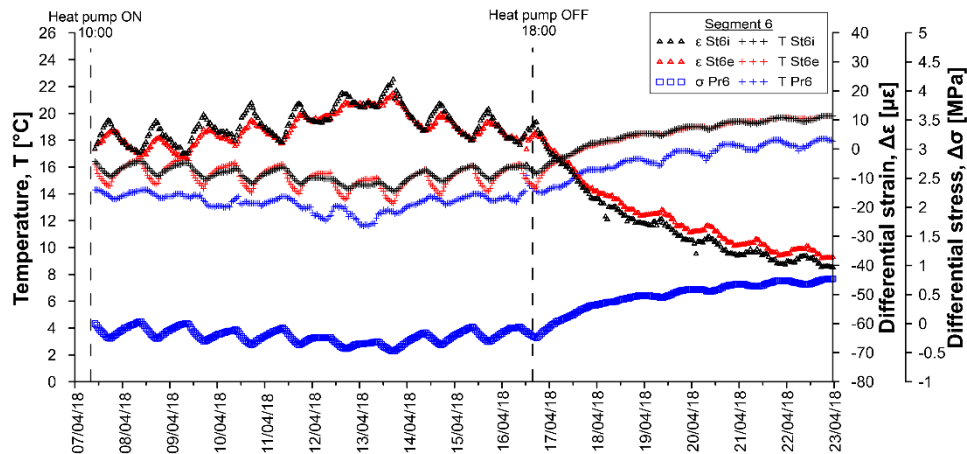


Figure A.125: Temperatures, differential strains and differential stresses in segment 6, ring 179 for test GH9.

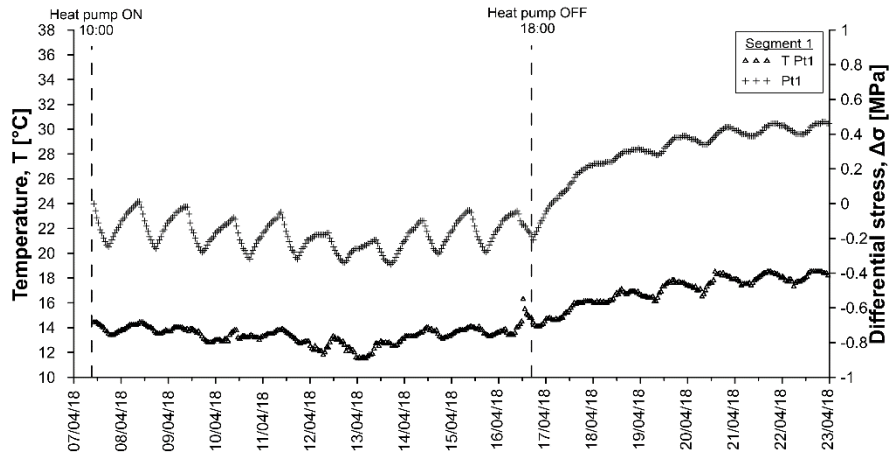


Figure A.126: Temperatures and differential stresses in segment 1, ring 179 for test GH9.

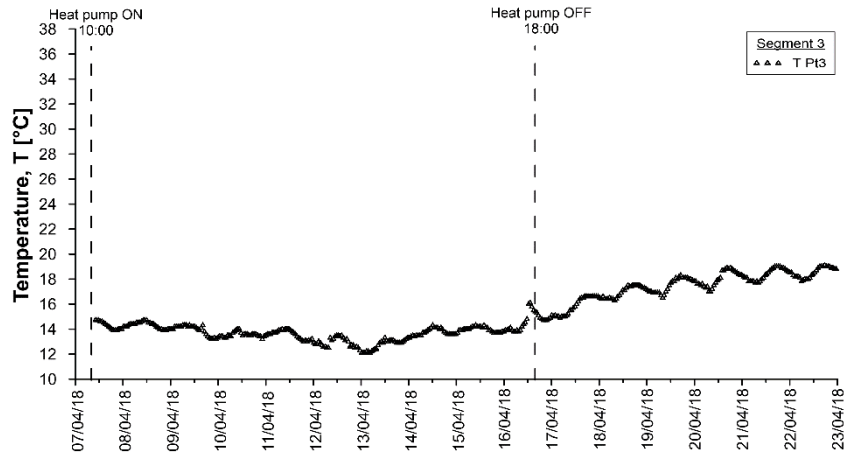


Figure A.127: Temperatures and differential stresses in segment 3, ring 179 for test GH9.

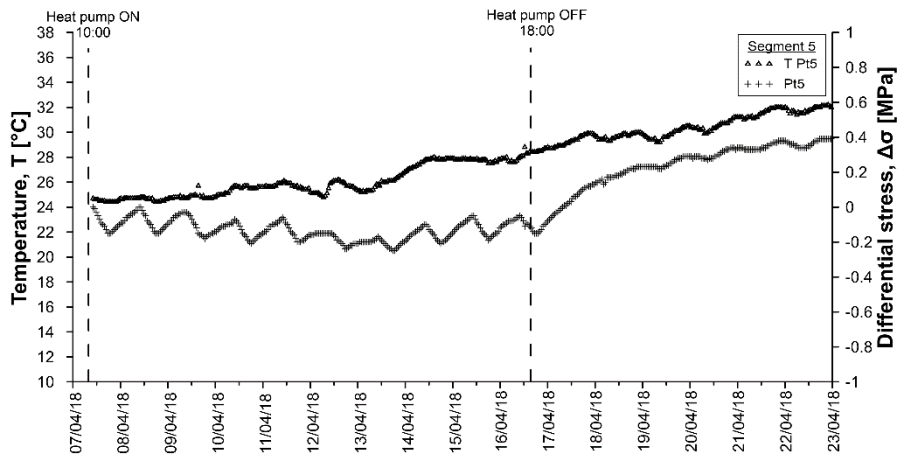


Figure A.128: Temperatures and differential stresses in segment 5, ring 179 for test GH9.

Date	T _{bl} [°C]	SI2i [μ€]	SI2i [°C]	SI2e [μ€]	SI2e [°C]	St4i [μ€]	St4i [°C]	St4e [μ€]	St4e [°C]	St6i [μ€]	St6i [°C]	St6e [μ€]	St6e [°C]
17/04/2018 22:06	18.0	-	16.3	3.94	16.1	1.81	15.9	2.13	15.8	-0.13	17.8	3.50	17.6
18/04/2018 02:06	17.8	-	16.3	3.21	16.2	1.56	16.0	1.30	16.0	-0.18	17.9	4.13	17.8
18/04/2018 06:06	17.7	-	16.4	-	16.4	1.37	16.0	2.27	16.1	-0.44	18.0	4.50	17.9
18/04/2018 10:06	17.6	-	16.5	4.23	16.5	1.44	16.1	3.18	16.2	-0.24	18.1	4.62	18.0
18/04/2018 14:06	19.6	-	16.9	-	16.7	2.38	16.4	2.26	16.4	0.28	18.3	4.52	18.2
18/04/2018 18:06	19.6	-	17.1	-	16.9	2.32	16.6	2.49	16.6	0.06	18.4	4.82	18.3
18/04/2018 22:06	18.8	-	17.2	-	17.1	2.08	16.7	3.35	16.7	0.31	18.5	5.06	18.5
19/04/2018 02:06	17.9	-	17.1	4.38	17.1	1.35	16.6	4.12	16.7	-0.39	18.5	5.57	18.5
19/04/2018 06:06	17.2	-	17.0	4.71	17.1	0.73	16.6	4.53	16.7	-0.72	18.4	5.81	18.5
19/04/2018 10:06	18.0	-	17.0	-	17.1	0.98	16.5	4.08	16.7	-0.70	18.4	5.58	18.5
19/04/2018 14:06	19.7	-	17.4	4.66	17.3	2.48	16.9	3.03	16.9	0.17	18.7	5.19	18.6
19/04/2018 18:06	20.7	-	17.7	-	17.5	2.91	17.2	2.99	17.1	0.57	18.9	5.22	18.8
19/04/2018 22:06	19.9	-	17.8	5.71	17.7	2.53	17.3	3.63	17.2	0.38	19.0	5.39	18.9
20/04/2018 02:06	19.0	-	17.8	5.05	17.7	1.96	17.3	4.39	17.3	-0.05	19.1	5.77	19.1
20/04/2018 06:06	17.8	-	17.6	-	17.7	1.09	17.1	4.45	17.3	-0.59	18.9	6.23	19.0
20/04/2018 10:06	18.6	-	17.5	-	17.6	1.25	17.0	3.98	17.2	-0.40	18.9	6.10	18.9
20/04/2018 14:06	20.1	-	17.9	-	17.7	2.67	17.4	2.52	17.3	0.15	19.1	5.60	19.1
20/04/2018 18:06	21.2	-	18.3	-	18.0	3.30	17.8	3.45	17.6	0.61	19.4	5.59	19.3
20/04/2018 22:06	19.9	-1.74	18.4	5.26	18.1	2.75	17.8	4.21	17.7	0.54	19.4	5.84	19.4
21/04/2018 02:06	19.1	-	18.2	6.04	18.2	1.90	17.7	4.87	17.7	0.14	19.4	6.18	19.4
21/04/2018 06:06	17.9	-	18.0	5.32	18.1	1.08	17.5	5.45	17.7	-0.26	19.3	6.61	19.4
21/04/2018 10:06	18.4	-	18.0	5.39	18.0	1.32	17.5	5.16	17.6	-0.09	19.2	6.46	19.3
21/04/2018 14:06	19.3	-1.69	18.3	5.63	18.1	2.52	17.8	4.27	17.7	0.52	19.4	5.96	19.5
21/04/2018 18:06	20.4	-	18.6	5.61	18.3	3.08	18.0	4.03	17.9	0.91	19.6	5.93	19.6
21/04/2018 22:06	19.1	-	18.6	5.95	18.5	2.51	18.0	4.94	18.0	0.69	19.7	6.31	19.7
22/04/2018 02:06	18.6	-	18.5	5.73	18.5	1.68	17.9	5.72	18.0	0.15	19.6	6.86	19.7
22/04/2018 06:06	18.0	-	18.3	5.93	18.4	0.72	17.8	6.31	18.0	-0.35	19.4	7.23	19.6
22/04/2018 10:06	18.3	-	18.2	5.85	18.3	0.99	17.7	5.79	17.9	-0.11	19.4	6.93	19.5
22/04/2018 14:06	19.3	-	18.5	5.19	18.4	2.17	17.9	4.86	18.0	0.55	19.6	6.41	19.6
22/04/2018 18:06	20.4	-	18.7	5.61	18.6	2.67	18.2	4.84	18.1	0.93	19.8	6.39	19.8
22/04/2018 22:06	19.2	-	18.8	6.12	18.6	2.38	18.2	5.29	18.2	0.93	19.8	6.55	19.9

Table A.38: Data sheet for test GH9 – stresses and temperatures.

Date	Pt1 [MPa]	Pt1 [°C]	Pl2 [MPa]	Pl2 [°C]	Pt3 [MPa]	Pt3 [°C]	Pr4 [MPa]	Pr4 [°C]	Pt5 [MPa]	Pt5 [°C]	Pr6 [MPa]	Pr6 [°C]
07/04/2018 10:06	0	14.4	0	14.5	-	14.7	0	14.4	0	24.7	0	14.3
07/04/2018 14:06	-0.16	14.1	0	14.3	-	14.5	-0.1	14.1	-0.08	24.5	-0.17	14.1
07/04/2018 18:06	-0.24	13.5	0	13.8	-	14	-0.14	13.6	-0.15	24.4	-0.25	13.7
07/04/2018 22:06	-0.15	13.6	0	13.8	-	14	-0.08	13.8	-0.12	24.5	-0.15	13.7
08/04/2018 02:06	-0.08	13.9	0	14	-	14.2	-0.04	14	-0.08	24.7	-0.07	14
08/04/2018 06:06	-0.02	14.2	0	14.2	-	14.4	0	14.2	-0.04	24.7	-0.01	14.1
08/04/2018 10:06	-0.01	14.4	0	14.5	-	14.7	0	14.4	0	24.8	0	14.3
08/04/2018 14:06	-0.17	14.1	0	14.3	-	14.5	-0.1	14.1	-0.09	24.6	-0.16	14.1
08/04/2018 18:06	-0.25	13.6	0	13.8	-	14	-0.14	13.6	-0.15	24.5	-0.24	13.7
08/04/2018 22:06	-0.15	13.7	0	13.7	-	13.9	-0.08	13.7	-0.11	24.6	-0.15	13.8
09/04/2018 02:06	-0.08	13.9	0	13.9	-	14.2	-0.04	13.9	-0.08	24.7	-0.07	13.9
09/04/2018 06:06	-0.04	14.1	0	14.1	-	14.2	-0.01	14.1	-0.04	24.9	-0.02	14
09/04/2018 10:06	-0.05	13.7	0	14	-	14.2	-0.03	13.9	-0.03	24.7	-0.03	13.7
09/04/2018 14:06	-0.21	13.7	0	13.8	-	14	-0.12	13.7	-0.11	25	-0.21	13.8
09/04/2018 18:06	-0.27	13.1	0	13.4	-	13.5	-0.16	13.2	-0.17	24.8	-0.3	13.3
09/04/2018 22:06	-0.2	12.8	0	13.1	-	13.3	-0.11	13.1	-0.15	24.7	-0.23	13.1
10/04/2018 02:06	-0.15	13	0	13.2	-	13.4	-0.08	13.2	-0.12	24.9	-0.17	13.1
10/04/2018 06:06	-0.11	12.9	0.01	13.2	-	13.4	-0.06	13.1	-0.1	25	-0.13	13
10/04/2018 10:06	-0.1	13.7	0	13.7	-	14	-0.06	13.8	-0.07	25.7	-0.12	13.7
10/04/2018 14:06	-0.26	13.3	0	13.4	-	13.6	-0.15	13.3	-0.15	25.7	-0.29	13.4
10/04/2018 18:06	-0.3	13.4	0	13.3	-	13.6	-0.18	13.2	-0.21	25.5	-0.35	13.3
10/04/2018 22:06	-0.21	13	0	13	-	13.3	-0.12	13.1	-0.16	25.5	-0.25	13.1
11/04/2018 02:06	-0.14	13.5	0	13.4	-	13.6	-0.08	13.5	-0.13	25.7	-0.18	13.4
11/04/2018 06:06	-0.09	13.6	0	13.6	-	13.8	-0.05	13.6	-0.09	25.7	-0.12	13.6
11/04/2018 10:06	-0.08	13.8	0	13.8	-	14	-0.05	13.8	-0.06	25.9	-0.11	13.8
11/04/2018 14:06	-0.24	13.4	0	13.5	-	13.7	-0.15	13.4	-0.14	25.9	-0.27	13.5
11/04/2018 18:06	-0.31	12.9	0	12.9	-	13.1	-0.18	12.9	-0.2	25.5	-0.36	13.1
11/04/2018 22:06	-0.22	12.9	0	12.9	-	13.2	-0.14	12.9	-0.17	25.4	-0.28	13
12/04/2018 02:06	-0.19	12.6	0.01	12.7	-	12.9	-0.11	12.7	-0.16	25.3	-0.24	12.7
12/04/2018 06:06	-0.18	12.1	0.01	12.3	-	12.6	-0.1	12.3	-0.15	24.9	-0.24	12.1
12/04/2018 10:06	-0.19	12.8	0	12.9	-	13.2	-0.11	12.9	-0.15	25.9	-0.27	12.7
12/04/2018 14:06	-0.3	13	0	13	-	13.3	-0.19	13	-0.2	26	-0.38	13
12/04/2018 18:06	-0.33	12	0	12.4	-	12.6	-0.21	12.3	-0.23	25.6	-0.43	12.3
12/04/2018 22:06	-0.27	12.1	0.01	12.4	-	12.6	-0.16	12.4	-0.21	25.6	-0.36	12.2
13/04/2018 02:06	-0.25	11.5	0.01	11.8	-	12	-0.15	11.8	-0.2	25.2	-0.35	11.6
13/04/2018 06:06	-0.23	11.8	0.01	12	-	12.3	-0.14	12	-0.2	25.3	-0.33	11.8
13/04/2018 10:06	-0.22	12.7	0	12.7	-	13	-0.14	12.8	-0.17	25.8	-0.33	12.6
13/04/2018 14:06	-0.32	12.8	0	12.7	-	13	-0.21	12.8	-0.21	26	-0.43	12.7
13/04/2018 18:06	-0.34	12.5	0	12.6	-	12.9	-0.22	12.6	-0.25	26.2	-0.46	12.6
13/04/2018 22:06	-0.26	13.1	0	12.8	-	13.2	-0.16	12.9	-0.21	26.6	-0.36	12.9
14/04/2018 02:06	-0.18	13.3	0.01	13.1	-	13.5	-0.11	13.2	-0.17	27.1	-0.27	13.2
14/04/2018 06:06	-0.13	13.4	0.01	13.3	-	13.5	-0.08	13.4	-0.14	27.4	-0.2	13.4
14/04/2018 10:06	-0.11	13.8	0	13.7	-	14	-0.07	13.7	-0.1	27.8	-0.18	13.7
14/04/2018 14:06	-0.24	13.8	0	13.7	-	14.1	-0.15	13.8	-0.16	27.9	-0.3	13.7
14/04/2018 18:06	-0.28	13.3	0	13.5	-	13.8	-0.16	13.3	-0.21	27.8	-0.35	13.3
14/04/2018 22:06	-0.19	13.3	0	13.3	-	13.6	-0.11	13.3	-0.17	27.9	-0.25	13.3
15/04/2018 02:06	-0.12	13.7	0	13.6	-	13.9	-0.07	13.6	-0.12	27.8	-0.17	13.6
15/04/2018 06:06	-0.07	13.8	0	13.7	-	14.1	-0.04	13.8	-0.09	27.9	-0.1	13.8
15/04/2018 10:06	-0.05	14.1	0	14	-	14.3	-0.04	14.1	-0.05	27.9	-0.08	14
15/04/2018 14:06	-0.21	14	0	14	-	14.3	-0.12	14	-0.13	27.8	-0.24	14
15/04/2018 18:06	-0.27	13.4	0	13.6	-	13.8	-0.15	13.4	-0.19	27.5	-0.3	13.5
15/04/2018 22:06	-0.17	13.5	0	13.5	-	13.7	-0.1	13.5	-0.15	27.7	-0.2	13.6
16/04/2018 02:06	-0.1	13.7	0	13.7	-	14	-0.05	13.8	-0.1	27.9	-0.12	13.7
16/04/2018 06:06	-0.06	13.6	0	13.7	-	13.9	-0.03	13.7	-0.08	27.8	-0.07	13.6
16/04/2018 10:06	-0.06	14.2	0	14.1	-	14.4	-0.04	14.1	-0.05	28	-0.07	14
16/04/2018 14:06	-0.14	15.1	-0.01	15.1	-	15.8	-0.09	14.9	-0.1	28.3	-0.18	14.6
16/04/2018 18:06	-0.19	14.2	0	14.6	-	14.9	-0.1	14.3	-0.15	28.4	-0.23	14.2
16/04/2018 22:06	-0.09	14.3	0	14.5	-	14.8	-0.04	14.3	-0.11	28.6	-0.11	14.2
17/04/2018 02:06	0	14.8	0	14.7	-	15.1	0.01	14.6	-0.05	28.7	-0.01	14.5
17/04/2018 06:06	0.03	14.7	0	14.7	-	15	0.04	14.6	-0.01	28.9	0.06	14.5
17/04/2018 10:06	0.08	15.2	0	15.1	-	15.5	0.07	15	0.02	29.1	0.13	14.9
17/04/2018 14:06	0.14	15.9	0	15.8	-	16.3	0.11	15.8	0.06	29.4	0.2	15.5
17/04/2018 18:06	0.19	16.1	0	16.1	-	16.6	0.14	15.9	0.1	29.7	0.27	15.7

Date	Pt1 [MPa]	Pt1 [°C]	Pl2 [MPa]	Pl2 [°C]	Pt3 [MPa]	Pt3 [°C]	Pr4 [MPa]	Pr4 [°C]	Pt5 [MPa]	Pt5 [°C]	Pr6 [MPa]	Pr6 [°C]
17/04/2018 22:06	0.22	16.2	0	16.2	-	16.6	0.16	16.1	0.13	30	0.31	15.8
18/04/2018 02:06	0.23	16.1	0	16.1	-	16.5	0.17	16	0.15	29.4	0.34	15.8
18/04/2018 06:06	0.24	16	0	16.2	-	16.4	0.18	16.1	0.17	29.4	0.37	16
18/04/2018 10:06	0.25	16.3	0	16.3	-	16.7	0.18	16.2	0.18	29.6	0.39	16.1
18/04/2018 14:06	0.29	16.8	0	16.9	-	17.4	0.21	16.8	0.2	29.8	0.43	16.4
18/04/2018 18:06	0.3	16.9	-0.01	17.1	-	17.5	0.22	16.9	0.22	29.8	0.46	16.5
18/04/2018 22:06	0.31	16.8	-0.01	17	-	17.3	0.23	16.8	0.23	30	0.48	16.6
19/04/2018 02:06	0.3	16.5	0	16.7	-	17	0.23	16.6	0.23	29.6	0.48	16.4
19/04/2018 06:06	0.29	16.4	0	16.6	-	16.9	0.22	16.5	0.23	29.5	0.47	16.3
19/04/2018 10:06	0.29	16.8	0	16.8	-	17.1	0.22	16.7	0.23	29.5	0.46	16.5
19/04/2018 14:06	0.34	17.6	-0.01	17.5	-	17.9	0.25	17.4	0.25	29.8	0.51	17
19/04/2018 18:06	0.38	17.6	-0.01	17.7	-	18.1	0.27	17.5	0.28	30.2	0.56	17.1
19/04/2018 22:06	0.39	17.6	-0.01	17.7	-	18	0.28	17.5	0.29	30.5	0.59	17.2
20/04/2018 02:06	0.37	17.3	-0.01	17.4	-	17.6	0.28	17.4	0.29	30.4	0.59	17.1
20/04/2018 06:06	0.35	17.1	-0.01	17.1	-	17.4	0.27	17.1	0.28	30.3	0.58	16.9
20/04/2018 10:06	0.34	17.4	-0.01	17.3	-	17.6	0.26	17.3	0.28	30.2	0.55	17.1
20/04/2018 14:06	0.39	18.4	-0.01	18.2	-	18.7	0.28	18.1	0.29	30.5	0.6	17.6
20/04/2018 18:06	0.43	18.4	-0.01	18.4	-	18.9	0.32	18.2	0.33	30.7	0.65	17.7
20/04/2018 22:06	0.43	17.9	-0.01	18.1	-	18.4	0.32	18	0.34	31.1	0.68	17.6
21/04/2018 02:06	0.41	17.8	-0.01	17.8	-	18.1	0.31	17.8	0.34	31.3	0.68	17.5
21/04/2018 06:06	0.39	17.5	-0.01	17.6	-	17.7	0.29	17.5	0.33	31.2	0.65	17.3
21/04/2018 10:06	0.39	17.8	-0.01	17.8	-	18	0.29	17.7	0.33	31.3	0.64	17.5
21/04/2018 14:06	0.42	18.3	-0.01	18.3	-	18.7	0.31	18.2	0.34	31.7	0.69	17.8
21/04/2018 18:06	0.46	18.5	-0.01	18.6	-	18.9	0.33	18.4	0.37	31.9	0.73	18
21/04/2018 22:06	0.46	18.2	-0.01	18.4	-	18.7	0.33	18.2	0.38	32	0.74	17.8
22/04/2018 02:06	0.44	17.8	-0.01	18	-	18.3	0.33	17.9	0.37	31.6	0.72	17.6
22/04/2018 06:06	0.41	17.4	-0.01	17.7	-	17.8	0.31	17.5	0.35	31.4	0.69	17.3
22/04/2018 10:06	0.4	17.8	-0.01	18	-	18.1	0.3	17.8	0.34	31.7	0.68	17.6
22/04/2018 14:06	0.43	18.4	-0.01	18.4	-	18.8	0.32	18.3	0.37	31.9	0.7	17.9
22/04/2018 18:06	0.46	18.5	-0.01	18.7	-	19	0.34	18.4	0.39	32.1	0.75	18.1
22/04/2018 22:06	0.47	18.4	-0.01	18.6	-	18.9	0.34	18.4	0.39	32.1	0.77	18

Date	T1 [°C]	T2 [°C]	T3 [°C]	T4 [°C]	T5 [°C]	Date	Tair [°C]	IN [°C]	OUT [°C]	U1 [°C]	U2 [°C]
18/04/2018 07:37	16	17.5	17.1	16.2	16.2	18/04/2018 00:55	15.4	16.2	16.4	16.1	16.4
18/04/2018 11:53	17	17.7	17.5	16.8	16.7	18/04/2018 04:59	15.4	16.4	16.6	15.7	16.2
18/04/2018 16:09	17	18.1	17.7	17.6	17.1	18/04/2018 09:03	15.3	16.5	16.7	15.5	15.9
18/04/2018 20:25	16.7	18.1	17.8	17.1	16.9	18/04/2018 13:06	17.3	16.7	16.9	15.8	16.1
19/04/2018 00:41	16.4	18	17.8	16.8	16.6	18/04/2018 17:10	19.5	16.9	17.1	18.3	18
19/04/2018 01:45	16.4	18	17.8	16.7	16.5	18/04/2018 21:14	16.5	17	17.2	17.5	17.3
19/04/2018 05:31	16.2	18	17.8	16.4	16.3	19/04/2018 01:18	15.7	17	17.2	16.7	16.8
19/04/2018 09:47	16.5	18.1	17.8	16.1	16.3	19/04/2018 05:21	15.2	17.1	17.3	16	16.5
19/04/2018 14:03	18.2	18.5	18.2	18.4	17.8	19/04/2018 09:25	15.1	17	17.2	15.4	15.9
19/04/2018 18:19	17.4	18.6	18.3	18.4	17.8	19/04/2018 13:29	18.4	17.2	17.4	16.2	16.4
19/04/2018 22:35	17.1	18.6	18.3	17.8	17.4	19/04/2018 17:33	20.3	17.5	17.7	19.3	18.9
20/04/2018 02:51	17	18.6	18.4	17.5	17.2	19/04/2018 21:36	17.5	17.5	17.8	18.5	18.2
20/04/2018 07:07	16.7	18.6	18.3	16.8	16.8	20/04/2018 01:40	16.5	17.6	17.8	17.4	17.7
20/04/2018 11:23	17.8	18.7	18.5	17.7	17.5	20/04/2018 05:44	15.7	17.6	17.8	16.7	17.3
20/04/2018 15:39	18.4	19.2	18.9	19.1	18.5	20/04/2018 09:48	15.9	17.6	17.8	16	16.6
20/04/2018 19:55	18	19.1	18.8	18.8	18.1	20/04/2018 13:51	18	17.7	17.9	16.7	16.9
21/04/2018 00:11	17.6	19.1	18.9	18.1	17.8	20/04/2018 17:55	20.1	18	18.2	19.6	19.5
21/04/2018 04:27	17.3	19	18.7	17.4	17.2	20/04/2018 21:59	17.6	18	18.2	18.8	18.6
21/04/2018 08:43	16.9	18.9	18.7	17.2	17.2	21/04/2018 02:02	16.9	18.1	18.2	17.7	18.1
21/04/2018 12:59	18	19.2	18.9	18.4	18	21/04/2018 06:06	15.8	18	18.2	16.8	17.4
21/04/2018 17:15	18.4	19.4	19.1	19	18.4	21/04/2018 10:10	16.6	18	18.2	16.4	16.9
21/04/2018 21:31	17.9	19.4	19.1	18.6	18.1	21/04/2018 14:14	18.2	18.1	18.3	16.9	17.1
22/04/2018 01:47	17.5	19.3	19	17.9	17.7	21/04/2018 18:17	19	18.3	18.5	19.5	19.3
22/04/2018 06:03	16.9	19.1	18.9	17.4	17.4	21/04/2018 22:21	17.1	18.3	18.5	18.5	18.3
22/04/2018 10:19	17.4	19.2	18.9	17.5	17.5	22/04/2018 02:25	16.5	18.3	18.5	17.6	17.8
22/04/2018 14:35	18.2	19.5	19.2	18.5	18.4	22/04/2018 06:29	15.6	18.3	18.5	16.9	17.3
22/04/2018 18:51	18.1	19.6	19.3	18.8	18.4	22/04/2018 10:32	16.6	18.3	18.5	16.6	17
22/04/2018 23:07	17.9	19.5	19.3	18.5	18.2	22/04/2018 14:36	18.3	18.4	18.6	17	17.2
						22/04/2018 18:40	18.6	18.5	18.7	19.4	19.1
						22/04/2018 22:44	17.1	18.5	18.7	18.4	18.3

Table A.40: Summary of test GH9 records.

Quantity	Unit	$x(t_0)$	$x(t_1)$	$x(t_1) - x(t_0)$	$\bar{x}(t_0, t_1)$
T _{DL}	[°C]	16.0	19.3	3.3	15.1
Sl2i	[με]	-328.41	-3192.03	-	13.6
	[με] _{comp}	0.00	-2853.86	-	
Sl2e	[°C]	14.8	14.0	-0.8	13.4
	[με]	-2612.18	-	-	
St4i	[με] _{comp}	-	-	-	13.6
	[°C]	14.7	13.1	-1.6	
St4e	[με]	-1765.49	-1762.89	2.60	13.5
	[με] _{comp}	0.00	6.26	6.26	
St6i	[°C]	14.4	14.1	-0.3	15.4
	[με]	-1506.92	-1510.18	-3.26	
St6e	[με] _{comp}	0.00	5.28	5.28	15.3
	[°C]	14.3	13.6	-0.7	
Pt1	[με]	-2174.44	-2177.26	-2.82	13.4
	[με] _{comp}	0.00	6.94	6.94	
Pl2	[°C]	16.4	15.6	-0.8	13.4
	[MPa]	-1801.66	-1814.77	-13.11	
Pr4	[με] _{comp}	0.00	5.19	5.19	13.4
	[°C]	16.2	14.7	-1.5	
Pt3	[MPa]	0.35	0.15	-0.20	13.7
	[°C]	14.4	14.3	-0.1	
Pr6	[MPa]	-0.05	-0.05	0.00	13.4
	[°C]	14.5	14.5	0.0	
T1	[MPa]	-	-	-	13.4
	[°C]	14.7	14.9	0.2	
T2	[MPa]	0.35	0.24	-0.11	26.0
	[°C]	14.4	14.3	-0.1	
T3	[MPa]	0.39	0.24	-0.15	13.4
	[°C]	24.7	28.4	3.7	
T4	[MPa]	0.72	0.49	-0.23	14.1
	[°C]	14.3	14.1	-0.2	
T5	[°C]	14.6	16.2	1.6	13.0
	[°C]	12.3	11.2	-1.1	
Air	[°C]	13.7	11.7	-2.0	14.0
	[°C]	14.6	16.9	2.3	
IN	[°C]	14.6	16.4	1.8	14.4
	[°C]	14.6	16.4	1.8	
OUT	[°C]	13.4	21.6	8.2	11.7
	[°C]	14.9	7.8	-7.1	
U1	[°C]	15.1	9.9	-5.2	12.6
	[°C]	15.0	48.1	33.1	
U2	[°C]	15.1	9.9	-5.2	29.9
	[°C]	14.3	42.3	28.0	

Test GH10 – cyclic test

Again, as in test GH9, this test was characterized by an intermittent operation mode. The heat pump was turned on from 10:00 to 18:00 every day.

Circuit:	Ground
Mode:	Heating
Secondary circuit temperature:	45°C
Activated rings:	179+180
Volumetric flow rate:	1.3 m ³ /h
Fluid velocity in primary circuit:	0.9 m/s
Starting time t_0 :	08/05/2018 10:04
Ending time t_1 :	20/05/2018 18:00
Duration:	12.33 days
Note:	Strange behaviour of SI2i, deleted from the charts.

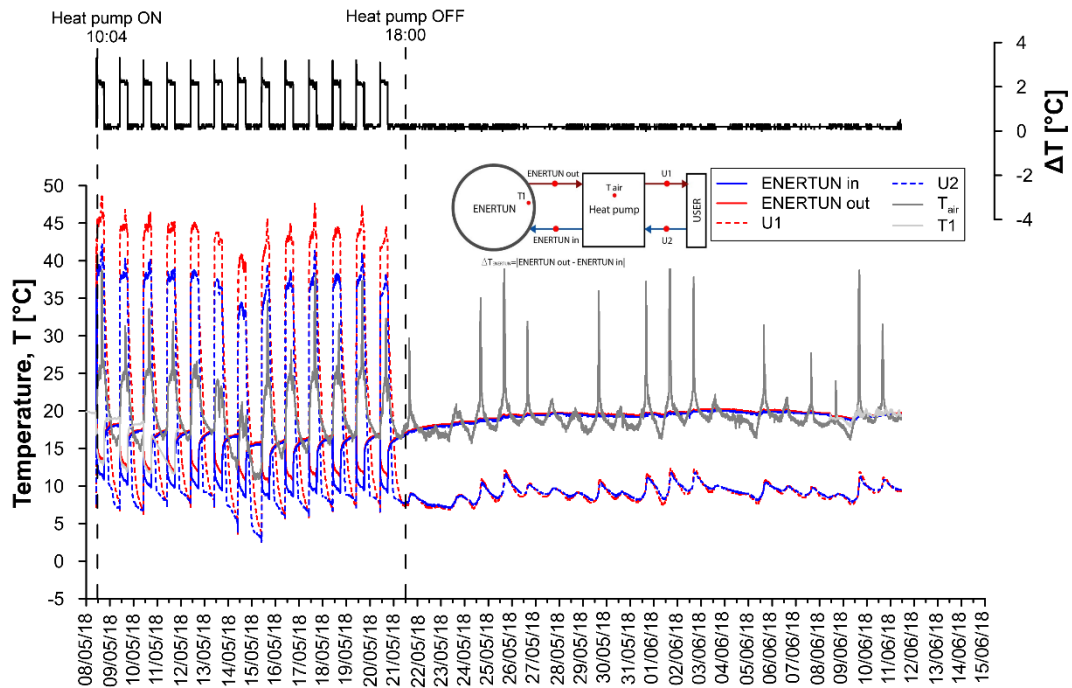


Figure A.129: Primary circuit, secondary circuit and air temperatures for test GH10.

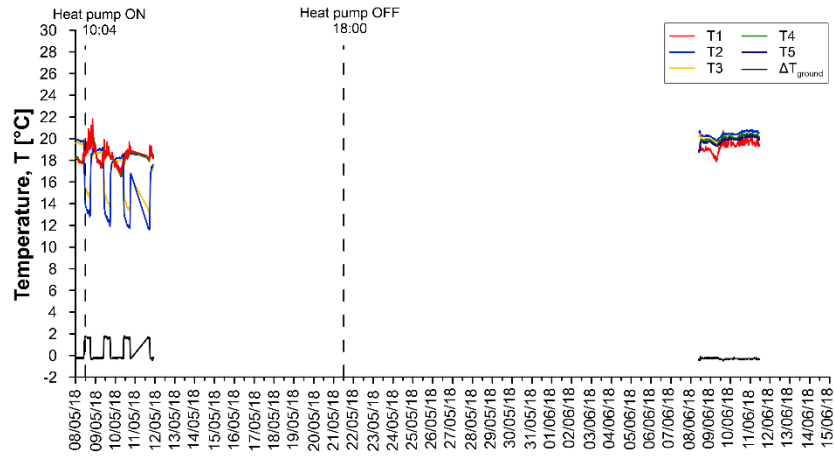


Figure A.130: Temperatures T1-T5 for test GH10.

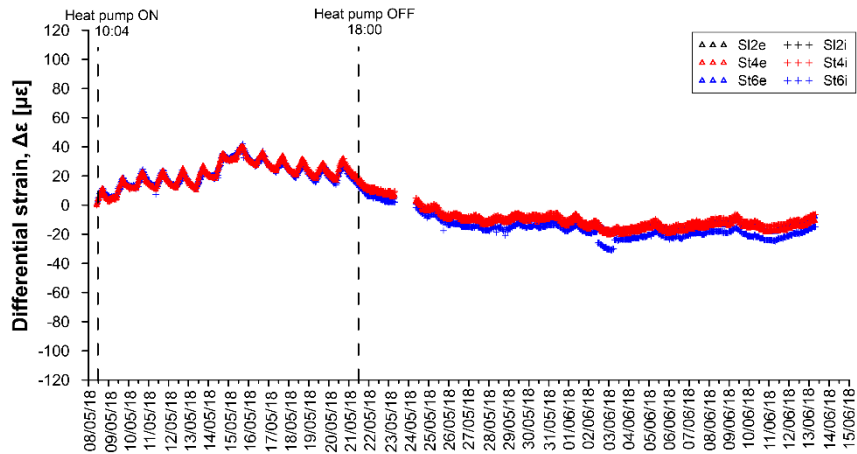


Figure A.131: Differential strains for test GH10.

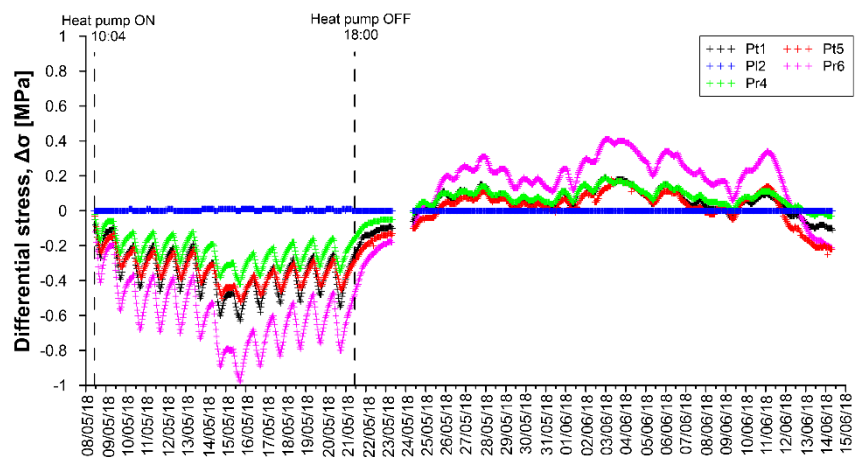


Figure A.132: Differential stresses for test GH10.

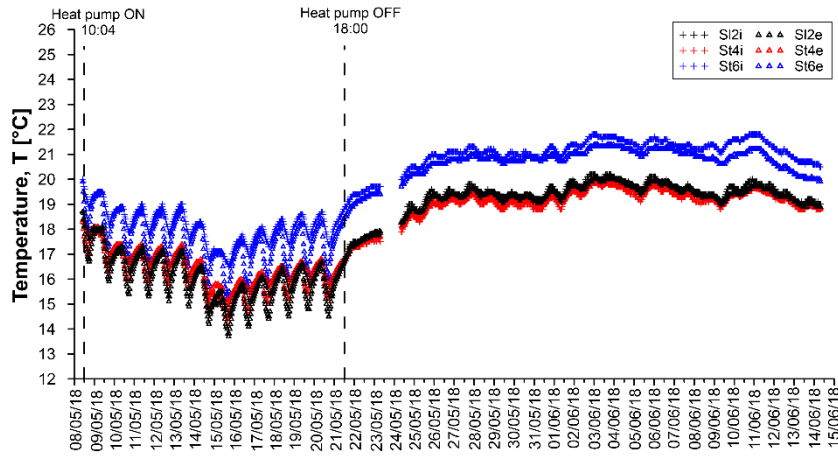


Figure A.133: Temperatures measured by VWSG for test GH10.

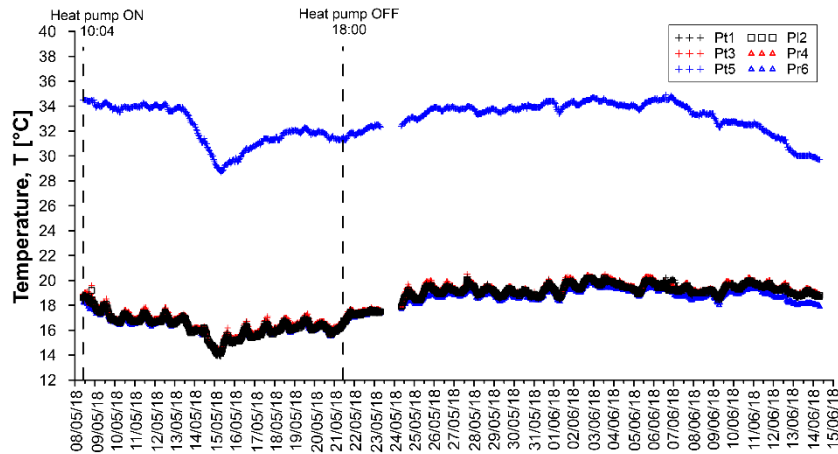


Figure A.134: Temperatures measured by PC for test GH10.

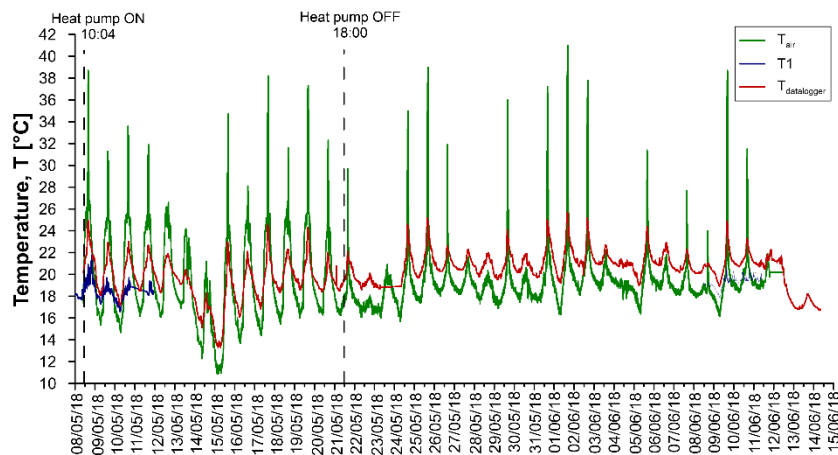


Figure A.135: Air temperatures for test GH10.

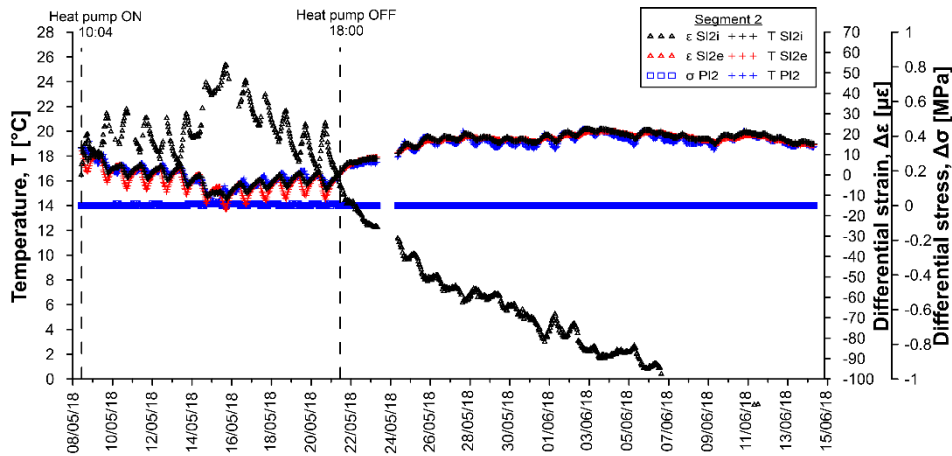


Figure A.136: Temperatures, differential strains and differential stresses in segment 2, ring 179 for test GH10.

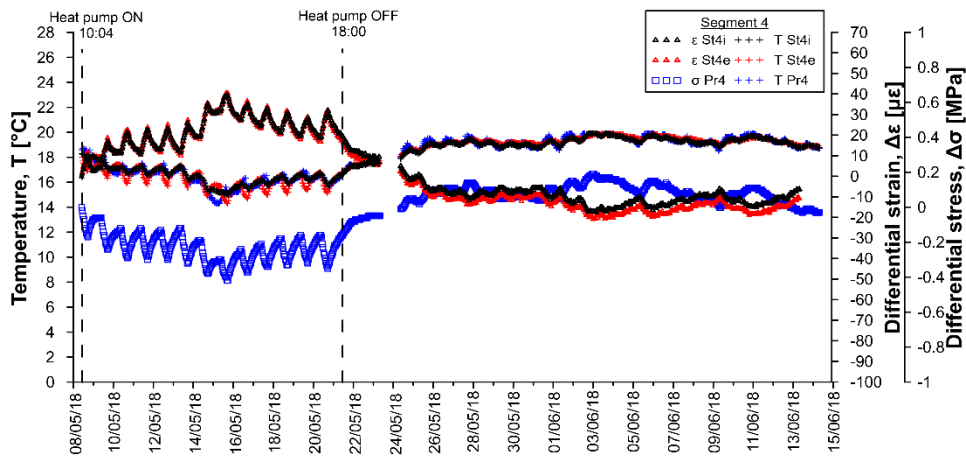


Figure A.137: Temperatures, differential strains and differential stresses in segment 4, ring 179 for test GH10.

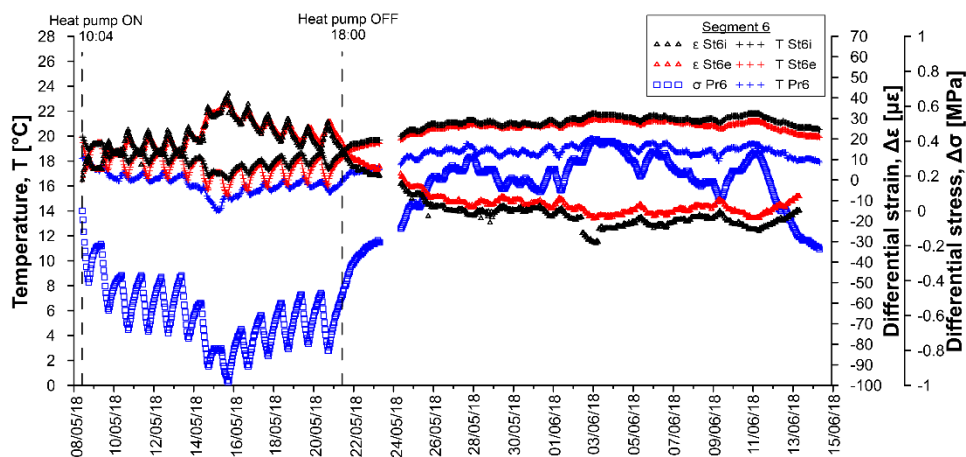


Figure A.138: Temperatures, differential strains and differential stresses in segment 6, ring 179 for test GH10.

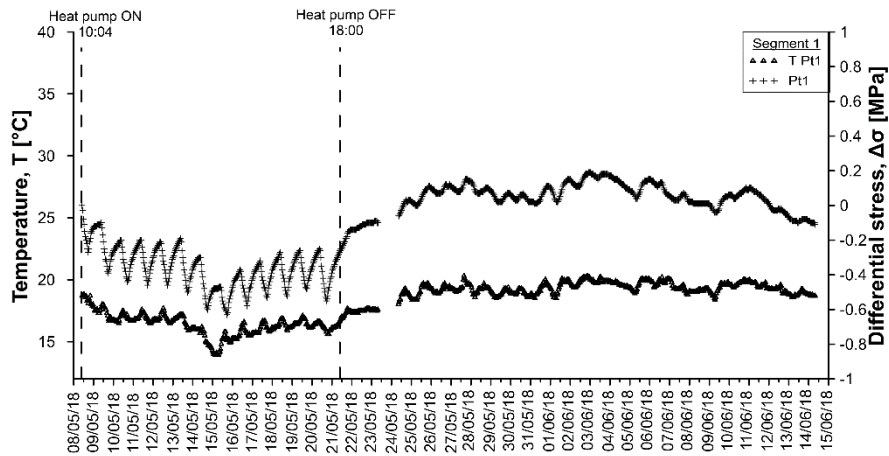


Figure A.139: Temperatures and differential stresses in segment 1, ring 179 for test GH10.

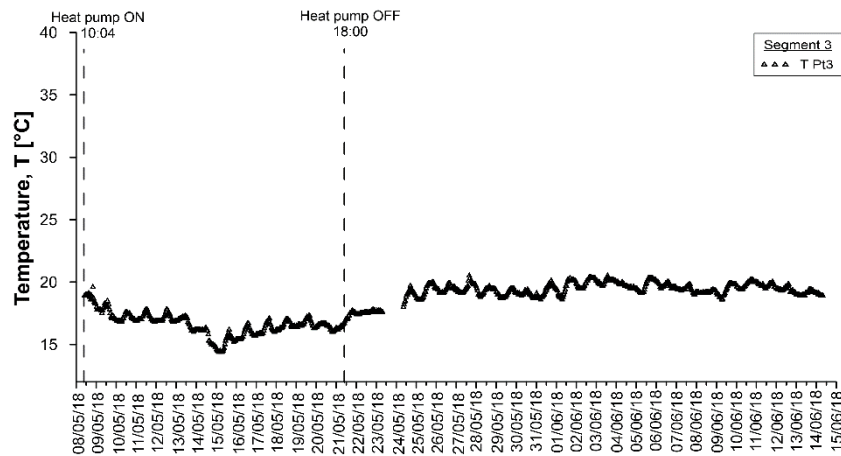


Figure A.140: Temperatures and differential stresses in segment 3, ring 179 for test GH10.

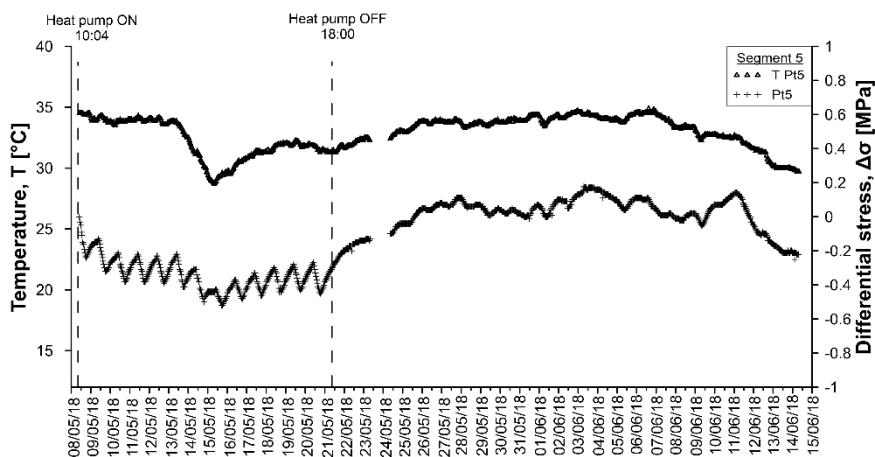


Figure A.141: Temperatures and differential stresses in segment 5, ring 179 for test GH10.

Table A.41: Data sheet for test GH10 – strains and temperatures.

Date	T _{DL} [°C]	SI2i [µε]	SI2i [°C]	SI2e [µε]	SI2e [°C]	St4i [µε]	St4i [°C]	St4e [µε]	St4e [°C]	St6i [µε]	St6i [°C]	St6e [µε]	St6e [°C]
08/05/2018 10:06	20.2	0.00	18.7	-	18.7	0.00	18.3	0.00	18.3	0.00	20.0	0.00	19.9
08/05/2018 18:06	23.1	1.24	17.6	-	16.7	1.82	17.7	-3.78	17.1	-2.77	18.8	-12.16	18.1
09/05/2018 02:06	19.3	3.13	18.0	-	17.9	-1.16	17.9	1.03	18.0	-1.87	19.4	-0.82	19.4
09/05/2018 10:06	19.5	3.14	18.1	-	17.9	0.42	17.9	-1.78	17.6	0.44	19.4	-2.84	19.1
09/05/2018 18:06	21.5	3.48	16.7	-	15.9	0.22	17.0	-3.39	16.6	-3.54	18.2	-13.74	17.5
10/05/2018 02:06	18.4	-	17.0	-	17.0	-2.47	17.2	0.18	17.3	-2.23	18.8	-1.77	18.7
10/05/2018 10:06	19.2	-	17.4	-	17.2	-0.44	17.3	-2.42	17.1	0.61	18.9	-3.56	18.5
10/05/2018 18:06	21.6	0.99	16.3	-	15.5	0.50	16.7	-4.91	16.1	-2.99	17.9	-15.08	17.0
11/05/2018 02:06	19.4	-	16.9	-	16.8	-1.72	17.1	-1.00	17.1	-1.57	18.7	-2.63	18.5
11/05/2018 10:06	19.9	-3.96	17.3	-	17.1	0.36	17.3	-2.86	17.0	0.77	19.0	-4.42	18.4
11/05/2018 18:06	21.9	-	16.2	-	15.4	0.26	16.5	-4.71	16.1	-3.37	17.8	-15.59	16.9
12/05/2018 02:06	19.5	-8.20	16.8	-	16.7	-1.36	17.0	-1.16	17.0	-1.88	18.6	-3.20	18.4
12/05/2018 10:06	19.7	-7.85	17.2	-	17.0	0.26	17.2	-3.31	16.9	0.57	18.9	-4.83	18.4
12/05/2018 18:06	21.2	-6.16	16.1	-	15.2	0.51	16.5	-5.01	16.0	-3.47	17.8	-16.40	16.9
13/05/2018 02:06	19.8	-13.09	16.8	-	16.6	-0.86	17.0	-1.53	17.0	-1.58	18.6	-3.33	18.4
13/05/2018 10:06	19.5	-9.94	17.2	-	16.9	0.57	17.2	-3.36	17.0	0.65	19.0	-4.80	18.4
13/05/2018 18:06	19.1	-8.35	15.6	-	15.0	-0.61	16.2	-4.63	15.8	-4.37	17.6	-16.17	16.7
14/05/2018 02:06	17.0	-11.55	16.2	-	16.2	-2.48	16.4	-1.10	16.7	-2.45	18.2	-2.59	18.1
14/05/2018 10:06	15.9	-4.85	16.4	-	16.4	-1.72	16.4	-2.38	16.3	-0.98	18.1	-3.70	17.7
14/05/2018 18:06	17.0	-	14.8	-	14.3	-2.10	15.3	-4.16	15.1	-4.70	16.8	-15.11	16.0
15/05/2018 02:06	13.7	-4.43	15.0	-	15.3	-5.61	15.3	-0.03	15.8	-4.36	17.1	-1.51	17.1
15/05/2018 10:06	14.9	-1.47	15.2	-	15.3	-3.82	15.2	-2.31	15.4	-1.52	17.0	-3.58	16.7
15/05/2018 18:06	20.5	-	14.5	-	13.8	-1.48	15.0	-5.77	14.6	-10.39	16.5	-15.57	15.5
16/05/2018 02:06	17.4	-	15.3	-	15.3	-3.07	15.6	-1.85	15.7	-1.44	17.4	-2.85	17.1
16/05/2018 10:06	18.2	-	15.8	-	15.6	-0.81	15.9	-3.53	15.6	0.82	17.8	-4.76	17.2
16/05/2018 18:06	20.7	-	15.0	-	14.2	0.06	15.5	-5.60	14.9	-2.11	17.0	-16.21	15.9
17/05/2018 02:06	18.1	-6.37	15.6	-	15.6	-2.16	15.9	-2.03	16.0	-0.98	17.8	-3.05	17.4
17/05/2018 10:06	18.6	-5.88	16.1	-	15.9	-0.32	16.1	-3.56	15.9	0.79	18.1	-4.97	17.4
17/05/2018 18:06	21.8	-	15.4	-	14.5	0.74	15.8	-5.47	15.2	-2.11	17.3	-15.84	16.2
18/05/2018 02:06	19.2	-8.82	16.0	-	15.8	-1.51	16.2	-2.06	16.2	-1.23	18.0	-3.18	17.7
18/05/2018 10:06	19.7	-9.29	16.5	-	16.2	0.39	16.5	-3.91	16.2	1.05	18.4	-5.00	17.7
18/05/2018 18:06	21.4	-8.44	15.5	-	14.7	0.61	15.9	-5.51	15.4	-2.91	17.4	-16.15	16.4
19/05/2018 02:06	19.4	-17.12	16.2	-	16.0	-1.10	16.4	-2.34	16.4	-1.67	18.3	-3.56	17.9
19/05/2018 10:06	19.5	-16.01	16.6	-	16.4	0.43	16.6	-3.82	16.3	0.35	18.6	-5.27	17.9
19/05/2018 18:06	21.9	-12.24	15.8	-	14.9	1.14	16.1	-5.77	15.6	-4.43	17.6	-16.20	16.5
20/05/2018 02:06	19.3	-21.55	16.3	-	16.2	-1.06	16.4	-2.18	16.5	-2.66	18.3	-2.98	17.9
20/05/2018 10:06	18.7	-18.35	16.7	-	16.5	0.38	16.7	-3.63	16.4	-0.35	18.6	-4.67	17.9
20/05/2018 18:06	20.6	-17.91	15.3	-	14.6	-0.19	15.7	-5.56	15.3	-5.27	17.4	-16.04	16.3
21/05/2018 02:06	19.0	-26.13	16.1	-	15.9	-1.26	16.3	-2.16	16.3	-2.87	18.2	-3.23	17.8
21/05/2018 10:06	19.1	-28.84	16.6	-	16.5	-0.95	16.6	-2.00	16.7	-1.61	18.7	-1.89	18.3
21/05/2018 18:06	21.1	-29.74	17.3	-	17.1	0.11	17.1	-2.07	17.1	-0.96	19.1	-1.32	18.8
22/05/2018 02:06	19.5	-28.85	17.5	-	17.4	-0.18	17.3	-1.12	17.4	-1.08	19.4	-0.56	19.1
22/05/2018 10:06	19.0	-31.60	17.6	-	17.6	-0.27	17.4	-0.99	17.5	-1.20	19.5	-0.32	19.2
22/05/2018 18:06	19.6	-35.29	17.8	-	17.8	-0.10	17.5	-1.01	17.7	-1.16	19.6	-0.31	19.4
23/05/2018 02:06	18.8	-36.00	17.8	-	17.9	-0.28	17.6	-0.71	17.7	-1.38	19.7	0.03	19.4
24/05/2018 10:06	19.8	-37.82	18.3	-	18.3	0.29	18.0	-0.55	18.1	-1.60	20.0	0.46	19.8
24/05/2018 18:06	22.9	-36.69	19.0	-	18.7	2.07	18.6	-1.19	18.5	-0.95	20.4	0.05	20.1
25/05/2018 02:06	20.0	-38.12	18.8	-	18.8	0.87	18.4	-0.09	18.5	-1.56	20.5	0.51	20.2
25/05/2018 10:06	20.7	-41.35	18.9	-	18.7	1.37	18.5	-0.50	18.5	-1.33	20.5	0.10	20.2
25/05/2018 18:06	23.3	-41.54	19.5	-	19.3	2.68	19.1	-1.26	18.9	-1.01	20.9	0.02	20.5
26/05/2018 02:06	20.8	-41.79	19.4	-	19.3	2.07	19.0	-0.39	19.0	-1.29	21.0	0.21	20.6
26/05/2018 10:06	20.4	-43.54	19.2	-	19.2	1.56	18.9	-0.18	19.0	-1.83	20.9	0.38	20.6
26/05/2018 18:06	21.9	-44.28	19.6	-	19.4	2.47	19.2	-0.62	19.2	-1.41	21.1	-0.01	20.7
27/05/2018 02:06	20.7	-46.29	19.4	-	19.4	1.77	19.1	0.15	19.2	-1.70	21.1	0.31	20.8
27/05/2018 10:06	20.4	-48.61	19.4	-	19.3	1.59	19.0	-0.32	19.1	-1.91	21.0	0.22	20.7
27/05/2018 18:06	21.8	-48.49	19.8	-	19.6	3.01	19.4	-0.92	19.3	-1.19	21.3	-0.36	20.9
28/05/2018 02:06	20.5	-46.34	19.6	-	19.6	1.89	19.3	0.59	19.4	-1.98	21.2	0.54	21.0
28/05/2018 10:06	20.7	-49.21	19.3	-	19.4	1.21	19.0	-0.04	19.2	-2.50	21.1	0.43	20.8
28/05/2018 18:06	21.5	-49.50	19.6	-	19.5	1.67	19.1	0.03	19.2	-2.22	21.2	0.06	20.9
29/05/2018 02:06	19.8	-51.07	19.4	-	19.4	0.83	19.0	0.34	19.2	-2.54	21.1	0.58	20.8
29/05/2018 10:06	20.4	-53.77	19.1	-	19.3	0.30	18.8	-0.03	19.0	-3.08	20.8	0.61	20.6
29/05/2018 18:06	22.3	-56.99	19.4	-	19.4	1.40	19.1	-0.80	19.1	-2.15	21.0	0.04	20.7
30/05/2018 02:06	20.4	-56.38	19.3	-	19.3	0.87	19.0	-0.41	19.1	-2.47	21.0	0.27	20.8

Date	T _{bl} [°C]	SI2i [μ€]	SI2i [°C]	SI2e [μ€]	SI2e [°C]	St4i [μ€]	St4i [°C]	St4e [μ€]	St4e [°C]	St6i [μ€]	St6i [°C]	St6e [μ€]	St6e [°C]
30/05/2018 10:06	21.4	-60.28	19.3	-	19.3	1.02	19.0	-0.75	19.1	-2.42	21.0	-0.07	20.7
30/05/2018 18:06	20.8	-61.34	19.3	-	19.3	0.89	19.0	-0.64	19.1	-2.60	21.0	0.08	20.9
31/05/2018 02:06	19.9	-64.63	19.1	-	19.2	0.46	18.8	-0.52	19.0	-2.72	20.9	0.24	20.8
31/05/2018 10:06	20.5	-69.11	19.2	-	19.2	0.69	18.8	-1.18	19.0	-2.41	20.9	-0.13	20.8
31/05/2018 18:06	23.7	-69.76	19.7	-	19.5	2.11	19.3	-1.89	19.2	-1.66	21.2	-0.48	20.9
01/06/2018 02:06	20.5	-63.16	19.5	-	19.5	0.97	19.1	-0.46	19.3	-2.41	21.2	0.24	20.9
01/06/2018 10:06	20.3	-67.85	19.2	-	19.3	0.56	18.9	-0.45	19.1	-2.78	20.9	0.24	20.7
01/06/2018 18:06	23.5	-64.33	19.9	-	19.7	2.36	19.5	-1.24	19.4	-1.78	21.3	-0.11	21.0
02/06/2018 02:06	21.2	-61.34	19.8	-	19.7	1.78	19.5	-0.55	19.5	-2.17	21.4	0.03	21.1
02/06/2018 10:06	21.1	-65.45	19.7	-	19.6	1.52	19.4	-0.75	19.5	-2.23	21.3	-0.06	21.0
02/06/2018 18:06	23.3	-66.96	20.2	-	19.9	2.51	19.8	-1.57	19.7	-8.30	21.7	-0.69	21.2
03/06/2018 02:06	21.1	-68.05	20.1	-	20.0	2.12	19.9	-1.05	19.9	-8.69	21.8	-0.34	21.4
03/06/2018 10:06	21.2	-71.19	20.0	-	19.9	1.92	19.7	-0.49	19.8	-3.10	21.6	-0.12	21.3
03/06/2018 18:06	21.6	-71.43	20.2	-	20.0	2.24	19.8	-0.61	19.9	-2.78	21.7	-0.05	21.3
04/06/2018 02:06	21.0	-71.94	20.1	-	20.0	1.89	19.8	-0.34	19.8	-2.79	21.7	0.03	21.3
04/06/2018 10:06	20.8	-71.65	19.9	-	19.9	1.51	19.7	-0.13	19.8	-2.93	21.6	0.13	21.3
04/06/2018 18:06	21.1	-73.75	19.7	-	19.8	1.01	19.5	-0.41	19.6	-3.43	21.5	0.14	21.2
05/06/2018 02:06	20.2	-74.74	19.6	-	19.7	0.46	19.3	-0.55	19.6	-3.48	21.4	0.13	21.1
05/06/2018 10:06	20.4	-77.52	19.5	-	19.6	0.66	19.2	-1.09	19.4	-3.36	21.3	-0.08	21.0
05/06/2018 18:06	22.6	-	20.0	-	19.9	2.09	19.7	-1.92	19.7	-2.55	21.6	-0.47	21.2
06/06/2018 02:06	21.1	-78.50	20.0	-	19.9	1.69	19.7	-1.20	19.7	-2.85	21.6	-0.42	21.3
06/06/2018 10:06	21.5	-79.90	19.8	-	19.8	1.09	19.5	-1.09	19.7	-3.45	21.5	-0.16	21.2
06/06/2018 18:06	21.5	-	19.7	-	19.8	1.10	19.5	-0.89	19.7	-4.21	21.4	-0.06	21.2
07/06/2018 02:06	20.4	-	19.6	-	19.7	0.50	19.4	-0.90	19.6	-3.54	21.3	-0.01	21.1
07/06/2018 10:06	20.5	-	19.5	-	19.6	0.40	19.3	-1.38	19.4	-3.29	21.3	-0.33	21.0
07/06/2018 18:06	21.2	-	19.7	-	19.7	0.87	19.4	-1.46	19.5	-3.17	21.4	-0.47	21.1
08/06/2018 02:06	20.1	-	19.4	-	19.5	0.02	19.1	-1.15	19.4	-3.53	21.2	-0.25	20.9
08/06/2018 10:06	20.4	-	19.4	-	19.4	0.03	19.1	-1.44	19.3	-3.52	21.2	-0.54	20.9
08/06/2018 18:06	20.9	-	19.4	-	19.3	0.93	19.2	-2.29	19.2	-1.97	21.4	-1.73	20.8
09/06/2018 02:06	20.0	-	19.3	-	19.3	0.53	19.1	-2.17	19.2	-2.29	21.3	-1.46	20.8
09/06/2018 10:06	19.9	-	19.1	-	19.1	0.50	18.9	-2.39	19.0	-2.26	21.1	-1.85	20.6
09/06/2018 18:06	22.7	-	19.6	-	19.4	2.00	19.4	-2.85	19.3	-1.53	21.5	-2.22	20.9
10/06/2018 02:06	21.0	-	19.6	-	19.5	1.60	19.4	-2.37	19.4	-1.96	21.6	-2.25	20.9
10/06/2018 10:06	21.1	-	19.6	-	19.4	1.58	19.4	-2.55	19.4	-2.21	21.6	-2.43	21.0
10/06/2018 18:06	22.3	-	19.9	-	19.7	2.29	19.7	-2.83	19.5	-1.90	21.8	-2.55	21.1
11/06/2018 02:06	21.1	-	19.9	-	19.7	2.18	19.7	-2.47	19.6	-2.15	21.8	-2.58	21.2
11/06/2018 10:06	21.0	-	19.7	-	19.7	1.59	19.5	-2.33	19.6	-3.38	21.7	-2.46	21.1
11/06/2018 18:06	21.3	-	19.8	-	19.6	1.42	19.5	-3.06	19.4	-4.71	21.4	-4.29	20.8
12/06/2018 02:06	21.2	-	19.5	-	19.4	0.61	19.3	-2.96	19.3	-5.92	21.2	-5.12	20.6
12/06/2018 10:06	20.7	-	19.4	-	19.2	0.68	19.2	-3.72	19.2	-6.09	21.1	-6.13	20.4
12/06/2018 18:06	18.0	-	19.4	-	19.3	0.45	19.1	-3.24	19.2	-6.06	21.0	-5.33	20.4
13/06/2018 02:06	16.9	-	19.2	-	19.1	-0.08	18.9	-3.18	19.0	-6.31	20.8	-5.43	20.2
13/06/2018 10:06	16.9	-	19.0	-	19.0	-0.32	18.8	-3.58	18.9	-5.94	20.7	-5.35	20.1
13/06/2018 18:06	18.0	-	19.2	-	19.0	0.43	19.0	-4.49	18.9	-8.03	20.7	-6.86	20.1
14/06/2018 02:06	17.1	-	19.1	-	19.0	-0.05	18.8	-3.95	18.9	-6.74	20.6	-6.55	20.0

Table A.42: Data sheet for test GH10 – stresses and temperatures.

Date	Pt1 [MPa]	Pt1 [°C]	Pl2 [MPa]	Pl2 [°C]	Pt3 [MPa]	Pt3 [°C]	Pr4 [MPa]	Pr4 [°C]	Pt5 [MPa]	Pt5 [°C]	Pr6 [MPa]	Pr6 [°C]
08/05/2018 10:06	0	18.7	0	18.6	-	18.9	0	18.6	0	34.5	0	18.2
08/05/2018 18:06	-0.26	18.5	0	18.5	-	18.9	-0.16	18.4	-0.24	34.4	-0.4	17.7
09/05/2018 02:06	-0.12	17.5	0	17.6	-	17.8	-0.06	17.6	-0.16	34	-0.22	17.3
09/05/2018 10:06	-0.13	18	0	18	-	18.4	-0.08	18	-0.13	34.2	-0.23	17.6
09/05/2018 18:06	-0.38	16.8	0	17	-	17.2	-0.24	16.9	-0.33	33.9	-0.57	16.8
10/05/2018 02:06	-0.25	16.7	0	16.7	-	16.9	-0.15	16.7	-0.26	33.7	-0.41	16.6
10/05/2018 10:06	-0.21	17.3	0	17.1	-	17.4	-0.15	17.2	-0.21	33.9	-0.4	17
10/05/2018 18:06	-0.43	16.8	0	16.9	-	17.2	-0.27	16.8	-0.38	33.9	-0.67	16.5
11/05/2018 02:06	-0.26	16.8	0.01	16.8	-	17	-0.17	16.8	-0.29	34	-0.47	16.6
11/05/2018 10:06	-0.21	17.5	0	17.3	-	17.6	-0.15	17.4	-0.23	34.3	-0.4	17.1
11/05/2018 18:06	-0.44	16.6	0	16.8	-	17	-0.28	16.6	-0.39	33.8	-0.68	16.4
12/05/2018 02:06	-0.27	16.8	0	16.7	-	16.9	-0.17	16.8	-0.3	34.1	-0.47	16.6
12/05/2018 10:06	-0.23	17.3	0	17.1	-	17.4	-0.15	17.2	-0.23	34.1	-0.42	17
12/05/2018 18:06	-0.45	16.7	0	16.7	-	17.1	-0.28	16.6	-0.39	33.5	-0.69	16.5
13/05/2018 02:06	-0.27	16.8	0	16.7	-	17	-0.17	16.9	-0.29	33.9	-0.48	16.6
13/05/2018 10:06	-0.21	17.2	0	17	-	17.2	-0.15	17.2	-0.22	33.8	-0.41	16.9
13/05/2018 18:06	-0.49	16	0	16	-	16.2	-0.31	16.1	-0.41	32.9	-0.72	16
14/05/2018 02:06	-0.33	16.1	0.01	16	-	16.2	-0.21	16.2	-0.33	32.2	-0.57	16
14/05/2018 10:06	-0.33	15.9	0.01	15.9	-	16.2	-0.22	16	-0.31	31.2	-0.59	15.7
14/05/2018 18:06	-0.59	14.9	0.01	15	-	15.1	-0.38	15	-0.48	30.2	-0.88	15
15/05/2018 02:06	-0.48	14	0.01	14.3	-	14.5	-0.31	14.4	-0.44	29.2	-0.79	14.2
15/05/2018 10:06	-0.48	14.8	0.01	14.7	-	14.9	-0.32	14.8	-0.43	28.9	-0.82	14.7
15/05/2018 18:06	-0.62	15.1	0	15.2	-	15.6	-0.4	15.2	-0.54	29.6	-0.96	15
16/05/2018 02:06	-0.44	15.3	0.01	15.1	-	15.4	-0.29	15.3	-0.43	29.8	-0.76	15.2
16/05/2018 10:06	-0.38	16.2	0.01	15.8	-	16.2	-0.26	16	-0.37	30.2	-0.7	15.8
16/05/2018 18:06	-0.56	15.7	0	15.6	-	16	-0.37	15.7	-0.48	30.6	-0.88	15.5
17/05/2018 02:06	-0.39	15.7	0.01	15.5	-	15.7	-0.26	15.6	-0.39	30.9	-0.69	15.5
17/05/2018 10:06	-0.35	16.2	0.01	16	-	16.3	-0.23	16.2	-0.33	31.3	-0.63	15.9
17/05/2018 18:06	-0.52	16	0	16	-	16.3	-0.33	15.9	-0.46	31.4	-0.82	15.8
18/05/2018 02:06	-0.35	16	0.01	15.9	-	16.1	-0.22	16	-0.37	31.4	-0.62	15.9
18/05/2018 10:06	-0.3	16.8	0	16.5	-	16.8	-0.2	16.6	-0.3	31.8	-0.55	16.4
18/05/2018 18:06	-0.51	16	0	16.1	-	16.4	-0.32	15.9	-0.44	32	-0.78	15.8
19/05/2018 02:06	-0.33	16.4	0.01	16.2	-	16.5	-0.21	16.3	-0.35	32.1	-0.58	16.1
19/05/2018 10:06	-0.28	16.8	0	16.5	-	16.8	-0.18	16.7	-0.28	32.1	-0.51	16.5
19/05/2018 18:06	-0.48	16.4	0	16.4	-	16.8	-0.3	16.3	-0.43	31.9	-0.75	16.1
20/05/2018 02:06	-0.32	16.4	0.01	16.2	-	16.5	-0.2	16.3	-0.34	31.8	-0.57	16.1
20/05/2018 10:06	-0.27	16.6	0	16.5	-	16.7	-0.18	16.6	-0.27	31.9	-0.5	16.3
20/05/2018 18:06	-0.54	15.8	0	15.8	-	16.2	-0.33	15.7	-0.45	31.3	-0.8	15.6
21/05/2018 02:06	-0.36	16.1	0.01	16	-	16.3	-0.22	16.1	-0.37	31.4	-0.6	15.9
21/05/2018 10:06	-0.26	16.7	0	16.5	-	16.8	-0.16	16.6	-0.29	31.4	-0.48	16.3
21/05/2018 18:06	-0.18	17.5	0	17.3	-	17.6	-0.11	17.3	-0.23	31.8	-0.36	17
22/05/2018 02:06	-0.14	17.4	0	17.2	-	17.4	-0.08	17.3	-0.19	31.7	-0.28	17.1
22/05/2018 10:06	-0.12	17.5	0	17.3	-	17.6	-0.06	17.4	-0.16	31.9	-0.24	17.2
22/05/2018 18:06	-0.1	17.7	0	17.5	-	17.7	-0.05	17.6	-0.15	32.3	-0.2	17.4
23/05/2018 02:06	-0.1	17.6	0	17.5	-	17.7	-0.05	17.5	-0.14	32.5	-0.18	17.4
24/05/2018 10:06	-0.05	18.4	0	18.2	-	18.4	-0.01	18.2	-0.1	32.6	-0.09	17.9
24/05/2018 18:06	0.03	18.9	0	19	-	19.3	0.05	18.8	-0.05	32.9	0.01	18.3
25/05/2018 02:06	0.01	18.4	0	18.5	-	18.6	0.04	18.4	-0.04	32.9	0.04	18.1
25/05/2018 10:06	0.02	19	0	18.8	-	19.1	10.73	18.8	-0.03	33.2	0.05	18.4
25/05/2018 18:06	0.09	19.5	0	19.5	-	19.9	0.1	19.4	0.02	33.7	0.15	18.8
26/05/2018 02:06	0.09	19.2	0	19.2	-	19.4	0.1	19.2	0.05	33.9	0.2	18.7
26/05/2018 10:06	0.07	19	0	19	-	19.2	0.08	19	0.04	33.6	0.18	18.6
26/05/2018 18:06	0.12	19.3	0	19.4	-	19.6	0.11	19.4	0.07	33.8	0.24	18.9
27/05/2018 02:06	0.1	19.2	0	19.1	-	19.3	0.11	19.1	0.07	33.8	0.25	18.8
27/05/2018 10:06	0.08	19.2	0	19.1	-	19.3	0.1	19.2	0.06	33.8	0.23	18.8
27/05/2018 18:06	0.15	19.9	0	19.7	-	20.1	0.14	19.7	0.11	34	0.3	19.3
28/05/2018 02:06	0.12	18.9	0	19.1	-	19	0.12	19.1	0.1	33.5	0.29	18.7
28/05/2018 10:06	0.07	19.2	0	19.1	-	19.3	0.09	19.1	0.06	33.5	0.22	18.8
28/05/2018 18:06	0.1	19.3	0	19.3	-	19.4	0.1	19.3	0.07	33.7	0.24	18.9
29/05/2018 02:06	0.07	18.8	0	19	-	19	0.09	18.9	0.06	33.6	0.22	18.6
29/05/2018 10:06	0.02	18.7	0	18.7	-	18.8	0.05	18.7	0.01	33.6	0.13	18.4
29/05/2018 18:06	0.06	19.3	0	19.3	-	19.5	0.07	19.3	0.04	33.9	0.17	18.8
30/05/2018 02:06	0.05	18.9	0	18.9	-	19.1	0.07	19	0.03	33.7	0.18	18.6

Date	Pt1 [MPa]	Pt1 [°C]	Pl2 [MPa]	Pl2 [°C]	Pt3 [MPa]	Pt3 [°C]	Pr4 [MPa]	Pr4 [°C]	Pt5 [MPa]	Pt5 [°C]	Pr6 [MPa]	Pr6 [°C]
30/05/2018 10:06	0.05	19.3	0	19.1	-	19.3	0.06	19.2	0.03	34	0.17	18.9
30/05/2018 18:06	0.05	18.8	0	18.9	-	18.9	0.07	18.9	0.04	34	0.17	18.6
31/05/2018 02:06	0.02	18.7	0	18.8	-	18.9	0.05	18.8	0.01	33.9	0.13	18.5
31/05/2018 10:06	0.02	19.2	0	19	-	19.1	0.05	19.1	0.01	34.1	0.12	18.8
31/05/2018 18:06	0.1	20	0	19.8	-	20.1	0.1	19.8	0.05	34.4	0.22	19.4
01/06/2018 02:06	0.08	18.9	0	19	-	19	0.1	19	0.06	33.9	0.23	18.7
01/06/2018 10:06	0.03	19.4	0	19.1	-	19.3	0.06	19.2	0	33.9	0.13	18.8
01/06/2018 18:06	0.13	19.8	0	19.8	-	20.1	0.13	19.8	0.07	34.2	0.25	19.2
02/06/2018 02:06	0.13	19.6	0	19.5	-	19.6	0.14	19.5	0.1	34.2	0.29	19.2
02/06/2018 10:06	0.12	19.7	0	19.5	-	19.7	0.11	19.6	0.09	34.3	0.28	19.2
02/06/2018 18:06	0.18	20.1	0	20.2	-	20.3	0.17	20.1	0.1	34.5	0.37	19.7
03/06/2018 02:06	0.18	19.9	0	19.9	-	20	0.18	20	0.13	34.6	0.41	19.6
03/06/2018 10:06	0.15	19.8	0	19.8	-	20	0.16	19.8	0.16	34.4	0.38	19.4
03/06/2018 18:06	0.18	19.9	0	19.9	-	20.2	0.17	19.9	0.17	34.3	0.4	19.5
04/06/2018 02:06	0.17	19.8	0	19.7	-	20	0.16	19.8	0.16	34.2	0.39	19.4
04/06/2018 10:06	0.14	19.6	0	19.6	-	19.7	0.14	19.6	0.13	34.1	0.36	19.3
04/06/2018 18:06	0.11	19.5	0	19.4	-	19.6	0.11	19.4	0.11	34	0.31	19.1
05/06/2018 02:06	0.08	19.3	0	19.2	-	19.3	0.1	19.3	0.08	34	0.27	19
05/06/2018 10:06	0.06	19.6	0	19.4	-	19.5	0.07	19.4	0.04	34	0.21	19.1
05/06/2018 18:06	0.14	20	0	20	-	20.3	0.14	19.9	0.1	34.4	0.3	19.4
06/06/2018 02:06	0.15	19.9	0	19.8	-	20	0.15	19.8	0.11	34.6	0.34	19.4
06/06/2018 10:06	0.11	19.7	0	19.6	-	19.7	0.12	19.6	0.1	34.5	0.31	19.2
06/06/2018 18:06	0.08	19.7	0	19.2	-	19.5	0.12	19.5	0.07	34.5	0.28	19.2
07/06/2018 02:06	0.04	19.8	0	19.2	-	19.4	0.09	19.3	0.03	34.4	0.23	18.7
07/06/2018 10:06	0.03	19.2	0	19.2	-	19.4	0.07	19.2	0.01	34.1	0.21	18.7
07/06/2018 18:06	0.06	19.2	0	19.3	-	19.4	0.09	19.3	0.02	33.7	0.23	18.7
08/06/2018 02:06	0.02	19.1	0	19	-	19.1	0.05	19.1	-0.01	33.3	0.17	18.5
08/06/2018 10:06	0.01	19.1	0	19	-	19.1	0.05	19.1	-0.02	33.3	0.15	18.6
08/06/2018 18:06	0.01	19.3	0	19.2	-	19.3	0.04	19.3	0.02	33.3	0.17	18.8
09/06/2018 02:06	-0.01	19	0	18.9	-	19	0.03	19	0.01	33	0.14	18.6
09/06/2018 10:06	-0.03	19.1	0	19	-	19.1	0.01	19.1	-0.04	32.6	0.07	18.6
09/06/2018 18:06	0.04	19.7	0	19.7	-	19.9	0.06	19.6	0.04	32.7	0.18	19
10/06/2018 02:06	0.06	19.6	0	19.4	-	19.6	0.08	19.5	0.07	32.7	0.23	18.9
10/06/2018 10:06	0.05	19.7	0	19.5	-	19.7	0.07	19.6	0.07	32.6	0.24	19.1
10/06/2018 18:06	0.09	19.9	0	19.9	-	20.1	0.1	19.9	0.11	32.5	0.29	19.4
11/06/2018 02:06	0.1	19.8	0	19.7	-	19.9	0.11	19.8	0.14	32.6	0.34	19.4
11/06/2018 10:06	0.07	19.5	0	19.5	-	19.6	0.1	19.5	0.1	32.2	0.29	19.1
11/06/2018 18:06	0.03	19.6	0	19.7	-	19.9	0.06	19.6	0.01	31.9	0.19	19
12/06/2018 02:06	-0.01	19.3	0	19.3	-	19.4	0.04	19.3	-0.07	31.5	0.07	18.7
12/06/2018 10:06	-0.03	19.3	0	19.3	-	19.6	0.02	19.3	-0.1	31.4	0	18.7
12/06/2018 18:06	-0.04	18.9	0	19.1	-	19.2	0.01	19.1	-0.14	30.5	-0.04	18.2
13/06/2018 02:06	-0.08	18.8	0	18.9	-	19	-0.01	18.8	-0.17	30.2	-0.11	18.2
13/06/2018 10:06	-0.1	18.7	0	18.8	-	18.9	-0.02	18.8	-0.2	30	-0.16	18.1
13/06/2018 18:06	-0.08	19.1	0	19.1	-	19.3	-0.01	19.1	-0.2	30	-0.17	18.2
14/06/2018 02:06	-0.1	18.7	0	18.8	-	19	-0.02	18.8	-0.21	29.8	-0.2	18

Table A.43: Data sheet for test GH10 - sensors T1-T5 and heat pump.

Date	T1 [°C]	T2 [°C]	T3 [°C]	T4 [°C]	T5 [°C]	Date	Tair [°C]	IN [°C]	OUT [°C]	U1 [°C]	U2 [°C]
08/05/2018 10:11	18.5	16.8	17.4	18.2	18.2	08/05/2018 10:00	17.9	18.8	19	7.8	8.2
08/05/2018 12:19	18.5	13.7	15.4	18.7	18.5	08/05/2018 16:03	37.5	11.6	13.7	48.4	41.9
08/05/2018 14:27	18.7	13.3	14.9	19.1	18.9	09/05/2018 00:03	19.4	17.8	18	17.1	10
08/05/2018 16:35	19	13	14.6	19.6	19.2	09/05/2018 08:02	16.3	18.1	18.2	8.4	7.1
08/05/2018 18:43	19.9	17.9	17.7	19.7	19.3	09/05/2018 16:02	29.2	10.7	12.8	46.1	39.6
08/05/2018 20:51	20.6	19	18.7	20.9	20.3	10/05/2018 00:01	16.9	17	17.3	15.5	8.1
08/05/2018 22:59	18.9	18.9	18.6	19.6	19.1	10/05/2018 08:01	15.7	17.3	17.5	7.3	6.8
09/05/2018 01:07	18.3	18.9	18.7	18.6	18.4	10/05/2018 16:00	31.8	10.2	12.3	45.3	38.9
09/05/2018 03:15	18.1	19	18.7	17.8	17.9	11/05/2018 00:00	18.8	16.7	16.9	16.9	9.3
09/05/2018 05:23	18	19	18.8	17.7	17.9	11/05/2018 07:59	17	17.2	17.4	8.4	8.2
09/05/2018 07:31	17.4	19	18.7	17.3	17.6	11/05/2018 15:59	31	10.1	12.3	45.1	38.6
09/05/2018 09:39	17.9	19.1	18.9	17.7	17.9	11/05/2018 23:58	18.7	16.6	16.8	15.9	9.2
09/05/2018 11:47	18.2	13.1	14.8	18.2	18.3	12/05/2018 07:58	16.5	17.1	17.4	8.3	8.2
09/05/2018 13:55	18.4	12.6	14.3	18.4	18.5	12/05/2018 15:57	24.8	10	12.2	44.2	37.8
09/05/2018 16:03	19.1	12.4	14	18.6	18.7	12/05/2018 23:57	18.7	16.6	16.8	16.3	9.2
09/05/2018 18:11	18.3	15.8	15.7	18.2	18.3	13/05/2018 07:56	17.3	17.2	17.4	8.6	8.6
09/05/2018 20:19	18.4	17.8	17.5	18.2	18.4	13/05/2018 15:56	22.3	9.7	12	42.8	36.4
09/05/2018 22:27	17.9	18	17.8	17.8	17.9	13/05/2018 23:55	16.4	16.2	16.5	14.4	7.4
10/05/2018 00:35	17.8	18.1	17.9	17.5	17.6	14/05/2018 07:55	13.8	16.7	16.9	6.3	5.7
10/05/2018 02:43	17.1	18.2	17.9	17.2	17.5	14/05/2018 15:54	16.9	8.8	11.1	38.6	32.2
10/05/2018 04:51	17	18.2	18	16.9	17.3	14/05/2018 23:54	13.1	15.4	15.6	15.1	5.4
10/05/2018 06:59	16.7	18.2	18	16.5	17	15/05/2018 07:53	11.7	15.6	15.8	4.5	3.3
10/05/2018 09:07	17.6	18.5	18.2	17.1	17.6	15/05/2018 15:53	33.3	9	11	45.3	39.1
10/05/2018 11:15	18.3	12.8	14.5	17.8	18	15/05/2018 23:52	17.2	15.2	15.4	15.6	7.7
10/05/2018 13:23	18.6	12.3	14	18.5	18.4	16/05/2018 07:52	14.8	15.8	16	6.7	6.2
10/05/2018 15:31	18.6	11.9	13.6	18.4	18.4	16/05/2018 15:51	28.1	9.1	11.2	44.1	37.9
10/05/2018 17:39	18.6	11.7	13.4	18.8	18.7	16/05/2018 23:51	17.6	15.5	15.7	16.3	8.1
11/05/2018 15:01	18.3	11.9	13.6	18.2	18.4	17/05/2018 07:50	14.6	16.1	16.3	7.2	6.8
11/05/2018 15:09	18.2	11.8	13.5	18.2	18.3	17/05/2018 15:50	34.6	9.6	11.6	46.9	40.6
11/05/2018 15:17	18.2	11.8	13.5	18.2	18.3	17/05/2018 23:49	18.2	15.8	16.1	16.6	8.7
11/05/2018 16:25	18.2	11.7	13.4	18	18.1	18/05/2018 07:49	16.2	16.4	16.6	7.6	7.8
11/05/2018 18:33	18.9	16.6	16.3	18.6	18.7	18/05/2018 15:48	26	9.5	11.7	44.1	37.8
11/05/2018 20:25	18.6	17.4	17.1	18.7	18.6	18/05/2018 23:48	18.4	16	16.2	16.6	8.8
11/05/2018 20:52	18.3	17.4	17.2	18.5	18.4	19/05/2018 07:47	16.7	16.6	16.8	7.8	8.3
11/05/2018 21:15	18.2	17.5	17.2	18.4	18.2	19/05/2018 15:46	35.4	9.9	12	46.6	40.3
08/06/2018 10:10	19	20.6	20.3	18.8	18.9	19/05/2018 23:46	18.5	16.1	16.3	18.6	8.9
08/06/2018 10:18	19	20.6	20.2	18.9	18.9	20/05/2018 07:45	16.9	16.7	16.9	8.3	8.2
08/06/2018 10:26	19	20.6	20.2	18.9	18.9	20/05/2018 15:45	30.3	9.6	11.8	44.2	37.9
08/06/2018 10:34	19	20.6	20.3	18.9	18.9	20/05/2018 23:44	18.4	15.9	16.1	18	8.8
08/06/2018 10:56	19	20.7	20.3	18.9	18.9	21/05/2018 07:44	16.6	16.6	16.8	8.1	7.9
08/06/2018 11:14	19.6	20.7	20.3	19	19	21/05/2018 15:43	27.4	17.2	17.4	8.3	8.3
08/06/2018 11:30	19.1	20.7	20.3	19	19	21/05/2018 23:43	18	17.5	17.7	8.5	8.5
08/06/2018 11:46	19.2	20.2	20	19.7	19.5	22/05/2018 07:42	16.7	17.7	17.9	7.5	7.8
08/06/2018 12:02	19.2	20.2	20	19.8	19.6	22/05/2018 15:42	17.4	17.8	18	7.2	7.5
08/06/2018 13:42	19.1	20.3	20	19.9	19.7	22/05/2018 23:41	16.6	17.9	18.1	7.2	7.4
08/06/2018 15:50	18.9	20.2	19.9	19.8	19.7	23/05/2018 07:41	16.2	18	18.2	7	7.1
08/06/2018 17:58	19.3	20.3	20	19.9	19.7	23/05/2018 15:40	19.9	18.3	18.4	8.5	8.4
08/06/2018 20:06	18.9	20.2	19.9	19.8	19.6	23/05/2018 23:40	18	18.4	18.6	8.5	8.5
08/06/2018 22:14	19	20.2	20	19.8	19.7	24/05/2018 07:39	16.5	18.3	18.5	7.2	7.7
09/06/2018 00:22	18.9	20.2	19.9	19.8	19.7	24/05/2018 15:39	29.2	18.8	18.9	9.2	9
09/06/2018 02:30	18.6	20.1	19.8	19.7	19.6	24/05/2018 23:38	18.7	18.8	19	9.5	9.4
09/06/2018 04:38	18.2	19.9	19.7	19.5	19.4	25/05/2018 07:38	17.8	18.8	18.9	8.1	8.5
09/06/2018 06:46	17.9	19.8	19.6	19.3	19.3	25/05/2018 15:37	32.9	19.3	19.5	10.2	9.9
09/06/2018 08:54	18.6	19.9	19.7	19.5	19.4	25/05/2018 23:37	19.3	19.2	19.4	10.4	10.3
09/06/2018 11:02	19	20.1	19.8	19.7	19.5	26/05/2018 07:36	18.5	19.2	19.4	8.6	9.2
09/06/2018 13:10	19.7	20.3	19.9	20	19.7	26/05/2018 15:36	28.4	19.5	19.7	9.7	9.6
09/06/2018 15:18	19.6	20.6	20.1	20.2	19.9	26/05/2018 23:35	18.9	19.4	19.6	9.6	9.6
09/06/2018 17:26	19.6	20.4	20.1	20.1	19.9	27/05/2018 07:35	18.3	19.4	19.6	8.6	9
09/06/2018 19:34	19.4	20.4	20.1	20.1	19.9	27/05/2018 15:34	21.2	19.5	19.7	9.3	9.3
09/06/2018 21:42	19.6	20.4	20.1	20.1	19.9	27/05/2018 23:34	19	19.6	19.8	9.4	9.4
09/06/2018 23:50	20.1	20.5	20.2	20.3	20.1	28/05/2018 07:33	17.8	19.5	19.7	8.4	8.8
10/06/2018 01:58	19.7	20.4	20.1	20.1	20	28/05/2018 15:33	19.5	19.5	19.7	8.8	8.8
10/06/2018 04:06	19.5	20.4	20.2	20.1	19.9	28/05/2018 23:32	18.1	19.5	19.7	8.9	9

Date	T1 [°C]	T2 [°C]	T3 [°C]	T4 [°C]	T5 [°C]	Date	Tair [°C]	IN [°C]	OUT [°C]	U1 [°C]	U2 [°C]
10/06/2018 06:14	19.3	20.4	20.1	20	19.9	29/05/2018 07:32	17.6	19.3	19.5	7.8	8.3
10/06/2018 08:22	19.6	20.4	20.1	20.1	19.9	29/05/2018 15:31	23.7	19.4	19.6	9.1	8.9
10/06/2018 10:30	19.4	20.5	20.1	20.1	19.9	29/05/2018 23:31	18.7	19.3	19.5	9.7	9.7
10/06/2018 12:38	20.1	20.6	20.3	20.3	20.1	30/05/2018 07:30	18	19.3	19.5	8.4	8.9
10/06/2018 14:46	19.9	20.7	20.4	20.4	20.2	30/05/2018 15:30	19.7	19.3	19.6	9.2	9.2
10/06/2018 16:54	19.7	20.7	20.3	20.3	20.1	30/05/2018 23:29	17.9	19.3	19.5	8.3	8.7
10/06/2018 19:02	19.6	20.7	20.4	20.3	20.1	31/05/2018 07:29	17.7	19.2	19.4	7.9	8.2
10/06/2018 21:10	19.9	20.7	20.4	20.4	20.2	31/05/2018 15:28	24.4	19.5	19.6	9.5	9.4
10/06/2018 23:18	19.7	20.7	20.4	20.4	20.2	31/05/2018 23:28	19.1	19.5	19.7	10.3	10.3
11/06/2018 01:26	20.2	20.8	20.4	20.5	20.3	01/06/2018 07:27	16.5	19.3	19.5	7.8	8.7
11/06/2018 03:34	19.7	20.7	20.4	20.3	20.2	01/06/2018 15:27	24.7	19.7	19.9	9.8	9.7
11/06/2018 05:42	19.4	20.6	20.3	20.2	20.1	01/06/2018 23:26	20.1	19.7	19.9	10.7	10.6
11/06/2018 07:50	19.8	20.7	20.3	20.4	20.1	02/06/2018 07:26	18.6	19.6	19.8	9	9.6
11/06/2018 09:58	19.3	20.5	20.2	20.1	19.9	02/06/2018 16:15	37.7	19.9	20.1	11.6	10.8
						03/06/2018 00:14	19.7	20	20.2	10.6	10.6
						03/06/2018 08:14	19.1	19.9	20.2	9.2	9.8
						03/06/2018 16:13	20.8	20	20.2	10	10
						04/06/2018 00:13	19.4	20	20.2	9.7	9.7
						04/06/2018 08:12	19.3	19.9	20.1	9.1	9.3
						04/06/2018 16:12	18.3	19.8	20	8.9	9.1
						05/06/2018 00:11	18.4	19.7	19.9	8.8	8.9
						05/06/2018 08:11	16.8	19.6	19.8	7.8	8.2
						05/06/2018 16:10	25.1	19.9	20.1	10.6	10.2
						06/06/2018 00:10	19.6	19.9	20.1	9.9	9.9
						06/06/2018 08:09	19	19.8	20	9.1	9.4
						06/06/2018 16:09	20.5	19.9	20.1	10.1	10
						07/06/2018 00:08	18.5	19.7	19.9	9.1	9.4
						07/06/2018 08:07	18.4	19.6	19.8	8.5	8.8
						07/06/2018 16:07	22.9	19.7	19.9	9.9	9.7
						08/06/2018 00:06	18.2	19.6	19.7	8.7	9.1
						08/06/2018 08:06	18.2	19.5	19.7	8.2	8.5
						08/06/2018 16:05	18.6	19	19.2	8.6	8.7
						09/06/2018 00:05	18.1	19	19.2	8.7	8.8
						09/06/2018 08:04	16.8	18.8	19	7.5	8
						09/06/2018 16:04	37.6	19.3	19.4	10.5	9.7
						10/06/2018 00:03	19.4	19.3	19.4	10	10
						10/06/2018 08:03	18.7	19.2	19.4	9	9.4
						10/06/2018 16:02	31.4	19.5	19.7	10.6	10.2
						11/06/2018 00:02	19.1	19.5	19.7	10	10
						11/06/2018 08:11	19.2	19.3	19.6	9.3	9.6
						11/06/2018 22:59	20.2	31.8	49.5	10.8	10.7
						12/06/2018 06:59	20.2	31.8	49.5	10.8	10.7

Table A.44: Summary of test GH10 records.

Quantity	Unit	$x(t_0)$	$x(t_1)$	$x(t_1) - x(t_0)$	$\bar{x}(t_0, t_1)$
T _{DL}	[°C]	20.2	20.7	0.5	19.4
Sl2i	[μϵ]	-3213.36	-3231.02	-17.66	16.3
	[μϵ] _{comp} [°C]	0.00 18.7	23.82 15.3	23.82 -3.4	
Sl2e	[μϵ]	-	-2610.45	-	-
	[μϵ] _{comp} [°C]	- 18.7	- 14.5	- -4.2	15.9
St4i	[μϵ]	-1763.74	-1763.74	0.00	-
	[μϵ] _{comp} [°C]	0.00 18.3	31.72 15.7	31.72 -2.6	16.5
St4e	[μϵ]	-1503.95	-1509.77	-5.82	-
	[μϵ] _{comp} [°C]	0.00 18.3	30.78 15.3	30.78 -3.0	16.3
St6i	[μϵ]	-2172.51	-2177.60	-5.09	-
	[μϵ] _{comp} [°C]	0.00 20.0	26.63 17.4	26.63 -2.6	18.1
St6e	[μϵ]	-1796.72	-1813.62	-16.90	-
	[μϵ] _{comp} [°C]	0.00 19.9	28.24 16.2	28.24 -3.7	17.5
Pt1	[MPa]	0.73	0.19	-0.54	16.4
	[°C]	18.7	15.8	-2.9	
Pl2	[MPa]	-0.06	-0.06	0.00	16.4
	[°C]	18.6	15.9	-2.7	
Pt3	[MPa]	-	-	-	16.7
	[°C]	18.9	16.3	-2.6	
Pr4	[MPa]	0.63	0.29	-0.34	16.4
	[°C]	18.6	15.7	-2.9	
Pt5	[MPa]	0.72	0.27	-0.45	32.3
	[°C]	34.5	31.3	-3.2	
Pr6	[MPa]	1.35	0.55	-0.80	16.2
	[°C]	18.2	15.6	-2.6	
T1	[°C]	18.5	18.2	-0.3	18.4
T2	[°C]	16.8	17.6	0.8	15.7
T3	[°C]	17.4	17.4	0.0	16.3
T4	[°C]	18.2	18.2	0.0	18.3
T5	[°C]	18.2	18.2	0.0	18.3
Air	[°C]	17.6	22.5	4.9	19.7
IN	[°C]	18.7	9.1	-9.6	14.1
OUT	[°C]	19.0	11.3	-7.7	15.0
U1	[°C]	7.5	42.6	35.1	25.2
U2	[°C]	7.6	36.3	28.7	20.3

Test GC1

This was the first test carried out to simulate heat injection in the ground with the aim to cool buildings' indoor environment.

Circuit:	Ground
Mode:	Cooling
Secondary circuit temperature:	10°C
Activated rings:	179+180
Volumetric flow rate:	1.4 m ³ /h
Fluid velocity in primary circuit:	0.97 m/s
Starting time t ₀ :	27/07/2018 11:29
Ending time t ₁ :	30/07/2018 11:31
Duration:	3.00 days
Note:	Some data are missing (great increase or decrease). Stops due to attainment of minimum U1 or set U2.

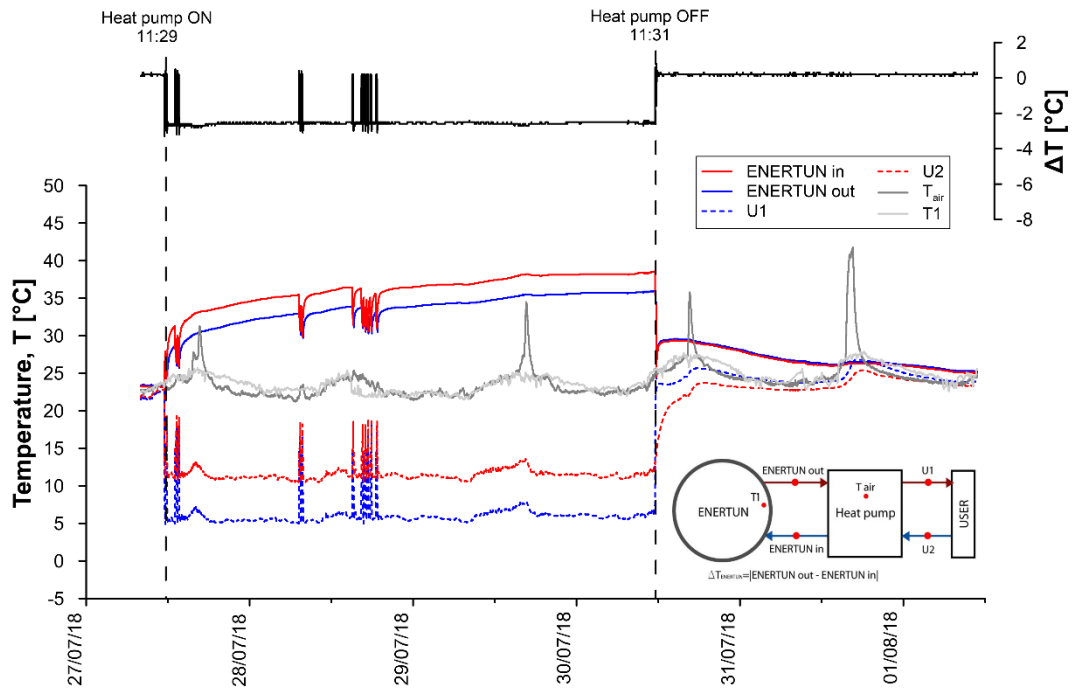


Figure A.142: Primary circuit, secondary circuit and air temperatures for test GC1.

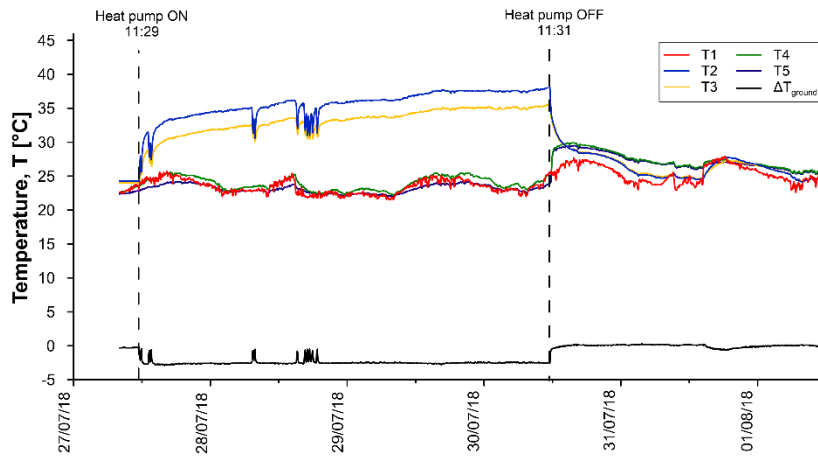


Figure A.143: Temperatures T1-T5 for test GC1.

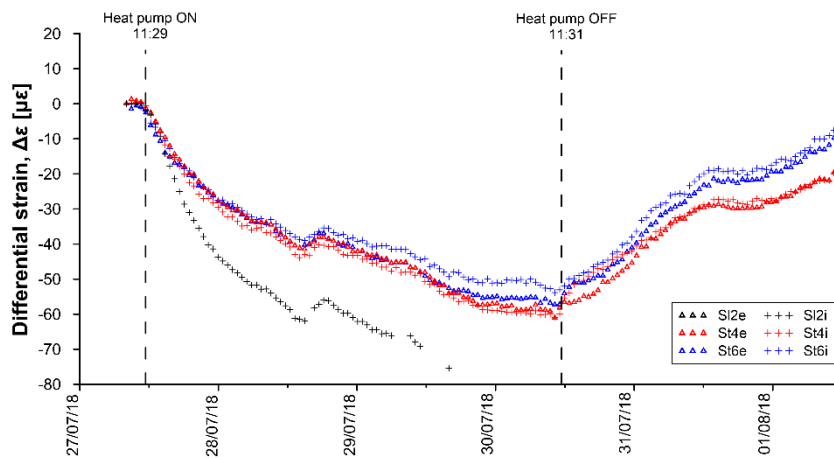


Figure A.144: Differential strains for test GC1.

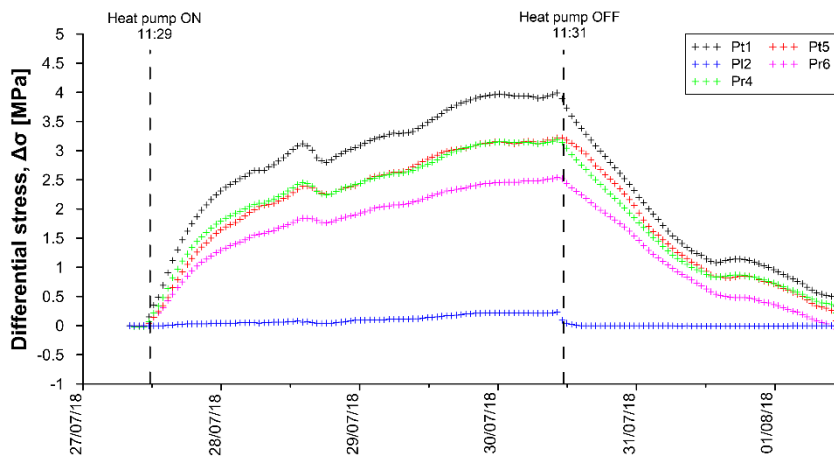


Figure A.145: Differential stresses for test GC1.

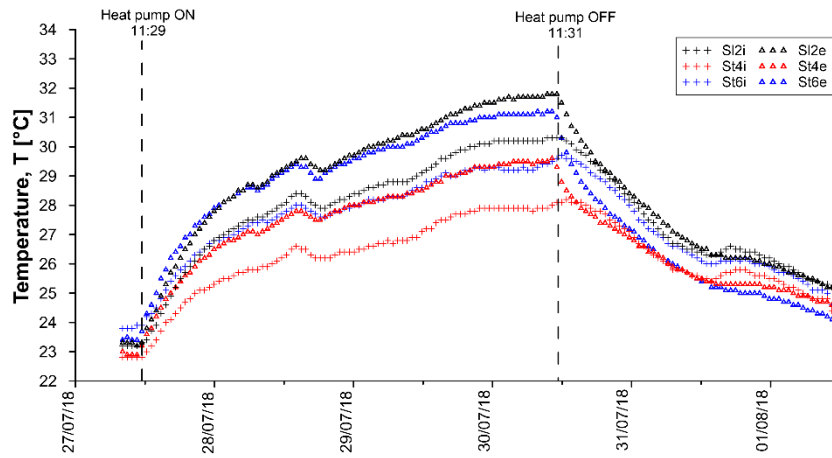


Figure A.146: Temperatures measured by VWSG for test GC1.

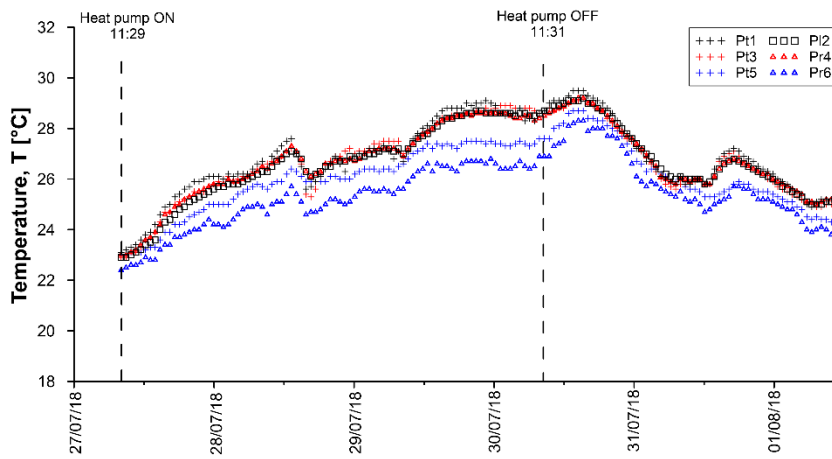


Figure A.147: Temperatures measured by PC for test GC1.

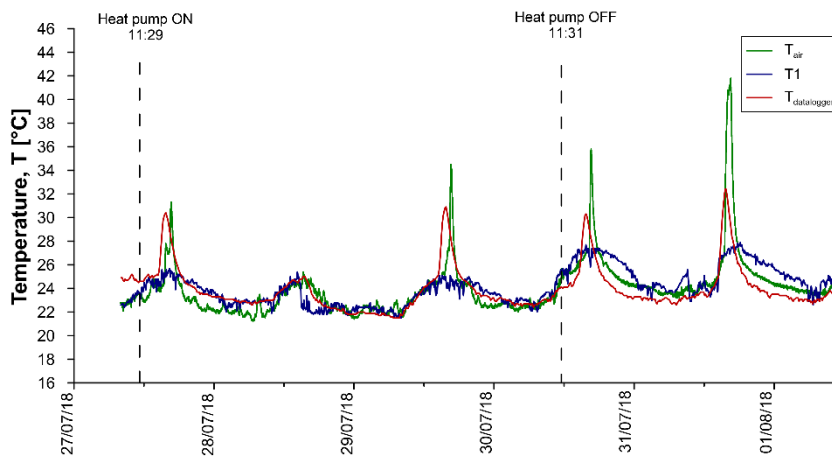


Figure A.148: Air temperatures for test GC1.

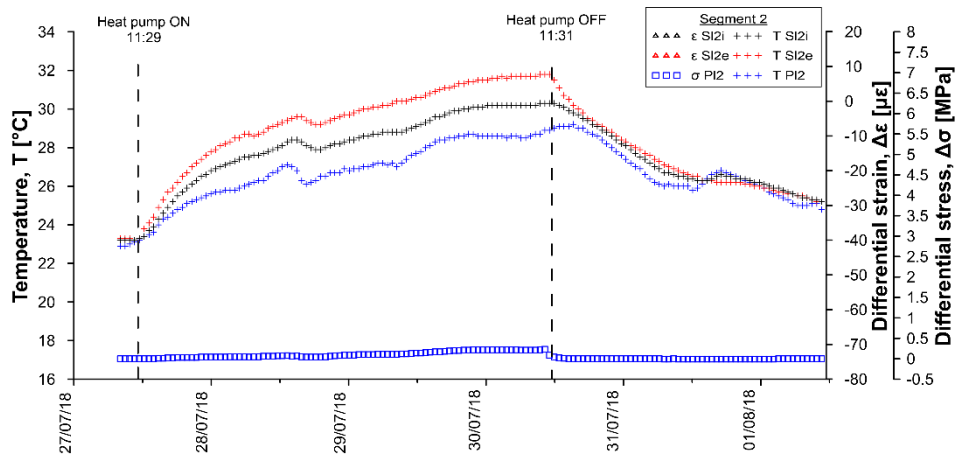


Figure A.149: Temperatures, differential strains and differential stresses in segment 2, ring 179 for test GC1.

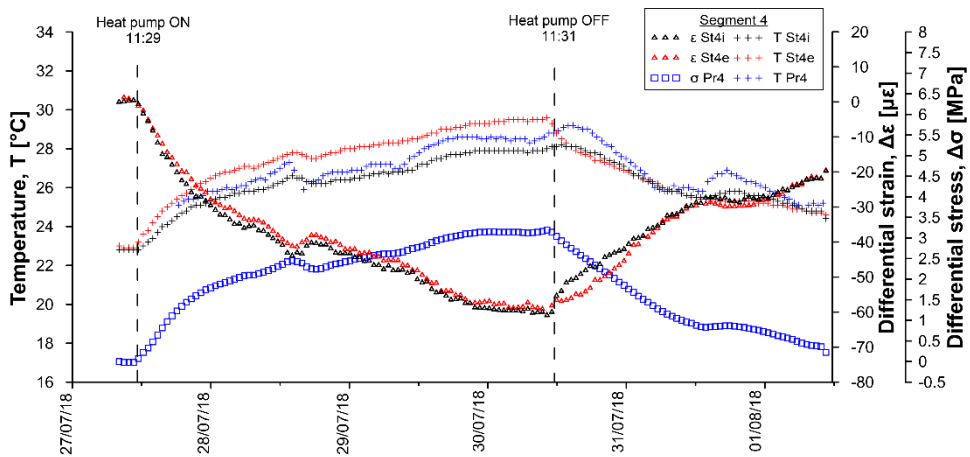


Figure A.150: Temperatures, differential strains and differential stresses in segment 4, ring 179 for test GC1.

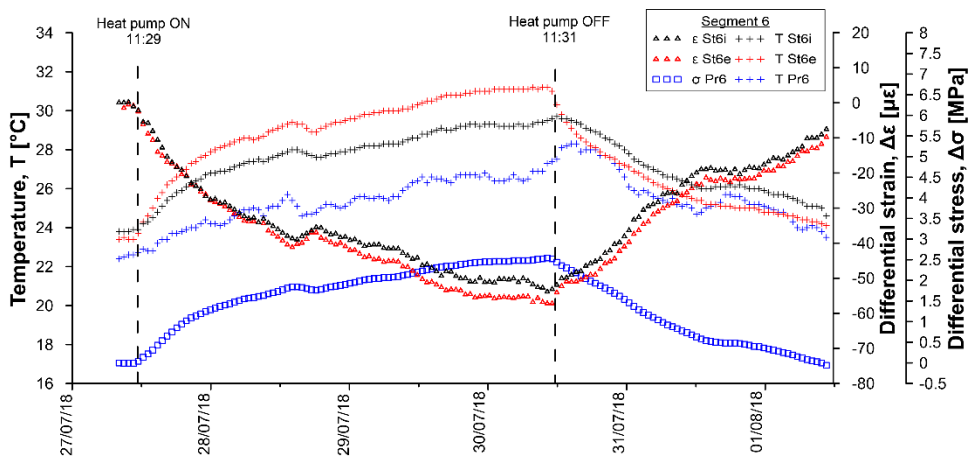


Figure A.151: Temperatures, differential strains and differential stresses in segment 6, ring 179 for test GC1.

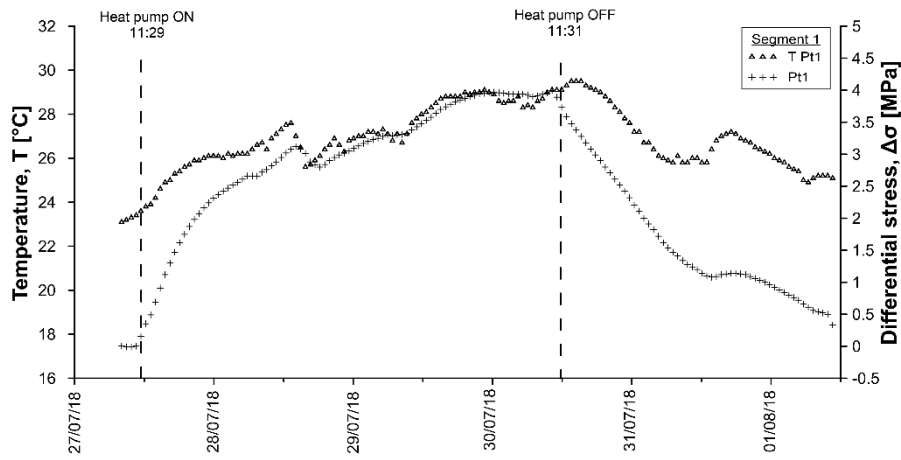


Figure A.152: Temperatures and differential stresses in segment 1, ring 179 for test GC1.

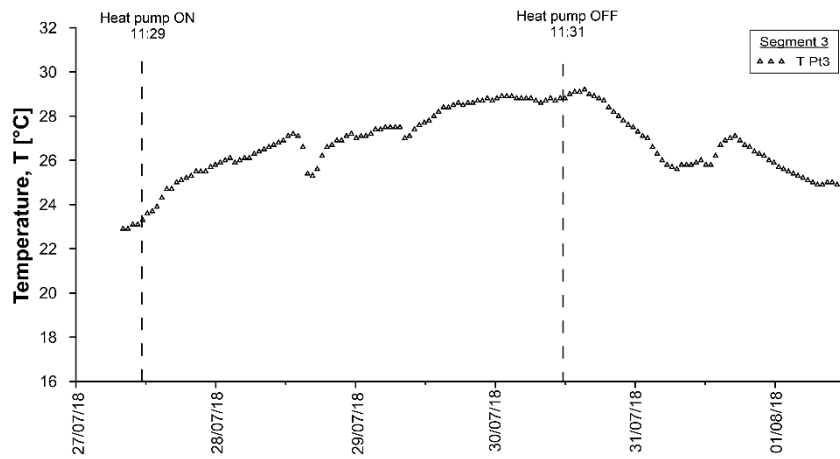


Figure A.153: Temperatures and differential stresses in segment 3, ring 179 for test GC1.

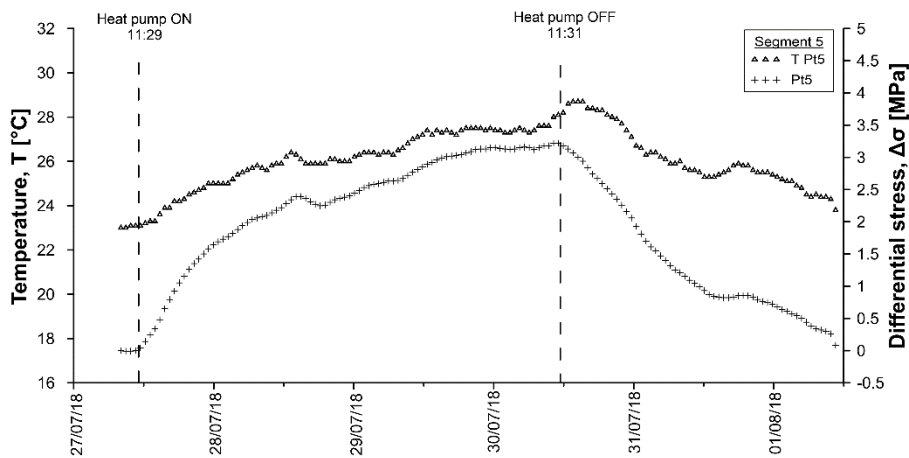


Figure A.154: Temperatures and differential stresses in segment 5, ring 179 for test GC1.

Table A.45: Data sheet for test GC1 – strains and temperatures.

Date	T _{DI} [°C]	SI2i [μϵ]	SI2i [°C]	SI2e [μϵ]	SI2e [°C]	St4i [μϵ]	St4i [°C]	St4e [μϵ]	St4e [°C]	St6i [μϵ]	St6i [°C]	St6e [μϵ]	St6e [°C]
27/07/2018 08:06	24.9	0.00	23.2	-	23.3	0.00	22.8	0.00	23.0	0.00	23.8	0.00	23.4
27/07/2018 10:06	25.1	-0.15	23.2	-	23.2	0.43	22.8	-0.46	22.9	0.19	23.9	-0.67	23.4
27/07/2018 12:06	24.8	-0.57	23.4	-	23.7	-1.13	23.0	4.46	23.6	-1.11	24.1	4.11	24.2
27/07/2018 14:06	25.1	-0.81	23.9	-	24.5	-0.93	23.4	7.22	24.2	0.59	24.6	9.42	25.1
27/07/2018 16:06	29.8	-0.67	24.8	-	25.5	-0.07	24.1	10.06	24.9	3.75	25.3	15.99	26.0
27/07/2018 18:06	25.4	-0.59	25.5	-	26.2	0.62	24.5	11.47	25.4	5.97	25.8	20.90	26.6
27/07/2018 20:06	24.2	-0.29	26.0	-	26.8	0.99	24.9	12.48	25.8	7.32	26.2	23.62	27.1
27/07/2018 22:06	23.5	0.02	26.5	-	27.4	0.98	25.1	14.14	26.2	8.22	26.5	25.66	27.6
28/07/2018 00:06	23.3	0.19	26.8	-	27.8	0.95	25.4	14.92	26.5	9.09	26.8	27.26	27.9
28/07/2018 02:06	23.1	0.29	27.1	-	28.1	0.63	25.5	15.89	26.7	9.34	26.9	28.84	28.2
28/07/2018 04:06	22.9	0.53	27.3	-	28.5	0.55	25.7	16.36	26.9	9.80	27.1	29.48	28.4
28/07/2018 06:06	22.8	0.68	27.5	-	28.7	0.61	25.8	16.70	27.1	10.41	27.3	29.92	28.6
28/07/2018 08:06	22.9	0.87	27.6	-	28.7	1.09	25.9	15.92	27.1	11.03	27.4	29.16	28.6
28/07/2018 10:06	23.0	0.84	27.8	-	29.0	1.08	26.0	16.83	27.3	11.08	27.5	30.77	28.9
28/07/2018 12:06	24.1	0.90	28.1	-	29.3	1.72	26.3	16.85	27.6	11.55	27.8	31.38	29.2
28/07/2018 14:06	24.6	1.96	28.4	-	29.5	2.48	26.6	17.37	27.8	12.56	28.0	32.06	29.4
28/07/2018 16:06	24.5	2.75	28.2	-	29.6	1.80	26.4	17.15	27.7	11.86	27.9	31.62	29.2
28/07/2018 18:06	23.0	1.27	27.9	-	29.2	1.19	26.2	16.87	27.5	10.97	27.7	29.99	29.0
28/07/2018 20:06	22.3	1.16	28.0	-	29.4	0.78	26.3	18.28	27.7	10.92	27.7	31.78	29.2
28/07/2018 22:06	22.3	1.25	28.2	-	29.6	0.77	26.4	18.82	27.9	11.59	27.8	33.08	29.4
29/07/2018 00:06	21.8	1.37	28.4	-	29.7	0.73	26.4	18.93	28.0	12.06	28.0	33.63	29.6
29/07/2018 02:06	21.9	1.44	28.5	-	29.9	0.88	26.6	19.00	28.1	12.70	28.1	33.88	29.7
29/07/2018 04:06	21.8	1.54	28.7	-	30.1	1.00	26.7	19.19	28.2	13.16	28.2	34.59	29.9
29/07/2018 06:06	21.7	-	28.8	-	30.2	1.03	26.7	19.42	28.2	13.44	28.3	35.15	29.9
29/07/2018 08:06	21.8	-	28.8	-	30.3	0.79	26.7	19.41	28.3	13.45	28.3	35.29	30.0
29/07/2018 10:06	22.6	1.55	28.9	-	30.4	1.15	26.9	19.15	28.4	13.73	28.5	34.95	30.1
29/07/2018 12:06	24.1	2.13	29.2	-	30.6	2.00	27.1	18.98	28.5	14.59	28.7	35.18	30.3
29/07/2018 14:06	24.9	-	29.4	-	30.8	2.60	27.3	18.97	28.8	15.06	28.9	35.53	30.5
29/07/2018 16:06	30.0	2.75	29.7	-	31.1	3.12	27.5	19.18	29.0	15.39	29.1	36.56	30.7
29/07/2018 18:06	25.2	-	29.8	-	31.2	3.36	27.7	19.29	29.1	15.26	29.0	37.04	30.8
29/07/2018 20:06	24.2	-	30.0	-	31.3	3.55	27.8	19.35	29.2	15.83	29.2	36.86	30.9
29/07/2018 22:06	23.4	-	30.1	-	31.5	3.46	27.9	19.57	29.3	16.04	29.3	37.39	31.0
30/07/2018 00:06	23.0	-	30.2	-	31.5	3.20	27.9	19.80	29.3	16.06	29.3	37.72	31.0
30/07/2018 02:06	23.0	-	30.2	-	31.6	2.83	27.9	20.45	29.4	15.65	29.2	38.50	31.1
30/07/2018 04:06	22.7	-	30.2	-	31.6	2.63	27.9	20.44	29.4	15.71	29.2	38.35	31.1
30/07/2018 06:06	22.6	-	30.2	-	31.7	2.32	27.9	20.77	29.5	15.85	29.2	38.77	31.1
30/07/2018 08:06	22.9	-	30.2	-	31.7	2.04	27.9	20.55	29.5	15.54	29.3	38.18	31.1
30/07/2018 10:06	23.4	-	30.3	-	31.8	2.37	28.0	19.46	29.5	16.20	29.4	38.06	31.2
30/07/2018 12:06	24.1	-	30.3	-	31.4	9.96	28.2	13.71	28.8	20.26	29.7	29.28	30.2
30/07/2018 14:06	24.9	-	30.0	-	30.5	13.64	28.1	6.39	28.1	20.82	29.5	20.15	29.2
30/07/2018 16:06	29.7	-	29.7	-	30.0	14.30	28.0	3.52	27.8	19.12	29.3	13.03	28.6
30/07/2018 18:06	25.4	-	29.3	-	29.5	13.92	27.8	2.74	27.5	17.32	28.9	9.01	28.2
30/07/2018 20:06	24.2	-	28.9	-	29.1	13.00	27.6	2.60	27.3	15.84	28.6	6.84	27.8
30/07/2018 22:06	23.5	-	28.5	-	28.7	11.67	27.3	2.50	27.1	14.40	28.3	5.54	27.4
31/07/2018 00:06	23.3	-	28.1	-	28.3	9.83	27.0	2.97	26.8	12.76	27.8	5.41	27.1
31/07/2018 02:06	23.1	-	27.7	-	28.0	7.51	26.6	3.20	26.6	11.37	27.4	5.13	26.8
31/07/2018 04:06	22.9	-	27.3	-	27.6	5.99	26.3	2.95	26.3	10.53	27.1	3.77	26.4
31/07/2018 06:06	23.0	-	26.9	-	27.3	4.53	26.0	2.63	26.1	9.33	26.8	2.97	26.1
31/07/2018 08:06	23.2	-	26.6	-	27.0	4.47	25.8	1.64	25.8	8.59	26.6	1.79	25.9
31/07/2018 10:06	23.3	-	26.5	-	26.7	4.24	25.6	1.29	25.6	8.25	26.3	1.43	25.6
31/07/2018 12:06	23.4	-	26.4	-	26.5	4.22	25.5	0.87	25.5	8.15	26.1	1.24	25.4
31/07/2018 14:06	24.6	-	26.2	-	26.3	4.89	25.5	-0.19	25.3	8.06	26.0	0.37	25.2
31/07/2018 16:06	31.2	-	26.5	-	26.3	7.42	25.7	-1.38	25.3	8.84	26.1	-0.79	25.1
31/07/2018 18:06	25.9	-	26.5	-	26.2	8.33	25.8	-1.57	25.3	9.17	26.2	-1.95	25.0
31/07/2018 20:06	24.2	-	26.5	-	26.1	7.71	25.7	-1.45	25.3	8.97	26.2	-2.27	25.0
31/07/2018 22:06	23.8	-	26.3	-	26.1	6.65	25.6	-1.31	25.3	8.25	26.0	-2.07	25.0
01/08/2018 00:06	23.5	-	26.2	-	25.9	5.77	25.5	-1.12	25.2	7.91	25.9	-2.27	24.8
01/08/2018 02:06	23.4	-	25.9	-	25.8	4.80	25.3	-1.05	25.1	7.33	25.7	-2.16	24.7
01/08/2018 04:06	23.2	-	25.8	-	25.7	3.90	25.2	-0.79	25.0	6.85	25.6	-2.26	24.6
01/08/2018 06:06	23.0	-	25.6	-	25.5	2.57	25.0	-0.42	24.9	6.08	25.3	-1.59	24.5
01/08/2018 08:06	23.2	-	25.4	-	25.4	2.41	24.8	-0.68	24.7	5.85	25.1	-1.91	24.3
01/08/2018 10:06	23.8	-	25.3	-	25.2	2.68	24.8	-0.83	24.6	5.41	25.0	-1.90	24.2

Table A.46: Data sheet for test GC1 – stresses and temperatures.

Date	Pt1 [MPa]	Pt1 [°C]	Pl2 [MPa]	Pl2 [°C]	Pt3 [MPa]	Pt3 [°C]	Pr4 [MPa]	Pr4 [°C]	Pt5 [MPa]	Pt5 [°C]	Pr6 [MPa]	Pr6 [°C]
27/07/2018 08:06	0	23.1	0	22.9	-	22.9	0	23	0	23	0	22.4
27/07/2018 10:06	-0.01	23.4	0	23.1	-	23.1	-0.02	23.2	-0.01	23.1	-0.01	22.7
27/07/2018 12:06	0.32	23.9	0	23.4	-	23.6	0.2	23.5	0.11	23.3	0.13	22.9
27/07/2018 14:06	0.73	24.3	0.01	23.8	-	24.1	0.52	24	0.37	23.5	0.34	23
27/07/2018 16:06	1.23	25	0.02	24.4	-	24.7	0.91	24.6	0.73	23.9	0.61	23.4
27/07/2018 18:06	1.62	25.4	0.03	24.8	-	25.1	1.23	25	1.05	24.2	0.85	23.7
27/07/2018 20:06	1.91	25.8	0.03	25.1	-	25.4	1.47	25.4	1.3	24.6	1.04	24
27/07/2018 22:06	2.14	26	0.04	25.4	-	25.6	1.65	25.6	1.49	24.8	1.18	24.2
28/07/2018 00:06	2.33	26.1	0.04	25.6	-	25.8	1.8	25.8	1.65	25	1.3	24.2
28/07/2018 02:06	2.44	26	0.04	25.7	-	26.1	1.9	25.9	1.75	25	1.38	24.1
28/07/2018 04:06	2.56	26.2	0.05	25.8	-	26	2	25.9	1.88	25.4	1.47	24.6
28/07/2018 06:06	2.67	26.3	0.05	26	-	26.1	2.1	26.1	2.02	25.6	1.56	24.9
28/07/2018 08:06	2.71	26.7	0.05	26.3	-	26.5	2.13	26.4	2.08	25.7	1.61	25
28/07/2018 10:06	2.83	26.9	0.06	26.5	-	26.7	2.22	26.6	2.15	25.7	1.67	24.9
28/07/2018 12:06	2.99	27.4	0.07	26.9	-	27	2.34	27	2.26	26.2	1.75	25.4
28/07/2018 14:06	3.12	27	0.06	27	-	27.1	2.45	27.1	2.39	26.3	1.84	25.4
28/07/2018 16:06	2.94	25	0.04	26	-	24.8	2.34	25.9	2.33	25.8	1.81	24.5
28/07/2018 18:06	2.8	26.2	0.03	26.3	-	26.1	2.24	26.3	2.26	26	1.76	25
28/07/2018 20:06	2.9	26.6	0.05	26.6	-	26.7	2.3	26.6	2.3	26.1	1.81	25.2
28/07/2018 22:06	3.01	26.4	0.07	26.7	-	27	2.38	26.8	2.38	26	1.88	25
29/07/2018 00:06	3.09	26.9	0.09	26.8	-	27	2.44	26.7	2.44	26.2	1.93	25.3
29/07/2018 02:06	3.18	27	0.1	26.9	-	27.1	2.52	26.9	2.54	26.4	1.99	25.6
29/07/2018 04:06	3.25	27.1	0.1	27.1	-	27.4	2.57	27.2	2.59	26.4	2.04	25.5
29/07/2018 06:06	3.3	26.9	0.11	27.2	-	27.5	2.61	27.2	2.63	26.4	2.07	25.5
29/07/2018 08:06	3.31	26.9	0.11	27.1	-	27.2	2.63	27	2.66	26.6	2.09	25.7
29/07/2018 10:06	3.38	27.6	0.12	27.4	-	27.4	2.7	27.4	2.77	27	2.14	26.1
29/07/2018 12:06	3.5	28.1	0.14	27.8	-	27.8	2.79	27.8	2.86	27.1	2.21	26.3
29/07/2018 14:06	3.63	28.4	0.16	28.1	-	28.1	2.88	28.2	2.95	27.4	2.28	26.6
29/07/2018 16:06	3.75	28.8	0.18	28.4	-	28.4	2.97	28.4	3.01	27.3	2.33	26.5
29/07/2018 18:06	3.83	28.8	0.2	28.5	-	28.5	3.03	28.5	3.03	27.3	2.36	26.4
29/07/2018 20:06	3.9	28.9	0.21	28.6	-	28.6	3.1	28.5	3.09	27.5	2.4	26.7
29/07/2018 22:06	3.95	29.1	0.22	28.7	-	28.8	3.13	28.6	3.13	27.5	2.43	26.7
30/07/2018 00:06	3.97	29.1	0.22	28.7	-	28.8	3.15	28.6	3.15	27.5	2.45	26.7
30/07/2018 02:06	3.95	28.4	0.22	28.6	-	28.9	3.14	28.6	3.13	27.3	2.45	26.3
30/07/2018 04:06	3.94	28.7	0.22	28.5	-	28.7	3.14	28.4	3.15	27.5	2.47	26.6
30/07/2018 06:06	3.92	28.4	0.21	28.5	-	28.8	3.13	28.5	3.15	27.3	2.48	26.4
30/07/2018 08:06	3.92	28.6	0.21	28.6	-	28.6	3.13	28.4	3.17	27.7	2.5	27
30/07/2018 10:06	3.98	29.1	0.23	28.9	-	28.7	3.18	28.7	3.21	27.9	2.53	27.2
30/07/2018 12:06	3.7	29.2	0.04	29	-	28.8	3.02	28.9	3.17	28.3	2.42	27.6
30/07/2018 14:06	3.42	29.5	0.01	29.1	-	29.1	2.79	29.1	3.03	28.7	2.26	28.2
30/07/2018 16:06	3.18	29.3	0	29	-	29	2.58	29	2.84	28.4	2.11	27.9
30/07/2018 18:06	2.95	29.1	0	28.8	-	28.7	2.39	28.8	2.63	28.4	1.96	28
30/07/2018 20:06	2.73	28.6	0	28.4	-	28.3	2.2	28.3	2.44	28	1.82	27.7
30/07/2018 22:06	2.49	28	0	27.9	-	27.7	2	27.9	2.24	27.6	1.67	27.2
31/07/2018 00:06	2.25	27.3	0	27.4	-	27.3	1.8	27.4	1.98	26.9	1.49	26.2
31/07/2018 02:06	2	26.7	0	27	-	27	1.59	26.9	1.7	26.3	1.29	25.7
31/07/2018 04:06	1.77	26.4	0	26.5	-	26.2	1.41	26.4	1.52	26.3	1.14	25.7
31/07/2018 06:06	1.56	25.9	0	26.1	-	25.7	1.22	25.9	1.34	25.9	0.99	25.4
31/07/2018 08:06	1.4	26.2	0	26.1	-	25.8	1.09	26	1.2	26	0.87	25.5
31/07/2018 10:06	1.26	25.9	-0.01	26	-	25.9	0.98	26	1.06	25.6	0.74	25.2
31/07/2018 12:06	1.14	25.8	-0.01	25.8	-	25.8	0.88	25.8	0.93	25.3	0.63	24.7
31/07/2018 14:06	1.08	26.5	-0.01	26.2	-	26.4	0.83	26.3	0.83	25.4	0.53	25
31/07/2018 16:06	1.13	27.1	-0.01	26.7	-	27.1	0.86	26.7	0.82	25.6	0.49	25.3
31/07/2018 18:06	1.14	27.1	-0.01	26.7	-	26.9	0.87	26.7	0.86	25.8	0.48	25.7
31/07/2018 20:06	1.1	26.7	-0.01	26.4	-	26.5	0.83	26.5	0.84	25.8	0.46	25.6
31/07/2018 22:06	1.03	26.4	-0.01	26.2	-	26.2	0.78	26.2	0.76	25.5	0.4	25.2
01/08/2018 00:06	0.95	26.1	-0.01	25.9	-	25.8	0.72	26	0.71	25.3	0.35	25
01/08/2018 02:06	0.85	25.8	-0.01	25.6	-	25.5	0.64	25.7	0.61	25.1	0.29	24.8
01/08/2018 04:06	0.75	25.5	0	25.4	-	25.2	0.57	25.5	0.53	24.9	0.22	24.6
01/08/2018 06:06	0.62	25	0	25.1	-	25	0.47	25.1	0.4	24.5	0.13	23.9
01/08/2018 08:06	0.54	25.2	0	25	-	24.9	0.39	25.1	0.32	24.4	0.05	24.1
01/08/2018 10:06	0.47	25.4	0	25.1	-	25.2	0.32	25.2	0.2	24.3	-0.01	23.9

Table A.47: Data sheet for test GC1 - sensors T1-T5 and heat pump.

Date	T1 [°C]	T2 [°C]	T3 [°C]	T4 [°C]	T5 [°C]	Date	Tair [°C]	IN [°C]	OUT [°C]	U1 [°C]	U2 [°C]
27/07/2018 08:02	22.6	24.3	24	22.6	22.3	27/07/2018 08:00	22.8	23.3	23.4	21.5	21.7
27/07/2018 10:02	23.4	24.3	24	23	22.6	27/07/2018 10:00	23	23.2	23.4	22.1	22.4
27/07/2018 12:02	24.5	28.4	26	23.9	23	27/07/2018 12:30	23.2	30.7	28	5.7	11.7
27/07/2018 14:02	24.7	31.2	28.6	24.7	23.5	27/07/2018 14:30	24.1	31.9	29.3	5.6	11.6
27/07/2018 16:02	25.3	33.1	30.3	25.2	23.9	27/07/2018 16:30	28.8	33.1	30.4	6.6	12.6
27/07/2018 18:02	25.2	33.5	30.8	25.4	24.1	27/07/2018 18:30	24	33.5	30.9	5.3	11
27/07/2018 20:02	24.5	33.8	31.2	25.1	24	27/07/2018 20:30	23.3	33.9	31.3	5.4	11.2
27/07/2018 22:02	23.9	34.1	31.5	24.8	23.9	27/07/2018 22:30	22.2	34.3	31.7	5.4	11.1
28/07/2018 00:02	23.6	34.4	31.9	24.4	23.7	28/07/2018 00:30	22.1	34.7	32.1	5.4	11
28/07/2018 02:02	22.2	34.5	31.9	23.3	22.9	28/07/2018 02:30	22	34.9	32.4	5.4	11.1
28/07/2018 04:02	22.8	34.7	32.1	22.9	22.6	28/07/2018 04:29	22.2	35.2	32.6	5.3	10.9
28/07/2018 06:02	22.8	35	32.4	23.4	22.8	28/07/2018 06:29	21.4	35.4	32.9	5.1	10.7
28/07/2018 08:02	23	33.5	31.2	23.5	22.9	28/07/2018 08:29	21.6	35.1	32.6	5.4	10.8
28/07/2018 10:02	22.4	35.1	32.5	23.1	22.5	28/07/2018 10:29	22.3	35.7	33.1	5.4	10.8
28/07/2018 12:02	24.2	35.8	33.2	24.2	23.2	28/07/2018 12:29	23.7	36.1	33.5	6	11.6
28/07/2018 14:02	24.7	36.1	33.5	24.8	23.5	28/07/2018 14:29	24.5	36.4	33.9	5.8	11.3
28/07/2018 16:02	22.1	35.6	33	23.6	23.1	28/07/2018 16:29	24.4	32.5	32.6	14.3	14.7
28/07/2018 18:02	21.9	32.6	30.8	22.6	22.5	28/07/2018 18:29	22.8	35.6	33.1	5.7	11.1
28/07/2018 20:02	22.4	35.5	32.9	22.5	22.2	28/07/2018 20:29	22.5	36.2	33.6	5.9	11.4
28/07/2018 22:02	22.2	35.8	33.3	22.9	22.3	28/07/2018 22:28	22.4	36.4	33.8	5.7	11.2
29/07/2018 00:02	22.1	35.9	33.4	22.5	22.2	29/07/2018 00:28	21.5	36.5	34	5.6	11.1
29/07/2018 02:02	22.5	36.1	33.6	23.1	22.4	29/07/2018 02:28	22.5	36.7	34.1	5.8	11.4
29/07/2018 04:02	21.9	36.1	33.6	23	22.3	29/07/2018 04:28	22.3	36.8	34.2	5.6	11.1
29/07/2018 06:02	22.1	36.3	33.8	22.8	22.3	29/07/2018 06:28	22.2	36.9	34.4	5.6	11.2
29/07/2018 08:02	21.7	36.1	33.6	22.2	22	29/07/2018 08:28	21.8	36.9	34.4	5.2	10.6
29/07/2018 10:02	23.1	36.5	34	23.2	22.6	29/07/2018 10:28	23.5	37.2	34.6	6.4	12
29/07/2018 12:02	23.6	36.9	34.3	24.2	23.1	29/07/2018 12:28	23.8	37.5	34.9	6.4	12
29/07/2018 14:02	23.4	37.2	34.6	24.8	23.5	29/07/2018 14:28	24.5	37.8	35.2	6.9	12.5
29/07/2018 16:02	24.4	37.5	34.9	25.2	23.8	29/07/2018 16:27	30.4	38.1	35.5	7.7	13.3
29/07/2018 18:02	23.4	37.4	34.8	24.8	23.6	29/07/2018 18:27	24.2	38	35.4	6	11.5
29/07/2018 20:02	24.5	37.6	35.1	25.4	24.1	29/07/2018 20:27	23.3	38.1	35.5	6.1	11.6
29/07/2018 22:02	23.8	37.6	35.1	25.1	23.9	29/07/2018 22:27	22.7	38.1	35.5	6.1	11.5
30/07/2018 00:02	23.7	37.5	35	24.7	23.7	30/07/2018 00:27	22.5	38.2	35.6	6.2	11.7
30/07/2018 02:02	22.8	37.4	34.9	23.7	23.1	30/07/2018 02:27	22.7	38.2	35.7	6	11.4
30/07/2018 04:02	22.7	37.5	35.1	23.4	23	30/07/2018 04:27	22.2	38.2	35.7	5.8	11.2
30/07/2018 06:02	22.8	37.5	35.1	23.8	23	30/07/2018 06:27	22.6	38.2	35.7	5.6	11
30/07/2018 08:02	23.2	37.6	35.1	23.4	22.9	30/07/2018 08:27	22.6	38.2	35.7	5.8	11.2
30/07/2018 10:02	23.7	37.8	35.3	24.3	23.3	30/07/2018 10:26	23.1	38.4	35.8	6.1	11.6
30/07/2018 12:02	25.3	33.1	32.7	28.4	28.2	30/07/2018 12:26	25.4	29.1	29.3	23.6	18.1
30/07/2018 14:02	26.7	29.7	29.6	29.7	29.3	30/07/2018 14:26	26.1	29.3	29.6	23.7	21.2
30/07/2018 16:02	27.1	28.7	28.9	29.8	29.5	30/07/2018 16:26	30	29.3	29.5	24.9	22
30/07/2018 18:02	27.4	28.4	28.4	29.5	29.2	30/07/2018 18:26	26.6	28.9	29.1	25.6	23.7
30/07/2018 20:02	26.6	28.2	28.2	29.2	28.9	30/07/2018 20:26	25.3	28.6	28.8	25.4	23.6
30/07/2018 22:02	26.2	27.7	27.8	28.8	28.5	30/07/2018 22:26	24.5	28.3	28.4	24.9	23.3
31/07/2018 00:02	25.1	26.9	27	28.2	28	31/07/2018 00:26	24.2	27.8	28.1	24.5	23.1
31/07/2018 02:02	24.2	25.7	25.9	27.6	27.4	31/07/2018 02:26	24	27.4	27.6	24.3	23
31/07/2018 04:02	24.4	25.2	25.4	27.4	27.2	31/07/2018 04:25	23.6	27	27.2	24.1	22.9
31/07/2018 06:02	23.7	24.9	25	27	26.9	31/07/2018 06:25	23.6	26.7	26.9	23.9	22.8
31/07/2018 08:02	24.5	24.8	25	26.8	26.8	31/07/2018 08:25	23.7	26.4	26.6	23.7	22.7
31/07/2018 10:02	23.5	24.8	24.8	26.5	26.4	31/07/2018 10:25	23.8	26.2	26.4	23.8	22.8
31/07/2018 12:02	25.1	24.8	25	26.6	26.4	31/07/2018 12:25	24.5	26.1	26.3	23.8	23
31/07/2018 14:02	24.3	24.6	24.7	26.4	26.2	31/07/2018 14:25	25	25.9	26.1	24	23.1
31/07/2018 16:02	27.2	26.5	26.2	27.3	26.9	31/07/2018 16:25	40.8	26.3	26.5	26.1	24.4
31/07/2018 18:02	27.6	27.6	27.1	27.4	27	31/07/2018 18:25	26.4	26.3	26.5	26.7	25.4
31/07/2018 20:02	26.9	27.6	27.2	27.2	26.9	31/07/2018 20:25	25.3	26.3	26.4	26.2	24.7
31/07/2018 22:02	26.3	27	26.8	27	26.7	31/07/2018 22:24	24.8	26.1	26.3	25.5	24.4
01/08/2018 00:02	25.7	26.7	26.6	26.8	26.6	01/08/2018 00:24	24.3	25.9	26.1	25	24.2
01/08/2018 02:02	25.1	26.1	26	26.4	26.2	01/08/2018 02:24	24.1	25.8	25.9	24.6	24
01/08/2018 04:02	24.9	25.7	25.7	26.2	26.1	01/08/2018 04:24	23.7	25.6	25.8	24.3	23.8
01/08/2018 06:02	23.1	24.9	24.9	25.6	25.5	01/08/2018 06:24	23.5	25.3	25.5	24	23.6
01/08/2018 08:02	24.5	24.2	24.3	25.7	25.5	01/08/2018 08:24	23.8	25.1	25.3	23.8	23.4
01/08/2018 10:02	24.2	24.7	24.7	25.6	25.5	01/08/2018 10:24	24.6	25	25.3	23.8	23.4

Table A.48: Summary of test GC1 records.

Quantity	Unit	$x(t_0)$	$x(t_1)$	$x(t_1) - x(t_0)$	$\bar{x}(t_0, t_1)$
T _{DL}	[°C]	24.6	24.1	-0.5	23.7
Sl2i	[με]	-343.47	-3282.63	-	
	[με] _{comp}	-1.78	-3026.51	-	
	[°C]	23.3	30.3	7.0	28.2
Sl2e	[με]	-	-	-	
	[με] _{comp}	-	-	-	
	[°C]	23.4	31.7	8.3	29.5
St4i	[με]	-1759.51	-1752.04	7.47	
	[με] _{comp}	-0.58	-57.94	-57.36	
	[°C]	22.9	28.1	5.2	26.4
St4e	[με]	-1502.61	-1488.14	14.47	
	[με] _{comp}	-1.18	-57.76	-56.58	
	[°C]	23.3	29.1	5.8	27.7
St6i	[με]	-2179.17	-2159.15	20.02	
	[με] _{comp}	-2.12	-23.03	-50.91	
	[°C]	23.9	29.7	5.8	27.9
St6e	[με]	-1793.66	-1762.51	31.15	
	[με] _{comp}	-2.49	-56.00	-53.51	
	[°C]	23.8	30.7	6.9	29.3
Pt1	[MPa]	1.81	5.44	3.63	
	[°C]	23.7	29.1	5.4	27.1
Pl2	[MPa]	-0.07	-0.01	0.06	
	[°C]	23.3	28.9	5.6	26.9
Pt3	[MPa]	-	-	-	
	[°C]	23.4	28.8	5.4	27.0
Pr4	[MPa]	1.59	4.59	3.00	
	[°C]	23.4	28.8	5.4	26.9
Pt5	[MPa]	1.72	4.89	3.17	
	[°C]	23.2	28.1	4.9	26.2
Pr6	[MPa]	2.55	4.98	2.43	
	[°C]	22.8	27.4	4.6	25.4
T1	[°C]	23.4	25.4	2.0	23.4
T2	[°C]	24.2	38.0	13.8	35.6
T3	[°C]	24.0	35.5	11.5	33.1
T4	[°C]	23.5	25.5	2.0	23.9
T5	[°C]	22.8	24.0	1.2	23.1
Air	[°C]	23.6	23.7	0.1	23.0
IN	[°C]	26.3	37.3	11.0	35.0
OUT	[°C]	23.3	34.8	11.5	32.5
U1	[°C]	17.6	6.2	-11.4	6.1
U2	[°C]	22.7	11.8	-10.9	11.5

Test AH1

On July 30th, 2018 the operating mode was reversed from cooling to heating and the air circuit was activated in place of the ground one. The main goal was to take advantage of the high summer temperatures to mimic mountain tunnels and try out the Enertun concept for tunnel cooling purposes.

Circuit:	Air
Mode:	Heating (tunnel cooling)
Secondary circuit temperature:	55°C
Activated rings:	179+180
Volumetric flow rate:	1.3 m ³ /h
Fluid velocity in primary circuit:	0.9 m/s
Starting time t_0 :	01/08/2018 10:56
Ending time t_1 :	03/08/2018 15:56
Duration:	2.21 days
Note:	Stops due to attainment of maximum or set U2.

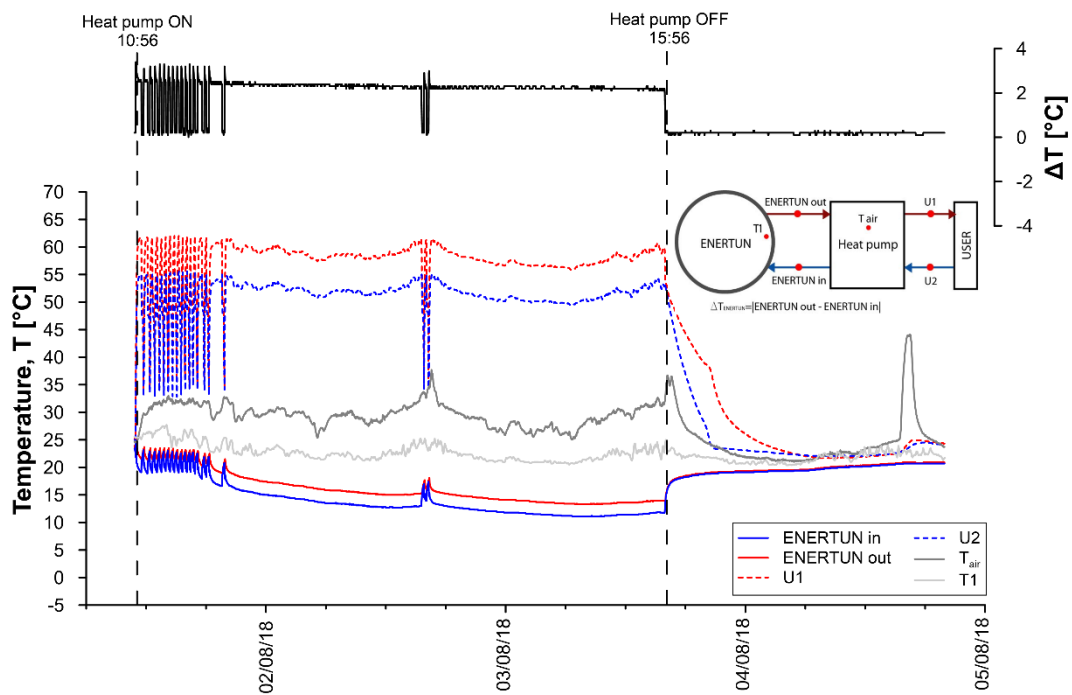


Figure A.155: Primary circuit, secondary circuit and air temperatures for test AH1.

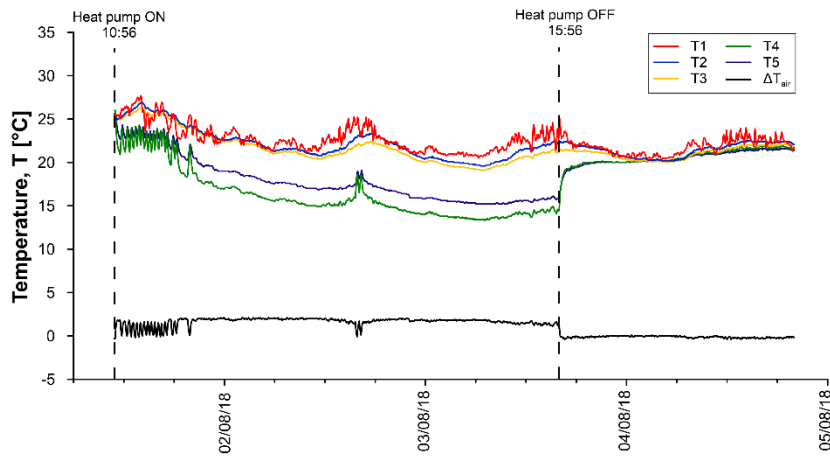


Figure A.156: Temperatures T1-T5 for test AH1.

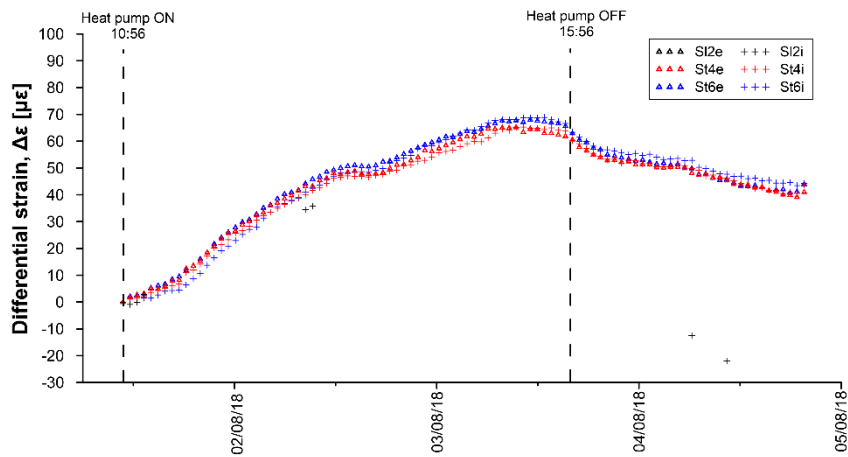


Figure A.157: Differential strains for test AH1.

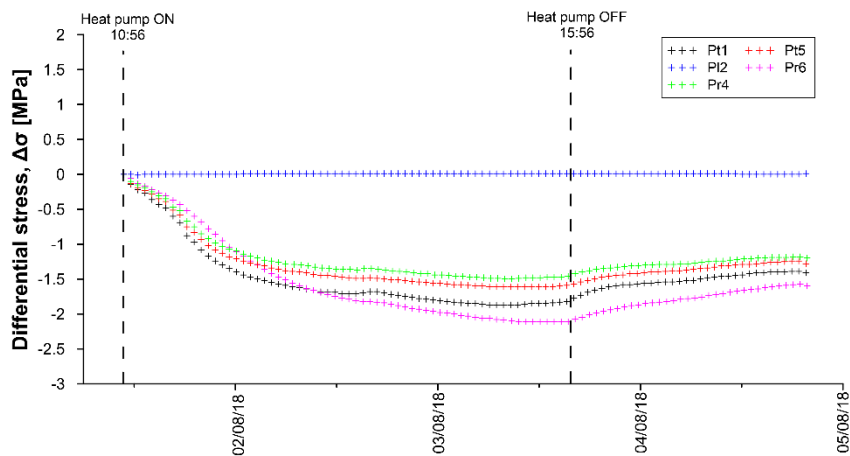


Figure A.158: Differential stresses for test AH1.

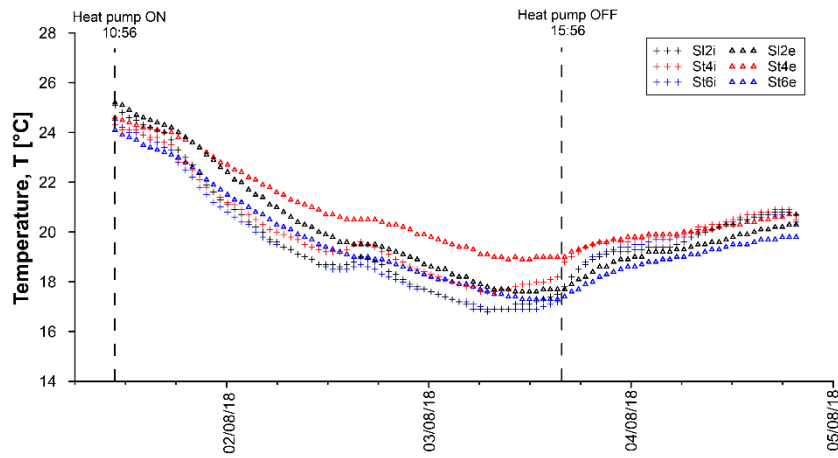


Figure A.159: Temperatures measured by VWSG for test AH1.

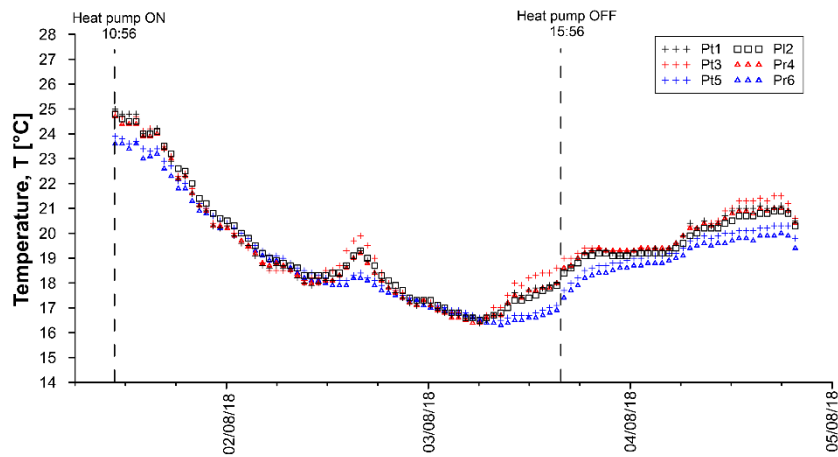


Figure A.160: Temperatures measured by PC for test AH1.

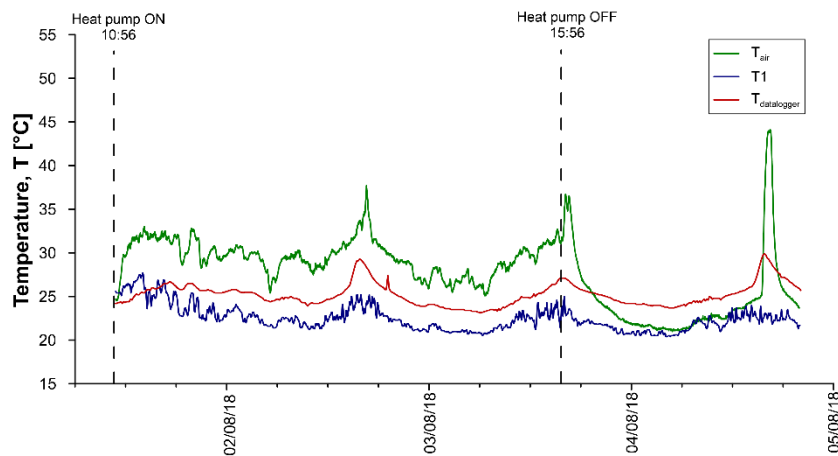


Figure A.161: Air temperatures for test AH1.

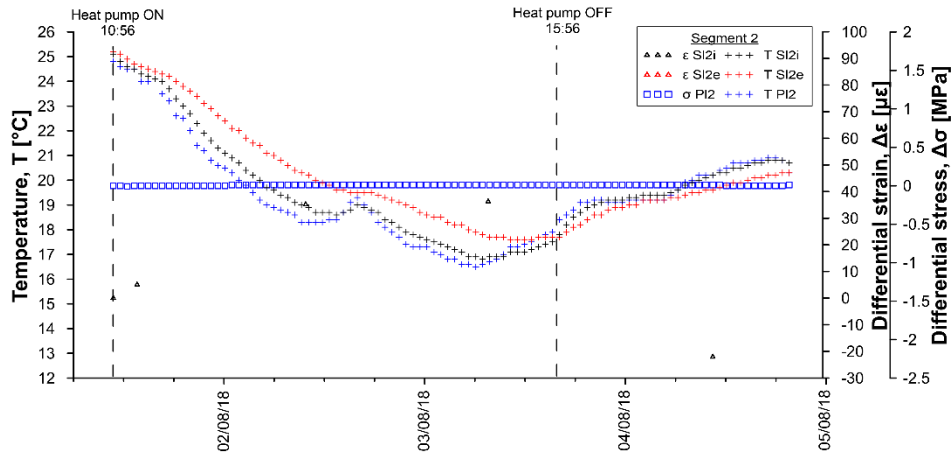


Figure A.162: Temperatures, differential strains and differential stresses in segment 2, ring 179 for test AH1.

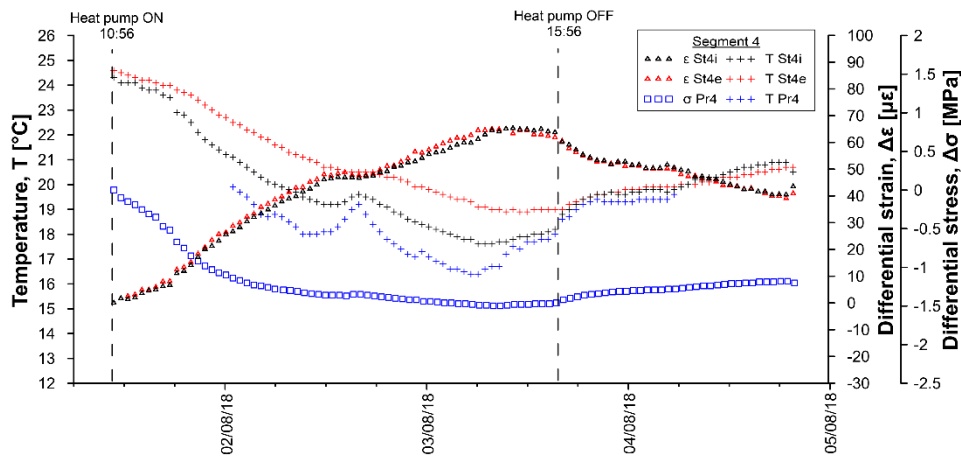


Figure A.163: Temperatures, differential strains and differential stresses in segment 4, ring 179 for test AH1.

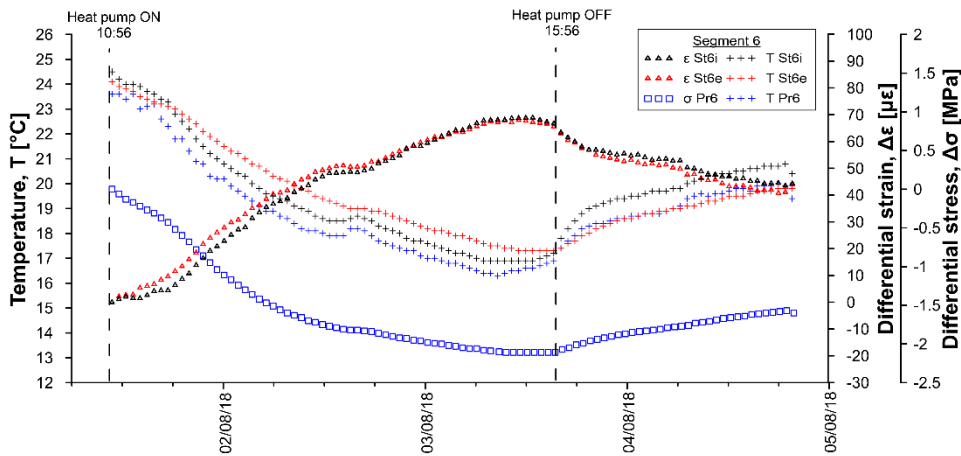


Figure A.164: Temperatures, differential strains and differential stresses in segment 6, ring 179 for test AH1.

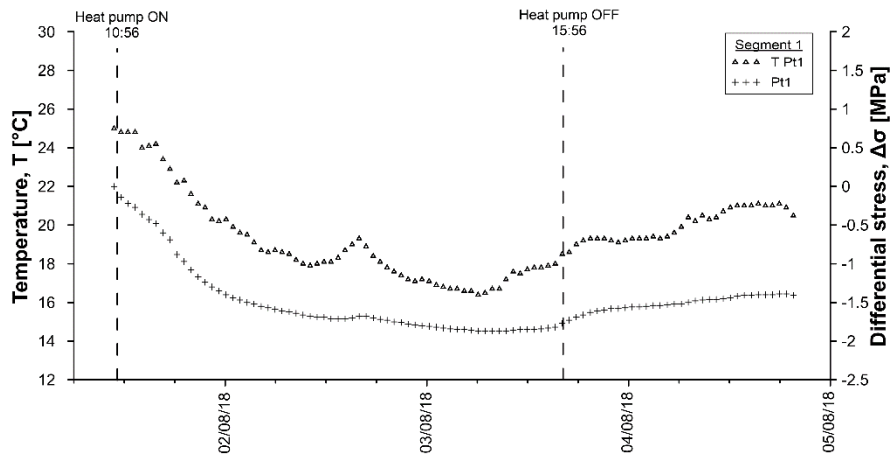


Figure A.165: Temperatures and differential stresses in segment 1, ring 179 for test AH1.

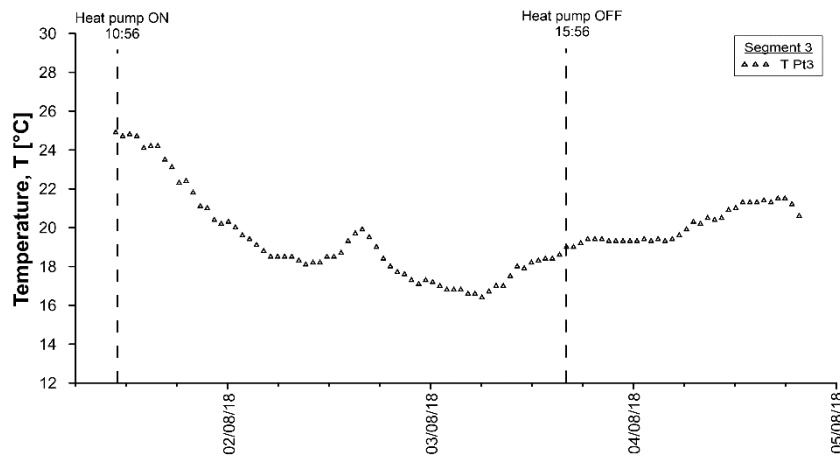


Figure A.166: Temperatures and differential stresses in segment 3, ring 179 for test AH1.

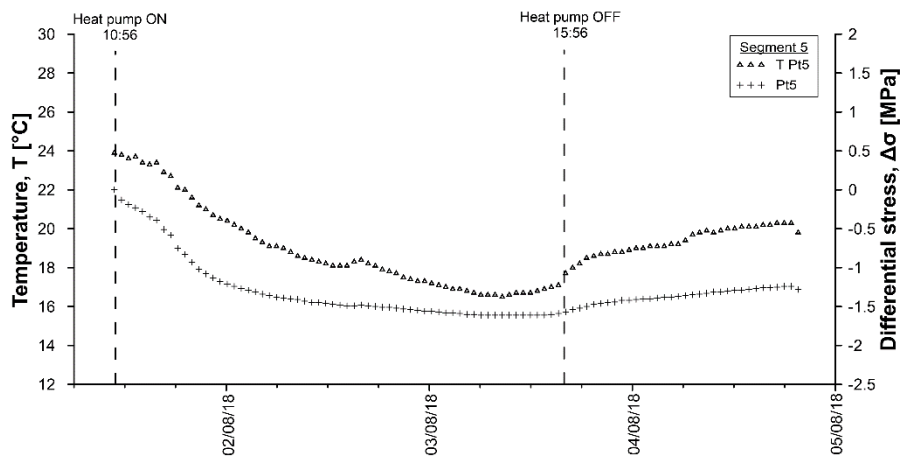


Figure A.167: Temperatures and differential stresses in segment 5, ring 179 for test AH1.

Table A.49: Data sheet for test AH1 – strains and temperatures.

Date	T _{DL} [°C]	SI2i [με]	SI2i [°C]	SI2e [με]	SI2e [°C]	St4i [με]	St4i [°C]	St4e [με]	St4e [°C]	St6i [με]	St6i [°C]	St6e [με]	St6e [°C]
01/08/2018 10:56	24.2	-1.79	25.1	-	25.2	0.07	24.3	0.30	24.6	-0.45	24.5	-0.05	24.1
01/08/2018 11:56	24.3	-	24.7	-	25.0	-0.91	24.1	-0.02	24.4	-3.48	24.1	-0.65	23.9
01/08/2018 12:56	24.9	-	24.5	-	24.8	-0.52	24.0	-0.40	24.3	-4.79	24.0	-1.66	23.7
01/08/2018 13:56	25.5	-	24.4	-	24.6	-1.05	23.9	0.06	24.3	-5.73	23.9	-1.99	23.6
01/08/2018 14:56	25.7	-	24.2	-	24.5	-1.56	23.8	-0.01	24.2	-7.08	23.7	-2.47	23.4
01/08/2018 15:56	26.0	-	24.1	-	24.3	-1.02	23.8	-0.24	24.1	-6.80	23.7	-2.98	23.3
01/08/2018 16:56	26.5	-	23.8	-	24.2	-2.73	23.5	0.51	24.0	-9.85	23.3	-2.80	23.2
01/08/2018 17:56	26.2	-	23.5	-	24.1	-4.94	23.2	2.20	23.9	-12.77	23.0	-2.08	23.1
01/08/2018 18:56	25.9	-	23.0	-	23.8	-6.65	22.8	2.39	23.7	-15.72	22.5	-2.32	22.8
01/08/2018 19:56	26.5	-	22.7	-	23.6	-7.81	22.5	3.07	23.6	-17.33	22.2	-2.30	22.6
01/08/2018 20:56	25.7	-	22.2	-	23.3	-9.94	22.0	3.60	23.4	-19.46	21.7	-2.39	22.3
01/08/2018 21:56	25.7	-	21.8	-	23.0	-10.86	21.8	3.81	23.1	-20.50	21.4	-2.75	22.1
01/08/2018 22:56	25.4	-	21.4	-	22.7	-12.08	21.4	3.91	22.9	-21.59	21.0	-3.03	21.8
01/08/2018 23:56	25.6	-	21.1	-	22.4	-12.21	21.2	3.46	22.7	-22.17	20.8	-3.76	21.6
02/08/2018 00:56	25.8	-	20.9	-	22.1	-12.30	21.1	3.16	22.5	-22.42	20.6	-4.36	21.3
02/08/2018 01:56	25.4	-	20.6	-	21.9	-13.29	20.9	3.20	22.3	-23.05	20.4	-4.70	21.1
02/08/2018 02:56	25.5	-	20.4	-	21.7	-13.75	20.7	3.02	22.2	-23.37	20.2	-5.11	20.9
02/08/2018 03:56	25.0	-	20.1	-	21.4	-14.86	20.4	3.01	22.0	-23.79	19.9	-5.22	20.7
02/08/2018 04:56	24.5	-	19.8	-	21.2	-16.22	20.2	2.91	21.8	-24.14	19.7	-5.36	20.5
02/08/2018 05:56	24.7	-	19.6	-	21.0	-16.09	20.0	1.96	21.6	-24.30	19.5	-6.04	20.3
02/08/2018 06:56	24.9	-	19.4	-	20.7	-15.74	19.9	1.85	21.4	-24.49	19.4	-6.69	20.1
02/08/2018 07:56	24.8	-	19.2	-	20.5	-15.93	19.7	1.60	21.3	-24.49	19.2	-7.06	20.0
02/08/2018 08:56	24.3	-	19.0	-	20.4	-16.53	19.6	1.57	21.1	-24.79	19.0	-7.14	19.8
02/08/2018 09:56	24.2	-40.36	18.9	-	20.2	-16.90	19.4	1.47	21.0	-24.92	18.9	-7.34	19.7
02/08/2018 10:56	24.2	-	18.7	-	20.0	-16.80	19.3	0.99	20.9	-25.00	18.7	-7.56	19.5
02/08/2018 11:56	24.7	-	18.7	-	19.9	-16.01	19.3	0.32	20.8	-24.99	18.6	-8.18	19.4
02/08/2018 12:56	25.0	-	18.6	-	19.7	-15.38	19.2	-0.14	20.7	-25.00	18.5	-8.81	19.3
02/08/2018 13:56	25.6	-	18.6	-	19.6	-14.43	19.2	-0.95	20.5	-24.82	18.5	-9.65	19.2
02/08/2018 14:56	27.5	-	18.7	-	19.5	-12.13	19.4	-1.97	20.5	-23.72	18.6	-11.40	19.1
02/08/2018 15:56	29.2	-	19.0	-	19.5	-10.66	19.6	-2.37	20.5	-22.32	18.7	-11.70	19.0
02/08/2018 16:56	27.8	-	19.0	-	19.5	-11.46	19.5	-2.15	20.5	-22.97	18.6	-11.30	19.0
02/08/2018 17:56	26.5	-	18.8	-	19.4	-12.66	19.3	-1.68	20.4	-23.59	18.4	-11.02	18.9
02/08/2018 18:56	25.8	-	18.5	-	19.4	-13.91	19.1	-1.35	20.4	-24.02	18.3	-10.83	18.8
02/08/2018 19:56	25.3	-	18.3	-	19.2	-14.86	18.9	-1.24	20.3	-24.31	18.1	-10.77	18.7
02/08/2018 20:56	24.8	-	18.1	-	19.1	-15.84	18.8	-0.91	20.2	-24.52	18.0	-10.77	18.6
02/08/2018 21:56	24.3	-	17.9	-	19.0	-17.18	18.6	-0.83	20.1	-24.59	17.8	-10.87	18.5
02/08/2018 22:56	23.9	-	17.7	-	18.8	-18.05	18.4	-0.76	19.9	-24.66	17.7	-11.01	18.3
02/08/2018 23:56	24.1	-	17.6	-	18.6	-17.51	18.4	-1.36	19.8	-24.72	17.6	-11.39	18.3
03/08/2018 00:56	24.0	-	17.5	-	18.5	-18.05	18.2	-1.32	19.7	-24.73	17.5	-11.50	18.2
03/08/2018 01:56	23.6	-	17.4	-	18.5	-18.94	18.1	-1.47	19.6	-24.73	17.4	-11.66	18.1
03/08/2018 02:56	23.5	-	17.2	-	18.3	-18.97	18.0	-1.60	19.5	-24.89	17.3	-11.84	18.0
03/08/2018 03:56	23.5	-	17.1	-	18.2	-19.13	17.9	-1.80	19.4	-24.84	17.2	-12.07	17.9
03/08/2018 04:56	23.4	-	17.0	-	18.1	-19.43	17.8	-1.96	19.3	-24.87	17.1	-12.27	17.8
03/08/2018 05:56	23.2	-52.69	16.9	-	18.0	-19.79	17.6	-2.09	19.2	-24.67	17.0	-12.48	17.7
03/08/2018 06:56	23.4	-	16.8	-	17.8	-18.73	17.6	-2.61	19.1	-24.98	16.9	-12.72	17.6
03/08/2018 07:56	23.5	-	16.8	-	17.7	-16.98	17.6	-3.87	19.0	-24.69	16.9	-13.31	17.5
03/08/2018 08:56	23.7	-	16.9	-	17.7	-16.26	17.7	-3.91	19.0	-24.77	16.8	-13.58	17.5
03/08/2018 09:56	24.1	-	17.0	-	17.6	-14.61	17.8	-4.73	18.9	-24.27	16.9	-14.42	17.4
03/08/2018 10:56	25.0	-	17.1	-	17.6	-13.29	17.9	-4.99	18.9	-24.00	16.9	-14.92	17.4
03/08/2018 11:56	24.8	-	17.1	-	17.6	-13.26	17.9	-5.08	18.9	-23.96	16.9	-15.29	17.3
03/08/2018 12:56	25.3	-	17.2	-	17.6	-12.28	18.0	-5.37	18.9	-23.86	17.0	-15.91	17.3
03/08/2018 13:56	25.8	-	17.3	-	17.6	-11.46	18.1	-5.46	19.0	-23.42	17.0	-16.34	17.3
03/08/2018 14:56	26.4	-	17.4	-	17.7	-11.58	18.1	-5.73	19.0	-23.19	17.1	-16.60	17.3
03/08/2018 15:56	27.1	-	17.7	-	17.7	-7.40	18.7	-7.53	19.0	-19.15	17.7	-18.68	17.4
03/08/2018 16:56	26.5	-	18.2	-	17.9	-5.57	19.0	-8.09	19.2	-15.41	18.2	-18.82	17.6
03/08/2018 17:56	25.8	-	18.5	-	18.1	-4.81	19.3	-8.47	19.3	-12.97	18.6	-18.55	17.8
03/08/2018 18:56	25.5	-	18.8	-	18.3	-4.25	19.4	-8.51	19.4	-10.83	18.8	-17.90	18.0
03/08/2018 19:56	25.3	-	19.0	-	18.5	-4.12	19.6	-8.37	19.5	-9.47	19.1	-17.23	18.1
03/08/2018 20:56	25.0	-	19.1	-	18.6	-4.09	19.6	-8.07	19.6	-8.39	19.2	-16.48	18.3
03/08/2018 21:56	24.6	-	19.2	-	18.8	-4.30	19.7	-7.64	19.7	-7.68	19.3	-15.69	18.4
03/08/2018 22:56	24.3	-	19.2	-	18.9	-4.48	19.7	-7.47	19.7	-7.07	19.4	-15.00	18.5
03/08/2018 23:56	24.2	-	19.2	-	19.0	-4.53	19.7	-7.30	19.8	-6.51	19.4	-14.35	18.6
04/08/2018 00:56	24.1	-	19.3	-	19.0	-4.53	19.7	-7.29	19.8	-6.12	19.5	-13.88	18.7

Date	T _{bl} [°C]	SI2i [μ€]	SI2i [°C]	SI2e [μ€]	SI2e [°C]	St4i [μ€]	St4i [°C]	St4e [μ€]	St4e [°C]	St6i [μ€]	St6i [°C]	St6e [μ€]	St6e [°C]
04/08/2018 01:56	24.0	-	19.4	-	19.1	-4.48	19.7	-7.19	19.9	-5.69	19.6	-13.28	18.8
04/08/2018 02:56	24.0	-	19.4	-	19.2	-4.47	19.8	-7.28	19.9	-5.40	19.7	-12.91	18.8
04/08/2018 03:56	23.8	-	19.4	-	19.2	-4.48	19.8	-7.08	19.9	-5.16	19.7	-12.34	18.9
04/08/2018 04:56	23.7	-	19.5	-	19.3	-4.46	19.8	-7.28	19.9	-4.83	19.7	-12.07	19.0
04/08/2018 05:56	24.0	-	19.6	-	19.3	-4.09	19.9	-7.89	20.0	-4.07	19.8	-12.09	19.0
04/08/2018 06:56	24.3	-	19.7	-	19.4	-3.35	20.0	-8.43	20.0	-4.55	20.0	-13.18	19.0
04/08/2018 07:56	24.3	-	19.9	-	19.5	-2.98	20.2	-8.56	20.0	-3.78	20.1	-13.20	19.1
04/08/2018 08:56	24.7	-	20.1	-	19.5	-2.57	20.3	-9.77	20.1	-3.60	20.2	-13.63	19.2
04/08/2018 09:56	24.8	-	20.1	-	19.6	-2.59	20.3	-8.28	20.2	-3.39	20.3	-12.87	19.3
04/08/2018 10:56	24.9	-	20.2	-	19.7	-2.48	20.4	-8.47	20.2	-3.38	20.4	-12.99	19.4
04/08/2018 11:56	25.3	-	20.3	-	19.8	-2.08	20.5	-8.56	20.3	-3.00	20.4	-12.78	19.5
04/08/2018 12:56	25.6	-	20.5	-	19.9	-1.68	20.6	-8.75	20.3	-2.72	20.5	-12.89	19.5
04/08/2018 13:56	26.0	-	20.6	-	19.9	-1.40	20.7	-9.16	20.4	-2.46	20.6	-12.55	19.6
04/08/2018 14:56	27.5	-	20.6	-	20.0	-1.29	20.7	-8.45	20.5	-2.41	20.6	-12.17	19.7
04/08/2018 15:56	29.8	-	20.7	-	20.1	-1.01	20.8	-8.93	20.5	-1.96	20.6	-11.90	19.7
04/08/2018 16:56	28.3	-	20.8	-	20.2	-1.03	20.9	-8.76	20.6	-1.98	20.7	-11.72	19.7
04/08/2018 17:56	27.2	-	20.8	-	20.2	-0.89	20.9	-8.85	20.6	-1.85	20.7	-11.73	19.8
04/08/2018 18:56	26.6	-	20.8	-	20.3	-1.04	20.9	-8.43	20.7	-1.74	20.8	-11.16	19.8
04/08/2018 19:56	25.9	-	20.5	-	20.3	-4.17	20.3	-5.66	20.6	-9.18	20.2	-7.52	19.8

Table A.50: Data sheet for test AH1 – stresses and temperatures.

Date	Pt1 [MPa]	Pt1 [°C]	Pl2 [MPa]	Pl2 [°C]	Pt3 [MPa]	Pt3 [°C]	Pr4 [MPa]	Pr4 [°C]	Pt5 [MPa]	Pt5 [°C]	Pr6 [MPa]	Pr6 [°C]
01/08/2018 10:56	-0.03	25	0	24.8	-	24.8	-0.03	24.7	-0.04	24	-0.01	23.7
01/08/2018 11:56	-0.17	24.7	0	24.5	-	24.6	-0.11	24.3	-0.14	23.7	-0.09	23.3
01/08/2018 12:56	-0.26	25	0	24.5	-	24.9	-0.18	24.5	-0.23	23.8	-0.15	23.6
01/08/2018 13:56	-0.36	24.1	0	24.1	-	24.2	-0.25	24	-0.29	23.4	-0.21	23.1
01/08/2018 14:56	-0.43	24.1	0	24	-	24.2	-0.31	23.9	-0.35	23.3	-0.27	23.1
01/08/2018 15:56	-0.5	24.1	0	24	-	24.1	-0.38	24	-0.43	23.3	-0.32	23.1
01/08/2018 16:56	-0.63	23.5	0	23.4	-	23.4	-0.47	23.3	-0.53	22.9	-0.39	22.7
01/08/2018 17:56	-0.81	22.4	0	22.8	-	22.6	-0.62	22.5	-0.69	22.3	-0.48	22
01/08/2018 18:56	-0.96	22.4	0	22.5	-	22.4	-0.72	22.3	-0.8	22	-0.58	21.8
01/08/2018 19:56	-1.08	21.6	0	22	-	21.8	-0.85	21.6	-0.93	21.6	-0.68	21.3
01/08/2018 20:56	-1.18	21.1	0	21.4	-	21.1	-0.93	21.1	-1.03	21.3	-0.79	21
01/08/2018 21:56	-1.26	20.6	0	21	-	20.8	-1	20.7	-1.1	20.9	-0.9	20.6
01/08/2018 22:56	-1.34	20.2	0	20.6	-	20.2	-1.05	20.2	-1.16	20.5	-1	20.2
01/08/2018 23:56	-1.39	20.3	0	20.5	-	20.2	-1.1	20.2	-1.2	20.4	-1.09	20.2
02/08/2018 00:56	-1.44	19.9	0.01	20.3	-	20	-1.14	19.9	-1.24	20.2	-1.17	19.9
02/08/2018 01:56	-1.47	19.6	0.01	19.9	-	19.5	-1.18	19.6	-1.27	19.9	-1.25	19.7
02/08/2018 02:56	-1.51	19.3	0.01	19.6	-	19.3	-1.21	19.4	-1.3	19.7	-1.33	19.4
02/08/2018 03:56	-1.54	18.9	0.01	19.3	-	18.9	-1.24	18.9	-1.33	19.4	-1.39	19.1
02/08/2018 04:56	-1.57	18.6	0.01	18.9	-	18.6	-1.26	18.7	-1.35	19.2	-1.46	18.9
02/08/2018 05:56	-1.59	18.7	0.01	18.9	-	18.5	-1.28	18.8	-1.38	19.1	-1.51	18.9
02/08/2018 06:56	-1.61	18.5	0.01	18.8	-	18.5	-1.29	18.6	-1.39	18.9	-1.56	18.7
02/08/2018 07:56	-1.63	18.3	0.01	18.6	-	18.3	-1.3	18.3	-1.41	18.7	-1.61	18.5
02/08/2018 08:56	-1.65	18	0.01	18.4	-	18.2	-1.32	18.1	-1.42	18.5	-1.65	18.3
02/08/2018 09:56	-1.67	18	0.01	18.3	-	18.2	-1.34	18	-1.45	18.4	-1.69	18.2
02/08/2018 10:56	-1.69	18	0.01	18.3	-	18.2	-1.35	18	-1.45	18.3	-1.72	18.1
02/08/2018 11:56	-1.7	18.1	0.01	18.4	-	18.5	-1.36	18.2	-1.46	18.2	-1.76	18
02/08/2018 12:56	-1.71	18.2	0.01	18.4	-	18.6	-1.36	18.2	-1.48	18.1	-1.78	17.9
02/08/2018 13:56	-1.71	18.7	0.01	18.7	-	19.1	-1.36	18.5	-1.49	18.1	-1.8	17.9
02/08/2018 14:56	-1.7	19.1	0.01	19	-	19.8	-1.36	19	-1.49	18.3	-1.82	18.2
02/08/2018 15:56	-1.68	19.3	0.01	19.3	-	19.9	-1.35	19.2	-1.48	18.4	-1.82	18.2
02/08/2018 16:56	-1.69	18.9	0.01	19	-	19.6	-1.36	18.8	-1.49	18.2	-1.83	18.1
02/08/2018 17:56	-1.71	18.3	0.01	18.5	-	18.7	-1.37	18.3	-1.5	18	-1.85	17.8
02/08/2018 18:56	-1.73	17.9	0.01	18.2	-	18.1	-1.38	17.9	-1.51	17.8	-1.88	17.7
02/08/2018 19:56	-1.74	17.6	0.01	17.9	-	17.8	-1.4	17.7	-1.52	17.7	-1.89	17.6
02/08/2018 20:56	-1.76	17.4	0.01	17.7	-	17.6	-1.41	17.4	-1.53	17.5	-1.92	17.4
02/08/2018 21:56	-1.78	17.2	0.01	17.4	-	17.3	-1.42	17.1	-1.55	17.4	-1.94	17.3
02/08/2018 22:56	-1.8	17.1	0.01	17.2	-	17.1	-1.43	17.1	-1.56	17.3	-1.95	17.2
02/08/2018 23:56	-1.8	17.2	0.01	17.3	-	17.4	-1.44	17.2	-1.56	17.2	-1.97	17.1
03/08/2018 00:56	-1.82	17	0.01	17.1	-	17	-1.45	16.9	-1.57	17.1	-1.99	17
03/08/2018 01:56	-1.83	16.8	0.01	17	-	16.8	-1.46	16.8	-1.58	17	-2	16.9
03/08/2018 02:56	-1.84	16.7	0.01	16.8	-	16.7	-1.46	16.7	-1.58	16.9	-2.02	16.7
03/08/2018 03:56	-1.85	16.7	0.01	16.7	-	16.7	-1.47	16.6	-1.59	16.8	-2.04	16.7
03/08/2018 04:56	-1.86	16.5	0.01	16.6	-	16.6	-1.48	16.5	-1.6	16.7	-2.05	16.6
03/08/2018 05:56	-1.86	16.5	0.01	16.5	-	16.4	-1.48	16.4	-1.61	16.7	-2.06	16.5
03/08/2018 06:56	-1.87	16.5	0.01	16.6	-	16.7	-1.49	16.6	-1.61	16.6	-2.08	16.4
03/08/2018 07:56	-1.87	16.7	0.01	16.8	-	17	-1.5	16.7	-1.61	16.6	-2.09	16.4
03/08/2018 08:56	-1.87	16.9	0.01	16.8	-	17.2	-1.5	17	-1.61	16.6	-2.1	16.3
03/08/2018 09:56	-1.86	17.4	0.01	17.3	-	17.8	-1.49	17.4	-1.61	16.7	-2.11	16.5
03/08/2018 10:56	-1.85	17.5	0.01	17.4	-	17.9	-1.48	17.4	-1.61	16.7	-2.11	16.5
03/08/2018 11:56	-1.85	17.7	0.01	17.4	-	18.2	-1.48	17.7	-1.61	16.7	-2.11	16.6
03/08/2018 12:56	-1.84	17.9	0.01	17.6	-	18.4	-1.47	17.8	-1.61	16.8	-2.11	16.6
03/08/2018 13:56	-1.84	18	0.01	17.7	-	18.5	-1.47	17.9	-1.61	16.9	-2.11	16.7
03/08/2018 14:56	-1.83	18	0.01	17.7	-	18.5	-1.47	17.9	-1.6	16.9	-2.11	16.7
03/08/2018 15:56	-1.78	18.5	0.01	18.4	-	19.1	-1.44	18.6	-1.57	17.6	-2.09	17.4
03/08/2018 16:56	-1.73	18.6	0.01	18.6	-	19	-1.41	18.7	-1.54	18	-2.05	17.7
03/08/2018 17:56	-1.68	19.1	0.01	18.9	-	19.4	-1.38	19.1	-1.51	18.4	-2.01	18.1
03/08/2018 18:56	-1.64	19.2	0.01	19.1	-	19.3	-1.36	19.2	-1.49	18.5	-1.98	18.2
03/08/2018 19:56	-1.62	19.3	0.01	19.1	-	19.4	-1.35	19.3	-1.47	18.6	-1.95	18.4
03/08/2018 20:56	-1.6	19.3	0.01	19.2	-	19.4	-1.33	19.3	-1.45	18.7	-1.93	18.5
03/08/2018 21:56	-1.58	19.2	0.01	19.1	-	19.3	-1.32	19.3	-1.44	18.8	-1.9	18.5
03/08/2018 22:56	-1.57	19.1	0.01	19.1	-	19.2	-1.31	19.2	-1.42	18.9	-1.88	18.6
03/08/2018 23:56	-1.57	19.2	0.01	19.1	-	19.3	-1.3	19.3	-1.41	18.9	-1.87	18.6
04/08/2018 00:56	-1.56	19.4	0.01	19.2	-	19.4	-1.3	19.4	-1.4	19	-1.85	18.7

Date	Pt1 [MPa]	Pt1 [°C]	PI2 [MPa]	PI2 [°C]	Pt3 [MPa]	Pt3 [°C]	Pr4 [MPa]	Pr4 [°C]	Pt5 [MPa]	Pt5 [°C]	Pr6 [MPa]	Pr6 [°C]
04/08/2018 01:56	-1.55	19.3	0.01	19.2	-	19.3	-1.3	19.3	-1.4	19	-1.83	18.7
04/08/2018 02:56	-1.54	19.4	0.01	19.2	-	19.4	-1.29	19.4	-1.39	19.1	-1.82	18.8
04/08/2018 03:56	-1.54	19.3	0.01	19.2	-	19.3	-1.29	19.4	-1.38	19.1	-1.81	18.8
04/08/2018 04:56	-1.53	19.5	0.01	19.3	-	19.5	-1.28	19.5	-1.37	19.2	-1.79	18.9
04/08/2018 05:56	-1.51	19.7	0.01	19.5	-	19.8	-1.28	19.7	-1.36	19.3	-1.78	19
04/08/2018 06:56	-1.5	20.3	0.01	19.9	-	20.3	-1.26	20.2	-1.35	19.6	-1.76	19.4
04/08/2018 07:56	-1.48	20.2	0.01	20	-	20.2	-1.25	20.2	-1.34	19.8	-1.74	19.5
04/08/2018 08:56	-1.47	20.5	0	20.2	-	20.6	-1.24	20.4	-1.32	19.8	-1.72	19.6
04/08/2018 09:56	-1.46	20.3	0.01	20.2	-	20.4	-1.24	20.3	-1.31	19.8	-1.7	19.5
04/08/2018 10:56	-1.45	20.7	0	20.4	-	20.9	-1.23	20.6	-1.3	20	-1.68	19.7
04/08/2018 11:56	-1.44	20.8	0	20.5	-	20.9	-1.22	20.7	-1.29	20	-1.67	19.7
04/08/2018 12:56	-1.42	21	0	20.7	-	21.3	-1.21	20.9	-1.29	20.1	-1.65	19.8
04/08/2018 13:56	-1.41	21	0	20.7	-	21.3	-1.2	20.9	-1.28	20.1	-1.64	19.8
04/08/2018 14:56	-1.41	21	0	20.7	-	21.3	-1.19	20.9	-1.27	20.2	-1.62	19.9
04/08/2018 15:56	-1.4	20.9	0	20.7	-	21.3	-1.19	20.9	-1.26	20.2	-1.61	19.8
04/08/2018 16:56	-1.4	21.1	0	20.9	-	21.5	-1.19	21	-1.25	20.3	-1.6	19.9
04/08/2018 17:56	-1.39	21.1	0	20.9	-	21.5	-1.18	21	-1.24	20.3	-1.58	20
04/08/2018 18:56	-1.39	20.9	0	20.8	-	21.1	-1.18	20.9	-1.24	20.3	-1.57	19.9
04/08/2018 19:56	-1.44	20	0.01	20	-	20.2	-1.21	20	-1.29	19.5	-1.6	19.1

Table A.51: Data sheet for test AH1 - sensors T1-T5 and heat pump.

Date	T1 [°C]	T2 [°C]	T3 [°C]	T4 [°C]	T5 [°C]	Date	Tair [°C]	IN [°C]	OUT [°C]	U1 [°C]	U2 [°C]
01/08/2018 10:54	25.4	24.8	24.8	26	25.7	01/08/2018 10:50	24.7	25	25.2	23.9	23.4
01/08/2018 11:54	26	25.4	25.2	22.6	23.9	01/08/2018 10:56	24.7	25	25.2	22.4	22.7
01/08/2018 12:54	26.3	25.9	25.5	23.9	23.8	01/08/2018 11:56	29.5	19.5	22	60.6	53.9
01/08/2018 13:54	27.4	26.8	26.2	23	24.1	01/08/2018 12:56	31.7	20.6	23.4	54	47.7
01/08/2018 14:54	25.3	26.2	25.7	21.3	22.9	01/08/2018 13:56	31.9	19.6	22.2	61	54.3
01/08/2018 15:54	26.7	26	25.5	23.6	23.5	01/08/2018 14:55	31.8	21.7	22.1	50.5	48
01/08/2018 16:54	25.4	25.9	25.6	21.4	23	01/08/2018 15:55	31.6	19.8	23	46.5	40.9
01/08/2018 17:54	25.6	25.4	25.1	22.4	23.1	01/08/2018 16:55	31.5	21	21.3	50.6	48.8
01/08/2018 18:54	23.1	24.4	24.1	18.8	20.7	01/08/2018 17:55	31.9	18.7	21.3	59	52.5
01/08/2018 19:54	25.4	24.2	24.1	22	22.1	01/08/2018 18:55	29.2	17.1	19.5	60.5	53.7
01/08/2018 20:54	22.6	23.7	23.5	17.9	19.9	01/08/2018 19:55	32.6	18.4	20.9	56.8	50.4
01/08/2018 21:54	23.6	23.2	23.1	17.7	19.6	01/08/2018 20:55	28.3	16.2	18.6	59.5	52.8
01/08/2018 22:54	22.6	22.9	22.7	17.2	19.1	01/08/2018 21:55	29.8	15.7	18.1	60.2	53.6
01/08/2018 23:54	22.6	22.6	22.4	16.9	19	01/08/2018 22:55	29.4	15.3	17.7	59.2	52.5
02/08/2018 00:54	23.7	22.7	22.5	17.2	19	01/08/2018 23:55	29.6	15	17.4	59.4	52.7
02/08/2018 01:54	22.3	22.7	22.4	16.7	18.6	02/08/2018 00:55	30.2	14.8	17.2	60.1	53.4
02/08/2018 02:54	22.6	22.5	22.1	16.4	18.5	02/08/2018 01:55	30.3	14.6	17	59.1	52.4
02/08/2018 03:54	22.1	22.3	21.9	16.2	18.2	02/08/2018 02:55	30	14.3	16.7	59.1	52.5
02/08/2018 04:54	21.6	21.7	21.4	15.8	17.8	02/08/2018 03:55	29.3	14.1	16.5	58.6	51.9
02/08/2018 05:54	21.5	21.3	21	15.5	17.5	02/08/2018 04:55	27.3	13.8	16.2	57.7	51
02/08/2018 06:54	22.5	21.5	21.2	15.8	17.6	02/08/2018 05:55	27	13.5	15.9	57.6	51
02/08/2018 07:54	21.9	21.5	21.2	15.5	17.5	02/08/2018 06:55	29.5	13.5	15.8	58.5	51.9
02/08/2018 08:54	21.4	21.4	21	15.2	17.2	02/08/2018 07:55	29.4	13.4	15.7	58.3	51.7
02/08/2018 09:54	21.3	21.1	20.7	15	17	02/08/2018 08:54	29	13.2	15.5	58	51.4
02/08/2018 10:54	21.9	20.9	20.5	15	17	02/08/2018 09:54	28.1	13	15.3	57.8	51.2
02/08/2018 11:54	22.3	21	20.6	15.1	17	02/08/2018 10:54	28.5	12.9	15.2	58.3	51.7
02/08/2018 12:54	22.4	21.3	20.8	15	17	02/08/2018 11:54	29.1	12.8	15	58.4	51.9
02/08/2018 13:54	22.3	21.6	21.1	15.3	17.1	02/08/2018 12:54	29.8	12.7	15	58.6	52
02/08/2018 14:54	24.3	22.3	21.6	15.8	17.4	02/08/2018 13:54	31.2	12.8	15.1	59.2	52.6
02/08/2018 15:54	25.2	23	22	18.4	19	02/08/2018 14:54	31.6	12.9	15.2	60.8	54.3
02/08/2018 16:54	25.2	23.1	22.3	16.3	17.8	02/08/2018 15:54	33.4	14.7	17	57.1	50.8
02/08/2018 17:54	24.3	23.1	22.2	15.5	17.2	02/08/2018 16:54	33.9	13.4	15.7	60.8	54.3
02/08/2018 18:54	22.7	22.7	22	15.1	17	02/08/2018 17:54	30.9	13	15.3	59.8	53.3
02/08/2018 19:54	22.4	22.3	21.6	14.9	16.8	02/08/2018 18:54	30.2	12.7	15	58.8	52.2
02/08/2018 20:54	21.6	21.8	21.2	14.5	16.5	02/08/2018 19:54	29.2	12.5	14.8	58.2	51.7
02/08/2018 21:54	21.6	21.4	20.8	14.3	16.3	02/08/2018 20:54	29	12.3	14.6	57.7	51.1
02/08/2018 22:54	21	20.8	20.3	14.1	15.9	02/08/2018 21:54	28.7	12.2	14.4	57.4	50.9
02/08/2018 23:54	20.9	20.4	20	14	15.8	02/08/2018 22:54	27	12	14.2	56.8	50.3
03/08/2018 00:54	21.6	20.6	20.2	14.2	15.9	02/08/2018 23:54	25.9	11.8	14.1	56.6	50.1
03/08/2018 01:54	21	20.3	19.8	13.8	15.6	03/08/2018 00:54	28.4	11.8	14.1	57.6	51
03/08/2018 02:54	21	20.1	19.6	13.7	15.5	03/08/2018 01:54	26.4	11.7	13.9	56.7	50.2
03/08/2018 03:54	21.2	20	19.5	13.7	15.5	03/08/2018 02:53	25.9	11.5	13.8	56.6	50.1
03/08/2018 04:54	21.1	19.9	19.4	13.6	15.4	03/08/2018 03:53	27.1	11.4	13.6	56.8	50.3
03/08/2018 05:54	20.9	19.8	19.2	13.5	15.3	03/08/2018 04:53	26.8	11.3	13.5	56.5	50
03/08/2018 06:54	20.7	19.6	19.1	13.4	15.2	03/08/2018 05:53	26.1	11.2	13.4	56.4	49.9
03/08/2018 07:54	21.4	19.9	19.4	13.6	15.2	03/08/2018 06:53	25.4	11.1	13.4	56.1	49.6
03/08/2018 08:54	21.5	20.1	19.6	13.6	15.2	03/08/2018 07:53	28.1	11.1	13.3	57	50.5
03/08/2018 09:54	22.3	20.5	19.9	13.8	15.3	03/08/2018 08:53	29	11.1	13.4	57	50.5
03/08/2018 10:54	22.6	21.2	20.4	14.2	15.6	03/08/2018 09:53	28.6	11.2	13.4	57.5	51.1
03/08/2018 11:54	22.6	21.6	20.7	14.2	15.6	03/08/2018 10:53	30.1	11.3	13.5	58.4	52
03/08/2018 12:54	24.3	21.6	20.7	14.3	15.6	03/08/2018 11:53	29.7	11.4	13.6	58.1	51.7
03/08/2018 13:54	23.4	22	21.1	14.5	15.8	03/08/2018 12:53	29.8	11.4	13.6	58.5	52.1
03/08/2018 14:54	23.5	22.1	21.2	14.6	15.8	03/08/2018 13:53	31.1	11.6	13.8	59.2	52.8
03/08/2018 15:54	22.7	22.2	21.3	14.4	15.8	03/08/2018 14:53	31.4	11.7	14	59.5	53.2
03/08/2018 16:54	23	22.4	21.5	19.3	19.1	03/08/2018 15:53	31.5	11.7	13.9	59.3	52.9
03/08/2018 17:54	21.8	22	21.3	19.5	19.4	03/08/2018 16:53	34	17.7	17.9	48.8	44.9
03/08/2018 18:54	22.4	21.9	21.3	20	19.8	03/08/2018 17:53	27.8	18.2	18.4	44.7	37.7
03/08/2018 19:54	21.8	21.7	21.2	20	19.9	03/08/2018 18:53	26.1	18.5	18.7	41.6	32.1
03/08/2018 20:54	21.7	21.5	21.1	20.1	20	03/08/2018 19:53	24.6	18.7	18.9	38.9	28.2
03/08/2018 21:54	21.1	21.3	20.9	20	20	03/08/2018 20:52	23.8	18.9	19.1	34.8	23.4
03/08/2018 22:54	21.3	21	20.7	20.1	20.1	03/08/2018 21:52	23.1	19	19.2	29.9	23.4
03/08/2018 23:54	20.7	20.6	20.4	20	20	03/08/2018 22:52	22.4	19.1	19.2	27.7	23.3
04/08/2018 00:54	20.9	20.5	20.3	20.2	20.1	03/08/2018 23:52	22	19.1	19.3	26.2	23.1

Date	T1 [°C]	T2 [°C]	T3 [°C]	T4 [°C]	T5 [°C]	Date	Tair [°C]	IN [°C]	OUT [°C]	U1 [°C]	U2 [°C]
04/08/2018 01:54	21.2	20.4	20.2	20.2	20.2	04/08/2018 00:52	21.8	19.1	19.4	25.1	23
04/08/2018 02:54	20.5	20.3	20.1	20.2	20.2	04/08/2018 01:52	21.6	19.2	19.4	24.2	22.8
04/08/2018 03:54	20.7	20.3	20.1	20.2	20.2	04/08/2018 02:52	21.4	19.3	19.5	23.5	22.6
04/08/2018 04:54	20.5	20.2	20.1	20.2	20.2	04/08/2018 03:52	21.4	19.3	19.5	22.9	22.5
04/08/2018 05:54	20.9	20.3	20.2	20.4	20.3	04/08/2018 04:52	21.1	19.4	19.5	22.5	22.3
04/08/2018 06:54	21.3	20.4	20.3	20.5	20.5	04/08/2018 05:52	21.2	19.4	19.6	22.1	22.2
04/08/2018 07:54	22.6	21.2	20.9	21.1	20.8	04/08/2018 06:52	21.4	19.5	19.7	21.8	22.1
04/08/2018 08:52	21.4	21.5	21.1	20.9	20.8	04/08/2018 07:52	22.1	19.7	19.9	21.7	22.1
04/08/2018 09:52	22	21.8	21.4	21.2	21	04/08/2018 08:52	22.4	19.9	20.1	21.7	22.1
04/08/2018 10:52	21.6	21.6	21.2	21	21	04/08/2018 09:52	22.6	20	20.2	21.9	22.1
04/08/2018 11:52	23	21.8	21.5	21.3	21.1	04/08/2018 10:52	22.4	20.1	20.2	21.8	22.1
04/08/2018 12:52	22.5	22.1	21.7	21.4	21.2	04/08/2018 11:52	23.1	20.2	20.4	21.9	22.1
04/08/2018 13:52	23	22.4	21.9	21.7	21.4	04/08/2018 12:52	23.7	20.3	20.5	22	22.2
04/08/2018 14:52	22.6	22.5	22	21.6	21.4	04/08/2018 13:52	24.2	20.4	20.6	22.2	22.3
04/08/2018 15:52	23.1	22.4	22	21.8	21.5	04/08/2018 14:51	24.8	20.5	20.7	22.5	22.5
04/08/2018 16:52	22.2	22.3	21.9	21.6	21.4	04/08/2018 15:51	38.1	20.7	20.9	23.4	23.1
04/08/2018 17:52	23.1	22.4	22	21.9	21.6	04/08/2018 16:51	34.2	20.7	20.9	24.9	24.1
04/08/2018 18:52	22.4	22.4	22.1	21.8	21.6	04/08/2018 17:51	26.1	20.7	20.9	24.8	24.5
04/08/2018 19:52	21.5	22.1	21.8	21.5	21.4	04/08/2018 18:51	24.8	20.7	20.9	24.6	24.3
						04/08/2018 19:51	23.7	20.7	20.9	24.3	24

Table A.52: Summary of test AH1 records.

Quantity	Unit	$x(t_0)$	$x(t_1)$	$x(t_1) - x(t_0)$	$\bar{x}(t_0, t_1)$
T _{DL}	[°C]	24.2	27.1	2.9	25.1
Sl2i	[$\mu\epsilon$]	-3294.24	-346.65	-	
	[$\mu\epsilon$] _{comp}	-1.79	3036.08	-	
	[°C]	25.1	17.7	-7.4	19.5
Sl2e	[$\mu\epsilon$]	-	-	-	
	[$\mu\epsilon$] _{comp}	-	-	-	
	[°C]	25.2	17.7	-7.5	20.4
St4i	[$\mu\epsilon$]	-1759.33	-1766.80	-7.47	
	[$\mu\epsilon$] _{comp}	0.07	60.92	60.85	
	[°C]	24.3	18.7	-5.6	19.9
St4e	[$\mu\epsilon$]	-1504.64	-1512.47	-7.83	
	[$\mu\epsilon$] _{comp}	0.3	60.79	60.49	
	[°C]	24.6	19.0	-5.6	21.1
St6i	[$\mu\epsilon$]	-2176.99	-2195.69	-18.70	
	[$\mu\epsilon$] _{comp}	-0.45	63.81	64.26	
	[°C]	24.5	17.7	-6.8	19.4
St6e	[$\mu\epsilon$]	-1796.99	-1815.62	-18.63	
	[$\mu\epsilon$] _{comp}	-0.05	63.06	63.11	
	[°C]	24.1	17.4	-6.7	19.8
Pt1	[MPa]	1.90	0.15	-1.75	
	[°C]	25.0	18.5	-6.5	19.1
Pl2	[MPa]	-0.07	-0.06	0.01	
	[°C]	24.8	18.4	-6.4	19.2
Pt3	[MPa]	-	-	-	
	[°C]	24.8	19.1	-5.7	19.3
Pr4	[MPa]	1.68	0.27	-1.41	
	[°C]	24.7	18.6	-6.1	19.1
Pt5	[MPa]	1.71	0.18	-1.53	
	[°C]	24.0	17.6	-6.4	19.0
Pr6	[MPa]	2.41	0.33	-2.08	
	[°C]	23.7	17.4	-6.3	18.7
T1	[°C]	25.4	22.7	-2.7	22.8
T2	[°C]	24.8	22.2	-2.6	22.3
T3	[°C]	24.8	21.3	-3.5	21.8
T4	[°C]	26.0	14.4	-11.6	16.3
T5	[°C]	25.7	15.8	-9.9	17.9
Air	[°C]	24.7	32.0	7.3	29.5
IN	[°C]	25.0	11.9	-13.1	14.1
OUT	[°C]	25.2	13.9	-11.3	16.2
U1	[°C]	22.4	59.4	37.0	57.3
U2	[°C]	22.7	53.4	30.7	51.2

Test AH2

This test was repeated just like AH1 to try to avoid the on-off cycles at the beginning of the test that was shown during test AH1.

Circuit:	Air
Mode:	Heating (tunnel cooling)
Secondary circuit temperature:	55°C
Activated rings:	179+180
Volumetric flow rate:	1.3 m ³ /h
Fluid velocity in primary circuit:	0.9 m/s
Starting time t_0 :	04/08/2018 20:00
Ending time t_1 :	06/08/2018 10:00
Duration:	1.58 days

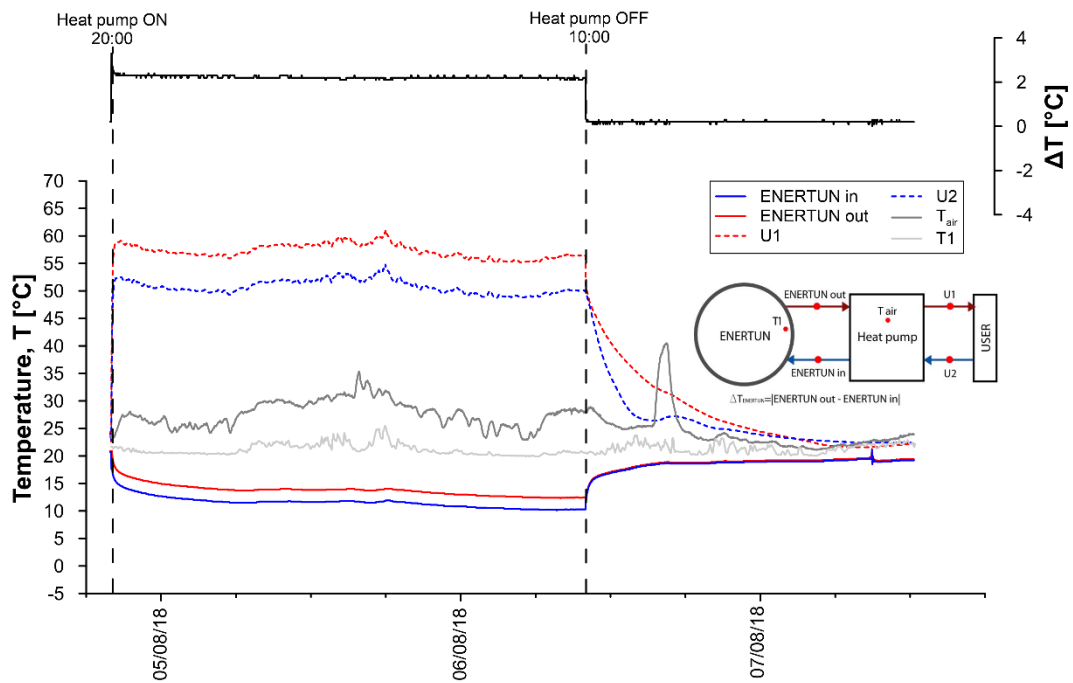


Figure A.168: Primary circuit, secondary circuit and air temperatures for test AH2.

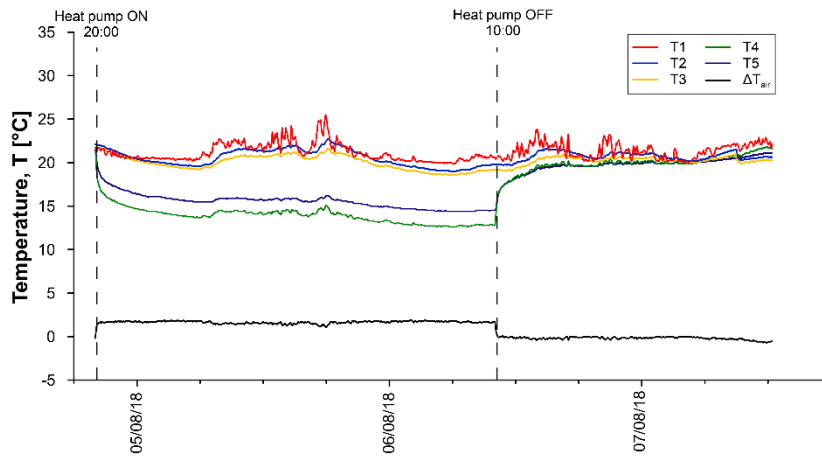


Figure A.169: Temperatures T1-T5 for test AH2.

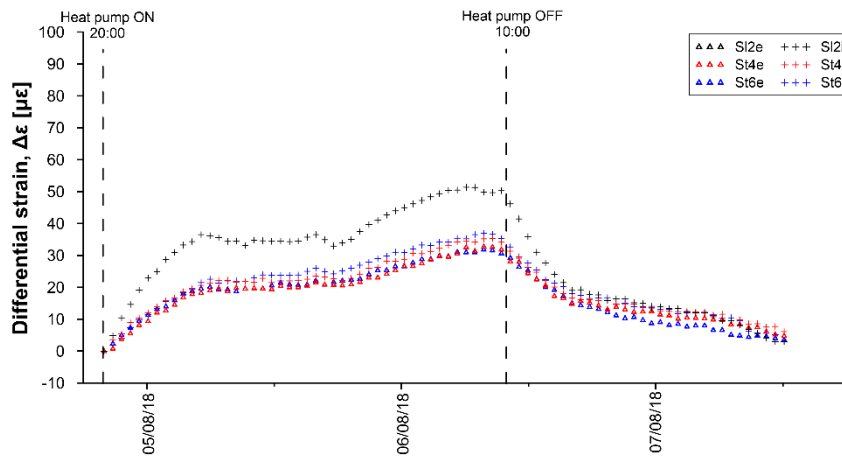


Figure A.170: Differential strains for test AH2.

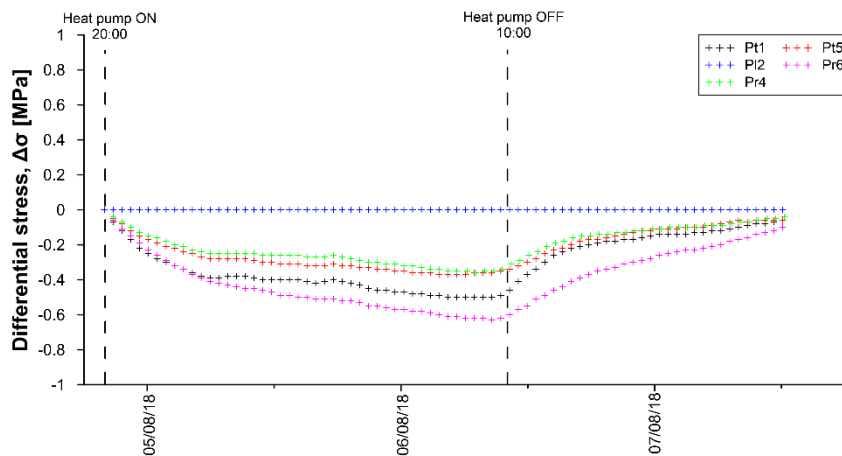


Figure A.171: Differential stresses for test AH2.

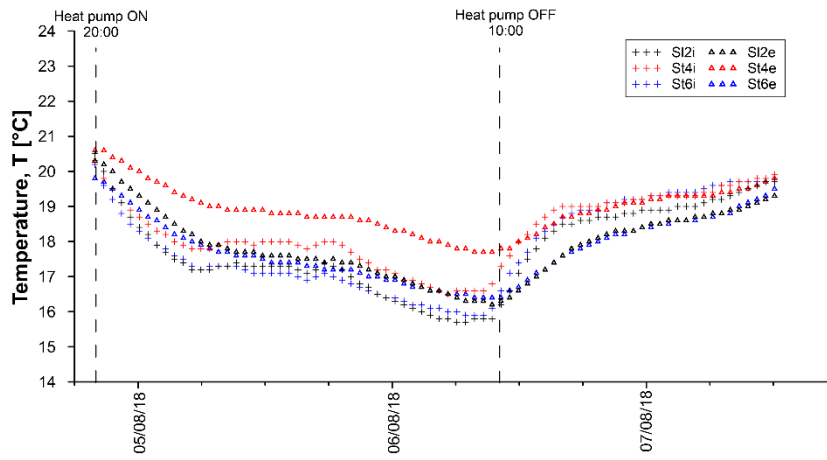


Figure A.172: Temperatures measured by VWSG for test AH2.

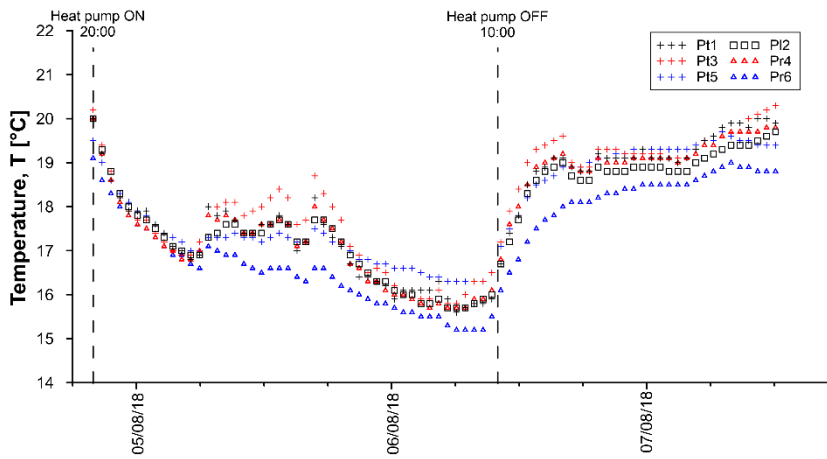


Figure A.173: Temperatures measured by PC for test AH2.

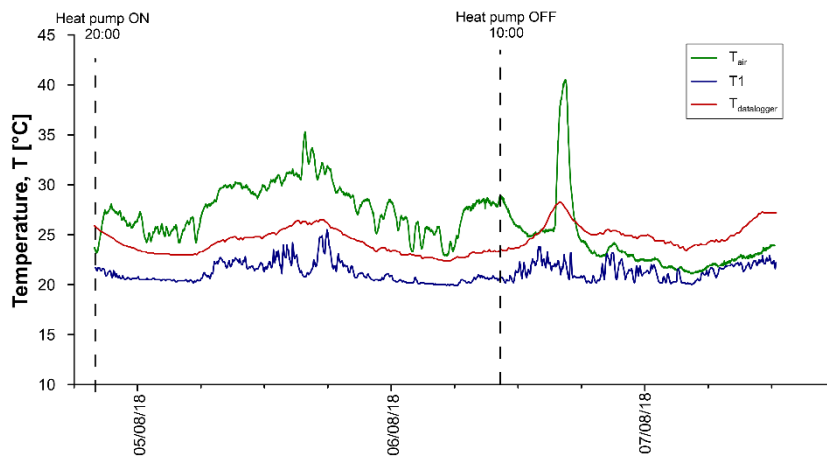


Figure A.174: Air temperatures for test AH2.

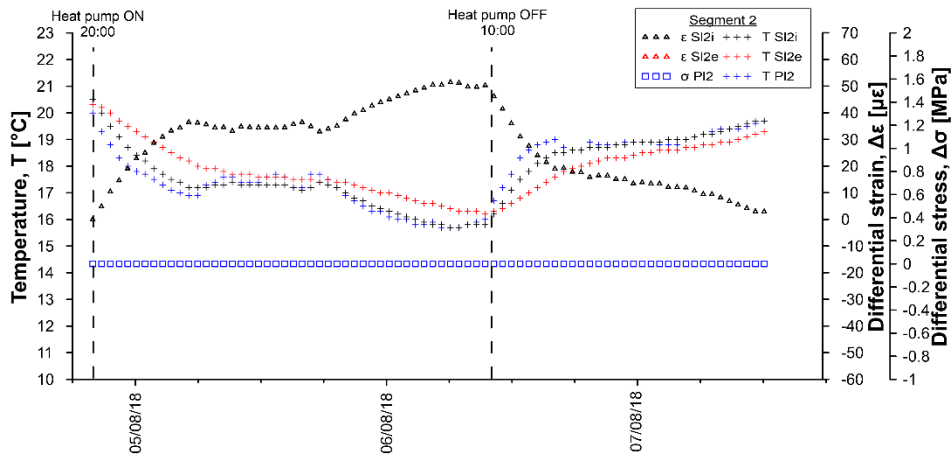


Figure A.175: Temperatures, differential strains and differential stresses in segment 2, ring 179 for test AH2.

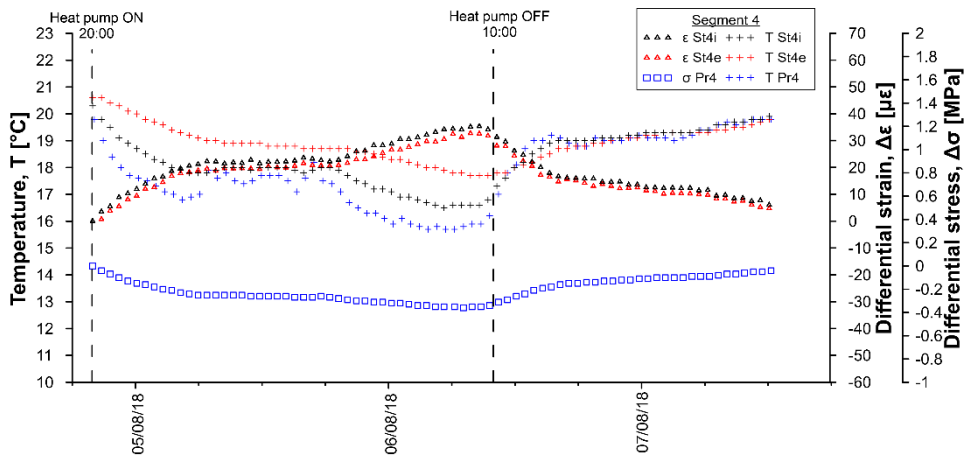


Figure A.176: Temperatures, differential strains and differential stresses in segment 4, ring 179 for test AH2.

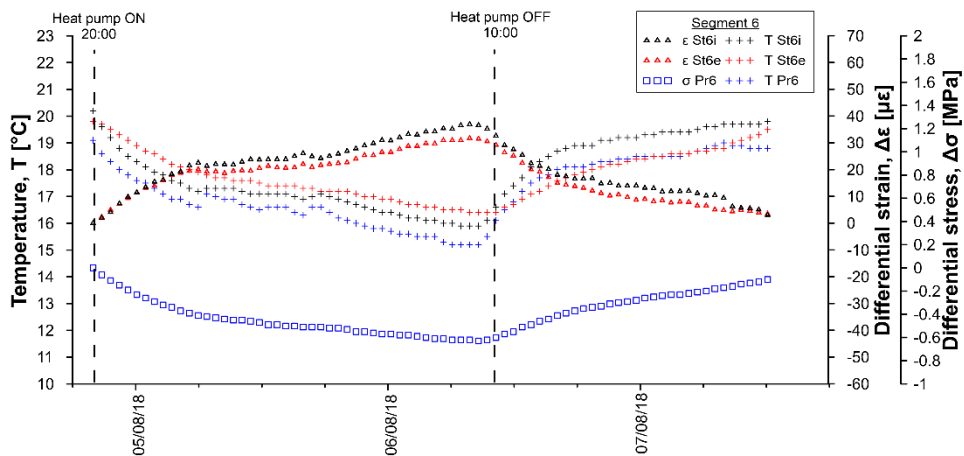


Figure A.177: Temperatures, differential strains and differential stresses in segment 6, ring 179 for test AH2.

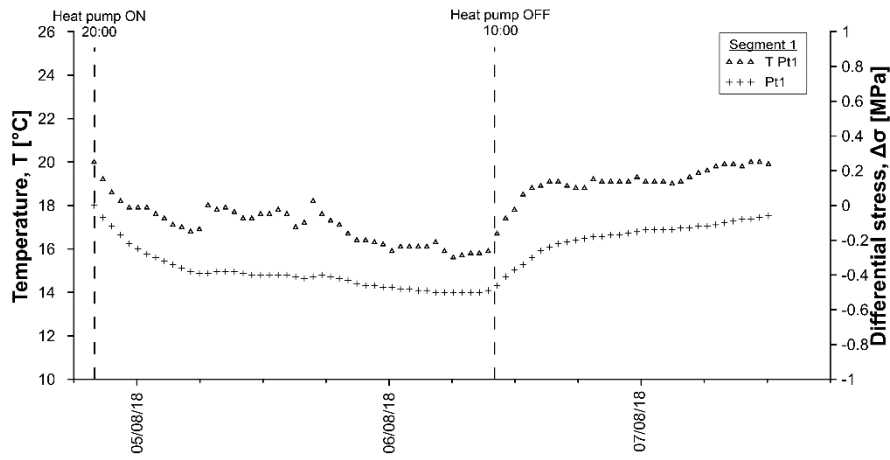


Figure A.178: Temperatures and differential stresses in segment 1, ring 179 for test AH2.

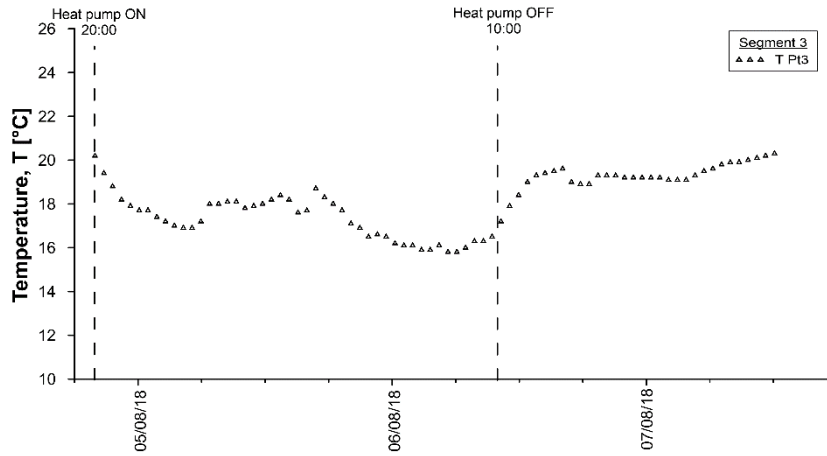


Figure A.179: Temperatures and differential stresses in segment 3, ring 179 for test AH2.

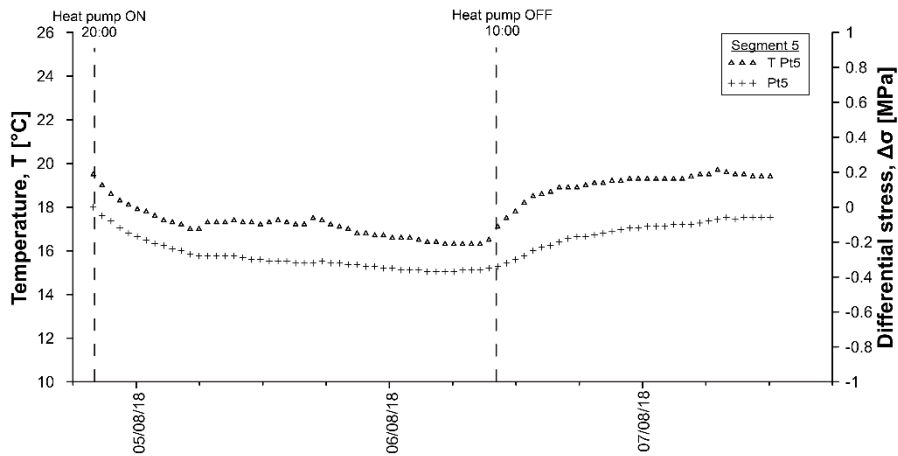


Figure A.180: Temperatures and differential stresses in segment 5, ring 179 for test AH2.

Table A.53: Data sheet for test AH2 – strains and temperatures.

Date	T _{DL} [°C]	SI2i [με]	SI2i [°C]	SI2e [με]	SI2e [°C]	St4i [με]	St4i [°C]	St4e [με]	St4e [°C]	St6i [με]	St6i [°C]	St6e [με]	St6e [°C]
04/08/2018 19:56	25.9	0.00	20.5	-	20.3	0.00	20.3	0.00	20.6	0.00	20.2	0.00	19.8
04/08/2018 21:06	25.0	-1.37	19.8	-	20.1	-3.28	19.7	1.53	20.5	-6.65	19.4	1.29	19.6
04/08/2018 22:16	24.2	-2.42	19.1	-	19.8	-5.48	19.2	1.75	20.3	-9.48	18.9	1.21	19.3
04/08/2018 23:26	23.7	-2.90	18.6	-	19.4	-6.93	18.9	2.10	20.1	-11.08	18.5	0.68	19.0
05/08/2018 00:36	23.3	-2.94	18.2	-	19.1	-7.91	18.5	1.97	19.9	-11.99	18.2	0.09	18.8
05/08/2018 01:46	23.1	-3.04	17.9	-	18.9	-8.54	18.3	1.71	19.7	-12.58	17.9	-0.71	18.6
05/08/2018 02:56	23.1	-3.27	17.7	-	18.6	-9.21	18.1	2.05	19.5	-13.13	17.7	-1.30	18.4
05/08/2018 04:06	23.0	-3.50	17.4	-	18.4	-9.61	17.9	2.05	19.3	-13.61	17.5	-1.89	18.2
05/08/2018 05:16	23.0	-4.05	17.2	-	18.2	-9.80	17.8	1.50	19.2	-14.00	17.3	-2.56	18.0
05/08/2018 06:26	23.5	-4.53	17.2	-	18.0	-8.86	17.8	0.27	19.1	-14.22	17.2	-4.11	17.8
05/08/2018 07:36	24.3	-4.65	17.3	-	17.9	-7.08	17.9	-0.80	19.0	-13.32	17.3	-6.33	17.7
05/08/2018 08:46	24.7	-4.66	17.4	-	17.8	-6.34	18.0	-1.16	18.9	-13.44	17.3	-7.11	17.7
05/08/2018 09:56	24.5	-4.55	17.4	-	17.7	-6.40	18.0	-1.09	18.9	-13.64	17.3	-7.22	17.6
05/08/2018 11:06	24.8	-4.63	17.3	-	17.7	-6.60	17.9	-1.22	18.9	-13.96	17.1	-7.31	17.5
05/08/2018 12:16	25.0	-4.88	17.3	-	17.6	-6.33	18.0	-1.71	18.9	-14.16	17.1	-7.86	17.5
05/08/2018 13:26	25.4	-4.74	17.3	-	17.6	-6.00	18.0	-1.98	18.8	-14.00	17.1	-8.49	17.4
05/08/2018 14:36	25.9	-4.44	17.3	-	17.6	-6.04	18.0	-1.80	18.8	-13.91	17.0	-8.58	17.4
05/08/2018 15:46	26.3	-5.04	17.1	-	17.5	-6.99	17.8	-1.57	18.8	-14.23	16.9	-8.43	17.3
05/08/2018 16:56	26.4	-5.59	17.3	-	17.5	-5.93	17.9	-2.56	18.7	-14.17	17.0	-9.96	17.3
05/08/2018 18:06	26.0	-5.12	17.3	-	17.5	-5.82	18.0	-2.79	18.7	-13.81	17.0	-9.82	17.3
05/08/2018 19:16	25.3	-5.21	17.2	-	17.4	-6.49	17.9	-2.31	18.7	-14.33	16.9	-9.36	17.2
05/08/2018 20:26	24.6	-5.36	16.9	-	17.4	-7.80	17.6	-1.56	18.7	-14.68	16.8	-9.03	17.1
05/08/2018 21:36	24.0	-5.38	16.7	-	17.3	-8.93	17.4	-1.20	18.6	-14.95	16.6	-8.82	17.1
05/08/2018 22:46	23.5	-6.19	16.5	-	17.1	-9.49	17.2	-1.51	18.5	-15.31	16.5	-8.78	17.0
05/08/2018 23:56	23.3	-6.17	16.3	-	17.0	-10.06	17.1	-1.41	18.4	-15.43	16.4	-8.84	16.9
06/08/2018 01:06	23.0	-6.32	16.2	-	16.9	-10.82	16.9	-1.46	18.3	-15.52	16.3	-8.94	16.8
06/08/2018 02:16	22.9	-6.48	16.1	-	16.8	-11.11	16.9	-1.78	18.2	-15.64	16.2	-9.03	16.7
06/08/2018 03:26	22.7	-6.67	15.9	-	16.7	-11.67	16.7	-1.95	18.1	-15.86	16.2	-9.06	16.6
06/08/2018 04:36	22.5	-6.91	15.8	-	16.5	-11.97	16.6	-2.33	18.0	-15.78	16.1	-9.38	16.6
06/08/2018 05:46	22.5	-7.19	15.7	-	16.5	-11.89	16.6	-2.02	17.9	-16.00	16.0	-9.34	16.5
06/08/2018 06:56	22.7	-7.26	15.7	-	16.3	-10.96	16.6	-2.88	17.8	-15.96	15.9	-9.32	16.5
06/08/2018 08:06	23.2	-7.57	15.8	-	16.3	-9.81	16.6	-2.70	17.7	-15.76	16.0	-10.03	16.4
06/08/2018 09:16	23.5	-7.31	15.8	-	16.2	-9.40	16.7	-3.31	17.7	-15.39	16.0	-10.48	16.4
06/08/2018 10:26	23.5	-6.16	16.3	-	16.3	-4.70	17.4	-6.23	17.8	-10.69	16.7	-12.39	16.4
06/08/2018 11:36	23.6	-5.73	16.9	-	16.5	-2.40	17.8	-7.17	17.9	-7.34	17.3	-12.69	16.7
06/08/2018 12:46	24.1	-5.57	17.5	-	16.8	-0.90	18.2	-8.12	18.1	-5.03	17.7	-12.81	16.9
06/08/2018 13:56	25.1	-5.40	18.0	-	17.1	0.32	18.6	-9.94	18.3	-2.62	18.2	-12.84	17.2
06/08/2018 15:06	27.2	-5.25	18.3	-	17.3	0.70	18.9	-10.30	18.5	-1.03	18.5	-12.23	17.4
06/08/2018 16:16	28.0	-5.09	18.5	-	17.7	0.80	19.0	-8.20	18.7	-0.01	18.7	-11.69	17.6
06/08/2018 17:26	26.3	-5.33	18.5	-	17.9	0.24	19.0	-7.18	18.8	0.54	18.8	-10.85	17.8
06/08/2018 18:36	25.2	-5.53	18.6	-	18.0	-0.05	19.0	-7.74	18.8	0.74	18.9	-10.01	17.9
06/08/2018 19:46	25.2	-5.60	18.7	-	18.1	0.06	19.0	-7.46	18.9	1.06	19.0	-9.72	18.0
06/08/2018 20:56	25.4	-5.50	18.7	-	18.2	-0.04	19.1	-6.57	19.0	1.47	19.1	-9.31	18.2
06/08/2018 22:06	24.9	-5.60	18.8	-	18.3	0.11	19.2	-6.04	19.0	1.72	19.2	-8.78	18.3
06/08/2018 23:16	24.6	-5.70	18.8	-	18.4	0.19	19.2	-5.86	19.1	1.84	19.2	-8.44	18.3
07/08/2018 00:26	24.9	-5.64	18.9	-	18.5	0.43	19.3	-5.63	19.2	2.19	19.3	-8.04	18.4
07/08/2018 01:36	24.4	-5.75	18.9	-	18.5	0.32	19.3	-5.95	19.2	2.12	19.3	-7.44	18.5
07/08/2018 02:46	23.9	-6.11	19.0	-	18.6	0.28	19.3	-5.66	19.2	2.16	19.4	-7.05	18.5
07/08/2018 03:56	23.4	-6.26	19.0	-	18.6	0.09	19.3	-5.48	19.3	2.18	19.4	-6.64	18.6
07/08/2018 05:06	23.9	-6.34	19.0	-	18.7	0.33	19.4	-6.00	19.3	2.57	19.5	-6.73	18.7
07/08/2018 06:16	24.4	-6.36	19.2	-	18.8	0.57	19.4	-6.07	19.3	2.95	19.6	-6.87	18.7
07/08/2018 07:26	24.4	-6.38	19.3	-	18.8	1.08	19.6	-6.34	19.4	3.28	19.7	-7.14	18.8
07/08/2018 08:36	25.1	-6.52	19.4	-	19.0	1.28	19.7	-5.96	19.5	0.84	19.7	-5.66	18.9
07/08/2018 09:46	26.1	-6.71	19.5	-	19.0	1.33	19.7	-6.15	19.5	-0.37	19.7	-3.86	19.1
07/08/2018 10:56	27.1	-6.81	19.6	-	19.1	1.49	19.8	-5.80	19.6	-0.94	19.7	-2.38	19.2
07/08/2018 12:06	27.2	-6.87	19.7	-	19.3	1.21	19.9	-5.03	19.8	-1.86	19.8	-0.15	19.5

Table A.54: Data sheet for test AH2 – stresses and temperatures.

Date	Pt1 [MPa]	Pt1 [°C]	Pl2 [MPa]	Pl2 [°C]	Pt3 [MPa]	Pt3 [°C]	Pr4 [MPa]	Pr4 [°C]	Pt5 [MPa]	Pt5 [°C]	Pr6 [MPa]	Pr6 [°C]
04/08/2018 19:56	0	20	0	20	-	20.2	0	20	0	19.5	0	19.1
04/08/2018 21:06	-0.09	18.9	0	19.1	-	19.1	-0.05	18.9	-0.06	18.9	-0.07	18.5
04/08/2018 22:16	-0.17	18.2	0	18.4	-	18.3	-0.09	18.1	-0.11	18.4	-0.14	18.1
04/08/2018 23:26	-0.22	17.9	0	17.9	-	17.9	-0.13	17.7	-0.15	18	-0.19	17.7
05/08/2018 00:36	-0.26	17.9	0	17.7	-	17.6	-0.15	17.5	-0.18	17.8	-0.24	17.5
05/08/2018 01:46	-0.3	17.6	0	17.5	-	17.4	-0.18	17.3	-0.21	17.6	-0.29	17.3
05/08/2018 02:56	-0.33	17.4	0	17.2	-	17.1	-0.2	17.1	-0.23	17.4	-0.33	17.1
05/08/2018 04:06	-0.36	17	0	17	-	16.9	-0.22	16.9	-0.25	17.2	-0.36	16.9
05/08/2018 05:16	-0.38	16.9	0	16.9	-	17	-0.24	16.9	-0.27	17	-0.39	16.7
05/08/2018 06:26	-0.39	17.6	0	17.1	-	17.7	-0.25	17.4	-0.28	17.1	-0.42	16.8
05/08/2018 07:36	-0.38	17.8	0	17.4	-	18	-0.25	17.7	-0.28	17.3	-0.43	17
05/08/2018 08:46	-0.38	17.8	0	17.6	-	18	-0.25	17.7	-0.28	17.3	-0.44	16.9
05/08/2018 09:56	-0.39	17.5	0	17.4	-	17.8	-0.25	17.5	-0.29	17.4	-0.45	16.7
05/08/2018 11:06	-0.4	17.4	0	17.4	-	17.9	-0.26	17.5	-0.3	17.3	-0.47	16.6
05/08/2018 12:16	-0.4	17.9	0	17.6	-	18.3	-0.26	17.8	-0.31	17.3	-0.48	16.5
05/08/2018 13:26	-0.4	17.8	0	17.7	-	18.4	-0.26	17.7	-0.31	17.4	-0.49	16.6
05/08/2018 14:36	-0.4	17.3	0	17.5	-	17.9	-0.26	17.4	-0.31	17.3	-0.5	16.6
05/08/2018 15:46	-0.42	17.2	0	17.3	-	17.7	-0.27	17.3	-0.32	17.2	-0.51	16.3
05/08/2018 16:56	-0.41	18.4	0	17.9	-	18.9	-0.26	18.2	-0.32	17.6	-0.51	16.7
05/08/2018 18:06	-0.41	17.5	0	17.6	-	18.1	-0.27	17.5	-0.31	17.3	-0.51	16.4
05/08/2018 19:16	-0.42	17.1	0	17.2	-	17.7	-0.28	17.2	-0.32	17.1	-0.52	16.2
05/08/2018 20:26	-0.44	16.5	0	16.8	-	17	-0.29	16.6	-0.33	16.9	-0.54	16.1
05/08/2018 21:36	-0.46	16.5	0	16.5	-	16.6	-0.3	16.3	-0.33	16.8	-0.55	16
05/08/2018 22:46	-0.46	16.2	0	16.3	-	16.6	-0.31	16.3	-0.34	16.7	-0.56	15.8
05/08/2018 23:56	-0.47	16	0	16.2	-	16.3	-0.31	16.1	-0.35	16.7	-0.57	15.7
06/08/2018 01:06	-0.48	16.1	0	16	-	16.1	-0.32	16	-0.36	16.6	-0.58	15.6
06/08/2018 02:16	-0.48	16	0	15.9	-	16	-0.33	15.9	-0.36	16.5	-0.59	15.5
06/08/2018 03:26	-0.49	16	0	15.7	-	15.9	-0.34	15.8	-0.37	16.4	-0.6	15.5
06/08/2018 04:36	-0.5	16.3	0	15.9	-	16.1	-0.35	15.8	-0.37	16.4	-0.61	15.5
06/08/2018 05:46	-0.5	15.7	0	15.7	-	15.8	-0.35	15.7	-0.37	16.3	-0.62	15.2
06/08/2018 06:56	-0.5	15.7	0	15.7	-	16	-0.35	15.7	-0.36	16.3	-0.62	15.2
06/08/2018 08:06	-0.5	15.8	0	15.8	-	16.2	-0.35	15.9	-0.36	16.3	-0.62	15.2
06/08/2018 09:16	-0.5	15.8	0	15.9	-	16.3	-0.35	15.9	-0.36	16.3	-0.63	15.3
06/08/2018 10:26	-0.45	16.7	0	16.8	-	17.3	-0.31	17	-0.33	17.2	-0.59	16.2
06/08/2018 11:36	-0.39	17.8	0	17.6	-	18.3	-0.27	17.9	-0.31	17.7	-0.56	16.7
06/08/2018 12:46	-0.34	18.5	0	18.3	-	19	-0.24	18.5	-0.28	18.2	-0.51	17.2
06/08/2018 13:56	-0.29	19	0	18.7	-	19.4	-0.21	19	-0.24	18.6	-0.47	17.6
06/08/2018 15:06	-0.24	19	0	18.9	-	19.4	-0.19	19	-0.22	18.7	-0.44	17.8
06/08/2018 16:16	-0.22	19	0	18.9	-	19.3	-0.16	19.1	-0.2	19	-0.4	18.1
06/08/2018 17:26	-0.2	18.8	0	18.7	-	19	-0.15	18.8	-0.17	19	-0.38	18.1
06/08/2018 18:36	-0.19	18.8	0	18.6	-	18.9	-0.14	18.8	-0.17	19	-0.35	18.1
06/08/2018 19:46	-0.18	19.2	0	18.9	-	19.3	-0.14	19	-0.16	19.1	-0.34	18.3
06/08/2018 20:56	-0.17	19.2	0	18.9	-	19.3	-0.13	19.1	-0.14	19.2	-0.31	18.3
06/08/2018 22:06	-0.17	19	0	18.8	-	19.2	-0.12	19	-0.13	19.2	-0.29	18.4
06/08/2018 23:16	-0.15	19.2	0	18.9	-	19.2	-0.12	19.1	-0.12	19.3	-0.28	18.5
07/08/2018 00:26	-0.14	19.1	0	18.9	-	19.2	-0.11	19.1	-0.11	19.3	-0.26	18.5
07/08/2018 01:36	-0.14	19	0	18.8	-	19.1	-0.1	19.1	-0.11	19.3	-0.25	18.5
07/08/2018 02:46	-0.14	19	0	18.8	-	19.1	-0.1	19	-0.1	19.3	-0.24	18.5
07/08/2018 03:56	-0.13	19.1	0	18.9	-	19.1	-0.1	19.1	-0.1	19.3	-0.23	18.5
07/08/2018 05:06	-0.12	19.4	0	19.1	-	19.4	-0.09	19.3	-0.09	19.5	-0.22	18.7
07/08/2018 06:16	-0.12	19.6	0	19.2	-	19.6	-0.09	19.4	-0.08	19.5	-0.2	18.8
07/08/2018 07:26	-0.1	19.8	0	19.3	-	19.8	-0.08	19.6	-0.07	19.5	-0.18	19
07/08/2018 08:36	-0.09	19.8	0	19.4	-	19.9	-0.07	19.6	-0.06	19.5	-0.16	18.9
07/08/2018 09:46	-0.08	19.9	0	19.4	-	20	-0.06	19.7	-0.06	19.4	-0.14	18.9
07/08/2018 10:56	-0.07	20.1	0	19.6	-	20.2	-0.05	19.8	-0.06	19.4	-0.12	18.9
07/08/2018 12:06	-0.06	19.9	0	19.7	-	20.3	-0.04	19.8	-0.06	19.4	-0.1	18.8

Table A.55: Data sheet for test AH2 - sensors T1-T5 and heat pump.

Date	T1 [°C]	T2 [°C]	T3 [°C]	T4 [°C]	T5 [°C]	Date	T _{air} [°C]	IN [°C]	OUT [°C]	U1 [°C]	U2 [°C]
04/08/2018 20:00	21.7	22.1	21.8	21.6	21.4	04/08/2018 19:54	23.7	20.7	20.9	24.3	24
04/08/2018 21:00	20.9	21.7	21.4	16.2	17.8	04/08/2018 20:00	23.5	18.4	20.9	25.8	22.7
04/08/2018 22:00	21.1	21.3	21	15.5	17.2	04/08/2018 21:00	27.2	14.3	16.6	58.5	51.9
04/08/2018 23:00	20.6	20.8	20.5	15	16.8	04/08/2018 22:00	27.2	13.6	15.9	58.2	51.6
05/08/2018 00:00	20.7	20.4	20.2	14.7	16.4	04/08/2018 23:00	26	13	15.3	57.4	50.7
05/08/2018 01:00	20.5	20.2	20	14.4	16.1	05/08/2018 00:00	26.5	12.7	14.9	57.3	50.8
05/08/2018 02:00	20.5	20.1	19.8	14.3	16.1	05/08/2018 01:00	24.7	12.4	14.7	56.9	50.3
05/08/2018 03:00	20.5	19.9	19.6	14.1	15.9	05/08/2018 02:00	25.1	12.2	14.5	56.7	50.1
05/08/2018 04:00	20.4	19.7	19.4	13.9	15.7	05/08/2018 03:00	24.9	12	14.2	56.5	50
05/08/2018 05:00	20.5	19.7	19.4	13.8	15.6	05/08/2018 04:00	24.2	11.8	14.1	56.3	49.8
05/08/2018 06:00	20.6	19.6	19.3	13.7	15.5	05/08/2018 05:00	26.5	11.6	13.9	56.5	50
05/08/2018 07:00	21.2	19.9	19.5	13.8	15.5	05/08/2018 06:00	26.8	11.5	13.7	56.6	50.1
05/08/2018 08:00	22.5	21	20.2	14.5	15.9	05/08/2018 07:00	28.2	11.5	13.7	57	50.5
05/08/2018 09:00	22.5	21.3	20.5	14.4	15.9	05/08/2018 07:59	29.7	11.7	13.9	58.2	51.7
05/08/2018 10:00	22.4	21.5	20.8	14.4	15.9	05/08/2018 08:59	29.8	11.7	13.9	58.2	51.7
05/08/2018 11:00	21.6	21.4	20.7	14.2	15.8	05/08/2018 09:59	29.8	11.7	14	58.2	51.8
05/08/2018 12:00	21.3	21.3	20.7	14	15.7	05/08/2018 10:59	29.1	11.7	13.9	58.3	51.8
05/08/2018 13:00	22.2	21.4	20.9	14.3	15.8	05/08/2018 11:59	29.8	11.6	13.8	58.1	51.6
05/08/2018 14:00	22.7	21.7	21	14.4	15.8	05/08/2018 12:59	30.2	11.6	13.8	58.7	52.3
05/08/2018 15:00	22.8	21.9	21.1	14.4	15.9	05/08/2018 13:59	30.8	11.7	13.9	59.1	52.7
05/08/2018 16:00	21	21.2	20.4	13.9	15.6	05/08/2018 14:59	31	11.8	14	59.5	53.1
05/08/2018 17:00	22.3	21.2	20.5	14.1	15.6	05/08/2018 15:59	33.5	11.6	13.8	58.2	51.8
05/08/2018 18:00	25.2	22.5	21.4	15.1	16.2	05/08/2018 16:59	30.6	11.5	13.7	58.9	52.5
05/08/2018 19:00	23.1	22.1	21.1	14.2	15.7	05/08/2018 17:59	31.7	11.9	14	61	54.6
05/08/2018 20:00	21.2	21.7	20.8	13.8	15.5	05/08/2018 18:59	29.4	11.6	13.8	58.8	52.4
05/08/2018 21:00	21.1	21.1	20.4	13.7	15.3	05/08/2018 19:59	29	11.5	13.7	57.6	51.2
05/08/2018 22:00	20.7	20.7	20	13.3	15.1	05/08/2018 20:59	27.6	11.2	13.4	57.2	50.8
05/08/2018 23:00	20.4	20.1	19.6	13.1	14.9	05/08/2018 21:59	28.2	11.1	13.3	56.8	50.3
06/08/2018 00:00	20.9	20.1	19.6	13.3	14.9	05/08/2018 22:59	26.9	10.9	13.1	56.4	49.9
06/08/2018 00:58	20.4	19.8	19.3	13	14.8	05/08/2018 23:59	28.3	10.8	13	56.7	50.3
06/08/2018 01:58	20.2	19.5	19.1	12.8	14.7	06/08/2018 00:59	26.9	10.7	12.9	56.1	49.7
06/08/2018 02:58	20.2	19.4	18.9	12.8	14.6	06/08/2018 01:58	23.3	10.6	12.8	55.4	48.9
06/08/2018 03:58	20.1	19.2	18.7	12.7	14.5	06/08/2018 02:58	23.8	10.5	12.7	55.4	49
06/08/2018 04:58	20	19.1	18.6	12.6	14.4	06/08/2018 03:58	25.2	10.4	12.6	55.3	48.9
06/08/2018 05:58	19.9	19	18.6	12.6	14.4	06/08/2018 04:58	23	10.3	12.5	55.2	48.8
06/08/2018 06:58	20.4	19.2	18.7	12.7	14.4	06/08/2018 05:58	23.7	10.3	12.5	55.4	49
06/08/2018 07:58	20.5	19.4	18.9	12.8	14.4	06/08/2018 06:58	27.6	10.3	12.4	55.9	49.5
06/08/2018 08:58	20.6	19.7	19.1	12.8	14.5	06/08/2018 07:58	28.1	10.2	12.4	56.3	49.9
06/08/2018 09:58	20.6	19.8	19.2	12.8	14.5	06/08/2018 08:58	28.4	10.3	12.4	56.4	50
06/08/2018 10:58	20.5	19.8	19.1	17.6	17.5	06/08/2018 09:58	27.9	10.3	12.5	56.4	50.1
06/08/2018 11:58	21.2	19.9	19.4	18.4	18.2	06/08/2018 10:58	27.6	16.2	16.4	44.7	41.2
06/08/2018 12:58	21.5	20.2	19.6	18.7	18.6	06/08/2018 11:58	25.8	16.9	17.1	40.7	34.6
06/08/2018 13:58	23.8	21.1	20.2	19.6	19.2	06/08/2018 12:58	24.9	17.4	17.6	37.9	30.1
06/08/2018 14:58	22.2	21.5	20.7	19.7	19.5	06/08/2018 13:58	25.2	17.9	18.1	35.5	27.3
06/08/2018 15:58	21.6	21.5	20.8	19.8	19.6	06/08/2018 14:58	25.4	18.3	18.5	33.4	26.5
06/08/2018 16:58	23.2	21.3	20.6	19.9	19.7	06/08/2018 15:58	37.9	18.6	18.8	32	26.6
06/08/2018 17:58	20.9	21	20.5	19.7	19.6	06/08/2018 16:58	30.2	18.6	18.8	31	27.2
06/08/2018 18:58	20.2	20.6	20.2	19.6	19.6	06/08/2018 17:58	24.5	18.6	18.8	29.6	26.9
06/08/2018 19:58	22.1	20.5	20.2	19.9	19.7	06/08/2018 18:58	23.2	18.6	18.8	28.3	26.1
06/08/2018 20:58	23.2	21.1	20.5	20.3	20	06/08/2018 19:57	22.9	18.7	18.8	27.2	25.2
06/08/2018 21:58	21.7	21.2	20.7	20.2	19.9	06/08/2018 20:57	24	18.8	19	26.3	24.9
06/08/2018 22:56	20.4	21	20.5	19.9	19.9	06/08/2018 21:57	23.3	18.8	19	25.7	24.6
06/08/2018 23:56	21.2	20.9	20.5	20.1	19.9	06/08/2018 22:57	22.7	18.9	19.1	25	24.2
07/08/2018 00:56	21.8	21.1	20.7	20.3	20.1	06/08/2018 23:57	22.4	18.9	19.1	24.5	23.9
07/08/2018 01:56	20.3	20.7	20.4	20	19.9	07/08/2018 00:57	22.7	19	19.2	24	23.6
07/08/2018 02:56	20.3	20.4	20.2	19.9	19.9	07/08/2018 01:57	21.8	19	19.2	23.5	23.3

Date	T1 [°C]	T2 [°C]	T3 [°C]	T4 [°C]	T5 [°C]	Date	Tair [°C]	IN [°C]	OUT [°C]	U1 [°C]	U2 [°C]
07/08/2018 03:56	20.1	20.3	20.1	19.9	19.9	07/08/2018 02:57	21.5	19	19.2	23	23.1
07/08/2018 04:56	20.5	20.2	20	20	20	07/08/2018 03:57	21.3	19	19.2	22.6	22.9
07/08/2018 05:56	21.1	20.4	20.2	20.3	20.1	07/08/2018 04:57	21.3	19	19.2	22.1	22.7
07/08/2018 06:56	21.1	20.7	20.4	20.3	20.2	07/08/2018 05:57	21.9	19.2	19.4	21.7	22.6
07/08/2018 07:56	21.9	21.2	20.7	20.7	20.4	07/08/2018 06:57	21.8	19.2	19.4	21.6	22.5
07/08/2018 08:56	21.9	21.5	21	20.8	20.5	07/08/2018 07:57	22.3	19.4	19.6	21.6	22.4
07/08/2018 09:56	21.7	20.4	20.1	21.1	20.7	07/08/2018 08:57	22.8	18.9	18.9	21.6	22.4
07/08/2018 10:56	22.3	20.5	20.2	21.5	20.9	07/08/2018 09:57	23	19	19.2	21.8	22.4
07/08/2018 11:56	22.3	20.7	20.4	21.8	21.1	07/08/2018 10:57	23.2	19.1	19.3	22	22.4
						07/08/2018 11:57	23.9	19.2	19.4	22.1	22.4

Table A.56: Summary of test AH2 records.

Quantity	Unit	$x(t_0)$	$x(t_1)$	$x(t_1) - x(t_0)$	$\bar{x}(t_0, t_1)$
T _{DL}	[°C]	25.7	23.3	-2.4	24.1
Sl2i	[$\mu\epsilon$]	-351.19	-357.15	-5.96	17.1
	[$\mu\epsilon$] _{comp} [°C]	0.72 20.4	48.44 16	47.72 -4.4	
Sl2e	[$\mu\epsilon$]	-	-	-	17.7
	[$\mu\epsilon$] _{comp} [°C]	- 20.3	- 16.3	- -4	
St4i	[$\mu\epsilon$]	-1764.19	-1769.87	-5.68	17.7
	[$\mu\epsilon$] _{comp} [°C]	0.6 20.2	32.74 17.1	32.14 -3.1	
St4e	[$\mu\epsilon$]	-1510.35	-1515.73	-5.38	18.8
	[$\mu\epsilon$] _{comp} [°C]	0.25 20.6	30.25 17.7	30.00 -2.9	
St6i	[$\mu\epsilon$]	-2187.17	-2198.43	-11.26	17.1
	[$\mu\epsilon$] _{comp} [°C]	0.99 20	33.65 16.4	32.66 -3.6	
St6e	[$\mu\epsilon$]	-1804.13	-1816.22	-12.09	17.5
	[$\mu\epsilon$] _{comp} [°C]	0.33 19.8	29.72 16.4	29.39 -3.4	
Pt1	[MPa]	0.48	0.02	-0.46	17.1
	[°C]	19.8	16.3	-3.5	
Pl2	[MPa]	-0.06	-0.06	0.00	17.0
	[°C]	19.9	16.4	-3.5	
Pt3	[MPa]	-	-	-	17.3
	[°C]	20	16.9	-3.1	
Pr4	[MPa]	0.49	0.18	-0.31	17.0
	[°C]	19.8	16.5	-3.3	
Pt5	[MPa]	0.45	0.12	-0.33	17.2
	[°C]	19.4	16.9	-2.5	
Pr6	[MPa]	0.81	0.21	-0.6	16.5
	[°C]	19	15.9	-3.1	
T1	[°C]	21.7	20.6	-1.1	21.2
T2	[°C]	22.1	19.8	-2.3	20.6
T3	[°C]	21.8	19.2	-2.6	20.0
T4	[°C]	21.6	12.8	-8.8	13.9
T5	[°C]	21.4	14.5	-6.9	15.6
Air	[°C]	23.5	27.9	4.4	27.7
IN	[°C]	18.4	10.3	-8.1	11.5
OUT	[°C]	20.9	12.5	-8.4	13.8
U1	[°C]	25.8	56.3	30.5	57.2
U2	[°C]	22.7	50.1	27.4	50.7

Test GC2

This test, similar to GC1, was intended to have a more complete set of thermomechanical data in the lining.

Circuit:	Ground
Mode:	Cooling
Secondary circuit temperature:	10°C
Activated rings:	179+180
Volumetric flow rate:	1.4 m ³ /h
Fluid velocity in primary circuit:	0.97 m/s
Starting time t_0 :	07/08/2018 12:22
Ending time t_1 :	09/08/2018 07:31
Duration:	1.80 days
Note:	Stops due to attainment of minimum U1.

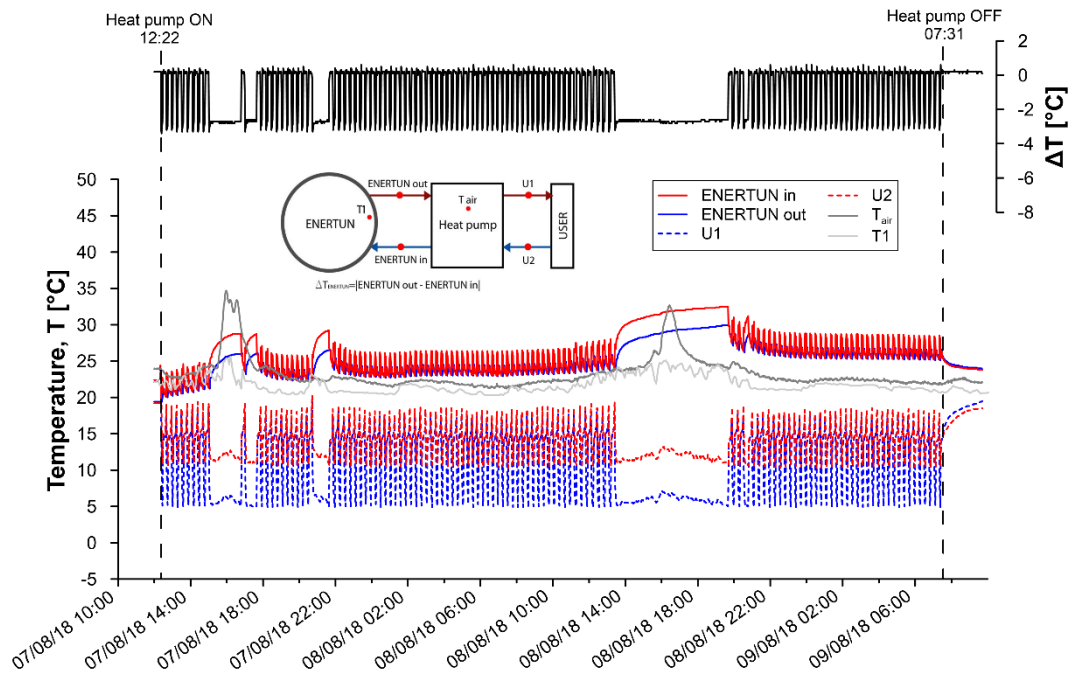


Figure A.181: Primary circuit, secondary circuit and air temperatures for test GC2.

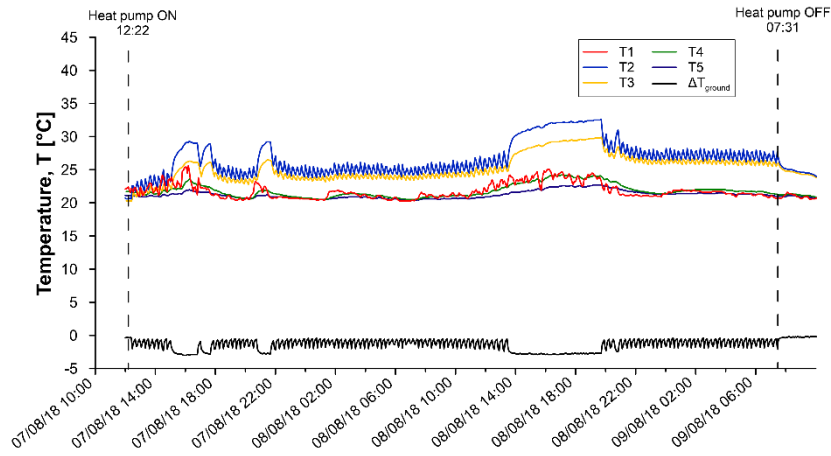


Figure A.182: Temperatures T1-T5 for test GC2.

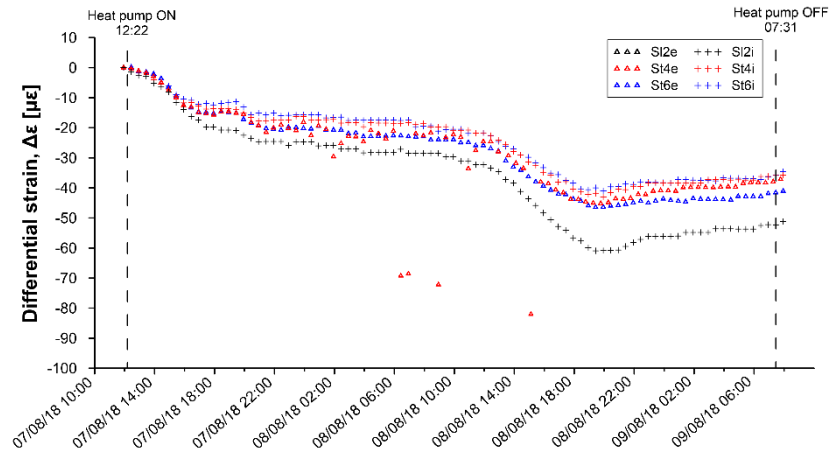


Figure A.183: Differential strains for test GC2.

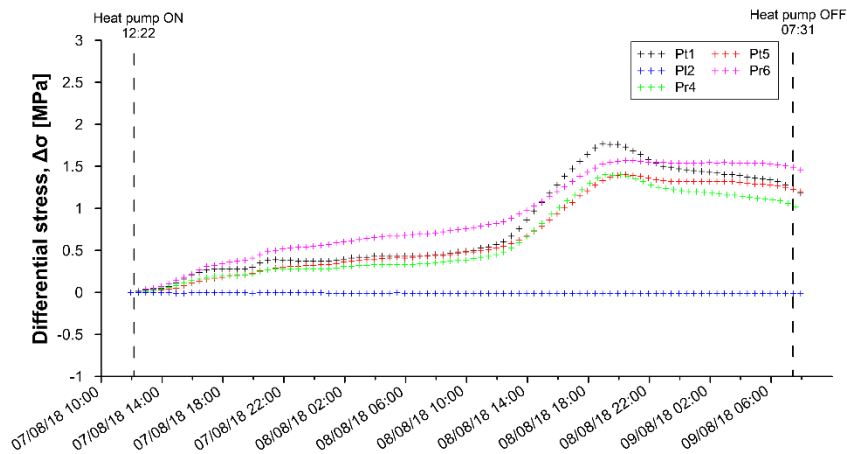


Figure A.184: Differential stresses for test GC2.

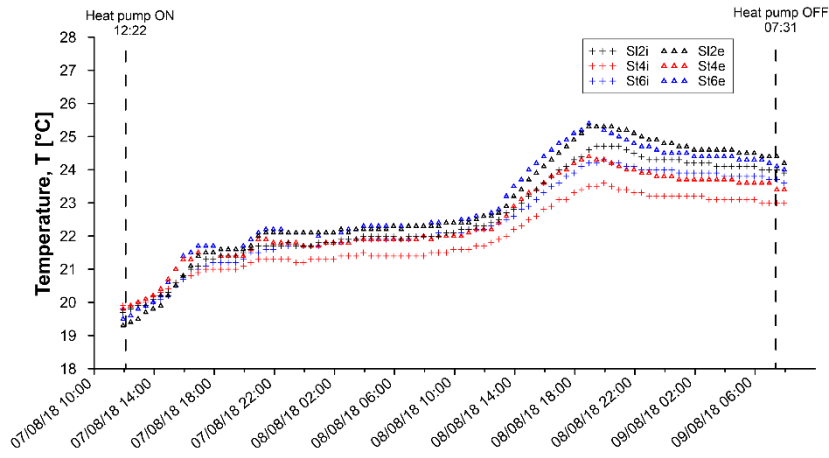


Figure A.185: Temperatures measured by VWSG for test GC2.

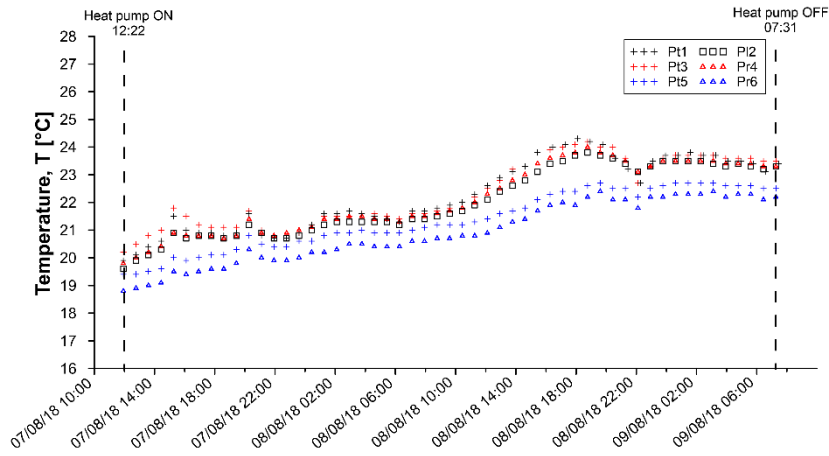


Figure A.186: Temperatures measured by PC for test GC2.

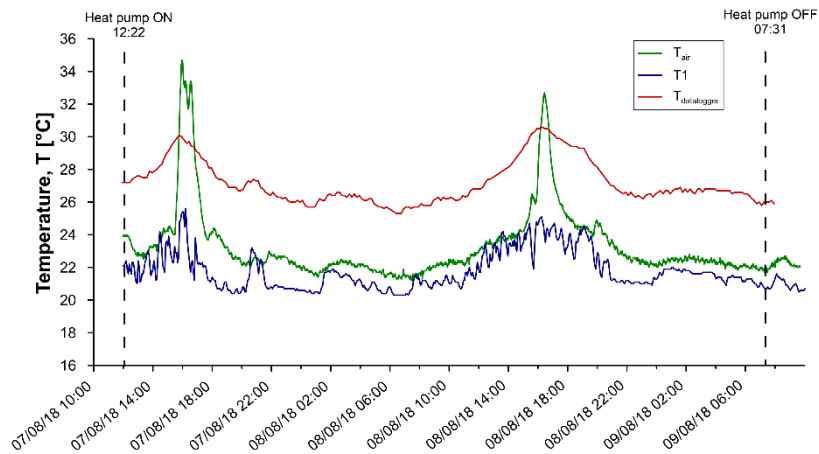


Figure A.187: Air temperatures for test GC2.

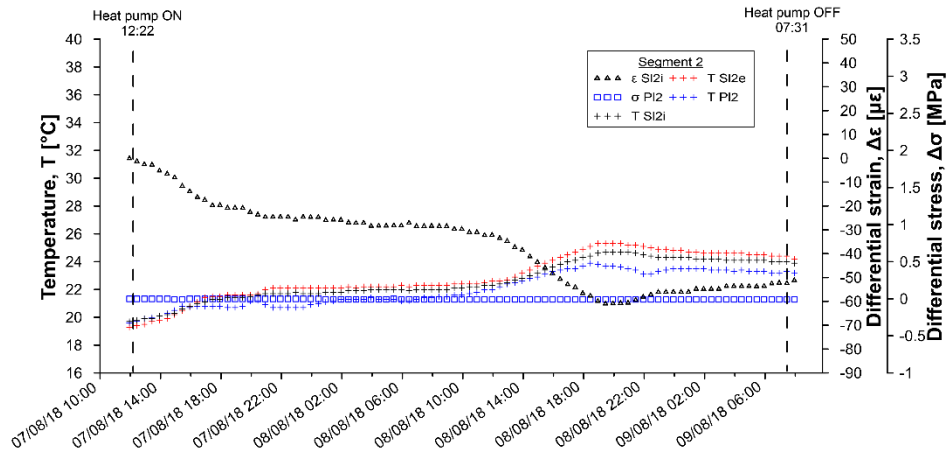


Figure A.188: Temperatures, differential strains and differential stresses in segment 2, ring 179 for test GC2.

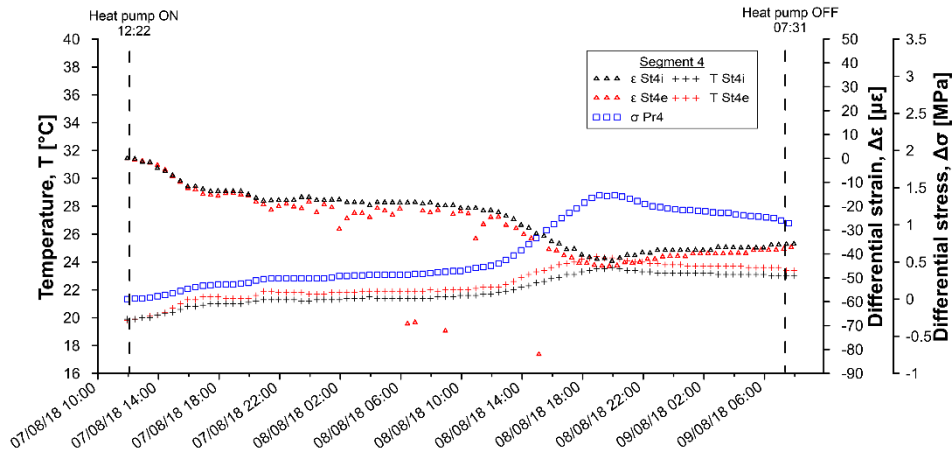


Figure A.189: Temperatures, differential strains and differential stresses in segment 4, ring 179 for test GC2.

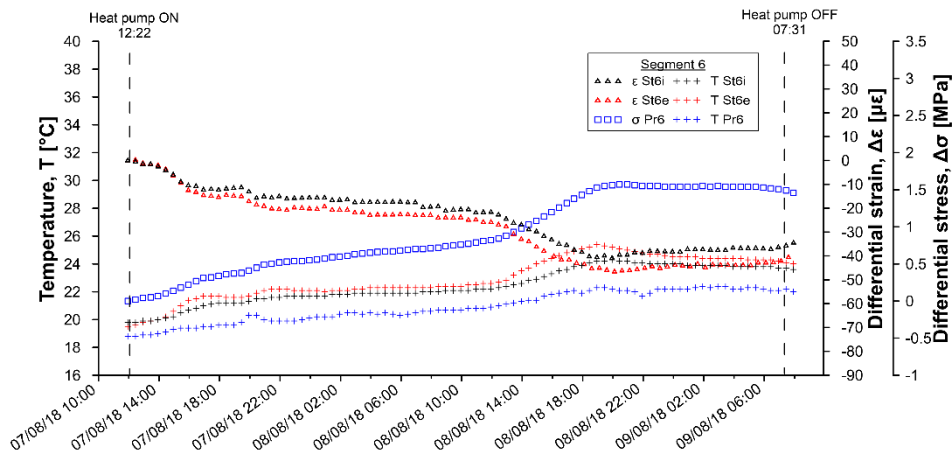


Figure A.190: Temperatures, differential strains and differential stresses in segment 6, ring 179 for test GC2.

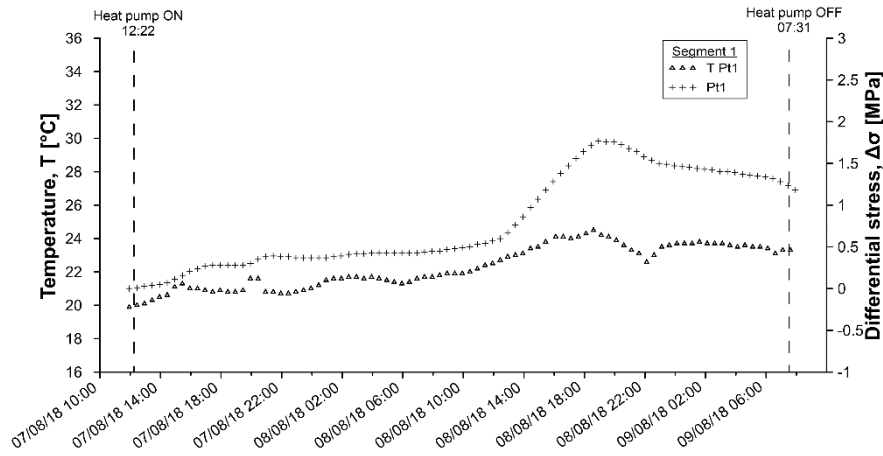


Figure A.191: Temperatures and differential stresses in segment 1, ring 179 for test GC2.

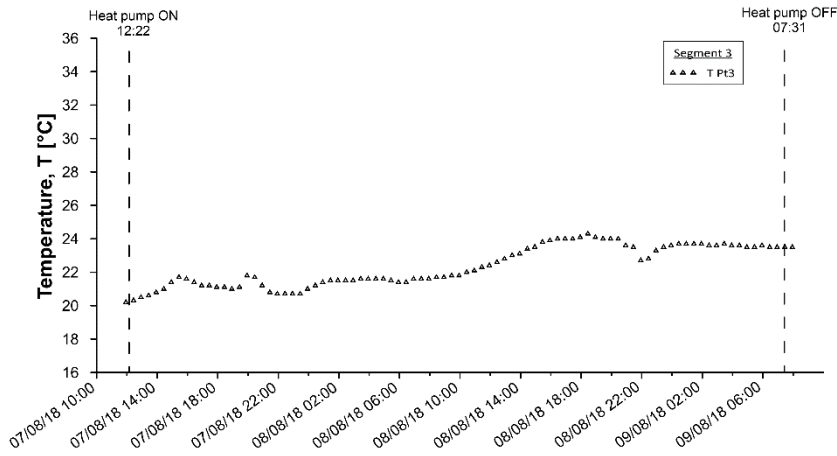


Figure A.192: Temperatures and differential stresses in segment 3, ring 179 for test GC2.

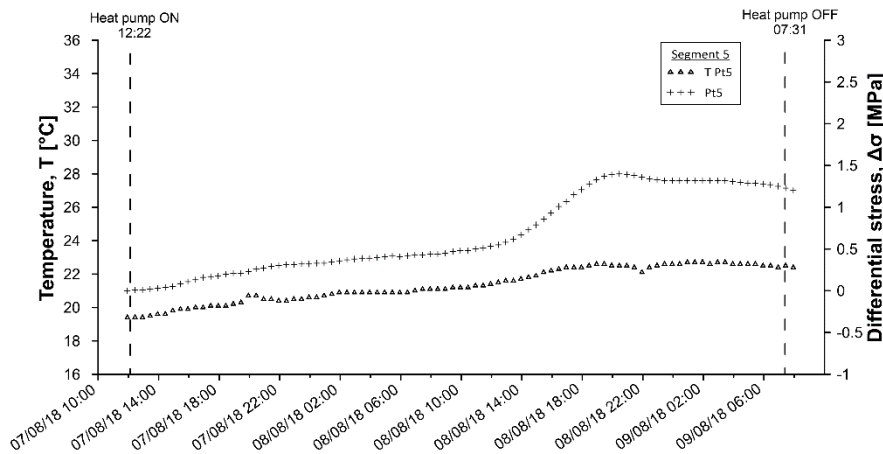


Figure A.193: Temperatures and differential stresses in segment 5, ring 179 for test GC2.

Table A.57: Data sheet for test GC2 – strains and temperatures.

Date	T _{DL} [°C]	SI2i [με]	SI2i [°C]	SI2e [με]	SI2e [°C]	St4i [με]	St4i [°C]	St4e [με]	St4e [°C]	St6i [με]	St6i [°C]	St6e [με]	St6e [°C]
07/08/2018 11:56	27.2	0.00	19.7	-	19.3	0.00	19.9	0.00	19.8	0.00	19.8	0.00	19.5
07/08/2018 12:26	27.2	-0.12	19.8	-	19.4	-0.21	19.9	0.74	19.9	-0.50	19.8	1.42	19.6
07/08/2018 13:26	27.5	-0.33	19.9	-	19.7	-0.38	20.0	1.85	20.1	-0.37	19.9	3.37	19.9
07/08/2018 14:26	28.2	-0.38	20.2	-	19.9	-0.55	20.3	2.49	20.4	-0.47	20.1	4.95	20.2
07/08/2018 15:26	29.7	-0.66	20.6	-	20.5	-0.93	20.6	4.71	21.0	-0.38	20.5	8.83	21.0
07/08/2018 16:26	29.7	-0.45	21.0	-	21.1	-0.69	20.8	5.23	21.3	1.36	20.8	11.11	21.5
07/08/2018 17:26	28.6	-0.23	21.3	-	21.5	-0.34	21.0	5.43	21.5	3.92	21.1	12.00	21.7
07/08/2018 18:26	27.4	-0.02	21.4	-	21.6	-0.25	21.0	4.87	21.4	5.25	21.2	11.10	21.6
07/08/2018 19:26	26.9	-0.18	21.4	-	21.6	-0.41	21.0	4.37	21.4	5.75	21.2	10.55	21.6
07/08/2018 20:26	27.3	-0.45	21.6	-	21.7	-0.73	21.2	3.80	21.6	5.04	21.5	10.79	21.9
07/08/2018 21:26	26.8	-0.16	21.7	-	22.1	-0.55	21.3	4.09	21.9	6.35	21.6	12.73	22.2
07/08/2018 22:26	26.3	-0.15	21.7	-	22.1	-0.41	21.3	5.40	21.8	7.12	21.7	12.16	22.2
07/08/2018 23:26	26.0	-0.21	21.7	-	22.1	-0.36	21.2	3.46	21.8	7.45	21.7	11.79	22.1
08/08/2018 00:26	25.7	-0.29	21.7	-	22.1	-0.42	21.3	0.65	21.7	7.56	21.7	11.34	22.1
08/08/2018 01:26	26.1	-0.16	21.8	-	22.1	-0.23	21.3	3.91	21.8	7.71	21.8	11.05	22.1
08/08/2018 02:26	26.6	-0.11	21.9	-	22.2	-0.10	21.4	-0.73	21.8	7.96	21.8	11.01	22.1
08/08/2018 03:26	26.3	-0.28	21.9	-	22.2	-0.05	21.4	2.68	21.9	8.18	21.9	11.24	22.2
08/08/2018 04:26	26.1	-0.25	22.0	-	22.2	-0.05	21.4	4.78	21.9	8.25	21.9	11.38	22.3
08/08/2018 05:26	25.7	-0.20	22.0	-	22.2	-0.12	21.4	2.03	21.9	8.26	21.9	11.45	22.3
08/08/2018 06:26	25.3	-0.31	21.9	-	22.2	-0.20	21.4	-43.65	21.9	8.06	21.9	11.53	22.3
08/08/2018 07:26	25.6	-0.40	22.0	-	22.3	-0.66	21.4	3.66	21.9	7.25	22.0	11.16	22.3
08/08/2018 08:26	25.8	-0.39	22.0	-	22.3	-0.16	21.5	3.95	21.9	7.57	22.0	11.38	22.4
08/08/2018 09:26	26.1	-0.42	22.1	-	22.4	-0.12	21.5	3.59	22.0	7.35	22.1	11.38	22.4
08/08/2018 10:26	26.1	-0.52	22.2	-	22.4	-0.10	21.6	3.76	22.0	7.53	22.1	11.66	22.5
08/08/2018 11:26	26.7	-0.60	22.3	-	22.5	0.15	21.7	1.73	22.2	7.53	22.2	11.97	22.6
08/08/2018 12:26	27.2	-0.52	22.4	-	22.6	0.62	21.8	4.74	22.2	7.79	22.3	12.14	22.7
08/08/2018 13:26	27.8	-0.63	22.7	-	22.9	0.11	22.0	5.95	22.6	6.70	22.5	14.19	23.2
08/08/2018 14:26	28.6	-0.91	23.0	-	23.4	0.16	22.3	7.02	23.1	7.63	22.8	17.17	23.7
08/08/2018 15:26	30.0	-0.73	23.4	-	23.9	0.49	22.6	-	23.4	8.53	23.1	19.34	24.2
08/08/2018 16:26	30.5	-0.64	23.8	-	24.3	0.88	22.9	9.15	23.8	10.08	23.5	21.53	24.6
08/08/2018 17:26	29.9	-0.44	24.1	-	24.7	1.11	23.1	9.68	24.0	11.33	23.8	23.69	24.9
08/08/2018 18:26	29.4	-0.38	24.4	-	25.1	1.30	23.4	9.94	24.3	12.15	24.1	25.24	25.2
08/08/2018 19:26	28.7	0.05	24.7	-	25.3	2.15	23.5	7.79	24.3	13.73	24.2	24.35	25.3
08/08/2018 20:26	27.6	0.21	24.7	-	25.3	2.24	23.5	7.78	24.2	14.02	24.2	22.36	25.1
08/08/2018 21:26	26.7	0.33	24.6	-	25.2	2.15	23.4	7.69	24.0	13.90	24.1	20.46	24.9
08/08/2018 22:26	26.4	0.19	24.4	-	25.0	1.89	23.3	7.70	23.9	13.27	24.0	19.08	24.7
08/08/2018 23:26	26.5	0.01	24.3	-	24.9	1.86	23.2	7.89	23.8	13.06	24.0	17.92	24.6
09/08/2018 00:26	26.5	0.05	24.3	-	24.8	1.88	23.2	7.87	23.8	12.88	24.0	16.91	24.5
09/08/2018 01:26	26.8	0.07	24.2	-	24.7	1.90	23.2	7.77	23.7	12.74	23.9	16.48	24.5
09/08/2018 02:26	26.6	0.08	24.2	-	24.6	1.83	23.2	7.75	23.7	12.52	23.9	16.07	24.4
09/08/2018 03:26	26.8	0.05	24.1	-	24.6	1.84	23.1	7.85	23.7	12.38	23.9	15.99	24.4
09/08/2018 04:26	26.7	0.04	24.1	-	24.6	1.69	23.1	7.87	23.7	12.02	23.8	15.79	24.4
09/08/2018 05:26	26.6	-0.02	24.1	-	24.5	1.66	23.1	8.02	23.6	11.93	23.8	15.71	24.3
09/08/2018 06:26	26.2	-0.01	24.0	-	24.4	1.61	23.0	8.00	23.6	11.53	23.8	15.72	24.3
09/08/2018 07:26	26.0	0.01	24.0	-	24.4	1.92	23.0	7.08	23.4	11.87	23.7	14.54	24.1

Table A.58: Data sheet for test GC2 – stresses and temperatures.

Date	Pt1 [MPa]	Pt1 [°C]	Pl2 [MPa]	Pl2 [°C]	Pt3 [MPa]	Pt3 [°C]	Pr4 [MPa]	Pr4 [°C]	Pt5 [MPa]	Pt5 [°C]	Pr6 [MPa]	Pr6 [°C]
07/08/2018 11:56	0	19.9	0	19.6	-	20.2	0	19.8	0	19.4	0	18.8
07/08/2018 12:26	0.01	20	0	19.7	-	20.3	0.01	19.8	0.01	19.4	0.02	18.8
07/08/2018 13:26	0.04	20.3	0	20	-	20.6	0.02	20.1	0.02	19.5	0.05	18.9
07/08/2018 14:26	0.07	20.6	0	20.3	-	21	0.06	20.4	0.04	19.6	0.1	19.1
07/08/2018 15:26	0.16	21.3	-0.01	20.8	-	21.7	0.11	20.9	0.08	19.9	0.18	19.4
07/08/2018 16:26	0.24	21	0	20.8	-	21.4	0.16	20.8	0.13	20	0.27	19.4
07/08/2018 17:26	0.28	20.8	0	20.8	-	21.2	0.19	20.8	0.17	20.1	0.32	19.5
07/08/2018 18:26	0.28	20.8	0	20.7	-	21.1	0.2	20.7	0.2	20.1	0.36	19.6
07/08/2018 19:26	0.28	20.9	0	20.8	-	21.1	0.21	20.8	0.21	20.3	0.38	19.8
07/08/2018 20:26	0.35	21.6	0	21.2	-	21.7	0.25	21.4	0.26	20.7	0.45	20.3
07/08/2018 21:26	0.39	20.8	0	20.7	-	20.8	0.28	20.9	0.29	20.5	0.5	19.9
07/08/2018 22:26	0.38	20.7	0	20.7	-	20.7	0.28	20.9	0.31	20.4	0.53	19.9
07/08/2018 23:26	0.37	20.9	0	20.7	-	20.7	0.28	21	0.32	20.5	0.54	20
08/08/2018 00:26	0.37	21.2	0	21	-	21.2	0.28	21.1	0.33	20.6	0.56	20.2
08/08/2018 01:26	0.38	21.6	-0.01	21.2	-	21.5	0.29	21.4	0.34	20.8	0.59	20.2
08/08/2018 02:26	0.41	21.7	-0.01	21.3	-	21.5	0.31	21.4	0.37	20.9	0.61	20.5
08/08/2018 03:26	0.42	21.6	-0.01	21.3	-	21.6	0.32	21.5	0.39	20.9	0.64	20.4
08/08/2018 04:26	0.43	21.6	-0.01	21.3	-	21.6	0.33	21.5	0.4	20.9	0.66	20.4
08/08/2018 05:26	0.43	21.4	0	21.3	-	21.5	0.33	21.4	0.42	20.9	0.67	20.4
08/08/2018 06:26	0.43	21.4	-0.01	21.2	-	21.4	0.33	21.3	0.42	20.9	0.69	20.4
08/08/2018 07:26	0.44	21.7	-0.01	21.4	-	21.6	0.34	21.5	0.43	21.1	0.7	20.6
08/08/2018 08:26	0.45	21.8	-0.01	21.5	-	21.7	0.36	21.6	0.44	21.1	0.72	20.7
08/08/2018 09:26	0.48	21.9	-0.01	21.6	-	21.8	0.38	21.7	0.47	21.2	0.75	20.7
08/08/2018 10:26	0.5	22	-0.01	21.7	-	22	0.4	21.8	0.48	21.2	0.77	20.8
08/08/2018 11:26	0.54	22.4	-0.01	22	-	22.3	0.43	22.1	0.51	21.3	0.81	20.8
08/08/2018 12:26	0.6	22.7	-0.01	22.2	-	22.6	0.48	22.3	0.55	21.5	0.84	21
08/08/2018 13:26	0.76	23	-0.01	22.5	-	23	0.59	22.7	0.62	21.6	0.93	21.2
08/08/2018 14:26	0.97	23.4	-0.01	22.8	-	23.4	0.74	23	0.73	21.8	1.03	21.4
08/08/2018 15:26	1.18	23.8	-0.01	23.1	-	23.8	-	23.4	0.86	22.1	1.14	21.7
08/08/2018 16:26	1.38	24	-0.01	23.4	-	24	1.06	23.6	1.01	22.3	1.26	21.9
08/08/2018 17:26	1.56	24	-0.01	23.5	-	24	1.2	23.7	1.15	22.4	1.38	22.1
08/08/2018 18:26	1.72	24.4	-0.01	23.9	-	24.3	1.34	24	1.28	22.5	1.48	22.1
08/08/2018 19:26	1.76	24	-0.01	23.7	-	24	1.39	23.8	1.37	22.6	1.55	22.3
08/08/2018 20:26	1.73	23.7	-0.01	23.6	-	24	1.39	23.7	1.4	22.5	1.57	22.1
08/08/2018 21:26	1.64	23.2	-0.01	23.4	-	23.5	1.33	23.4	1.38	22.4	1.56	22
08/08/2018 22:26	1.54	22.9	-0.01	23.1	-	22.8	1.26	23.1	1.34	22.4	1.55	21.9
08/08/2018 23:26	1.49	23.6	-0.01	23.4	-	23.5	1.23	23.4	1.32	22.6	1.54	22.2
09/08/2018 00:26	1.46	23.7	-0.01	23.5	-	23.7	1.21	23.5	1.32	22.6	1.54	22.2
09/08/2018 01:26	1.44	23.8	-0.01	23.5	-	23.7	1.19	23.5	1.32	22.7	1.54	22.3
09/08/2018 02:26	1.42	23.7	-0.01	23.4	-	23.6	1.17	23.5	1.32	22.6	1.54	22.3
09/08/2018 03:26	1.4	23.7	-0.01	23.4	-	23.7	1.16	23.5	1.32	22.7	1.54	22.4
09/08/2018 04:26	1.37	23.5	-0.01	23.4	-	23.6	1.14	23.4	1.3	22.6	1.54	22.2
09/08/2018 05:26	1.35	23.5	-0.01	23.3	-	23.5	1.12	23.4	1.29	22.6	1.54	22.3
09/08/2018 06:26	1.32	23.2	-0.01	23.2	-	23.5	1.09	23.3	1.27	22.5	1.52	22.1
09/08/2018 07:26	1.23	23.4	-0.01	23.3	-	23.5	1.04	23.3	1.23	22.5	1.49	22.2

Table A.59: Data sheet for test GC2 - sensors T1-T5 and heat pump.

Date	T1 [°C]	T2 [°C]	T3 [°C]	T4 [°C]	T5 [°C]	Date	T _{air} [°C]	IN [°C]	OUT [°C]	U1 [°C]	U2 [°C]
07/08/2018 12:00	22.1	20.7	20.3	21.7	21.1	07/08/2018 12:00	23.9	19.2	19.4	22.1	22.4
07/08/2018 12:24	22.2	20.6	20.2	21.6	21.1	07/08/2018 12:22	23.9	19.2	19.4	23.9	24.2
07/08/2018 13:24	21.9	22.9	21.9	21.2	20.9	07/08/2018 13:22	22.6	21.2	21.3	14.2	14.7
07/08/2018 14:24	23.5	22.6	21.9	21.5	21	07/08/2018 14:23	23.4	23.8	21.1	15.2	19.4
07/08/2018 15:24	22.3	27.2	24.5	22	21.3	07/08/2018 15:24	24	27.1	24.4	5.4	11.3
07/08/2018 16:24	22.9	29.1	26.2	23.3	21.9	07/08/2018 16:25	32	28.7	25.9	5.8	11.8
07/08/2018 17:24	22	28.5	25.8	22.5	21.6	07/08/2018 17:26	24.5	28.4	25.8	5	11
07/08/2018 18:24	20.7	24.6	23.8	21.5	21.1	07/08/2018 18:27	24	26.1	22.9	12.9	18.1
07/08/2018 19:24	20.4	25.2	23.2	20.8	20.8	07/08/2018 19:28	22.6	22.7	22.9	14.6	14.6
07/08/2018 20:24	21.2	23.9	23.2	20.6	20.7	07/08/2018 20:29	22.2	25.4	22.7	5.2	11.1
07/08/2018 21:24	22.1	29.2	26.4	21.9	21.2	07/08/2018 21:30	22.3	29.1	26.4	5.8	11.7
07/08/2018 22:24	20.9	25.4	24.4	21.2	20.9	07/08/2018 22:31	22.7	26.1	23.2	6.1	12
07/08/2018 23:24	20.7	24.9	23.4	20.9	20.8	07/08/2018 23:32	22.3	23.3	23.5	15	14.8
08/08/2018 00:24	20.5	24.2	23.6	20.7	20.6	08/08/2018 00:33	21.7	24	24.2	13.7	14.2
08/08/2018 01:24	20.8	25	24	20.5	20.5	08/08/2018 01:34	21.9	25.9	22.9	7.1	12.8
08/08/2018 02:24	21.7	24.3	23.7	21.2	20.8	08/08/2018 02:35	22.3	23.4	23.7	15.1	15.2
08/08/2018 03:24	21.3	25.7	24.4	21.4	20.9	08/08/2018 03:36	22.1	25.9	23	5.6	11.5
08/08/2018 04:24	20.7	24.3	23.8	21.1	20.7	08/08/2018 04:37	21.9	23.5	23.7	15.2	14.9
08/08/2018 05:24	20.5	25.5	24.3	20.9	20.6	08/08/2018 05:38	21.5	24	24.4	13.5	14.2
08/08/2018 06:24	20.3	24	23.5	20.6	20.5	08/08/2018 06:39	21.5	26.4	23.2	11.5	16.9
08/08/2018 07:22	20.6	24.9	24	20.5	20.4	08/08/2018 07:39	21.4	23.4	23.6	15	14.6
08/08/2018 08:20	21.2	24.3	23.7	20.9	20.6	08/08/2018 08:40	21.8	24.3	24.6	13.6	14.2
08/08/2018 09:18	21	25.6	24.6	21	20.6	08/08/2018 09:41	22.2	23.3	23.5	17.3	17.9
08/08/2018 10:18	21.3	24.6	24	21.2	20.7	08/08/2018 10:42	22.3	24.5	24.7	14	14.5
08/08/2018 11:18	21.8	26.8	24.7	21.2	20.7	08/08/2018 11:43	22.8	24	24.2	15.4	15.2
08/08/2018 12:18	22.8	26.7	25.4	21.6	20.9	08/08/2018 12:44	23.6	23.8	24	18	18.6
08/08/2018 13:18	23.1	26.7	25.6	22.4	21.3	08/08/2018 13:45	23.6	29.3	26.7	5.4	11.2
08/08/2018 14:18	23.6	30.5	27.8	23	21.6	08/08/2018 14:46	24.3	30.8	28.2	5.7	11.5
08/08/2018 15:18	24.3	31.4	28.5	23.4	22	08/08/2018 15:47	26	31.4	28.7	5.7	11.7
08/08/2018 16:18	24.8	32	29.1	24.1	22.4	08/08/2018 16:48	29.3	32	29.2	6.2	12.2
08/08/2018 17:18	23.7	32.1	29.4	24.1	22.6	08/08/2018 17:49	25.3	32.2	29.5	5.7	11.8
08/08/2018 18:18	23.2	32.3	29.6	23.9	22.6	08/08/2018 18:50	24.5	32.3	29.7	5.6	11.5
08/08/2018 19:18	24	32.5	29.8	24.1	22.7	08/08/2018 19:51	24.6	27.7	27.9	14.4	15.9
08/08/2018 20:18	21.4	28.9	27	23.2	22.3	08/08/2018 20:52	23.4	28.5	28.5	14.3	14.6
08/08/2018 21:18	21.1	27.4	26.8	22.4	21.9	08/08/2018 21:53	22.8	25.9	26.1	16.9	17.5
08/08/2018 22:18	21	28.3	26.4	21.7	21.6	08/08/2018 22:54	22.3	26.8	27	13.9	14.5
08/08/2018 23:18	21.1	26.8	26.2	21.4	21.3	08/08/2018 23:55	22.2	28.8	25.6	11	16.2
09/08/2018 00:18	21.6	28.2	26.4	21.5	21.3	09/08/2018 00:55	22.4	25.8	26	14.8	14.8
09/08/2018 01:18	21.9	26.7	26.1	21.9	21.4	09/08/2018 01:56	22.6	28.2	25.4	5.8	11.5
09/08/2018 02:18	21.7	28.2	26.4	22	21.5	09/08/2018 02:57	22.4	25.8	26	15	14.7
09/08/2018 03:18	21.7	26.6	26.1	22	21.4	09/08/2018 03:58	22.4	28.6	26.3	4.9	10.6
09/08/2018 04:18	21.4	28.1	26.3	21.9	21.4	09/08/2018 04:59	22.3	25.7	25.8	15.4	15.1
09/08/2018 05:18	21.4	26.6	26.1	21.8	21.4	09/08/2018 06:00	22.1	26.3	26.6	13.2	14
09/08/2018 06:18	21.3	27.9	26.1	21.7	21.3	09/08/2018 07:01	21.9	25.2	25.4	16.7	17.3
09/08/2018 07:18	20.7	26.4	25.8	21.3	21	09/08/2018 07:30	21.8	25.4	25.7	14.8	14.7
09/08/2018 08:18	21.4	25	24.7	21.3	21.1	09/08/2018 08:03	22.4	24.3	24.5	17.8	16.7
09/08/2018 09:18	20.9	24.5	24.3	21.1	20.9	09/08/2018 09:04	22.2	23.9	24.1	18.9	18.3

Table A.60: Summary of test GC2 records.

Quantity	Unit	$x(t_0)$	$x(t_1)$	$x(t_1) - x(t_0)$	$\bar{x}(t_0, t_1)$
T _{DL}	[°C]	27.2	26.0	-1.2	27.2
Sl2i	[με]	-357.61	-357.48	0.13	22.6
	[με] _{comp} [°C]	-1.34 19.8	-52.45 24.0	-51.11 4.2	
Sl2e	[με]	-	-	-	23.0
	[με] _{comp} [°C]	- 19.4	- 24.4	- 5.0	
St4i	[με]	-1762.45	-1760.32	2.13	22.0
	[με] _{comp} [°C]	-0.21 19.9	-35.9 23.0	-35.69 3.1	
St4e	[με]	-1515.04	-1508.70	6.34	22.5
	[με] _{comp} [°C]	-0.48 19.9	-36.84 23.4	-36.36 3.5	
St6i	[με]	-2187.91	-2175.54	12.37	22.5
	[με] _{comp} [°C]	-0.5 19.8	-35.71 23.7	-35.21 3.9	
St6e	[με]	-1803.61	-1790.49	13.12	23.0
	[με] _{comp} [°C]	0.2 19.6	-41.58 24.1	-41.78 4.5	
Pt1	[MPa]	0.44	1.66	1.22	22.3
	[°C]	20.0	23.4	3.4	
Pl2	[MPa]	-0.06	-0.07	-0.01	22.0
	[°C]	19.7	23.3	3.6	
Pt3	[MPa]	-	-	-	22.4
	[°C]	20.3	23.5	3.2	
Pr4	[MPa]	0.47	1.50	1.03	22.2
	[°C]	19.8	23.3	3.5	
Pt5	[MPa]	0.41	1.63	1.22	21.4
	[°C]	19.4	22.5	3.1	
Pr6	[MPa]	0.73	2.20	1.47	20.9
	[°C]	18.8	22.2	3.4	
T1	[°C]	22.2	20.7	-1.5	21.8
T2	[°C]	20.6	27.7	7.1	26.8
T3	[°C]	20.2	25.9	5.7	25.3
T4	[°C]	21.6	21.3	-0.3	21.8
T5	[°C]	21.1	21.0	-0.1	21.2
Air	[°C]	23.8	21.8	-2.0	23.3
IN	[°C]	22.6	25.4	2.8	26.3
OUT	[°C]	19.4	25.7	6.3	25.1
U1	[°C]	18.6	14.8	-3.8	11.1
U2	[°C]	23.4	14.7	-8.7	13.9

Undisturbed phase (summer 2018)

In the morning of August 9th, 2018 the construction site disconnected the heat pump and the monitoring system for matters related to the yard. The system has no longer been connected up to the time this manuscript has been drawn up. During the following days, we could not but monitor the T1-T5 probes.

Starting time t_0 :	09/08/2018 10:06
Ending time t_1 :	20/08/2018 11:28
Duration:	11.1 days

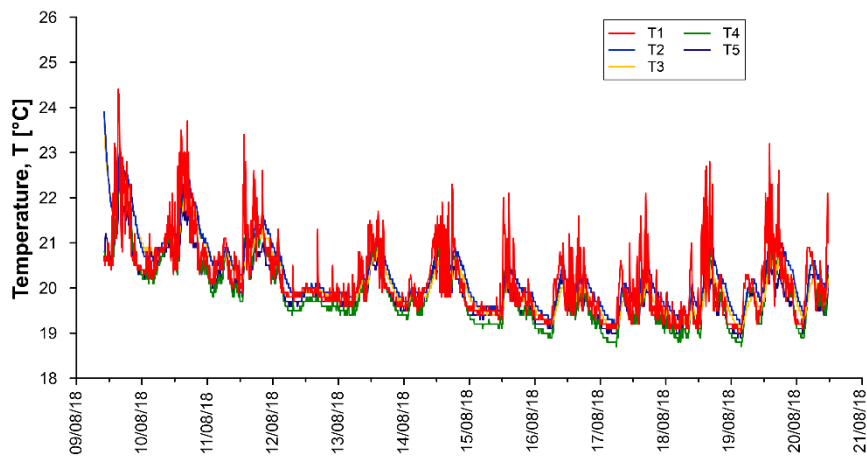


Figure A.194: Temperatures T1-T5 for undisturbed phase.

Table A.61: Data sheet for undisturbed phase (summer 2018)- sensors T1-T5 and heat pump.

Date	T1 [°C]	T2 [°C]	T3 [°C]	T4 [°C]	T5 [°C]
09/08/2018 10:06	20.6	23.9	23.8	20.8	20.7
09/08/2018 13:06	20.7	21.8	21.9	20.6	20.7
09/08/2018 16:06	23.1	23	22.6	22.8	22.3
09/08/2018 19:06	21.6	22.4	22.3	21.8	21.4
09/08/2018 22:06	20.6	21.4	21.4	20.6	20.5
10/08/2018 01:06	20.4	20.7	20.8	20.2	20.2
10/08/2018 04:06	20.2	20.6	20.7	20.1	20.2
10/08/2018 07:06	20.8	20.9	20.9	20.7	20.7
10/08/2018 10:06	21.7	21.3	21.2	21.1	20.9
10/08/2018 13:06	22.4	21.1	21	20.7	20.4
10/08/2018 16:06	22	22.3	21.9	22	21.6
10/08/2018 19:06	21.3	21.9	21.7	21.4	21
10/08/2018 22:06	20.8	21.1	21.1	20.5	20.4
11/08/2018 01:06	20.2	20.7	20.6	20	20.1
11/08/2018 04:06	20.7	20.6	20.5	20.2	20.3
11/08/2018 07:06	20.8	20.9	20.8	20.7	20.7
11/08/2018 10:06	20.6	20.5	20.4	20	20.1
11/08/2018 13:06	22.2	20.5	20.4	20.2	20.1
11/08/2018 16:06	21.2	21	20.8	20.7	20.4
11/08/2018 19:06	21.2	21.4	21.1	21	20.7
11/08/2018 22:04	20.9	21.3	21.1	20.7	20.5
12/08/2018 01:04	20.7	20.8	20.7	20.3	20.2
12/08/2018 04:04	19.9	20.4	20.3	19.7	19.8
12/08/2018 07:04	19.8	19.9	19.9	19.4	19.7
12/08/2018 10:04	19.9	19.9	19.8	19.6	19.7
12/08/2018 13:04	20	20	19.9	19.7	19.9
12/08/2018 16:04	19.9	20	20	19.7	19.9
12/08/2018 19:04	19.8	19.9	19.9	19.6	19.7
12/08/2018 22:04	19.8	19.9	19.9	19.6	19.8
13/08/2018 01:04	19.7	19.9	19.8	19.5	19.6
13/08/2018 04:04	19.6	19.8	19.7	19.4	19.6
13/08/2018 07:04	20	19.9	19.8	19.6	19.7
13/08/2018 10:04	19.7	20.1	20	19.7	19.7
13/08/2018 13:04	21	20.9	20.7	20.8	20.5
13/08/2018 16:04	19.9	20.7	20.5	20.2	20.2
13/08/2018 19:04	19.9	20.2	20.1	19.8	19.8
13/08/2018 22:04	19.6	19.9	19.8	19.4	19.6
14/08/2018 01:04	19.6	19.7	19.6	19.3	19.5
14/08/2018 04:04	20	20	19.8	19.7	19.8
14/08/2018 07:04	20	19.9	19.7	19.6	19.7
14/08/2018 10:04	20.5	20.3	20.1	20.1	20.1
14/08/2018 13:04	20.9	21	20.6	20.8	20.5
14/08/2018 16:04	21.4	20.7	20.4	20.4	20.1
14/08/2018 19:04	20.3	20.8	20.5	20.4	20.2
14/08/2018 22:04	20.1	20.4	20.2	19.9	19.8
15/08/2018 01:04	19.5	19.8	19.7	19.3	19.4
15/08/2018 04:04	19.6	19.6	19.5	19.2	19.4
15/08/2018 07:04	19.6	19.6	19.5	19.2	19.4
15/08/2018 10:04	19.8	19.6	19.5	19.2	19.4
15/08/2018 13:04	21.3	20.4	20	20.4	20.4
15/08/2018 16:04	21.1	20.4	20.1	20.1	19.8
15/08/2018 19:04	19.7	20	19.8	19.4	19.5
15/08/2018 22:04	19.7	19.9	19.7	19.4	19.5
16/08/2018 01:04	19.3	19.6	19.4	19.1	19.2
16/08/2018 04:04	19.3	19.4	19.3	19	19.2
16/08/2018 07:04	20.2	19.5	19.4	19.4	19.4
16/08/2018 10:04	20.2	20.4	20	20.2	20.1
16/08/2018 13:04	19.5	20	19.8	19.4	19.5
16/08/2018 16:04	21.6	20.1	19.9	19.8	19.7
16/08/2018 19:04	19.9	20.2	19.9	19.7	19.7
16/08/2018 22:04	19.3	19.7	19.6	19.2	19.3
17/08/2018 01:04	19.2	19.5	19.3	18.9	19.1
17/08/2018 04:04	19.2	19.3	19.2	18.8	19

Date	T1 [°C]	T2 [°C]	T3 [°C]	T4 [°C]	T5 [°C]
17/08/2018 07:04	20.2	19.5	19.3	19.3	19.5
17/08/2018 10:04	19.7	20	19.7	19.6	19.5
17/08/2018 13:04	19.4	19.8	19.5	19.2	19.3
17/08/2018 16:04	20	20.1	19.8	19.7	19.7
17/08/2018 19:04	19.4	20.1	19.8	19.4	19.4
17/08/2018 22:04	19.8	19.8	19.6	19.4	19.4
18/08/2018 01:04	19.2	19.6	19.4	19.1	19.2
18/08/2018 04:04	19.1	19.4	19.2	18.9	19
18/08/2018 07:04	19.5	19.5	19.3	19.1	19.3
18/08/2018 10:04	19.3	19.9	19.6	19.5	19.6
18/08/2018 13:04	21.1	19.7	19.5	19.5	19.4
18/08/2018 16:04	22.8	20.8	20.2	20.7	20
18/08/2018 19:04	19.7	20.3	20	19.6	19.4
18/08/2018 22:04	19.5	20	19.7	19.4	19.3
19/08/2018 01:04	19.1	19.4	19.2	18.9	19
19/08/2018 04:04	19.4	19.3	19.1	18.9	19
19/08/2018 07:04	20.1	20.1	19.7	19.9	19.8
19/08/2018 10:04	19.3	19.8	19.6	19.2	19.2
19/08/2018 13:04	21	20.6	20.1	20.3	20.2
19/08/2018 16:04	20.8	20.8	20.3	20.2	19.8
19/08/2018 19:04	20.4	20.9	20.4	20.3	20
19/08/2018 22:04	20.3	20.4	20.1	20	19.7
20/08/2018 01:04	19.2	19.7	19.5	19	19.1
20/08/2018 04:04	20.9	20	19.7	20	19.9
20/08/2018 07:04	19.5	20.4	20	19.8	19.7
20/08/2018 10:04	20	20.1	19.8	19.6	19.5

Table A.62: Summary of undisturbed phase (summer 2018) records.

Quantity	Unit	$x(t_0)$	$x(t_1)$	$x(t_1) - x(t_0)$	$\bar{x}(t_0, t_1)$
T1	[°C]	20.6	21.0	0.4	20.2
T2	[°C]	23.9	20.5	-3.4	20.3
T3	[°C]	23.8	20.2	-3.6	20.1
T4	[°C]	20.8	20.2	-0.6	19.9
T5	[°C]	20.7	20.1	-0.6	19.9

Appendix B

In situ testing equipment

B.1 Contents

For the sake of clarity and completeness, in this Appendix the datasheets of circulation pump, vibrating wire strain gauges, heat pump, pressure cells and Fiber Bragg Grating sensors are reported, as provided by the producers.

Table B.1: Datasheet of the circulation pump DAB EVOPLUS B 120/250.4

Q=m ³ /h	0	4.2	5.4	7.2	9.6	12	14.4	18	24	30	36	42	54	72
Q=l/min	0	70	90	120	160	200	240	300	400	500	600	700	900	1200
H [m]	12			11.5	10.1	8.7	7.3	5.2						

" TABELLA A "			
Descrizione prodotto		ESTENSIMETRO A CORDA VIBRANTE	
Modello	0VK4000VS00	Quantità	6
Numero di serie		Lotto Numero	07/17
Paese di Origine	ITALIA-EC	Rintracciabilità per	IST 8/01
CORREDO	Modello	Numero di Serie	Descrizione articolo
	<input checked="" type="checkbox"/> 0VK400JIG00		Dima posizionamento VK4000VS
	<input type="checkbox"/> 0VK400MB200		Coppia blocchetti VK4000VS
Cert.di taratura	<input type="checkbox"/> SI	<input checked="" type="checkbox"/> NO	
Collegamenti	Rosso/Nero = sensore - Bianco/Verde = termistore		
Gauge Factor Reale	3.422		

Figure B.1: Certificate of conformity of the vibrating wire strain gauges

Apparecchiatura		WPG-07-1 HT	WPG-10-1 HT	WPG-15-1 HT
Versione				
Fonte di calore lato primario ¹⁾		Energia geotermale ²⁾		
Dissipatore di calore lato secondario		Acqua ³⁾		
Controller		TERMOTRONIC 3000 WEB		
Installazione - apparecchiatura		Interna		
Installazione - unità di controllo		Incorporata nella pompa di calore		
Compressore		1 x scroll		
Riscaldatore elettrico		3 x 2 kW		
Avvio soft		Sì (optional)		
Pompa di cir. – il primario		/		
Pompa di cir. – il secondario		/		
Capacità				
Riscaldamento		Potenza di riscaldamento / potenza elettrica / COP¹¹⁾		
W10/W30-35	kW / kW / -	7,4 / 1,4 / 5,48	10,3 / 1,9 / 5,42	15,0 / 2,7 / 5,50
W10/W47-55	kW / kW /	6,6 / 2,0 / 3,30	9,2 / 2,7 / 3,41	13,2 / 3,9 / 3,38
B0/W30-35 ⁴⁾	kW / kW / -	5,4 / 1,2 / 4,53	7,8 / 1,7 / 4,58	11,4 / 2,5 / 4,60
B0/W47-55 ⁴⁾	kW / kW / -	4,8 / 1,6 / 3,00	7,1 / 2,4 / 2,95	10,3 / 3,5 / 2,90
Raffrescamento⁵⁾		Potenza di raffrescamento / potenza elettrica / EER¹²⁾		
W20/W12-7	kW / kW / -	5,7 / 1,3 / 4,46	8,1 / 1,8 / 4,52	11,8 / 2,6 / 4,61
B20/W12-7	kW / kW / -	5,7 / 1,3 / 4,46	8,1 / 1,8 / 4,52	11,8 / 2,6 / 4,61
Dati elettrici				
Voltaggio nominale		3N~ 400 V; 50 Hz		
Max. corrente operativo	A	15,4	16,7	19,0
Max. potenza elettrica	kW	8,8	9,8	11,1
Z _{max} ¹⁴⁾	Ω	Senza limiti		0,065
Corrente del rotore bloccato (LRA)	A	26	32	64
Fusibili ¹⁵⁾	A	3 x 16	3 x 16	3 x 20
Cavo d'alimentazione ^{6), 7)}				
Unità interna	mm ²	5 x 2,5	5 x 2,5	5 x 2,5
Sistema di raffreddamento				
WPG H				
Fluido refrigerante – tipo		R407C		
Fluido refrigerante – quant.tà	kg	1,6	2,1	2,3
Max. pressione operativa	MPa	2,9		
WPG HK				
Fluido refrigerante – tipo		R407C		
Fluido refrigerante – quant.tà	kg	2,1	2,2	2,5
Max. pressione operativa	MPa	2,9		
Lato primario¹⁾ (fonte di calore) – acqua				
Min. / Max. pressione nel sistema	MPa	0,05 / 0,3 (0,5 / 3 bar)		
Tubatura		G 1" (fil. interna)	G 1" (fil. interna)	G 5/4" (fil. interna)
Dimensioni raccomandate di tubi verso l'apparecchio ⁸⁾	DN	25	25	32
Temp. d'acqua all'ingresso nell'apparecchiatura 10 °C (p.es. acqua sotterranea) – funzionamento »acqua-acqua«				
Flusso nominale	m ³ / h	1,7	2,3	3,4
Calo di pressione a flusso nominale	kPa	14	18	15
Riscaldamento				
Limiti di funzionamento –temp. dell'acqua min. / max.	°C	7 / 25		
Raffrescamento				
Limiti di funzionamento –temp. dell'acqua min. / max	°C	10 / 40		

Figure B.2: Datasheet of the heat pump – part 1

Apparecchiatura		WPG-07-1 HT	WPG-10-1 HT	WPG-15-1 HT
Temperatura d'entrata della soluzione 30% etilene-glicol nell'apparecchiatura 0 °C (p.es collettore geotermico, geosonda) – funzionamento »terra-acqua«				
Flusso nominale	m ³ / h	1,1	1,6	2,2
Calo di pressione a flusso nominale	kPa	9	13	9
Riscaldamento				
Limiti di funzionamento– temp. medio min. / max.	°C	-7 / 25		
Raffrescamento				
Limiti di funzionamento– temp. medio min. / max.	°C	10 / 40		
Pompa di circolazione primaria raccomandata ⁸⁾	YONOS	Yonos PARA RS 25/7.0	Yonos PARA RS 25/7.5	Yonos PARA RS 25/7.5
Lato secondario¹⁾ (dissipatore di calore) – voda³⁾				
Pressione nel sistema min. / max.	MPa	0,05 / 0,3 (0,5 / 3 bar)		
Tubatura		G 1" (fil. interna)	G 1" (fil. interna)	G 1" (fil. interna)
Dimensioni raccomandate di tubi verso l'apparecchio	DN	25	25	25
Pompa di circolazione primaria raccomandata ⁸⁾	WILO	Yonos PARA RS 25/7.0		Yonos PARA RS 25/7.5
Riscaldamento				
Limiti di funzionamento– temp. d'acqua min. / max.	°C	25 / 65		
Raffrescamento				
Limiti di funzionamento– temp. d'acqua min. / max	°C	7 ⁵⁾ / 25		
Temp. d'acqua all'entrata nella pompa di calore 10 °C (p.es. acqua sotterranea) – funzionamento »acqua-acqua«				
Flusso nominale	m ³ / h	1,2	1,7	2,5
Calo di pressione a flusso nominale	kPa	12	16	14
Temperatura d'entrata della soluzione 30% etilene-glicol nella pompa di calore 0 °C (p.es collettore geotermico, geosonda) – funzionamento »terra-acqua«				
Flusso nominale	m ³ / h	0,9	1,2	1,8
Calo di pressione a flusso nominale	kPa	9	11	10
Dimensioni e massa				
WPG H				
Dimensioni (L x A x P)	mm	700 x 1150 x 480		
Massa – trasporto	kg	108	113	133
Massa – netto	kg	98	103	123
WPG HK				
Dimensioni (L x A x P)	mm	700 x 1150 x 600		
Massa – trasporto	kg	110	122	134
Massa – netto	kg	100	112	124
Rumorosità⁹⁾				
Livello potenza sonora	dB (A)	53	54	55
Livello pressione sonora a distanza di 1 m	dB (A)	45	46	47
Livello pressione sonora a distanza d5 m	dB (A)	31	32	33
Livello pressione sonora a distanza d10 m	dB (A)	25	26	27
Comunicazione				
Collegamento a BMS		Protocollo MODBUS (cavo UTP – terminali RJ45) – RS 485		
Collegamento internet ¹⁰⁾		Cavo UTP 5e – terminale RJ45 - Ethernet		
Varie				
Classe di protezione		IP20		
Unità esterna		IP20		

Figure B.3: Datasheet of the heat pump – part 2

CERTIFICATO DI TARATURA						
Modello: Trasduttore di pressione		PK45HE5000		Numero di Serie: P170275		
Tipologia: Corda vibrante				Numero di Serie: 08-2216-18		
Cliente: POLITECNICO				O.L.: 17-00117		
Lunghezza cavo: 1 m				Data: 20/02/2017		
Condizioni di prova :				Alimentazione [Vcc] : 0		
				Temperatura [°C] : 21		
				Umidità [%] : 34		
				Pressione atmosferica [mbar] : 0		
La taratura è stata realizzata in accordo al Sistema di Qualità UNI EN ISO 9001:2008 IST. 10/01						
Catena metrologica						
Primari: Digital Pressure Indicator Druck mod. DPI 515 s/n 51500575, Calibratore Yokogawa mod. 7651 s/n 51WK0176,						
Generatore di funzioni Hameg mod. HM8030-5 s/n 54710037, Calibratore HBM mod. K307 s/n 34200.						
Secondari: Unità di lettura Sigeeo s/n 087						
Incertezze di misura: ± 0,00137 MPa / 6E-04 Hz						
pressione	letture [digit]			statistiche		
MPa	l up	l down		med [digit]	lin. [MPa]	polin. [MPa]
0,00	8436	8437		8436	0,01	0,00
1,00	7829	7832		7831	1,00	1,00
2,00	7220	7223		7222	1,99	2,00
3,00	6607	6611		6609	2,99	3,00
4,00	5991	5995		5993	4,00	4,00
5,00	5374	5376		5375	5,01	5,00

MPa

◆ dati
— regr.lin.
— regr.polin.

RISULTATI			
Fattore di sensibilità lineare		S	err.max.
		[digit/MPa]	%F.S.
		-612,34798	0,23954
Fattori di sensibilità polinomiale		A	B
$[MPa] = A \cdot [digit]^2 + B \cdot [digit] + C$		[MPa/digit ²]	[MPa/digit]
		-6,820E-09	-1,539E-03
		1,347E+01	err.max.
		[MPa]	%F.S.
		0,07349	
NOTE : L'errore riportato tiene conto degli effetti di linearità ed isteresi.			
Con il software "Multilogger" il fattore lineare S è da inserire invertito (1/S)			
digit = Hz2x10-3			
coefficiente di temperatura K = -0,000496 MPa/°C			
Colleg.: rosso=bobina; nero=bobina; bianco=termistore; verde=termistore			
Responsabile qualità :		Responsabile :	
<i>Roberta Puppo</i>		<i>Marcus...</i>	

Figure B.4: Certificate of conformity of the pressure cell P170275 corresponding to Pr6

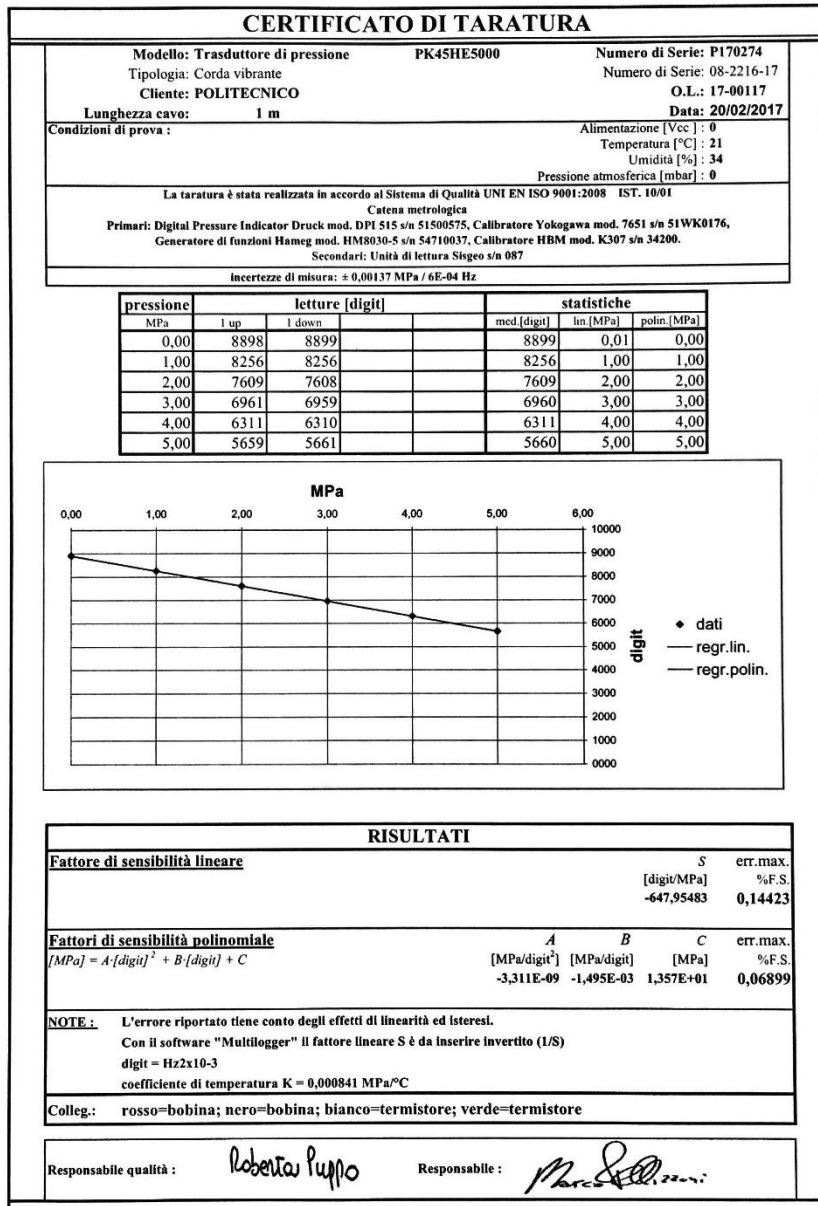


Figure B.5: Certificate of conformity of the pressure cell P170274 corresponding to PI2

CERTIFICATO DI TARATURA						
Modello: Trasduttore di pressione		PK45HE5000		Numero di Serie: P170273		
Tipologia: Corda vibrante				Numero di Serie: 08-2216-16		
Cliente: POLITECNICO				O.L.: 17-00117		
Lunghezza cavo: 1 m				Data: 20/02/2017		
Condizioni di prova :				Alimentazione [Vcc] : 0		
				Temperatura [°C] : 21		
				Umidità [%] : 34		
				Pressione atmosferica [mbar] : 0		
La taratura è stata realizzata in accordo al Sistema di Qualità UNI EN ISO 9001:2008 IST. 10/01 Catena metrologica Primari: Digital Pressure Indicator Druck mod. DPI 515 s/n 51500575, Calibratore Yokogawa mod. 7651 s/n 51WK0176, Generatore di funzioni Hameg mod. HM8030-S s/n 54710037, Calibratore HBM mod. K307 s/n 34200. Secondari: Unità di lettura Siggeo s/n 087						
Incertezze di misura: ± 0,00137 MPa / 6E-04 Hz						
pressione MPa	letture [digit]		statistiche			
	1 up	1 down	med.[digit]	lin [MPa]	polin. [MPa]	
0,00	9106	9106		9106	0,00	0,00
1,00	8450	8450		8450	1,00	1,00
2,00	7794	7793		7793	2,00	2,00
3,00	7136	7136		7136	3,00	3,00
4,00	6477	6478		6478	4,00	4,00
5,00	5819	5821		5820	5,00	5,00

RISULTATI				
Fattore di sensibilità lineare		S	err.max.	
		[digit/MPa]	%F.S.	
		-657,36195	0,05707	
Fattori di sensibilità polinomiale		A	B	C
		[MPa/digit ²]	[MPa/digit]	[MPa]
		-8,911E-10	-1,508E-03	1,381E+01
		err.max. %F.S. 0,03563		
NOTE: L'errore riportato tiene conto degli effetti di linearità ed isteresi.				
Con il software "Multilogger" il fattore lineare S è da inserire invertito (1/S)				
digit = Hzx10-3				
coefficiente di temperatura K = 0,000127 MPa/°C				
Colleg.: rosso=bobina; nero=bobina; bianco=termistore; verde=termistore				
Responsabile qualità :		Responsabile :		

Figure B.6: Certificate of conformity of the pressure cell P170273 corresponding to Pt5

CERTIFICATO DI TARATURA						
Modello: Trasduttore di pressione		PK45HE5000		Numero di Serie: P170272		
Tipologia: Corda vibrante				Numero di Serie: 08-2216-15		
Cliente: POLITECNICO				O.L.: 17-00117		
Lunghezza cavo: 1 m				Data: 20/02/2017		
Condizioni di prova:				Alimentazione [Vcc]: 0		
				Temperatura [°C]: 21		
				Umidità [%]: 34		
				Pressione atmosferica [mbar]: 0		
La taratura è stata realizzata in accordo al Sistema di Qualità UNI EN ISO 9001:2008 IST. 10/01						
Catena metrologica						
Primari: Digital Pressure Indicator Druck mod. DPI 515 s/n 51500575, Calibratore Yokogawa mod. 7651 s/n 51WK0176,						
Generatore di funzioni Hameg mod. HM8030-S s/n 54710037, Calibratore HBM mod. K307 s/n 34200.						
Secondari: Unità di lettura Sigseo s/n 087						
Incertezze di misura: ± 0,00137 MPa / 6E-04 Hz						
pressione MPa	letture [digit]		statistiche			
	1 up	1 down	med.[digit]	lin.[MPa]	polin.[MPa]	
0,00	9259	9260	9260	0,01	0,00	
1,00	8615	8616	8616	1,00	1,00	
2,00	7967	7968	7968	1,99	2,00	
3,00	7315	7315	7315	2,99	3,00	
4,00	6658	6660	6659	4,00	4,00	
5,00	5998	5999	5998	5,01	5,00	

RISULTATI				
Fattore di sensibilità lineare		S	err.max.	
		[digit/MPa]	%F.S.	
		-652,25769	0,23621	
Fattori di sensibilità polinomiale		A	B	C
		[MPa/digit ²]	[MPa/digit]	[MPa]
		-7,422E-09	-1,420E-03	1,378E+01
				err.max.
				%F.S.
				0,02899
NOTE: L'errore riportato tiene conto degli effetti di linearità ed isteresi.				
Con il software "Multilogger" il fattore lineare S è da inserire invertito (1/S)				
digit = Hzx10-3				
coefficiente di temperatura K = 0,000108 MPa/°C				
Colleg.: rosso=bobina; nero=bobina; bianco=termistore; verde=termistore				
Responsabile qualità :		Responsabile :		
Roberto Puppo		[Signature]		

Figure B.7: Certificate of conformity of the pressure cell P170272 corresponding to Pt1

CERTIFICATO DI TARATURA							
Modello: Trasduttore di pressione		PK45HE5000		Numero di Serie: P170271			
Tipologia: Corda vibrante				Numero di Serie: 08-2216-14			
Cliente: POLITECNICO				O.L.: 17-00117			
Lunghezza cavo: 1 m				Data: 20/02/2017			
Condizioni di prova :				Alimentazione [Vcc] : 0			
				Temperatura [°C] : 21			
				Umidità [%] : 34			
				Pressione atmosferica [mbar] : 0			
La taratura è stata realizzata in accordo al Sistema di Qualità UNI EN ISO 9001:2008 IST. 10/01							
Catena metrologica							
Primari: Digital Pressure Indicator Druck mod. DPI 515 s/n 51500575, Calibratore Yokogawa mod. 7651 s/n 51WK0176, Generatore di funzioni Hameg mod. HM8030-5 s/n 54710037, Calibratore HBM mod. K307 s/n 34200.							
Secondari: Unità di lettura Siggeo s/n 087							
Incertezze di misura: ± 0,00137 MPa / 6E-04 Hz							
pressione	letture [digit]				statistiche		
	MPa	1 up	1 down		med.[digit]	lin [MPa]	polin [MPa]
0,00	8639	8639			8639	0,00	0,00
1,00	8005	8003			8004	1,00	1,00
2,00	7369	7364			7367	2,00	2,00
3,00	6730	6724			6727	3,00	3,00
4,00	6090	6084			6087	4,00	4,00
5,00	5449	5450			5449	5,00	5,00

RISULTATI				
Fattore di sensibilità lineare		<i>S</i>	err.max.	
		[digit/MPa]	%F.S.	
		-638,32550	0,16436	
Fattori di sensibilità polinomiale		<i>A</i>	<i>B</i>	<i>C</i>
$[MPa] = A \cdot [digit]^2 + B \cdot [digit] + C$		[MPa/digit ²]	[MPa/digit]	[MPa]
		-1,570E-09	-1,544E-03	1,346E+01
		err.max. %F.S. 0,14648		
NOTE : L'errore riportato tiene conto degli effetti di linearità ed isteresi.				
Con il software "Multilogger" il fattore lineare <i>S</i> è da inserire invertito (1/ <i>S</i>)				
digit = Hz2x10-3				
coefficiente di temperatura K = 0,000488 MPa/°C				
Colleg.: rosso=bobina; nero=bobina; bianco=termistore; verde=termistore				
Responsabile qualità :		Responsabile :		
<i>Roberta Puppo</i>		<i>Mario...</i>		

Figure B.8: Certificate of conformity of the pressure cell P170271 corresponding to Pt3

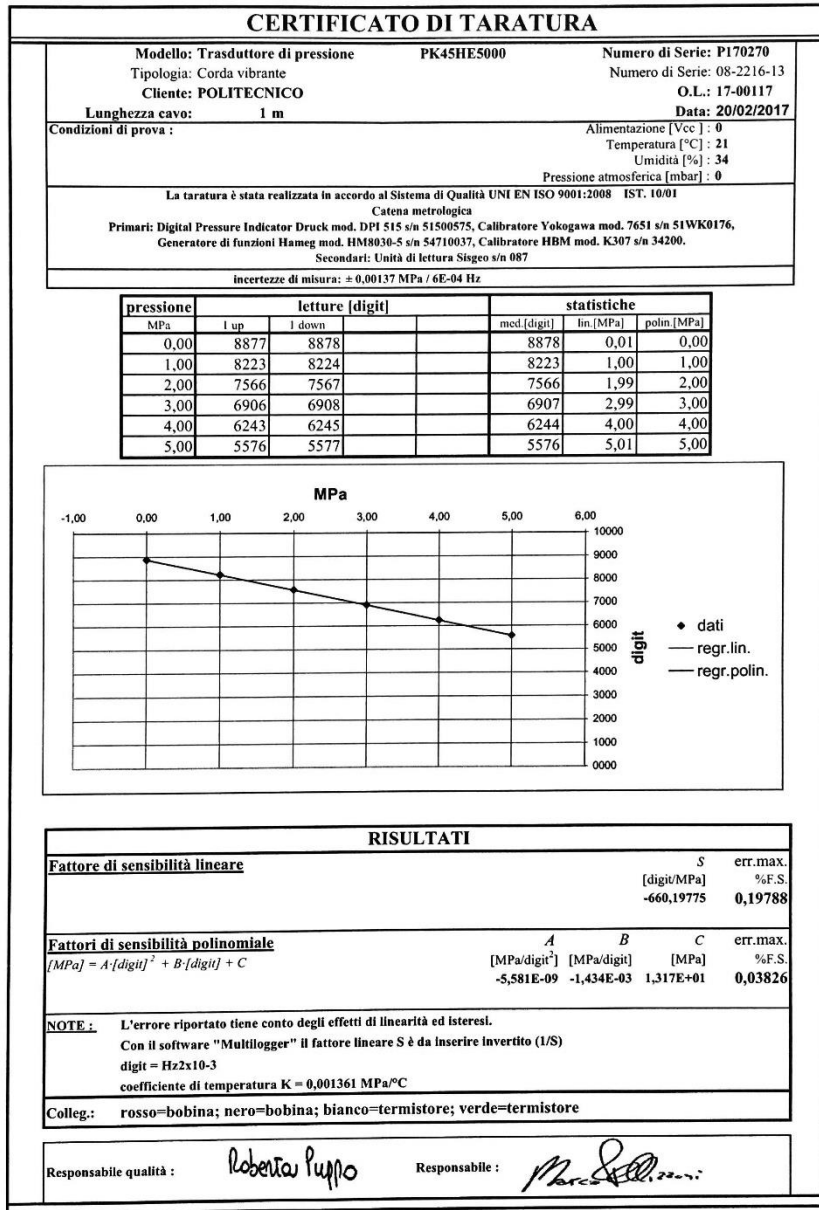


Figure B.9: Certificate of conformity of the pressure cell P170270 corresponding to Pr4

Production Name: FBG Strain Sensor

P/T: MS-01

S/N: 170315-1

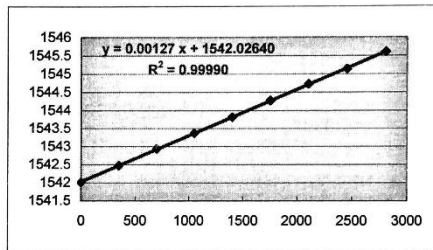
Date: 2017.03.15

The temperature Characteristic

No.	FBG1(1539)	FBG2(1543)
Thermal Coeff.(pm/°C)	8.7	26.2

FBG Strain Calibration:

Strain (µε)	CW(nm)
0	1542.009
350.877	1542.475
701.754	1542.937
1052.632	1543.37
1403.509	1543.814
1754.386	1544.27
2105.263	1544.723
2456.140	1545.137
2807.018	1545.603



Other Information

Cable Type: Dia. 6mm Armored cable

Connector: FC/APC

Connector1 IL (dB) : 0.11

Sensor Bony Material: SS316

Connector1 IL (dB) : 0.12

Figure B.10: Calibration datasheet of FGB number 170315-1 corresponding to FBG3e

Production Name: FBG Strain Sensor

P/T: MS-01

S/N: 170315-2

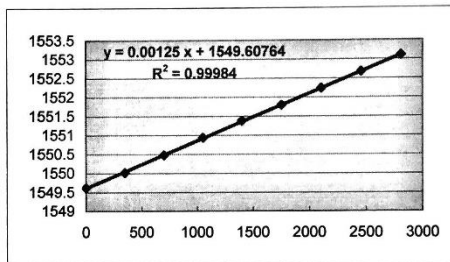
Date: 2017.03.15

The temperature Characteristic

No.	FBG1(1547)	FBG2(1551)
Thermal Coeff.(pm/°C)	9.2	26.7

FBG Strain Calibration:

Strain (µε)	CW(nm)
0	1549.622
350.877	1550.017
701.754	1550.475
1052.632	1550.94
1403.509	1551.377
1754.386	1551.794
2105.263	1552.241
2456.140	1552.674
2807.018	1553.107



Other Information

Cable Type: Dia. 6mm Armored cable

Connector: FC/APC

Connector1 IL (dB) : 0.1

Sensor Bony Material: SS316

Connector1 IL (dB) : 0.13

Figure B.11: Calibration datasheet of FGB number 170315-2 corresponding to FBG1i

Production Name: FBG Strain Sensor

P/T: MS-01

S/N: 170315-3

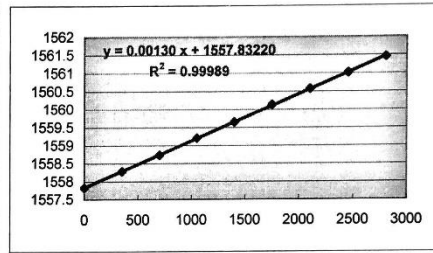
Date: 2017.03.15

The temperature Characteristic

No.	FBG1(1555)	FBG2(1559)
Thermal Coeff.(pm/°C)	9	27.3

FBG Strain Calibration:

Strain (µε)	CW(nm)
0	1557.828
350.877	1558.278
701.754	1558.737
1052.632	1559.207
1403.509	1559.65
1754.386	1560.133
2105.263	1560.571
2456.140	1561.014
2807.018	1561.453



Other Information

Cable Type: Dia. 6mm Armored cable

Connector: FC/APC

Connector1 IL (dB) : 0.1

Sensor Bosity Material: SS316

Connector1 IL (dB) : 0.14

Figure B.12: Calibration datasheet of FGB number 170315-3 corresponding to FBG5e

Production Name: FBG Strain Sensor

P/T: MS-01

S/N: 170315-4

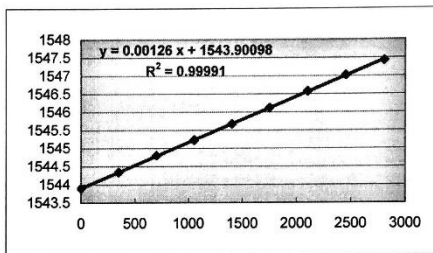
Date: 2017.03.15

The temperature Characteristic

No.	FBG1(1541)	FBG2(1545)
Thermal Coeff.(pm/°C)	9.1	25.5

FBG Strain Calibration:

Strain (µε)	CW(nm)
0	1543.895
350.877	1544.339
701.754	1544.799
1052.632	1545.226
1403.509	1545.67
1754.386	1546.116
2105.263	1546.571
2456.140	1547.016
2807.018	1547.423



Other Information

Cable Type: Dia. 6mm Armored cable

Connector: FC/APC

Connector1 IL (dB) : 0.14

Sensor Bosity Material: SS316

Connector1 IL (dB) : 0.13

Figure B.13: Calibration datasheet of FGB number 170315-4 corresponding to FBG3i

Production Name: FBG Strain Sensor

P/T: MS-01

S/N: 170315-5

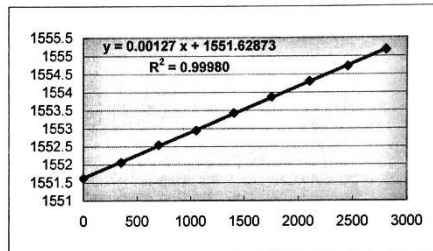
Date: 2017.03.15

The temperature Characteristic

No.	FBG1(1549)	FBG2(1553)
Thermal Coeff.(pm/°C)	9	25.7

FBG Strain Calibration:

Strain (µε)	CW(nm)
0	1551.62
350.877	1552.056
701.754	1552.536
1052.632	1552.948
1403.509	1553.426
1754.386	1553.873
2105.263	1554.303
2456.140	1554.72
2807.018	1555.172



Other Information

Cable Type: Dia. 6mm Armored cable

Connector: FC/APC

Connector1 IL (dB) : 0.12

Sensor Bosity Material: SS316

Connector1 IL (dB) : 0.1

Figure B.14: Calibration datasheet of FBG number 170315-5 corresponding to FBG1e

Production Name: FBG Strain Sensor

P/T: MS-01

S/N: 170315-6

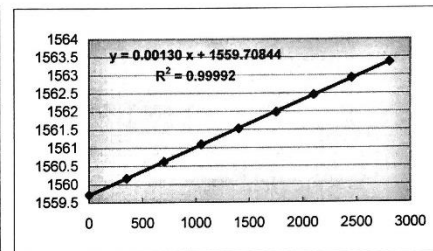
Date: 2017.03.15

The temperature Characteristic

No.	FBG1(1557)	FBG2(1561)
Thermal Coeff.(pm/°C)	9	25.6

FBG Strain Calibration:

Strain (µε)	CW(nm)
0	1559.708
350.877	1560.166
701.754	1560.62
1052.632	1561.096
1403.509	1561.527
1754.386	1561.973
2105.263	1562.457
2456.140	1562.918
2807.018	1563.36



Other Information

Cable Type: Dia. 6mm Armored cable

Connector: FC/APC

Connector1 IL (dB) : 0.13

Sensor Bosity Material: SS316

Connector1 IL (dB) : 0.11

Figure B.15: Calibration datasheet of FBG number 170315-6 corresponding to FBG5i